Peter S. Conti
Aarti Kaushik *Editors*

PET-CT

A Case-Based Approach

Second Edition

Springer

PET-CT

Peter S. Conti, MD, PhD, FACNP, FACR
Aarti Kaushik, MD

Editors

PET-CT

A Case-Based Approach

Second Edition

Springer

Editors
Peter S. Conti, MD, PhD, FACNP, FACR
Professor of Radiology
Biomedical Engineering and Pharmaceutical Sciences
Director, Molecular Imaging Center and PET Clinic
Keck School of Medicine
University of Southern California
Los Angeles, CA, USA

Aarti Kaushik, MD
Kaiser Permanente
Southern California Permanente Medical Group
Riverside, CA, USA

Molecular Imaging Center and PET Clinic
University of Southern California
Los Angeles, CA, USA

ISBN 978-1-4419-5810-5 ISBN 978-1-4419-5811-2 (eBook)
DOI 10.1007/978-1-4419-5811-2

Library of Congress Control Number: 2015957390

Springer New York Heidelberg Dordrecht London

Printed on acid-free paper

Springer Science+Business Media LLC New York is part of Springer Science+Business Media (www.springer.com)

To my wife and children, for their many years of love, understanding and support.

—P.S.C.

To my husband and children for believing in me and to all my teachers without whom I would not be here today.

—A.K.

To our friends and colleagues, whose understanding and support have been invaluable in the preparation of this book.

—P.S.C., A.K.

Preface

PET-CT: A Case-Based Approach, Second Edition, provides practical clinical examples of studies performed with FDG on a state-of-the-art dedicated PET-CT device. Detailed histories and correlative imaging findings are given in each case to demonstrate the level of detail required for image interpretation and the capabilities of this instrumentation. Impressions are followed by relevant discussion points designed to provide novice as well as experienced readers a brief but concise summary of the advantages and limitations of using this technology in the clinical setting. Images are presented in PET only, CT only, and fused format to highlight the advantages of this hybrid technology in displaying the spectrum of normal and pathological findings in the cases selected.

Chapter 1 explores the fundamentals of PET-CT imaging with FDG, including normal physiology, normal variants, and technical artifacts. Chapters 2–10 discuss a spectrum of clinical applications in oncology, such as common malignancies involving the lung, breast, and colon and less common cancers, such as adrenal and germ cell tumors. Chapter 11 details the use of F-18 NaF in diagnosing prostate, breast, and lung cancers and presents cases in which this method is deployed with nonmalignant findings. Chapters 12 and 13 examine brain tumors and general neurological applications such as epilepsy. Pediatric imaging cases with both benign and malignant findings are discussed in Chapter 14. Cardiac and granulomatous disease applications are described in Chapters 15 and 16. Finally, Chapter 17 highlights images of newer PET-CT tracers.

This book is ideal for nuclear medicine practitioners, radiologists, residents/fellows, and referring clinicians interested in learning more about how this medical imaging technology can be applied in their patient populations.

Los Angeles, CA — Peter S. Conti, MD, PhD, FACNP, FACR
Riverside, CA — Aarti Kaushik, MD

Acknowledgments

We wish to acknowledge the dedicated work of the faculty of the USC Department of Radiology for their assistance in case selection and discussions in the preparation of this book. We would like to thank the USC PET technologists for their assistance in acquiring and processing the images shown in this book. Finally, we wish to thank all the USC PET fellows who over the years have contributed to the teaching file established at the USC PET Center and have provided a source of inspiration for the entire faculty.

Contents

Contributors

Shahram Bonyadlou, MD Department of Radiology, Keck School of Medicine, University of Southern California, Los Angeles, CA, USA

Peter S. Conti, MD, PhD, FACNP, FACR Keck School of Medicine, University of Southern California, Los Angeles, CA, USA

Bhushan Desai, MBBS, MS Department of Radiology, Keck School of Medicine, University of Southern California, Los Angeles, CA, USA

Abtin Doroudinia, MD Keck School of Medicine, University of Southern California, Los Angeles, CA, USA

Shereif H. Gamie, MD Long Beach Memorial Medical Center, Long Beach, CA, USA

John Go, MD Department of Radiology, Keck School of Medicine, University of Southern California, Los Angeles, CA, USA

Saman Hazany, MD Rancho Research Institute, Downey, CA, USA

Robert W. Henderson, MD Department of Radiology, Keck School of Medicine, University of Southern California, Los Angeles, CA, USA

Linh T. Ho, MD Department of Radiology, Keck School of Medicine, University of Southern California, Los Angeles, CA, USA

Nova M. Isaac, MD Department of Radiology, Keck School of Medicine, University of Southern California, Los Angeles, CA, USA

Hossein Jadvar, MD, PhD, MPH, MBA Department of Radiology, Keck School of Medicine, University of Southern California, Los Angeles, CA, USA

Aarti Kaushik, MD Kaiser Permanente, Southern California Permanente Medical Group, Riverside, CA, USA

Molecular Imaging Center and PET Clinic, University of Southern California, Los Angeles, CA, USA

Paul Kim, MD Department of Radiology, Keck School of Medicine, University of Southern California, Los Angeles, CA, USA

Hollie A. Lai, MD Department of Radiology and Nuclear Medicine, Children's Hospital Los Angeles, Los Angeles, CA, USA

Meng Law, MBBS, FRACR Keck School of Medicine, University of Southern California, Los Angeles, CA, USA

Sindu Sheth, MD Keck School of Medicine, University of Southern California, Los Angeles, CA, USA

Heidi Wassef, MD Department of Radiology, Keck School of Medicine, University of Southern California, Los Angeles, CA, USA

Ella Yevdayev, MD Keck School of Medicine, University of Southern California, Los Angeles, CA, USA

1 Normal Patterns and Artifacts

Aarti Kaushik and Peter S. Conti

Bone Marrow Hyperplasia

Granulocyte colony-stimulating factor is a glycoprotein hormone that regulates proliferation and differentiation of granulocyte precursors. It is used to accelerate recovery from chemotherapy-related neutropenia in cancer patients. Intense increased FDG uptake is commonly observed in the bone marrow and/or spleen following GCSF therapy; however, the bone marrow response to GCSF can be differentiated from pathological infiltration by its intense homogeneous nature without focally increased areas of FDG uptake. Increased FDG uptake attributable to GCSF uptake rapidly decreases following completion of therapy and generally resolves within a month (Fig. 1.1).

P.S. Conti, A. Kaushik (eds.), *PET-CT*, DOI 10.1007/978-1-4419-5811-2_1

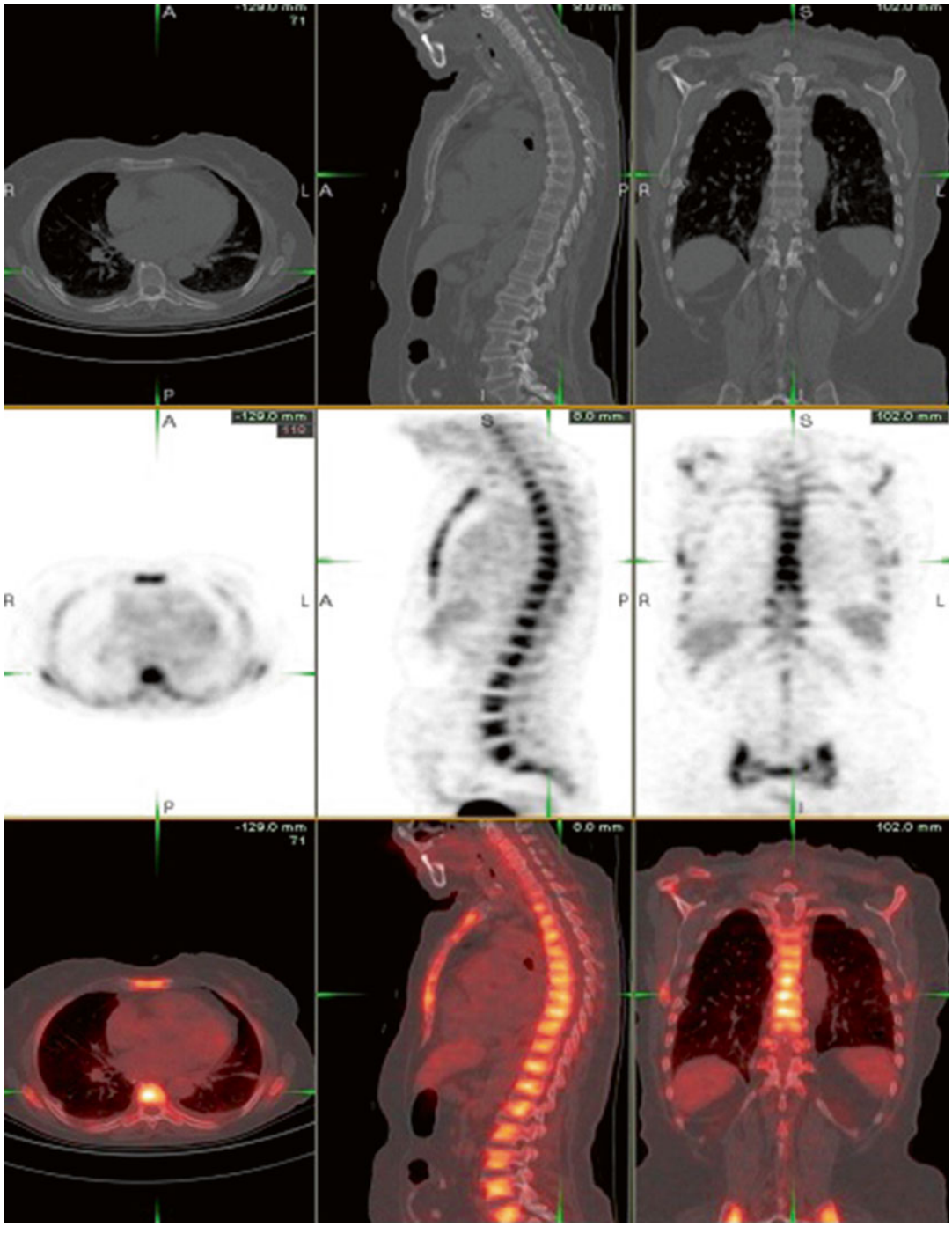

Fig. 1.1

Metal Implants

The presence of metal implants in the body produces streak artifact on CT imaging and degrades image quality. When CT images are used for attenuation correction, the presence of metal results in over-attenuation of PET activity in this region and can result in artifactual "hot spots." Metal prostheses, dental fillings, indwelling ports, breast expanders, and sometimes contrast media are common causes of streak artifact secondary to high photon absorption and can cause attenuation correction artifacts. In order to avoid false positives, particularly when imaging metallic implants, careful attenuation should be paid to the non-attenuation-corrected images, which do not produce this artifact (Fig. 1.2).

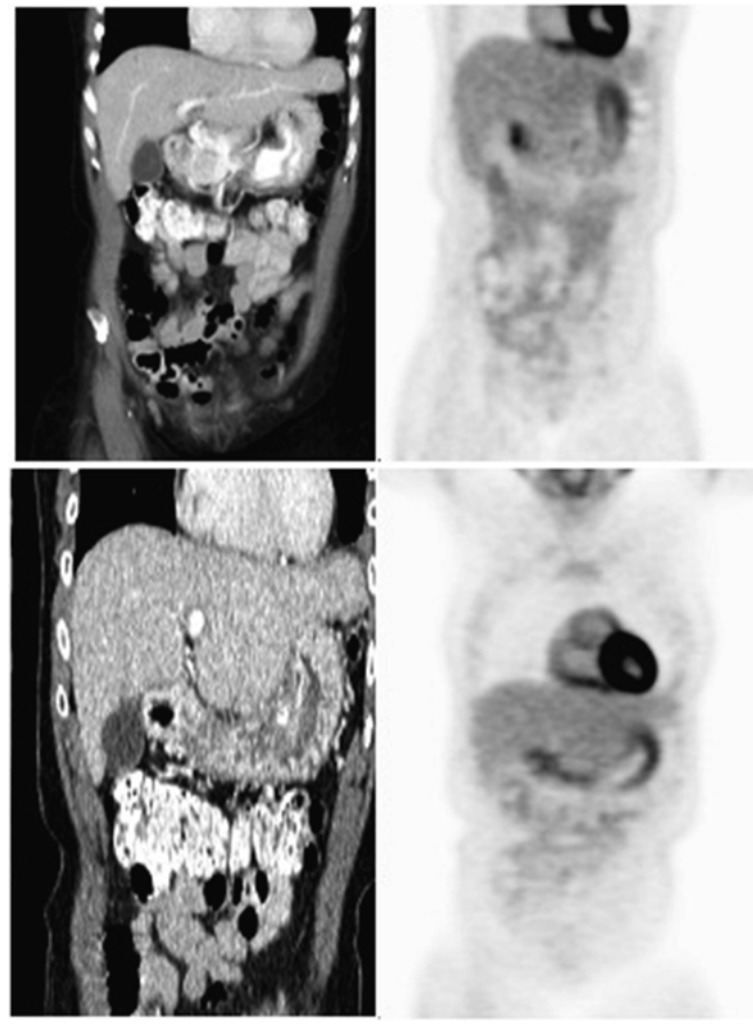

Fig. 1.2

Pacemaker Artifact

See Fig. 1.3.

Epidural Stimulator Artifact

See Fig. 1.4.

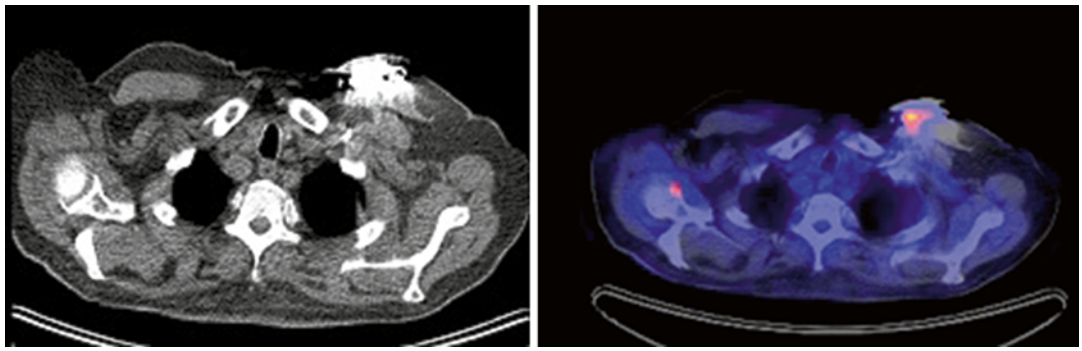

Fig. 1.3

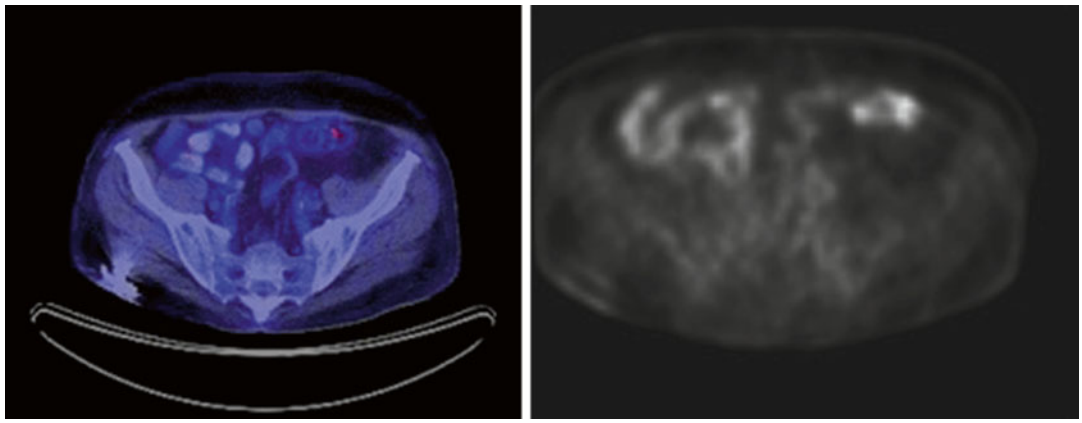

Fig. 1.4

Vascular Uptake [Aorta] and Bilateral Hip Joint with Peripheral Uptake: Inflammatory Degenerative Changes

See Fig. 1.5.

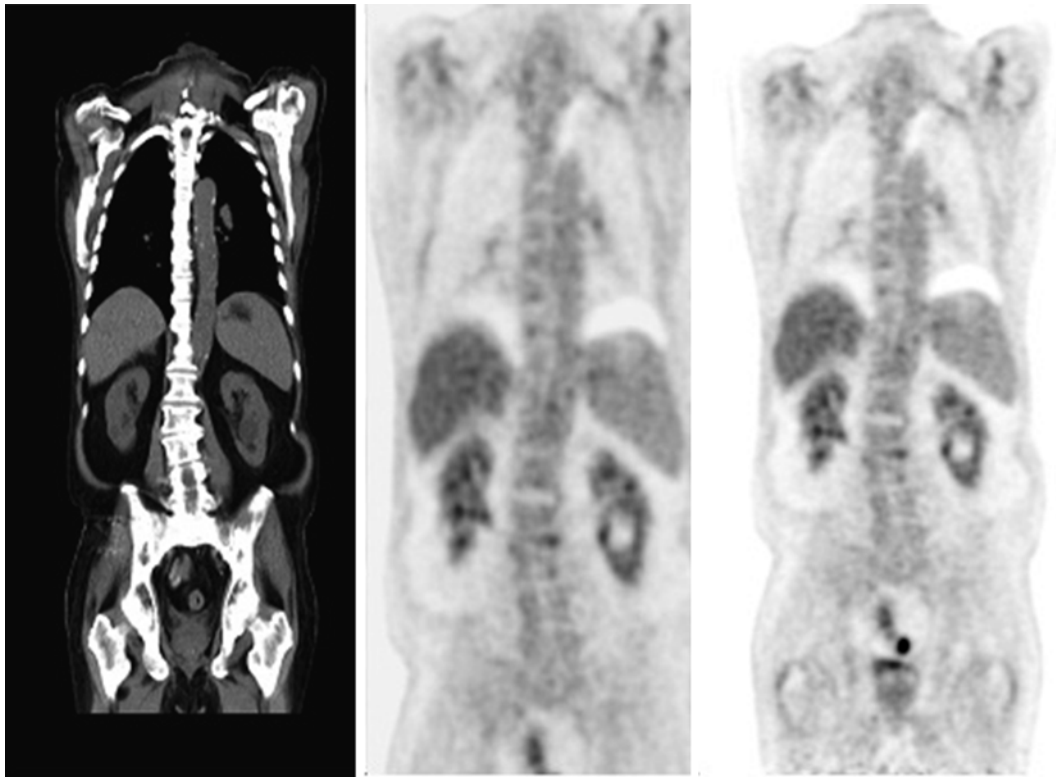

Fig. 1.5

Post-RFA Assessment Lesions

See Fig. 1.6.

Post-RFA of Hepatic Lesion Photopenia (Absent Uptake) on PET Images on the Left Correlating with Low Attenuation Region on CT

Post-RFA (radio-frequency ablation) assessment of lesion PET is useful as it distinguishes treated lesion by whether it is actively metabolizing glucose or dead in the area of destruction (photopenia) (Fig. 1.7).

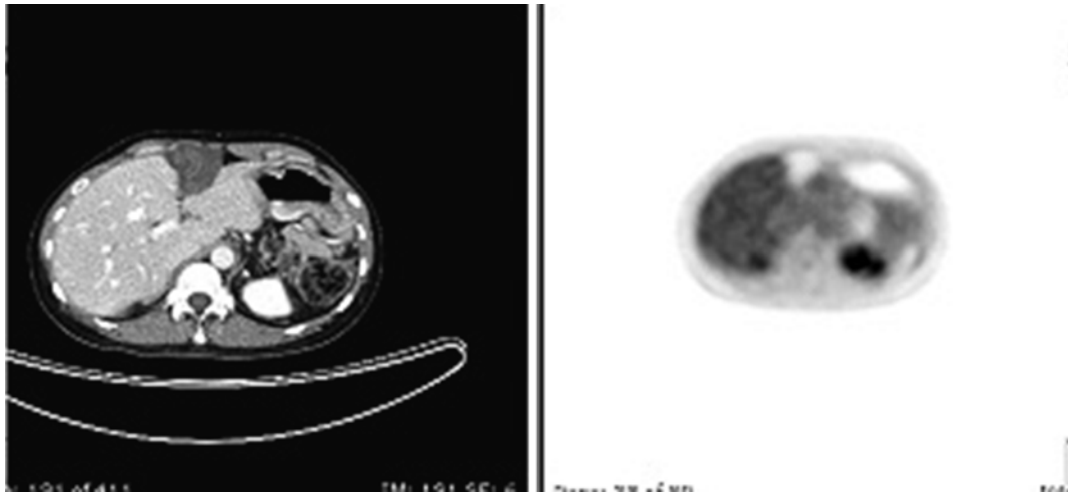

Fig. 1.6

Fig. 1.7

Subclinical Aspiration

Inflammatory changes in the lungs can be noted in asymptomatic patients related to subclinical aspiration (Fig. 1.8).

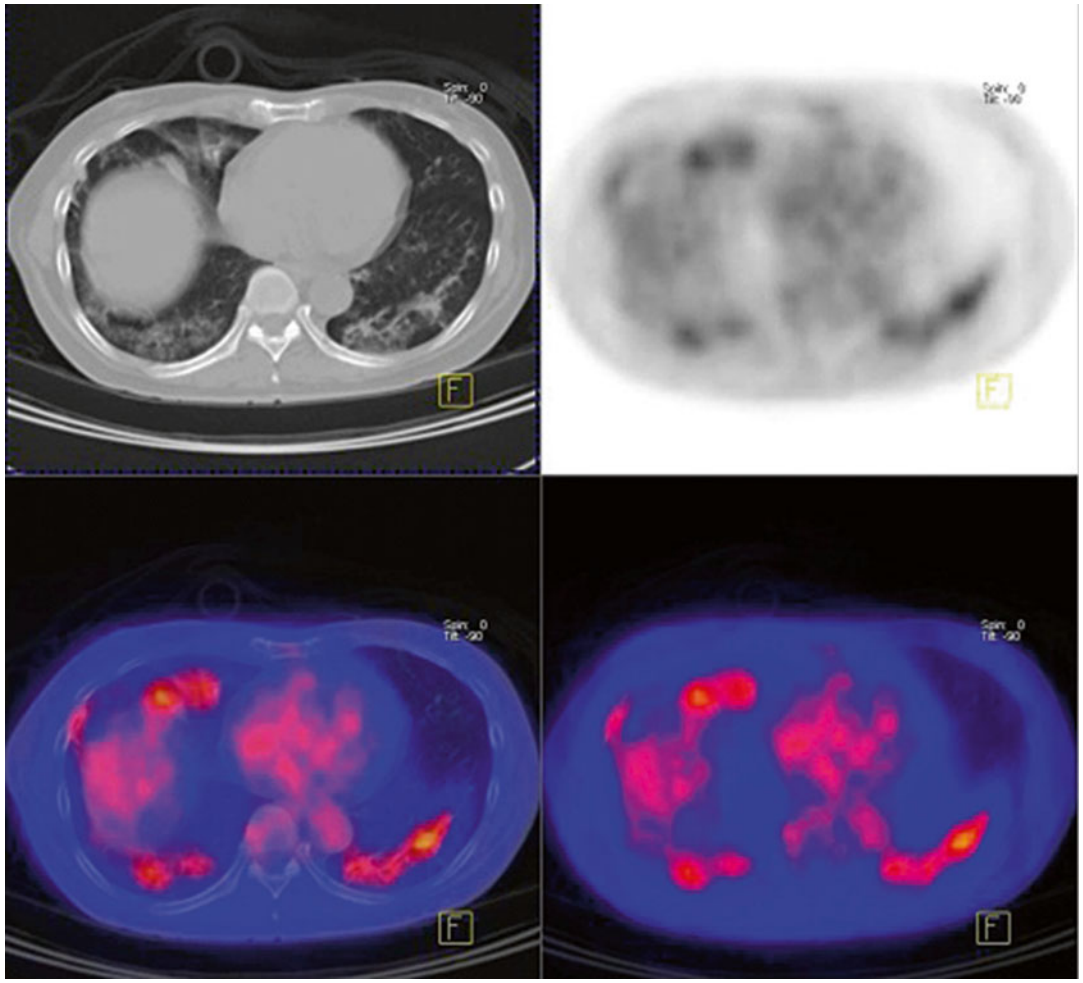

Fig. 1.8

Postradiation Changes in the Mid Spine with Low Bone Mineral Density on CT and Photopenia (Absent Uptake) on PET

See Fig. 1.9.

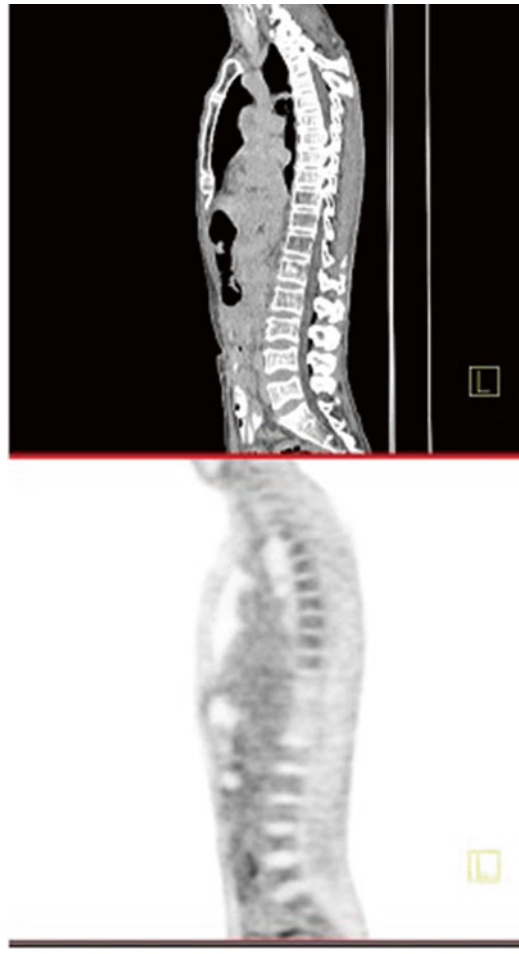

Fig. 1.9

Thymic Hyperplasia Post Chemotherapy

Thymic hyperplasia post chemotherapy is a well-described phenomenon. It is generally seen in children and young adults post chemotherapy. The presence of increased FDG uptake in the anterior mediastinum can be attributed to thymic hyperplasia by identification of a triangular soft tissue density seen retrosternally on CT with a characteristic bilobed anatomical appearance. In the presence of thymic hyperplasia, there is generally preservation of the normal shape of the gland despite an increase in size (Figs. 1.10 and 1.11).

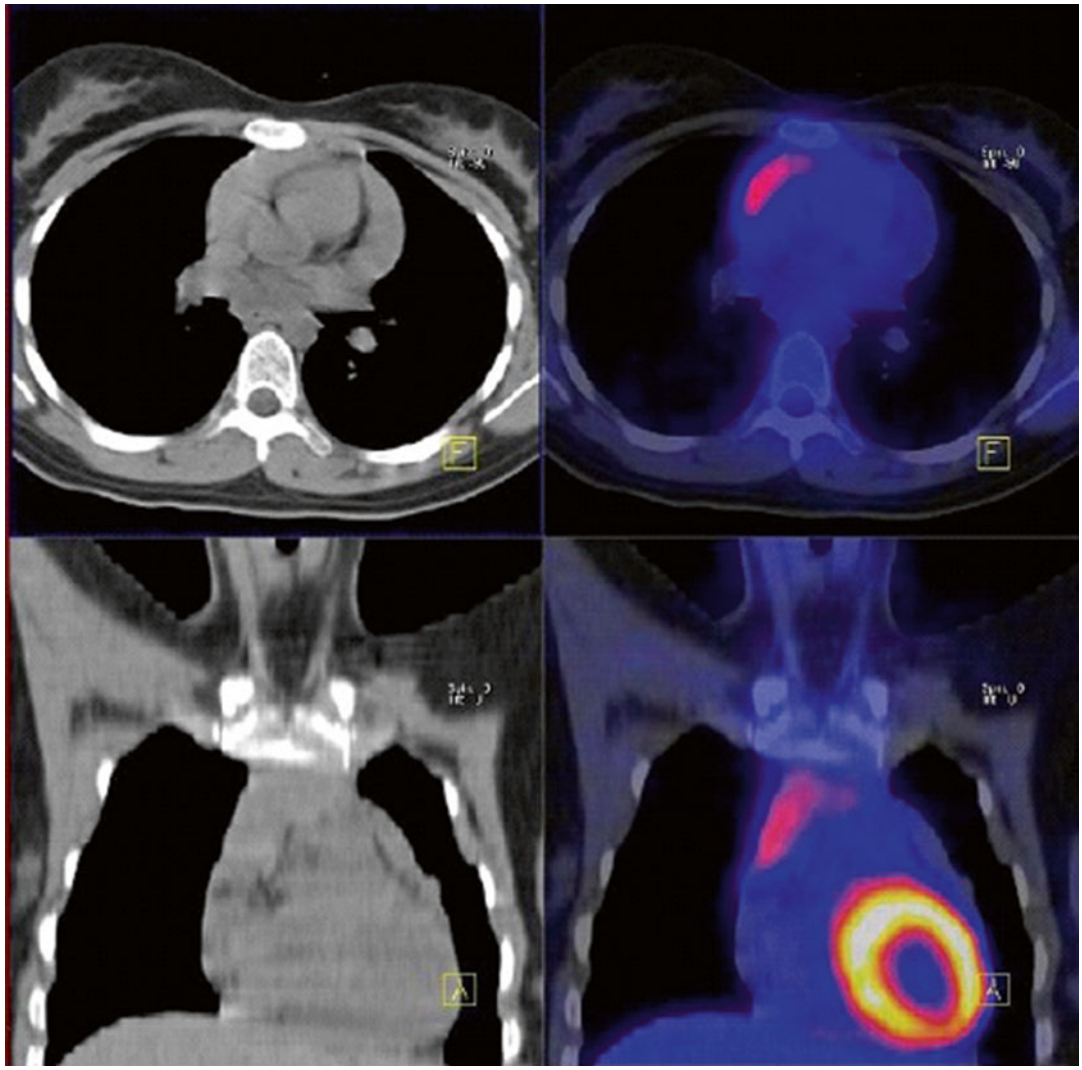

Fig. 1.10

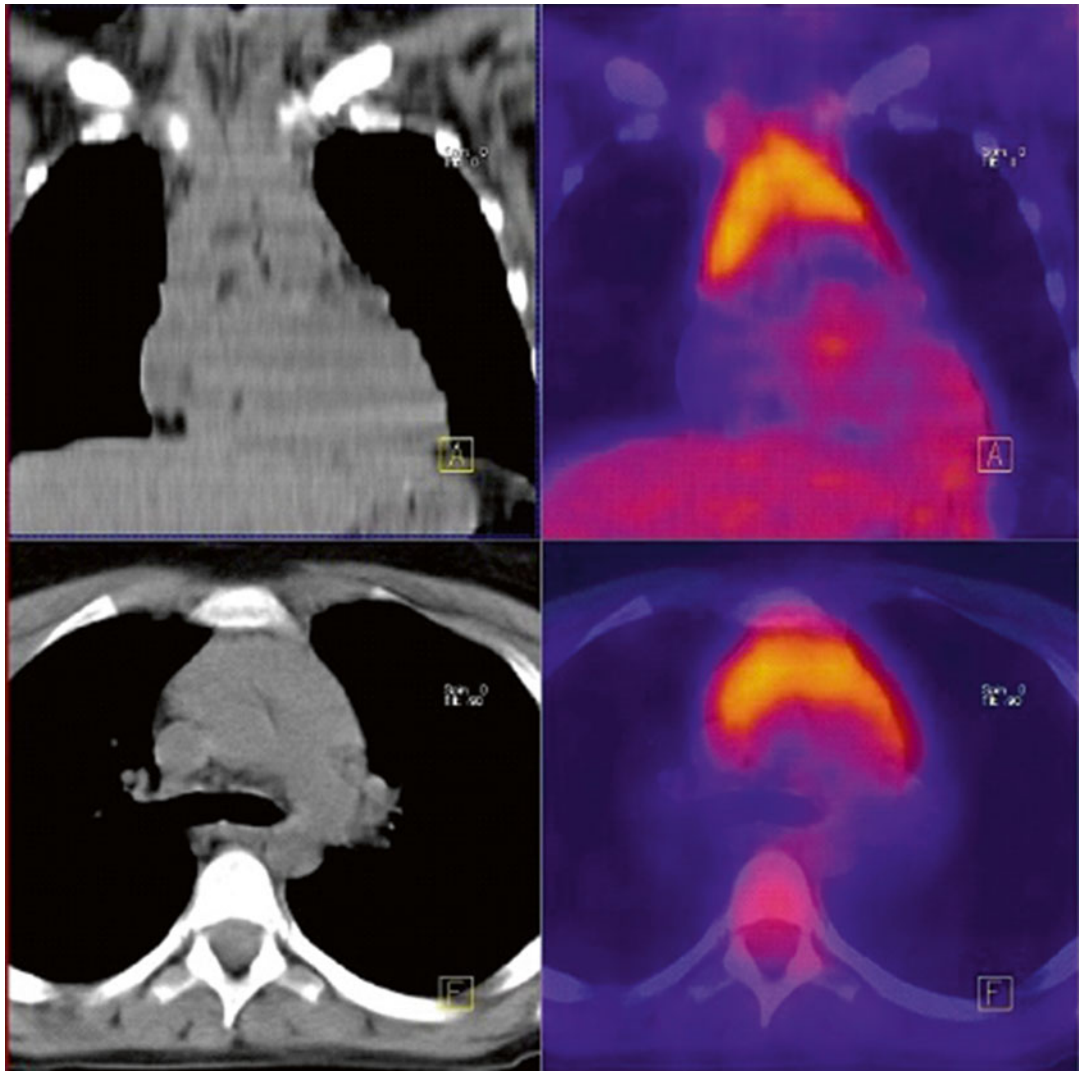

Fig. 1.11

Dextrocardia

See Fig. 1.12.

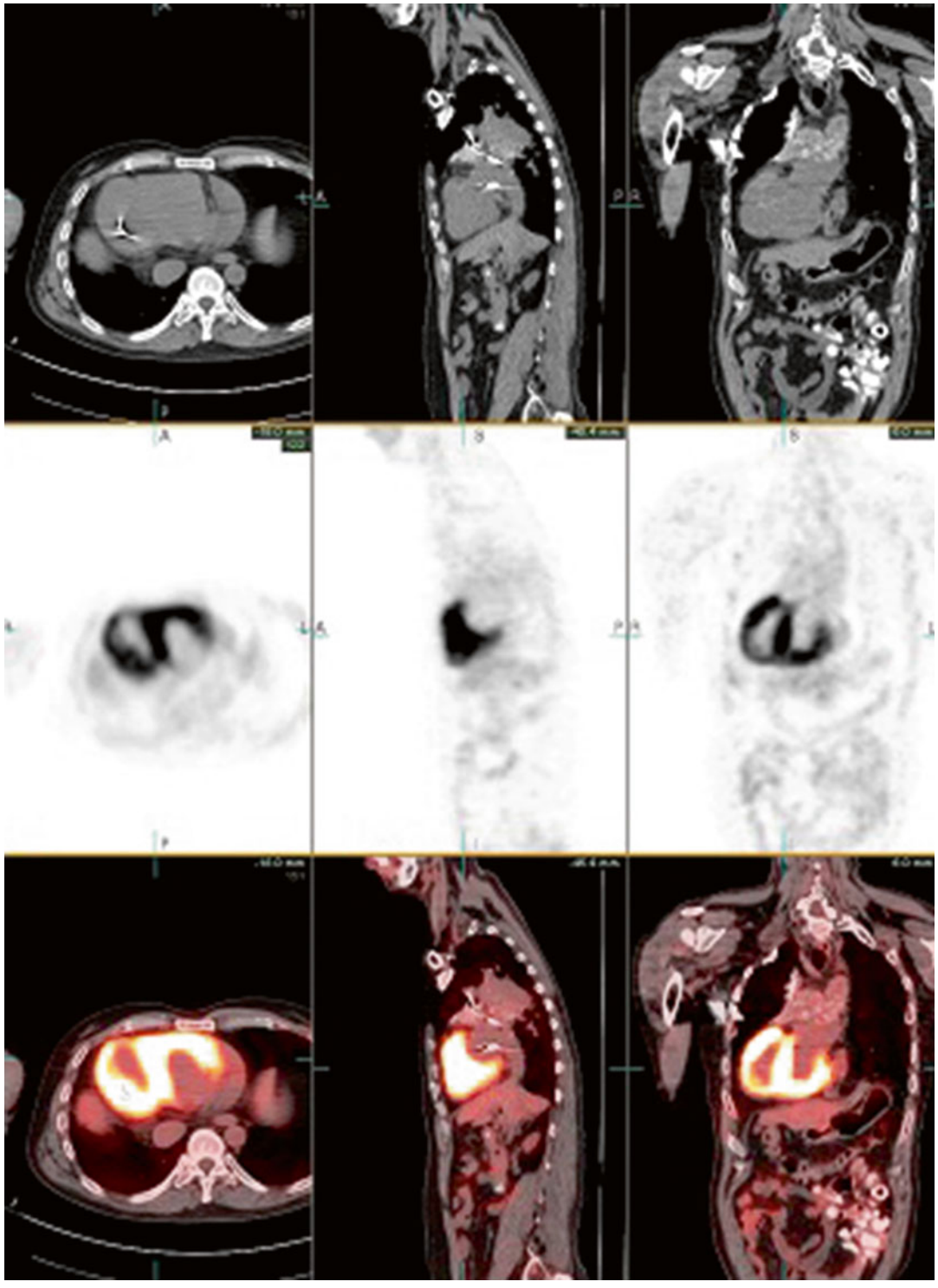

Fig. 1.12

Muscular Uptake Variations on PET/CT Scan

Normal muscles accumulate little ^{18}F-FDG, but muscles exercised just before or around the time of ^{18}F-FDG injection can exhibit intense ^{18}F-FDG uptake. Muscle uptake can be attributed to voluntary or involuntary muscle activity, increased insulin, and surgical interventions. Voluntary muscle activity consists of activities such as talking, chewing, and exercising. Involuntary muscle activity would include labored breathing or muscle spasms/tension. Postradiation treatment or injection-related inflammatory changes in the muscles can also cause F-18 FDG uptake.

Radiation Myositis

See Fig. 1.13.

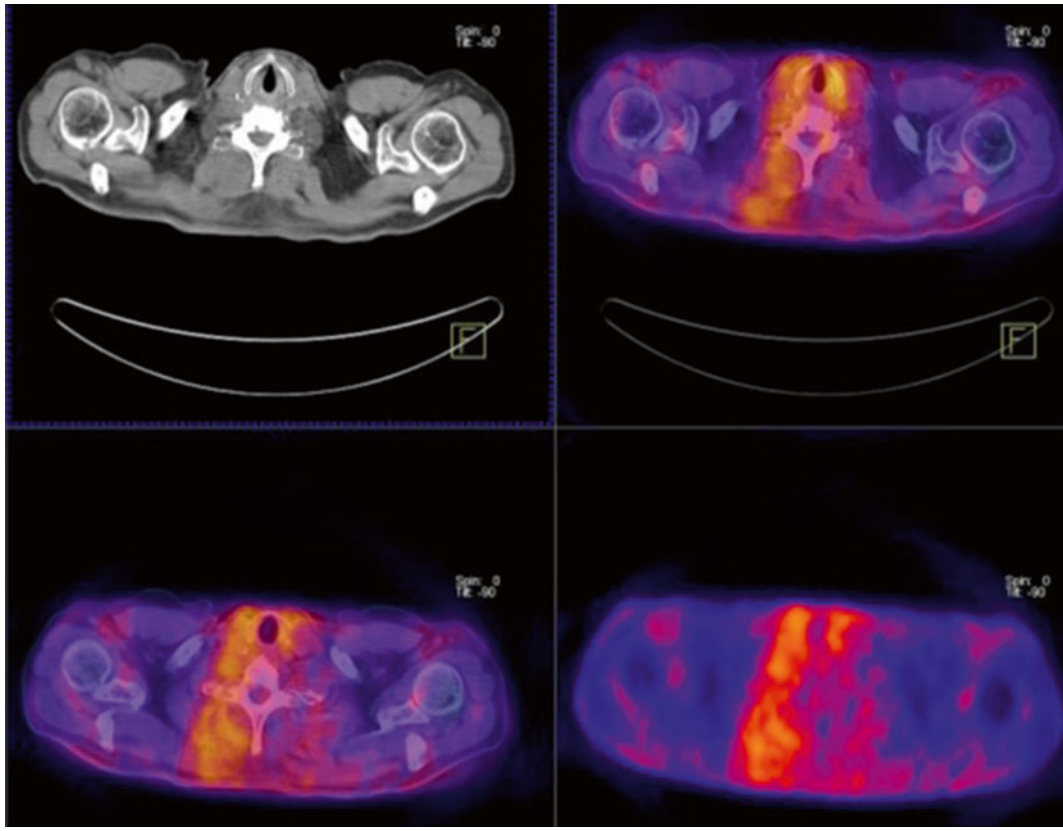

Fig. 1.13

Weight Lifting

See Fig. 1.14.

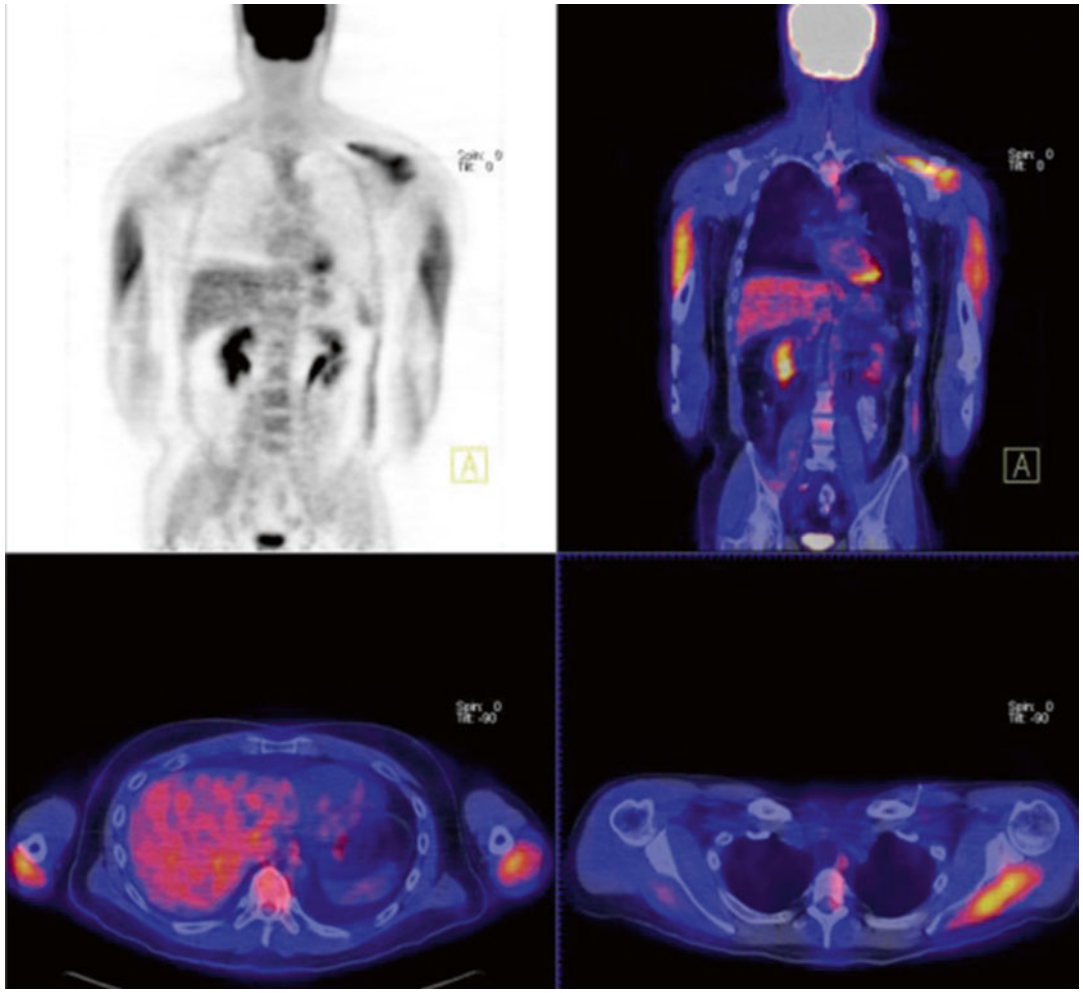

Fig. 1.14

Sit-Ups Prior to Injection

See Fig. 1.15.

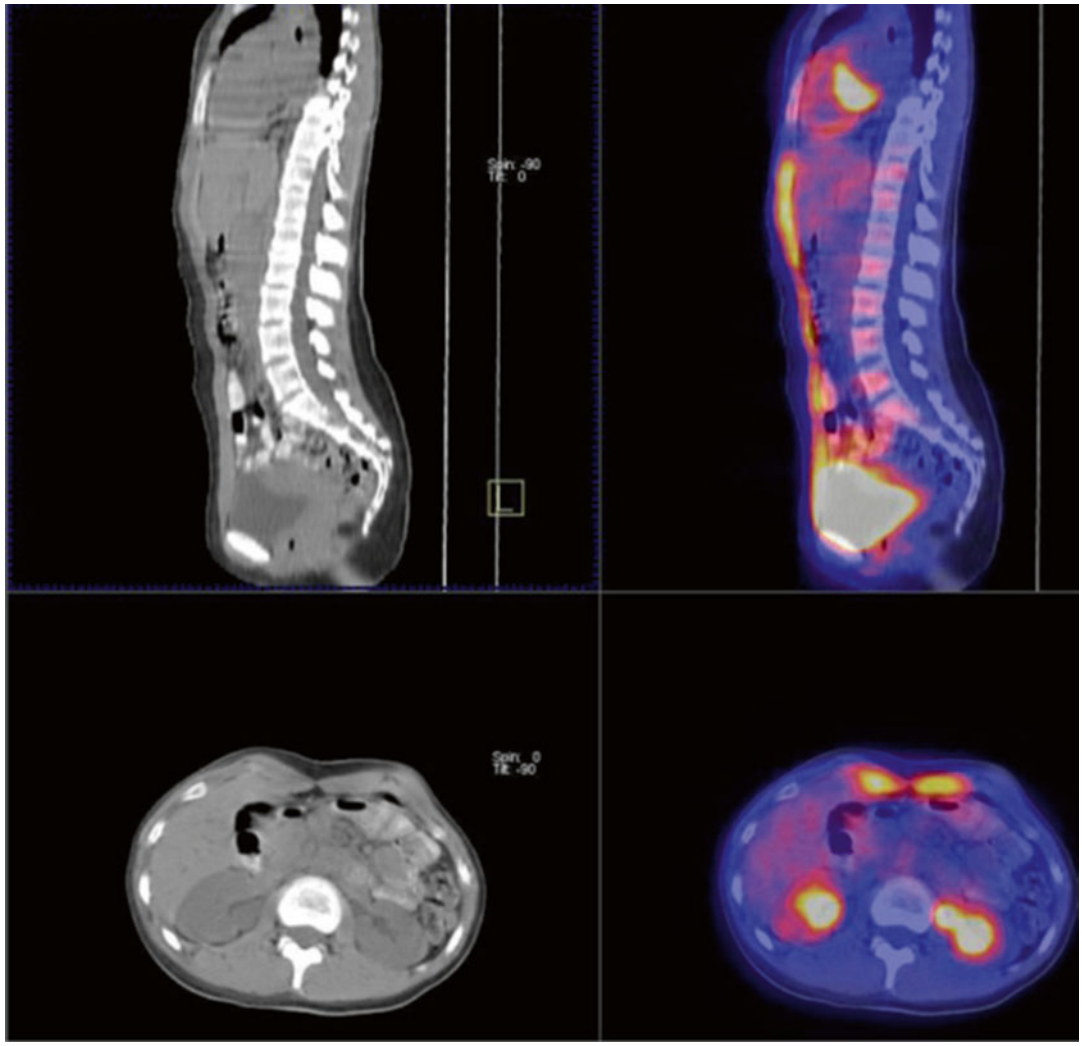

Fig. 1.15

Tense, Cervical, and Intercostal Muscular Uptake

See Fig. 1.16.

Fig. 1.16

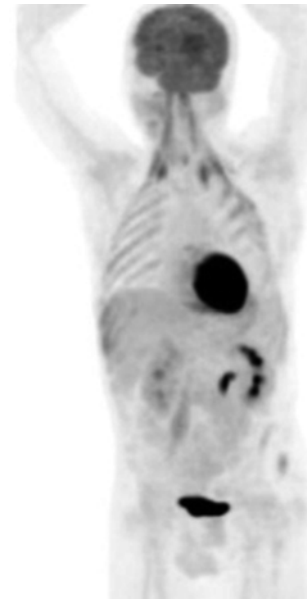

PET Uptake Secondary to Inflammatory Changes Post Subcutaneous Injections

Gluteal Subcutaneous Uptake, Postinjection Soft Tissue Changes on CT

See Fig. 1.17.

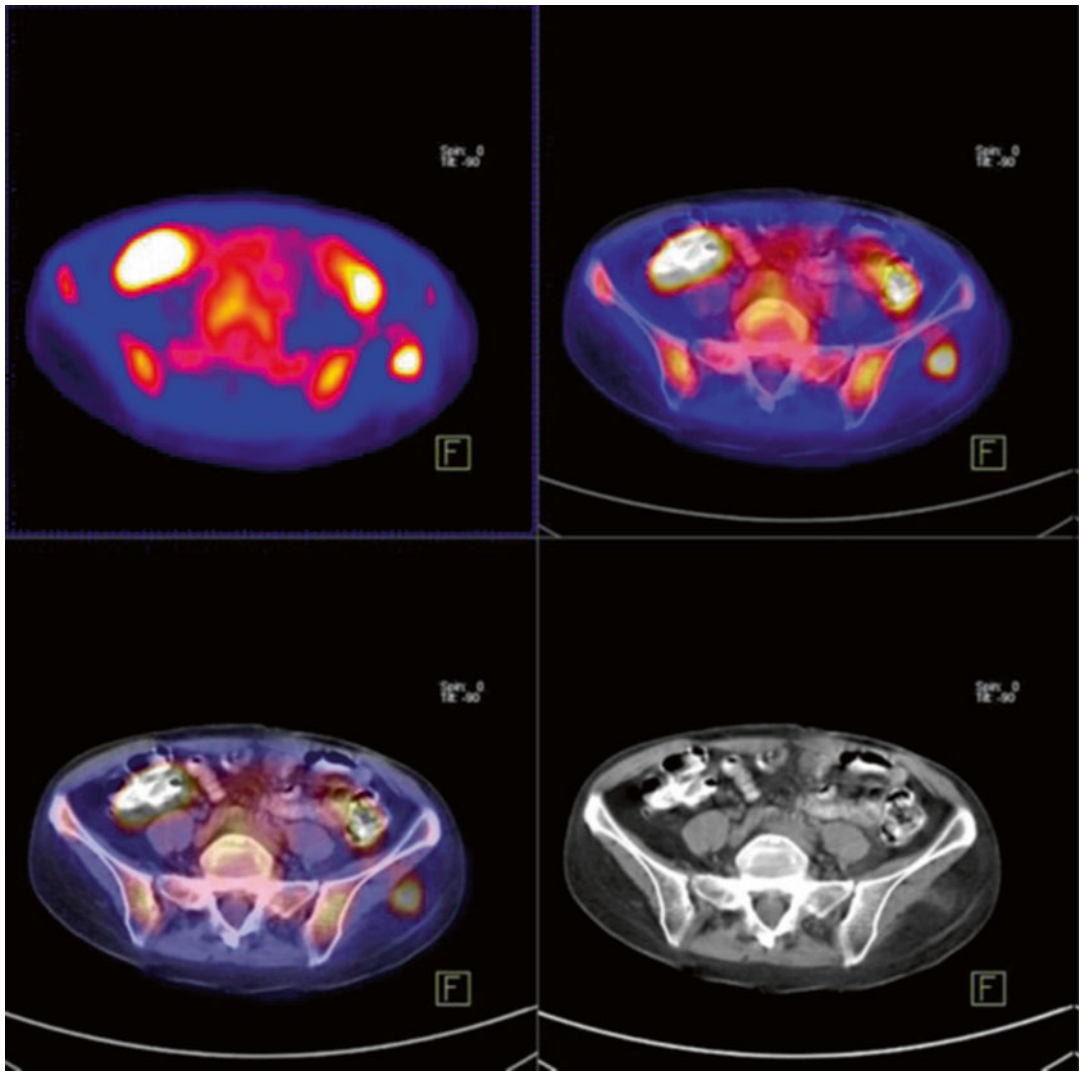

Fig. 1.17

Thigh Subcutaneous Uptake, Postinjection Soft Tissue Changes on CT

See Fig. 1.18.

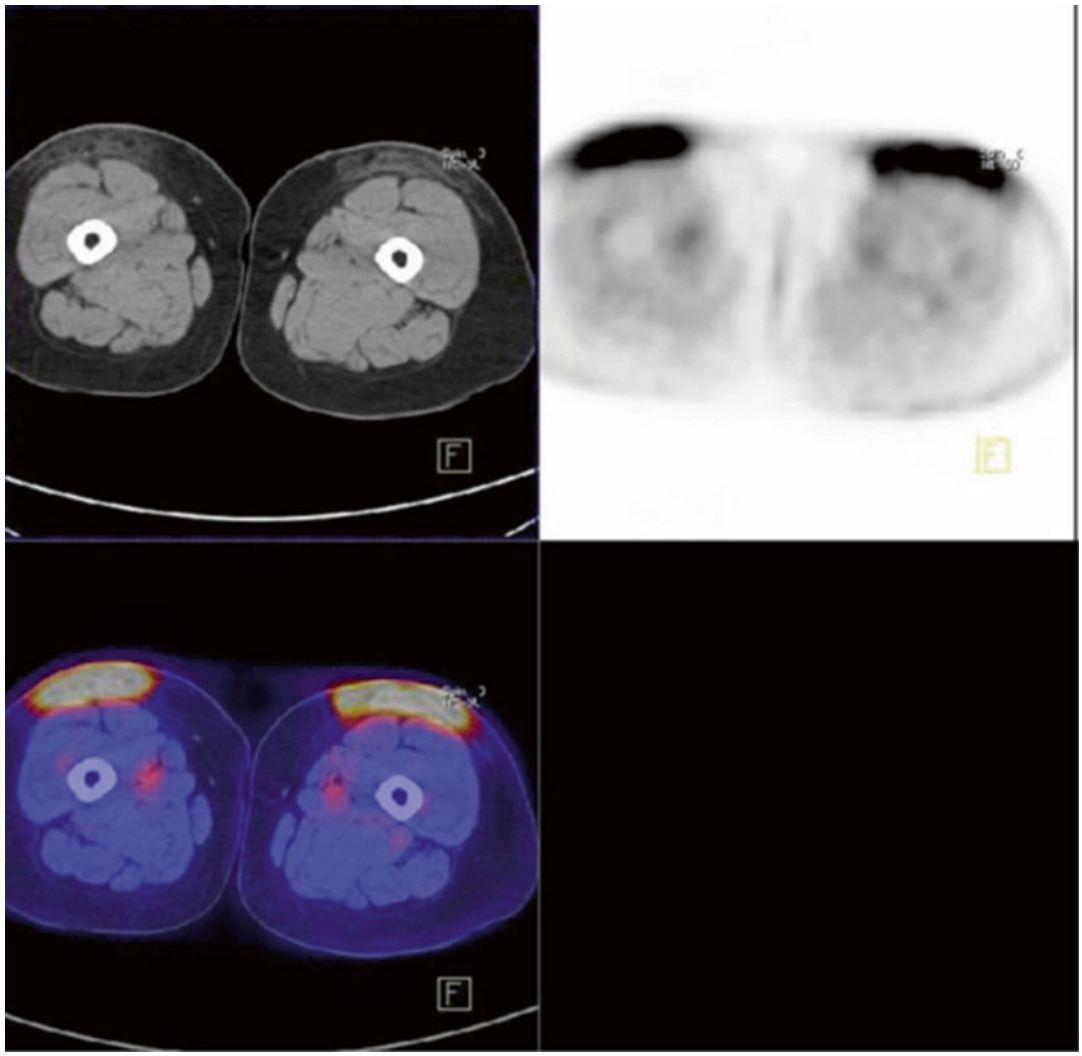

Fig. 1.18

Attenuation Correction Artifact

Vertebroplasty Artifact, Increase Uptake on AC Images (Left) with no Uptake on NAC Images (Right)

Comparison of the attenuation-corrected and non-attenuation-corrected images is important as it demonstrated that the activity was due to an artifact of attenuation correction. The CT scan correlated the site of vertebroplasty to the foci of increased uptake of ^{18}F-FDG. The cement for the vertebroplasty has high density (much denser than normal bone). PET/CT uses the transmission scan from the CT as a density map for attenuation correction of the measured activity. In this case, the attenuation correction algorithm added back too many counts to compensate for attenuation by the extremely dense cement (Fig. 1.19).

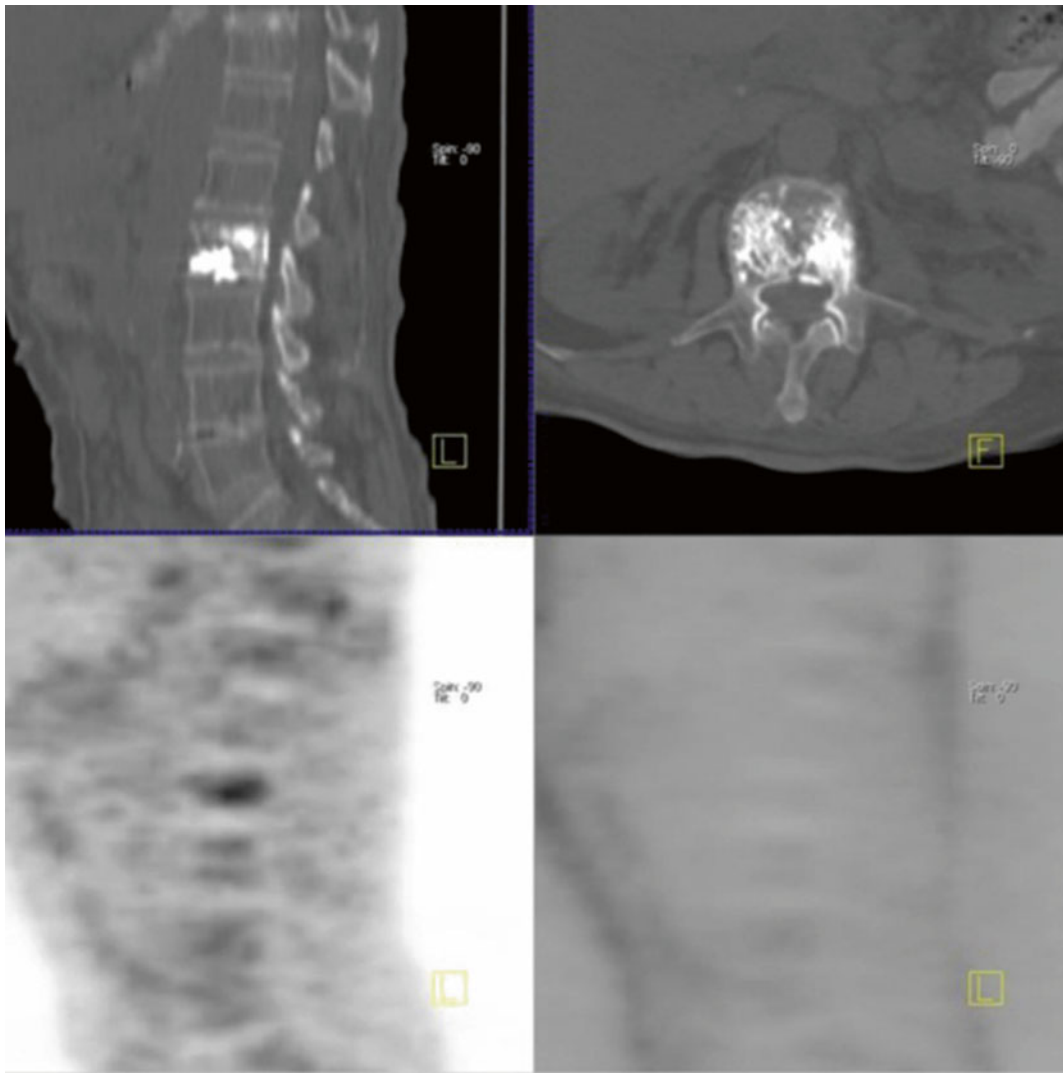

Fig. 1.19

2 Lung Neoplasms

Nova M. Isaac and Peter S. Conti

Case 2.1: Solitary Pulmonary Nodule

History

A 50-year-old male, incidentally diagnosed with a lung nodule in the right lung apex on X-ray and confirmed on CT. Patient was referred for PET/CT evaluation of solitary pulmonary nodule.

Findings (Fig. 2.1)

Hypermetabolic right upper lobe pulmonary nodule with pleural tag (yellow arrow), measures 1.9 × 0.9 cm, anterolaterally, SUVmax 2.9, worrisome for neoplastic process. Remainder of the study was unremarkable.

Impression

Hypermetabolic solitary pulmonary nodule, worrisome for primary neoplasm. (Patient underwent Rt. Upper lobe wedge resection. Pathology: granulomatous caseating inflammation.)

Pearls and Pitfalls

A major application of PET is in the workup of indeterminate solitary pulmonary nodules, defined as noncalcified nodules, 3 cm or smaller, in the lung parenchyma that are found on chest radiography or CT (both of which play vital role in the diagnosis and management of many pulmonary disorders) [1]. However, FDG-PET studies can be falsely positive, primarily due to inflammatory and granulomatous changes, as might be seen in tuberculosis, fungal infections, and sarcoidosis [1].

P.S. Conti, A. Kaushik (eds.), *PET-CT*, DOI 10.1007/978-1-4419-5811-2_2

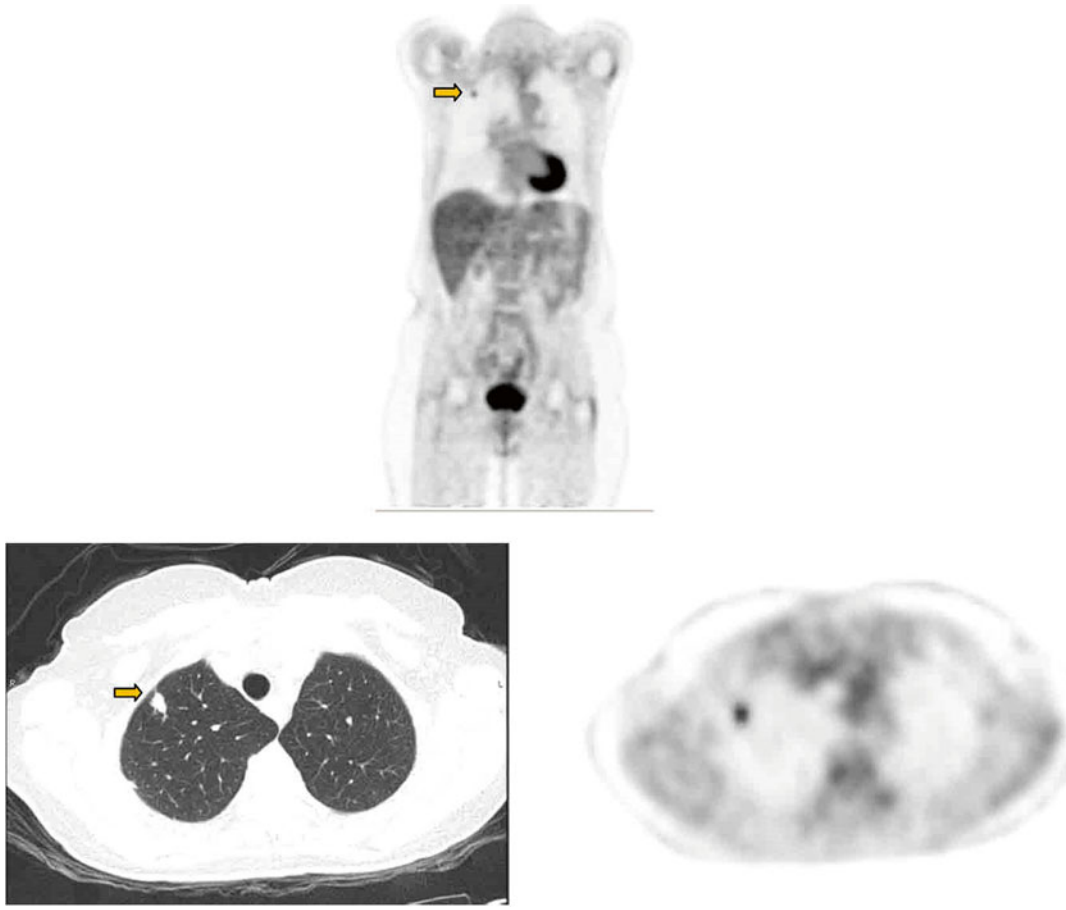

Fig. 2.1

Discussion

Solitary pulmonary nodule (SPN) is defined as a single spherical lesion within the lung parenchyma without associated atelectasis or adenopathy. Current convention is that SPNs are 3 cm or less in diameter. Larger lesions should be referred to as pulmonary masses and should be managed with the understanding that they are most likely malignant; prompt diagnosis and resection are usually advisable [2].

SPNs are caused by a variety of benign and malignant processes. Solitary pulmonary nodules are commonly encountered in clinical practice—about 150,000 new ones are discovered each year in the United States, of which 30–50 % are malignant [1]. Of the benign lesions, 80 % are caused by infectious granulomas, 10 % are caused by hamartomas, and the remaining 10 % are caused by a variety of rarer disorders including noninfectious granulomas and other benign tumors [2].

Fine-needle aspiration (FNA) biopsy is recommended as the first-line diagnostic approach in the workup of SPN.

PET should be reserved for those situations in which a biopsy is inconclusive or contraindicated [3].

Initial studies indicated that a standardized uptake value of 2.5 might distinguish benign from malignant processes; however, later studies have shown that there can be some overlap in these values between benign and malignant processes [1].

Case 2.2: Non-small Cell Lung Cancer

History

A 60-year-old female with history of adenocarcinoma involving the right lung. Additional history of left breast cancer in the past.

Findings (Fig. 2.2)

Pretherapy images demonstrate hypermetabolic pulmonary nodule measuring 2.4 × 1.6 cm in the right lung base, SUVmax 3.2.

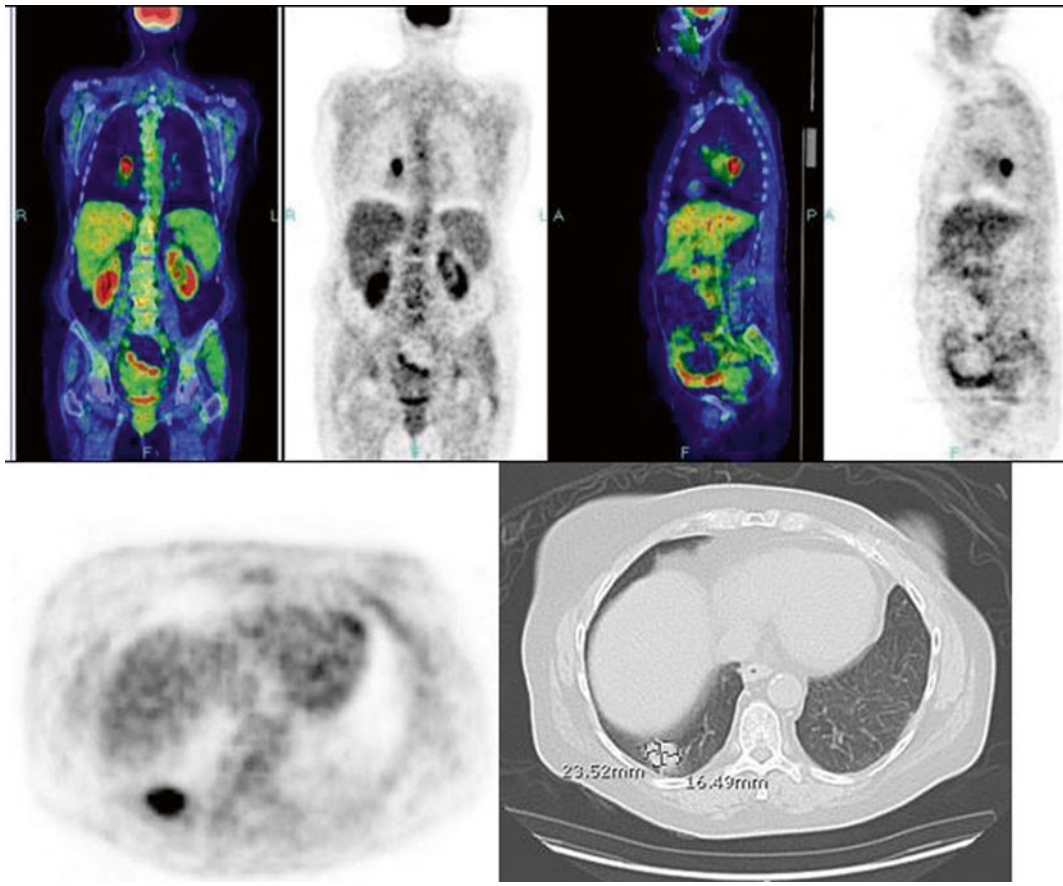

Fig. 2.2 PET/CT (pretreatment)

Impression

Hypermetabolic solitary pulmonary nodule in the right lung base, consistent with malignancy (on biopsy). (The patient later underwent surgical resection of the right lower lobe with nodal dissection.)

Findings (Fig. 2.3)

Posttreatment/follow-up PET/CT demonstrates findings consistent with status post resection of previously noted hypermetabolic pulmonary nodule (seen in Fig. 2.1) at the right lung base. Mild hypermetabolic activity at the lower right costovertebral junction represents inflammation from recent resection. Linear, left chest wall uptake is related to prior breast cancer therapy.

Impression

Post-therapy scan, compatible with treated disease with no scan evidence of local recurrence or distant metastasis.

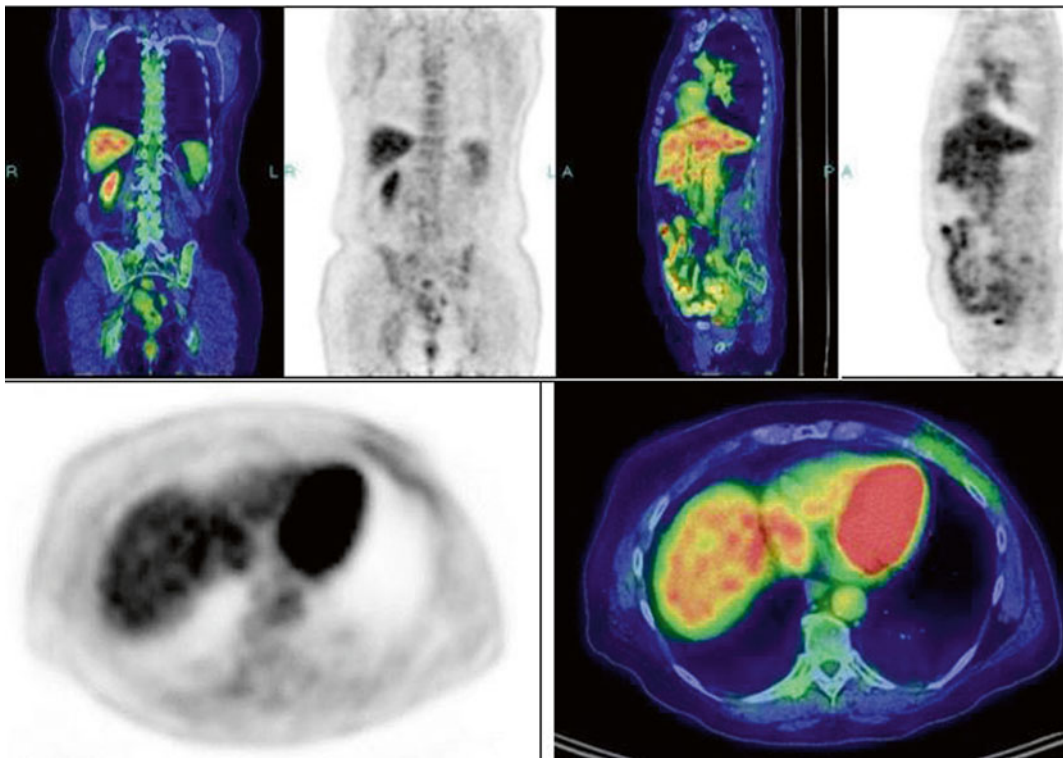

Fig. 2.3 PET/CT (posttreatment/surgery)

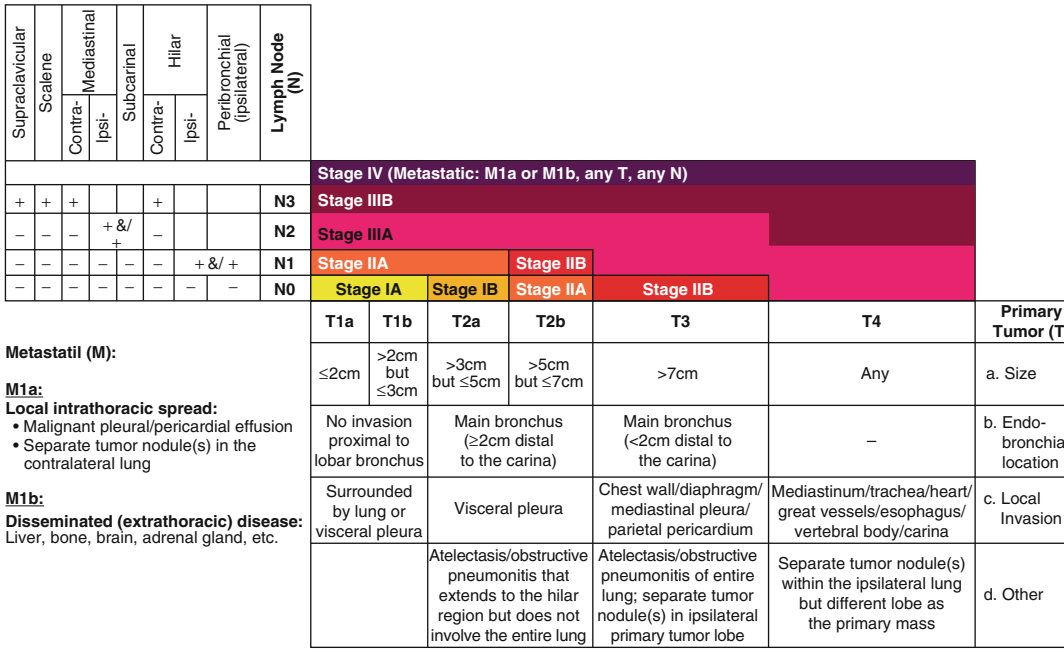

Fig. 2.4

Pearls and Pitfalls

Most solitary pulmonary nodules without increased FDG uptake are highly unlikely to be malignant. However, FDG-PET scans are occasionally falsely negative in cases of well-differentiated adenocarcinoma, bronchoalveolar cell carcinoma, and carcinoid. The spatial resolution of most commercial PET scanners is about 5–6 mm; FDG-PET is less accurate for pulmonary nodules smaller than 1 cm [1].

Discussion

Figure 2.4 illustrates the descriptors from the seventh edition of the TNM staging system for lung cancer [4].

Case 2.3: Squamous Cell Carcinoma of the Lung

History

A 67-year-old female with right lung, pleural-based squamous cell carcinoma (biopsy proven).

Findings (Fig. 2.5)

Large 6.4 cm hypermetabolic, pleural-based mass in the right middle lobe (RML), SUVmax 8.2, with area of central necrosis (yellow arrow) within it. Hypermetabolic focus in the (contralateral) left axillary region (red arrow) corresponds to lymph node on CT.

Impression

Stage III lung cancer. Hypermetabolic pleural-based RML lung malignancy (proven on biopsy as squamous cell carcinoma) with contralateral left axillary lymph node metastasis.

Pearls and Pitfalls

With regard to PET/CT imaging, patient motion (e.g., respiratory motion) can produce significant artifacts on fused images and may cause confusion as to the correct position of the origin of the detected photon [5]. It is recommended to review CT and PET images separately for comparison.

Discussion

National Comprehensive Cancer Network (NCCN) guidelines were reviewed on March 13, 2012 for utilization of F18 fluorodeoxyglucose (FDG) PET and PET/CT.

Practice guidelines from the SNM, NCCN, and other professional groups summarized for lung cancer [6]:

1. Characterization of an indeterminate pulmonary nodule which is at least 8–10 mm in diameter
2. Initial staging in patients with non-small cell lung cancer and selected patients with small cell lung cancer
3. Delineation of gross tumor volume in patients receiving radiation therapy

PET and PET/CT are approved by the Centers for Medicare and Medicaid Services (CMS) for:

a. Characterization of solitary pulmonary nodules.
b. Development of initial treatment strategy and subsequent treatment strategy in patients with NSCLC.
c. Development of initial treatment strategy in patients with SCLC. The use of PET/CT for subsequent treatment strategy falls under "CED" (coverage with evidence of development) category.

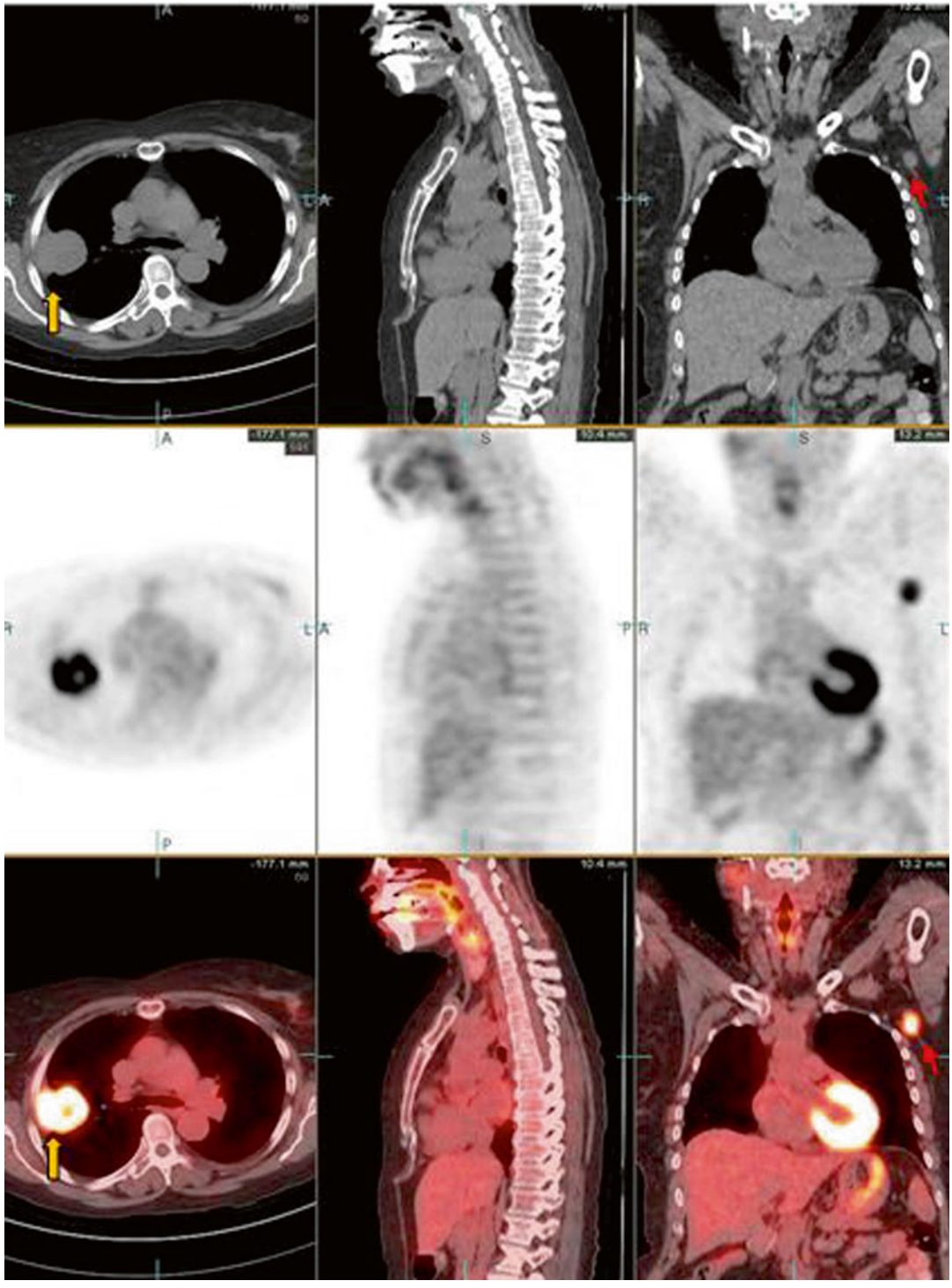

Fig. 2.5

Case 2.4: Stage IIIB Non-small Cell Lung Cancer (NSCLC)

History

A 75-year-old male with right middle lobe non-small cell lung cancer, clinical T4b N2 M0, stage IIIB.

Findings (Fig. 2.6)

Large, irregular, hypermetabolic mass (>7 cm), SUVmax 13.6, in the medial segment of the right middle lobe, with central necrosis (appearing photopenic on PET). There is invasion of the tumor into the right minor fissure and extends superiorly into the right upper lobe. A satellite hypermetabolic nodule, SUVmax 6.6, seen posterior to the dominant mass (yellow arrow).

Impression

Non-small cell lung carcinoma (biopsy proven), in the RML, stage IIIB.

Pearls and Pitfalls

PET is a useful tool for identifying patients at high risk for disease recurrence and restaging following neoadjuvant chemotherapy with or without radiation. PET is particularly useful when posttreatment scarring and pleural thickening limit the role of CT for disease assessment [7].

Discussion

Malignant lung neoplasms arise from respiratory epithelium (bronchi, bronchioles, and alveoli).

Four major cell types make up 90 % of all primary lung neoplasms:

1. Squamous cell or epidermoid carcinoma
2. Small cell (also called oat cell) carcinoma
3. Adenocarcinoma (including bronchoalveolar)
4. Large cell (also called large cell anaplastic) carcinoma

Remainder include:

5. Undifferentiated carcinomas
6. Carcinoids
7. Bronchial gland tumors (including adenoid cystic carcinomas and mucoepidermoid tumors)
8. Other rarer tumor types

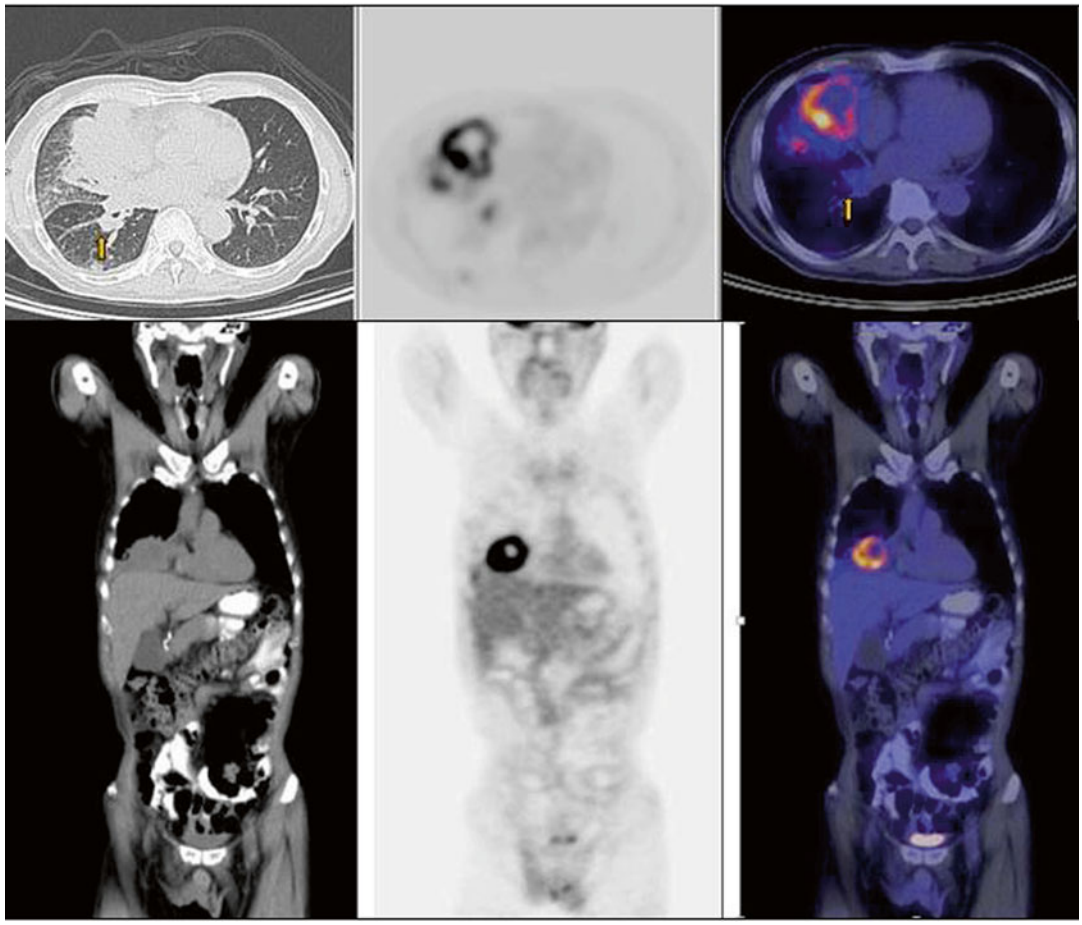

Fig. 2.6

Adenocarcinoma has replaced squamous cell carcinoma as the most frequent histologic subtype for unclear reasons [8].

Case 2.5: Stage IV NSCLC

History

A 79-year-old female with history of locally advanced non-small cell lung cancer in the left upper lobe.

Pretreatment PET CT images and follow-up surveillance PET/CT following cyber knife radiation therapy are shown below.

Findings (Figs. 2.7 and 2.8)

Large, hypermetabolic left posterior apical 4.8 × 4.0 cm mass which abuts the medial pleura and left paravertebral margin, SUVmax of 19.7. In addition, there is subtle erosion of the lateral margin of T3 vertebral body cortex. The mass extends through the left T3/4 neural foramen with epidural involvement at this level. The epidural portion of the mass is inactive on PET, probably related to small size.

Impression

Stage IV lung cancer.

Fig. 2.7 Initial PET/CT, axial view

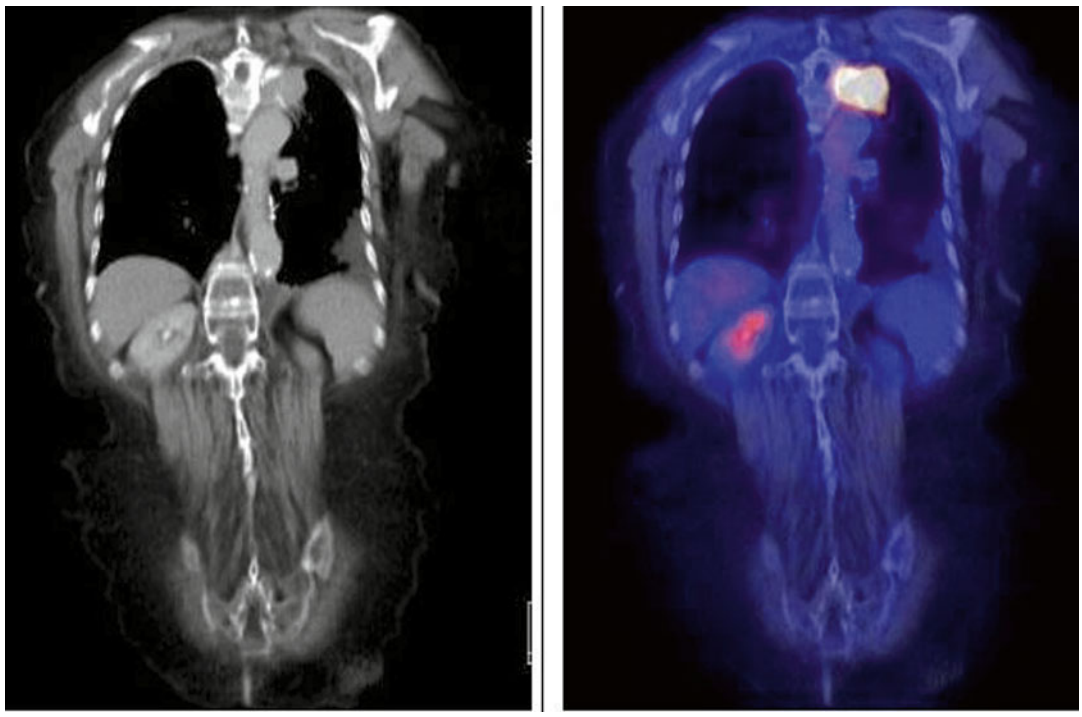

Fig. 2.8 Initial PET/CT, coronal view

Findings (Figs. 2.9 and 2.10)

There is linear hypermetabolic activity associated with fibrotic changes in the left lung apex which appears more confluent and demonstrates SUVmax at 4.4 (compared to pretreatment PET/CT) (which was stable from intermittent post-therapy scan from 6 months prior, not shown).

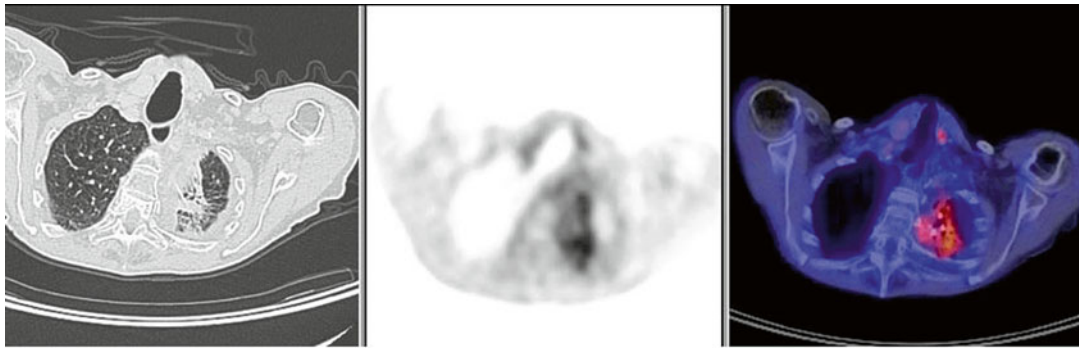

Fig. 2.9 Surveillance PET/CT (2 yrs. following radiation therapy), axial view

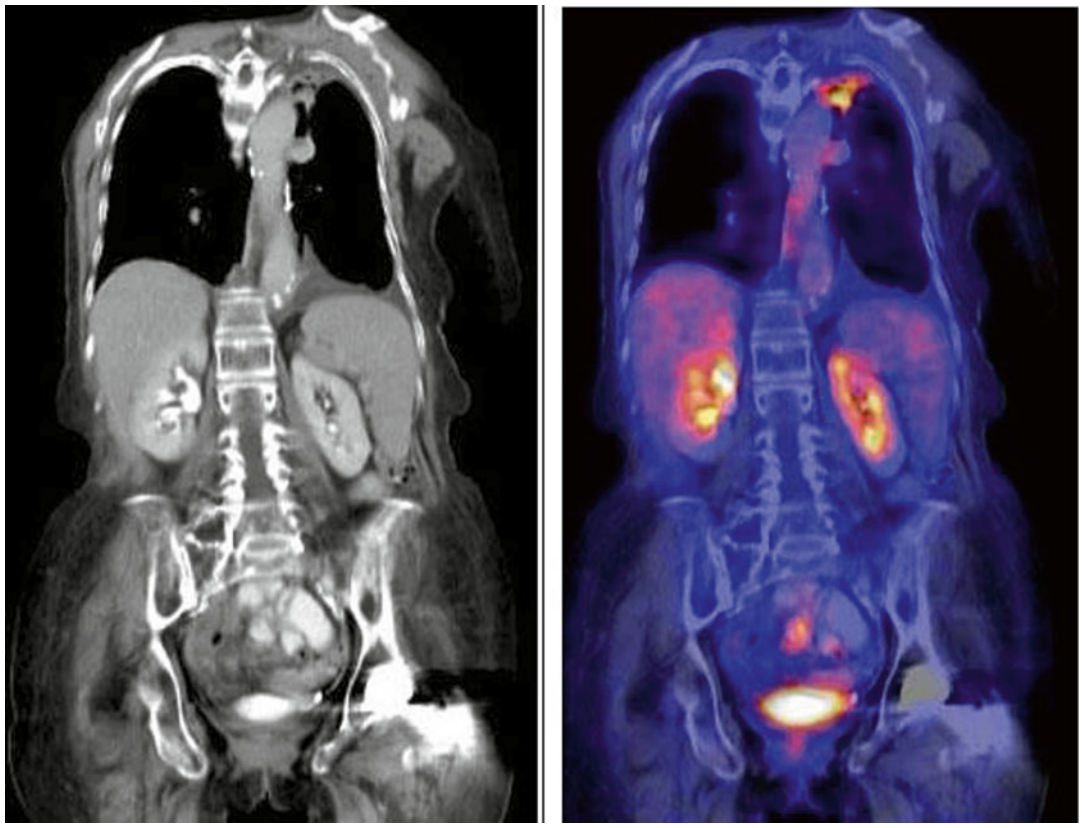

Fig. 2.10 Surveillance PET/CT (2 yrs. following radiation therapy), coronal view

There is associated traction bronchiectasis, left lung volume loss, and mediastinal shift to the left. Findings compatible with postradiation changes. Remainder of the study was unremarkable for metabolically active metastatic disease.

Impression

Stable postradiation-induced inflammation in the left lung apex.

Pearls and Pitfalls

Radiation pneumonitis (RP) has a characteristic linear border and diffuse intense uptake [7]. Uptake on PET can be seen before radiation changes are seen radiographically. Tumor recurrence is usually more focal and can be differentiated from radiation pneumonitis. However, sometimes RP can occasionally have heterogeneous uptake in the early treatment stages. PET imaging should be delayed by 3–6 months following radiation therapy.

Discussion

See Fig. 2.11.

Treatment Recommendations and Future Research Directions in the Management of Non-Small Cell Lung Cancer

Stage	Standard Management	Future Directions
Stage I	Surgical resection	Adjuvant therapy (chemotherapy/radiation or a combination of the two) Chemoprevention
Stage II	Surgical resection	Same as stage I
Stage IIIA	Chemoradiotherapy Surgical resection in selected patients	Neoadjuvant combined-modality therapy to downstage primary tumor
Stage IIIB	Chemoradiotherapy	Neoadjuvant combined-modality therapy to downstage primary tumor
Stage IV	Cisplatin-based chemotherapy* Surgical resection if solitary metastatic lesion with resectable primary tumor	More efficacious single-agent and combination chemotherapy

*Chemotherapy beneficial only in patients with good performance status and weight loss less than 10% of their body weight

Fig. 2.11

Case 2.6: Small Cell Lung CA (SCLC)

History

A 65-year-old female with history of limited stage small cell lung carcinoma.

Findings (Fig. 2.12)

Initial scan shows hypermetabolic pulmonary nodule in the left lower lobe (adjacent to the left hilum), measuring 1.9 × 2.9 cm, SUVmax 34.3, most consistent with malignant tumor.

Impression

Left lower lobe hypermetabolic pulmonary nodule consistent with neoplasm (primary versus secondary).

Pathology on biopsy: Small cell lung carcinoma.

The patient underwent chemoradiation and prophylactic cranial radiation. Follow-up PET/CT, 1 year since initial diagnosis was obtained. (fig 2.13)

Findings (Fig. 2.13)

Posttreatment scan shows traction bronchiectasis, peribronchial thickening, and fibrotic changes related to radiation therapy in the left lower lobe, demonstrating low-grade activity, SUVmax 3.8. There is volume loss within the left lung with shift of mediastinum to the left.

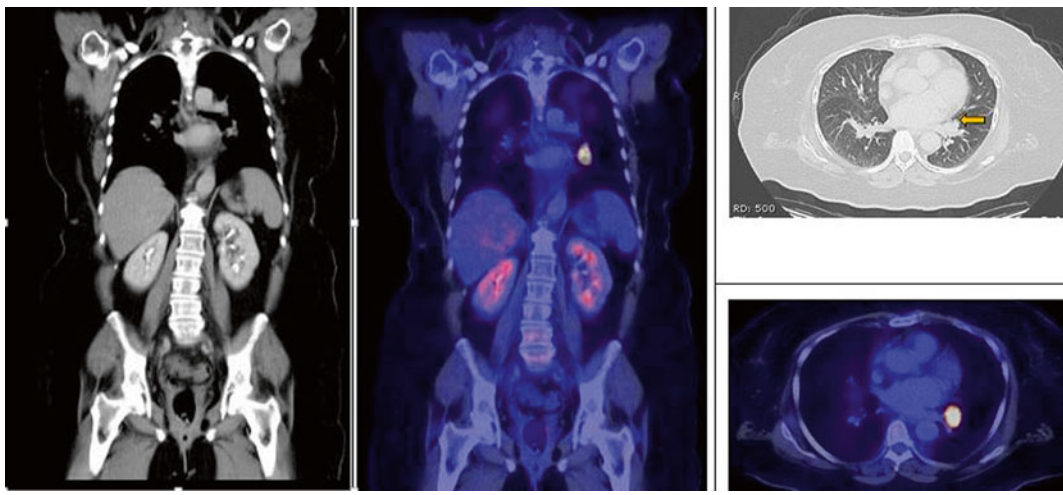

Fig. 2.12

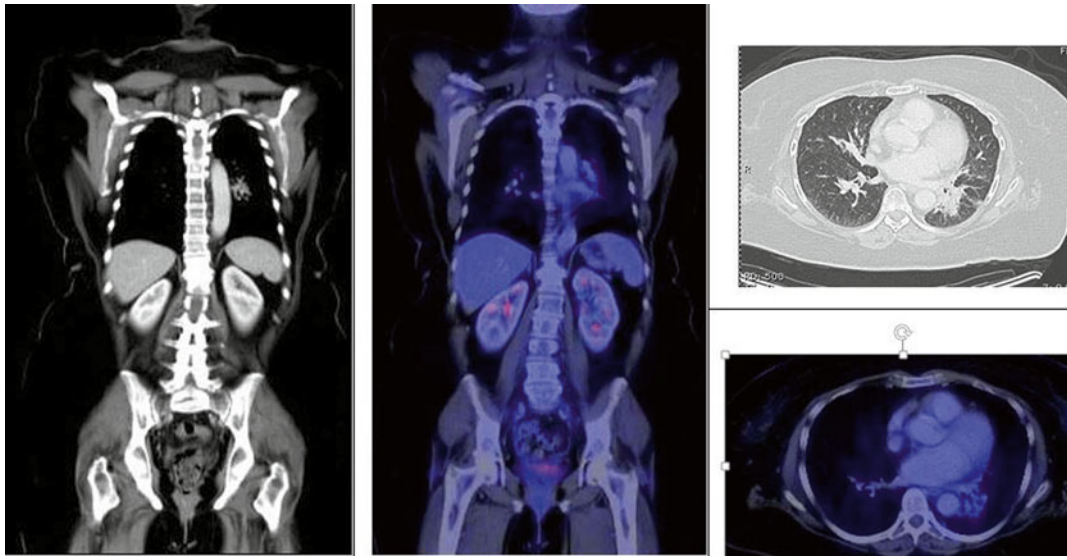

Fig. 2.13

Impression

Findings consistent with radiation-related changes in the left lower lobe.

Pearls and Pitfalls

Limited data indicate that PET and PET/CT are more accurate than conventional imaging in the staging and follow-up of SCLC with superior accuracy for mediastinal, hilar, and extra thoracic lymph nodes, distant metastases, and bone marrow metastases [9]. Compared to conventional imaging, PET/CT can result in a change in stage in 10–17 % of patients.

Discussion

SCLC is considered a systemic disease. The clinical course, prognosis, and treatment options are clearly different from those of other lung cancers. Clinically, lung cancers are often categorized into SCLC and non-SCLC (NSCLC) [10].

SCLC is categorized into two stages: limited disease and extensive disease. The disease is termed limited when it is confined to an area of the chest that can be encompassed by a single irradiation port; supraclavicular nodes may be included. The disease is called extensive when metastasis outside the thorax is present or when intrathoracic disease cannot be contained in a single irradiation port.

Patients with SCLC are rarely surgical candidates, and they are usually treated with irradiation and/or chemotherapy.

Case 2.7: Neuroendocrine Tumor Favoring Small Cell Lung Cancer

History

A 49-year-old male presents with anterior mediastinal mass.

Findings (Fig. 2.14)

(Red arrow) hypermetabolic, heterogeneous, left anterior mediastinal mass centered in the prevascular space/AP window, SUVmax 9.7.

Impression

Hypermetabolic anterior mediastinal mass corresponding to biopsy-proven diagnosis of neuroendocrine tumor favoring small cell carcinoma.

Pearls and Pitfalls

The maximum SUVs of neuroendocrine tumors are significantly different for carcinoid tumors, large cell neuroendocrine carcinomas (LCNEC), and small cell lung cancers (SCLC). A high maximum SUV suggests short survival of patients with (LCNEC) or (SCLC).

Discussion

Neuroendocrine tumors of the lung arise from Kulchitsky cells of the bronchial mucosa and comprise typical carcinoid, atypical carcinoid, large cell neuroendocrine carcinoma (LCNEC), and small cell lung cancer (SCLC) [11]. Pulmonary or bronchial carcinoid tumors account for over 25 % of all carcinoid tumors and for 1–2 % of all pulmonary neoplasms.

National Comprehensive Cancer Network (NCCN) guidelines were reviewed on March 13, 2012 for utilization of F18 fluorodeoxyglucose (FDG) PET and PET/CT.

Specific indications for PET and PET/CT in (SCLC) [12]:

For initial staging of small cell lung carcinoma and high-grade/large cell neuroendocrine carcinoma: PET/CT is recommended if limited stage is suspected (staging). PET/CT has replaced bone scan in NCCN guidelines; bone scan is now only recommended if PET/CT is not available.

PET/CT is not recommended for routine follow-up after initial therapy (restaging).

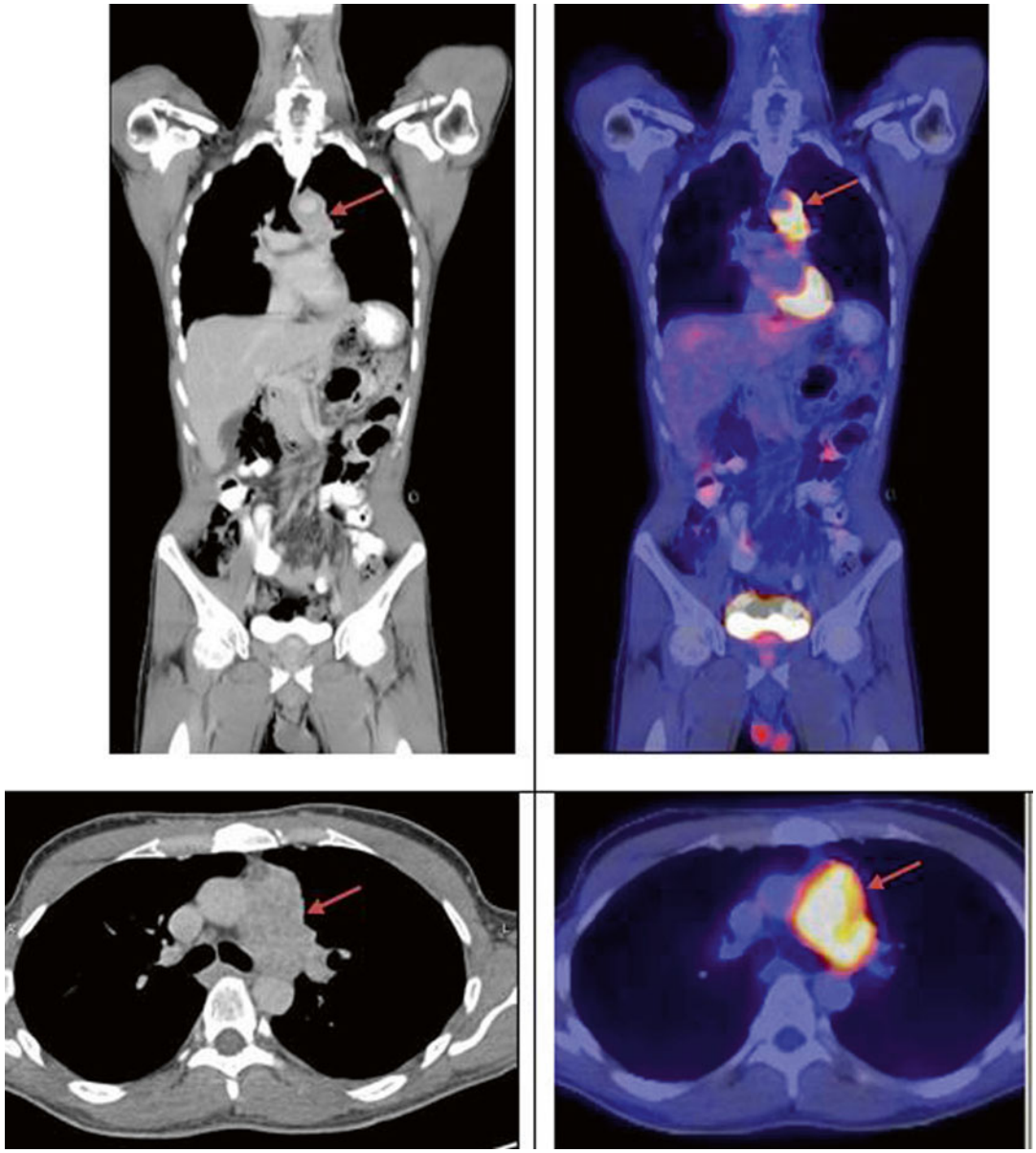

Fig. 2.14

PET/CT is also suggested for radiation treatment planning purposes.

For low- and intermediate-grade neuroendocrine carcinomas (e.g., carcinoid tumor): PET scan is considered optional (staging). Currently, PET is undergoing evaluation in clinical trials and should only be considered as a supplement and not a replacement to other studies in such cases [12].

Case 2.8: Mesothelioma

History

An 80-year-old male with history of unresectable left malignant pleural mesothelioma.

Findings (Fig. 2.15)

Multiple hypermetabolic pleural-based nodules in the left hemithorax demonstrating circumferential distribution causing encasement of the left lower lobe with loss of lung volume (yellow arrow). Pleural-based

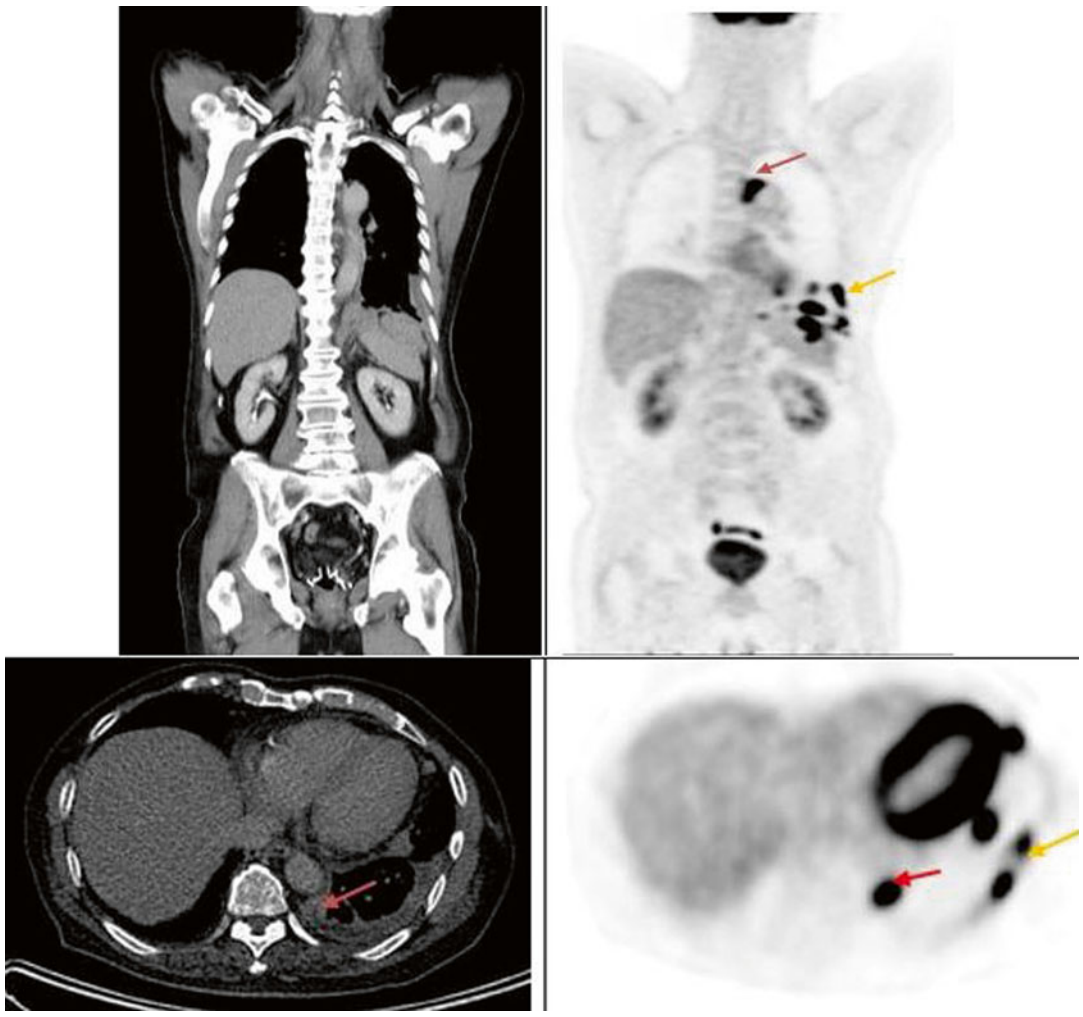

Fig. 2.15

lesions seen at the medial aspect of left lung apex, between the trachea and posterior arch of aorta and in the left costovertebral region shows SUVmax in the range of 25.0–26.0 (red arrow). No FDG avid pleural plaques in the right hemithorax. Left pleural effusion.

Impression

Findings compatible with biopsy-proven diagnosis of left hemithorax mesothelioma.

Pearls and Pitfalls

The findings in talc pleurodesis are very similar to mesothelioma and pleural metastasis. In patients with mesothelioma, talc pleurodesis is used in treating recurrent pleural effusions, which also limits future PET/CT evaluation as they both show similar scan patterns. The activity of both pleural implants and talc-induced inflammation will be high. Careful evaluation of the PET/CT images in the pleural reflections adjacent to diaphragm is important to allow confident identification of loculated talc (radiodense material on CT) at these sites [13].

Discussion

Malignant pleural mesothelioma (MPM) is an uncommon neoplasm that arises from the pleura or, rarely, the pericardium or peritoneum. There are approximately 2000–3000 new cases diagnosed in the United States every year, the majority of which are associated with prior asbestos exposure. Patients frequently present with dyspnea, chest pain, cough, and weight loss. The tumor can invade both visceral and parietal pleura and frequently extends to adjacent structures [14]. The prognosis is poor, with a median survival time of 12 months after diagnosis.

Case 2.9: Mesothelioma (with low SUV)

History

A 65-year-old male with biopsy-proven right pleural mesothelioma.

Findings (Fig. 2.16)

Circumferential pleural thickening with associated hypermetabolism, SUVmax up to 7.2, with presence of calcified pleural plaques in the right hemithorax. Large right pleural effusion.

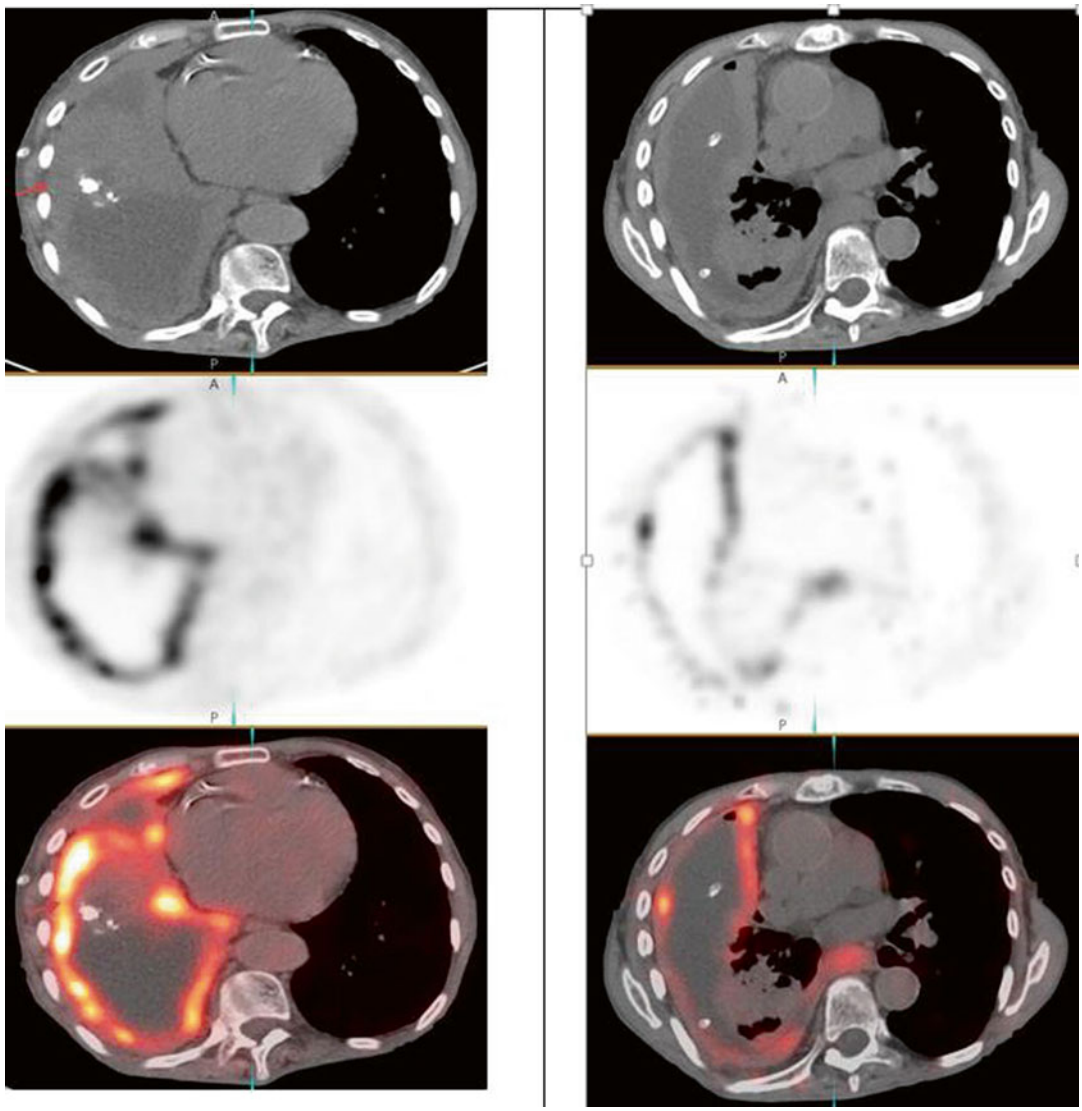

Fig. 2.16

Impression

Findings compatible with known mesothelioma in the right hemithorax.

Pearls and Pitfalls

Patients with highly active mesotheliomas on FDG-PET imaging have a poor prognosis. High FDG uptake in these tumors indicates shorter patient survival [15].

Discussion

Several factors have been shown to correlate with reduced survival time: intrathoracic lymph node metastases, distant metastatic disease, and extensive pleural involvement [14].

Case 2.10: Solitary Fibrous Tumor (SFT) in the Lung

History

A 65-year-old male with right lower lobe mass on the CT chest, status post biopsy of tumor.

Findings (Fig. 2.17)

Mild-to-moderately active, pleural-based soft tissue mass in the right costophrenic angle (yellow arrow), measuring approximately 7.1 cm × 5.0 cm × 8.2 cm (TR XAP X CC), SUVmax 2.9.

Impression

Pleural-based right lower lobe mass with low-grade FDG activity, consistent with biopsy-proven diagnosis of benign solitary fibrous tumor.

Pearls and Pitfalls

Benign SFT exhibits low-grade activity in PET, whereas malignant SFT tends to be strongly hypermetabolic. In addition to FDG activity on PET scans, lesion multiplicity is a helpful feature in identifying malignant disease [16]. However, benign pleural SFT sometimes causes adjacent rib destruction, mimicking an aggressive or malignant lesion. Ultimately, benign SFT has a local recurrence rate of 8 %, and malignant lesions recur within 2 years in as many as 63 % of cases.

Discussion

Solitary fibrous tumors (SFTs) are uncommon neoplasms of mesenchymal origin that can be benign or malignant. Although SFTs most commonly occur in the pleura, numerous extra pleural sites of involvement have been reported. SFTs most commonly present during the fifth and sixth decades of life, and there is no significant sex predilection. SFT can be associated with hypoglycemia secondary to production of insulin-like

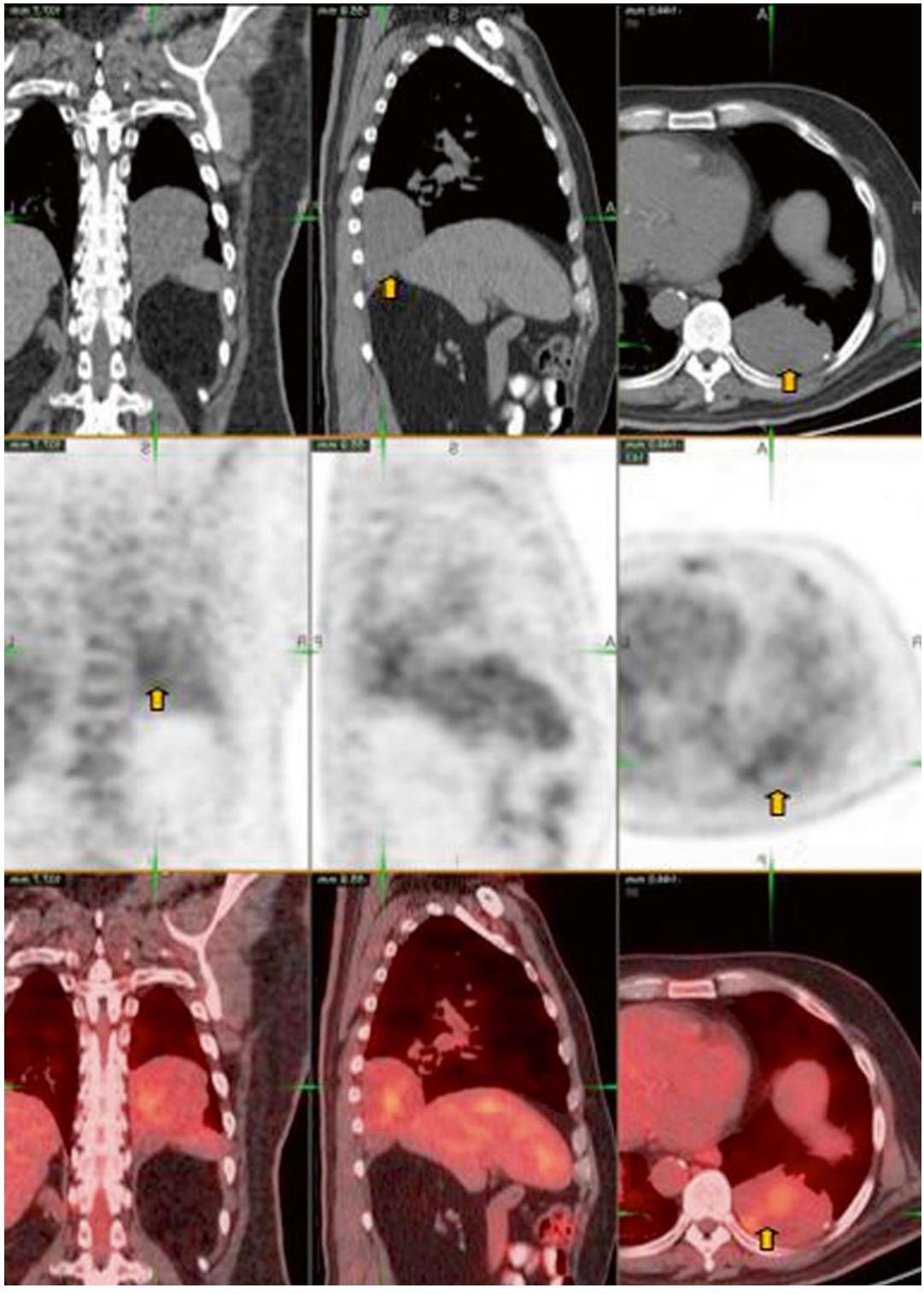

Fig. 2.17

growth factor, osteoarthropathy, arthralgia, and clubbing. Histologically, SFTs are composed of spindle cells within a background of collagen stroma, often in a whorled pattern or patternless. These tumors are highly vascular and have a propensity to undergo myxoid degeneration [16]. The diagnosis is confirmed by characteristic positive immunohistochemical staining for CD34 and negative staining for S-100. Overall, approximately 15–20 % of SFTs are malignant, and even benign SFTs have indeterminate malignant potential. Therefore, complete resection is the treatment of choice.

References

1. Bybel B, et al. PET and PET/CT imaging: what clinicians need to know. Cleve Clin J Med. 2006;73(12):1075–87.
2. Ost D, et al. Evaluation and management of the solitary pulmonary nodule. Am J Respir Cri Care Med. 2000;162(3):782–7.
3. Guidelines summary. http://www.guideline.gov/content.aspx?id=12137&search=Malignant+neoplasm+of+lung.
4. UyBico SJ, et al. Lung cancer staging essentials: the new TNM staging system and potential imaging pitfalls. Radiographics. 2010;30:1163–81.
5. Kapoor V, et al. An introduction to PET-CT imaging. Radiographics. 2004;24:523–43. doi:10.1148/rg.242025724.
6. PET PROS. 18F-fludeoxyglucose (FDG) PET and PET/CT practice guidelines in oncology (March 2012). http://www.snm.org/docs/PET_PROS/OncologyPracticeGuidelineSummary.pdf.
7. Lin EC, et al. Thoracic neoplasms. In: PET and PET/CT: a clinical guide. 2nd ed. Stuttgart: Thieme; 2005. p. 150–151.
8. Lung Cancer; General. http://www.harrisonspractice.com/practice/ub/view/Harrisons%20Practice/141188/all/lung_cancer__general.
9. Lin EC, et al. Thoracic neoplasms. In: PET and PET/CT: a clinical guide. 2nd ed. Stuttgart: Thieme; 2005. p. 151.
10. Imaging in small cell lung cancer. http://emedicine.medscape.com/article/358274-overview.
11. Chong S, et al. Neuroendocrine tumors of the lung: clinical, pathologic, and imaging findings. Radiographics 2006;26:41–57. doi:10.1148/rg.261055057January.
12. PET PROS. 18F-fludeoxyglucose (FDG) PET and PET/CT practice guidelines in oncology (March 2012). http://www.snm.org/docs/PET_PROS/NCCNPracticeGuidelinesII.pdf.
13. Peller P. Talc pleurodesis on PET/CT. In: Hartman T, editor. Pearls and pitfalls in thoracic imaging: variants and other difficult diagnoses. Cambridge: Cambridge University Press; 2011. p. 206.
14. Wang Z, et al. Malignant pleural mesothelioma: evaluation with CT, MR imaging, and PET. Radiographics 2004;24:105–19. doi:10.1148/rg.241035058January.
15. Benard F, et al. Prognostic value of FDG PET imaging in malignant pleural mesothelioma. J Nucl Med. 1999;40(8):1241–5.
16. Ginat DT, et al. Imaging features of solitary fibrous tumors. Am J Roentgenol. 2011;196(3):487–95. doi:10.2214/AJR.10.4948AJR.

3 Breast Neoplasms

Nova M. Isaac and Peter S. Conti

Case 3.1: Ductal Carcinoma In Situ of Breast

History

A 45-year-old female with biopsy-proven diagnosis of ductal carcinoma in situ of right breast. PET/CT was performed for initial staging.

Findings (Fig. 3.1)

Hypermetabolic right breast mass, SUVmax 13.8 (*black arrow*). Intensely hypermetabolic right axillary lymph nodes (LN), most avid LN demonstrates SUVmax 16.4 (*yellow arrow*).

Impression

Hypermetabolic right breast mass with at least two hypermetabolic right axillary LN, consistent with biopsy-proven malignancy.

Pearls and Pitfalls

Positron emission tomography (PET) with fluorine 18 fluorodeoxyglucose (FDG) is used to diagnose, stage, and monitor breast cancer. FDG-PET has the capability to depict abnormal metabolic activity before any anatomic change occurs. The most important advantage of FDG-PET/CT compared with other imaging modalities is the capability of detecting unsuspected distant metastases during a single whole-body examination. However, the results of most studies show that the capability of PET to depict lesions smaller than 1 cm in diameter is constrained by limited spatial resolution. PET also is of limited use for identifying tumors that are well differentiated histologically, such as ductal carcinoma in situ, and slow-growing cancers such as tubular carcinoma [1].

P.S. Conti, A. Kaushik (eds.), *PET-CT*, DOI 10.1007/978-1-4419-5811-2_3

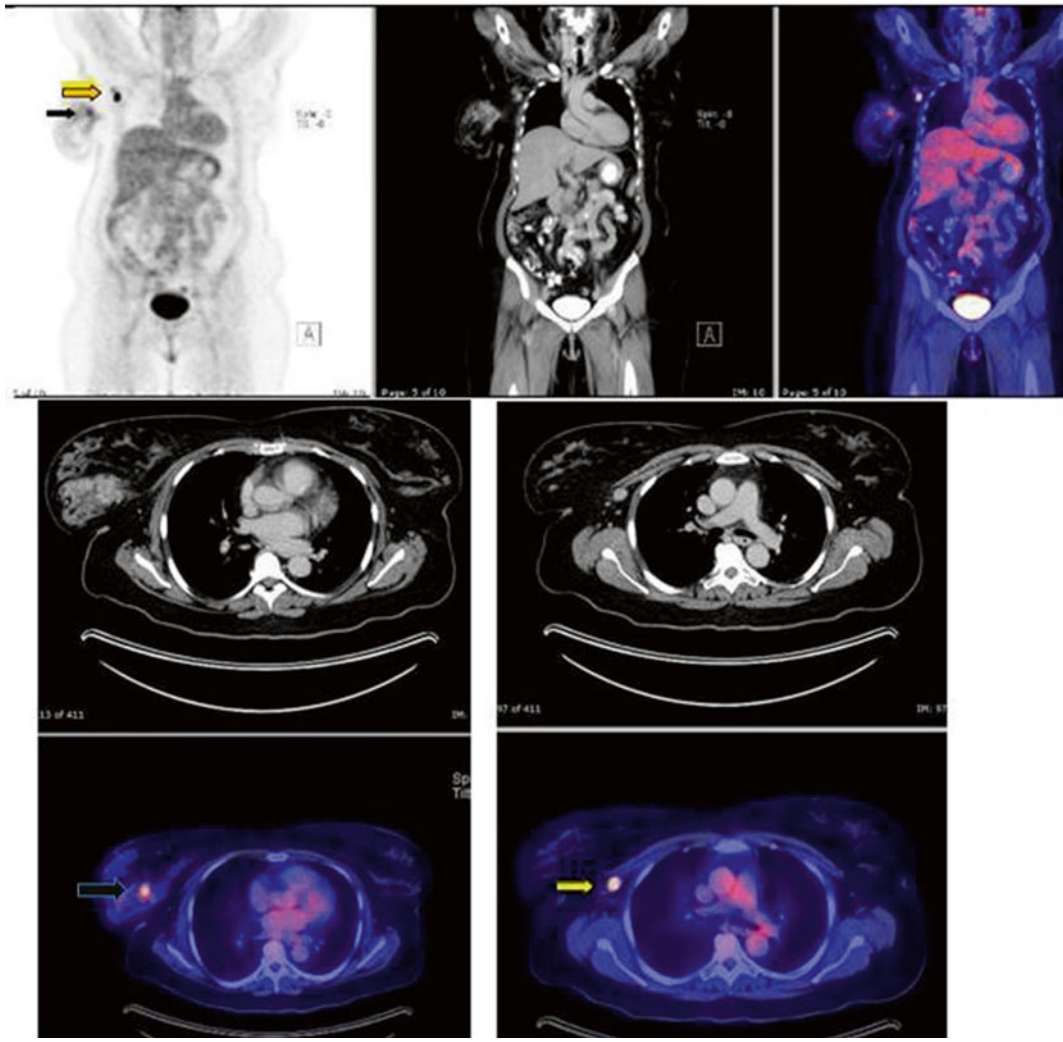

Fig. 3.1

Discussion

DCIS is defined as proliferation of epithelial cells confined to mammary ducts. The frequency of the diagnosis of DCIS has increased markedly in the United States since the widespread use of screening mammography [2]. DCIS comprises of a heterogeneous group of histopathological lesions that have been classified into several subtypes based primarily on architectural pattern: micropapillary, papillary, solid, cribriform, and comedo. Comedo-type DCIS appears to be more aggressive, with a higher probability of associated invasive ductal carcinoma [3].

Treatment options for patients with DCIS [2]:

1. Breast-conserving surgery and radiation therapy with or without tamoxifen
2. Total mastectomy with or without tamoxifen
3. Breast-conserving surgery without radiation therapy

Case 3.2: Invasive Breast Cancer

History

A 31-year-old female diagnosed with invasive right breast cancer and positive axillary metastases. She underwent modified radical mastectomy (MRM) and sentinel lymph node dissection, followed by chemotherapy.

Findings (Fig. 3.2)

(Right breast) Irregular enhancing mass measuring approximately $1.7 \times 1.3 \times 2.8$ cm, approximately 6 cm from the nipple, in the deep outer right breast (*white arrow*). No scan evidence of overlying skin, underlying muscle, or nipple involvement. (Left breast) No occult masses or abnormal areas of enhancement or adenopathy.

Findings (Fig. 3.3)

Hypermetabolic mediastinal lymph nodes seen best in coronal image on *left* (subcarinal lymph node showed SUVmax 6.6). Postsurgical changes in the right axilla. Minimally lytic, hypermetabolic lesion at L4, SUVmax 6.6 (*coronal view and bottom right axial image*).

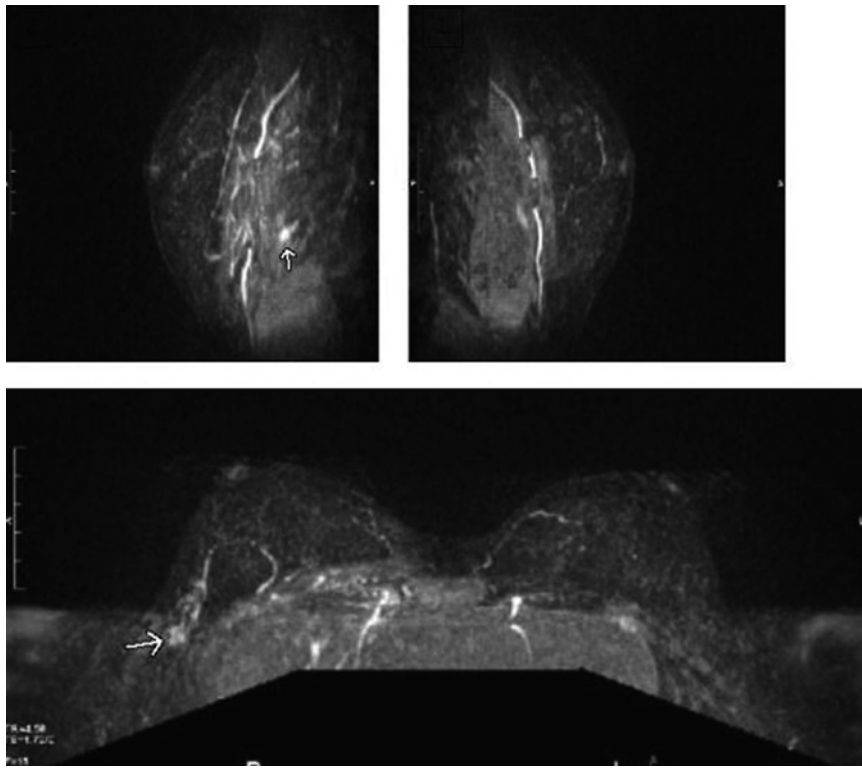

Fig. 3.2

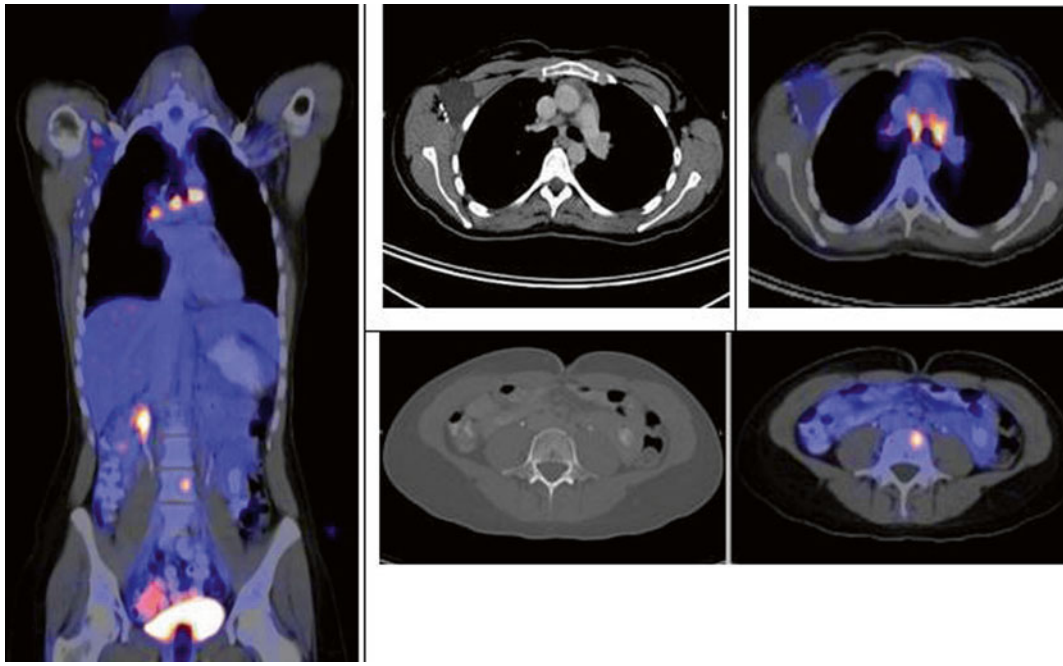

Fig. 3.3

Findings (Fig. 3.4)

Follow-up PET/CT (obtained 2 years from initial diagnosis and chemotherapy). Metabolic activity in the surgical bed of right axilla may represent chronic postsurgical changes versus residual disease. Resolution of hypermetabolic lymphadenopathy in the mediastinum. Resolution of hypermetabolic, L4 lytic lesion, now replaced by inactive, dense sclerosis, consistent with treated disease.

Impression

Interval resolution of activity within previously seen hypermetabolic mediastinal lymph nodes and L4 lytic lesion. Mild activity at the right axillary tail, likely postsurgical inflammation. No scan evidence of local recurrence.

Pearls and Pitfalls

FDG-PET is valuable for monitoring the effects of chemotherapy [4, 5]. Clinical examination and mammography are of limited use for monitoring the treatment response because of the difficulty in distinguishing fibrosis from residual tumor [1].

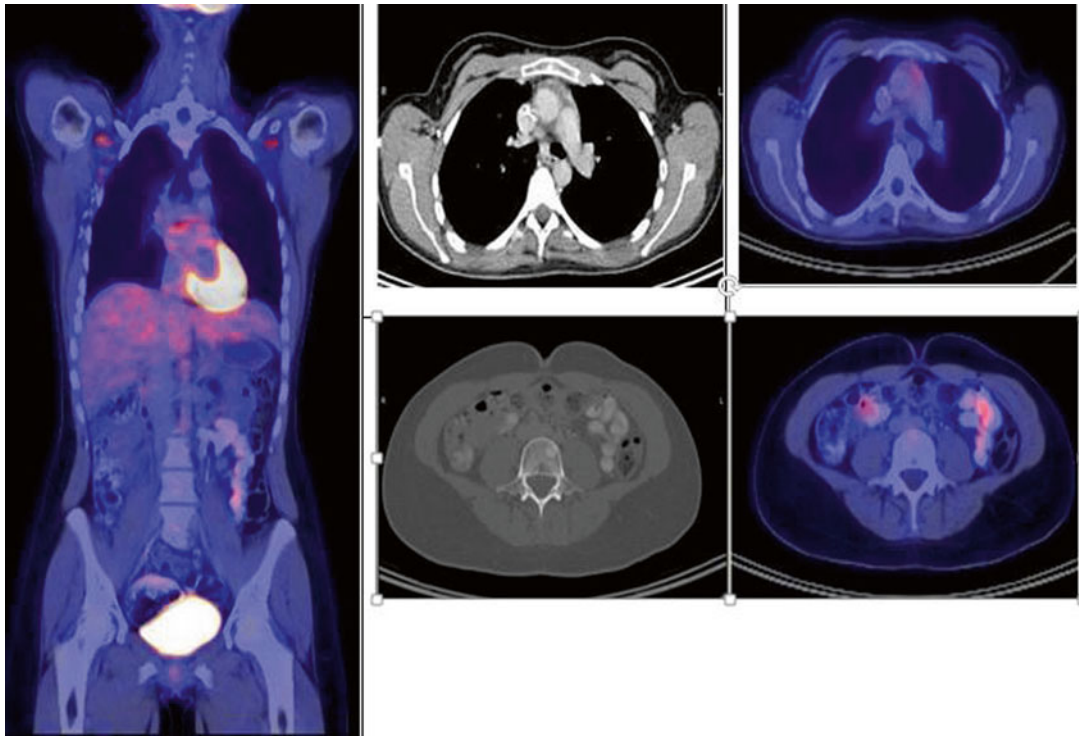

Fig. 3.4

However, false-positive FDG uptake has been observed in some benign breast diseases, e.g., in the presence of fibrocystic change, atypical ductal hyperplasia, ductal ectasia, and phyllodes tumor [1].

Discussion

PET can demonstrate changes in tumor metabolism before morphologic changes occur; thus, unresponsive tumors can be identified quickly. The uptake of FDG in a tumor after chemotherapy is predictive of the response to therapy; a treatment-induced reduction in metabolic activity correlates with a positive clinical response [1].

Practice guidelines from the SNM, National Comprehensive Cancer Network (NCCN), and other professional groups summarized for Breast Cancer (March, 2012):

1. Initial staging of patients with locally advanced or metastatic breast cancer when conventional staging studies (e.g., CT or bone scan) are equivocal or suspicious
2. Follow-up or surveillance of patients with breast cancer when conventional studies (e.g., CT or bone scan) are equivocal or suspicious

Case 3.3: Osseous Metastatic Disease Secondary to Intraductal Breast Carcinoma

History

A 54-year-old female, previously diagnosed with intraductal carcinoma (IDCA) of right breast, refused therapy, and now presents with stage IV disease.

Findings (Fig. 3.5)

Hypermetabolic, right subareolar mass also involving skin (known primary neoplasm), SUVmax 13.0, hypermetabolic satellite lesion lateral to the primary lesion (*yellow arrow*), right axillary lymph nodes, hypermetabolic contralateral left internal mammary lymph node (*axial PET image*), hypermetabolic retroperitoneal and pelvic lymphadenopathy (*coronal PET/CT images*). Multiple hypermetabolic osseous lesions (*coronal PET/CT images*) involving C5, left scapula, sternum, T7, L3 vertebrae. Pathologic compression fracture of L5. Hypermetabolic lesion involving sacral promontory, predominantly lytic left iliac bone lesion extending to the posterior left acetabulum (*red arrow*).

Impression

Stage IV, metastatic breast cancer with hypermetabolic nodal disease above and below the diaphragm and multiple osseous metastases.

Pearls and Pitfalls

^{18}F-FDG-PET/CT may be an independent prognostic factor for disease recurrence in patients with invasive ductal carcinoma [6]. Intraductal carcinoma also refers to as ductal carcinoma in situ (DCIS).

Discussion

Skeletal metastases of breast cancer mainly occur from lymphatic spread and hematogenous dissemination. A part of the sternal metastasis could occur via lymphatic vessels to parasternal lymph node. The prognosis of patients with solitary metastatic bone lesions, especially sternal metastasis, may be different from that of multiple skeletal metastasis, because

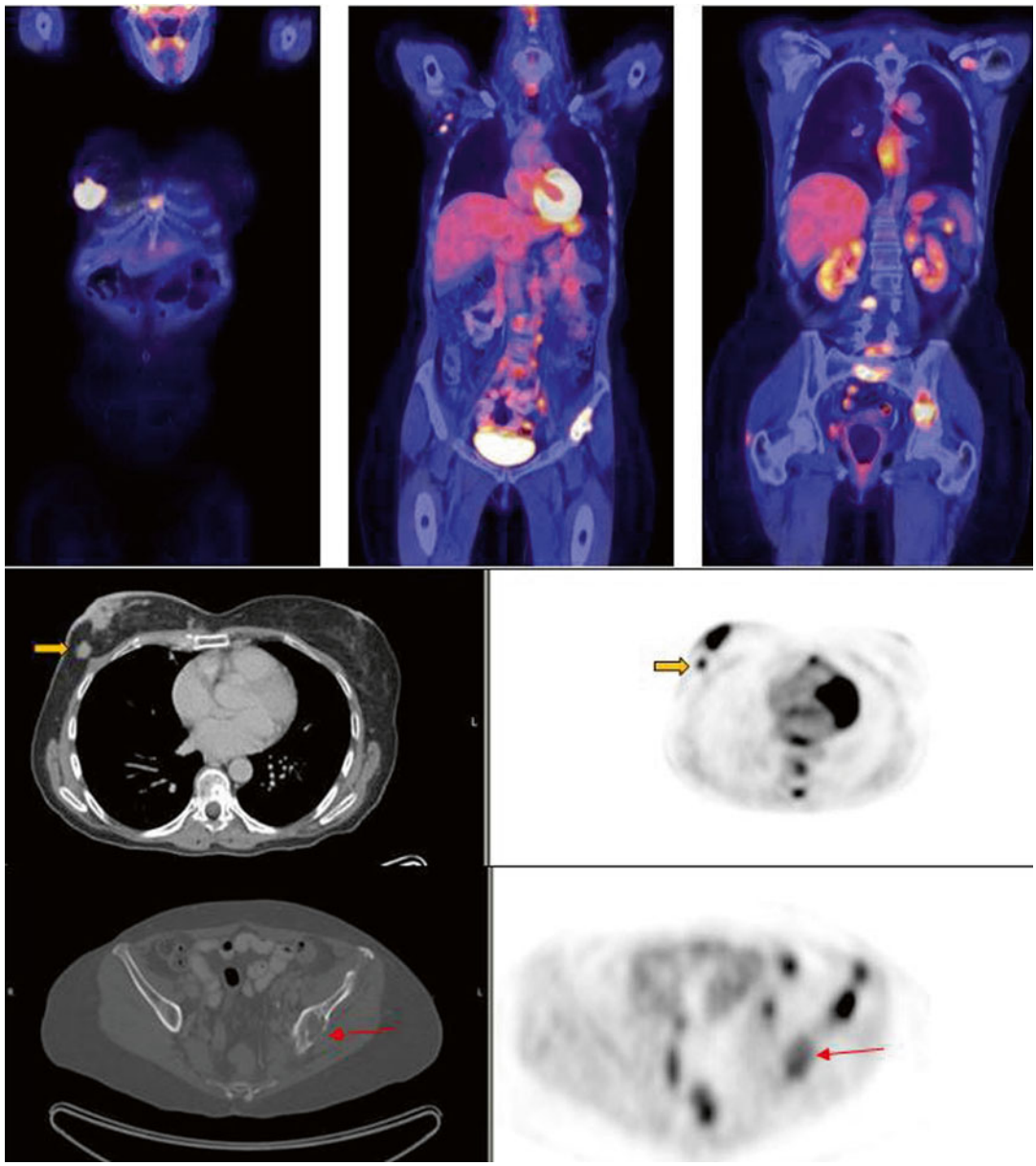

Fig. 3.5

sternal metastasis may be caused by local tumor invasion from either the primary site or adjacent lymph nodes [7]. Coleman et al. [8] reported that important prognostic factors for survival after the development of osseous metastasis in breast cancer depended on the histopathological grade of the primary tumor, ER status, presence of skeletal metastasis at initial breast cancer diagnosis, disease-free interval, and age.

Case 3.4: Metastatic Breast Cancer

History

A 5-year-old female with right breast cancer and hepatic metastases, on chemotherapy.

Findings (Fig. 3.6)

(*Top row image*) Hypermetabolic solitary right axillary LN, SUVmax 6.8, consistent with metastatic disease. (*Middle row image*) Hypermetabolic

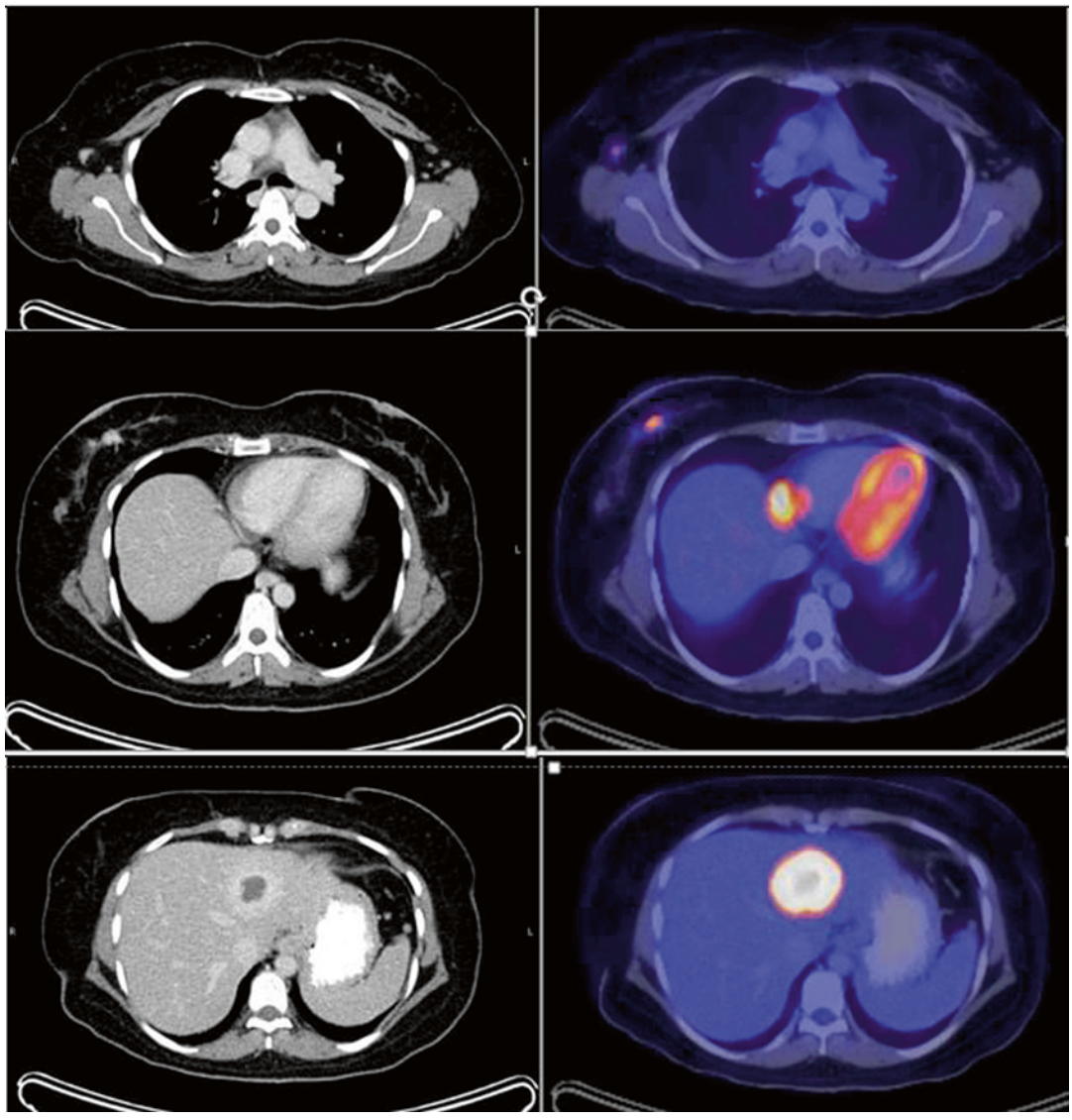

Fig. 3.6

soft tissue density in the medial quadrant of the lower right breast, SUVmax 8.3, consistent with known breast primary. (*Bottom row image*) Large hypermetabolic left hepatic lobe lesion, SUVmax 14.0, with central necrosis.

Impression

Hypermetabolic right breast primary neoplasm with ipsilateral right axillary LN metastasis and hypermetabolic hepatic metastasis.

Pearls and Pitfalls

PET/CT may be more sensitive than serum tumor markers in detecting relapse of breast cancer [9].

Discussion

$^{(90)}$Y radio embolization (selective internal radiation therapy [SIRT]) has emerged as a valuable therapeutic option in unresectable, chemotherapy-refractory hepatic metastases from breast cancer. The change in SUV (max) as assessed by (18)F-FDG-PET/CT before and 3 mos after SIRT was identified as the only independent predictor of survival in patients with hepatic metastases of breast cancer [10].

Case 3.5: Stage IV Breast

History

A 55-year-old female presented with pathologic fracture of the left femoral neck. Shown below are images from the initial PET/CT *(top row in figs 3.7, 3.8, 3.9, 3.10)* and follow-up PET/CT (performed 6 months following chemotherapy, *bottom row in figs 3.7, 3.8, 3.9, 3.10*).

Findings (Figs. 3.7, 3.8, 3.9, and 3.10, *top rows*)

Pretherapy images showed focally hypermetabolic, spiculated right breast lesion, SUVmax 5.2, with mildly hypermetabolic right axillary lymph node, SUVmax 2.4, and FDG avid right hilar lymph node. Intense activity at the left femoral neck corresponds to a lytic lesion causing pathologic fracture, seen best in Fig. 3.10 (*top*).

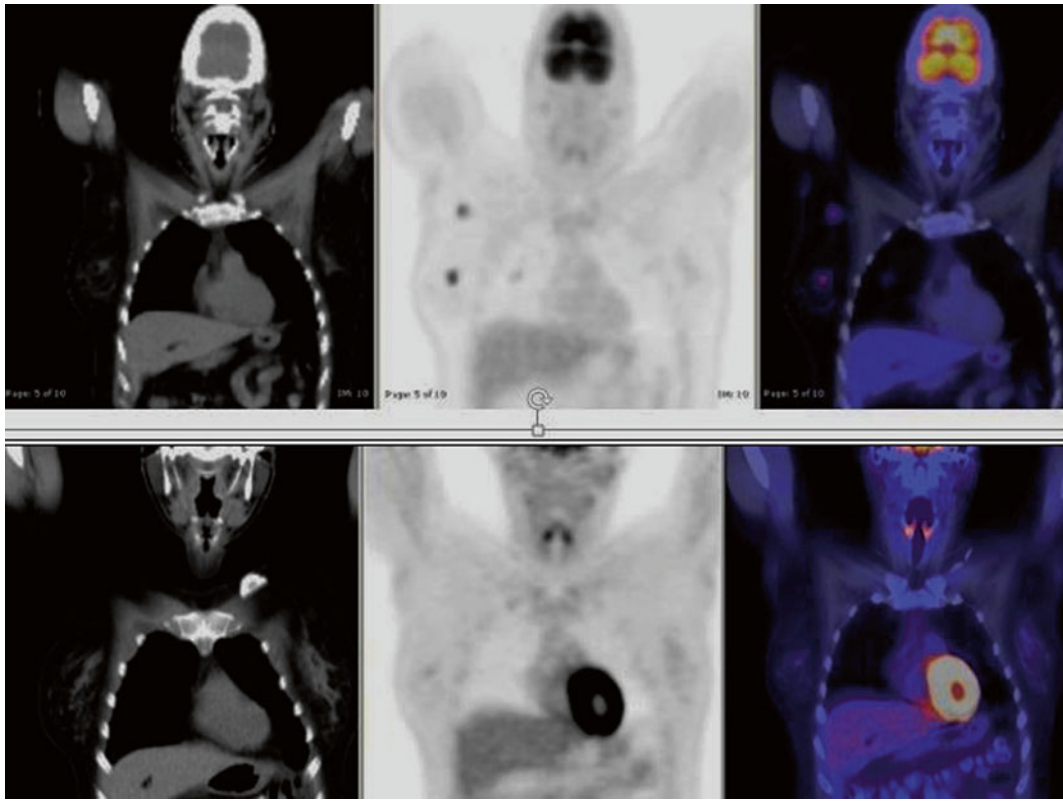

Fig. 3.7

Findings (Figs. 3.7, 3.8, 3.9, and 3.10, *bottom rows*)

Post-therapy images showed resolution of metabolic activity within previously noted primary breast neoplasm and hypermetabolic right axillary lymph node.

No abnormal activity in the right breast (status post lumpectomy), resolution of metabolic activity within previously noted hypermetabolic right axillary lymph node. Status post left hip arthroplasty, with resection of previously noted hypermetabolic osseous lesion. No scan evidence of metabolically avid disease elsewhere.

Impression

Stage IV breast cancer demonstrating excellent response to chemotherapy by scan pattern.

Pearls and Pitfalls

FDG-PET/CT can improve staging and alter therapeutic options in patients suspected to have breast cancer recurrence with or without distant metastatic disease, primarily by demonstrating local or distant nodal

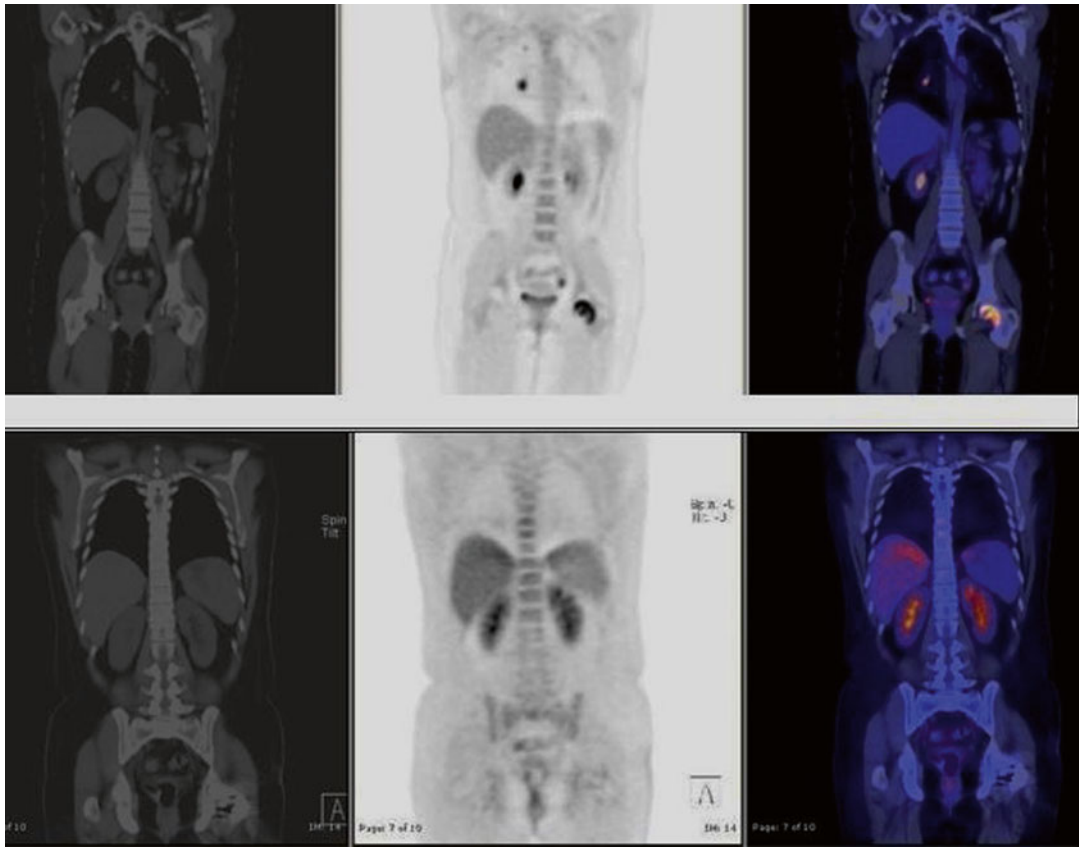

Fig. 3.8

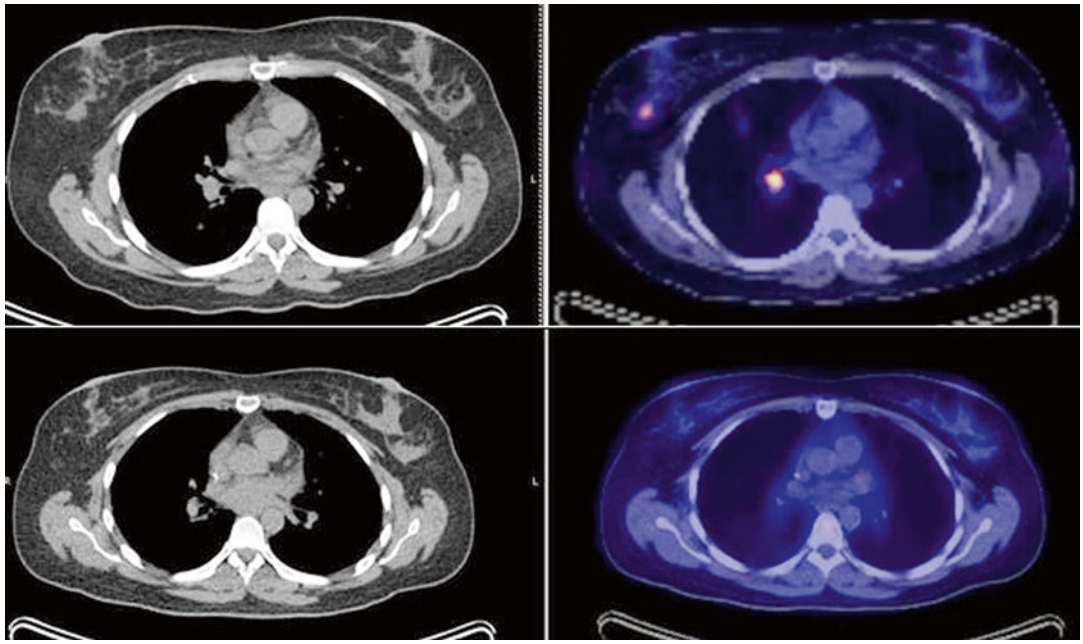

Fig. 3.9

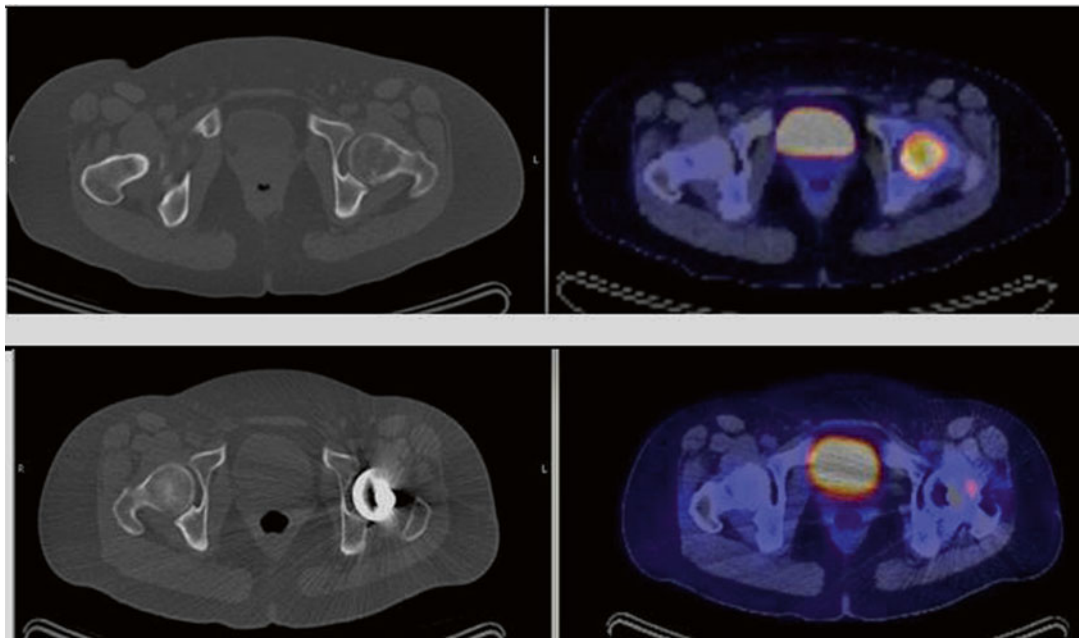

Fig. 3.10

involvement, which may present as occult at other imaging studies [11]. FDG-PET is complementary to bone scintigraphy, which remains the standard imaging procedure for surveying the skeleton for metastatic involvement. FDG-PET can be particularly useful in this setting to evaluate the response of metastatic breast cancer to systemic therapy, since conventional imaging is often challenging in this setting.

Discussion

There are two major patterns of disease spread in metastatic breast carcinoma, excluding patients with extensive diffuse metastases [12]. Patients with ER+/PR+ tumors tend to develop osseous but not brain metastases. Patients with ER−/PR− tumors tend to develop brain but not osseous metastases. Appreciation of these distributions can aid the radiologist in detecting metastatic lesions and will help the clinician to estimate the likelihood of metastases to various organ systems as well as to potentially target therapy.

Case 3.6: Invasive Ductal Carcinoma

History

A 53-year-old female, undergoing workup for invasive ductal carcinoma of right breast.

Findings (Fig. 3.11)

(Right breast; top left) Retroareolar spiculated mass corresponding to known invasive ductal carcinoma. Evidence of nipple involvement including enhancement and inversion, diffuse skin thickening and enhancement, consistent with inflammatory breast carcinoma. BI-RADS 6. An additional 1.5 cm enhancing mass at the 11:00 axis. The position of this second mass relative to the retroareolar mass above results in a total span of disease of approximately 5.6 cm. BI-RADS 5. Multiple abnormal level one right axillary lymph nodes, the largest of which measures approximately 4.4 cm AP × 3.2 cm ML × 2.3 cm SI, consistent with metastases. BI-RADS 5. (Left breast; top right): Normal appearing 1.1 cm intramammary lymph node. No significant MR abnormalities identified. BI-RADS: 1

Findings (Figs. 3.12 and 3.13)

Hypermetabolic primary neoplasm with satellite lesion in the right breast, presence of metastatic right axillary lymph node (seen best in coronal images, Fig. 3.12) with overlying skin thickening, demonstrating inflammatory changes (Fig. 3.13).

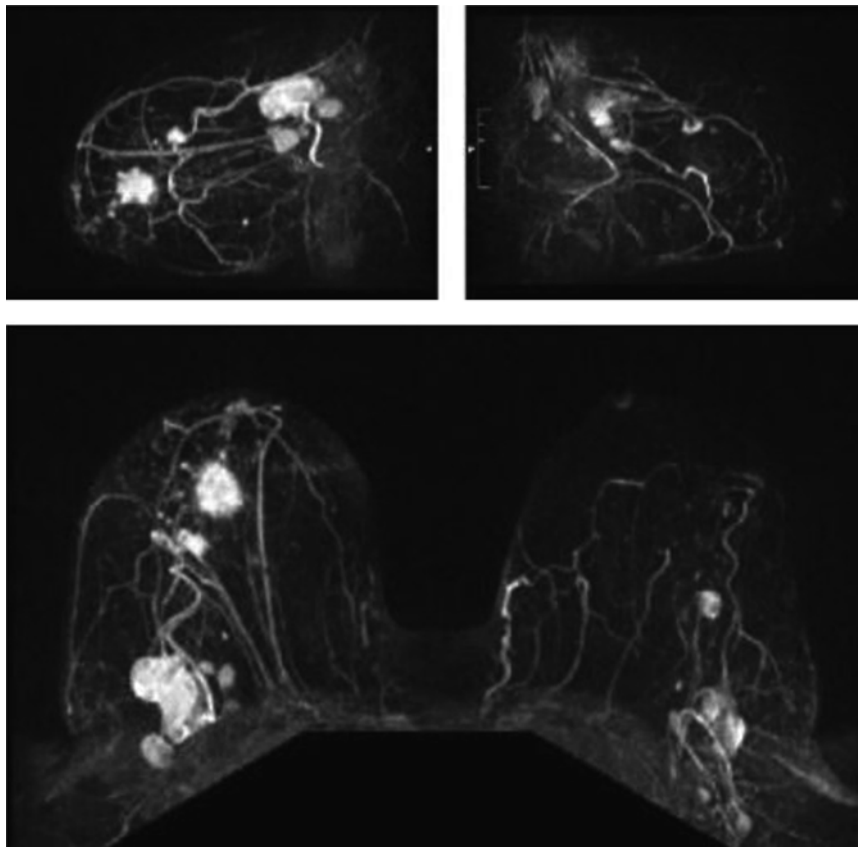

Fig. 3.11

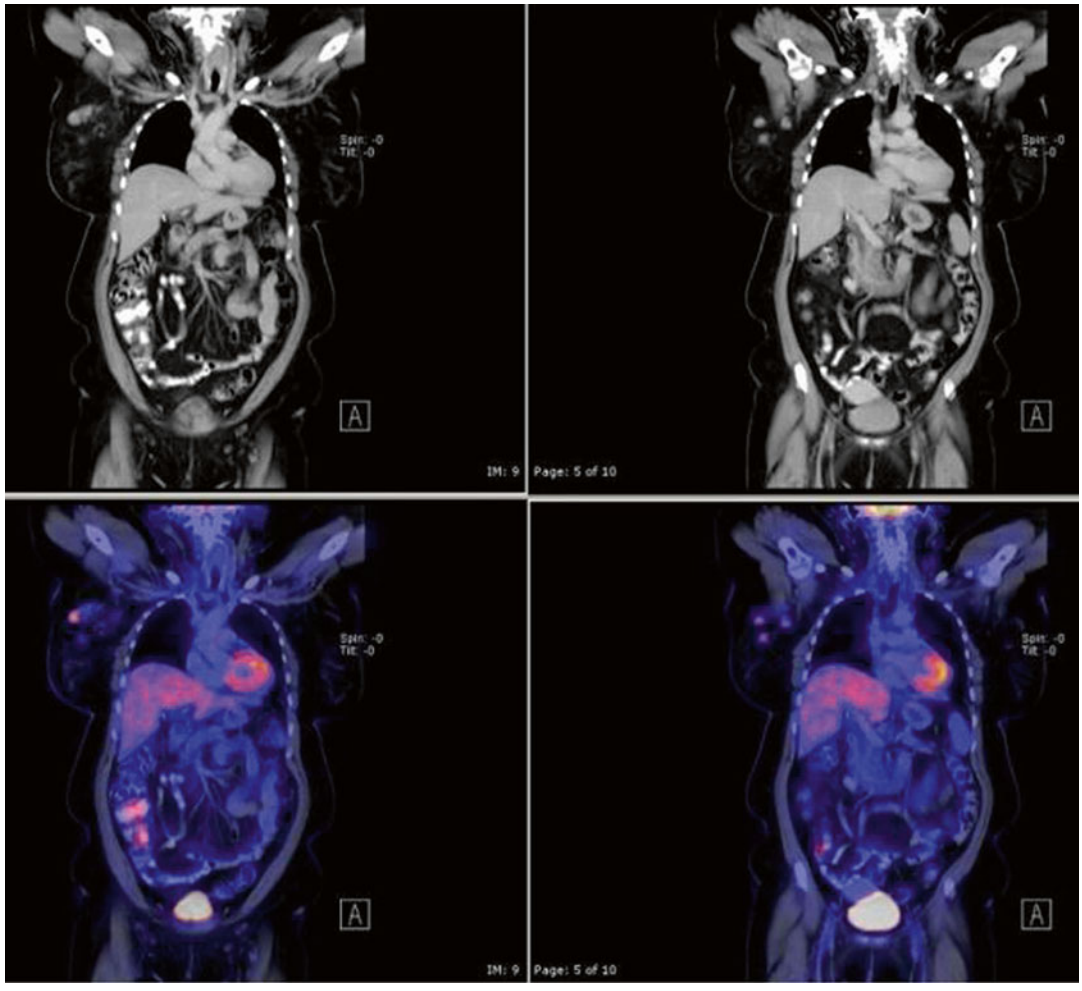

Fig. 3.12

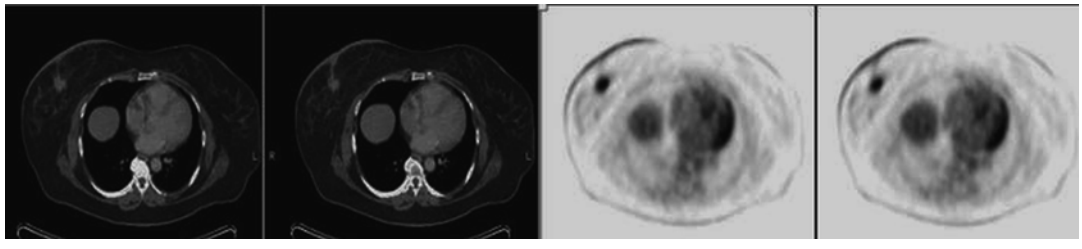

Fig. 3.13

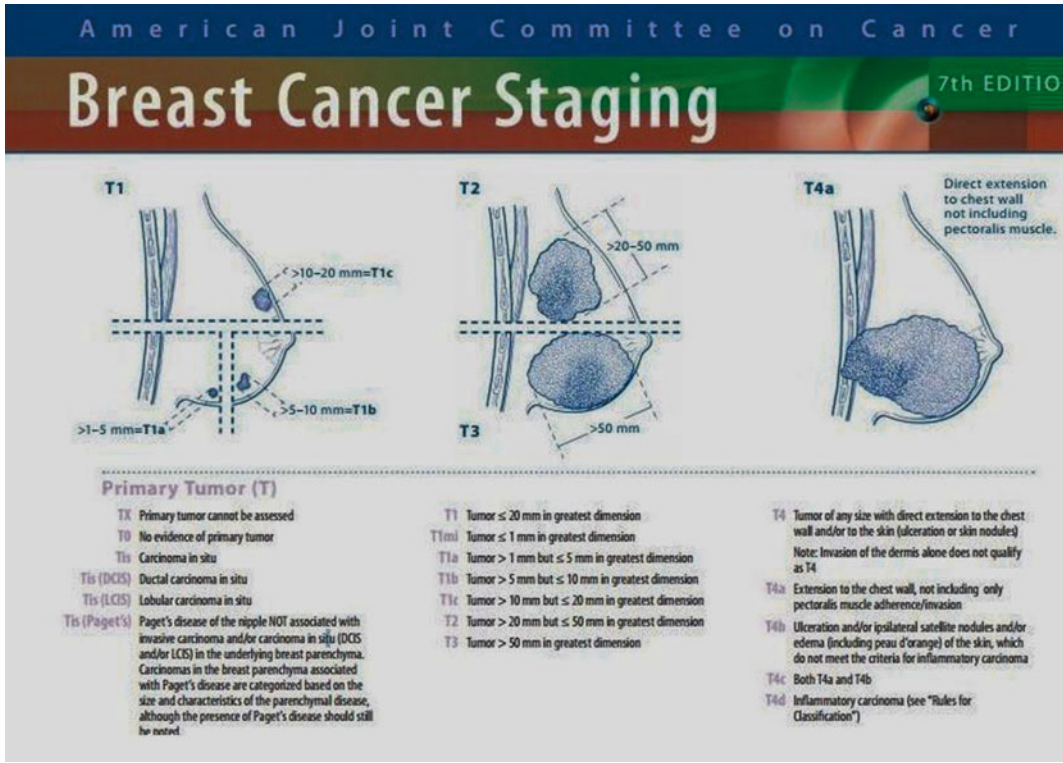

Fig. 3.14

Impression

Stage IIIB, breast cancer.

Discussion (Fig. 3.14)

The most common system used to describe the stages of breast cancer is the American Joint Committee on Cancer (AJCC) TNM system [13].

Case 3.7: Male Breast Cancer

History

A 73-year-old male with history of right breast carcinoma, status post (s/p) right mastectomy, showed disease progression over the course of 4 years.

Findings (Fig. 3.15)

Initial PET images showed hypermetabolic metastatic disease in T6 and T9 vertebrae and the left hepatic lobe. Similar study obtained 4 years later showed disseminated osseous metastasis, numerous hepatic lesions, metastatic pleural disease, and metastatic nodal disease.

Impression

Progression of hypermetabolic metastatic disease in a case of male breast ca, s/p mastectomy.

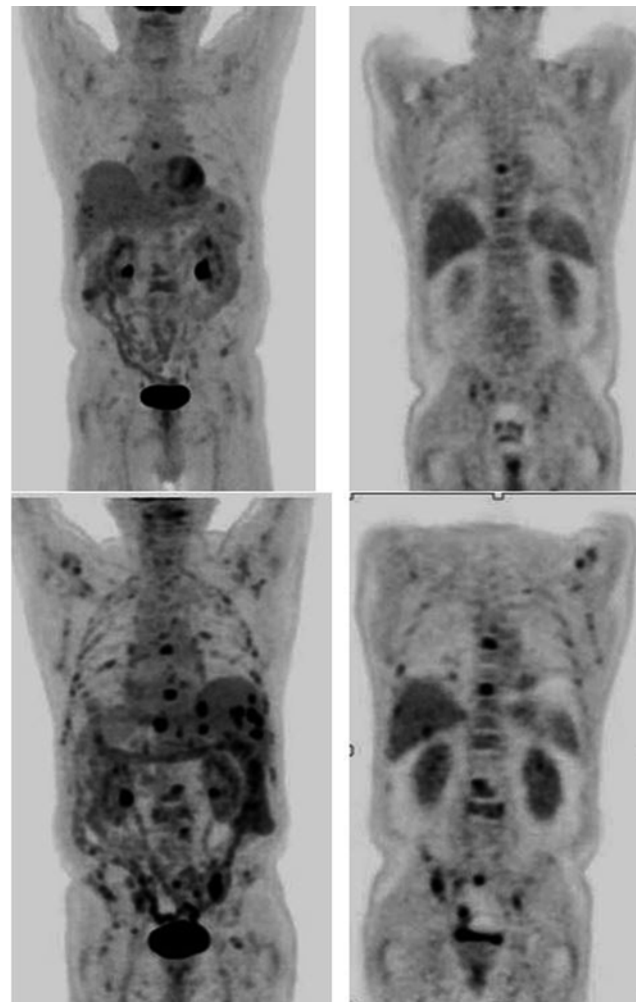

Fig. 3.15

Discussion

Men at any age may develop breast cancer, but it is usually seen in men between 60 and 70 years of age. Male breast cancer makes up less than 1 % of all cases of breast cancer. Risk factors for breast cancer in men may include the following [14]:

1. History of radiation exposure
2. Having a disease related to high levels of estrogen in the body, such as cirrhosis (liver disease) or Klinefelter syndrome (a genetic disorder)
3. Having several female relatives who have had breast cancer, especially relatives who have an alteration of the BRCA2 gene

---

Case 3.8: Role of Positron Emission Mammography (PEM) in Breast Cancer

History

A 50-year-old female, newly diagnosed with invasive breast cancer in the upper outer quadrant of the right breast.

Findings (Fig. 3.16)

(Right breast; top left) In the central 10 o'clock axis approximately 5 cm deep to the nipple, there is a 2.9 × 2.6 × 2.2 cm spiculated enhancing mass, consistent with the site of biopsy-proven invasive malignancy. No evidence of nipple, skin, or chest wall involvement. No satellite lesions identified. Remainder of the breast and the right axilla appears unremarkable. Right breast MRI BI-RADS: 6. (Left breast; top right): No occult masses, abnormal areas of enhancement, or adenopathy. Left breast MRI BI-RADS: 1.

Findings (Fig. 3.17)

Known breast neoplasm demonstrating intense FDG uptake in the 10 o'clock axis of the right breast, SUVmax = 8.2. The remainder of the right breast was normal. Right breast PEM BI-RADS: 6. (No abnormality in the left breast; left breast PEM BI-RADS1—image not shown).

Impression

Intensely hypermetabolic right breast mass, corresponding to known primary neoplasm, proven on biopsy.

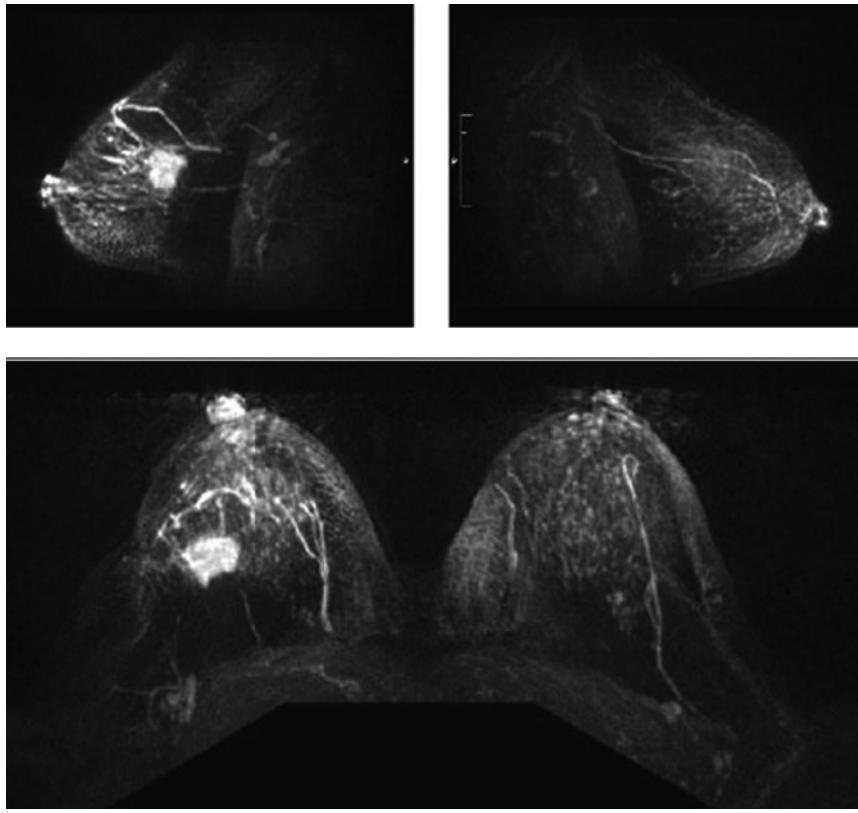

Fig. 3.16

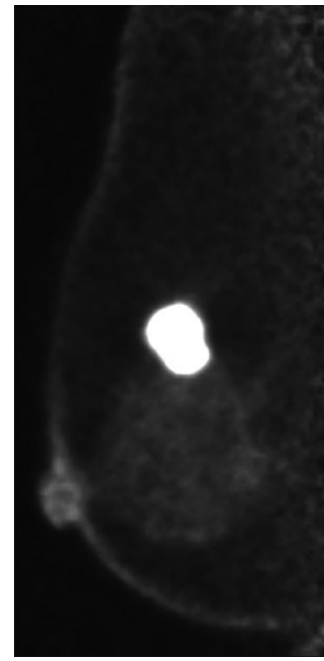

Fig. 3.17

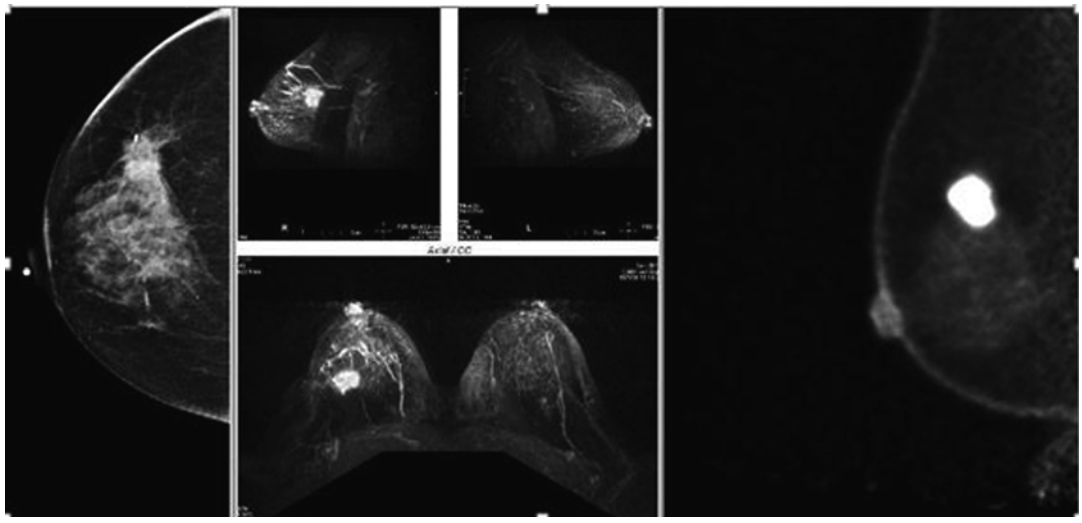

Fig. 3.18 Comparison view, mammogram, MRI breast, and PEM of the same patient

Discussion

Dedicated breast positron emission mammography (PEM) units have been developed to overcome the limitations of whole-body PET and to provide a positron emission imaging platform capable of detection and depiction of primary breast carcinoma [11]. In general, these systems consist of two planar detectors placed opposite a gently compressed breast. The advantages of such dedicated systems include improved geometric sensitivity, higher spatial resolution, shorter imaging time, and reduced attenuation compared with whole-body PET systems. They also have a small physical footprint, which makes their use in a breast imaging facility feasible and allows correlation of the results with those of conventional breast imaging as well as PEM-guided biopsy.

Case 3.9: Breast Activity in a Case of Nodal Non-Hodgkin's Lymphoma

History

A 38-year-old female, newly diagnosed with NHL following biopsy of a left neck mass.

Findings (Fig. 3.19)

Asymmetric, diffuse left breast activity (SUVmax 4.3), corresponding to dense left breast tissue on concurrent CT. Diffuse, increased FDG activity involving medial two-third of left clavicle and adjacent soft tissue, medial head of left clavicle, shows SUVmax 4.4, corresponding to biopsy-proven diagnosis of NHL.

Impression

Finding consistent with preferential lactating breast status in a setting of active NHL.

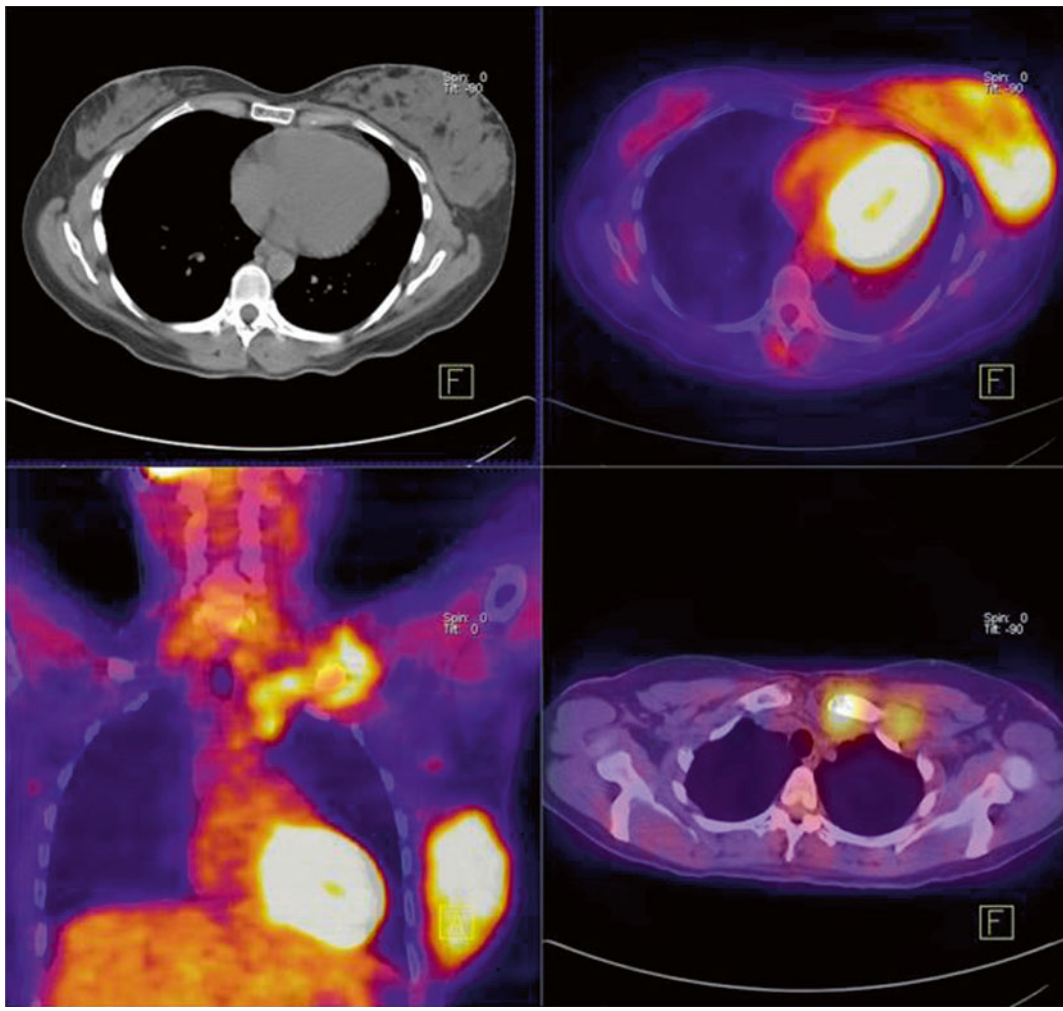

Fig. 3.19

Pearls and Pitfalls

The lactating breast has been reported to show FDG uptake related to increased glucose trapping in active glandular tissue, causing false-positive readouts. Tissue density and hormonal status also affect the uptake of FDG in the breast; dense breasts have significantly greater FDG uptake than do fatty breasts. However, the ability to discriminate between benign and malignant breast lesions is unlikely to be affected by normal physiologic uptake in the breast, because the average SUV of normal breast tissue is low [1].

Discussion

Some of the administered ^{18}F-FDG might be excreted in small amounts in breast milk. Normally, the scan should be delayed until breast-feeding has stopped. But if the scan is needed urgently, then it is advisable to collect milk before the scan, so that this can be used to provide a feed after the scan [15]. Furthermore, milk should be collected and discarded for 2 h after the scan. Normal breast-feeding can resume after that.

Case 3.10: Diffuse Large Cell Lymphoma of Breast

History

A 48-year-old female presents with diffuse large cell lymphoma (DLBCL) of the right breast.

Findings (Fig. 3.20)

Hypermetabolic soft tissue density anterior to the right breast implant, SUVmax 7.5. Left breast tissue is relatively less dense with low-grade activity, possibly related to postsurgical changes following left breast implant removal.

Impression

Diffuse soft tissue activity within the right breast consistent with biopsy-proven diagnosis of DLBCL. Likely postsurgical changes in the left breast.

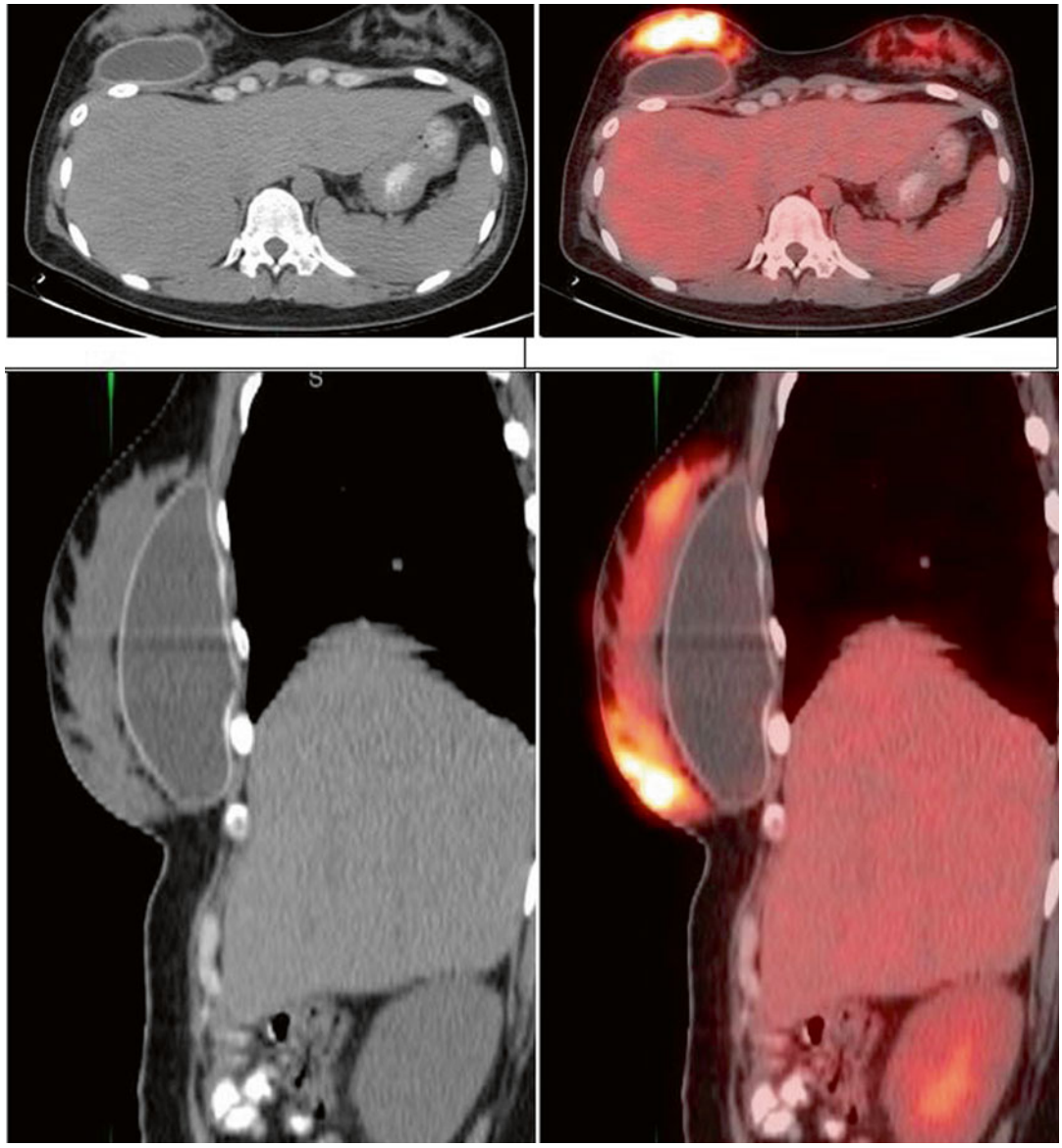

Fig. 3.20

Discussion

Primary breast lymphoma (PBL) and breast involvement in systemic lymphoma are rare [16]. Primary breast DLBCL appears to have a worse prognosis than early stage DLBCL in nodal or other extra nodal sites.

There is no consensus on the question of how to best treat PBL. Mastectomy offers no benefit in the treatment of PBL. The combined

therapy approach, with chemotherapy and radiotherapy, is the most successful treatment. PBL is poorly represented in rituximab-containing trials in DLBCL patients; there is not much experience with this agent in breast DLBCL. Because of the high incidence of central nervous system (CNS) involvement in PBL patients, many authors strongly believe that patients with aggressive forms of PBL should receive CNS infiltration prophylaxis [17].

References

1. Lim HS, Yoon W, et al. FDG PET/CT for the detection and evaluation of breast diseases: usefulness and limitations. Radiographics. 2007;27:S197–213. doi:10.1148/rg.27si075507October.
2. Ductal carcinoma in situ. http://www.cancer.gov/cancertopics/pdq/treatment/breast/healthprofessional/page4.
3. Fisher ER, Dignam J, Tan-Chiu E, et al. Pathologic findings from the National Surgical Adjuvant Breast Project (NSABP) eight-year update of protocol B-17: intraductal carcinoma. Cancer. 1999;86(3):429–38 [PUBMED Abstract].
4. Jansson T, Westlin JE, Ahlstrom H, Lilja A, Langstrom B, Bergh J. Positron emission tomography studies in patients with locally advanced and/or metastatic breast cancer: a method for early therapy evaluation? J Clin Oncol. 1995;13:1470–7.
5. Bassa P, Kim EE, Inoue T, et al. Evaluation of preoperative chemotherapy using PET with fluorine-18-fluorodeoxyglucose in breast cancer. J Nucl Med. 1996;37:931–8.
6. Song BI, Lee SW, et al. ^{18}F-FDG uptake by metastatic axillary lymph nodes on pretreatment pet/ct as a prognostic factor for recurrence in patients with invasive ductal breast cancer. J Nucl Med. 2012;53(9):1337–44.
7. Koizumi M, et al. Comparison between solitary and multiple skeletal metastatic lesions of breast cancer patients. Ann Oncol. 2003;14(8):1234–40. doi:10.1093/annonc/mdg348.
8. Coleman RE, Smith P, Rubens RD. Clinical course and prognostic factors following bone recurrence from breast cancer. Br J Cancer. 1998;77:336–40.
9. Diagnosis of breast cancer metastasis with PET/CT in patients with elevation of tumor markers. http://www.asco.org/ASCOv2/Meetings/Abstracts?&vmview=abst_detail_view&confID=100&abstractID=60273.
10. Haug AR, Tiega Donfack BP, et al. 18F-FDG PET/CT predicts survival after radio embolization of hepatic metastases from breast cancer. J Nucl Med. 2012;53(3):371–7. Epub 2012 Feb 13.
11. Rosen EL, et al. FDG PET, PET/CT, and breast cancer imaging. Radiographics. 2007;27:S215–29. doi:10.1148/rg.27si075517October.
12. Maki DD, et al. Patterns of disease spread in metastatic breast carcinoma: influence of estrogen and progesterone receptor status. AJNR Am J Neuroradiol. 2000;21:1064–6.
13. Cancer staging poster series. http://www.cancerstaging.org/staging/index.html.
14. Male breast cancer. http://www.cancer.gov/cancertopics/pdq/treatment/malebreast/Patient/page5.

15. Radiation protection of patients. https://rpop.iaea.org/RPOP/RPoP/Content/InformationFor/HealthProfessionals/6_OtherClinicalSpecialities/PETCTscan.htm#PETCT_FAQ08.
16. Pisani F, et al. Diffuse large B cell lymphoma involving the breast: a report of four cases. J Exp Clin Cancer Res. 2006;25(2):277–81.
17. Mouna B, et al. Primary malignant non-Hodgkin's lymphoma of the breast: a study of seven cases and literature review. World J Surg Oncol. 2012;10:151. doi:10.1186/1477-7819-10-151.

4 Esophageal and Gastric Neoplasms

Shahram Bonyadlou and Abtin Doroudinia

Case 4.1

History

A 73-year-old male with history of metastatic gastric carcinoma and peritoneal disease, on chemotherapy. Patient is status post total gastrectomy and splenectomy.

Findings

Review of images demonstrates a large hypermetabolic mass in the left mid to upper abdomen at the site of multiple surgical clips with SUVmax of 10.0 (Fig. 4.1). A hypermetabolic mesenteric focus in the mid abdomen inferior to the left hepatic lobe demonstrates SUVmax of 5.3 is identified (Fig. 4.2). Focal activity along the medial aspect of colon in the right lower quadrant is compatible with serosal involvement with SUVmax of 4.1 (Fig. 4.3). Focal FDG activity at the presacral area likely represents a hypermetabolic iliac lymph node with SUVmax of 8.4 (Fig. 4.4). Correlation of the areas with increased PET activity with specific anatomic locations was difficult due to the complete lack of intraperitoneal fat causing poor definition of intra-abdominal structures.

Impression

1. Multiple hypermetabolic peritoneal and mesenteric metastatic disease
2. Pelvic nodal metastatic disease

P.S. Conti, A. Kaushik (eds.), *PET-CT*, DOI 10.1007/978-1-4419-5811-2_4

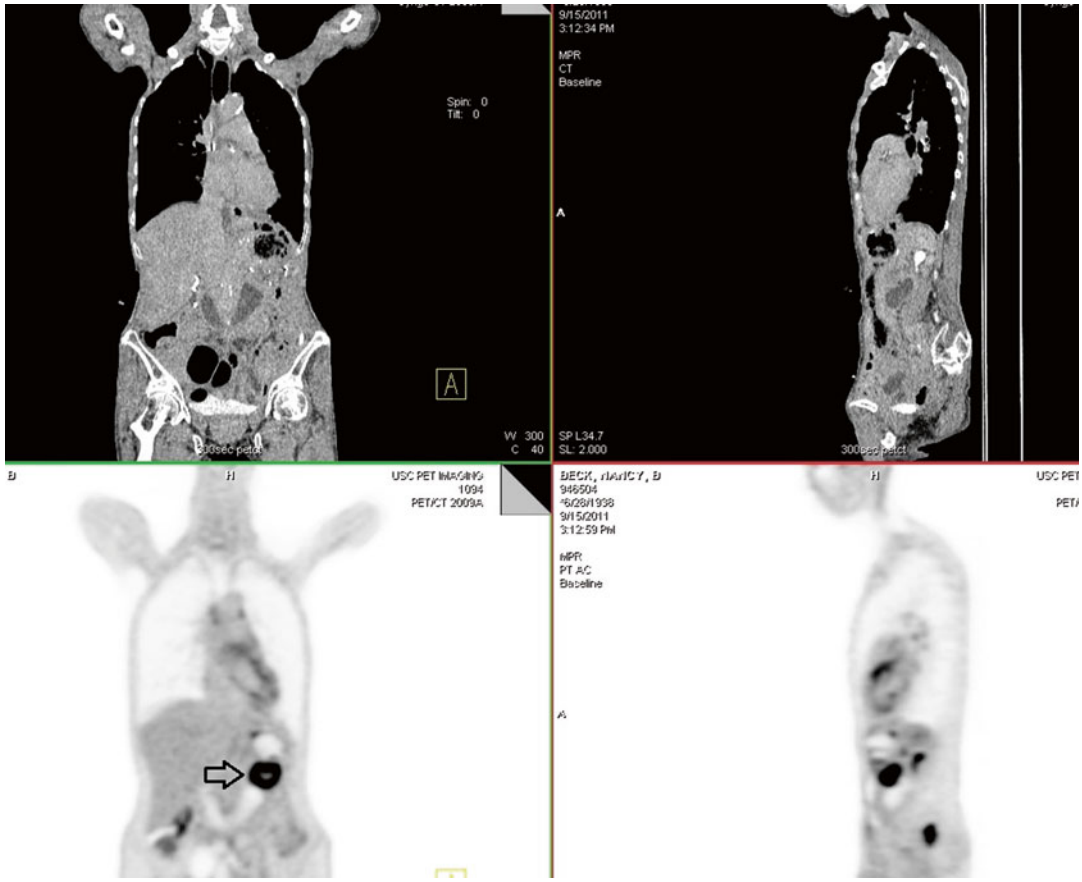

Fig. 4.1

Pearls and Pitfalls

1. FDG PET may be useful in evaluation of recurrent gastric cancer as well as detecting distant metastatic disease
2. Staging of gastric cancer with FDG PET scanning will alter the clinical management in patients with recurrence and complement standard staging methods such as laparoscopy, which are more effective at staging local nodal spread and peritoneal disease

Discussion

Gastric cancer is one of the most prevalent cancers worldwide and is a leading cause of cancer mortality. Complete resection of gastric cancer is the only method of achieving permanent control. However, surgeries can be morbid and futile in patients who have advanced disease, making appropriate staging and characterization of disease burden of paramount importance.

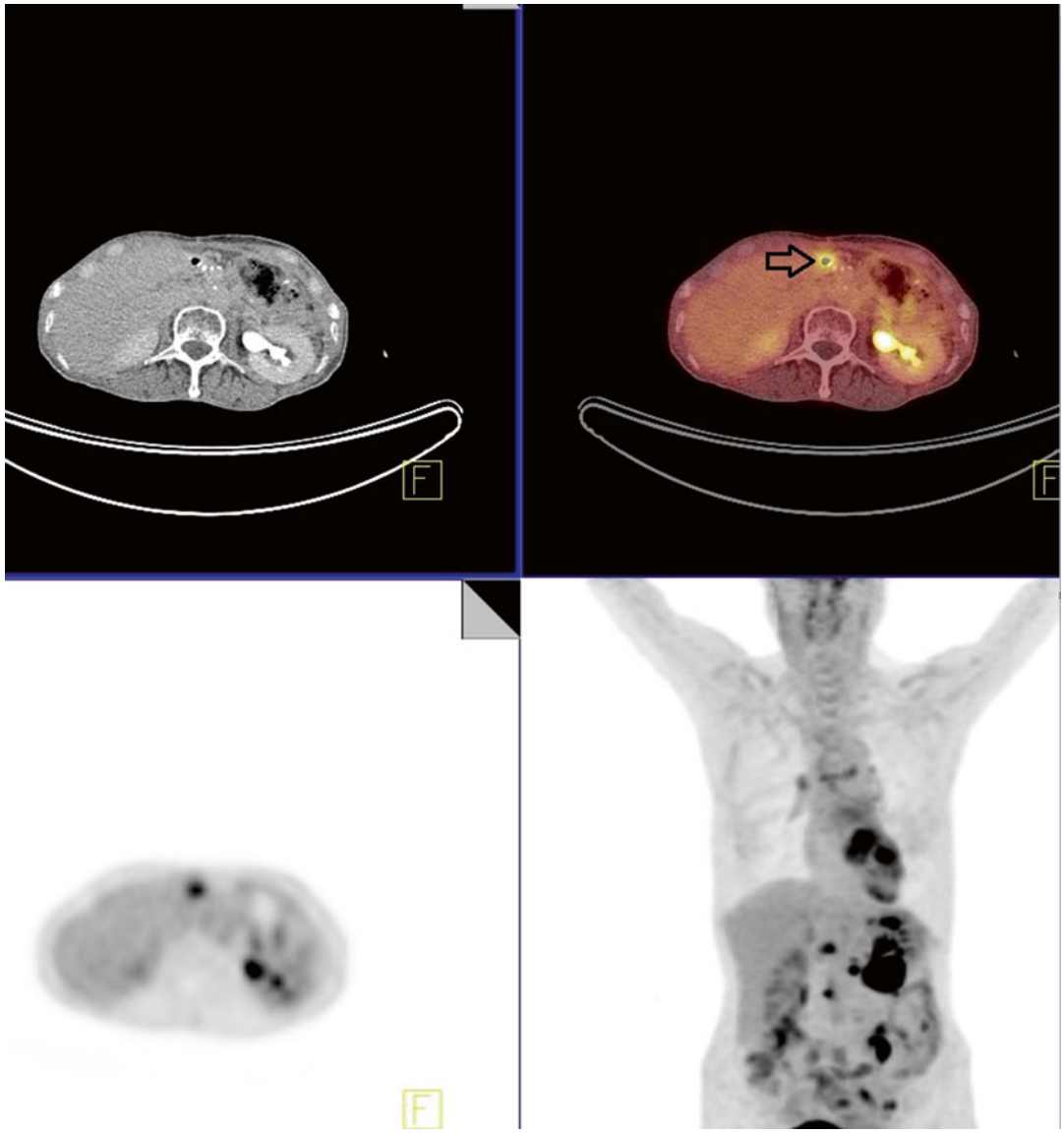

Fig. 4.2

The value of PET-CT has been of increasing interest among clinicians and increased its use in the detection, staging, and management of a variety of malignancies. During and after therapy, PET-CT may be useful in determining response to chemotherapy. It may be helpful for restaging and diagnosing recurrence at an earlier time or with greater certainty.

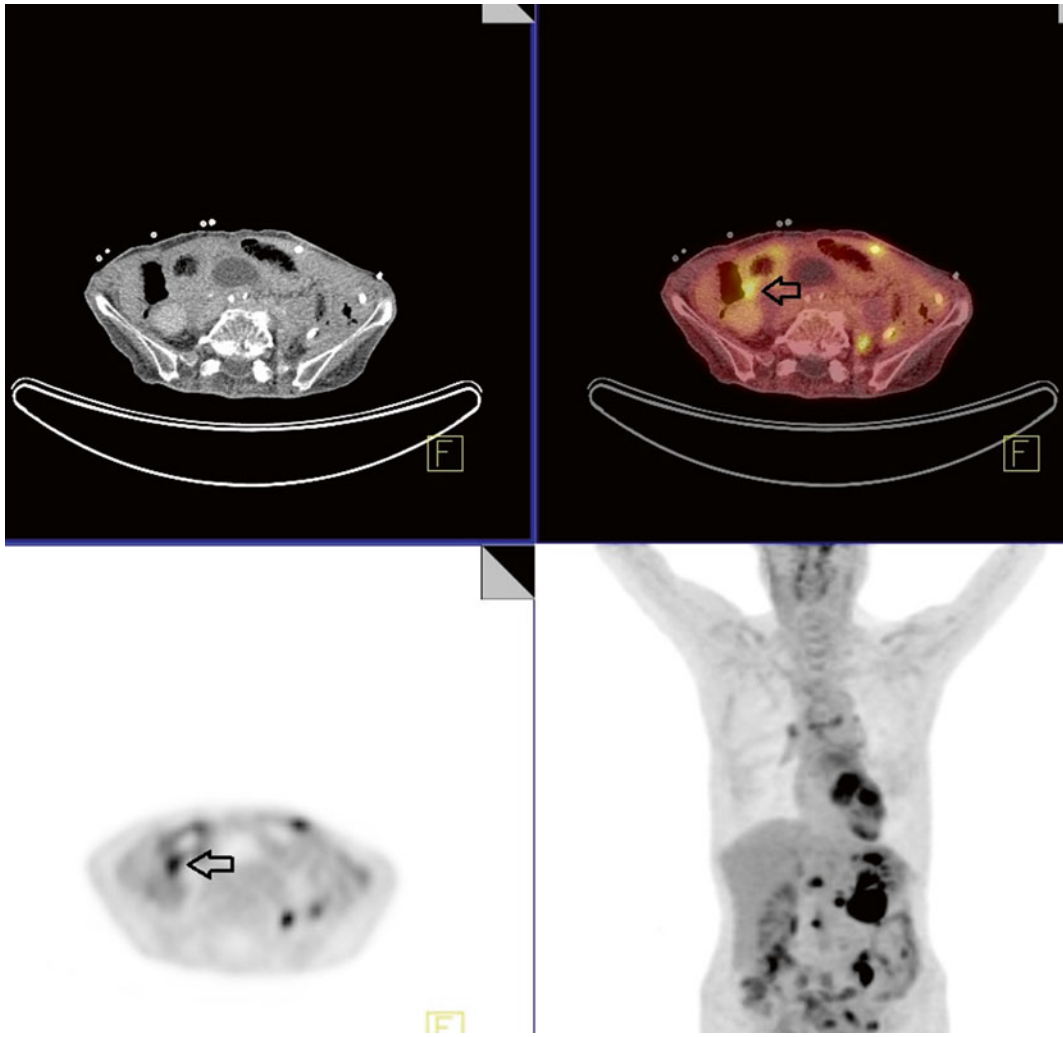

Fig. 4.3

Case 4.2

History

A 53-year-old male patient with submucosal squamous cell carcinoma of the esophagus, status post thoracic laparoscopic esophagectomy with gastric pull-up.

Findings

A hypermetabolic mass measuring 4 × 4.1 × 4.2 cm with SUVmax 19.9 in the proximal esophageal anastomosis is identified. There were no enlarged or hypermetabolic hilar, mediastinal, or axillary lymph nodes (Fig. 4.5).

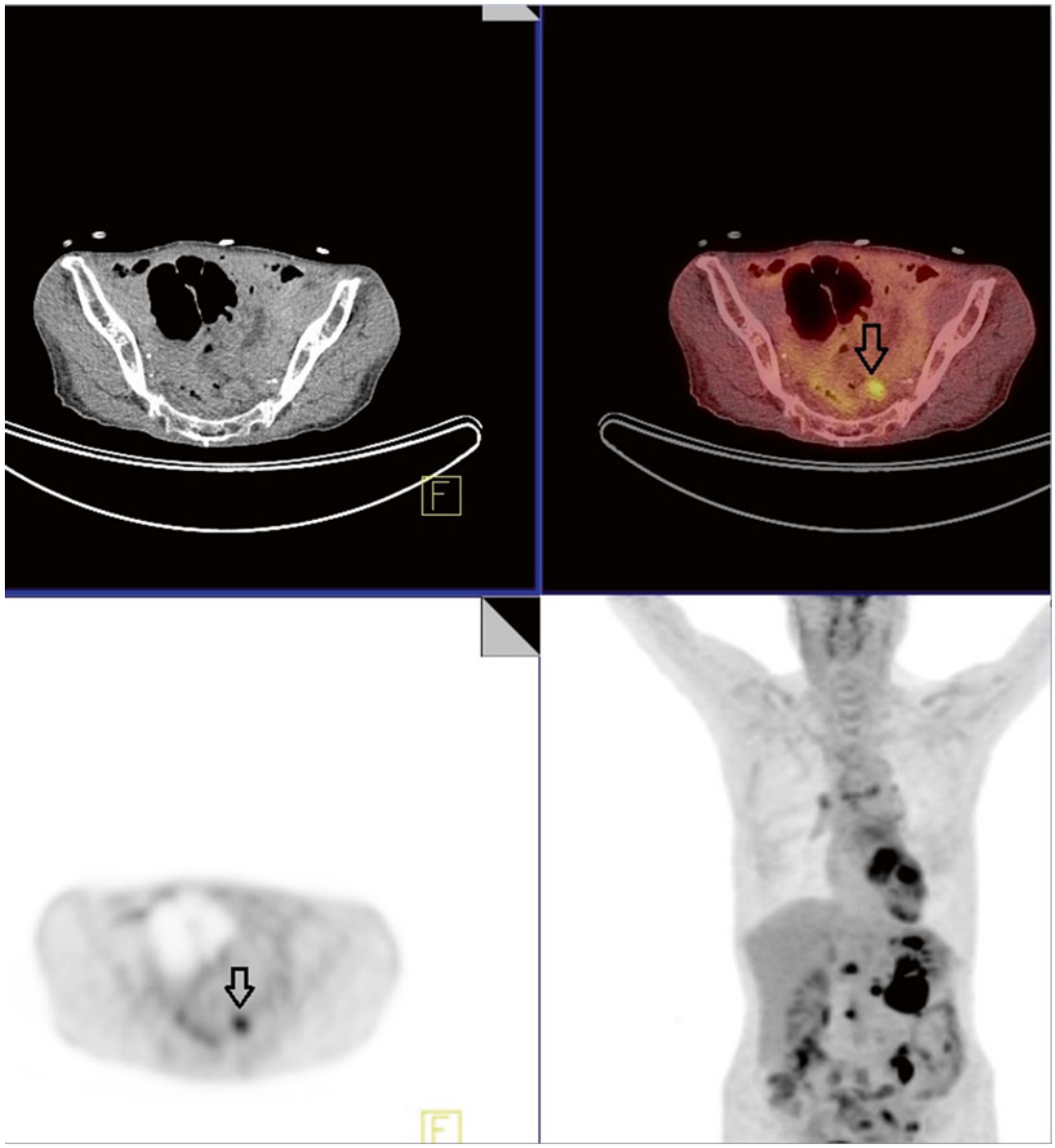

Fig. 4.4

Impression

1. Hypermetabolic mass at the proximal esophagogastric anastomotic site, consistent with locally recurrent disease
2. No nodal or distant metastatic disease

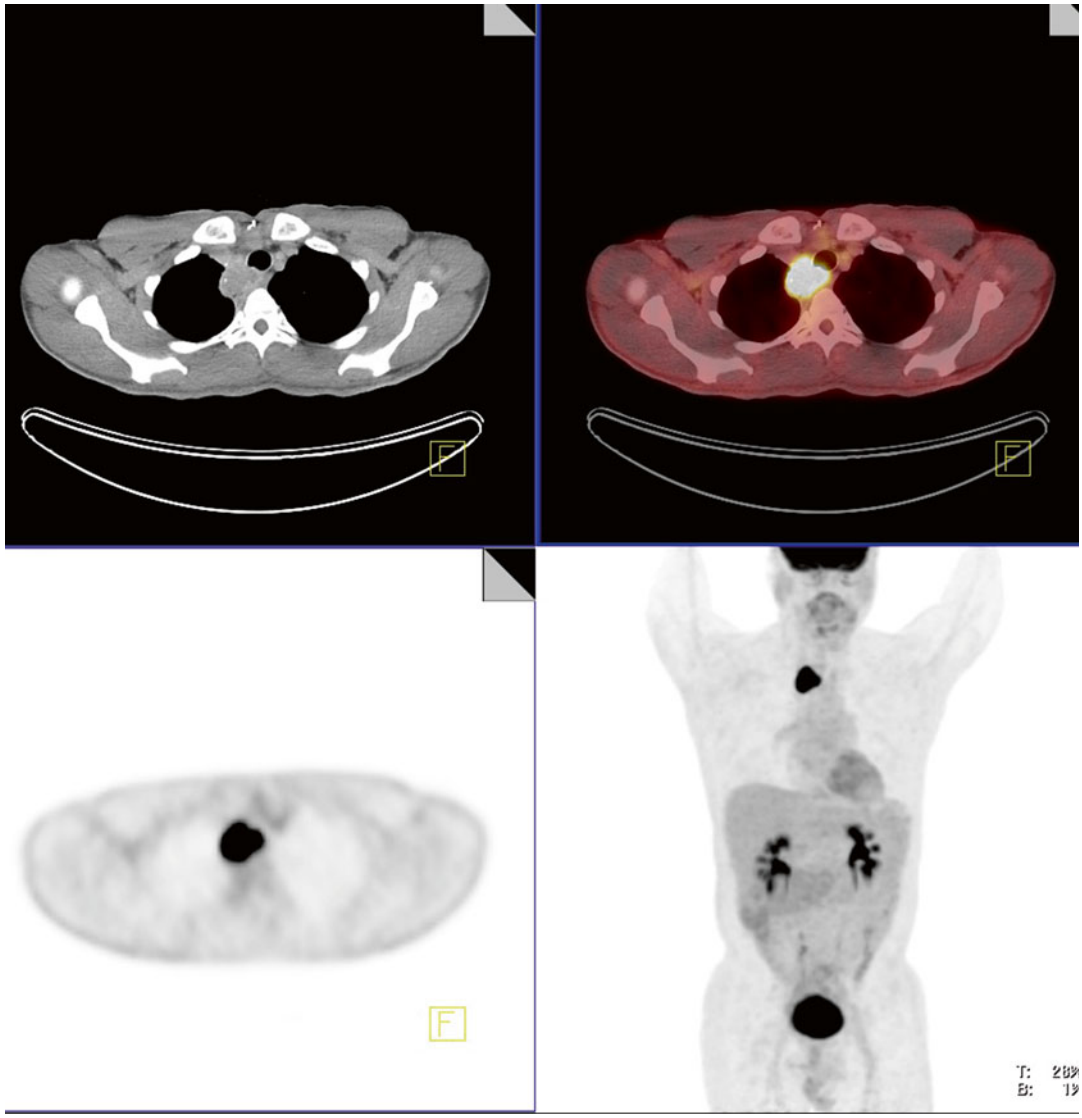

Fig. 4.5

Pearls and Pitfalls

1. Sensitivities for FDG PET imaging are between 91 and 100 %. False-positive uptake can occur due to inflammation, and there can be normal mild FDG activity from muscular contractions.
2. Accuracy of FDG PET in the staging of regional lymph node metastases ranges from 24 to 90 %. The major limitation of FDG PET with regard to the detection of nodal metastases adjacent to the primary tumor is its relatively poor spatial resolution (approximately 6 mm for a dedicated PET scanner) which reduces sensitivity. The level of metabolic activity and pattern of mediastinal and hilar lymph nodes as well as coexisting nodal calcification is helpful in determining inflammatory versus metastatic etiology.
3. Recurrence is most common near the esophagogastric anastomosis.

Discussion

Because esophageal cancer is associated with unfavorable prognosis, proper assessment of primary tumor and regional/distant metastasis is necessary for treatment selection and follow-up planning. The depth of invasion and presence of lymph node metastasis are independent prognostic variables in esophageal cancer. Open esophagectomy with comprehensive lymph node dissection is the most accurate method for pathologic staging as well as the most common treatment method for esophageal cancer. However, this operation is frequently associated with significant morbidity, and a mortality rate from experienced institutes is reported in the range of 6–7 %. There are several noninvasive staging methods for esophageal cancer. Endoscopic ultrasound (EUS) and ^{18}F-FDG PET have recently shown good results for clinical staging in esophageal cancer. The degree of ^{18}F-FDG uptake in the primary tumor presenting as the standardized uptake value (SUV) is associated with prognosis in esophageal cancer.

Case 4.3

History

Patient with invasive well-differentiated adenocarcinoma of the distal esophagus.

Findings

There is a hypermetabolic distal esophageal circumferential thickening with SUVmax of 17.4, consistent with biopsy-proven tumor (Fig. 4.6). There are subcentimeter subcarinal and right hilar nodes with SUVmax of 3.3 and 2.9, respectively. Constellation of latter findings is most suggestive of granulomatous disease by pattern. There was also an AP window node with SUVmax of 4.5, measuring 6 mm (white arrow), also more suggestive of inflammatory (likely granulomatous disease) than malignant etiology (Fig. 4.7). There are several subcentimeter mediastinal nodes with no PET activity but below PET resolution. No enlarged or hypermetabolic axillary lymph nodes are identified.

Impression

1. Hypermetabolic distal esophageal mass consistent with biopsy-proven malignancy
2. Hypermetabolic mediastinal lymph nodes as noted above

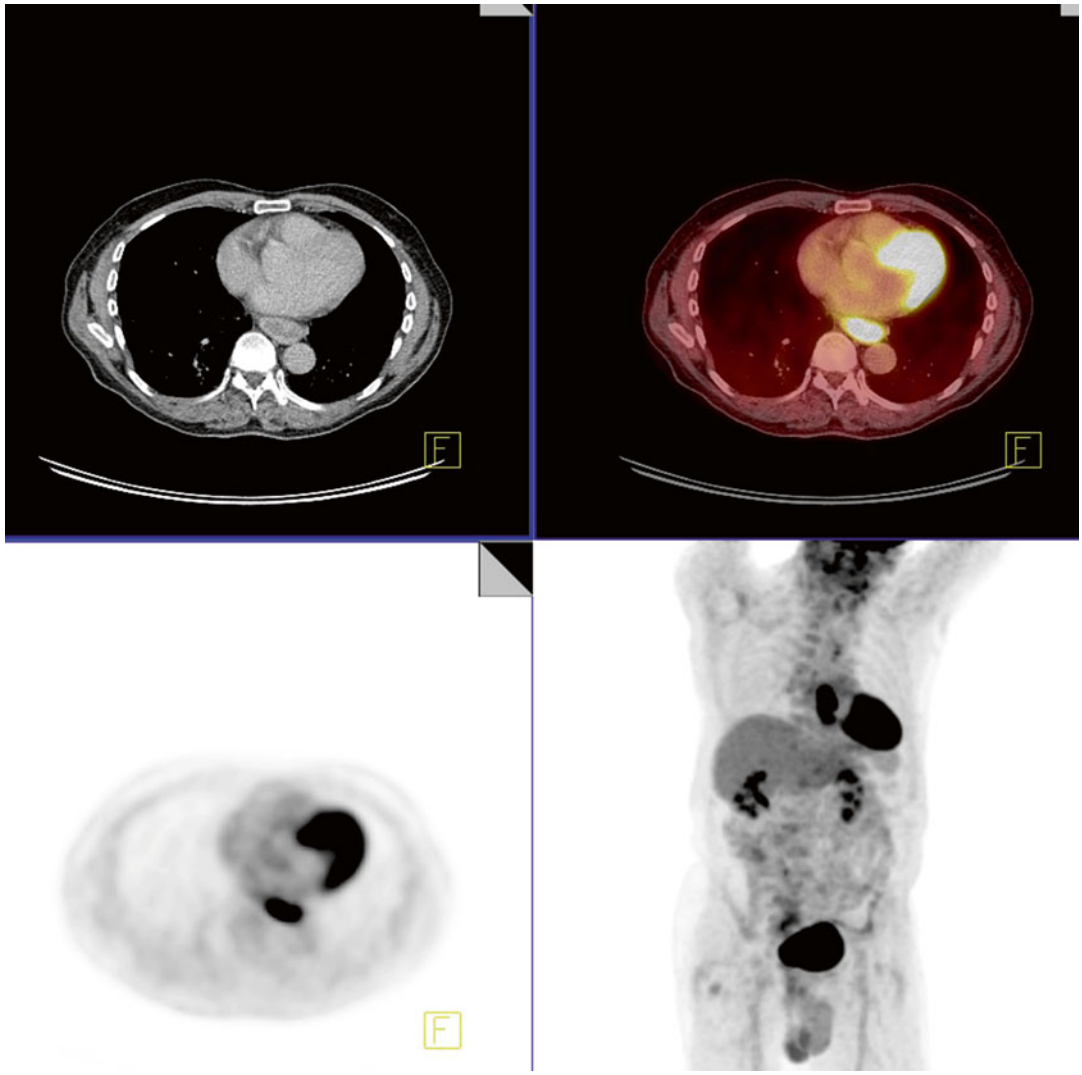

Fig. 4.6

Pearls and Pitfalls

1. PET is a useful tool for staging in esophageal cancer prior to surgical intervention and has higher accuracy in comparison with CT (88 % versus 65 %).
2. PET is not sensitive enough to assess local invasion.
3. Carcinoma in situ and small volume tumors are predisposing factors for false-negative PET.

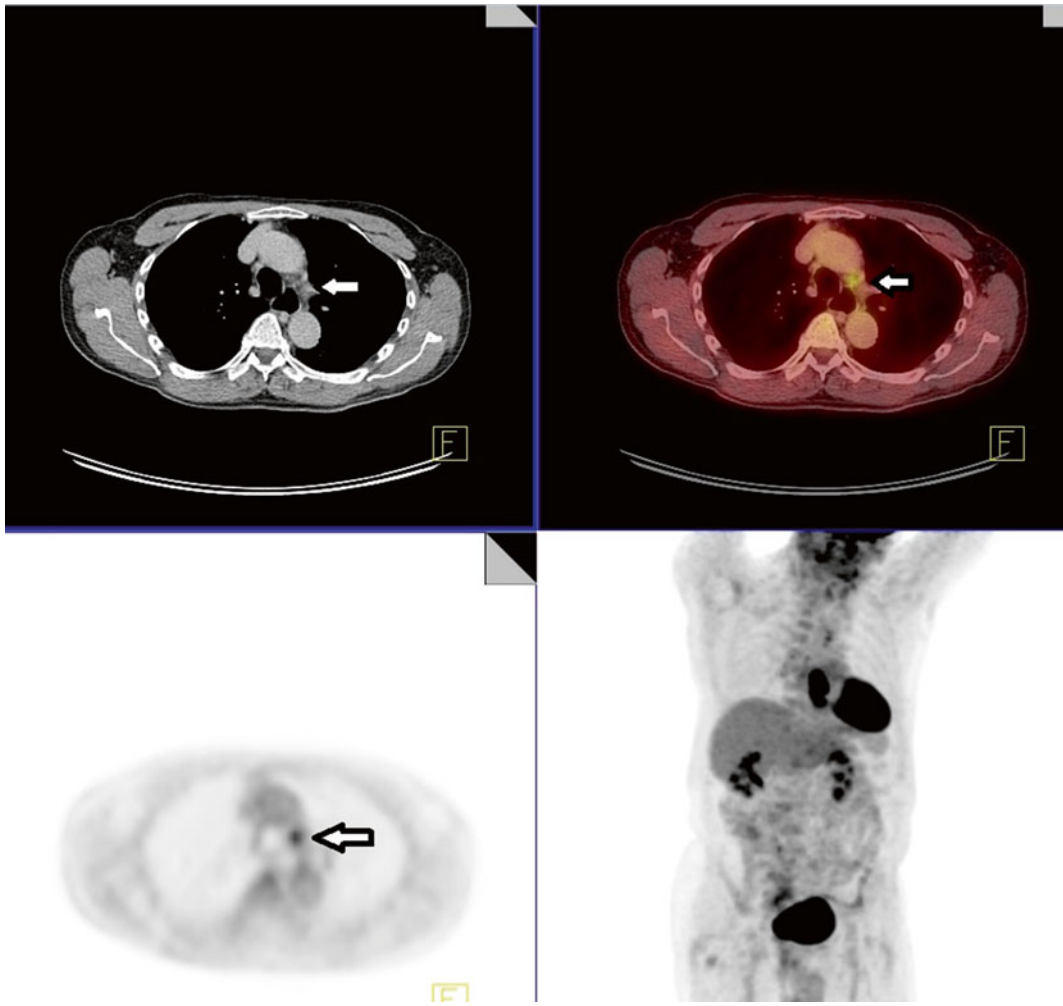

Fig. 4.7

Discussion

There are two histologic types of esophageal carcinoma that account for the majority of malignant cases: squamous cell carcinoma (>75 to 90 %) and adenocarcinoma. Esophageal cancer tends to be aggressive in its behavior. It invades locally, spreads to local lymph nodes, and then metastasizes throughout the body. Approximately 15 % of esophageal cancers occur in the upper third of the esophagus, 45 % in the middle third of the esophagus, and 40 % in the distal third of the esophagus.

Esophageal carcinoma carries a poor prognosis. Although it is a disease that can be treated, it can rarely be cured. By the time the patient becomes symptomatic, the disease is usually at an advanced stage.

The overall 5-year survival rate in patients who undergo surgery ranges from 5 to 20 %, while the 5-year survival rate in patients with lymph node metastases (nonsurgical patients) ranges from 0 to 7 %. Once the diagnosis of esophageal cancer has been made, staging is the next critical step in determining the most appropriate treatment plan for the patient.

Case 4.4

History

Patient with a history of moderate to poorly differentiated adenocarcinoma of the distal esophagus, status post trans-hiatal esophagectomy and gastric pull-up. Patient had biopsy-proven metastatic disease involving the mesentery and liver and was on chemotherapy at the time of imaging.

Findings

There is status post esophagectomy and gastric pull-up with prominent physiologic and/or inflammatory metabolic activity (white arrow) (Fig. 4.8). There are reticular nodular fibrotic changes, predominantly in the lower lungs, suggestive of posttreatment changes (red arrow).

Several metabolic active hypoattenuating hepatic lesions are identified. One of which demonstrates SUVmax of 4.5 in the lateral right lobe; another lesion is seen in the inferior posterior right hepatic lobe with SUVmax of 3.7 (Fig. 4.9).

Two hypermetabolic mesenteric nodules are identified that are most consistent with metastatic disease. One of these nodules is at the level of L3–L4 (ventral to third part of duodenum), measuring 2.1 cm with SUVmax of 4.5 (Fig. 4.10).

Impression

Enlarged and metabolically active metastatic disease involving mesentery and liver parenchyma.

Pearls and Pitfalls

1. ^{18}F-FDG PET is sensitive and accurate in the preoperative staging of distant metastases in patients with cancer of the esophagus and leads to upstaging.
2. Though performance of PET in assessing N1 disease is not better than that of current staging methods, there is a significant advantage in detection of M1 disease, avoiding unnecessary surgery.

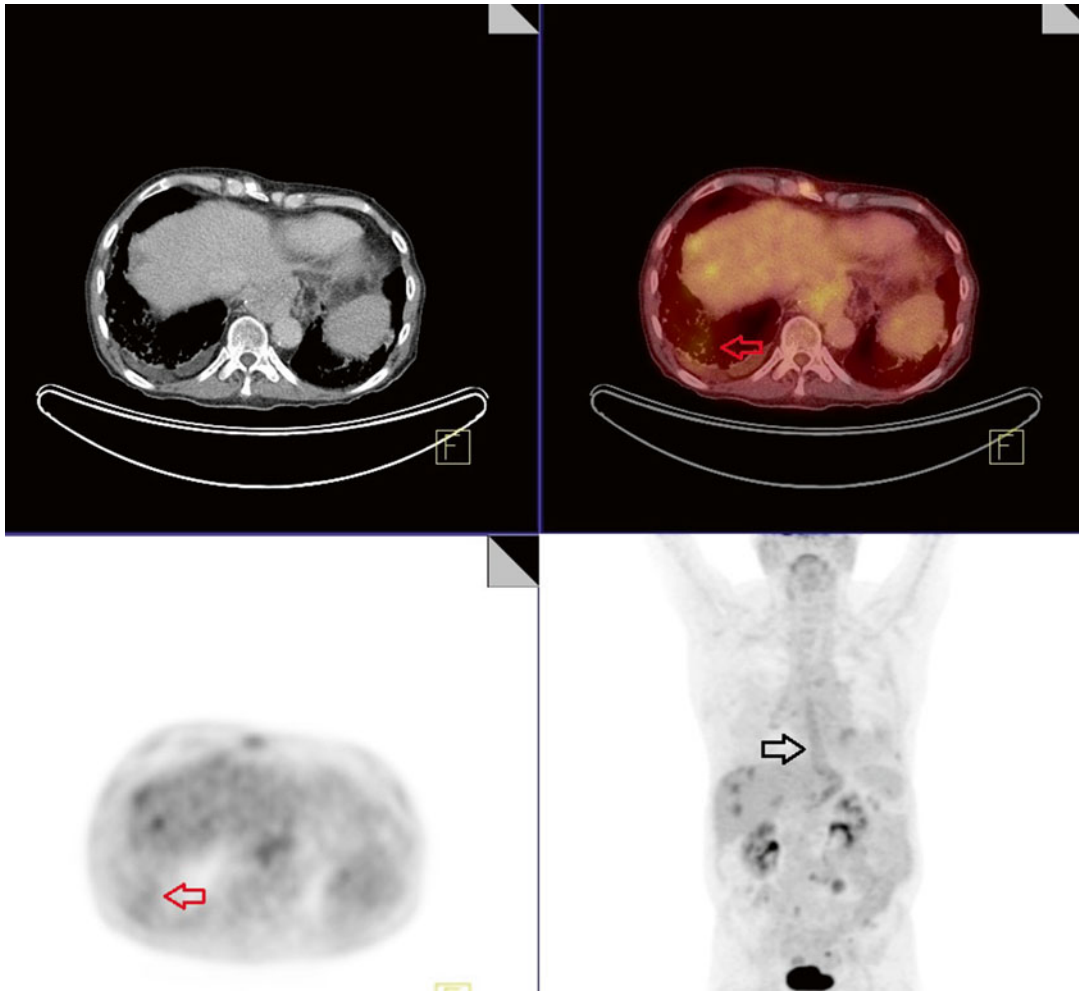

Fig. 4.8

Discussion

Performance of PET in assessing N1 disease is not better than that of current staging methods. There is a significant advantage in detection of M1 disease, avoiding unnecessary surgery. ^{18}F-FDG PET detects 95 % of the primary esophageal tumors. To identify unsuspected M1 disease, ^{18}F-FDG PET performed better than the combination of CT and EUS. The rate of M1 metastases only detected by ^{18}F-FDG PET in conventionally staged tumors is 10–20 %. ^{18}F-FDG PET upstaged the disease in about 20 % as M1 disease. The accuracy of 69 % for detecting M1 disease with CT and EUS increased to 86 % when combined with ^{18}F-FDG PET.

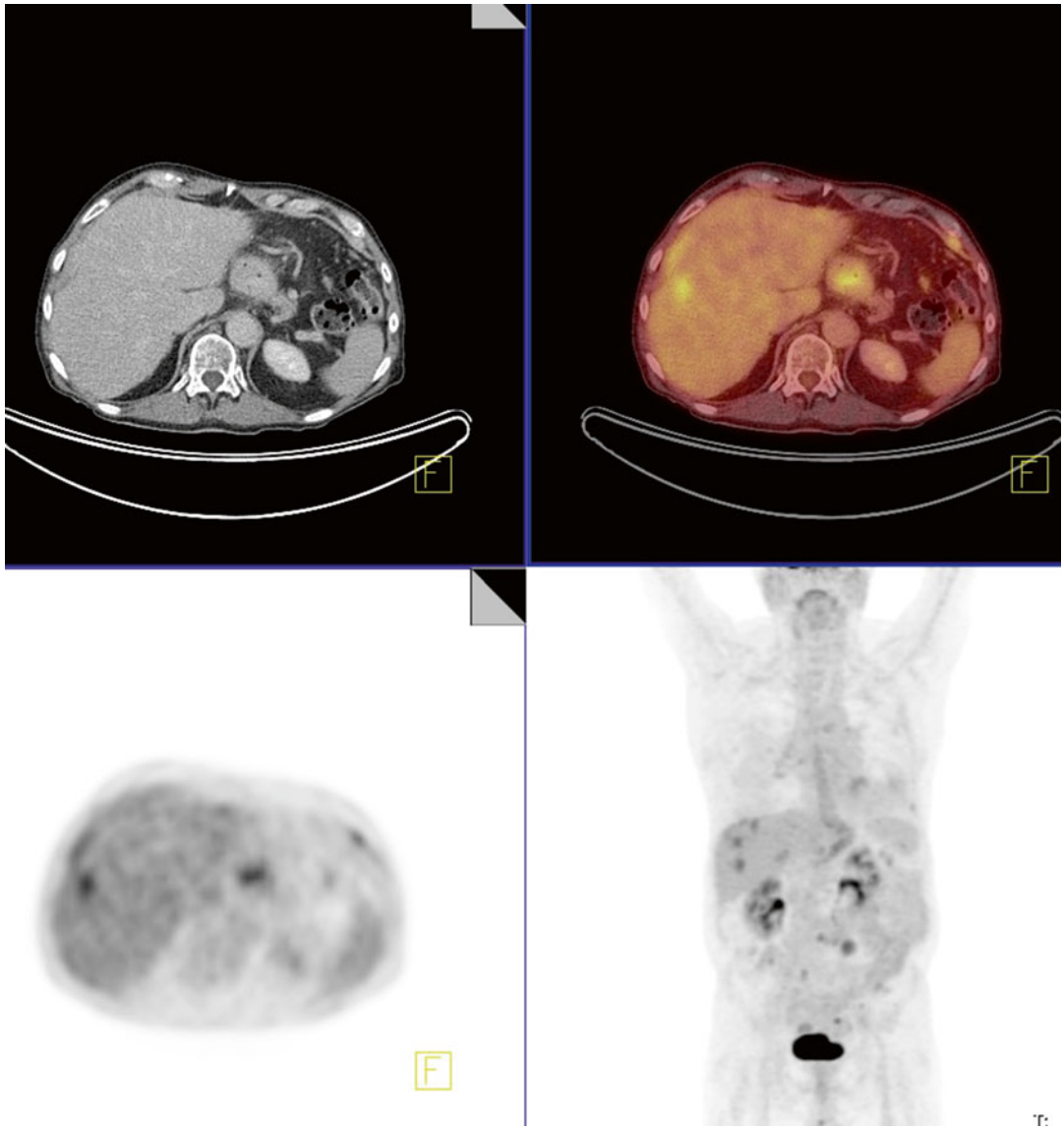

Fig. 4.9

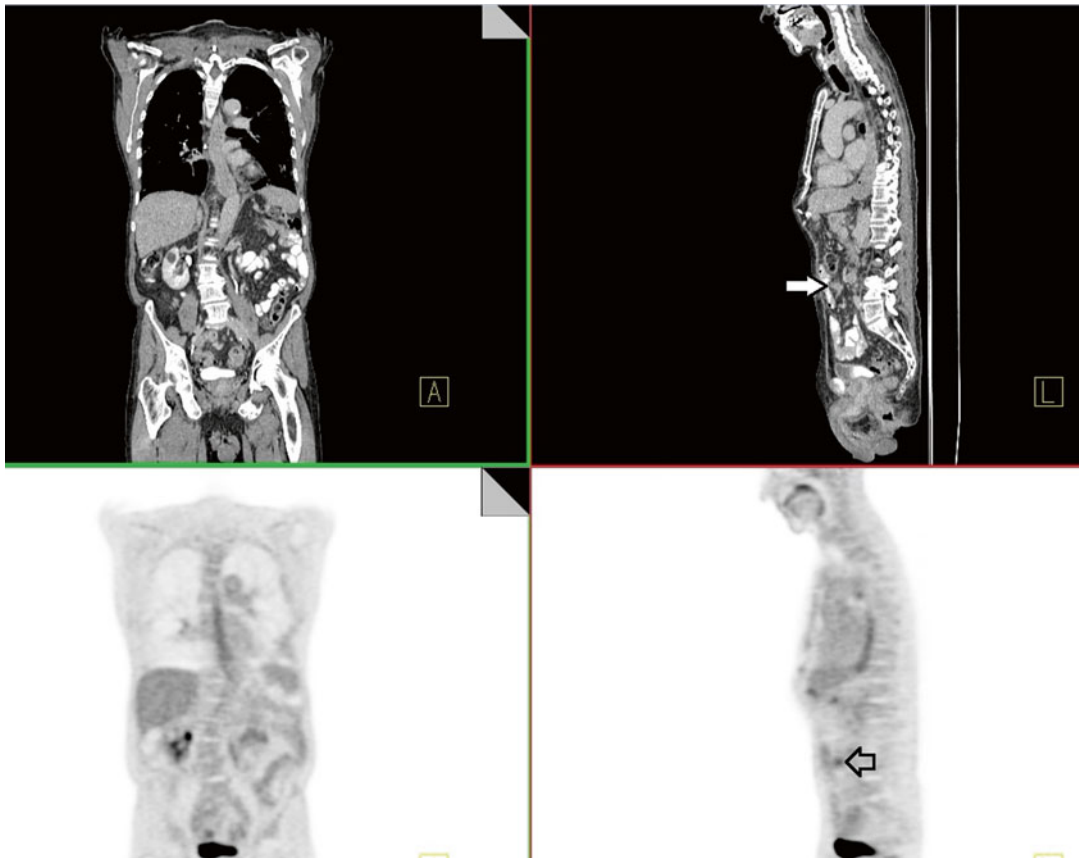

Fig. 4.10

Case 4.5

History

Patient with biopsy-proven well-differentiated adenocarcinoma of the esophagus.

Findings

There is a hypermetabolic mass in the mid to distal esophagus, protruding into the lumen, with generalized wall thickening at SUVmax of 7.4. There are inactive small paraesophageal nodes near the gastroesophageal junction (Fig. 4.11).

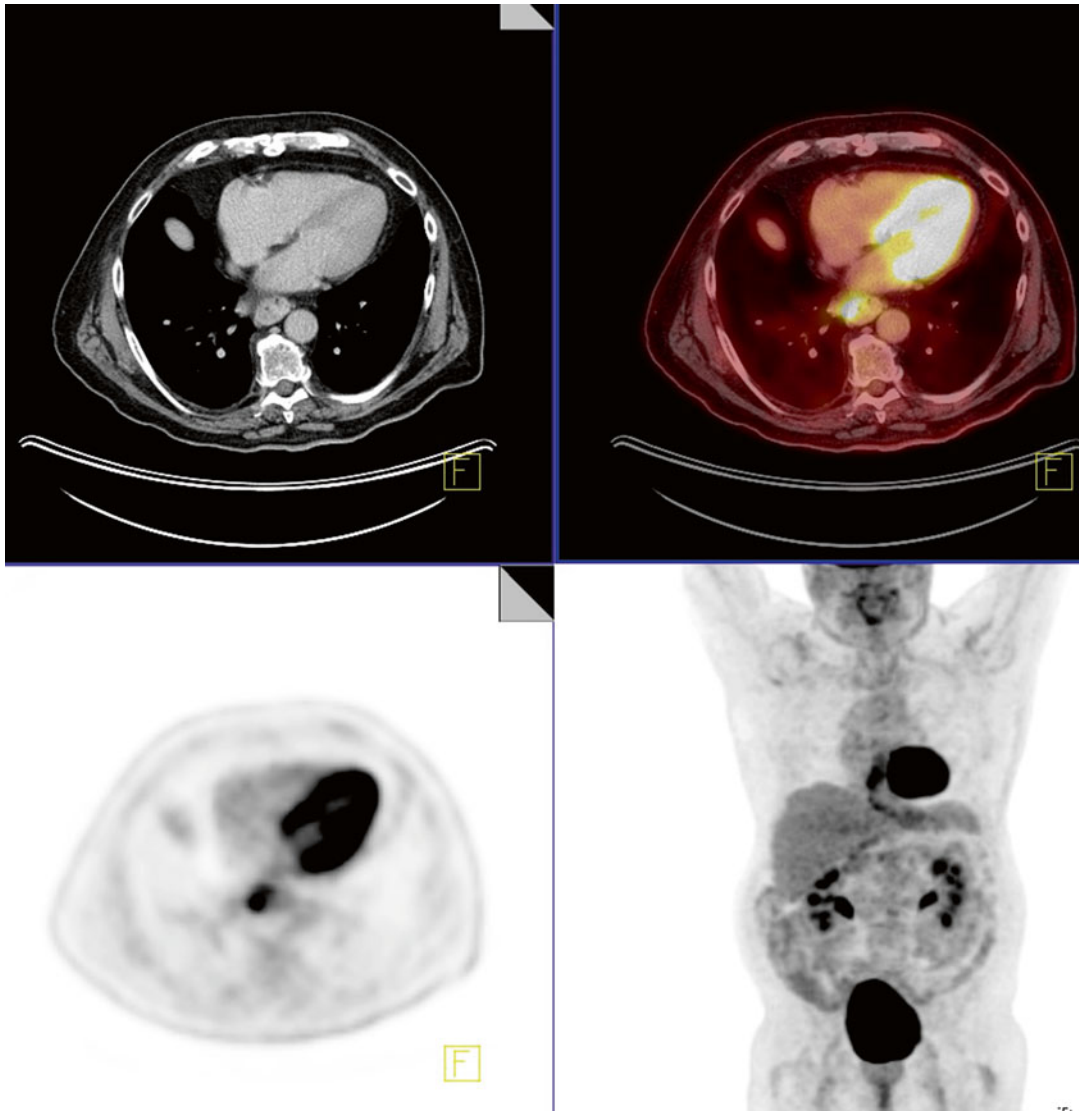

Fig. 4.11

Impression

Hypermetabolic mid to distal primary esophageal tumor with small adjacent nodes that despite being metabolically inactive can statistically be involved with tumor deposits.

Pearls and Pitfalls

Performance of PET in assessing N1 disease is not better than that of current staging methods. The sensitivity, specificity, and accuracy of FDG PET for nodal metastatic disease are 30 %, 90 %, and 82 %, respectively.

Discussion

^{18}F-FDG PET does not add much in the detection of regional nodes. The direct vicinity of the primary tumor, obscuring ^{18}F-FDG uptake, probably causes false-negative results in peritumoral N1 nodes. Moreover, small metastatic nodes could cause false negativity by limitations in the spatial resolution. Specificity of 71 % with PET in assessing regional metastases is comparable with that of other series. FDG PET is slightly less specific than CT for depicting metastases, but the difference in specificity between the two modalities is statistically significant. Both FDG PET and CT have low sensitivity for depicting nodal metastasis. The relatively low specificity of FDG PET for depiction of nodal metastasis compared with that of CT is caused mainly by a high rate of false-positive hilar node interpretations.

Case 4.6

History

A 50-year-old male with submucosal adenoid cystic carcinoma of esophagus.

Findings

There is a hypermetabolic low attenuating heterogeneous retrotracheal esophageal mass which appears to be arising from right anterior wall of the esophagus. The bulk of the mass is at the level of thyroid, extending inferiorly to the level of manubrium, compressing the trachea with SUVmax of 5.4, compatible with primary neoplasm (Fig. 4.12). Focal activity is also seen in the terminal ileum (Fig. 4.13) with prominent mucosal enhancement, demonstrating SUVmax of 4.2. Subsequent imaging revealed resolution of focal ileal activity.

Impression

1. Hypermetabolic retrotracheal esophageal mass, compatible with known primary neoplasm
2. No definite evidence of distant metastasis
3. Focal activity in the terminal ileum with prominent mucosal enhancement, likely inflammatory or physiologic

Pearls and Pitfalls

1. Sensitivities for ^{18}F-FDG PET imaging are between 91 % and 100 %. False-positive uptake can occur due to inflammation, and there can be normal mild FDG activity from muscular contractions.
2. Recurrence is most common near the esophagogastric anastomosis.

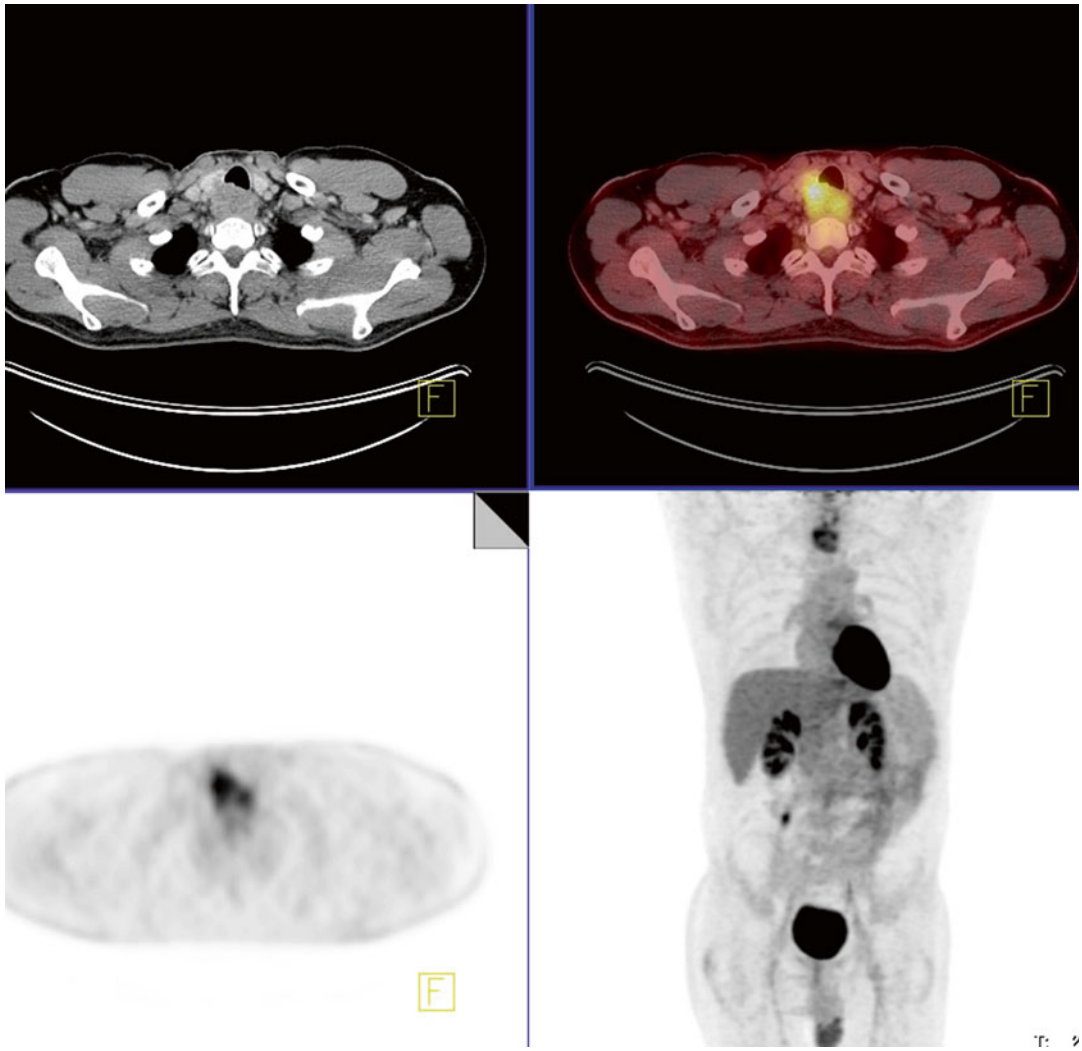

Fig. 4.12

Discussion

Esophageal adenoid cystic carcinoma (EACC) accounts for 0.1 % of esophageal malignancies. The clinical behavior of EACC is not well known due to the small number of reported cases. The average age of patients is 65 years, with a male-to-female ratio of 3.4:1. The most common symptom is progressive dysphagia. EACCs have most frequently been reported in the middle third of the esophagus (63 %), less often in the lower third (30 %), and rarely in the upper third (7 %). The most common endoscopic findings include a fungating or polypoid mass rather than an ulcerative or infiltrative growth pattern.

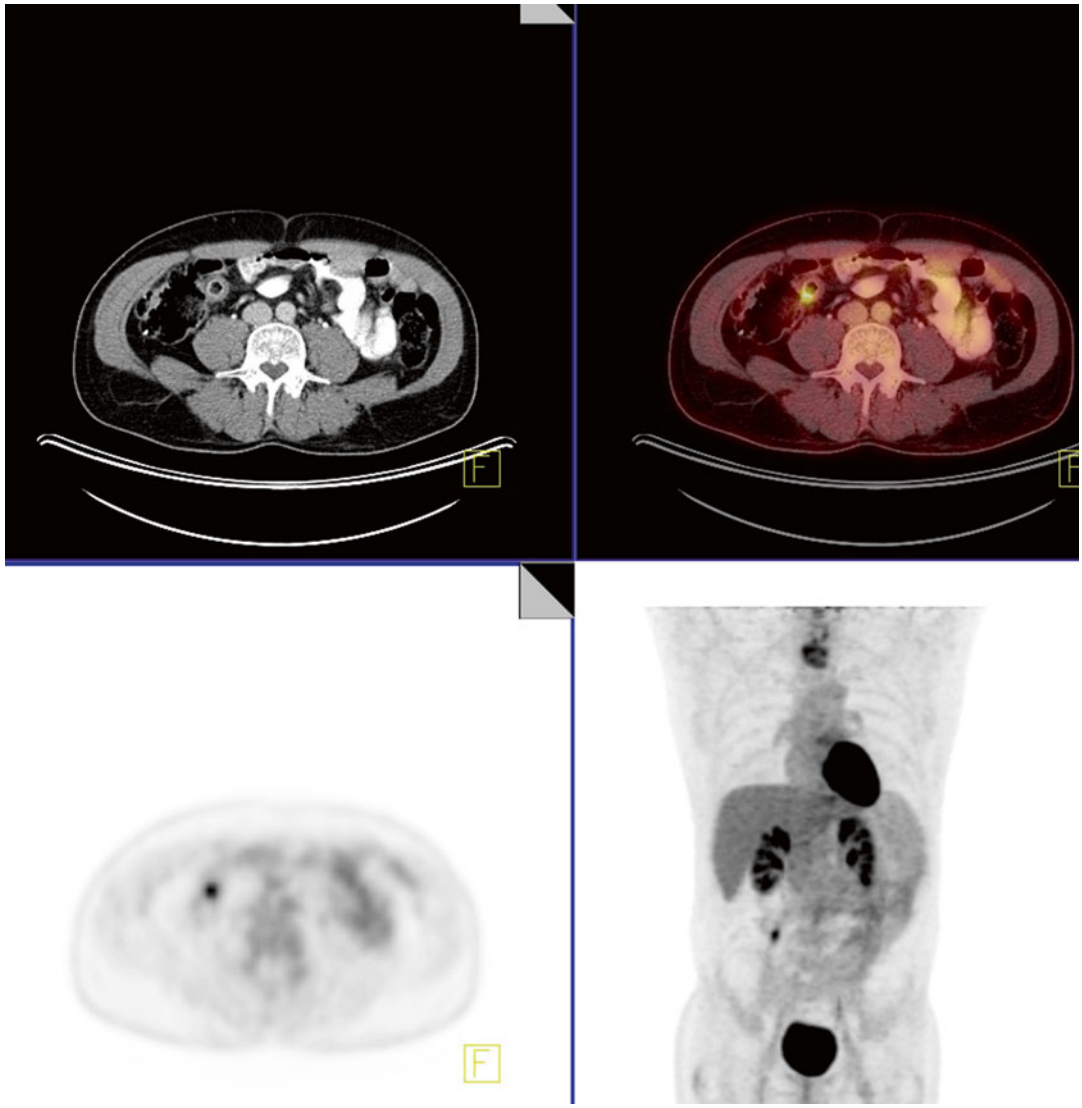

Fig. 4.13

The treatment of choice for EACC is radical excision. When the surgical margin is positive, postoperative radiotherapy is recommended. Chemotherapy is not usually chosen due to a poor response rate. The 5-year survival rate is approximately 35 %, and the long-term survival is poor. Eighty to 90 % of patients die of this disease within 10–15 years. Poor prognostic factors that influence survival include solid histological pattern, advanced clinical stage, and positive surgical margins. The role of chemotherapy, through either adjuvant or primary chemotherapy, is not clear. Postoperative radiotherapy may help the improvement of progressive dysphagia.

Case 4.7

History

Patient with distal esophagus/gastroesophageal junction mass with a superficial biopsy showing severe dysplasia and focal adenocarcinoma in situ.

Findings

There is a large area of fairly intense hypermetabolism with some necrosis in the distal esophagus and medial gastric fundus with SUVmax of 13.4 (estimated tumor volume of 148 cm^3 at a threshold of SUV 3, with mean SUV of 5.5, indicating significant tumor necrosis) (Fig. 4.14).

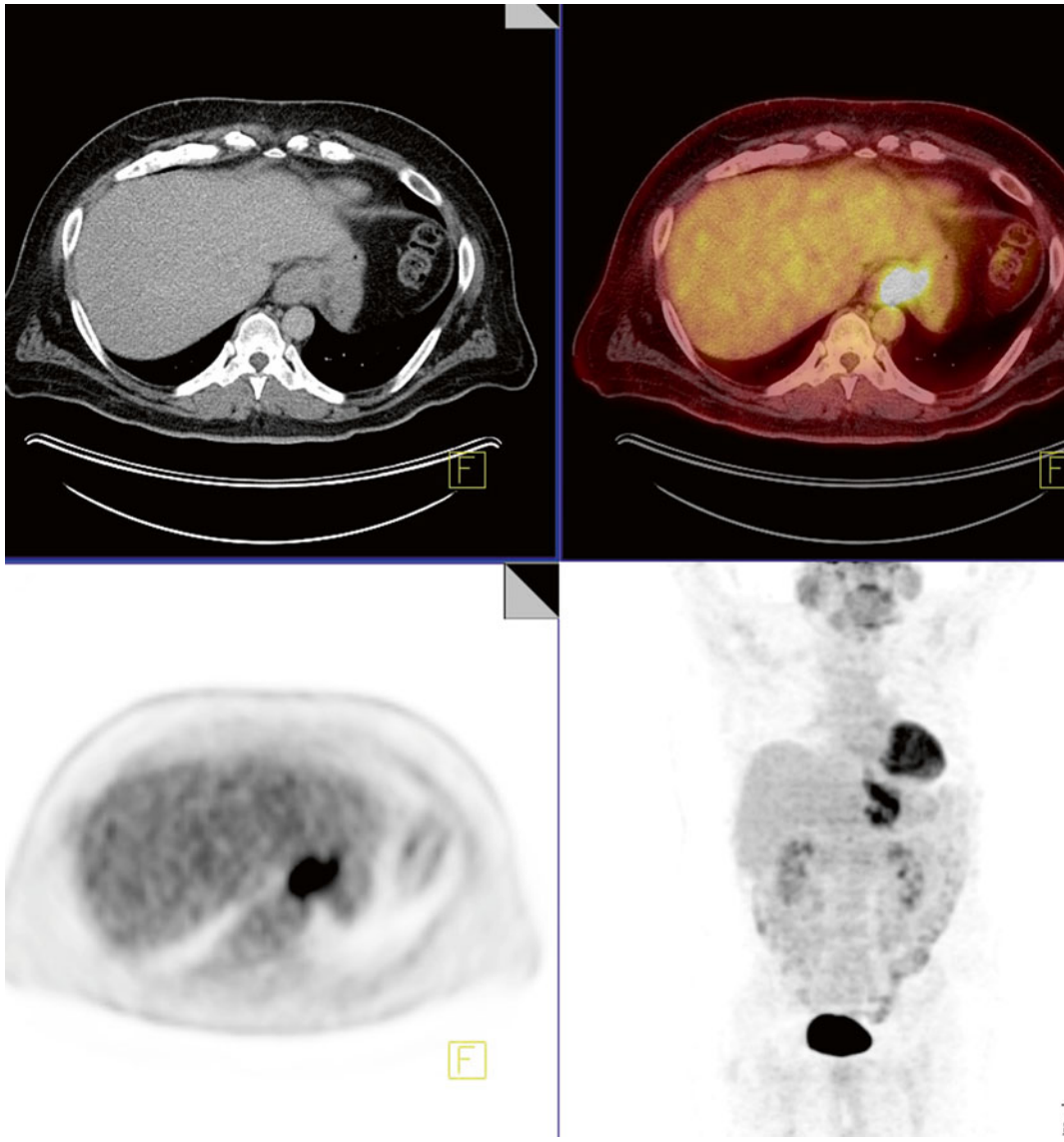

Fig. 4.14

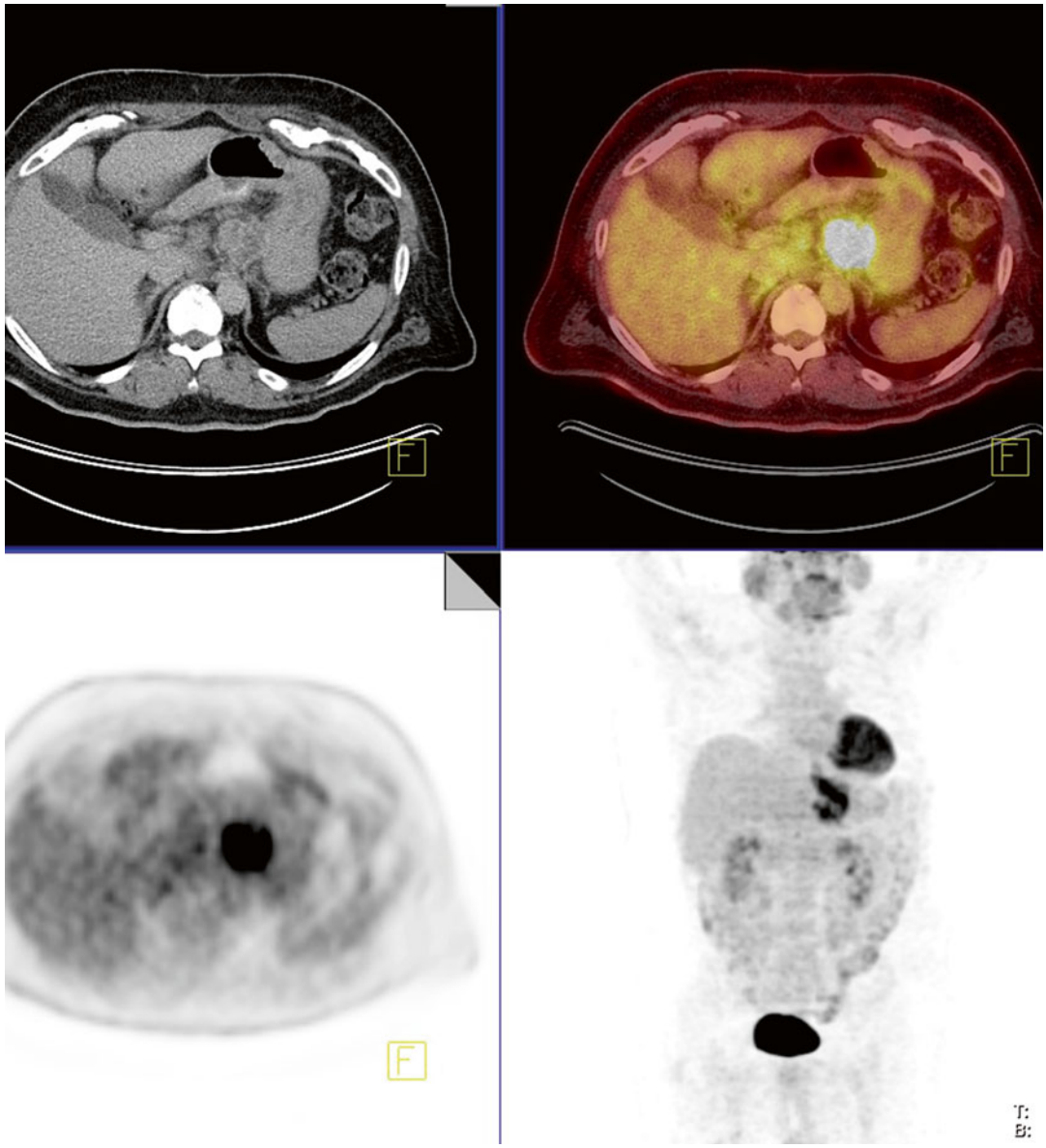

Fig. 4.15

There are regional perigastric/gastroduodenal nodes with SUVmax up to 9.2 (Fig. 4.15). There are no hypermetabolic or enlarged lymph node in the celiac axis or retroperitoneal stations.

Impression

Large hypermetabolic tumor involving the distal esophagus and medial gastric fundus with regional lymph node metastasis.

Pearls and Pitfalls

1. Sensitivities for FDG PET imaging are between 91 and 100 %. False-positive uptake can occur due to inflammation, and there can be normal mild FDG activity from muscular contractions.
2. Accuracy of FDG PET in the staging of regional lymph node metastases ranges from 24 to 90 %. The major limitation of FDG PET with regard to the detection of nodal metastases adjacent to the primary tumor is its relatively poor spatial resolution (approximately 6 mm for a dedicated PET scanner), which reduces sensitivity. The level of metabolic activity and pattern of mediastinal and hilar lymph nodes as well as coexisting nodal calcification is helpful in determining inflammatory versus metastatic etiology.
3. Recurrence is most common near the esophagogastric anastomosis.

Discussion

^{18}F-FDG PET does not add much in the detection of regional nodes. The direct vicinity of the primary tumor, obscuring ^{18}F-FDG uptake, probably causes false-negative results in peritumoral N1 nodes. Moreover, small metastatic nodes could cause false negativity by limitations in the spatial resolution. Specificity of 71 % with PET in assessing regional metastases is comparable with that of other series. FDG PET is slightly less specific than CT for depicting metastases, but the difference in specificity between the two modalities is statistically significant. Both FDG PET and CT have low sensitivity for depicting nodal metastasis. The relatively low specificity of FDG PET for depiction of nodal metastasis compared with that of CT is caused mainly by a high rate of false-positive hilar node interpretations.

Case 4.8

History

A 64-year-old male with history of esophageal adenocarcinoma.

Findings

There is long segmental hypermetabolic wall thickening of the esophagus from the T3 level to the gastroesophageal junction with SUVmax of 14.9. The segmental thickening is more pronounced and concentric as it reaches the gastroesophageal junction (Figs. 4.16 and 4.17). Several hypermetabolic cervical and supraclavicular lymph nodes were noted. Evaluation of the abdomen demonstrated innumerable hypermetabolic hepatic lesions (most active at the dome with SUVmax of 12.2), some of which correspond to hypodense lesions on transmission CT scan (Figs. 4.18 and 4.19). A nodule was identified within the right adrenal gland with intense increased metabolic activity. Enlarged lymph nodes were seen within the celiac axis that also demonstrated increased

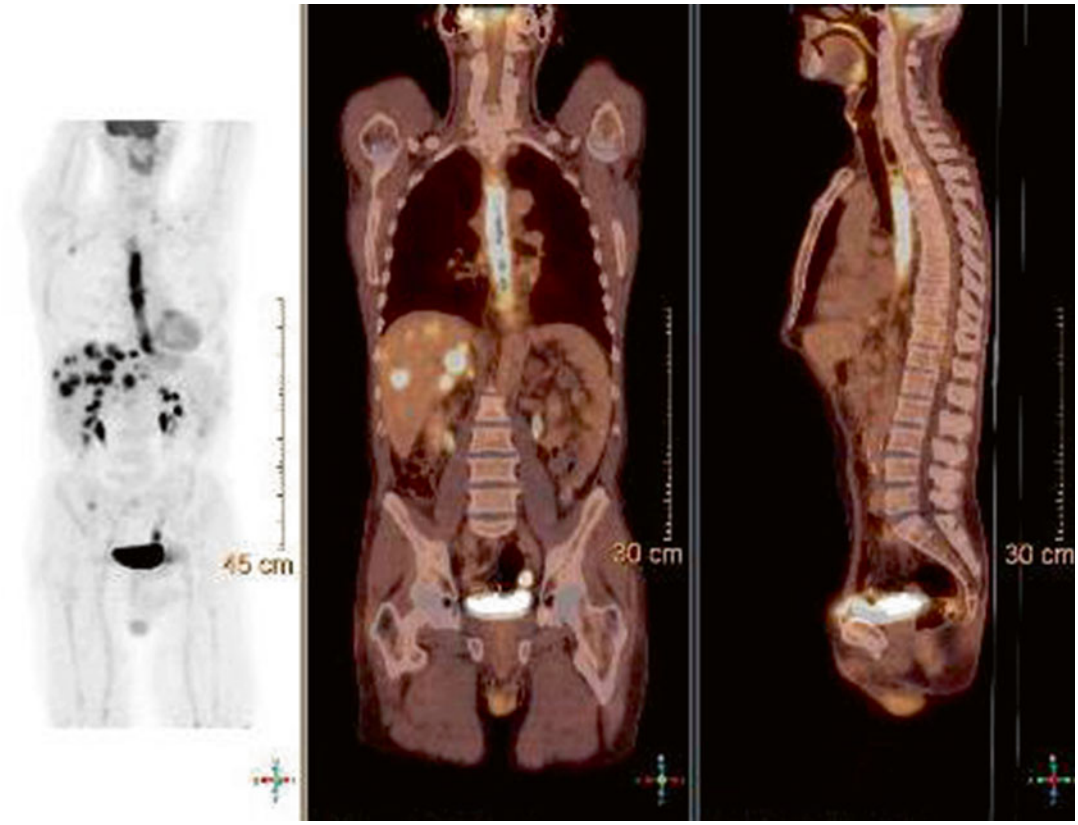

Fig. 4.16

metabolic activity. Numerous areas of increased metabolic activity were seen within skeleton, consistent with metastatic osseous disease. The majority of these lesions do not demonstrate any lytic or cortical disruption on CT (Figs. 4.20 and 4.21).

Impression

1. Esophageal wall thickening with intense increased metabolic activity, consistent with known esophageal adenocarcinoma
2. Metastatic disease to the liver, skeleton, and right adrenal gland
3. Metastatic nodal disease as described above

Pearls and Pitfalls

1. F-FDG PET is sensitive and accurate in the preoperative staging of distant metastases in patients with cancer of the esophagus and leads to upstaging. Though performance of PET in assessing N1 disease is not better than that of current staging methods, there is a significant advantage in detection of M1 disease, avoiding unnecessary surgery.
2. Sensitivity to identify locoregional metastases was highest for EUS (69 %) but was not different for CT and PET (44 % and 55 %, respectively).

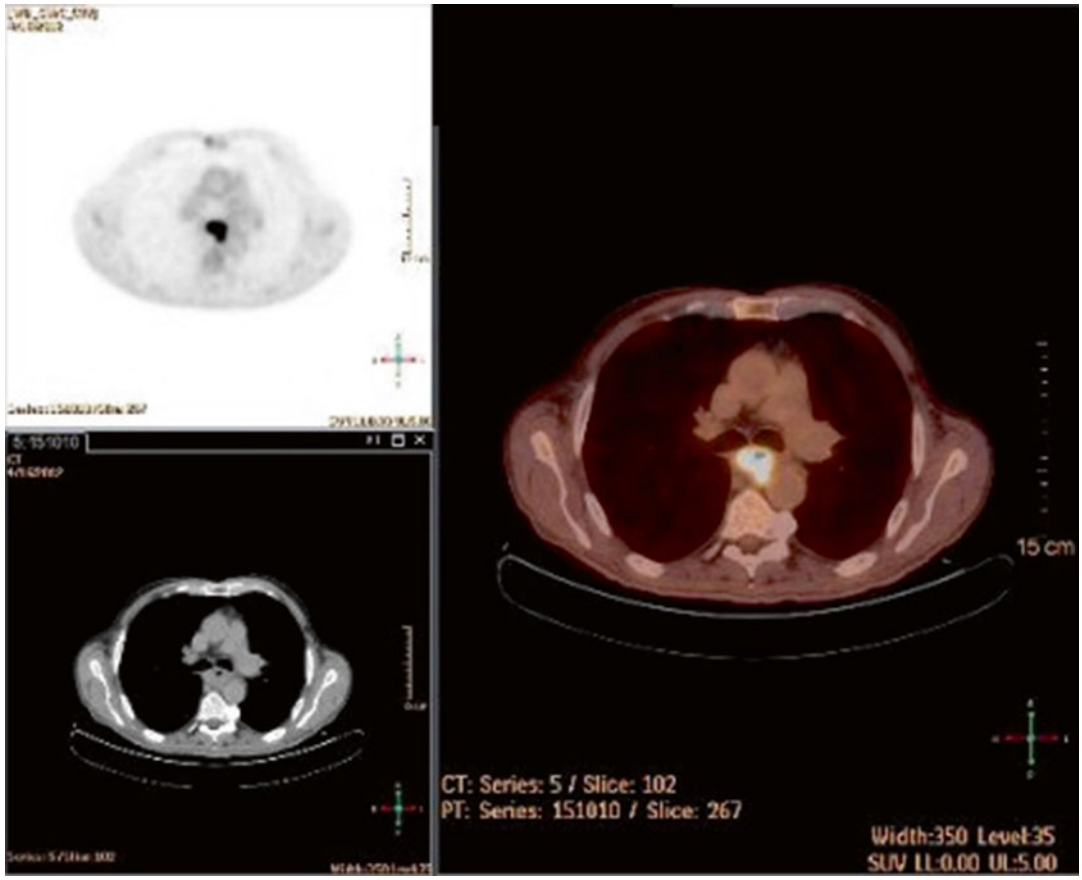

Fig. 4.17

Discussion

This study clearly shows the additional value of ^{18}F-FDG PET in staging carcinoma of the esophagus and GE Junction. Though performance of PET in assessing N1 disease is not better than that of current staging methods, there is a significant advantage in detection of M1 disease, avoiding unnecessary surgery.

To identify unsuspected M1 disease, ^{18}F-FDG PET performed better than the combination of CT/EUS. The rate of M1 metastases only detected by ^{18}F-FDG PET in conventionally staged tumors is 10–20 %. ^{18}F-FDG PET upstaged the disease in about 20 % as M1 disease. A combination of all three modalities increased the accuracy for detecting M1 disease up to 92 % as was the result of a more sensitive detection of both distant node and organ metastases. PET improves the currently applied staging of esophageal and GEJ tumors, particularly by ameliorating the detection of M1 disease.

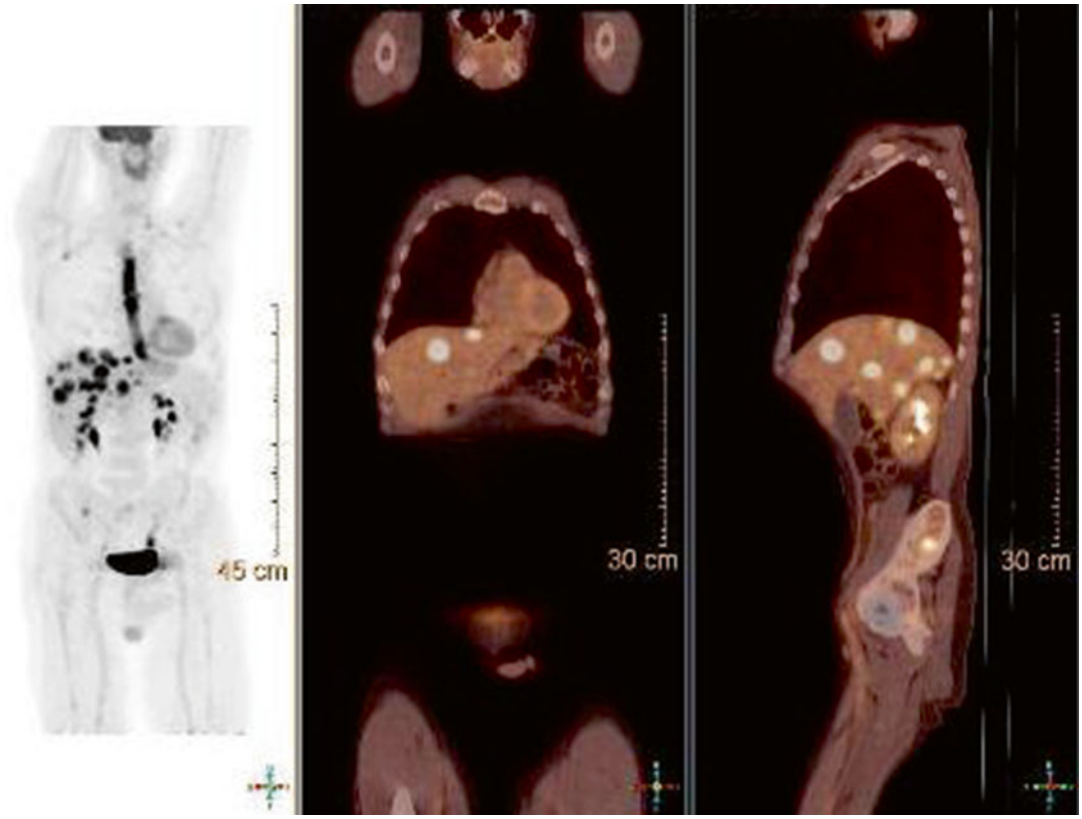

Fig. 4.18

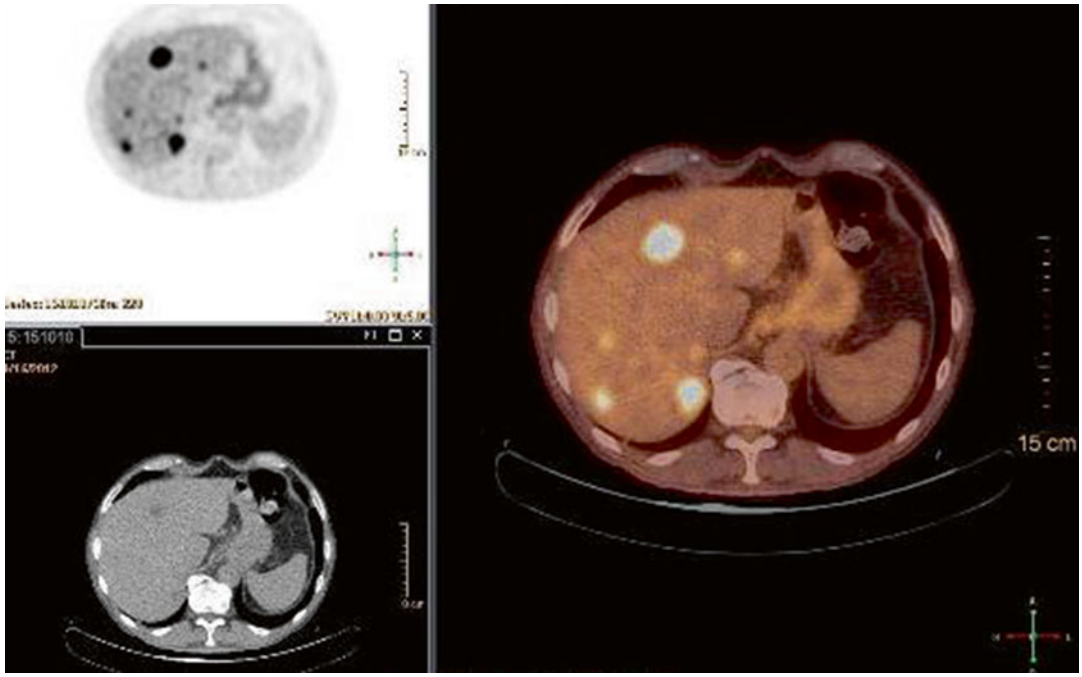

Fig. 4.19

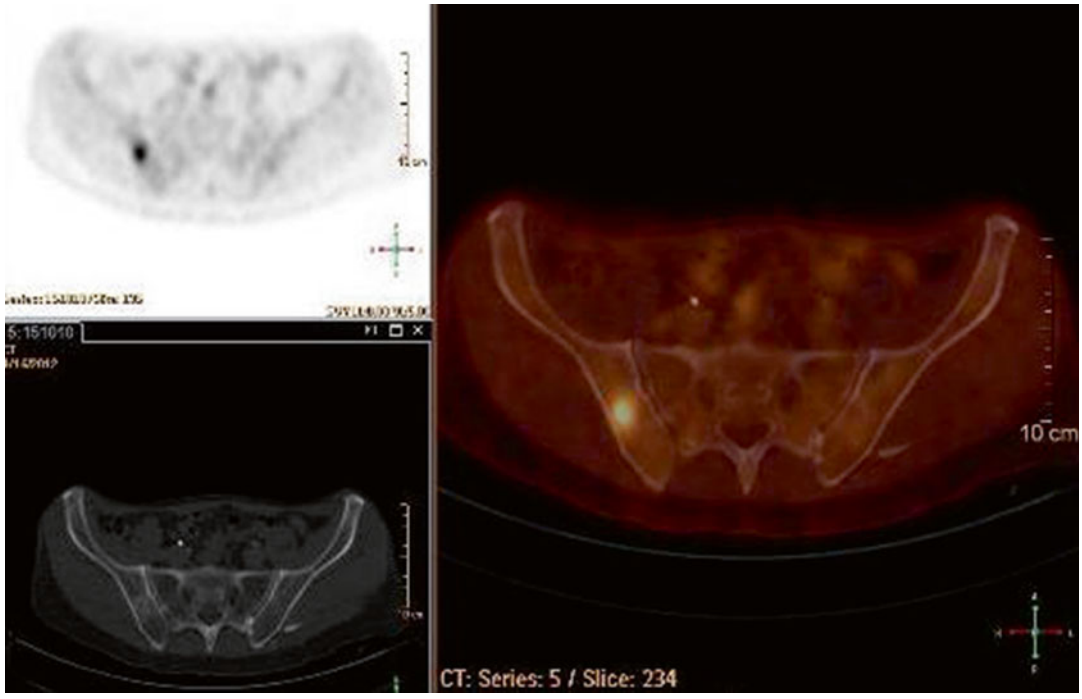

Fig. 4.20

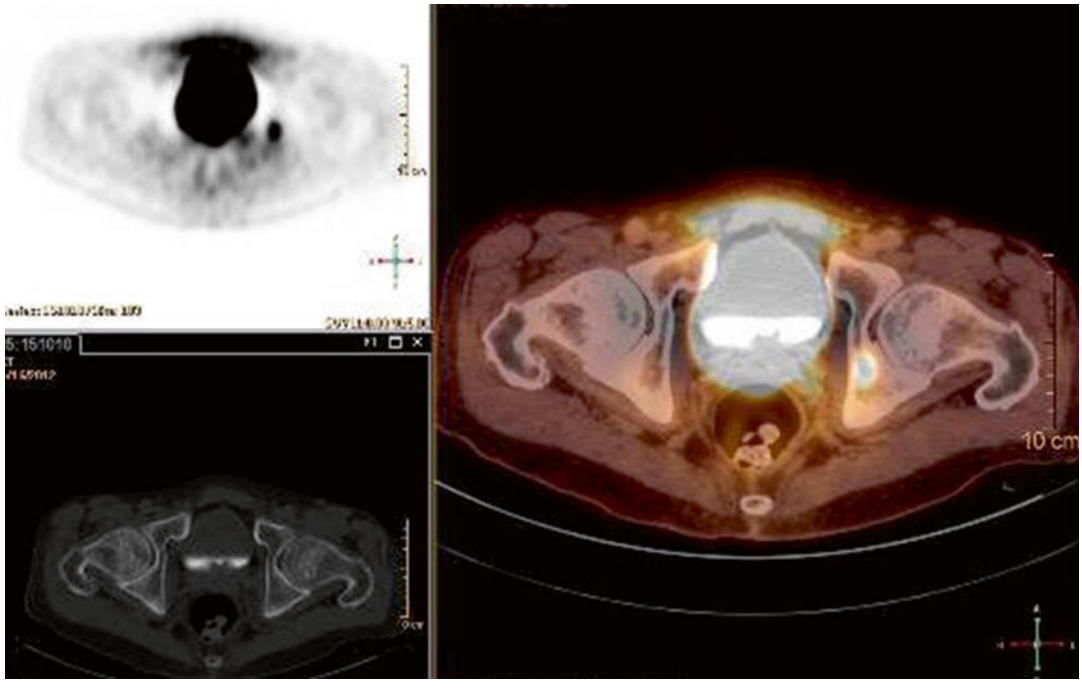

Fig. 4.21

Case 4.9

History

Patient with esophageal cancer.

Findings

There is a hypermetabolic right paratracheal node with SUVmax of 10, consistent with metastatic node (Fig. 4.22, white arrow). There is a hypermetabolic distal esophageal circumferential thickening extending to the gastroesophageal junction with SUVmax of 22 consistent with known

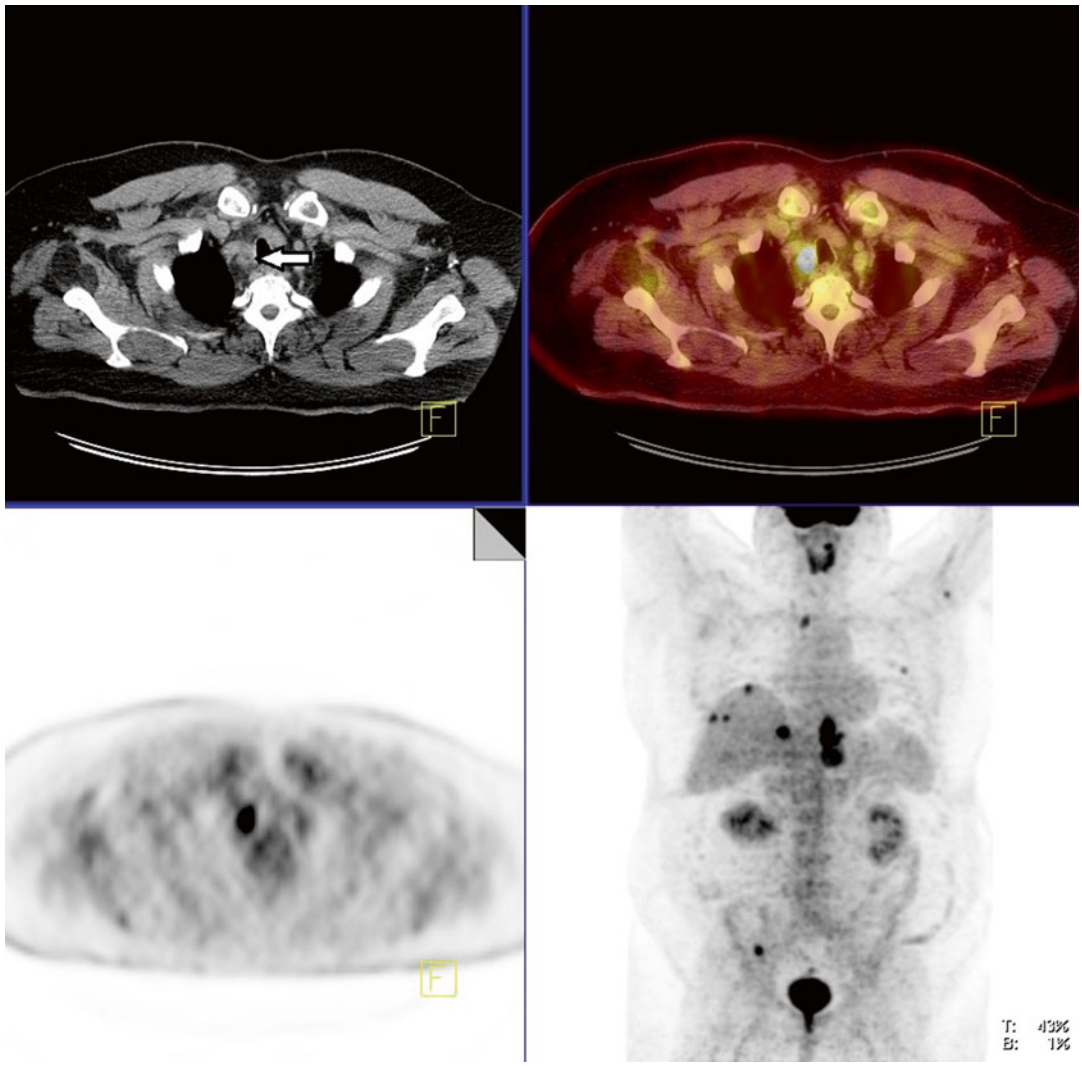

Fig. 4.22

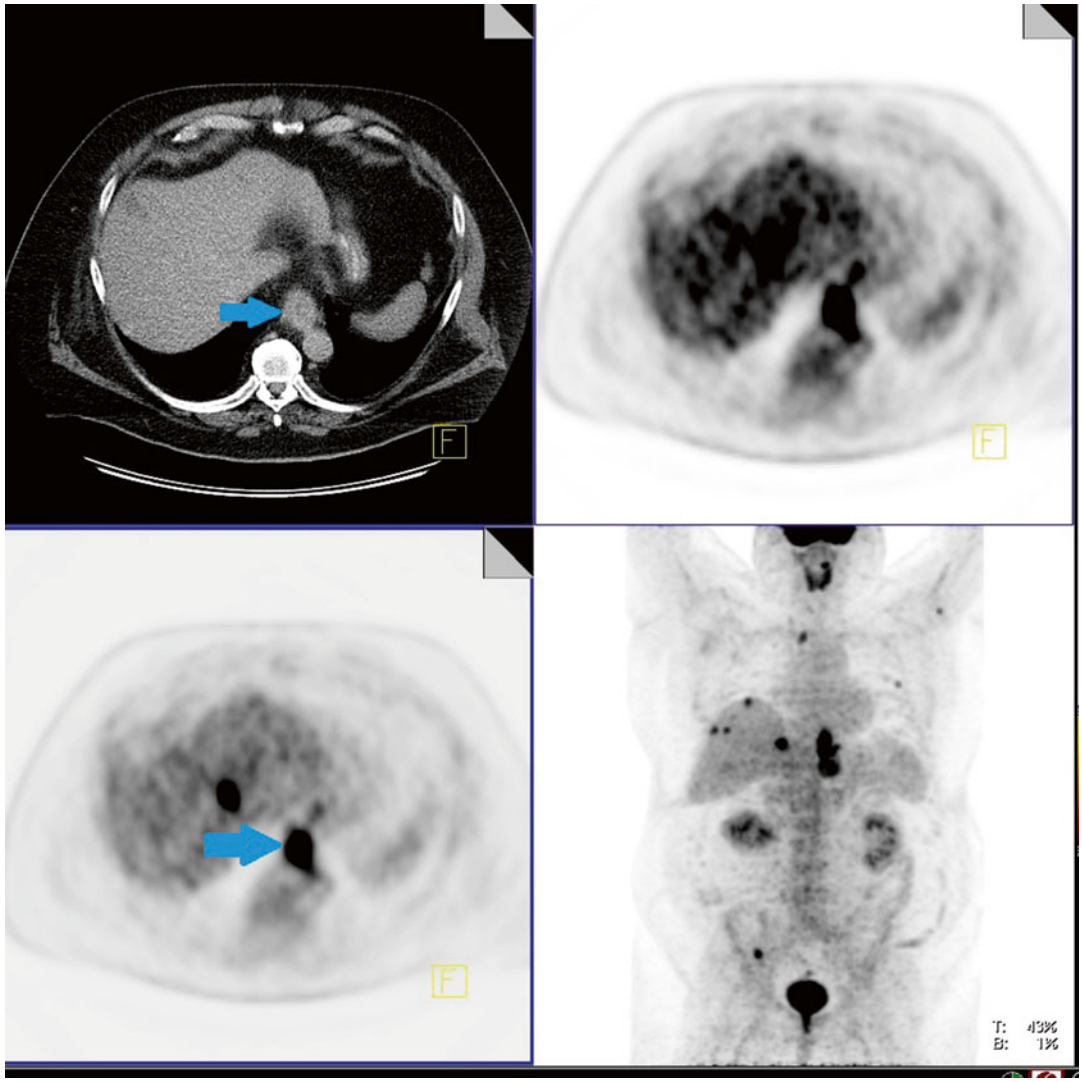

Fig. 4.23

esophageal tumor with a hypermetabolic lymph node at gastroesophageal junction with SUVmax of 16.4 (Fig. 4.23, blue arrow). There are multiple hypoattenuating, hypermetabolic foci within hepatic parenchyma consistent with metastases (Figs. 4.24 and 4.25, red arrow). There is focal activity in the right iliacus muscle with SUVmax of 15.9 with slight adjacent osseous erosion, also consistent with metastasis (Fig. 4.26, green arrow).

Impression

1. Hypermetabolic distal esophageal mass extending to gastroesophageal junction, consistent with known primary tumor with adjacent regional nodal metastasis
2. Mediastinal nodal disease

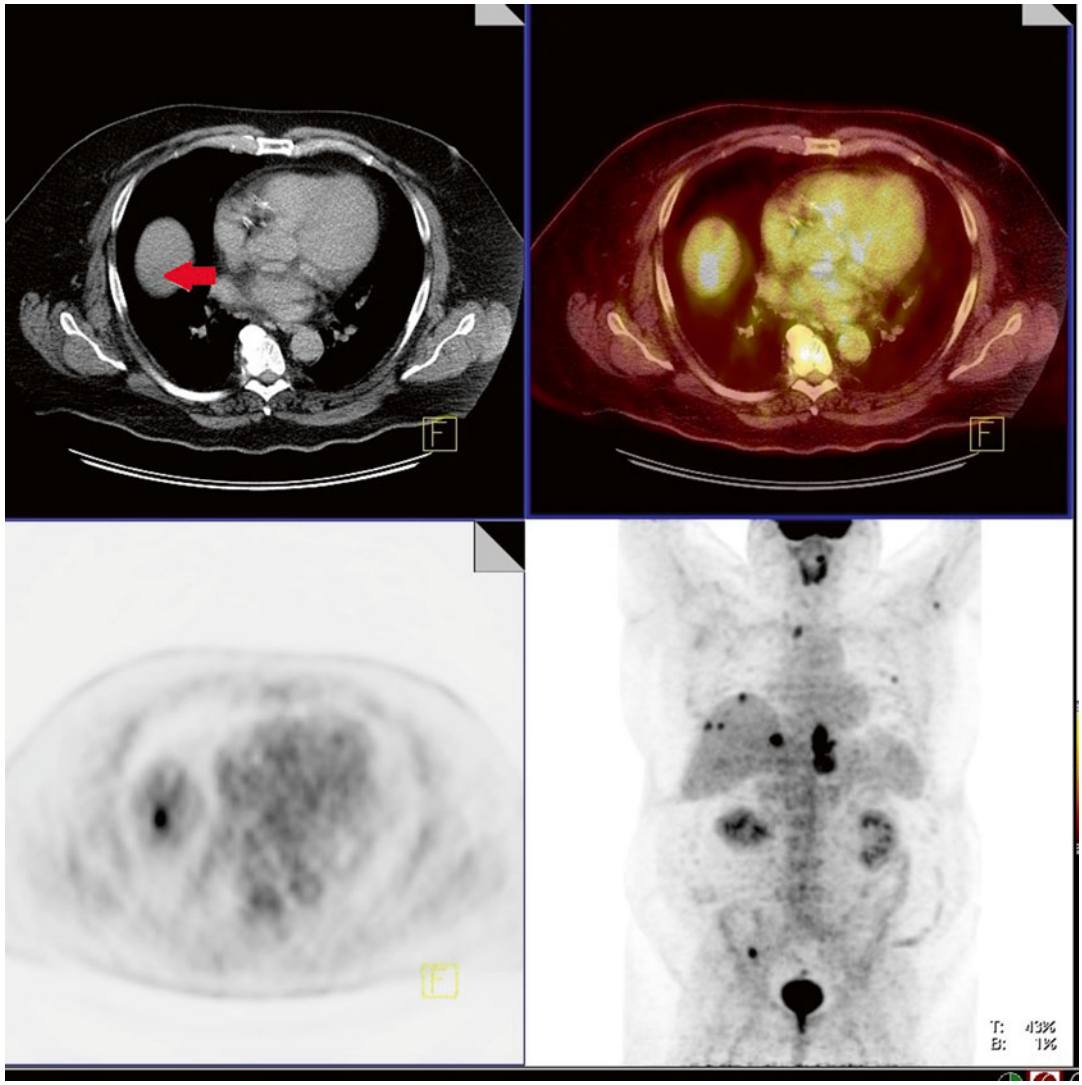

Fig. 4.24

3. Hepatic metastatic disease
4. Multiple osseous metastases
5. Right iliacus muscular metastasis with adjacent osseous erosion

Pearls and Pitfalls

1. ^{18}F-FDG PET is sensitive and accurate in the preoperative staging of distant metastases in patients with cancer of the esophagus and leads to upstaging. Though performance of PET in assessing N1 disease is not better than that of current staging methods, there is a significant advantage in detection of M1 disease, avoiding unnecessary surgery.
2. Sensitivity to identify locoregional metastases is highest for EUS (69 %) but is not different for CT and PET (44 % and 55 %, respectively).

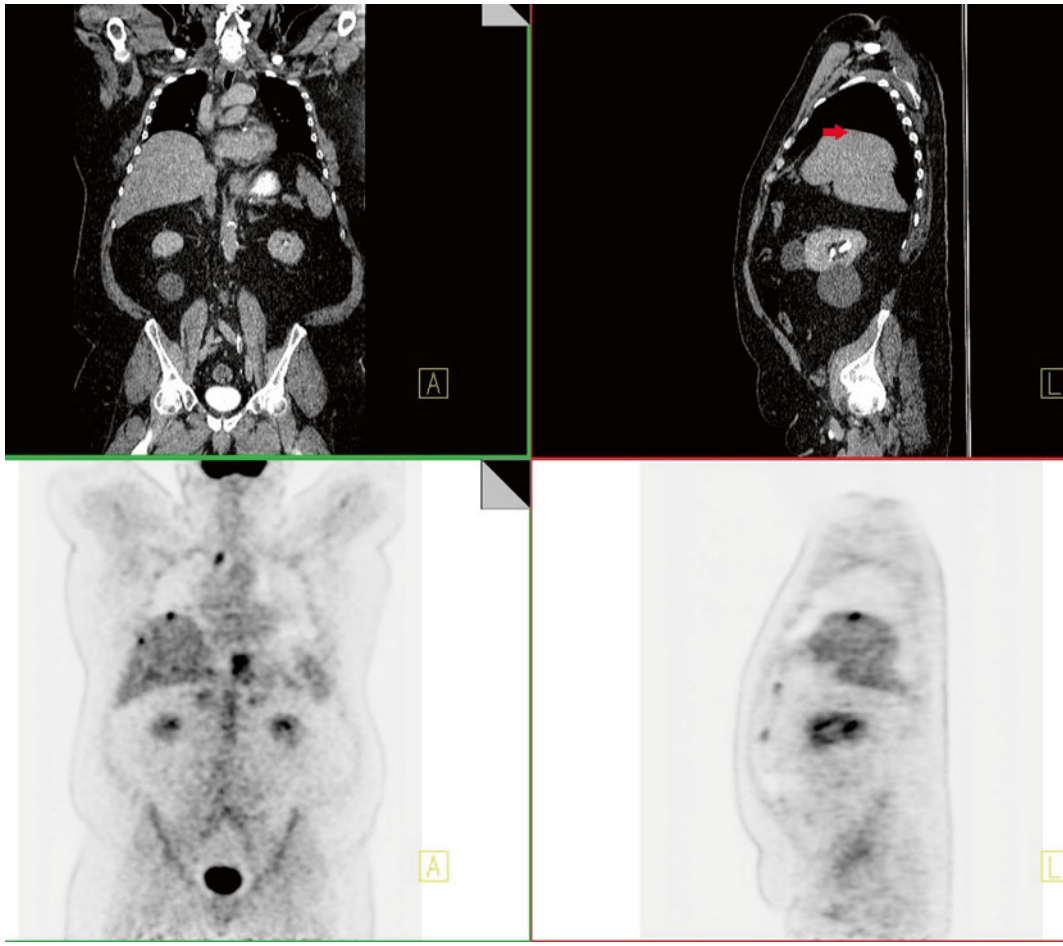

Fig. 4.25

Discussion

This study clearly shows the additional value of ^{18}F-FDG PET in staging carcinoma of the esophagus and gastroesophageal junction. Though performance of PET in assessing N1 disease is not better than that of current staging methods, there is a significant advantage in detection of M1 disease, avoiding unnecessary surgery.

To identify unsuspected M1 disease, ^{18}F-FDG PET performed better than the combination of CT/EUS. The rate of M1 metastases only detected by ^{18}F-FDG PET in conventionally staged tumors is 10–20 %. ^{18}F-FDG PET upstaged the disease in about 20 % as M1 disease. A combination of all three modalities increased the accuracy for detecting M1 disease up to 92 % as was the result of a more sensitive detection of both distant node and organ metastases. PET improves the currently applied staging of esophageal and gastroesophageal junction tumors, particularly by ameliorating the detection of M1 disease.

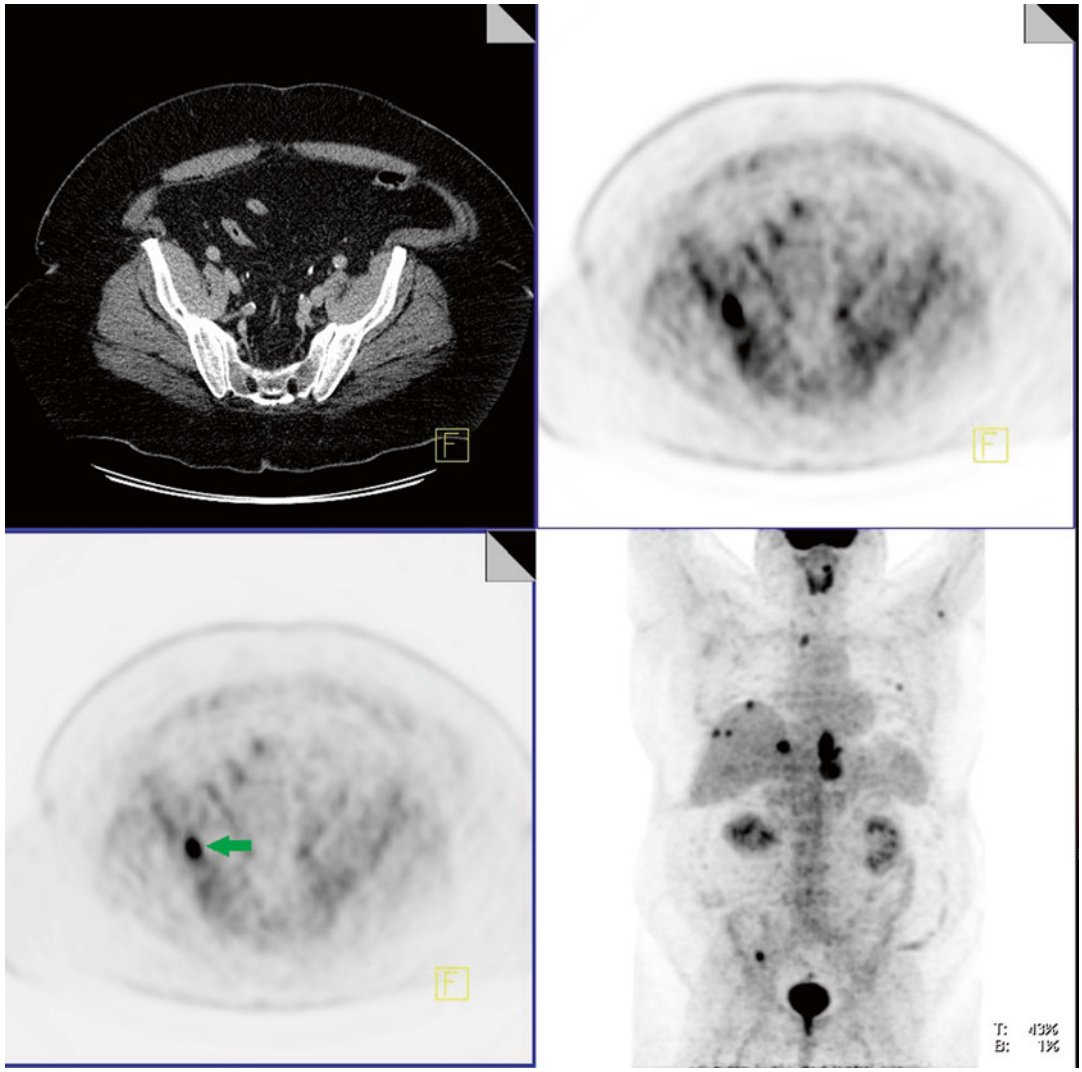

Fig. 4.26

Suggested Reading

Barber TW, Duong CP, Leong T, Bressel M, Drummond EG, Hicks RJ. ^{18}F-FDG PET/CT has a high impact on patient management and provides powerful prognostic stratification in the primary staging of esophageal cancer: a prospective study with mature survival data. J Nucl Med. 2012;53:864–71.

Bruzzi JF, Munden RF, Truong MT, Marom EM, Sabloff BS, Gladish GW, Iyer RB, Pan TS, Macapinlac HA, Erasmus JJ. PET/CT of esophageal cancer: it's role in clinical management. Radiographics. 2007;27(11):1635–52.

Gamboa EO, Cohen S, Ghesani M. The utility of PET/CT in monitoring treatment response and detecting unusual metastases in esophageal cancer. On-line HemOnc Today. 2009;10(12)

Heeren PAM, Jager PL, Bongaerts F, Van Dullemen H, Sluiter W, Plukker THM. Detection of distant metastases in esophageal cancer with 18F-FDG PET. J Nucl Med. 2004;45(6):980–7.

Hopkins S, Yang GY. Positron emission tomography's utility in esophageal cancer management. J Thorac Dis. 2009;1:29–33.
Hopkins S, Yang GY. FDG PET imaging in the staging and management of gastric cancer. J Gastrointest Oncol. 2011;2(1):39–44.
Iyer R, DuBrow R. Imaging of esophageal cancer. Cancer Imaging. 2004;4(2):125–31.
Kim TJ, Kim HY, Lee KW, Kim MS. Multimodality assessment of esophageal cancer: preoperative staging and monitoring of response to therapy. Radiographics. 2009;29(2):403–21.
Kitada H, Takashima KYM, Tanaka M. Adenoid cystic carcinoma of the esophagus: report of a case. Surg Today. 1997;27(3):238–42.
Kostakoglu L, Agress HJ, Goldsmith SJ. Clinical role of FDG-PET in evaluation of cancer patients. Radiographics. 2003;23(3):315–40.
Lieberman MD, Franceschi D, Marsan B, Burt M. Esophageal carcinoma; the unusual variants. J Thorac Cardiovasc Surg. 1994;108:1138–46.
Line BR, Maragh MR, Ahamed TB. Positron emission tomography imaging of lung and esophageal cancer. Appl Radiol. 2002;31(6):137–45.
Luketich JD, Friedman DM, Weigel TL, Meehan MA, Keenan RJ, Townsend DW, Meltzer CC. Evaluation of distant metastases in esophageal cancer: 100 consecutive positron emission tomography scans. Ann Thorac Surg. 1999;68:1133–6.
Ott K, Herrmann K, Krause BJ, Lordick F. The value of PET imaging in patients with localized gastroesophageal cancer. Gastrointest Cancer Res. 2008;2(6):287–94.
Skehan SK, Brown AL, Thompson M, Young EM, Coates G, Nahmias C. Imaging features of primary and recurrent esophageal cancer at FDG PET. Radiographics. 2000;20(5):713–23.
Turlakow A, Yeung HW, Salmon SA, Macapinlac HA, Larson SM. Peritoneal carcinomatosis: role of ^{18}F-FDG PET in peritoneal carcinomatosis. J Nucl Med. 2003;44(9):1407–12.
Van Westreenen HL, Westerterp M, Bossuyt PMM, Pruim J, Sloof GW, Van Lanschot JJB, Groen H, Plukker JTM. Systematic review of the staging performance of 18F-fluorodeoxyglucose positron emission tomography in esophageal cancer. J Nucl Med. 2004;22(18):3805–12.
Yeung HW, Macapinlac H, Karpeh M, Finn RD, Larson SM. Accuracy of FDG-PET in gastric cancer. Preliminary experience. Clin Positron Imaging. 1998;1(4):213–21.
Yoon YC, Lee KS, Shim YM, Kim BT, Kim K, Kim TS. Metastasis to regional lymph nodes in patients with esophageal squamous cell carcinoma: CT versus FDG PET for presurgical detection prospective study. Radiology. 2003;227(3):764–70.
Youn JN, Shim KN, Kang MJ, Jung JM, Chang YH, Jung HS, Baik SJ, Kim SE, Jung SA, Yoo K, Moon H, Cho MS. Primary esophageal adenoid cystic carcinoma. Gut Liver. 2007;1(2):178–81.
Young CY, Lee KS, Shim YM, Kim TB, Kwhanmien K, Kim TS. Metastasis to regional lymph nodes in patients with esophageal squamous cell carcinoma: CT versus FDG PET for presurgical detection—prospective study. Radiology. 2003;227(6):764–70.
Young JC, Jang HJ, Shim YM, Kwhanmien K, Lee KS, Lee KH, Yong C, Yearn SC. 18F-FDG PET in patients with esophageal squamous cell carcinoma undergoing curative surgery: prognostic implications. J Nucl Med. 2004;45(11):1843–50.

5 Hepatobiliary, Pancreas, Adrenal, Melanoma, and GIST

Heidi Wassef and Linh T. Ho

Case 5.1

History

A 55-year-old man with recently diagnosed hepatocellular carcinoma (HCC). PET-CT requested for staging.

Findings

The small HCC is associated with focal enhancement at the dome of the liver on the contrast-enhanced axial image (Fig. 5.1a) but is not appreciated on the non-contrast-enhanced image (Fig. 5.1b). The HCC is not associated with hypermetabolism as shown on the fused PET-CT image (Fig. 5.1c) and the FDG PET image (Fig. 5.1d). Contrast-enhanced CT would be the follow-up study of choice since this HCC is not ^{18}F-FDG avid.

Pearls and Pitfalls

- The reported sensitivity of PET-CT for the detection of HCC is 55 % while for CT is 90 %, thus CT with IV contrast is the preferred study for diagnosis, staging, and restaging of HCC.
- Hypermetabolism in the hepatic tissue adjacent to a lesion can be seen up to 3 months following transarterial chemoembolization as a reaction to the infarcted tumor.
- Mild hypermetabolism in the parenchyma peripheral to the tumor occurs 2–3 days following radiofrequency ablation (RFA). The recommended ideal imaging time is 24–48 h following RFA because the cellular damage caused by thermocoagulation in RFA is immediate.

P.S. Conti, A. Kaushik (eds.), *PET-CT*, DOI 10.1007/978-1-4419-5811-2_5

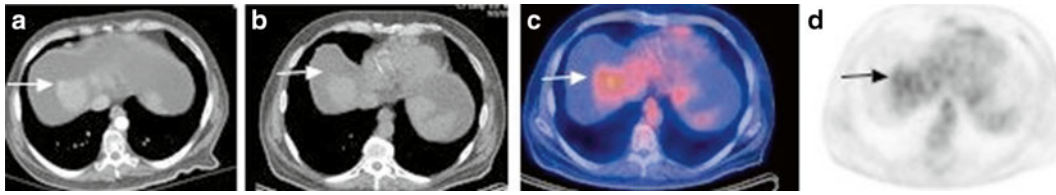

Fig. 5.1

Discussion

PET-CT has low sensitivity for the detection of HCC partly due to the high levels of glucose-6-phosphatase in the liver which dephosphorylates FDG-6-PO4 allowing it to leave the cell. Unlike the liver, other tissue do not have glucose-6-phosphatase, and thus FDG-6-PO4 is trapped within the cell allowing radiotracer accumulation and visualization. High-grade HCCs are less well differentiated and thus have less glucose-6-phosphatase.

Every year, there are nearly half a million people diagnosed with HCC. HBV or HCV infections and probably nonalcoholic liver disease are risk factors for HCC. The most common sites of extrahepatic metastatic HCC are the lung, abdominal lymph nodes, and bone.

Case 5.2

History

A 75-year-old man with newly diagnosed gallbladder carcinoma. PET-CT was requested to evaluate for metastatic disease.

Findings

A 2.7×1.4 cm intensely active soft tissue lesion within the gallbladder (Fig. 5.2), with SUVmax of 5.7, represents the primary neoplasm. In addition, there is mild wall thickening of the gallbladder with pericholecystic fluid, with no definite discernible activity, probably due to inflammation.

Several celiac axis (Fig. 5.2), retroperitoneal, and retrocrural lymph nodes are seen, consistent with metastases. The largest celiac axis adenopathy (near the stomach) measures 1.6×1.7 cm and has a SUVmax of 5.6.

Pearls and Pitfalls

- PET-CT is valuable for detecting regional lymph node involvement and distant metastases that are not diagnosed by multi-detector CT (MDCT).
- PET-CT shows no significant advantage over MDCT for the diagnosis of the primary gallbladder tumor.
- PET is helpful in detecting residual gallbladder carcinoma after cholecystectomy but has low sensitivity for detecting carcinomatosis.

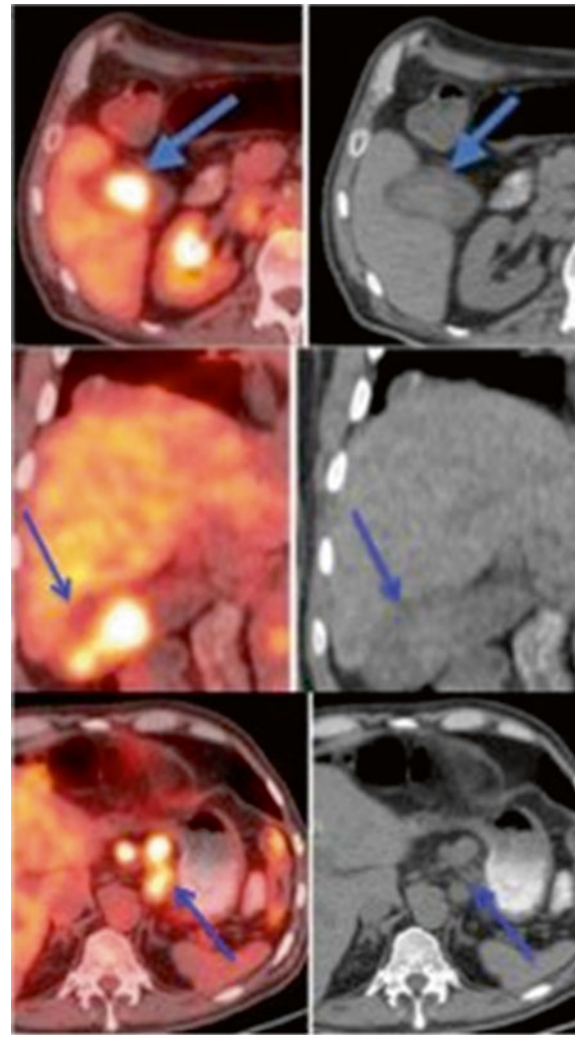

Fig. 5.2

Discussion

PET-CT shows a significantly higher positive predictive value (94.1 % vs. 77.5 %, $p = 0.04$) than that found for MDCT in the diagnosis of regional lymph node metastasis. In addition, PET-CT also demonstrates a significantly higher sensitivity (94.7 % vs. 63.2 %, $p = 0.02$) than MDCT in the diagnosis of distant metastases. A SUVmax of 3.65 was found to be the best cutoff value for detecting a gallbladder malignant tumor. PET-CT findings resulted in a change of management in 17 % of patients deemed resectable after standard workup.

Case 5.3

History

A 67-year-old man underwent an ERCP with biopsy revealing cholangiocarcinoma. PET-CT requested for staging.

Findings

There is an ill-defined, intensely hypermetabolic large mass involving the medial segment of the left lobe and the anterior segment of the right lobe of the liver (Fig. 5.3, arrowheads), consistent with the known cholangiocarcinoma (CC). The tumor likely involves and engulfs the gallbladder due to the apparent indistinctness of the gallbladder wall. A small, active hepatoduodenal lymph node is present (not shown). In addition, there is also mild hypermetabolism involving the entire pancreas (Fig. 5.3, arrows) due to post-ERCP pancreatitis. Hypermetabolism surrounding the biliary stent is due to foreign body reaction, but in this case, there may also be tumor involvement.

Pearls and Pitfalls

- PET-CT is valuable for detecting regional lymph node involvement and unsuspected distant metastases that are not diagnosed by MDCT.
- Hypermetabolism could be seen in patients with primary sclerosing cholangitis or known granulomatous disease as well as biliary stents, which could mimic neoplasm.

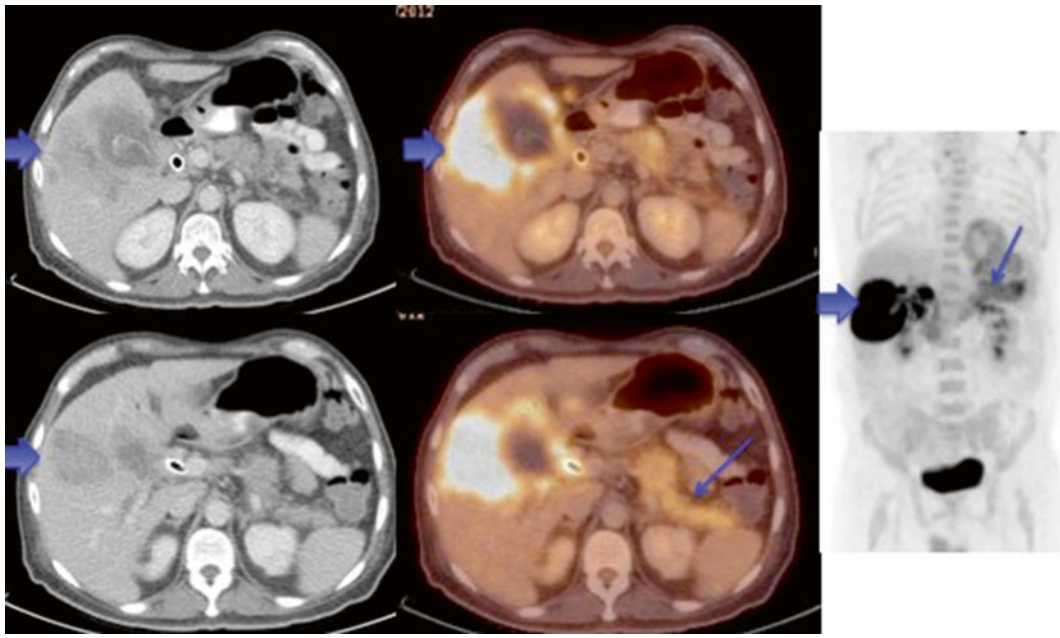

Fig. 5.3

Discussion

For cholangiocarcinoma, PET-CT shows significantly higher accuracy over CT in the diagnosis of regional lymph nodes (75.9 % vs. 60.9 %, $p = 0.004$) and distant metastases (88.3 % vs. 78.7 %, $p = 0.004$). There is no significant advantage of PET-CT over multi-detector CT (MDCT) for the diagnosis of a primary biliary tumor. FDG PET was shown to change management in 30 % of patients with CC. Additionally, FDG PET-CT is useful in patients with CC (except for infiltrating type) for detection of recurrent disease and for assessment of treatment response.

Case 5.4

History

A 73-year-old woman with recently discovered pancreatic head mass.

Findings

There is a $7 \times 7 \times 4$ cm hypermetabolic pancreatic head mass with a SUVmax of 13 (Fig. 5.4).

Pearls and Pitfalls

- For accurate staging of pancreatic carcinoma, the size of the tumor, relationship to adjacent vessels, and invasion of nearby tissue and spread of disease outside the pancreas must be assessed. Endoscopic ultrasound (EUS) has been found to be more accurate than CT in local staging of pancreatic malignancies and in predicting vascular invasion and resectability.
- Pancreatic cancer spreads to regional lymph nodes followed by the liver and lung. Osseous metastases are rare.
- PET can reliably detect hepatic, peritoneal, and other distant metastases that are at least 1 cm.

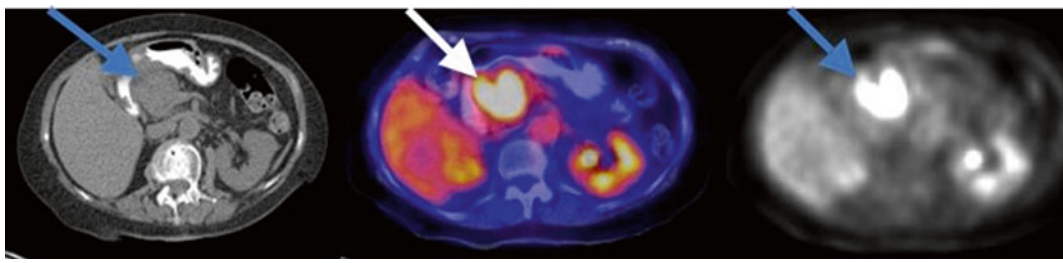

Fig. 5.4

Discussion

The pancreatic head is defined as the segment to the right of the left border of the superior mesenteric vein (SMV). The body extends from the left border of the SMV to the left border of the aorta. The narrow segment between the head and body is defined as the neck. The segment of pancreas posterior to the SMV is the uncinate process. PET-CT is helpful in differentiating benign and malignant pancreatic masses using a SUVmax cutoff of 2.5.

Case 5.5

History

Patient had a Whipple procedure for moderately differentiated pancreatic adenocarcinoma. PET-CT performed to assess response following chemotherapy.

Findings

There is peripheral increased FDG uptake at the liver surface (Fig. 5.5) with SUVmax up to 5.3 consistent with peritoneal carcinomatosis. Some of the foci of hypermetabolism demonstrate no CT correlate and some show peritoneal thickening or nodularity.

Pearls and Pitfalls

Peritoneal metastases can appear to lie within the liver. Careful evaluation of the coronal and sagittal images is helpful in differentiating peritoneal implants from peripheral hepatic lesions particularly if the peritoneal deposits are not evident on CT.

Discussion

Tumors that may involve the peritoneal cavity include malignant peritoneal mesothelioma, pseudomyxoma peritonei, and metastases from the stomach, colon, appendix, gallbladder, pancreas, ovary, breast, lung, uterus, and lymphoma. CT has a sensitivity of 43 % and positive predictive value of 100 % for evaluation of peritoneal carcinomatosis, while PET-CT has a sensitivity of 78 % and positive predictive value of 96 %.

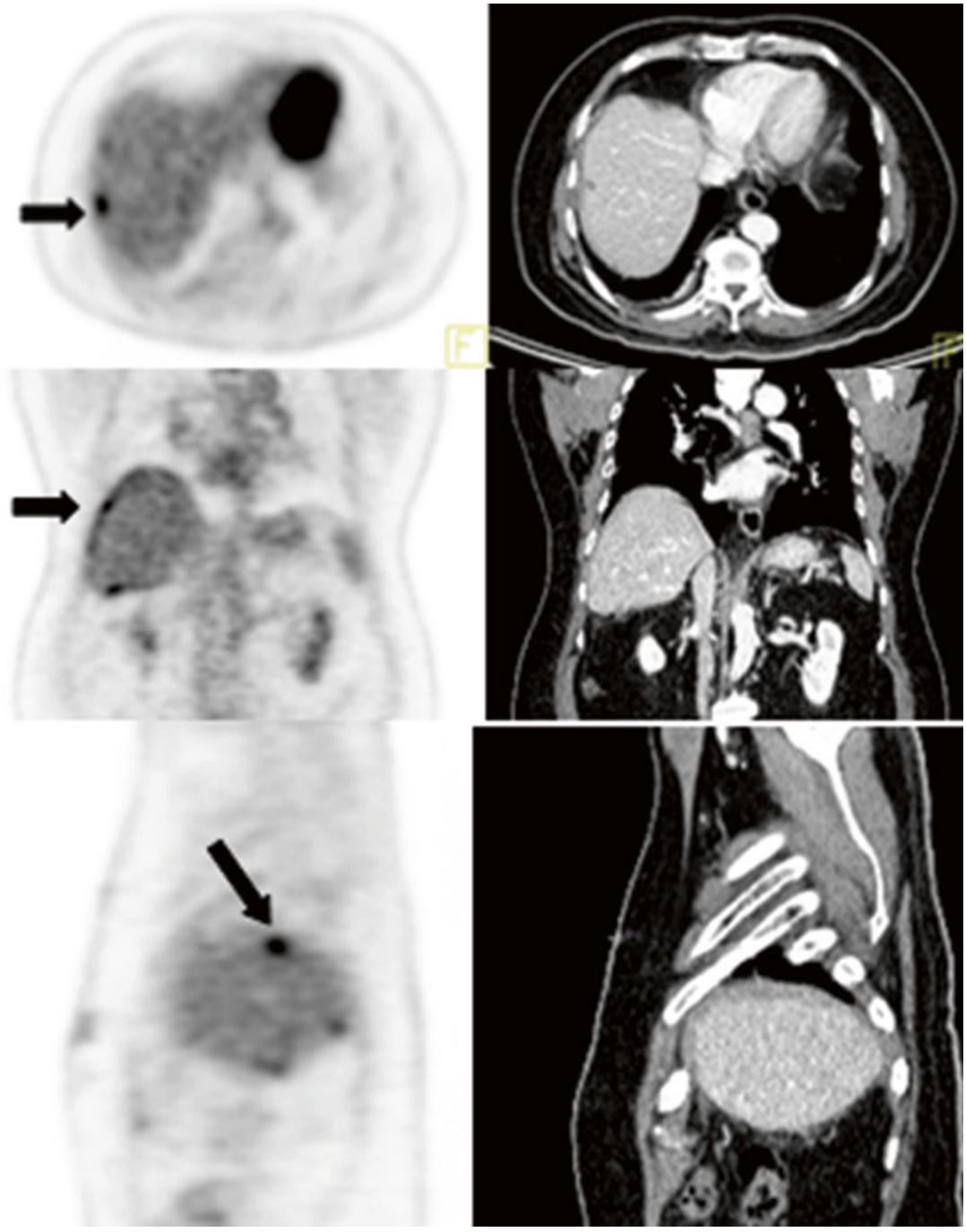

Fig. 5.5

Case 5.6

History

Patient with moderately differentiated adenocarcinoma of the ampulla who is status post hepaticojejunostomy, right hemicolectomy, and partial hepatectomy in February 2010 had his last chemotherapy dose 2 months ago.

Findings

Patient had interval progression of right paratracheal and precarinal adenopathy and interval development of multiple right axillary and subpectoral nodes.

Pearls and Pitfalls

The histological differentiation of periampullary cancer is more important than the anatomical location. Pancreatobiliary histology carries a worse prognosis than intestinal histology in periampullary cancers.

Discussion

Periampullary cancers can arise from the pancreas, duodenum, distal common bile duct (CBD), or the ampullary duct. Ampullary carcinoma most commonly presents as obstructive jaundice in 80 % of patients and is treated with a Whipple procedure (pancreaticoduodenectomy). Pneumonia, abdominal infection, anastomotic leaks, and delayed gastric emptying are the most common complications following a Whipple procedure.

Case 5.7

History

Woman diagnosed with pancreatic cancer. PET-CT requested for staging.

Findings

A solitary focus of hypermetabolism was consistent with hepatic metastases (Fig. 5.6).

Pearls and Pitfalls

Hepatic metastasis appeared as a vertically oriented linear lesion due to patient breathing.

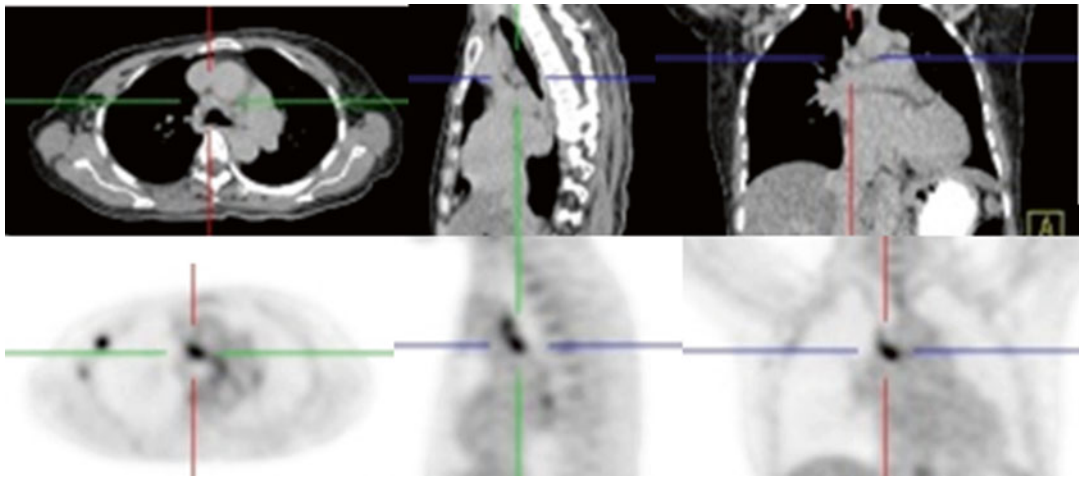

Fig. 5.6

Discussion

Only 15–20 % of patients with pancreatic cancer are resectable at diagnosis and have a 20 % 5-year survival rate. Gallium-68 DOTATATE positron emission tomography/computed tomography (PET-CT neuroendocrine tumors) changed therapy in 35 % of patients Pancreatic ductal adenocarcinomas are characterized by invasiveness, rapid progression and resistance to treatment. Potentially curative resection followed by adjuvant systemic chemotherapy is the most common therapeutic strategy.Pancreatic cancer has a proclivity for perineural invasion. It is characterized by lymphatic spread to adjacent and distant lymph nodes and metastases to the liver, peritoneum and the lung. Higher metabolic activity on FDG PET correlates with higher initial stage of pancreatic adenocarcinoma and with decreased overall survival.

Case 5.8

History

A 61-year-old male with history of gastrointestinal stromal tumor (GIST) for follow-up evaluation.

Findings

The patient is status post partial gastrectomy and splenectomy. There is interval development of a hypermetabolic focus in the caudate lobe (segment 1) consistent with recurrent disease (Fig. 5.7).

Pearls and Pitfalls

PET-CT can predict malignant potential of GISTs. An SUV greater than 5 indicates a higher likelihood of having a malignant potential.

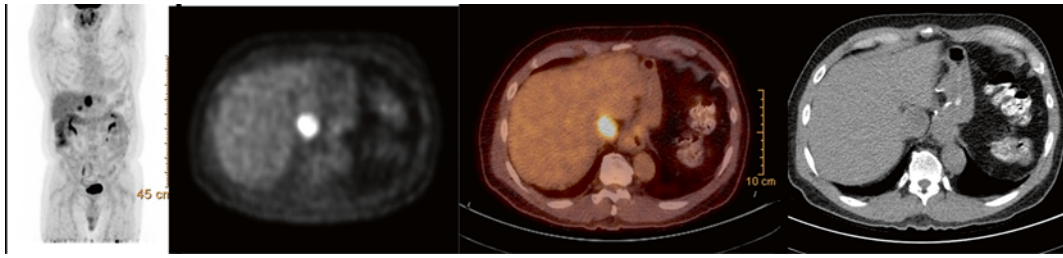

Fig. 5.7

Discussion

PET-CT no earlier than 6–8 weeks following GIST resection improves the diagnostic accuracy and influences treatment. Studies performed less than 6 weeks following resection have a higher incidence of false-negative, false-positive, and indeterminate findings.

Case 5.9

History

A 64-year-old male diagnosed with GIST 7 years ago. The patient is on sixth line chemotherapy. PET-CT requested to evaluate response to chemotherapy.

Findings

Hypermetabolic metastases are seen in the posterior segment of the right lobe and lateral segment of the left lobe (Fig. 5.8, arrows). Although the lesions as seen on CT are unchanged in size compared to the prior study, the hypermetabolism has increased in size and activity. Patient was admitted due to bleeding. Hemoglobin became stable, and thus no surgical or radiologic interventional procedure was required.

Pearls and Pitfalls

The size of the lesion on a post-therapy scan as determined by CT is not an accurate assessment of response to therapy.

Discussion

A decrease in metabolic activity indicating response to therapy is seen weeks to months prior to a significant decrease in the size of the lesion. Post-chemotherapy studies revealing no change in metabolism indicates primary resistance of the tumor to the administered chemotherapy.

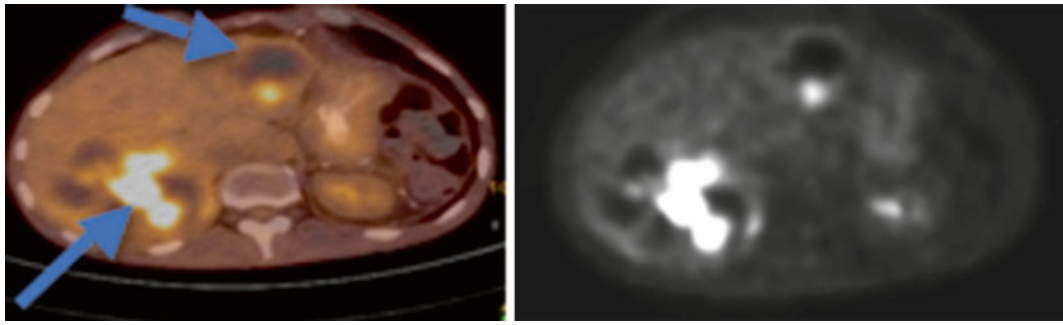

Fig. 5.8

Case 5.10

History

A 64-year-old man with esophageal adenocarcinoma. PET-CT is requested for staging.

Findings

There is diffuse esophageal wall thickening with intensely increased metabolic activity involving the distal 2/3 of the esophagus consistent with the reported recent diagnosis of esophageal adenocarcinoma via endoscopy. Multiple scattered hypermetabolic foci involving the liver, bone, retroperitoneal and cervical nodes, and right adrenal gland (Fig. 5.9, arrows) are consistent with metastases. There is also mild activity in the left adrenal gland which is physiologic.

Pearls and Pitfalls

Several groups have evaluated using a cutoff of 1 for the ratio of SUVmax of adrenal gland to SUVmax of the liver to differentiate benign from malignant adrenal lesions. Blake et al. found the sensitivity, specificity, positive predictive value, negative predictive value, and accuracy to be 100 %, 93.8 %, 81.8 %, 100 %, and 95.1 %, respectively. Potential false negatives include a very small malignant tumor, tumors with significant necrosis, and metastases from tumors with limited 18F-FDG uptake such as mucinous or neuroendocrine tumors. Potential false positives include rare hypermetabolic adenomas and pheochromocytoma. Ten percent of pheochromocytomas are malignant, 10 % are bilateral, 10 % are in children, and 10 % are extra-adrenal.

Discussion

An adrenal lesion with Hounsfield unit (HU) < 10 indicates a lipid-rich adenoma. If HU ≥ 10, 18F-FDG PET, CT washout test, magnetic resonance chemical shift imaging with in-phase and out-of-phase images, or

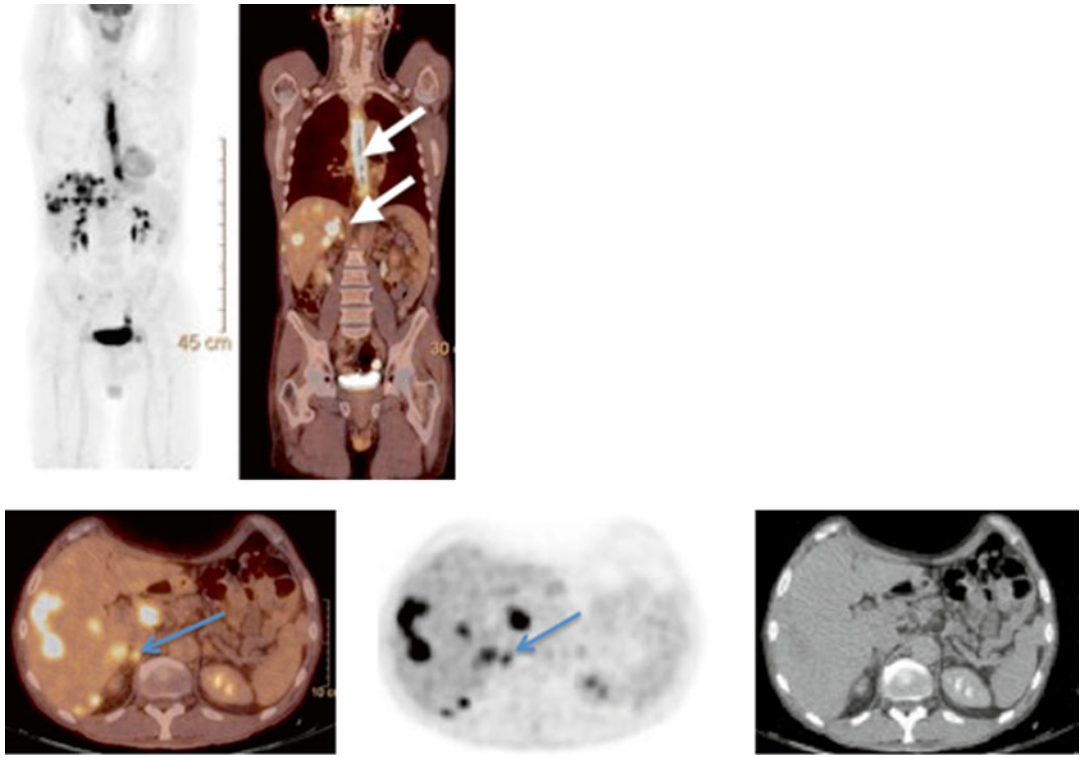

Fig. 5.9

biopsy may be used to differentiate between benign and malignant lesions. Greater than 60 % intravenous contrast washout at 15 min compared to uptake at 60 s in the adrenal lesion indicates that it is an adenoma.

Case 5.11

History

Newly diagnosed right adrenal cortical carcinoma.

Findings

There is an 8 cm heterogeneous, hypermetabolic mass superior to the right kidney (Fig. 5.10, arrows). There were no enlarged lymph nodes. Pathology examination revealed adrenal cortical carcinoma with lymphovascular invasion. Periaortic lymph nodes were negative.

Pearls and Pitfalls

Adrenal cortical carcinoma (ACC) is often large at presentation. ACC appears heterogeneous due to the presence of necrosis, hemorrhage, and

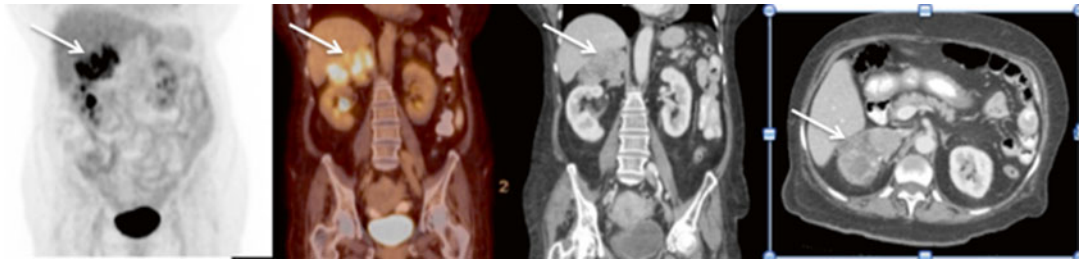

Fig. 5.10

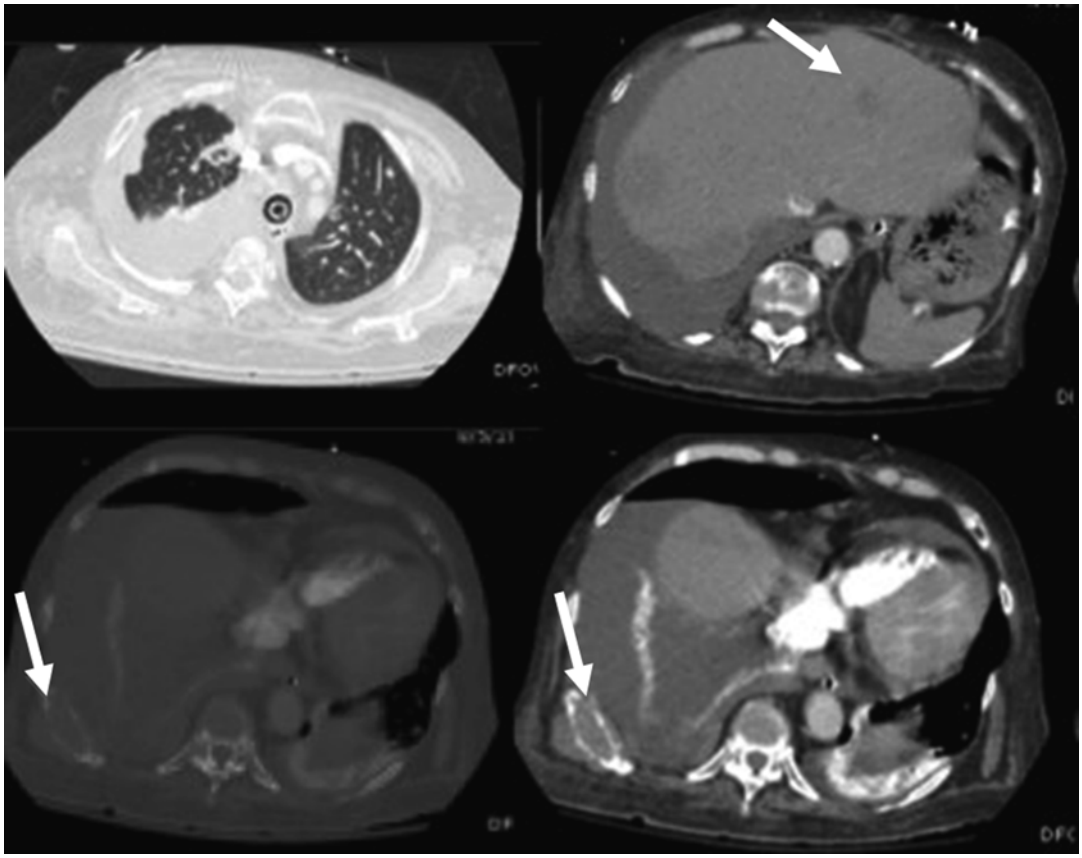

Fig. 5.11

calcification. Large tumors may invade the adrenal vein and inferior vena cava. Metastases commonly involve the lung, liver, and bone (Fig. 5.11, 1 year later) but can involve cervical and mediastinal lymph nodes, ovaries, pancreas, thyroid, brain, spleen, and peritoneum.

Discussion

ACC is rare with an incidence of 2 per million. Age of presentation is between 30 and 70 years. ACC may present due to excess hormone production or due to mass effect. Cushing's syndrome which involves excess

cortisol production may present with weak muscles, fat on the back of neck and upper back, abnormal hair growth, mood changes, high blood pressure, and high blood sugars. In most patients with ACC, detection of the first metastasis occurs within 4 months of diagnosis. Five-year survival drops to 0–24 % in patients with metastases compared to 58–66 % in patients without metastatic disease.

Case 5.12

History

A 51-year-old woman with recently diagnosed melanoma following shave biopsy overlying the left mandible. The patient has a palpable left cervical lymph node. PET-CT was requested for staging.

Findings

A 1 cm left cervical level 2 lymph node has a SUVmax of 2.2 (Fig. 5.12, arrows). This lymph node was biopsied revealing metastatic disease.

Pearls and Pitfalls

PET-CT has a high sensitivity and specificity in detecting distant metastases from melanoma. The sensitivity of PET-CT for the detection of melanoma in regional lymph nodes is reported to be only 16.7 %, and thus PET-CT cannot replace lymphoscintigraphy for evaluation of regional nodes. Reports indicate that PET-CT may aid in the detection of primary disease in patients with metastatic melanoma of unknown primary.

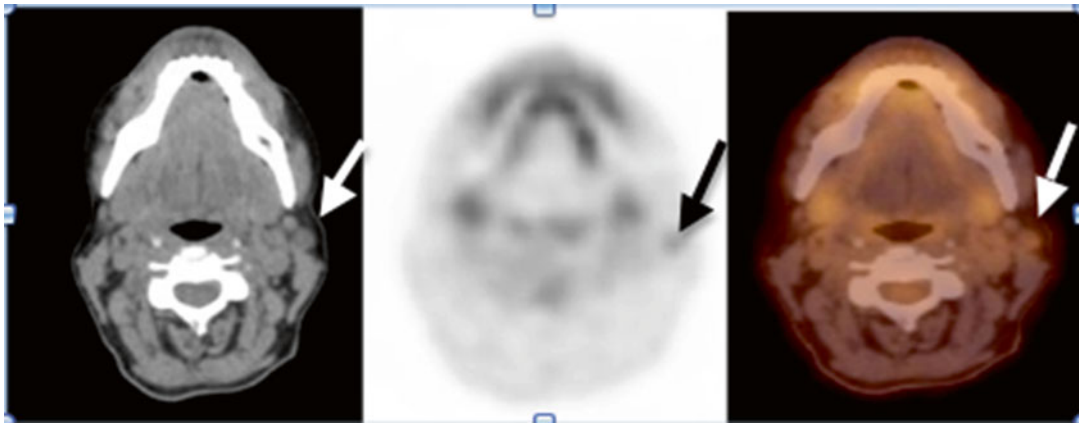

Fig. 5.12

Discussion

The T stage depends on the tumor thickness with lesions less than 1.0 mm thick, 1.01–2.0, 2.01–4.0, and >4.0 mm classified as T1, T2, T3, and T4, respectively. Sentinel lymph node (SLN) biopsy is recommended for patients with Breslow thickness 1–4 mm melanomas. Completion lymph node dissection is performed if the SLN is positive.

Case 5.13

History

A 64-year-old man who had resection 2 yrs ago of a 6 mm lentigo maligna subtype of melanoma on his left cheek with perineural and subcutaneous invasion. The patient underwent radiation 1 year ago. Restaging PET-CT is requested following chemotherapy to determine response to therapy.

Findings

There has been interval progression of disease with interval increase in size of hypermetabolic left cervical level 1B lymph node (Fig. 5.13, arrow) as well as increase in number of pulmonary nodules.

Pearls and Pitfalls

PET-CT has higher accuracy (97.2 %) than PEt alone (92.8 %) and CT alone (78.8 %) for N (lymph node) and M (metastases) staging. The sensitivity of PET-CT for the detection of pulmonary melanoma metastases depends on size. The sensitivity is 100 % for nodules 12 mm or larger, 63.6 % for 10–11 mm, 56.8 % for 8–9 mm, 33.3 % for 6–7 mm, and 7.9 % for 4–5 mm nodules.

Discussion

The most common location for melanoma is the upper back in men and the lower legs and upper back in women. Superficial spreading, lentigo maligna, nodular, and acral lentiginous are subtypes of melanoma that

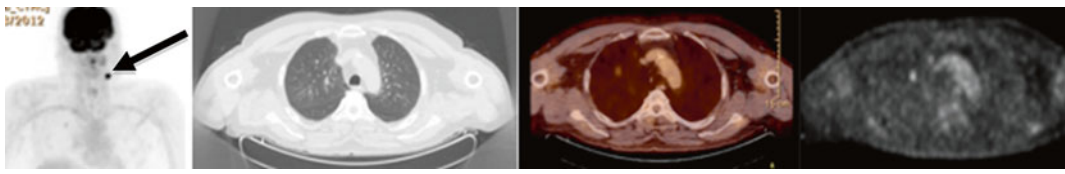

Fig. 5.13

are distinguished by their growth patterns. Review of the patient records is important. Recurrent disease in patients with stage I and II melanomas is most likely locoregional, while in stage III disease is likely distant. Common sites of metastases are the skin, subcutaneous tissue, lymph node, liver, bone, lung, brain, and visceral organs.

Suggested Reading

Anderson CD, Rice MH, Pinson CW, et al. Fluorodeoxyglucose PET imaging in the evaluation of gallbladder carcinoma and cholangiocarcinoma. J Gastrointest Surg. 2004;8(1):90–7.

Assie G, Antoni G, Tissier F, et al. Prognostic parameters of metastatic adrenocortical carcinoma. J Clin Endocrinol Metab. 2007;92(1):148–54.

Bertz-Lepel J, Rahm J, Pink D, et al. Influence of PET/CT on therapeutic management after resection of high-risk or very high-risk GIST. J. Clin Oncol 2011;29(suppl; abstr e20516).

Blake MA, Slattery JM, Kaira MK. Adrenal lesions: characterization with fused PET/CT image in patients with proved or suspected malignancy—initial experience. Radiology. 2006;238:970–7.

Chin BB, Wahl RL. 18F-Fluoro-2-deoxyglucose positron emission tomography in the evaluation of gastrointestinal malignancies. Gut. 2003;52 Suppl 4:iv23–9.

Chuang TY, Coleman 3rd JJ. Current therapy of cutaneous melanoma. Plast Reconstr Surg. 2001;105:1774–99.

Donghiui L, Keping X, Wolff R, et al. Pancreatic cancer. Lancet. 2004;363:15841–8.

Elsayes KM, Caoili EM. Adrenal imaging: a practical guide to diagnostic workup and spectrum of imaging findings. Appl Radiol. 2011;40(9):14–9.

El-Serag HB. Hepatocellular carcinoma. N Engl J Med. 2011;365(12):1118–27.

Ghazali N, Collyer JC, Tighe J. Navigation-assisted localisation and resection of subclinical metastatic malignant melanoma of unknown primary based on 18-fluorodeoxyglcose positron emission tomography computed tomography fusion imaging. Int J Oral Maxillofac Surg. 2012;14(1):5–8. Epub 2011 Oct 22.

Gress F, Hawes R, Thomas S, et al. Role of EUS in the preoperative staging of pancreatic cancer: a large single-center experience. Gastrointest Endosc. 1999;50:786–91.

Heinrick S, Pierre-Alain C. Ampullary cancer. Curr Opin Gastroenterol. 2010;26:280–5.

Icard P, Goudet P, Charpenay C, et al. Adrenocortical carcinomas: surgical trends and results of a 253-patient series from the French Association of Endocrine Surgeons study group. World J Surg. 2001;25:891–7.

Jadvar H, Henderson RW, Conti PS. [F-18]fluorodeoxyglucose positron emission tomography and positron emission tomography: computed tomography in recurrent and metastatic cholangiocarcinoma. J Comput Assist Tomogr. 2007;31(2):223–8.

Kim JY, Kim MH, Lee TY, et al. Clinical Role of ^{18}F-FDG PET-CT in suspected and potentially operable cholangiocarcinoma: a prospective study compared with conventional imaging. Am J Gastroenterol. 2008;103(5):1145–51.

Lee SW, Kim HJ, Park JH, et al. Clinical usefulness of 18F-FDG PET-CT for patients with gallbladder cancer and cholangiocarcinoma. J Gastroenterol. 2010;45(5):560–6.

Levy A, et al. Secondary tumors and tumorlike lesions of the peritoneal cavity: imaging features with pathologic correlation. Radiographics. 2009;29:347–73.

Mayerhoefer ME, Prosch H, Herold CJ, et al. Assessment of pulmonary melanoma metastases with (18)F-FDG PET/CT: which PET-negative patients require additional tests for definitive staging? Eur Radiol. 2012;22(11):2451–7.

Metser U, Miller E, Lerman H, et al. 18F-FDG PET/CT in the evaluation of adrenal masses. J Nucl Med. 2006;47(1):32–7.

Petrowsky H, Wildbrett P, Husarik DB, et al. Impact of integrated positron emission tomography and computed tomography on staging and management of gallbladder cancer and cholangiocarcinoma. J Hepatol. 2006;45(1):43–50.

Purandare NC, Rangarajan V, Shah SA, et al. Therapeutic response to radiofrequency ablation of neoplastic lesions: FDG PET/CT findings. Radiographics. 2011;31(1): 201–13.

Romano E, Scordo M, Dusza SW, et al. Site and timing of first relapse in stage III melanoma patients: implications for follow-up guidelines. J Clin Oncol. 2010;28(18): 3042–7. Epub 2010 May 17.

Ryan D, Mamon H, Fernandez-del Castillo C. Ampullary carcinoma: treatment and prognosis. http://www.uptodate.com/contents/ampullary-carcinoma-treatment-and-prognosis. Accessed 19 Nov 2012.

Tamm EP, Fleming JB, Varadhachary GR. In: Silverman P, editor. Oncologic imaging: a multidisciplinary approach. Elsevier, Philadelphia; 2012.

Turlakow A, et al. Peritoneal carcinomatosis: role of 18F-FDG PET. J Nucl Med. 2003;44:1407–12.

Van den Abbeele AD. The lessons of GIST-PET and PET/CT: a new paradigm for imaging. Oncologist. 2008;13 Suppl 2:8–13.

Wagner JD, Schauwecker D, Davidson D, et al. Prospective study of fluorodeoxyglucose-positron emission tomography imaging of lymph node basins in melanoma patients undergoing sentinel node biopsy. J Clin Oncol. 1999;17(5):1508–15.

Wagner JD, Gordon MS, Jaeger U, et al. Diagnostic performance of whole body dual modality 18F-FDG PET/CT imaging for N- and M-staging of malignant melanoma: experience with 250 consecutive patients. J Clin Oncol. 2006;24(7):1178.

Wong SL, Balch CM, Agarwala SS, et al. Sentinel lymph node biopsy for melanoma: American Society of Clinical Oncology and Society of Surgical Oncology Joint Clinical Practice Guideline. Ann Surg Oncol. 2012;19(11):3313–24.

Yoshikawa K, Shimada M, Sato H, et al. The utility of PET-CT in predicting malignant potential of GIST. J Clin Oncol 2012;30(suppl 4, abstr 38)

6 Colon Neoplasms

Aarti Kaushik and Robert W. Henderson

Case 6.1: Ascending Colon Cancer

History

Patient is a 35-year-old female with ascending colon cancer for initial staging.

Findings

A soft tissue mass in the colonic hepatic flexure with SUV max 7.7 consistent with primary tumor (Fig. 6.1). There are focal areas of increased uptake which could represent mesenteric nodes and/or peritoneal/omental metastases. There are innumerable hypermetabolic panlobar metastases in the enlarged liver.

Case 6.2: Mid-ascending Colon Cancer

History

49-year-old male newly diagnosed with adenocarcinoma of the ascending colon, with possible metastasis to the lung and liver.

Findings

There are hypermetabolic metastatic lesions seen in the right hepatic lobe (involving segments 5, 6, and 7), with the most avid lesion seen in segment 6, demonstrating SUV max 9.4 (Fig. 6.2). There is an annular lesion in the mid-ascending colon, demonstrating SUV max 18.3, compatible with known site of primary neoplasm.

P.S. Conti, A. Kaushik (eds.), *PET-CT*, DOI 10.1007/978-1-4419-5811-2_6

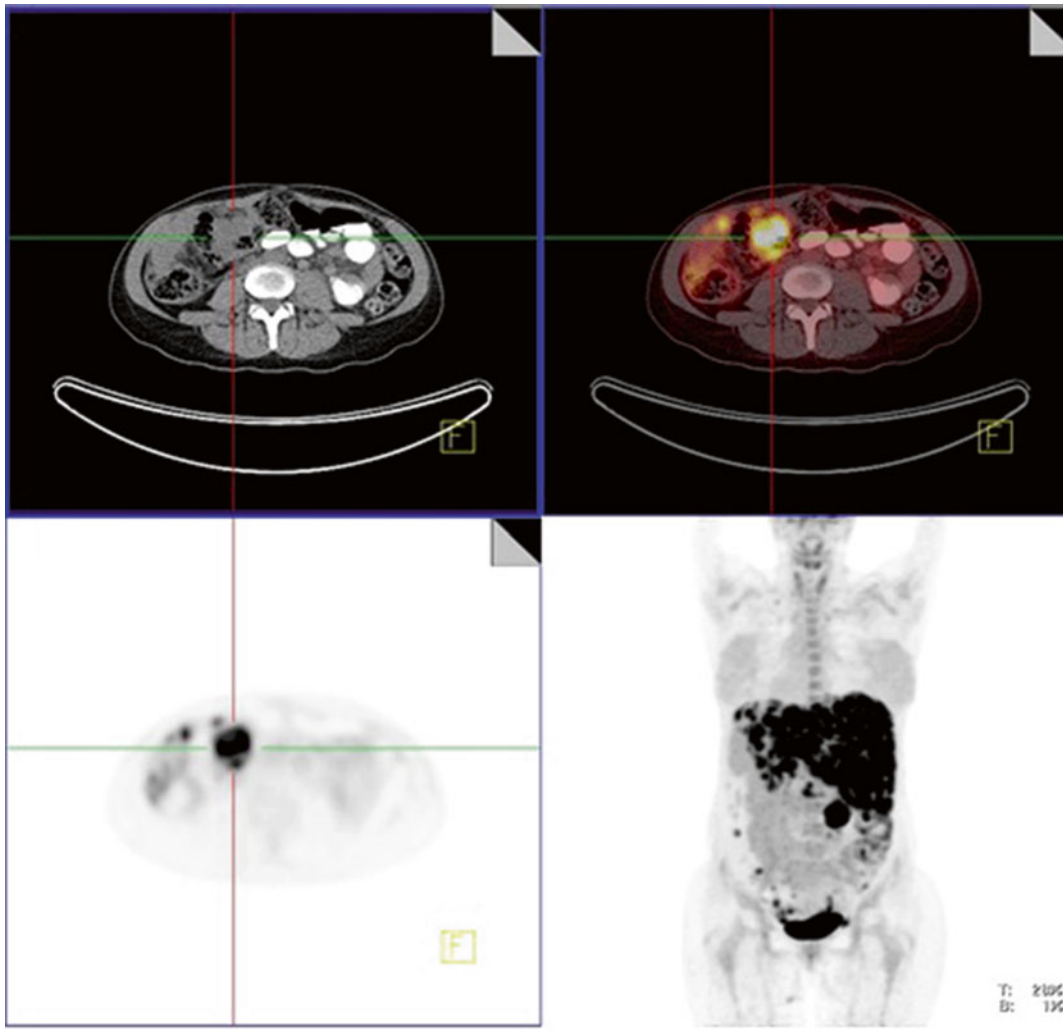

Fig. 6.1

Pearls and Pitfalls

Accurate preoperative staging is essential for the planning of optimal therapy considering the many therapeutic options available.

Discussion

CRC is the third most commonly diagnosed cancer in males and females. The survival rate depends on the stage at the time of diagnosis. Approximate 5-year survival rates are stage I 90 %, IIA 85 %, IIB 72 %, IIIA 83 %, IIIB 64 %, IIIC 44 %, and IV 8 %.

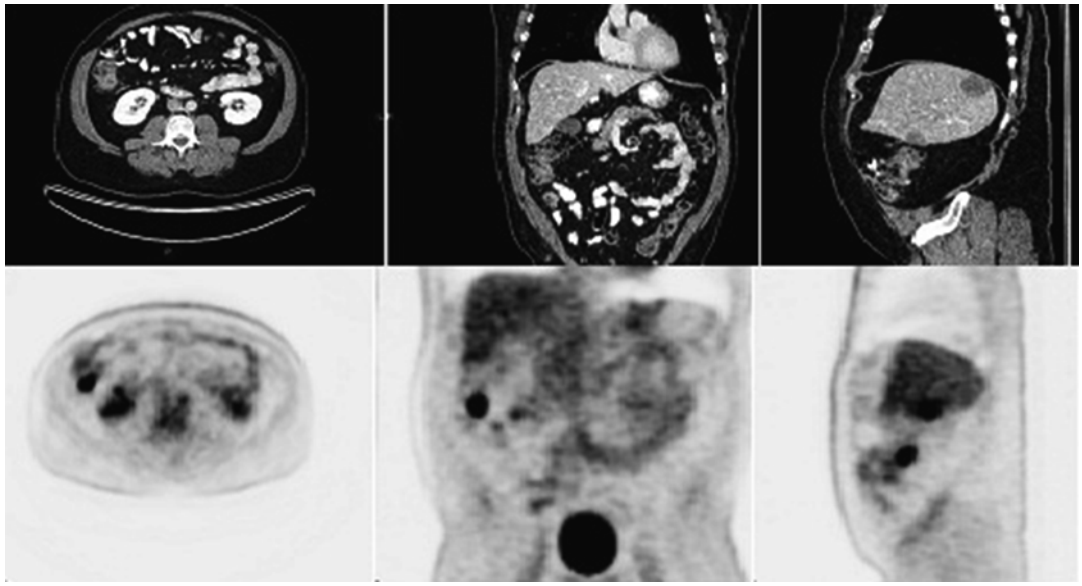

Fig. 6.2

Case 6.3: Peritoneal Metastases from Colon Cancer

History

Patient with metastatic colorectal cancer has history of cholecystectomy. Patient had last chemotherapy in 2005. This scan is being done for suspected recurrence in 2011.

Findings

There is a peritoneal nodule with adjacent peritoneal thickening measuring 1.2 cm in the right false pelvis with SUV max 16.3 (Fig. 6.3). There is an intensely active lesion anterior to the capsule of the liver at the gallbladder fossa measuring 1.7×0.7 cm, with SUV max 7.3.

Pearls and Pitfalls

1. Roughly one in five patients with colorectal cancer develops peritoneal minimal residual disease after surgical resection.
2. About one in seven patients develops peritoneal carcinomatosis.

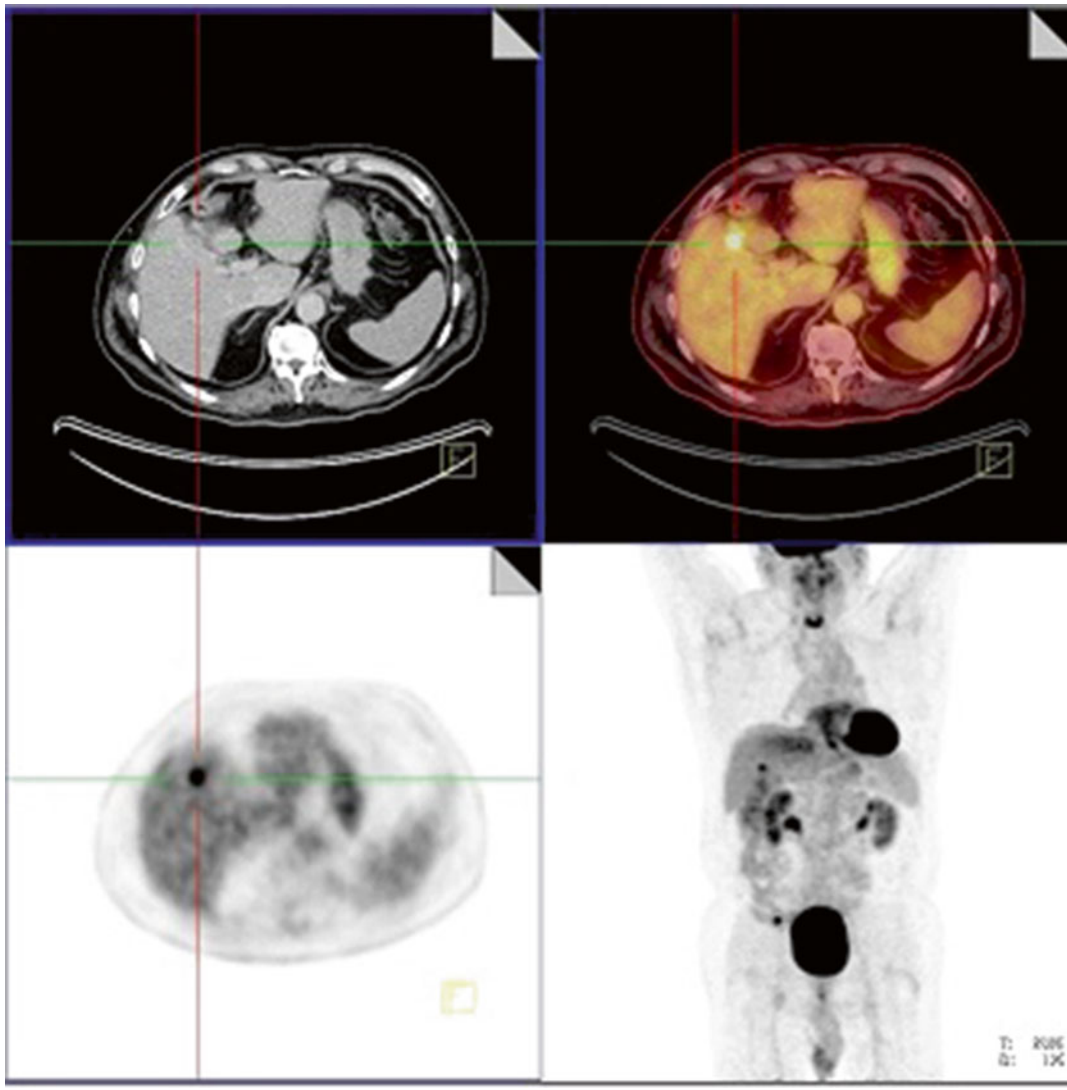

Fig. 6.3

Discussion

There is a vast body of research addressing hematogenous metastasis; little is known about the biology of peritoneal spread of colorectal cancer. The development of peritoneal carcinomatosis involves well-defined steps including cell shedding and transport, adhesion to the mesothelial layer, invasion of and proliferation into the submesothelial stroma, and potential access to the systemic circulation.

Case 6.4: Recurrent Adenocarcinoma of the Rectum Manifesting as Solitary Inguinal Adenopathy

History

Patient with moderately differentiated adenocarcinoma of the rectum diagnosed in 2005 status post resection with nodal and lung metastases. Patient underwent resection of the left upper lung lesion in April 2008. Patient is status post chemotherapy in April 2008 and radiation therapy in August 2005. No interval treatment. Scan being done for restaging.

Findings

A new 2 × 2.3 cm left inguinal nodal mass with SUV max 12.8 is consistent with recurrent metastatic disease (Fig. 6.4).

Pearls and Pitfalls

Low rectal carcinoma is more likely to present with pulmonary, osseous, and ilioinguinal metastases because of hemorrhoidal venous circulation.

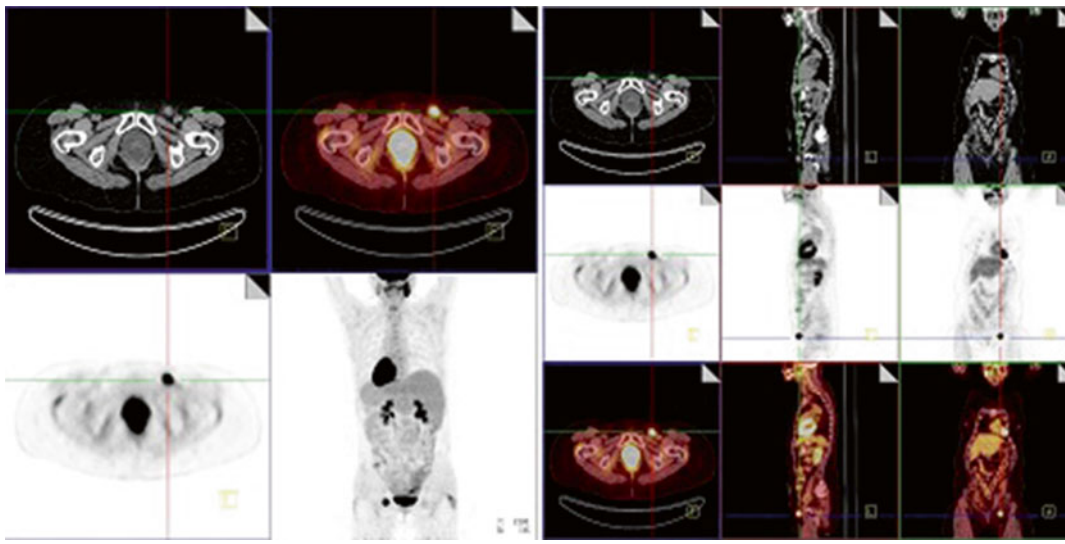

Fig. 6.4

Discussion

The usual pattern of regional lymph node metastasis in colorectal carcinoma follows the vascular distribution in the mesocolon. Tumors originating from the cecum spread to the ileocolic nodes, whereas tumors of the ascending and the proximal transverse colon drain in lymph nodes of the right colic and middle colic arteries reaching the superior mesenteric artery lymph nodes. Tumors originating from the descending colon spread to the left colic artery nodes, whereas those of the sigmoid colon reach the sigmoid artery nodes ending in the inferior mesenteric artery lymph nodes. Both the inferior and the superior mesenteric artery nodes belong to the preaortic nodes. Tumors in the rectum can spread by two different routes. The lymphatic drainage of tumors of the upper rectum reaches the inferior mesenteric artery lymph nodes via the superior rectal arteries. Metastases of tumors originating from the lower rectum reach the internal iliac nodes by following the pathway of the middle and the inferior rectal arteries and then the common iliac and the para-aortic nodes. Tumors of the anal region spread to the superficial inguinal lymph nodes ascending along the femoral vessels to the deep inguinal nodes and along the iliac vessels to the para-aortic nodes. After radical surgery for carcinoma of the rectum with interruption of the normal pathway of lymphatic drainage, recurrent disease may find an alternative retrograde route to the superficial and deep inguinal nodes.

Case 6.5: Psoas Muscle Metastasis from Colon Cancer

History

Patient is an 83-year-old female with appendiceal cancer (mucinous adenocarcinoma) with mass in the right iliopsoas muscle. Patient has radiation therapy in 2007 and is on chemotherapy, last dose in December 2010, with scan being done for restaging.

Findings

There is a peripherally enhancing hypermetabolic right distal psoas muscle mass with central photopenia (SUV max 6.2) (Fig. 6.5). On bone windows, there is no definite iliac bone involvement.

Pearls and Pitfalls

Skeletal muscles are an unusual site of blood-borne metastasis, but direct spread from adjacent tumor can occur.

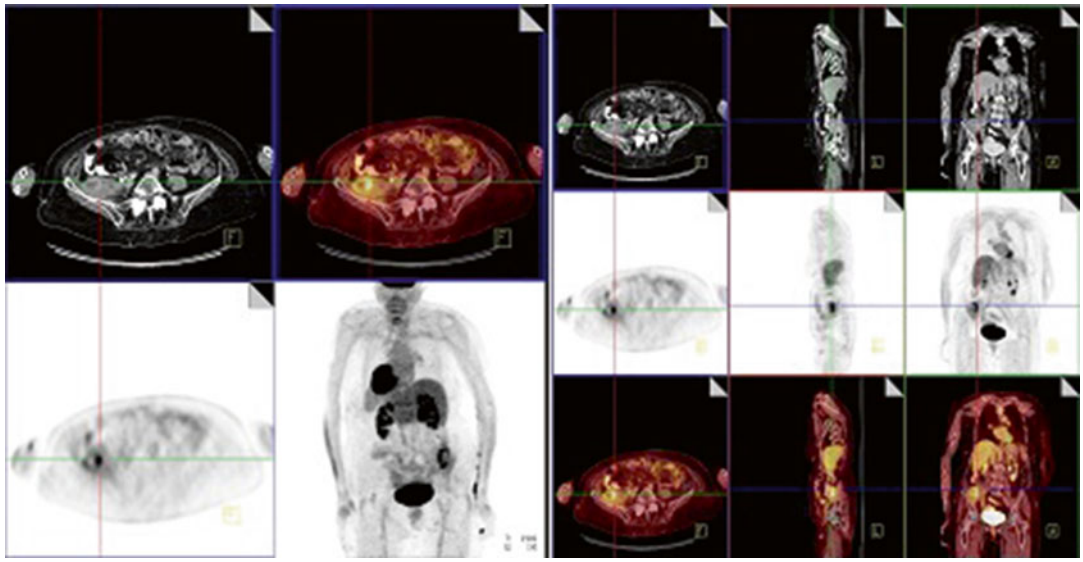

Fig. 6.5

Discussion

Skeletal muscle is an unusual site for blood-borne metastasis. The most common neoplasm metastasizing to the muscle is from the breast, lungs, or melanoma. The most common muscles involved are psoas and paravertebral muscles. The low incidence of muscular metastasis may be related to the anatomical characteristics and/or biochemical environment of the skeletal muscle. In this case, this is direct spread from appendiceal tumor to the psoas muscle.

Case 6.6: Colon Cancer with Hepatic Pulmonary and Nodal Involvement

History

The patient had moderately to poorly differentiated adenocarcinoma of the sigmoid status post sigmoidectomy and left oophorectomy. Patient has metastases to the left ovary, liver, and lung, with scan being done for evaluation with PET/CT.

Findings

There are panlobar hepatic metastases with central necrosis with SUV max up to 17.1 (Fig. 6.6). These are replacing almost half of the liver.

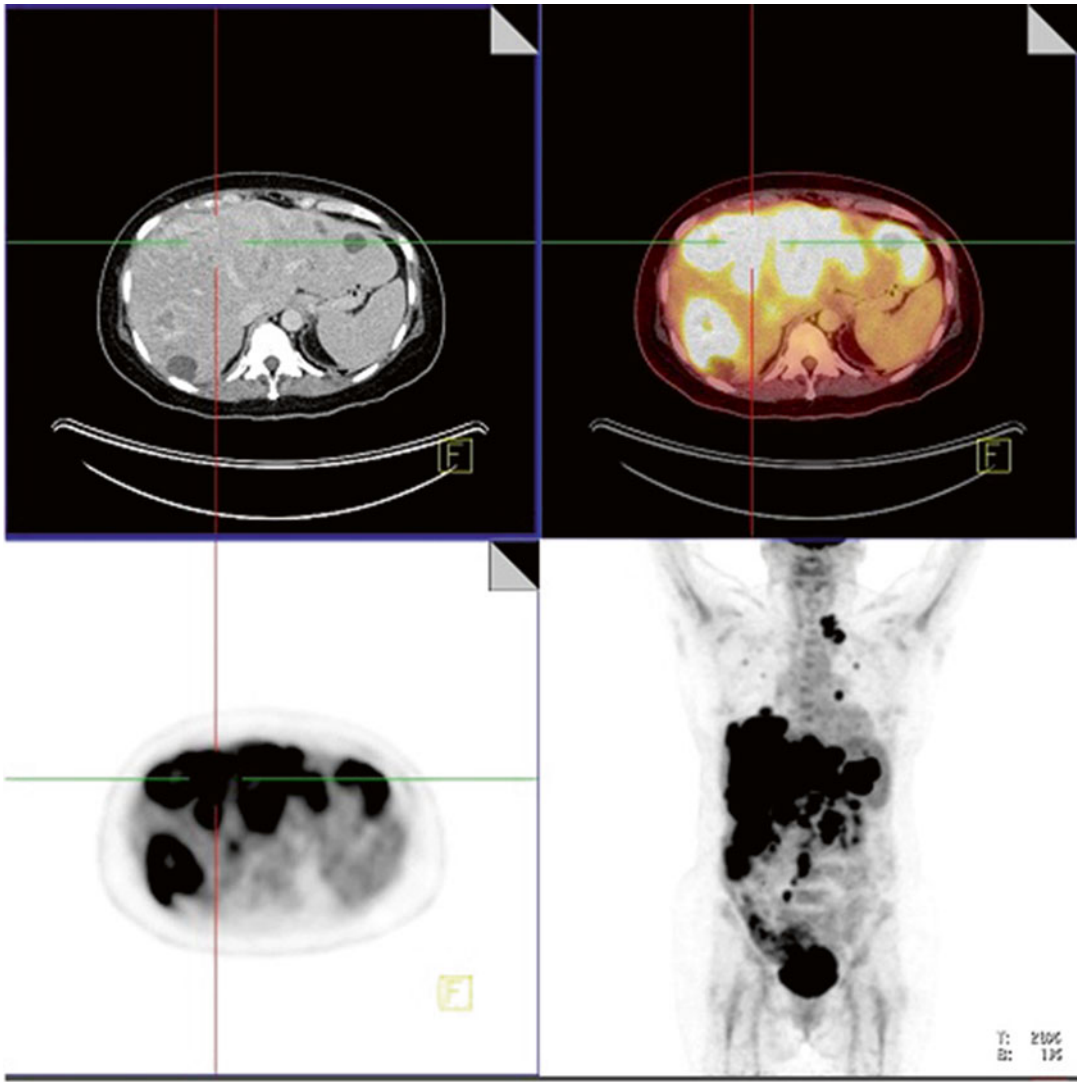

Fig. 6.6

There is continuous chain of hypermetabolic retroperitoneal adenopathy extending from the porta hepatis/gastroduodenal level to beyond the bifurcation involving a right common iliac node with SUV max up to 8.8.

Pearls and Pitfalls

Tumors arising in the low rectum may metastasize initially to the lungs because the inferior rectal vein drains into the inferior vena cava rather than into the portal venous system.

Discussion

Because the venous drainage of the intestinal tract is via the portal system, the first site of hematogenous dissemination is usually liver, followed by the lungs, bone, and many other sites, including the brain. However, tumors arising in the distal rectum may metastasize initially to the lungs because the inferior rectal vein drains into the inferior vena cava rather than into the portal venous system. The true prevalence of metastatic disease is unknown, but approximately 20–25 % of patients with colorectal cancer have liver metastases at the time of diagnosis. Studies based on autopsy results showed that up to 70 % of colon cancer patients have liver metastases at autopsy.

Case 6.7: Cecal Cancer

History

Patient with moderately differentiated adenocarcinoma of the cecum for initial staging.

Findings

There is a hypermetabolic right internal mammary node with SUV max 3.3 (Fig. 6.7). There is extraordinarily intense hypermetabolic cecal mass with SUV max up to 75 likely the site of primary malignancy. There is a large complex hypermetabolic mass with both solid and cystic components in the left pelvis which could either be an ovarian metastasis (Krukenberg tumor) or a serosal implant of the sigmoid mesocolon SUV max 32.4.

There are hypermetabolic mesenteric nodules and pelvic nodes with SUV max up to 7.5. There were multiple hypermetabolic hepatic lesions too (not seen in images above).

Discussion

A Krukenberg tumor is a rare tumor of the ovary derived from metastatic tissue, most frequently from a tumor of gastrointestinal origin. Gastric cancer is the most frequent primary source, followed by the breast, colon, and appendix. For those carcinomas originating from the intestinal tract, about 80 % are found within either the sigmoid colon or rectum. Colorectal cancers can be found anywhere from the cecum to the rectum, in the following distribution: rectosigmoid, 55 %; cecum and ascending colon, 22 %; transverse colon, 11 %; and descending colon, 6 %.

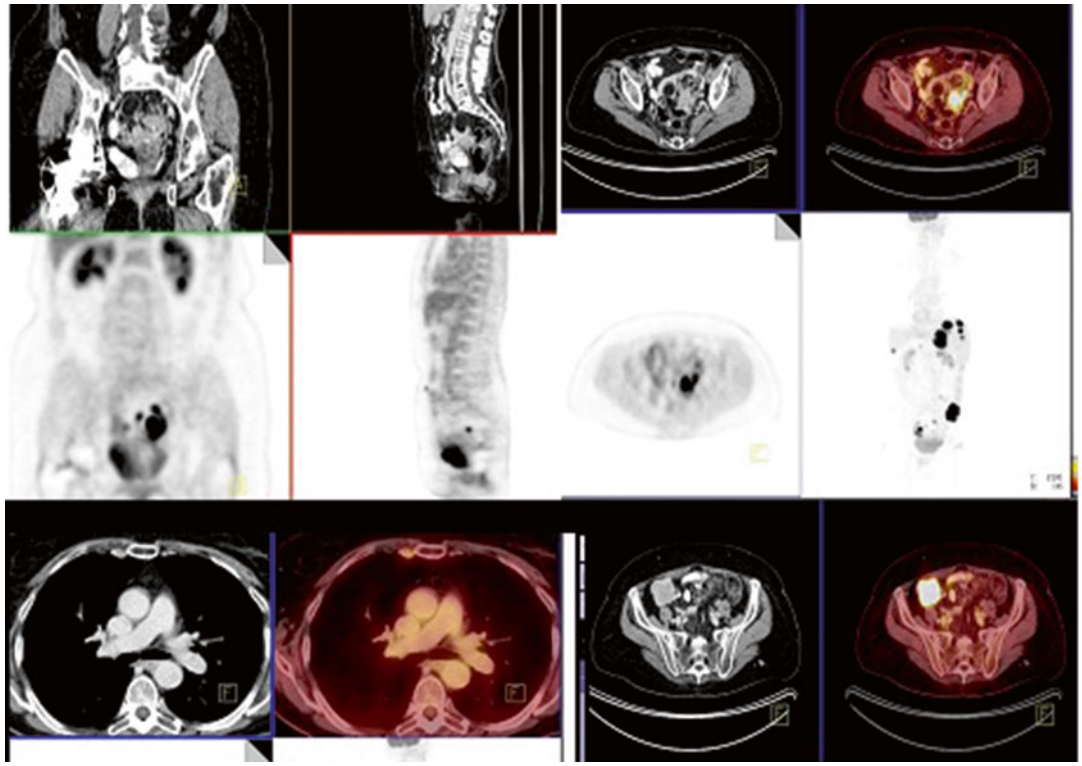

Fig. 6.7

Pearls and Pitfalls

A Krukenberg tumor is a rare tumor of the ovary derived from metastatic gastrointestinal tissue.

Case 6.8

Findings

Adenocarcinoma of the rectum, villous tumor of the cecum (situs inversus); ileal conduit to stoma s/p cystectomy (Fig. 6.8).

Pearls and Pitfalls

Normally, colon adenocarcinoma is relatively active with exceptions being villous and mucinous tumors.

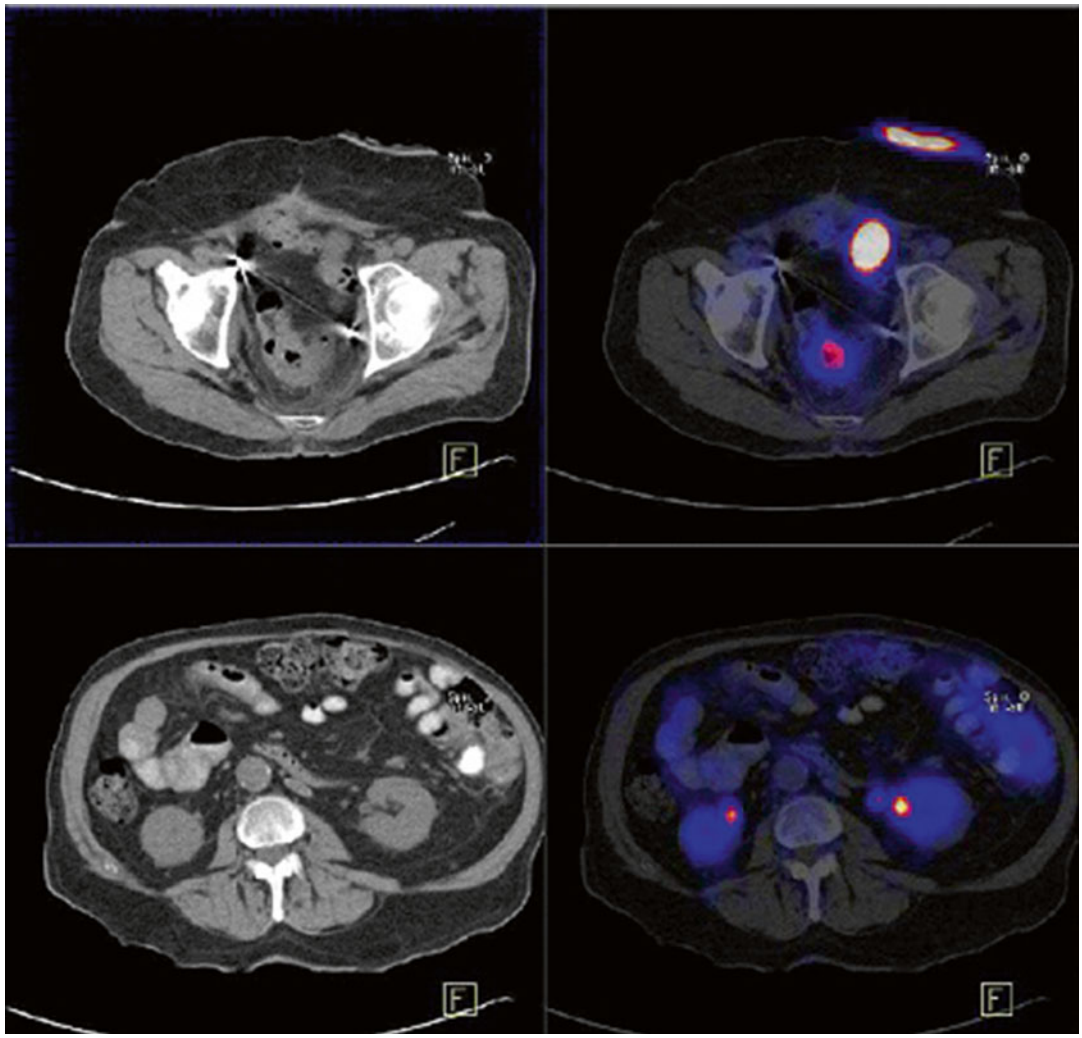

Fig. 6.8

Case 6.9: Anastomotic Recurrence

Findings

There is general wall thickening from radiation with one active focus suspect for anastamotic recurrence (Fig. 6.9).

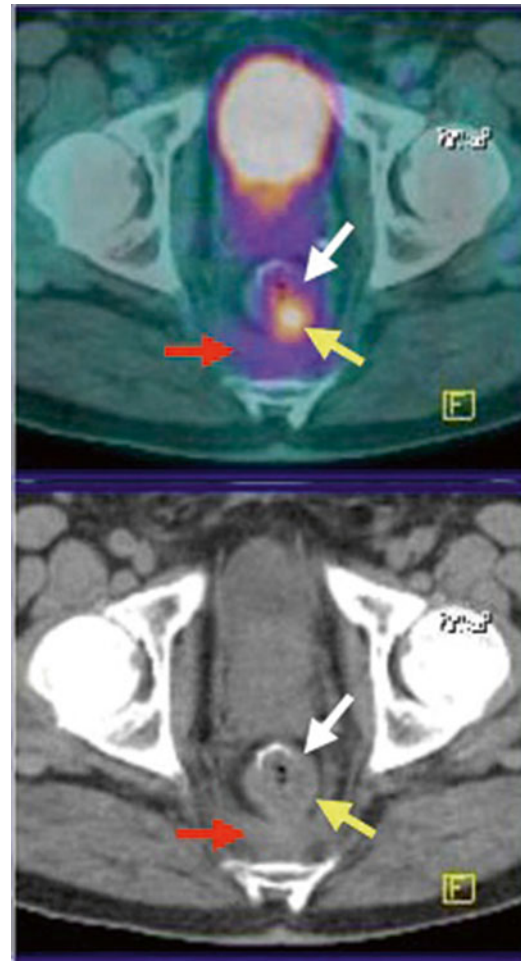

Fig. 6.9

Case 6.10

Findings

Perirectal space recurrence, 5 cm above the anal verge at 10 o' clock as viewed from below (Fig. 6.10).

Case 6.11

Findings

Presacral recurrence within postsurgical scar at 5 o' clock as viewed from below (Fig. 6.11).

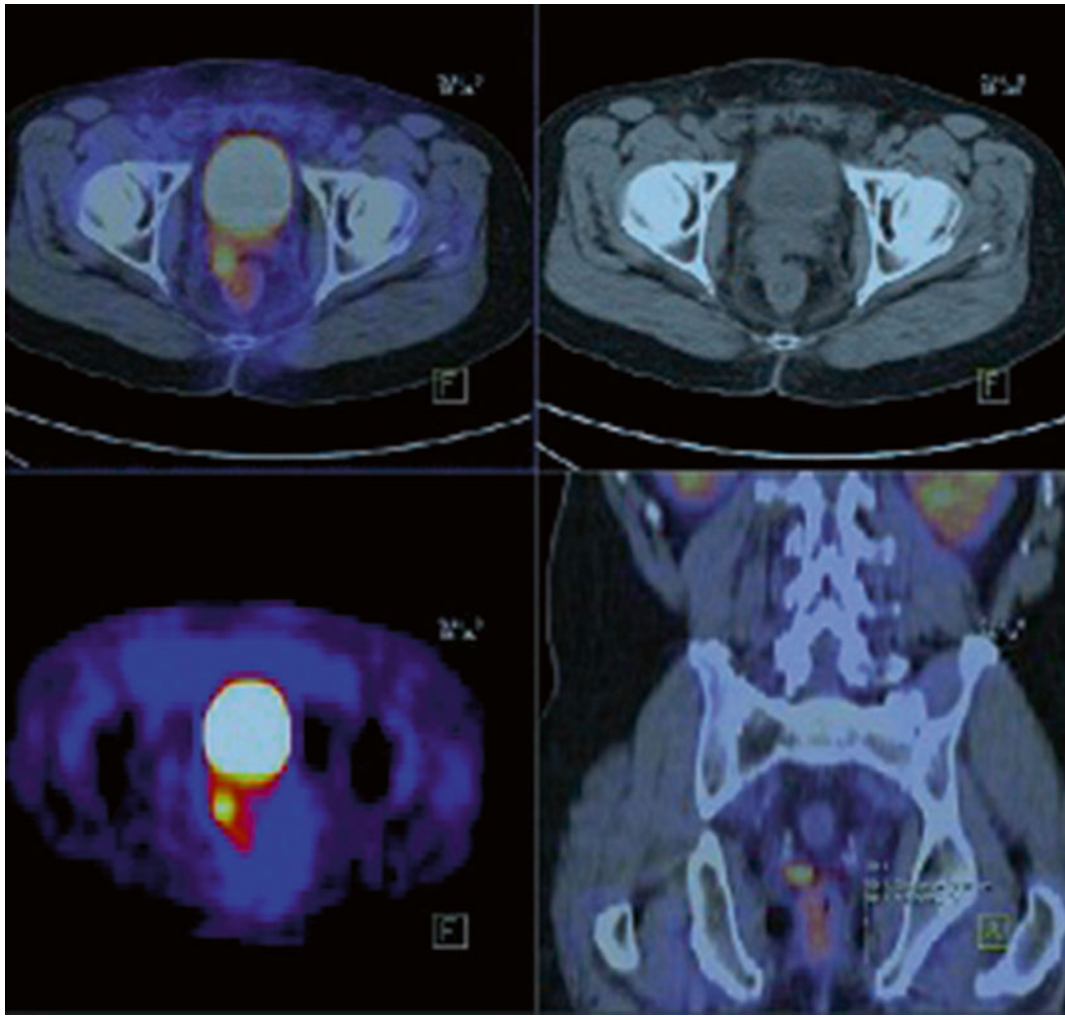

Fig. 6.10

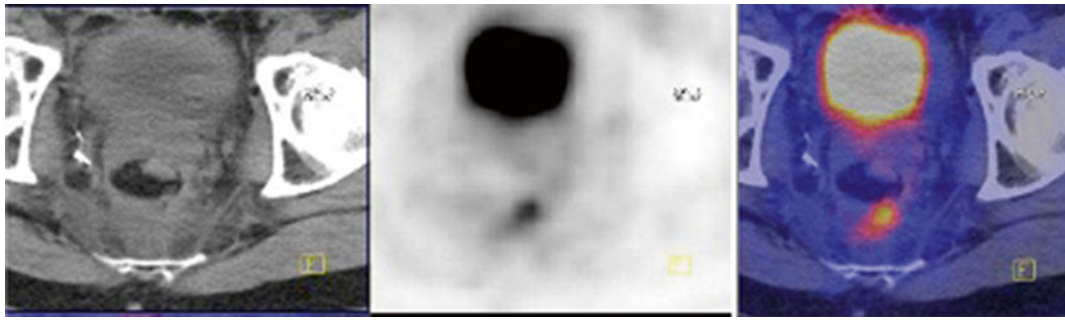

Fig. 6.11

Discussion

A considerable proportion of local failures is caused by anastomotic or suture line recurrence, which reportedly develops in 5–15 % of patients undergoing colorectal resection [1–3]. However, the true incidence of anastomotic recurrence, after restorative rectal cancer surgery, is unclear in the era of total mesorectal excision (TME). Although anastomotic recurrence could be rather easily controlled, compared to other types of local recurrence, curative-intent surgery is not always feasible, and reoperation itself is a significant burden to the patient, both physically and economically [4, 5]. Anastomotic recurrence may develop outside of the rectum and spread inside to the suture line. Conversely, tumor regrowth on the mucosal surface of the intestinal anastomosis may present along with a recurrence involving the suture line [8, 9]. Differentiation of these two possibilities is difficult in clinical practice.

Pearls and Pitfalls

1. Anastomotic recurrence may develop outside of the rectum and spread inside to the suture line.
2. Conversely, tumor regrowth on the mucosal surface of the intestinal anastomosis may present along with a recurrence involving the suture line [8, 9]. Differentiation of these two possibilities is difficult in clinical practice.

Suggested Reading

Ben-Jacob TK, Gordon CR, Koniges F. Krukenberg tumors: a review. J Surg Radiol. 2010;1:56–9.

Ceelen WP, Bracke ME. Peritoneal minimal residual disease in colorectal cancer: mechanisms, prevention, and treatment. Lancet Oncol. 2009;10:72–9.

Iyer RB, SiIverman PM, DuBrow RA, Charnsangavej C. Imaging in the diagnosis, staging, and follow-up of colorectal cancer. Am J Roentgenol. 2002;179(1):3–13.

Jones PF. Anastomotic recurrence of colorectal cancer. Gut. 1987;28:1691–2.

Kumar V, Fausto N, Abbas A. Robbins & Cotran pathologic basis of disease. 7th ed. Philadelphia: WB Saunders; 2005.

Lopez-Kostner F, Fazio VW, Vignali A, et al. Locally recurrent rectal cancer; predictors and success of salvage surgery. Dis Colon Rectum. 2001;44:173–8.

Phillips RKS, Hittinger R, Blesovsky L, et al. Local recurrence following "curative" surgery for large bowel cancer. I. The overall picture. Br J Surg. 1984;71:12–6.

Pihl E, Hughes ES, McDermott FT, et al. Recurrence of carcinoma of the colon and rectum at the anastomotic suture line. Surg Gynecol Obstet. 1981;153:495–6.

Keighley MR, Hall C. Anastomotic recurrence of colorectal cancer—a biological phenomenon or an avoidable calamity? Gut. 1987;28:786–91.

Sagar PM, Pemberton JH. Surgical management of locally recurrent rectal cancer. Br J Surg. 1996;83:293–304.

Siegel R, Naishadham D, Jemal A. Cancer statistics, 2012. CA Cancer J Clin. 2012;62:10–29.

Umpleby HC, Williamson RC. Anastomotic recurrence in large bowel cancer. Br J Surg. 1987;74:873–8.

7 Gynecologic Neoplasms: Cervical, Ovarian, Vulvar, Uterine, and Endometrial Cancer

Bhushan Desai and Hossein Jadvar

Cervical Cancer

Case 7.1

History

A 59-year-old female presenting with newly diagnosed cervical carcinoma on biopsy. PET/CT was ordered as a part of the initial treatment strategy evaluation.

Findings

The uterus is anteverted, demonstrating physiologic FDG activity (Fig. 7.1). Intense metabolic activity is seen in the cervical region with associated thickening, SUVmax 16.3, which is compatible with biopsy-proven diagnosis of primary neoplasm. There is a fat plane between the cervix and urinary bladder anteriorly which excludes the direct tumor invasion.

Impression

Cervical thickening demonstrating intense hypermetabolism, which is compatible with biopsy-proven diagnosis of primary neoplasm.

P.S. Conti, A. Kaushik (eds.), *PET-CT*, DOI 10.1007/978-1-4419-5811-2_7

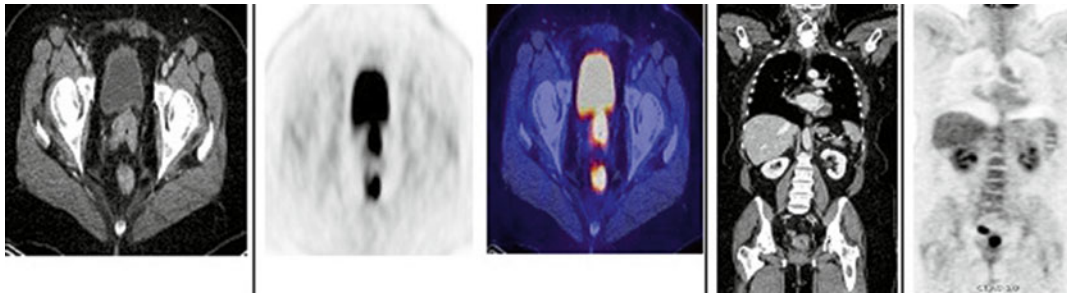

Fig. 7.1

Case 7.2

History

A 51-year-old female with history of cervical cancer.

Findings

1. There are bilateral supraclavicular, bilateral internal mammary, left axillary, and mediastinal lymph nodes, demonstrating intense FDG activity which is compatible with distant metastatic spread (Fig. 7.2). As a reference, right precarinal lymphadenopathy demonstrates SUVmax 12.9, measuring approximately 2.4 × 3.6 cm, subcarinal lymph node measures approximately 1.7 cm with SUVmax 8.9, left internal mammary lymph node demonstrates SUVmax 7.8, and AP window lymphadenopathy shows SUVmax 10.8.
2. There is a large hypermetabolic uterine cervical mass demonstrating intense FDG activity, SUVmax 13.8. Exact tumor margins cannot be identified due to lack of IV contrast. There is no fat plane between the tumor and posterior wall of urinary bladder anteriorly, which also abuts the ventral surface of the rectal wall posteriorly, worrisome for local tumor invasion.
3. There are several hypermetabolic, enlarged retrocrural, retroperitoneal, bilateral common iliac lymph nodes extending inferiorly to involve bilateral external iliac lymph nodes, compatible with metastatic disease. As a reference, left para-aortic lymph node at the level of L1 demonstrates SUVmax 7.5; a right retrocrural lymph node, measuring approximately 1.5 cm at the level of T11 and T12, demonstrates SUVmax 5.5; right common iliac lymphadenopathy also shows SUVmax 5.5; and right internal iliac lymph nodes demonstrate SUVmax 12.1.
4. Solitary hypermetabolic osseous focus identified at the posterolateral aspect of left eleventh rib, demonstrating SUVmax 5.0.

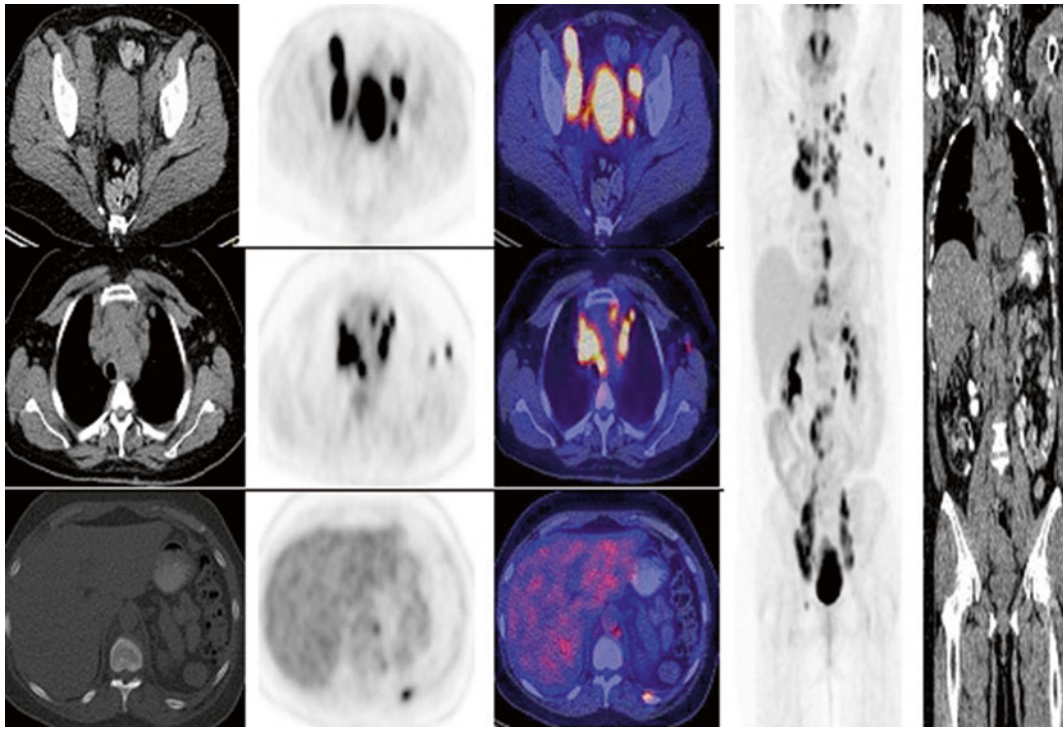

Fig. 7.2

Impression

1. Hypermetabolic, large, uterine cervical mass which is worrisome for local tumor invasion.
2. Metastatic lymphadenopathy involving multiple nodal stations in the neck, chest, abdomen, and pelvis.
3. Findings compatible with early metastatic disease within the lungs.

Pearls and Pitfalls

1. FDG PET/CT has no significant role in screening/diagnosis of cervical cancer.
2. Lymph node staging with PET/CT provides unique prognostic information [1, 2].
3. Early response assessments using PET/CT might help to avoid unnecessary and ineffective treatments.
4. The sensitivity and specificity of PET for early recurrent cervical cancer is 90 % and 76 %, respectively [3].

Discussion

Cervical cancer was once the most common cause of cancer death in women, but the mortality rate has decreased by 50 % due to widespread screening. Worldwide, cervical cancer is the third commonest cancer diagnosed, and it remains the major gynecologic cancer in underdeveloped countries. Squamous cell carcinoma is the most frequent cervical cancer with 85–90 % being invasive. The most common risk factors include lower socioeconomic groups, smoking, early initial sexual activity and/or multiple sexual partners, and history of sexually transmitted disease like gonorrhea, syphilis, and herpes simplex.

MRI is considered the method of choice in the staging of primary tumor since it can evaluate tumor depth and stromal invasion. However, it lacks the ability to accurately diagnose nodal involvement. For this reason, PET is used to assess nodal malignancy as well as regional and distant metastatic disease. Frequency and pattern of cervical cancer lymph node metastasis on FDG PET is influenced by FIGO staging [12, 13]. PET has a 91 % positive value for pelvic and para-aortic lymphadenopathy. In a prospective study on 560 patients, Kidd et al. concluded that the PET findings correlated with the risk of disease progression and survival. In another study looking at the prognostic value of SUVmax, on 73 patients with operable cervical cancer, Chung et al. concluded that FDG tumor uptake correlated with FIGO stage, tumor size, parametrial involvement, and lympho-vascular invasion. These results will likely have important implications for management of cervical cancer patients with lymph node metastasis on FDG PET.

Ovarian Cancer

Case 7.3

History

A 61-year-old female with metastatic stage IV ovarian carcinoma, post gamma knife radiosurgery for left frontal and left cerebellar metastasis. PET/CT was done as part of the subsequent treatment strategy evaluation.

Findings

Three hypermetabolic peritoneal implants are seen in the abdomen (Fig. 7.3). These include a hypermetabolic lesion at the hepatorenal surface of segment 6 of the liver measuring 4.2 cm (long axis) with SUVmax 14.8; peritoneum implant in the splenic flexure, measuring 2.0 cm with SUVmax 8.3; and peritoneal implant in the right hemipelvis internal to the right internal iliac vessels showing SUVmax 10.2. Hypermetabolic subcarinal lymph node is seen with increase in size and activity, SUVmax 8.2. Physiologic brown fat activity is seen in the superior mediastinal and bilateral paravertebral regions.

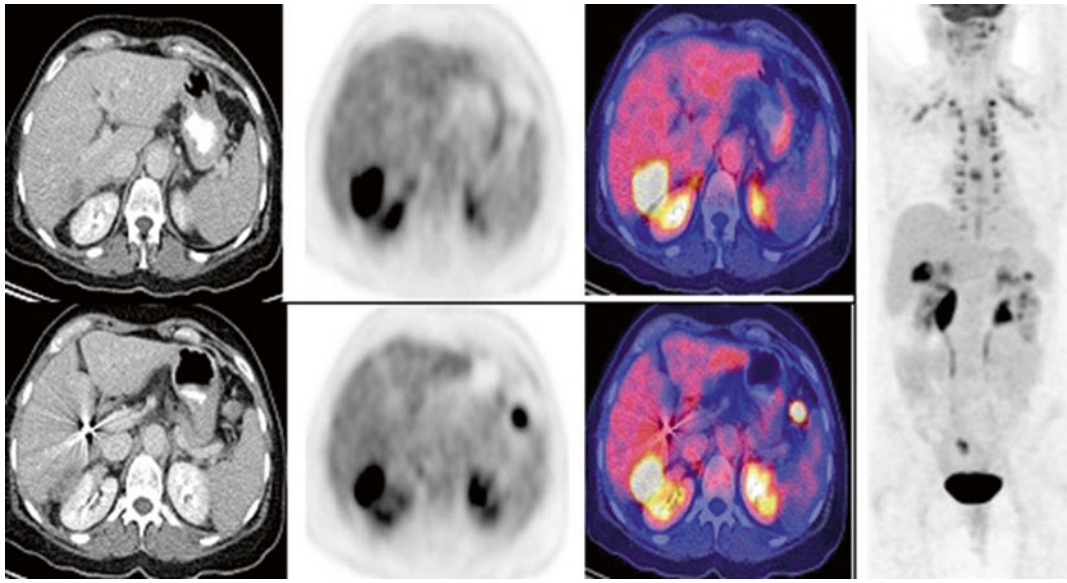

Fig. 7.3

Impression

Three peritoneal implants with increased size and metabolic activity.

Case 7.4

History

A 53-year-old female with stage IV ovarian carcinoma, status post hysterectomy, bilateral salpingo-oophorectomy, omentectomy, and bilateral lymph node dissection with appendectomy, currently on chemotherapy (Taxol). PET/CT was done as part of subsequent treatment strategy evaluation.

Findings

Overall, previously seen majority of the hypermetabolic abdominal lymph nodes have resolved (Fig. 7.4). Exceptions include a porta hepatis lymph node which has decreased in FDG activity and currently demonstrates SUVmax 6.5, previously 9.5; a mesenteric lymph node near the terminal ileum has increased in FDG activity and currently demonstrates SUVmax 12.1 previously 9.3. Additionally, there is a new right retrocrural lymph node which currently demonstrates SUVmax 8.6.

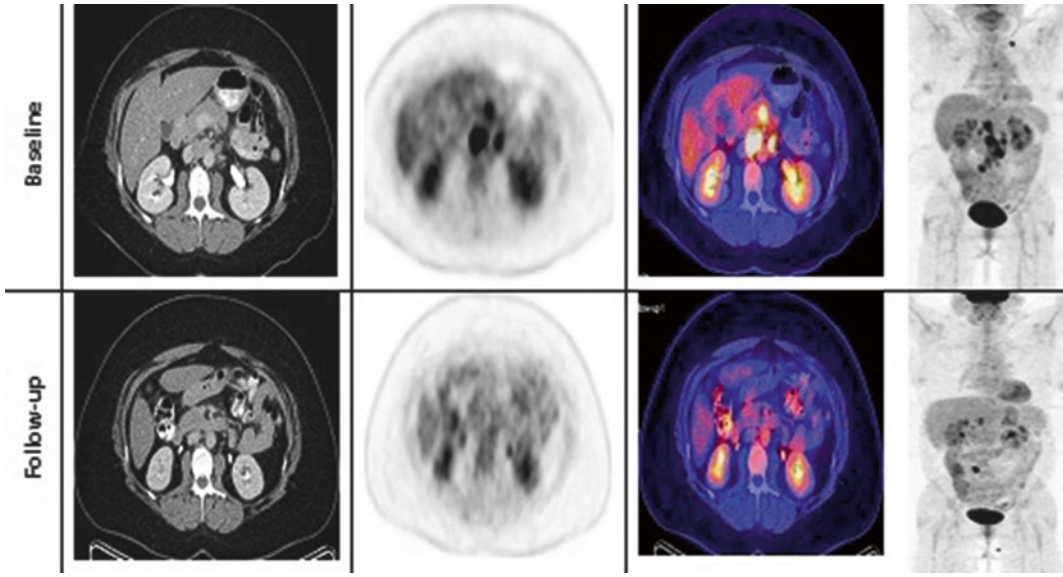

Fig 7.4

Impression

1. Resolution of majority of hypermetabolic abdominal and chest lymph nodes with the exception of the porta hepatis lymph node and mesenteric lymph node adjacent to the terminal ileum.
2. New hypermetabolic right retrocrural lymph node.
3. Overall findings consistent with a substantial partial response to interval chemotherapy.

Case 7.5

History

A 65-year-old female with ovarian cancer, currently on chemotherapy.

Findings

Multiple hypermetabolic omental/peritoneal metastases are seen, like the peritoneal implant lateral to psoas in the left iliac fossa with SUVmax 9.3 (Fig. 7.5). The lymph nodes are involved which are intensely hypermetabolic, for example, retroaortic node at L4 with SUVmax 12.3, left common iliac with SUVmax 8.8, left external iliac with SUVmax 7.1, and left hypogastric with SUVmax 5.7.

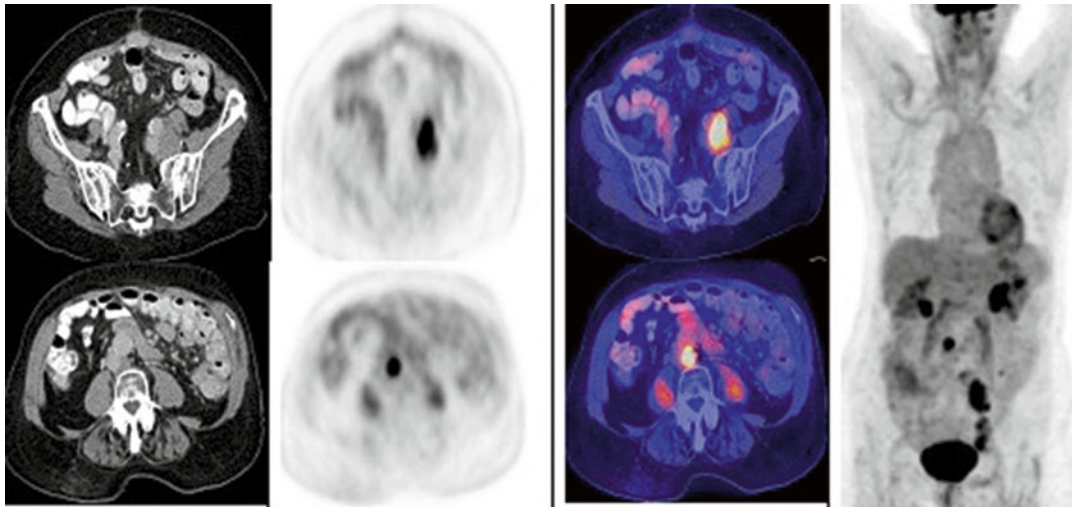

Fig. 7.5

Impression

Widespread metastases in the abdomen and pelvis.

Case 7.6

History

A 66-year-old female with well-differentiated papillary serous adenocarcinoma of the ovary, status post total abdominal hysterectomy and left salpingo-oophorectomy.

Findings

PET/CT showed multiple hypermetabolic calcified masses in the abdomen and pelvis consistent with metastatic disease (Fig. 7.6).

Pearls and Pitfalls

1. PET has the sensitivity of 80–90 %, specificity of 92–100 %, and accuracy of 79–92 % for detecting recurrent ovarian tumor [4–6].
2. PET has a sensitivity of 73 %, specificity of 92 %, accuracy of 86 %, positive predictive value of 89 %, and negative predictive value of 86 % for detecting lymph node involvement. The sensitivity of CT for detecting lymph node involvement ranges from 40 to 63 %; the specificity of CT for detecting the same ranges from 81 to 83 % [4–6].

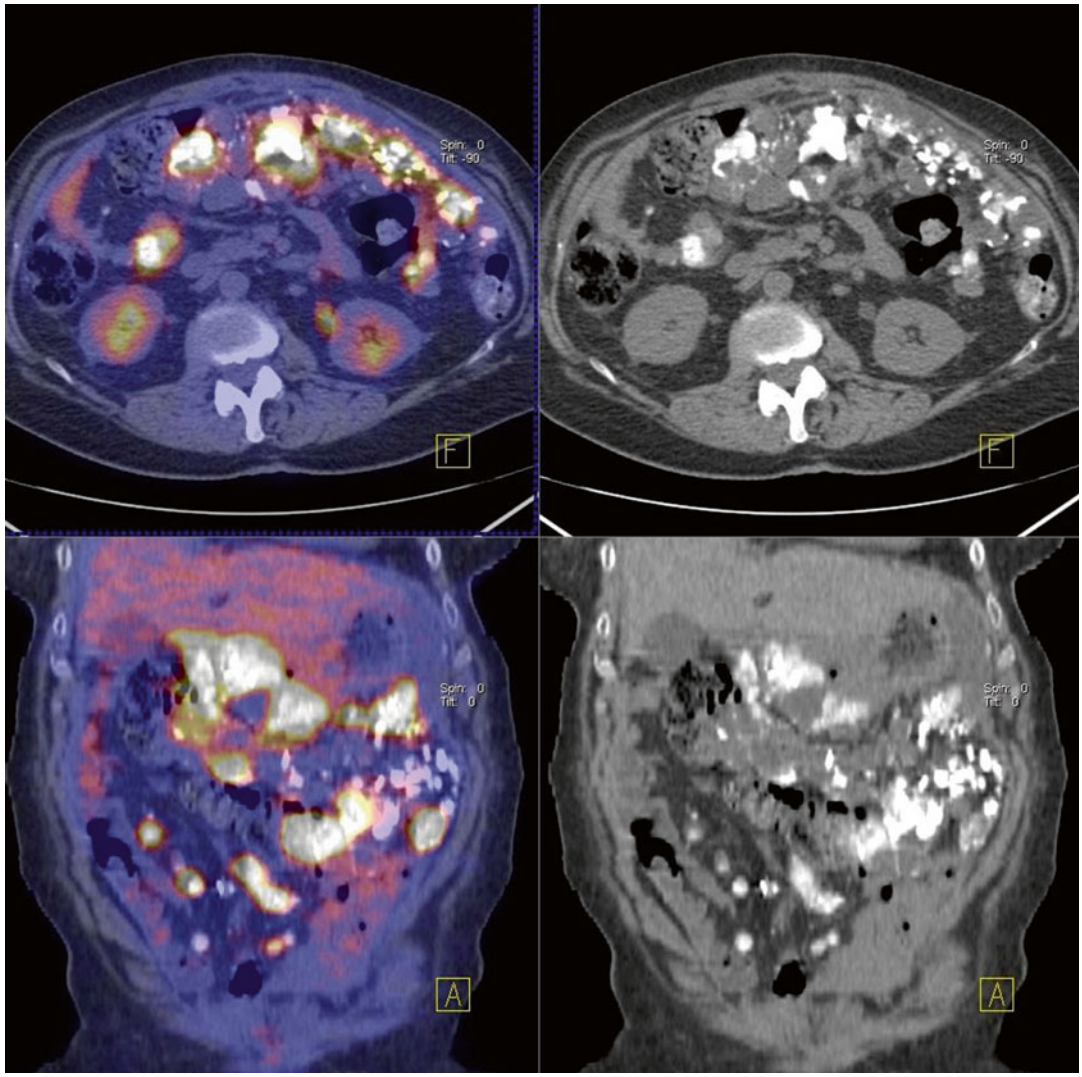

Fig. 7.6

3. FDG PET has a sensitivity of 71 %, specificity of 100 %, positive predictive value of 100 %, negative predictive value of 76 %, and accuracy of 85 % in the detection of peritoneal carcinomatosis [4–6].
4. Peritoneal metastases along the serosa of the colon may be mistaken for physiologic bowel activity, while calcified metastases along the bowel can be mistaken for oral contrast and is typical of mucinous cystadenocarcinoma histology [7].

Discussion

Ovarian cancer is the fifth cause of cancer-related death in women. 24,000 new cases of ovarian cancer were detected in the USA in 2010 with 16,000 deaths/year. More women die of ovarian cancer than of endometrial and

cervical cancer combined. Age-specific incidence peaks in the eighth decade. Some of the common risk factors associated with ovarian cancer are BRCA1 and 2, infertility, nulliparity, family Hx, and endometriosis. At the time of initial evaluation, about 80–85 % of patients have CA-125 > 35 U/mL (postmenopausal women with asymptomatic pelvic mass and CA-125 > 65 U/mL: 78 % specific and 97 % sensitive for cancer). Ovarian tumors can be of epithelial cell, stromal cell, or germ cell origin. Two thirds of patients will have metastatic disease outside the pelvis at the time of diagnosis. Approximately 85 % of the malignant ovarian tumors are epithelial origin of which 50 % are benign, 33 % malignant, and around 15 % borderline with a good prognosis.

In a prospective study on 60 patients who underwent PET/CT scan within 2 weeks prior to surgery, Risum et al. found that the presurgical SUVmax was not predictive of the outcome in patients with primary ovarian cancer. PET/CT scans are accurate for staging but probably not very relevant since impact on management and outcome is small [8]. PET/CT has a high accuracy and positive predictive value in diagnosing recurrent ovarian cancer and can alter patient management [14, 15]. Restaging with PET/CT is not only accurate but also provides the foundation for monitoring of chemotherapy which can help in shortening the duration of ineffective treatments and reduce costs. PET can detect an intra-abdominal relapse with peritoneal carcinomatosis in 40–60 % of the cases. Most recurrent ovarian carcinomas present with peritoneal seeding from para-aortic or peritoneal lymphatics. Unfortunately, false-positive examinations can occur with associated non-malignancy physiology including inflammatory adnexal mass or corpus luteum. Urine activity can also potentially mask the lesions. Some institutions recommend the use of bladder lavage in order to minimize this artifact.

Endometrial/Uterine Cancer

Case 7.7

History

An 81-year-old female with endometrial adenocarcinoma, status post total abdominal hysterectomy with bilateral salpingo-oophorectomy, pelvic radiation therapy, and chemotherapy. PET/CT is done as part of the subsequent treatment strategy evaluation.

Findings

There is an intensely hypermetabolic left adrenal lesion, measures 1.4 cm with SUVmax 5.0, consistent with metastatic disease (Fig. 7.7). There are several hypermetabolic peritoneal/serosal implants, some of which demonstrate central necrosis, again compatible with progression of metastatic disease. A serosal implant overlying the right hepatic lobe demonstrates SUVmax 13.2. Serosal implants are also seen adjacent to the sigmoid and in the region of lower rectum (SUVmax 18.5). Most avid omental implant

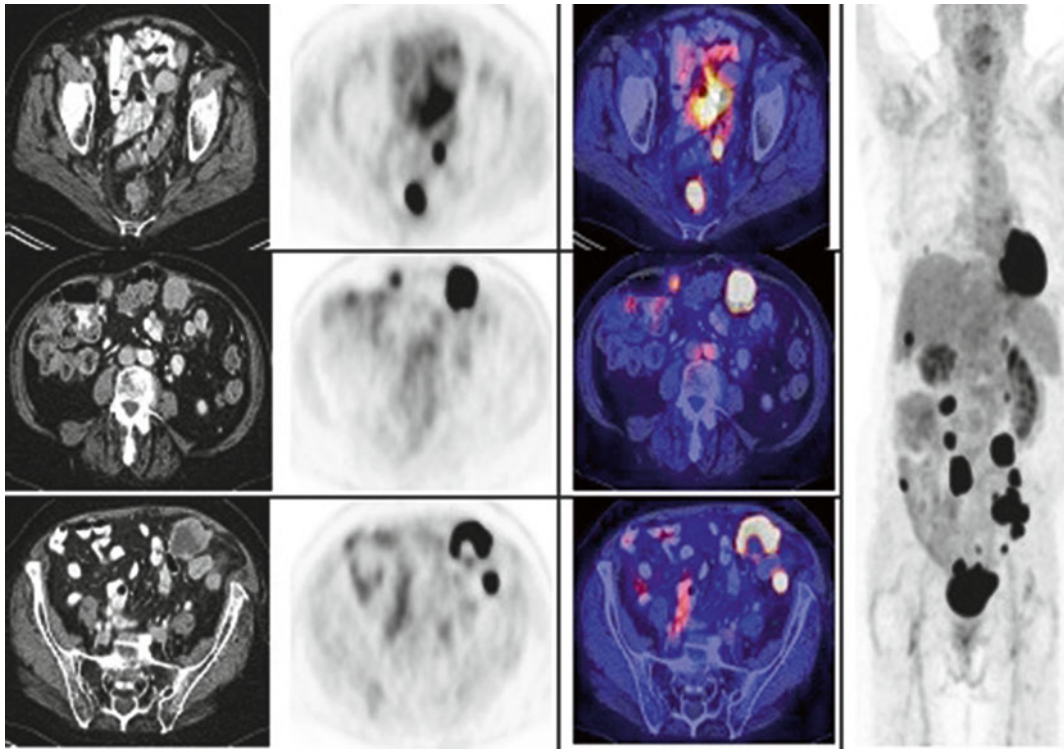

Fig. 7.7

is seen in the lower right abdomen, adjacent to the anterior abdominal wall at the level of L5, demonstrating (SUVmax 19.9).

Impression

Overall findings compatible with progression of metastatic disease.

Case 7.8

History

An 88-year-old female with history of recurrent uterine carcinoma, currently on chemotherapy. PET/CT is done as part of the subsequent treatment strategy evaluation.

Findings

Bilateral adrenal glands demonstrate interval increase in PET activity, suspect for metastatic disease (Fig. 7.8). As a reference, right adrenal

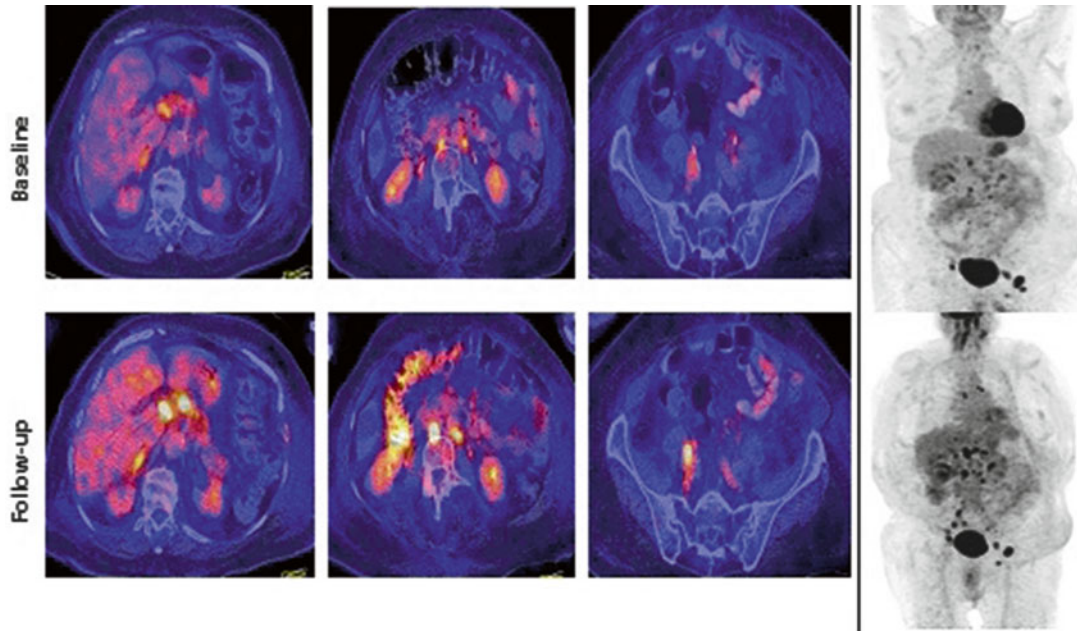

Fig. 7.8

gland currently shows SUVmax 5.0 (previously 3.9), and left adrenal shows SUVmax 4.5 (previously 4.3). There is an interval increase in hypermetabolic activity within gastrohepatic, portacaval, celiac, right retrocaval, mesenteric, retroperitoneal and bilateral common, external and internal iliac, right obturator, and left inguinal and bilateral femoral lymph nodes with marginal increase in size of some of them, compatible with progression of disease. As a reference, gastrohepatic lymph node currently shows SUVmax 4.2 (previously 2.3), and portacaval lymph nodes show SUVmax 9.1 (previously 6.3).

Impression

Progression of metastatic disease.

Case 7.9

History

A 72-year-old female with poorly differentiated endometrial carcinoma, status post-radiation therapy. Approximately 1 year later, she developed a recurrent mass in the vaginal vault and metastases to the lungs.

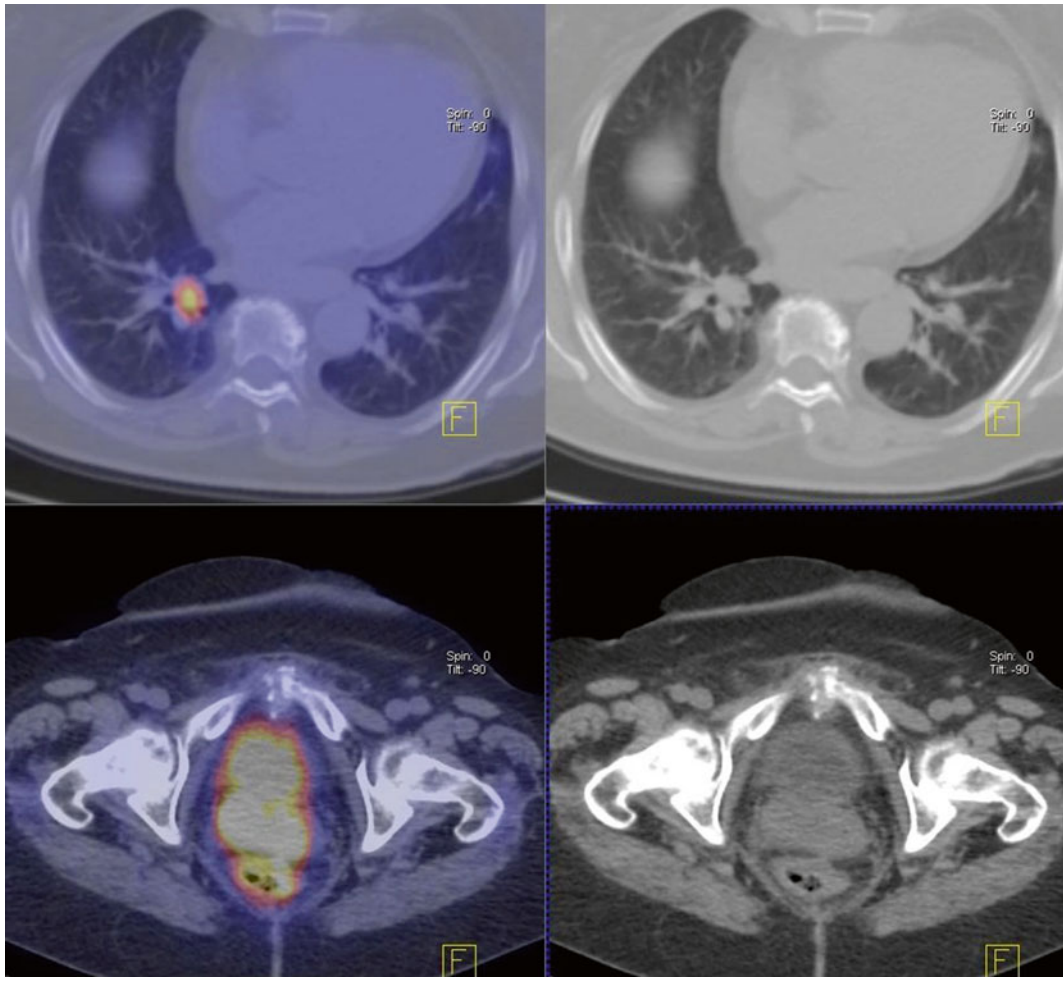

Fig. 7.9

Findings

Hypermetabolic mass in the vagina and lung consistent with recurrent and metastatic disease (Fig. 7.9).

Pearls and Pitfalls

1. Need to avoid pitfalls associated with benign pathology or physiological processes (fibroids, menstruation).
2. FDG PET/CT is insensitive for presurgical LN staging in endometrial CA [9].
3. Highly accurate for detecting recurrence and distant metastasis which can help in clinical decision-making: sensitivity 93 %, specificity 93 %, and accuracy 93 % [10].
4. Very limited data on treatment monitoring [11].

Discussion

Uterine cancer is the most common cancer of the female pelvic organs. Around 40,000 new cases of uterine cancer were detected in the USA in 2010, and the mortality rate was 7400 deaths/year. The most common cancer in the uterus is adenocarcinoma (75–80 % adenocarcinomas, 10 % adenocarcinomas with squamous differentiation, 5 % mucinous carcinoma, and 5–10 % papillary serous carcinoma). Postmenopausal bleeding is the most common presentation in 90 % of the patients; 70–75 % are diagnosed with surgical stage I disease. The most common risk factors include obesity, low fertility index, early menarche, late menopause, chronic anovulation, unopposed estrogen replacement, and hypertension. Clinical staging underestimates the extent of disease, and thus the FIGO staging system requires surgical and histopathologic evaluation. Most endometrial cancers are diagnosed in stage I and surgery alone is adequate. Beyond that, adjuvant radiotherapy may be necessary for treatment. The 5-year survival rate for endometrial carcinoma in stage I is 74–92 % depending on histologic grade.

There is physiologic uptake of FDG in the endometrium in premenopausal women that increases during the menstrual and ovulatory phases [16]. FDG PET/CT is helpful in the staging of endometrial carcinoma because it can detect distant metastatic disease which can change patient management [17]. In a prospective study on 88 patients by Park et al. [18] they found that PET/CT scan helped in clinical decision-making in 22 % of the patients. In another study by Nakamura et al., they concluded that the SUVmax of 18F FDG PET correlated with the histological grade in endometrial cancer ($p = 0.017$). Around 10–30 % of women with clinical stage I or II disease will have metastasis to the pelvic and para-aortic lymph nodes at the time of surgery [19, 20]. However, lymph nodes that are too small may not be detected. Physiologic uptake in the ovaries, ureters, bladder diverticulum, and blood vessels may be mistaken for metastatic disease.

Vulvar Cancer

Case 7.10

History

A 60-year-old female with history of recurrent vulvar cancer, who had undergone a recent perianal biopsy which showed invasive squamous cell carcinoma, status post-radiation therapy to the rectal/vaginal region. PET/CT is done as part of the subsequent treatment strategy evaluation.

Findings

Focal activity seen in the region of anal verge with SUVmax 8.0, presumed to correspond to biopsy site of known neoplasm (Fig. 7.10).

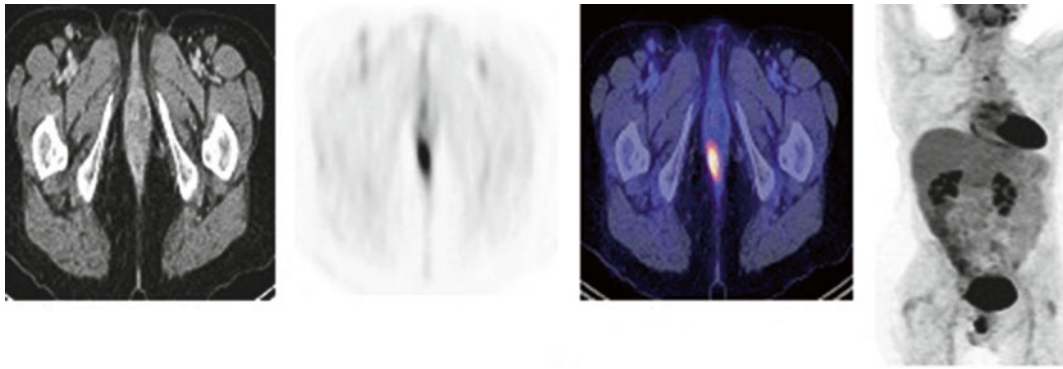

Fig. 7.10

Impression

Focal metabolic activity in the region of anal verge corresponds to known biopsy site of neoplasm.

Case 7.11

History

A 72-year-old female with recent history of vulvar intraepithelial neoplasm, level 3, status post modified radical vulvectomy. PET/CT is done as part of the subsequent treatment strategy evaluation.

Findings

There is linear tracer activity in the perineal region which likely represents urinary contamination (Fig. 7.11).

Impression

Probable perineal urine soiling that reduces the sensitivity for local recurrence evaluation.

Pearls and Pitfalls

1. Currently, there is no data in the literature to evaluate the sensitivity and specificity of PET for detecting vulvar carcinoma.
2. PET scanning has the ability to identify small nodal metastasis.

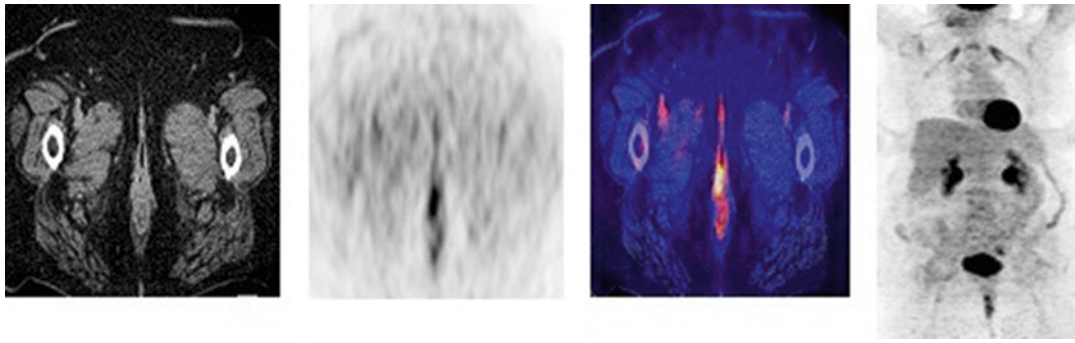

Fig. 7.11

Discussion

Vulvar carcinoma represents 1 % of the female genital cancers. The majority arises in the labia majora and minora. Vulvar carcinoma includes squamous cell carcinoma, adenocarcinoma, and melanoma. Human papillomavirus, sexually transmitted disease, smoking, and multiple sexual partners are risk factors. Patients may be asymptomatic or present with a mass, pruritus, bleeding, or pain. Biopsy is confirmatory. Imaging studies may be helpful. CT can evaluate adenopathy with a sensitivity of 30 %. MRI can evaluate lymphatic involvement. PET can also help in detecting nodal metastasis. Radical primary tumor excision and en bloc lymph nodes dissection are the treatment of choice. Cure rate is 80 % if malignancy is contained in stages I and II. Stage III has a 68 % 5-year survival rate vs. stage IV with 20 %.

References

1. Chung H, et al. Preoperative [^{18}F] FDG PET/CT maximum standardized uptake value predicts recurrence of uterine cervical cancer. Eur J Nucl Med Mol Imaging. 2010;37:1467–73.
2. Kidd E, et al. Lymph node staging by positron emission tomography in cervical cancer: relationship to prognosis. J Clin Oncol. 2010;28:2108–13.
3. Ryu SY, et al. Detection of early recurrence with 18F FDG PET in patients with cervical cancer. J Nucl Med. 2003;44:347–52.
4. Nakamoto Y, et al. Clinical value of positron emission tomography with FDG for recurrent ovarian cancer. Am J Roentgenol. 2001;176:1449–54.
5. Turlakow A, et al. Peritoneal carcinomatosis: role of 18F FDG PET. J Nucl Med. 2003;44:1407–12.
6. Risum S, et al. The diagnostic value of PET/CT for primary ovarian cancer—a prospective study. Gynecol Oncol. 2007;105:145–9.
7. Burkill GJ, et al. Significance of tumor calcification in ovarian carcinoma. Br J Radiol. 2009;82:640–4.
8. Risum S, et al. Standardized FDG uptake as a prognostic variable and as a predictor of incomplete cytoreduction in primary advanced ovarian cancer. Acta Oncol. 2010;50:415–9.

9. Horowitz N, et al. Prospective evaluation of FDG-PET for detecting pelvic and para-aortic lymph node metastasis in uterine corpus cancer. Gynecol Oncol. 2004;95:546–51.
10. Kazuhiro K, et al. Performance of FDG-PET/CT in the diagnosis of recurrent endometrial cancer. Ann Nucl Med. 2008;22:103–9.
11. Nishiyama Y, et al. Monitoring the neoadjuvant therapy response in gynecological cancer patients using FDG PET. Eur J Nucl Med. 2008;35:287–95.
12. Kaur H, et al. Diagnosis, staging, and surveillance of cervical carcinoma. Am J Roentgenol. 2003;180:1621–32.
13. Schwarz J, et al. The role of 18F-FDG PET in assessing therapy response in cancer of the cervix and ovaries. J Nucl Med. 2009;50:64S–73S.
14. Seung J, et al. CT and MR imaging of ovarian tumors with emphasis on differential diagnosis. Radiographics. 2002;22:1305–25.
15. Prakash P, et al. Role of PET/CT in ovarian cancer. Am J Roentgenol. 2010;194:W464–70.
16. Lerman H, et al. Normal and abnormal 18F-FDG endometrial and ovarian uptake in pre- and postmenopausal patients: assessment by PET/CT. J Nucl Med. 2004;45:266–71.
17. Subhas N, et al. Imaging of pelvic malignancies with in-line FDG PET–CT: case examples and common pitfalls of FDG PET. Radiographics. 2005;25:1031–43.
18. Park J, et al. Comparison of the validity of magnetic resonance imaging and positron emission tomography/computed tomography in the preoperative evaluation of patients with uterine corpus cancer. Gynecol Oncol. 2008;108:486–92.
19. Picchio M, et al. High-grade endometrial cancer: value of [18F] FDG PET/CT in preoperative staging. Nucl Med Commun. 2010;31:506–12.
20. Gambir SS, et al. A tabulated summary of the FDG PET literature. J Nucl Med. 2001;42:1S–93S.

8 Urologic Neoplasms: Prostate, Bladder, and Renal Cell Carcinoma

Bhushan Desai and Hossein Jadvar

Prostate Cancer

Case 8.1

History

A 60-year-old Caucasian male with castrate-resistant metastatic adenocarcinoma of prostate, status post radical prostatectomy (Gleason score 4 + 5) and androgen ablation therapy.

Findings

FDG PET-CT scan performed 4 months after the baseline showed an interval increase in extent and degree of hypermetabolism diffusely throughout both hepatic lobes with maximum SUV of 9.1 (Fig. 8.1). There is also an interval increase in number and size of diffuse pulmonary nodules. Patient died from disseminated disease 2 months later.

Impression

Interval progression of metastatic disease.

Case 8.2

History

A 55-year-old male with history of end-stage renal disease and metastatic prostate cancer, initially diagnosed in June 2005, status post radiation treatment and currently on Casodex and monthly Lupron.

P.S. Conti, A. Kaushik (eds.), *PET-CT*, DOI 10.1007/978-1-4419-5811-2_8

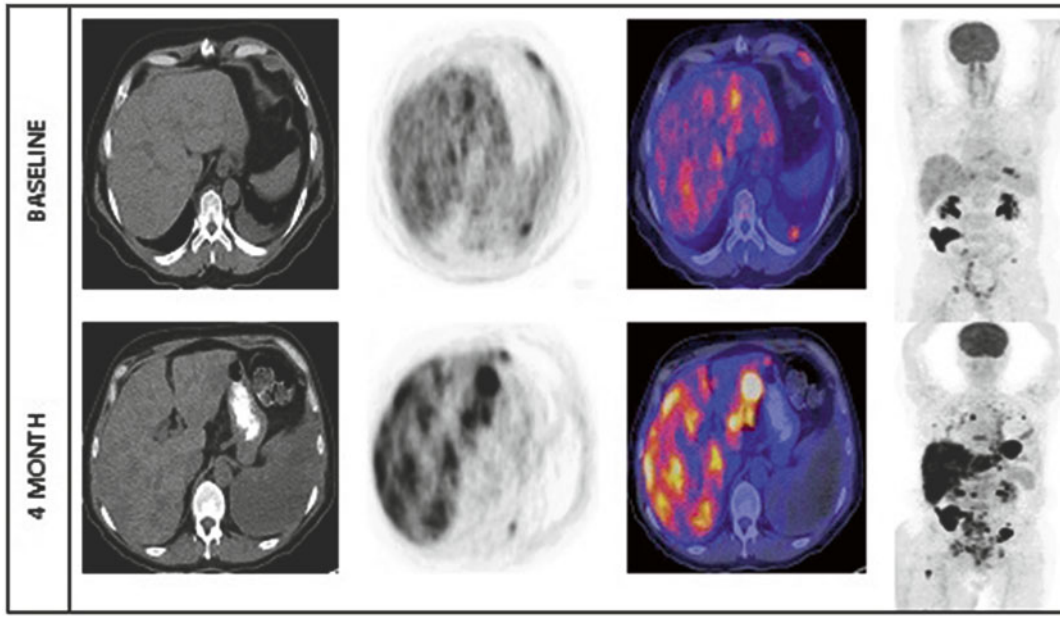

Fig. 8.1

Findings

There has been an interval increase in the size and metabolic activity of previously seen mesenteric, retroperitoneal, and right common iliac lymph nodes (Fig. 8.2). For example, the hypermetabolic left para-aortic lymph nodes, at L2 level, now have a maximum SUV of 2.7 (from 2.1). A newly apparent, hypermetabolic left supraclavicular lymph node has a SUVmax of 3.0 and measures 1.5 cm × 2.9 cm. There has also been an interval increase in the intensity and extent of previously seen hypermetabolic osseous lesions.

Impression

Progressive retroperitoneal, left supraclavicular lymphadenopathy, and osseous metastatic disease.

Case 8.3

History

A 63-year-old male with castrate-resistant metastatic prostate cancer (primary Gleason score 4 + 5).

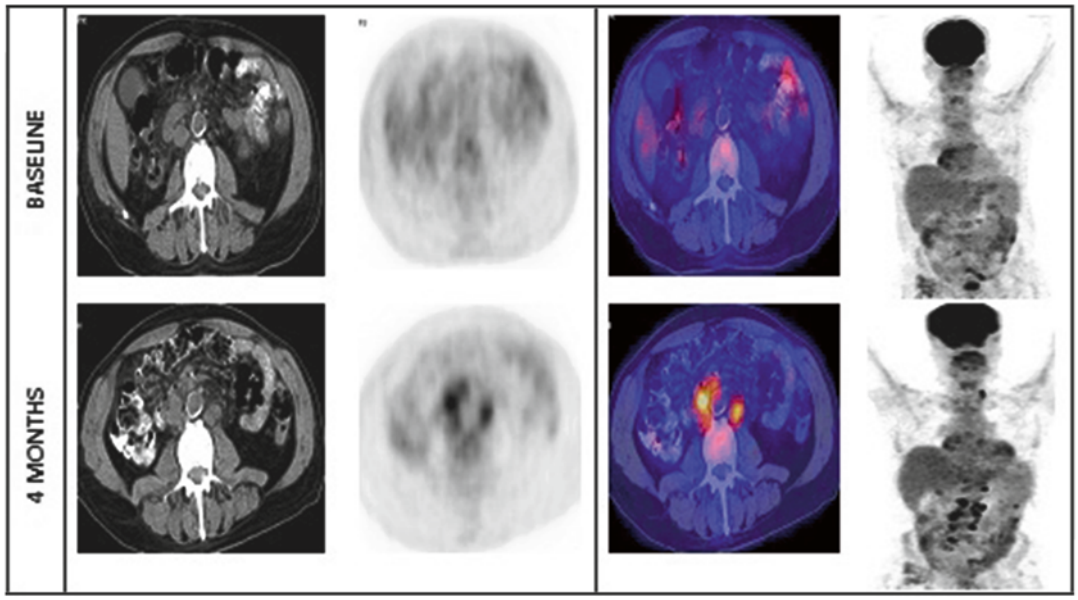

Fig. 8.2

Findings

Serial FDG PET-CT scans showed that the lesions' metabolic activity, as depicted by SUVmax, kept on decreasing showing a good response to therapy and was also correlated with decline in PSA values, but the CT density, as depicted by HU (Hounsfield unit), continued to increase (Fig. 8.3).

Impression

Metabolic activity of metastatic osseous lesions tends to decrease, while CT density tends to increase with successful therapy.

Case 8.4

History

An 86-year-old male, recently diagnosed with small cell carcinoma of the prostate gland. PET-CT is done as part of the initial treatment strategy evaluation.

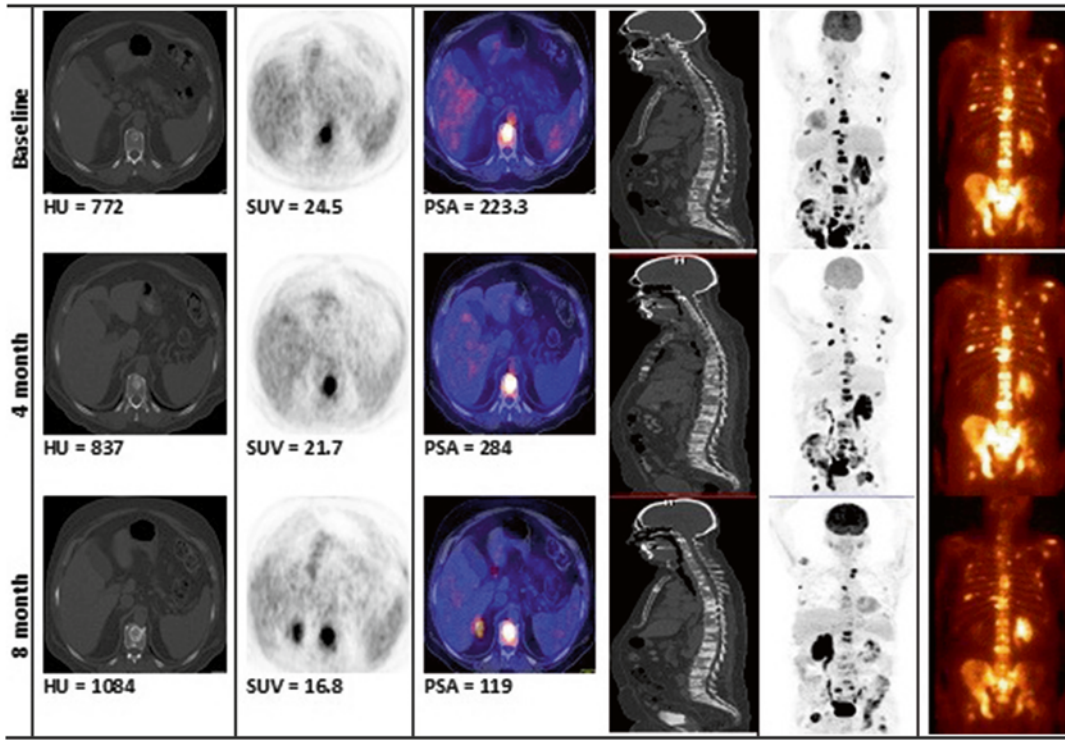

Fig. 8.3

Findings

The prostate gland is extensively bulky with areas of calcification (Fig. 8.4). Intense metabolic activity is seen at the right posterior and central aspect of prostate (SUVmax 11.2), compatible with known primary neoplasm. The prostate tumor appears to encroach the urethra with no fat plane identified between the prostate tumor and anterior wall of the rectum posteriorly or the urinary bladder anteriorly. There are several hypermetabolic bilateral external and internal iliac and presacral/perirectal lymph nodes, compatible with metastatic disease. The highest level of FDG-avid lymph node is seen at the level of left proximal external iliac bifurcation, involving the left external iliac lymph node, measuring approximately 2.7 cm in long axis with SUVmax 13.3. The largest hypermetabolic right external iliac lymph node measures approximately 2.6 cm long axis with SUVmax 14.6. Two hypermetabolic presacral lymph nodes are seen: one in the midline shows SUVmax 7.0, and the left paramedian presacral lymph node shows SUVmax 9.4. A right perirectal lymph node at the level of S4 shows SUVmax 13.1.

Impression

Hypermetabolic, large, bulky tumor involving right and central posterior aspect of prostate with hypermetabolic, metastatic bilateral internal and external iliac and perirectal/presacral lymphadenopathy.

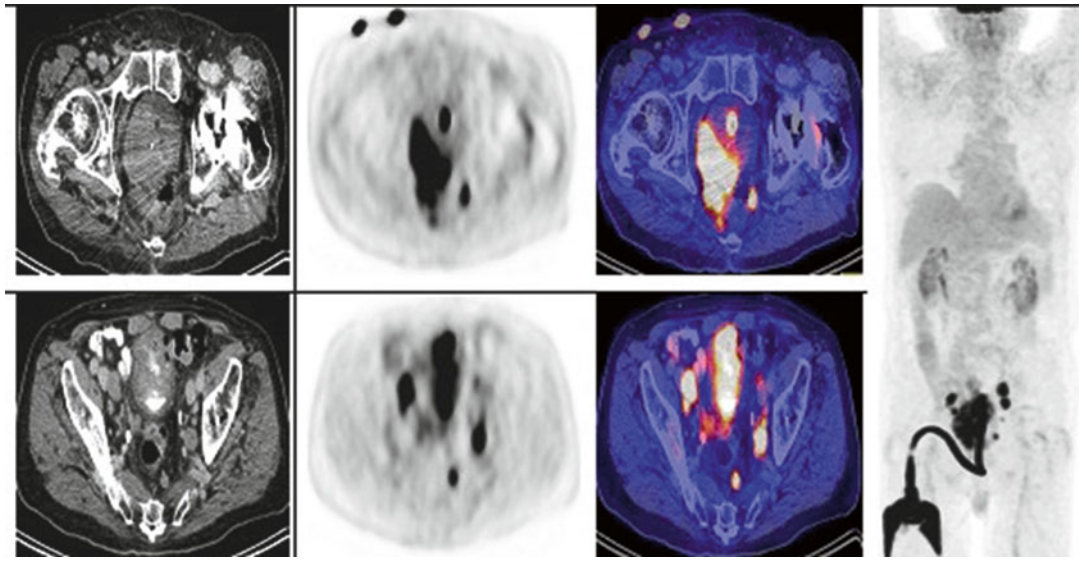

Fig. 8.4

Pearls and Pitfalls

- FDG PET may be useful for detecting, staging, and restaging poorly differentiated, hypoxic, high Gleason score tumors, monitoring treatment response in metastatic disease, assessment of extent of metabolically active castrate-resistant disease, and prognostication.
- FDG PET-CT has limited utility to differentiate between primary prostate cancer vs. BPH and post-op scarring and in patients with local recurrence after primary therapy.
- Higher FDG uptake with higher Gleason grade, advanced clinical stage, and higher serum PSA levels.
- Conventional morphologic (CT) and functional (99m Tc-MDP bone scintigraphy) imaging methods for qualitative treatment response assessment of bone metastases have been inaccurate and pose a challenge in routine oncological practice and in clinical trials, as skeletal lesions have been considered as nonmeasurable disease [2].
- Semiquantitative analysis of 18F FDG PET-CT might address an urgent need to develop an objective method for assessing tumor response in bone lesions which can clinically help physicians determine the effectiveness of systemic therapy [11, 13].

Discussion

Prostate cancer is the most common CA (30 % of all male CA) and second leading cause of CA death in men (exceeded by lung cancer) [1]. Incidence of adenocarcinoma is much higher than sarcoma and transitional cell carcinoma of the prostate. Routine diagnostic tests include digital rectal examination (DRE), PAP and PSA (nonspecific), and Gleason score (min 2, max 10). PSA and DRE have a limited positive predictive

value. Imaging modalities currently in use are ultrasonography (standard gray scale, enhanced transrectal with contrast agents, color and power Doppler, elastrography), computed tomography (CT), MRI (endorectal probe, contrast, spectroscopic imaging, lymphotropic nanoparticles, DWI), scintigraphy (bone scan, radioimmunoscintigraphy—*Prostascint*™), and positron emission tomography (PET), PET-CT, and PET-MRI.

Prostate cancer is biologically and clinically a heterogeneous disease, and its imaging evaluation needs to be tailored to the specific phases of the disease in a patient-specific, risk-adapted manner. Within 10 years after successful treatment for localized disease, 15–40 % experience PSA rise which is termed as biochemical recurrence. About 25–35 % of men with an increasing serum PSA level will develop locally recurrent disease only, 20–25 % will develop metastatic disease only, and 45–55 % will develop both local recurrence and metastatic disease. Median survival time for patients detected with metastatic disease is around 5 years, while the medial survival is only 8–18 months for those who have become refractory to hormonal therapy. As shown in Case 1, the patient had developed castrate-resistant metastatic prostate cancer and died 2 months after his 4-month scan due to disease progression.

Bone is the most common site to which prostate cancer metastasizes. Response to treatment is typically estimated by using a combination of methods, including diagnostic imaging, measurement of biochemical markers, and evaluation of patients' symptoms. Three patterns of bone metastasis commonly noted depending on the stage of treatment are (a) FDG uptake without corresponding morphological changes on CT; (b) FDG uptake with concomitant morphological changes on CT as sclerotic, lytic, and/or mixed lesions; and (c) negative FDG PET but dense sclerosis on CT. Metabolic and anatomic details provided by the combined PET-CT may provide a good imaging tool for quantitatively assessing response of metastatic skeletal lesions to various forms of systemic therapy.

Several novel PET tracers which are being tested for use in prostate cancer are radiolabeled acetate (11C, 18F), choline (11C, 18F), 11C-methionine, dihydrotestosterone (18F-FDHT), anti-1-amino-3-18F--fluorocyclobutane-1-carboxylic acid (anti-18F-FACBC), 1-(2′-deoxy-2′-fluoro-b-D-arabinofuranosyl)thymidine (18F-FMAU), and [18F]DCFBC (PSMA inhibitor) [12, 14, 15].

Bladder Cancer

Case 8.5

History

A 68-year-old male with high-grade urothelial carcinoma primary involving his kidney and bladder with metastasis in the retroperitoneum and liver, status post open nephroureterectomy with excision of the bladder cuff and left pelvic lymph node dissection and chemotherapy. Scan is being done for restaging.

Findings

Interval progression of hepatic disease now pan lobar with interval increase in extent of right hepatic confluent metastatic disease with new active left hepatic lobe lesions (Fig. 8.5). The confluent disease in the right correlates to low attenuation and now measures 9.8 × 9.2 × 10.4 cm, with SUVmax 25.1 (9 × 6.6 × 4.1 cm with SUVmax 23.1 in prior). There is an interval increase in size and activity of portacaval nodes now with SUVmax 14.1 (right 13.5 in prior). Also noted is a new hypermetabolic gastroduodenal (SUVmax 16) celiac axis node which is normal sized. There are also new multiple retroperitoneal hypermetabolic nodes, for example, aortocaval nodes with SUVmax up to 8.9. Interval increase is seen in the extent of left anterior pillar of acetabulum medullary sclerosis with stable metabolic activity, now involving superior pubic ramus, with SUVmax 10.6 (SUVmax 9.8 in prior).

Impression

Interval progression of disease with increasing hepatic, nodal, and osseous metastases.

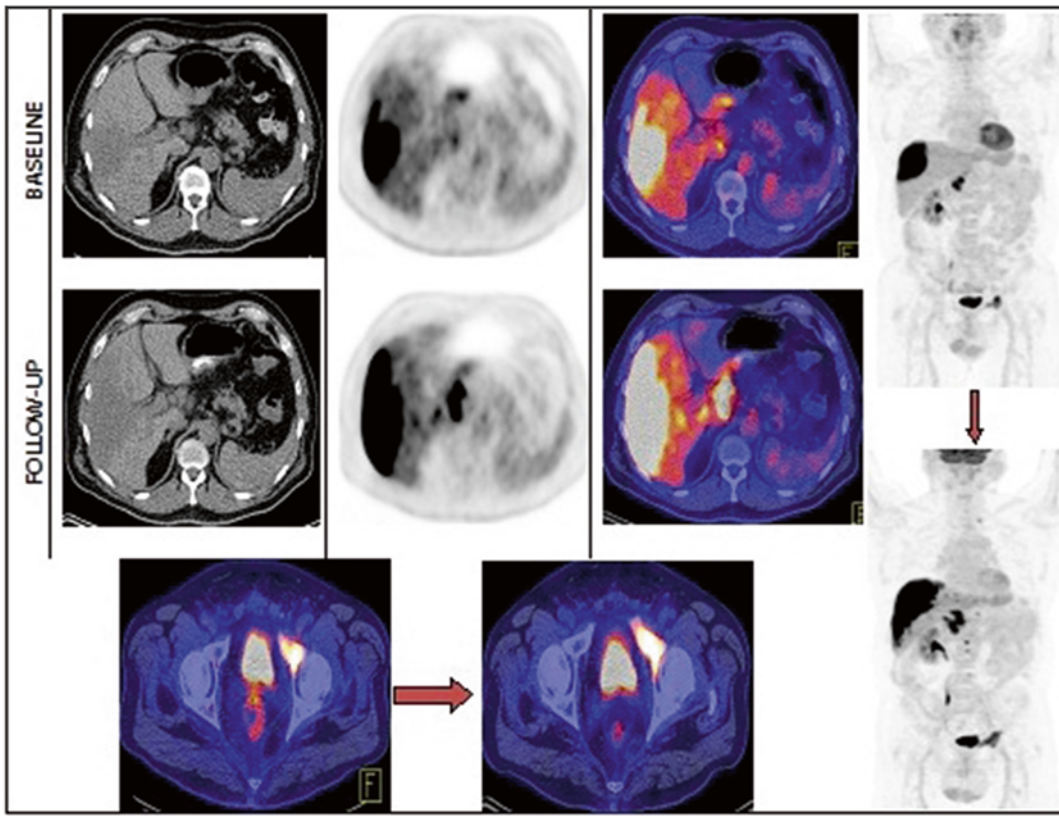

Fig. 8.5

Case 8.6

History

A 50-year-old male with history of metastatic bladder cancer, status post cystoprostatectomy with extensive lymph node dissection and seminal vasectomy with neobladder and ureteral diversion. The PET-CT was done for restaging purposes.

Findings

There is a slight misregistration of hypermetabolic activity with SUVmax 10.0 that most likely corresponds to the left supraclavicular lymph node, measuring approximately 0.6 × 0.8 cm (Fig. 8.6). There is large portacaval single lymph node or nodal conglomerate, approximately measuring 5.1 cm × 3.2 cm and demonstrating intense hypermetabolic activity (SUVmax 14.3). Patient is status post cystoprostatectomy with extensive lymph node dissection and seminal vasectomy with neobladder and ureteral diversion. The bilateral ureters are connected to the ileal conduit to Studer pouch and to urethra. There is stasis and dilatation of the left ureter and normal caliber of the right ureter, suggestive of stenosis at the anastomosis from left ureter to the conduit.

Impression

Scattered hypermetabolic lymph nodes above and below the diaphragm, with most active and largest lymph node/nodal conglomerate at portacaval location, consistent with metastatic disease.

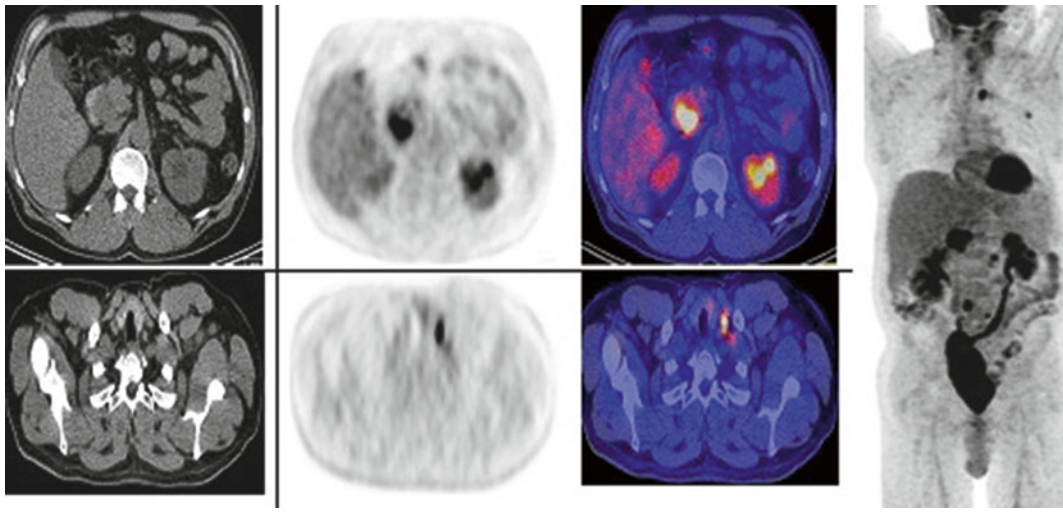

Fig. 8.6

Case 8.7

History

A 27-year-old male with bladder cancer, status post radical cystectomy and chemotherapy, with scan requested for initial staging.

Findings

There are several hypermetabolic periaortic and retroperitoneal lymph nodes noted; most of them are along the surgical clips (Fig. 8.7). The largest and the most active left aortic lymph node at the level of L4 vertebral body measures 1.3 cm with maximum SUV of 18.4. The left peritoneal nodule adjacent to the left psoas muscle measures 1.4 cm with maximum SUV of 8.6. The largest of right retroperitoneal lesion adjacent to the right psoas medially at the level of L5 vertebral body measures 2.9 cm × 2.4 cm with maximum SUV of 11.6. There are multiple presacral lesions with the largest presacral lesion next to the surgical clips on the left measures 3.1 cm × 2.5 cm with maximum SUV of 16. The midline presacral lesion measures 1.6 cm × 1.2 cm with maximum SUV of 10.7.

Impression

Multiple hypermetabolic abdominal and pelvic lymphadenopathy consistent with recurrent disease in the retroperitoneum.

Case 8.8

History

A 52-year-old female with recurrent high-grade urothelial carcinoma of the urinary bladder, status post radical cystectomy and anterior pelvic exenteration with multiple postoperative complications necessitating

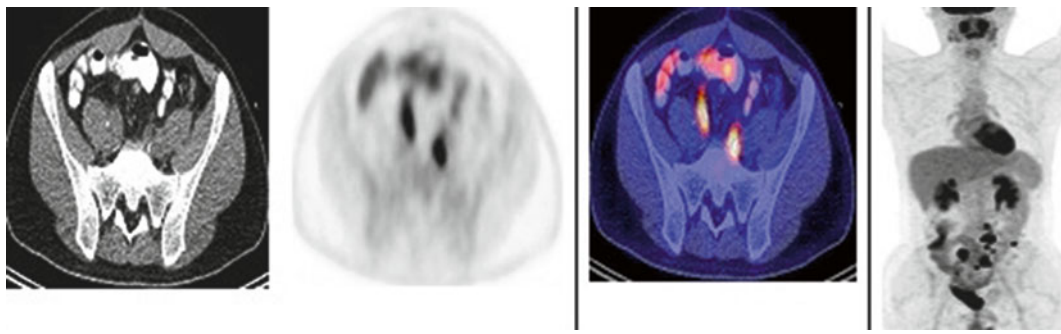

Fig. 8.7

additional six repair surgeries. Her last surgery included cystectomy with removal of the neobladder and ileal conduit urinary diversion and placement of bilateral open indwelling ureteral stents and biopsy of vaginal cuff. CABG pathology of the vaginal cuff revealed recurrent high-grade urothelial carcinoma. PET-CT is done to assess for local versus distant metastasis in order to plan further treatment strategy.

Findings

Left and right hydronephrosis and hydroureter are present (Fig. 8.8). Both ureters show mild circumferential wall thickening and terminate at the level of the large soft tissue mass at the L5–S1 level, suspicious for tumor involvement. There is hypermetabolic heterogeneous presacral mass, anterior to L5–S1, now measuring approximately $5.5 \times 5.3 \times 4.8$ with SUVmax 19.0. This tumor mass causes new bony erosion of approximately the anterior two-thirds of the upper sacrum. A focal intramuscular activity is noted laterally to the right ischial tuberosity, measuring approximately 1.0 cm and SUVmax 3.6, which may represent local inflammation versus metastatic implant.

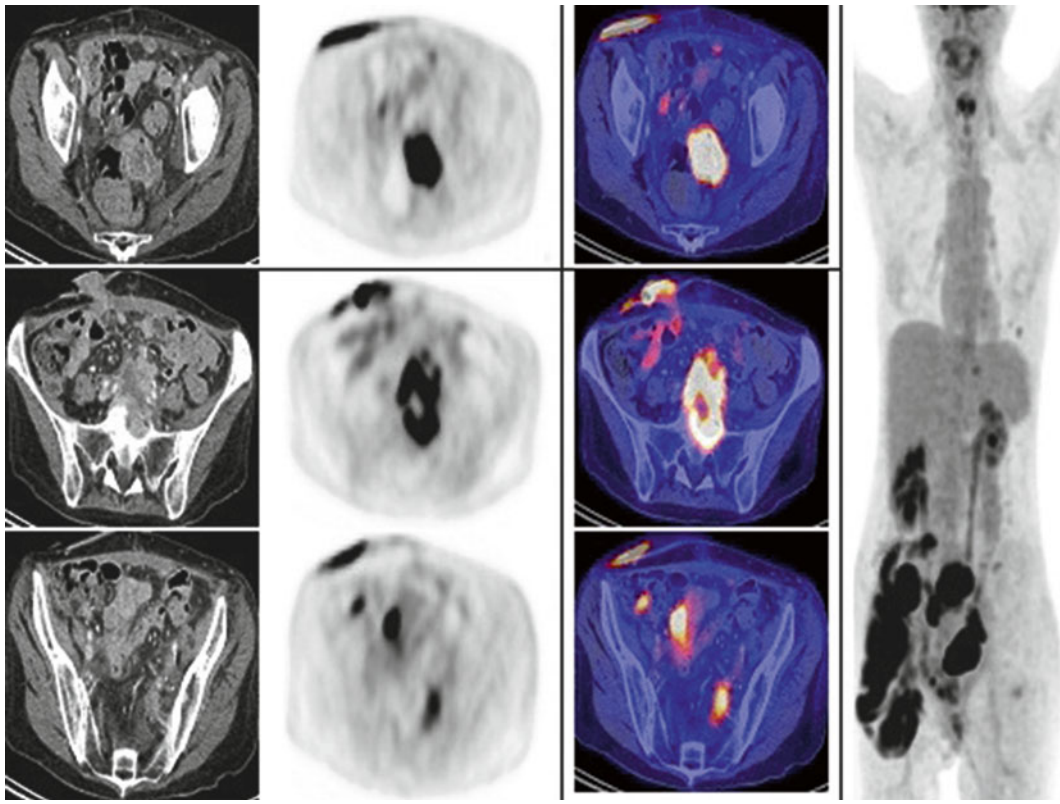

Fig. 8.8

Impression

Hypermetabolic lesions in the pelvis, significant in the presacral lesion which demonstrates bone erosion involving approximately the anterior two-thirds of the upper sacrum.

Pearls and Pitfalls

1. FDG is not generally used for the detection of primary bladder cancer since the tracer is excreted through urine. However, distant metastatic disease is usually seen.
2. 11C-choline and 11C-acetate have potential for bladder tumor imaging because they are not excreted in the urine [3].
3. PET has sensitivity of 67 %, specificity of 86 %, and an accuracy of 80 % for staging bladder cancer [4–6].

Discussion

Most cases of bladder cancer are transitional cell carcinoma. It is more common in whites than blacks. The median age is 68 years. Smoking, industrial carcinogen exposure, and prior radiation are risk factors. Microscopic hematuria is a common finding. IVP can be used to image the upper-tract urothelium in patients presenting with hematuria. CT and ultrasonography can be effective for lesion detection, but they can miss urothelial tumors in the upper tract. Cystoscopy and urine cytology are diagnostic. More than 70 % of the cancers are carcinoma in situ. Intravesical immunotherapy and intravesical chemotherapy are common treatment modalities. The methotrexate, vinblastine, Adriamycin, and cisplatin combination is the standard treatment for metastatic bladder cancer. For superficial bladder cancer, the 5-year survival is 82–100 %. For T2, T3, and T4 tumors, the 5-year survival rates are 63–83 %, 45–55 %, and 0–22 %. Recognition of epidural disease should prompt urgent consultation to initiate local therapy (radiation or surgery) if there is compromise of the spinal cord on MRI.

Renal Cell Carcinoma

Case 8.9

History

An 85-year-old female with history of right renal cell carcinoma, status post right radical nephrectomy. Patient developed metastasis to the left lung 11 years later for which she underwent left wedge resection with mediastinal lymphadenectomy. PET-CT is done as part of the subsequent treatment strategy evaluation.

Findings

Status post interval resection of hypermetabolic metastatic mass in the left upper lobe with postsurgical changes in comparison to baseline PET-CT (Fig. 8.9). There is increased confluence of airspace disease/bronchiectatic changes seen in the inferior right middle lobe which has increased in metabolic activity, currently demonstrating SUVmax 13.4 (previously 7.1). Again noted, patient is status post right nephrectomy with right adrenalectomy.

Impression

Status post interval resection of hypermetabolic metastatic mass in the left upper lobe. Bronchiectatic changes are seen in the right middle lobe which demonstrates increased metabolic activity, most probably inflammatory.

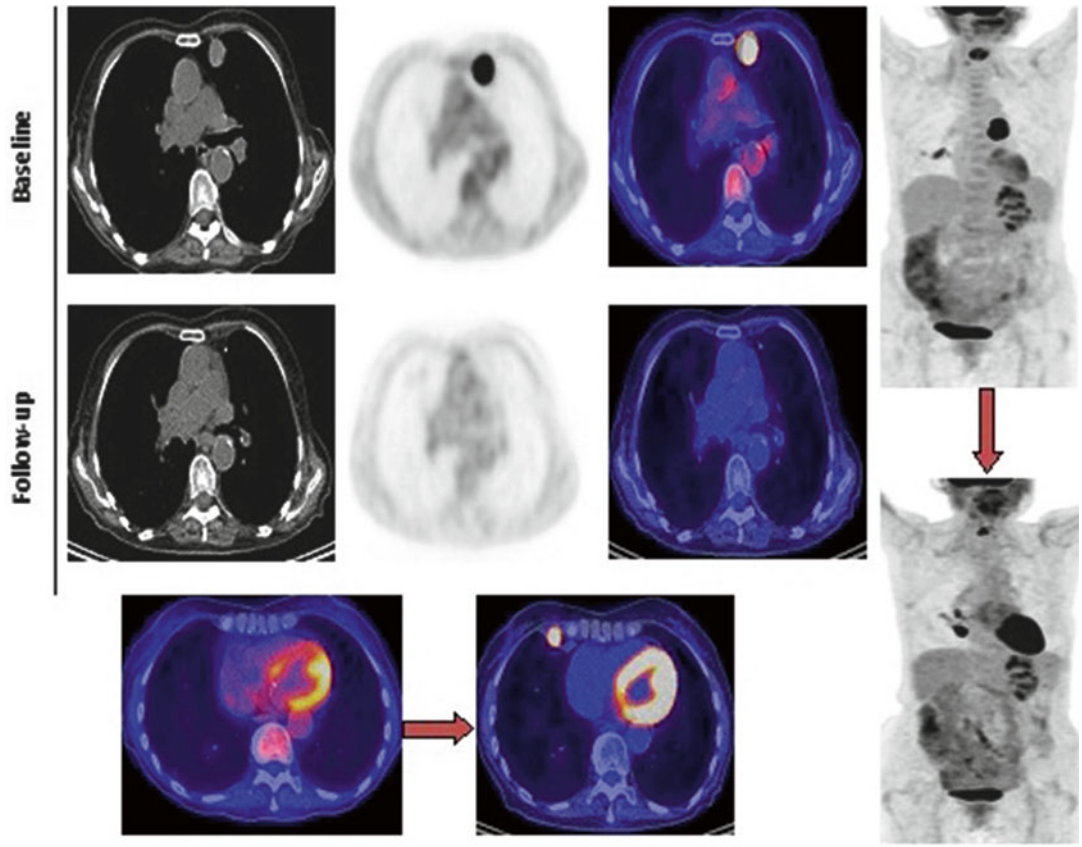

Fig. 8.9

Case 8.10

History

A 90-year-old male with high-grade transitional renal cell carcinoma and recurrent hematuria, status post resection of right renal lower pole. Pathology report showed high-grade papillary urothelial carcinoma, grade 4/4. PET-CT was done for staging purposes.

Findings

Within the right low pelvicalyceal system, in the expected area of filling defect on the CT, there is focal hyperactivity (SUVmax 7.7) (Fig. 8.10). Central calyx of the right kidney showed SUVmax 5.0, probably related to the urine. The close proximity to the urine makes it somewhat difficult to differentiate; however, the area of activity related to filling defect is suspicious for recurrent carcinoma. There is an exophytic renal cyst in the right upper pole and an intra-cortical cyst in the lower pole.

Impression

Suspect hypermetabolic recurrent malignancy within the low right renal pelvicalyceal system.

Pearls and Pitfalls

1. Seventy-seven percent of the renal cell carcinomas may be identified correctly with PET [7, 8].
2. Both PET and CT perform well in detecting metastatic lesions, 80 % as opposed to 83 %, respectively [7, 8].
3. The sensitivity, specificity, and diagnostic accuracy of PET is 82 %, 88 %, and 84 %, respectively [7, 8].
4. PET can alter patient management in 40 % of the cases [7, 8].

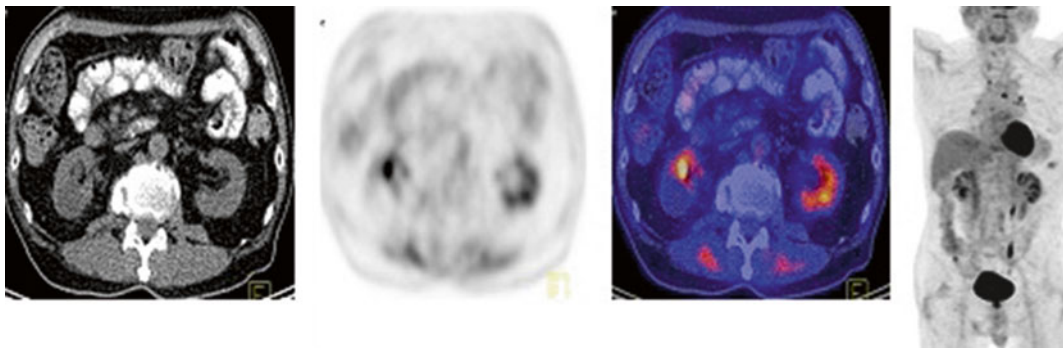

Fig. 8.10

Discussion

Renal cell carcinoma represents 3 % of all cancers in the adult population; mostly within the age range of 50–70 years of age. The widespread use of conventional CT, MRI, and ultrasonography of the abdomen has resulted in the identification of an increased number of incidental renal abnormalities, which may need further investigation. CT scanning is currently the commonly used noninvasive imaging tool to assess the nature of these abnormalities. In a study involving 53 patients, the accuracy of this technique in identifying renal masses was 83 % [9, 10]. Other larger studies showed the sensitivity and specificity of CT were both over 90 % [9, 10, 17]. CT and MRI also provide important information on size, tumor extension, and vascular invasion, factors which are essential for staging patients, prognosis, and planning of surgery.

Metastatic renal cell carcinoma has a median survival of 10 months despite of nephrectomy. A shortcoming regarding FDG PET is that its success is highly dependent on tumor histology type and tumor grade [16].

References

1. SEER: The Surveillance, Epidemiology, and End Results Program (http://seer.cancer.gov)-based within the Surveillance Research Program (SRP) at the National Cancer Institute (NCI).
2. Even-Sapir E, et al. The detection of bone metastases in patients with high-risk prostate cancer: 99mTc-MDP planar bone scintigraphy, single- and multi-field-of-view SPECT, 18F-fluoride PET, and 18F-fluoride PET/CT. J Nucl Med. 2006;47:287.
3. Heicappell R, et al. Staging of pelvic lymph nodes in neoplasms of the bladder and prostate by positron emission tomography with 18F FDG. Eur Urol. 1999;36:582–7.
4. Ahlstrom H, et al. Positron emission tomography in the diagnosis and staging of urinary bladder cancer. Acta Radiol. 1996;37:180–5.
5. Bachor R, et al. Lymph node staging of bladder neck carcinoma with positron emission tomography. Urologe. 1999;38:46–50.
6. Mantzarides M, Papathanassiou D, Bonardel G, et al. High-grade lymphoma of the bladder visualized on PET. Clin Nucl Med. 2005;30:478–80.
7. Shvarts O, et al. Positron emission tomography in urologic oncology. Cancer Control. 2002;9:335–42.
8. Steffens MG, et al. Clinical role of F-18 fluorodeoxyglucose positron emission tomography for detection and management of renal cell carcinoma. J Urol. 2002;168:2127–8.
9. Powles T, Murray I, Brock C, et al. Molecular positron emission tomography and PET/CT imaging in urological malignancies. Eur Urol. 2007;51(6):1511–20.
10. Aide N, et al. Efficiency of [(18)F]FDG PET in characterizing renal cancer and detecting distant metastases: a comparison with CT. Eur J Nucl Med Mol Imaging. 2003;30:1236–45.
11. Oyama N, et al. FDG PET for evaluating the change of glucose metabolism in prostate cancer after androgen ablation. Nucl Med Commun. 2001;22:963.
12. Beheshti M, et al. Detection of bone metastases in patients with prostate cancer by 18F fluorocholine and 18F fluoride PET-CT: a comparative study. Eur J Nucl Med Mol Imaging. 2008;35:1766.

13. Jadvar H. Molecular imaging of prostate cancer with [F-18]-fluorodeoxyglucose PET. Nat Rev Urol. 2009;6:317–23.
14. Hamaoka T, et al. Tumor response interpretation with new tumor response criteria vs. the World Health Organization criteria in patients with bone-only metastatic breast cancer. Br J Cancer. 2010;102:651–7.
15. Jadvar H. Prostate cancer: PET with 18F-FDG, 18F- or 11C-acetate, and 18F- or 11C-choline. J Nucl Med. 2011;52:81–9.
16. Subhas N, Patel PV, Pannu HK, et al. Imaging of pelvic malignancies with in-line FDG PET-CT: case examples and common pitfalls of FDG PET. Radiographics. 2005;25:1031–43.
17. Kang DE, et al. Clinical use of fluorodeoxyglucose F 18 positron emission tomography for detection of renal cell carcinoma. J Urol. 2004;171:1806–69.

9 Lymphoma

Aarti Kaushik and Robert W. Henderson

Case 9.1: Transformation of Follicular Lymphoma Grade

History

A 63-year-old female with recurrent lymphoma. Patient had low-grade (grade 1A) follicular B-cell lymphoma initially in the left inguinal region. The current disease is follicular B cell (grade 3). Scan is requested for restaging.

Findings

There are at least two subcentimeter left cervical level 2 lymph nodes with the most active with maximum SUV of 8.6 (Fig. 9.1). There is a subcentimeter left level 5 lymph node with maximum SUV of 7.9. These are consistent with lymphomatous involvement. There are multiple splenic lesions noted with the largest and most active measuring 2.4 cm × 1.8 cm, with maximum SUV of 13.9 correlating to hypodense region on CT.

Pearls and Pitfalls

Recurrent disease with histopathological transformation from grade 1–3 (Fig. 9.1).

P.S. Conti, A. Kaushik (eds.), *PET-CT*, DOI 10.1007/978-1-4419-5811-2_9

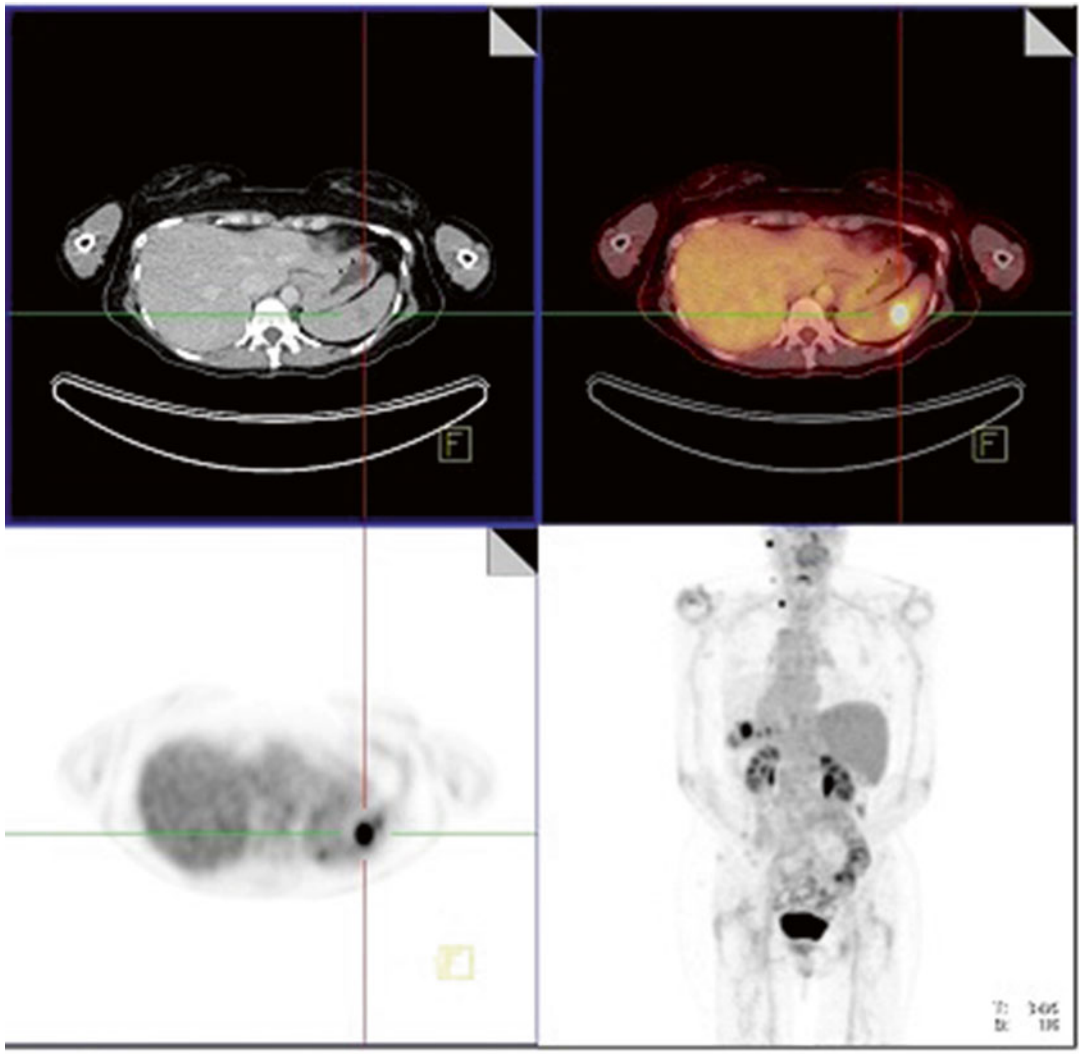

Fig. 9.1

Case 9.2: Multiple Recurrences with High-Grade Transformation of Lymphoma

History

A patient with low-grade follicular lymphoma initially diagnosed in the sacrum in 1998, treated with chemotherapy and radiation. A patient had recurrence in 2004 involving the right groin, bilateral iliac region, and right base of the tongue, treated with chemotherapy and radiation therapy. No interval treatment since then. Current study in 2011.

Findings

Interval increase in size and metabolic activity of a left level 4 node now measuring 1.2 cm in short axis with SUVmax 4.5 (normal size and inactive in prior) (Fig. 9.2). New intensely active and enlarged left porta hepatis nodes, SUVmax up to 12. There is interval increase in metabolic activity but unchanged size of a left retroaortic node, now with SUVmax 4.3 (SUVmax 3.8 in prior).

Pearls and Pitfalls

1. Multiple recurrences with progressive more biologic activity as noted with SUVmax in the current study.
2. Zevalin (90Yt Rituxan) with higher response rate than Rituxan alone.

Discussion

Follicular lymphoma is the second most common type of lymphoma in high-income countries, representing nearly 20 % of all non-Hodgkin's lymphomas. The pathogenesis of follicular lymphoma remains elusive, and evidence exists that t(14;18)(q32;q21), the most common genetic alteration in follicular lymphoma cells, which results in an overproduction of the antiapoptotic BCL-2 protein, is not sufficient to cause the disease [26]. By contrast, the role of infiltrating cells in the tumor microenvironment has gained attention in the past few years [1]. The clinical course of follicular lymphoma is quite variable, with some patients having an indolent, waxing, and waning disease for years, without the need for therapy, and others presenting with a more disseminated and rapidly growing disease. Most patients with follicular lymphoma have incurable disease, with a generally indolent course, frequent relapses, and a progressive decrease in duration of responses with every subsequent relapse. A major advance in the treatment of follicular lymphoma was the introduction of monoclonal antibodies to therapeutic regimens, mainly antibodies against CD20. These antibodies have contributed to the improvements in survival of patients with follicular lymphoma recorded in the past decade [2]. But, even in the immunotherapy era, relapses will occur (Fig. 9.2).

Case 9.3: Diffuse Large B-Cell Lymphoma Scapula

History

A patient with diffuse large B-cell lymphoma, stage 4, involving the right scapula (biopsy dated 12/13/2010). No treatment yet.

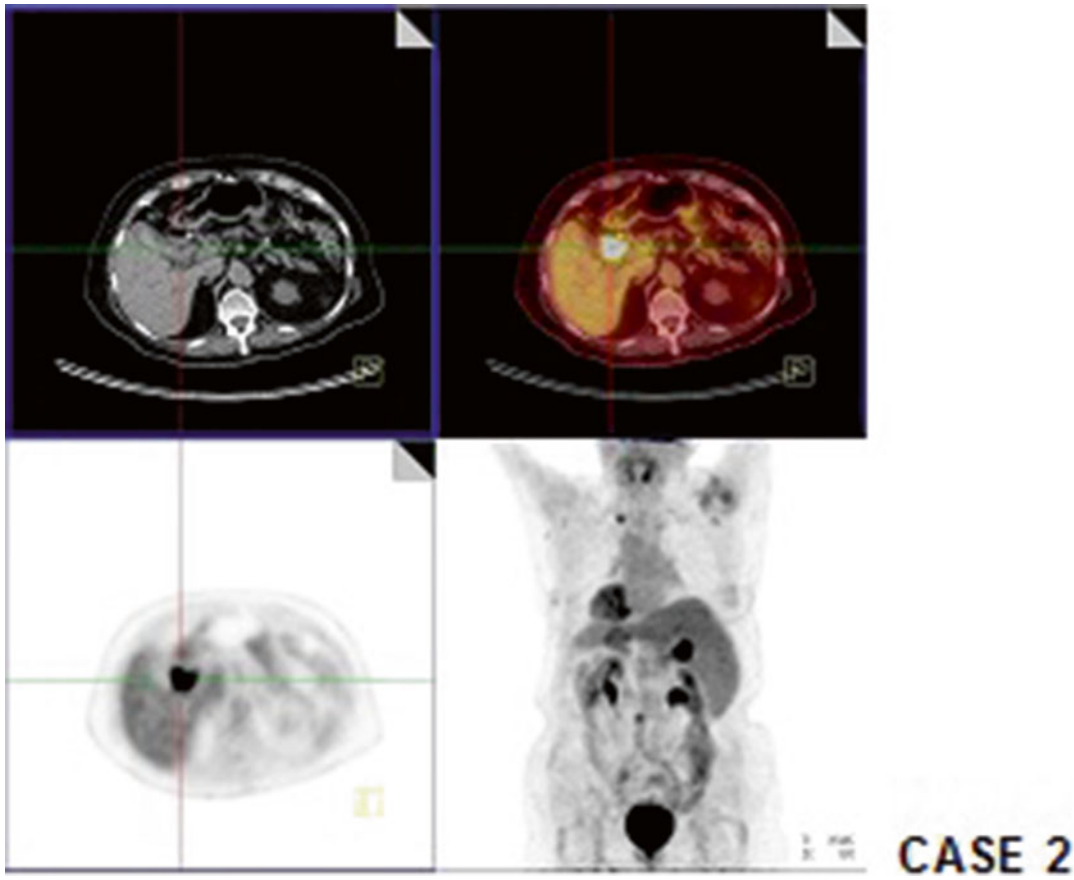

Fig. 9.2

Findings

A hypermetabolic, osteolytic right scapular body mass involving the wing and extending into the glenoid, with SUVmax 10.3 consistent with biopsy-proven lymphoma (Fig. 9.3). Hypermetabolic, right supraclavicular and right axillary nodes (faintly visible) with SUVmax up to 6.5 and hypermetabolic right inguinal node (1.3 cm, with SUVmax 13.2) are consistent with lymphomatous involvement (Fig. 9.3).

Case 9.4: Hodgkin's Lymphoma Involving Spine

History

A 47-year-old female presenting with neurologic symptoms, undergoing workup with PET-CT for T5 lesion, status post bone biopsy which was

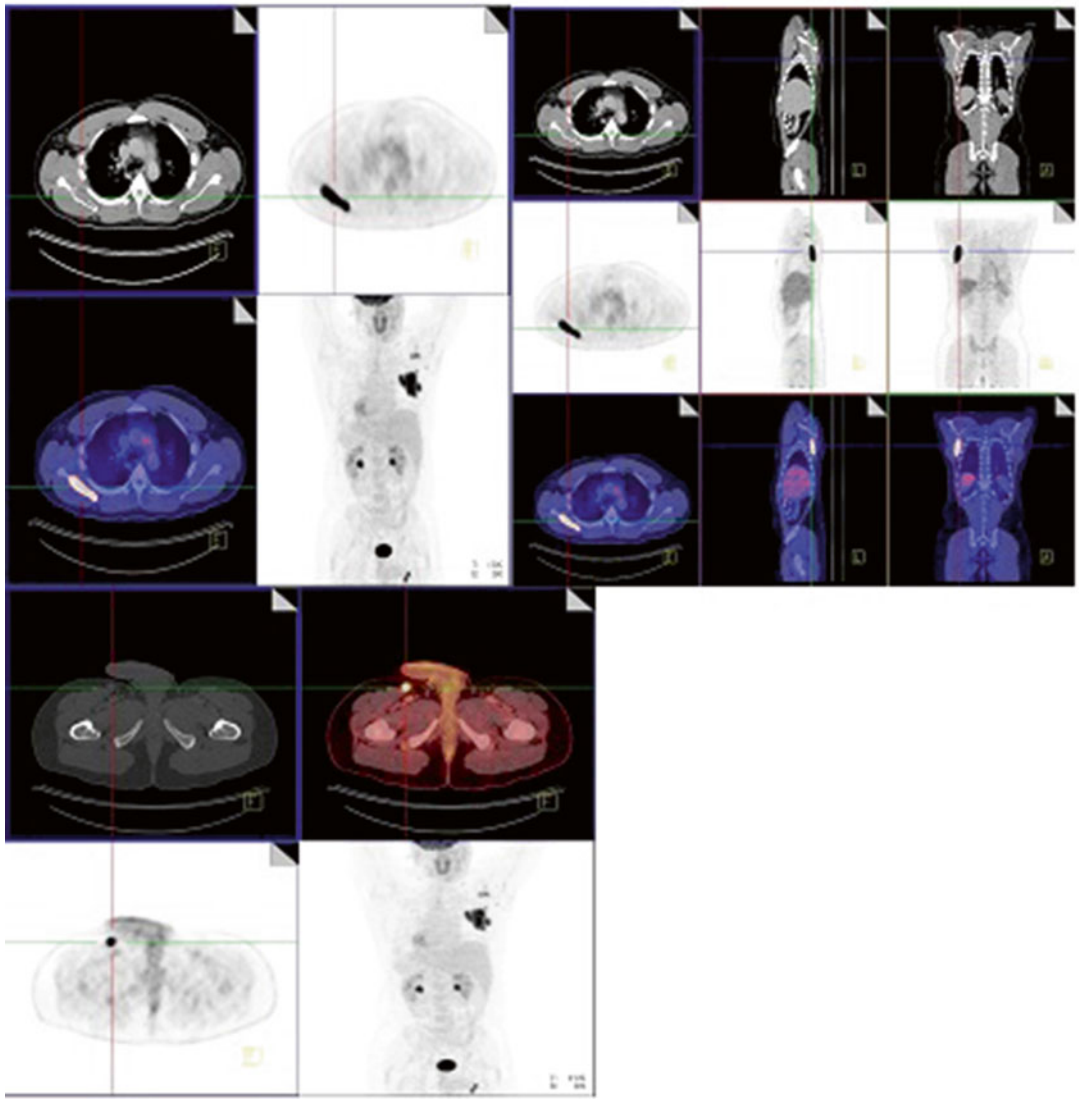

Fig. 9.3

nondiagnostic. However, post scan biopsy reported classic Hodgkin's lymphoma.

Findings

There is a large hypermetabolic mass involving T5 with its soft tissue component causing bony destruction and extending posteriorly abutting and possibly causing mass effect on the spinal cord, SUVmax 13.3 (Fig. 9.4). This lesion extends anteriorly to abut the posterior aspect of the trachea and extends laterally involving adjacent paravertebral space (Fig. 9.4).

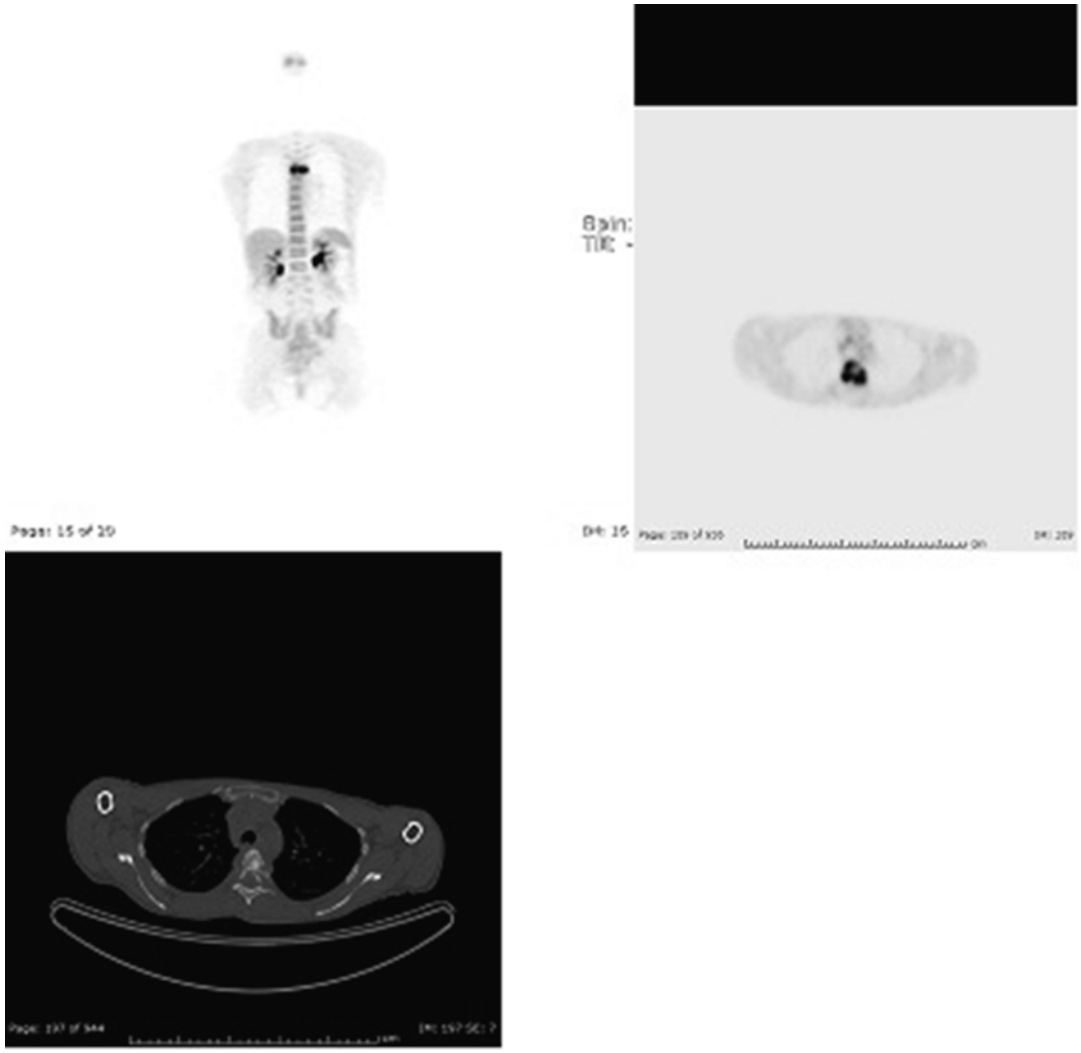

Fig. 9.4

Case 9.5: Sacral Lymphoma

History

A 59-year-old male with B-cell lymphoma of the right sacrum.

Findings

Intensely active destructive lytic mass involving the right sacral wing and body with presacral extension of the soft tissue, with maximum SUV of 12.5 (Fig. 9.5). In addition, there is extension of this lesion into the adjacent

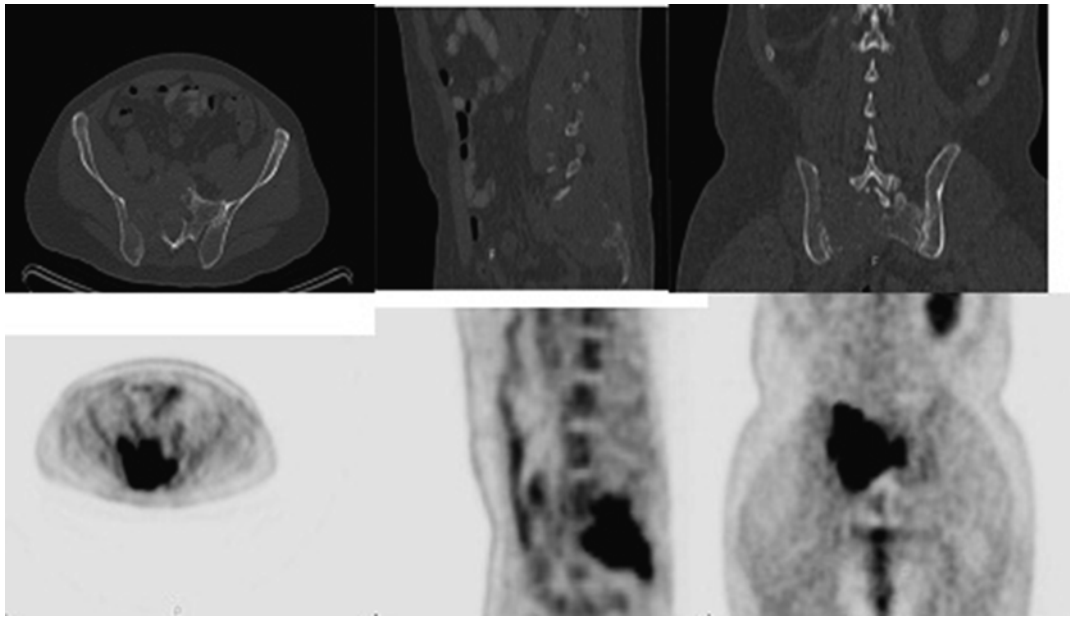

Fig. 9.5

iliacus musculature. There is extension into the lower bony spinal canal with involvement of the first and second sacral foramina (Fig. 9.5).

Case 9.6: Right Maxillary Lymphoma

History

A 71-year-old male with history of diffuse large B-cell lymphoma involving the right maxilla and right neck nodes for initial staging.

Findings

There is a large right maxillary sinus mass with SUVmax 15 (Fig. 9.6). There is osseous destruction involving the anterior and medial walls of the right maxillary sinus as well as the maxilla.

Discussion

Primary lymphoma of the bone is a rare malignant condition that accounts for less than 5 % of all primary bone tumors [3]. It has also been called reticulum cell sarcoma [4], malignant lymphoma of the bone [5], and more

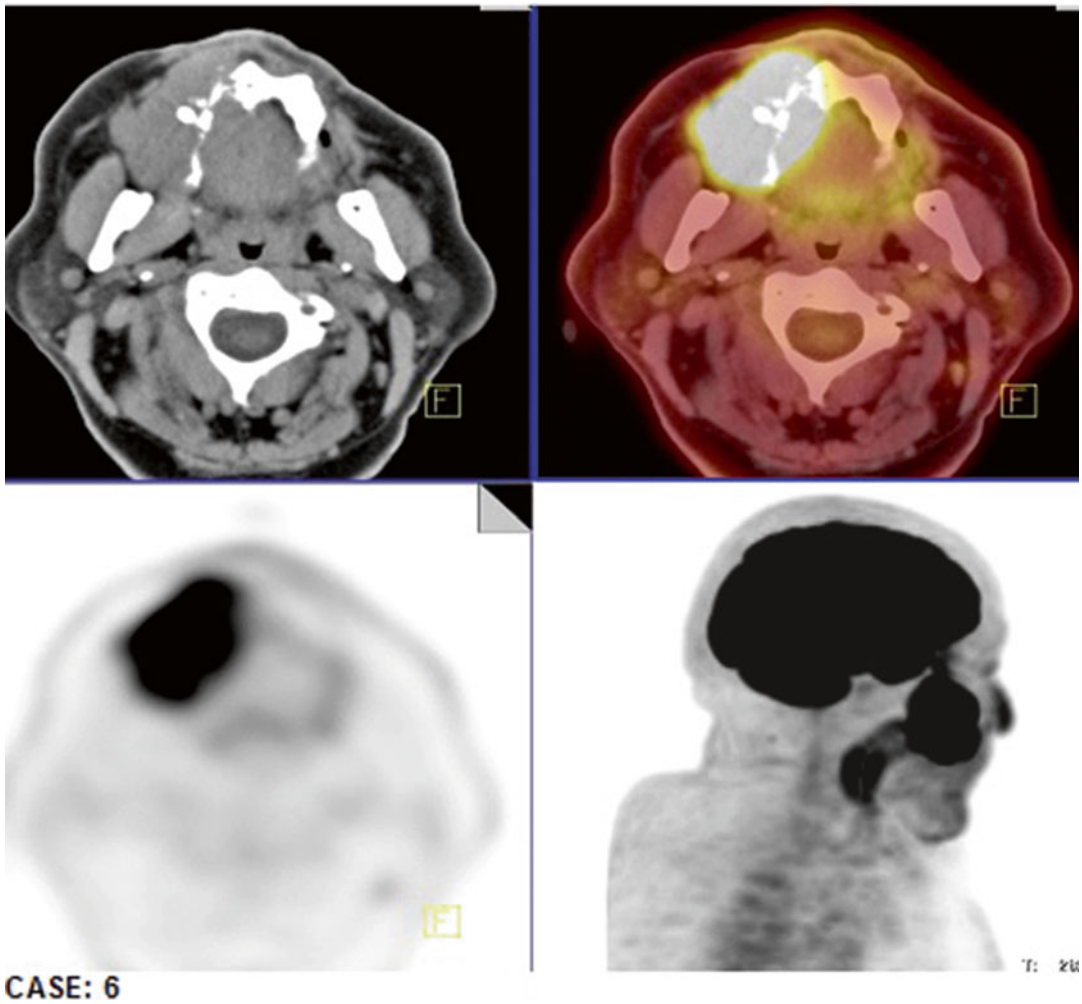

Fig. 9.6

recently osteolymphoma [6]. The vast majority of cases are of the non-Hodgkin type, with Hodgkin's disease accounting for 6 % of cases in one series [3]. Lymphomas of the bone are uncommon, comprising only 8 % of primary malignant bone tumors [3]. Most malignant lymphomas of the bone are diffuse non-Hodgkin's lymphomas of B-cell type [4] (Fig. 9.6).

Case 9.7: NHL Bladder

History

Primary urinary bladder non-Hodgkin's lymphoma in an 80-year-old female. She presented with difficulty urinating and urinary frequency and

urgency along with weak stream of urine. On physical examination, she was found to have bladder neck mass for which she underwent transurethral resection of the mass. The pathology was consistent with diffuse large B-cell lymphoma.

Findings

Staging PET-CT study demonstrated a hypermetabolic, soft tissue mass at the base of the urinary bladder, measuring $6.3 \times 3.8 \times 3.4$ cm and maximum SUV of 21.8 (Fig. 9.7). She had received chemotherapy and demonstrated excellent response on the follow-up PET-CT study.

Pearls and Pitfalls

Lymphomas of the bladder are rare lesions, representing approximately 0.2 % of the primary neoplastic lesions and approximately 1.8 % of the secondary lesions in this organ [7, 8, 27].

Discussion

Primary lymphoma of the bladder represents 0.2 % of all bladder malignancies. Secondary involvement of the bladder by malignant lymphoma occurs in 10–50 % of cases. Most lymphomas of the bladder are non-Hodgkin's lymphomas of the B-cell type, with preponderance among women. Patients with bladder lymphomas can be divided into three

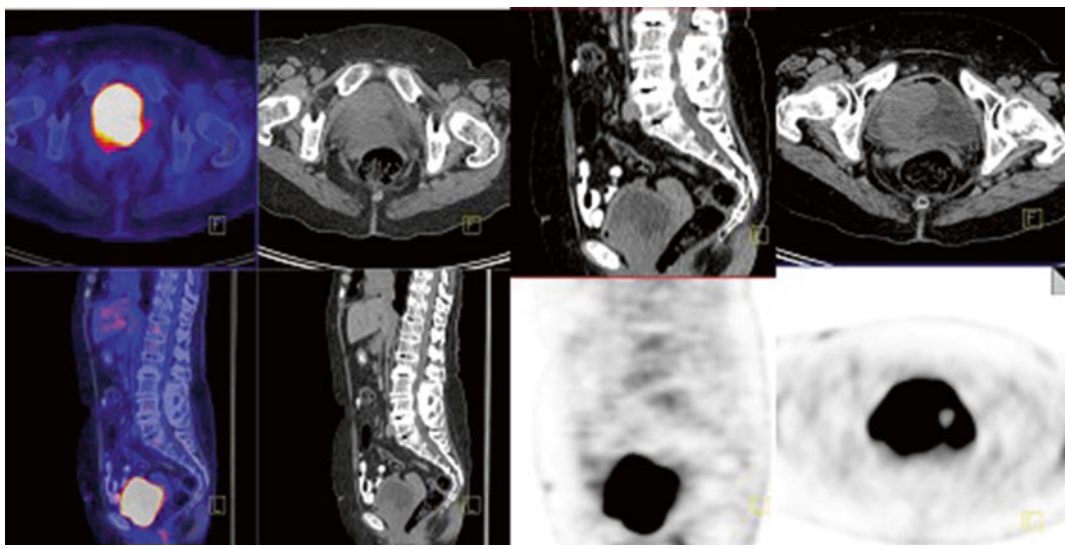

Fig. 9.7

groups, according to their clinical presentation: (1) primary cases in the bladder, (2) cases occurring in the bladder as a manifestation of systemic disease, and (3) secondary cases, with clinical history of malignant lymphoma recurring in the bladder. In the latter case, the main sites of involvement are peripheral lymph nodes, the bone marrow, and the spleen [8] (Fig. 9.7).

Case 9.8: Parotid Lymphoma

History

A 48-year-old female with non-Hodgkin's lymphoma in the left parotid diagnosed in 2012, for initial staging.

Findings

There is intensely hypermetabolic soft tissue density noted in the left parotid with the maximum SUV of 10.4 with photopenic hypoattenuating center which may be related to necrosis or seroma, consistent with the known left parotid tumor (Fig. 9.8). There is brown fat activity noted in the bilateral posterior cervical region in the images.

Pearls and Pitfalls

The following clinical features might suggest the diagnosis: development of a parotid mass in a patient with a known history of malignant lymphoma; occurrence of a parotid mass in a patient with an immune disorder, such as Sjogren's syndrome, rheumatoid arthritis, or acquired immunodeficiency syndrome; occurrence of a parotid mass in a patient with a previous diagnosis of "benign lymphoepithelial lesion"; multiple masses in a unilateral parotid gland or bilateral parotid masses; or parotid mass associated with multiple, enlarged unilateral or bilateral cervical lymph nodes.

Discussion

Sjogren's disease is the commonest collagen vascular disorder involving the parotid gland causing enlargement. The parotid node maybe involved in lymphoma. Parotid glands are the only salivary glands with lymph nodes. Primary malignant lymphomas of the salivary glands are uncommon, comprising only 1.7–3.1 % of all salivary neoplasms [9–11] and 0.6–5 % of all tumors and/or tumor like lesions of the parotid gland [9, 12]. The lymphoma may arise in intraglandular lymph nodes normally found

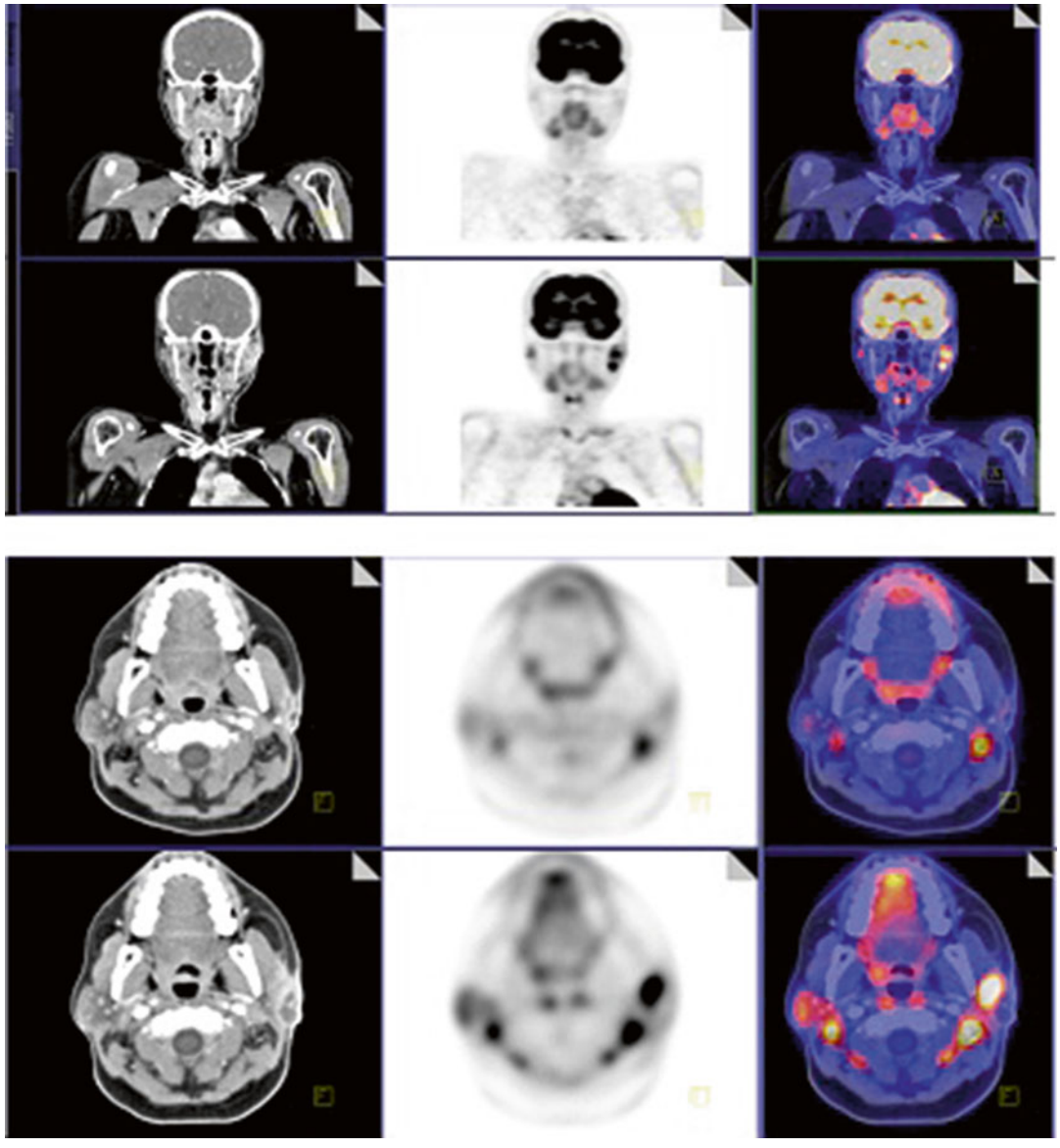

Fig. 9.8

in the parotid gland or from the parenchyma (mucosa-associated lymphoid tissue [MALT]) or both. The distinction of nodal vs parenchymal (MALT) origin of a salivary lymphoma has some clinical significance, since many of the parenchymal (MALT) lymphomas tend to be low grade, are localized at the time of diagnosis and often remain so for extended periods, frequently are associated with a "benign lymphoepithelial lesion," and are often curable. 18–25 A few, however, may disseminate to lymph nodes or other MALT sites or even transform to a higher-grade lymphoma (Fig. 9.8).

Case 9.9: Renal Non-Hodgkin's Lymphoma

History

A patient is a 70-year-old male with history of non-Hodgkin's lymphoma. The study is requested for staging.

Findings

Bilateral kidneys are markedly enlarged and demonstrate intense activity on PET, consistent with lymphomatous infiltration (Fig. 9.9). The right kidney measures approximately 14.5 cm AP × 13.7 cm transverse × 19.5 cm craniocaudal and has a maximum SUV up to 11.5. The left kidney measures approximately 16.9 cm AP × 16 cm transverse × 18.2 cm craniocaudal and has a maximum SUV of 9.8. There is a right ureteral stent, with the distal pigtail terminating in the urinary bladder.

Numerous enlarged lymph nodes in are seen multiple nodal basins in the neck, chest, abdomen, and pelvis, consistent with the documented lymphoma abdomen, and pelvis. For reference, the largest right axillary adenopathy measures 2.0 × 4.6 cm and has a maximum SUV of 7.0.

Pearls and Pitfalls

1. Primary renal lymphoma should be suspected if there is bilateral enlargement of the kidneys.
2. Imaging techniques and renal histology have a central role in establishing the diagnosis.

Discussion

Primary renal lymphoma is an uncommon variant of extranodal non-Hodgkin's lymphoma. Manifestations are usually nonspecific hematuria, fever, flank pain, and renal insufficiency [13, 14]. Renal lymphoma, however, is important to include in the differential diagnosis of renal masses, because generally it is a systemic disease and treatment is nonsurgical. Primary renal NHL is a rare disease [15, 16]. It is defined as an NHL arising primarily in the renal parenchyma, not resulting from invasion of an adjacent lymphomatous mass [16]. It affects middle-aged people and is usually of B-cell lineage. Clinical presentation includes symptoms of flank pain and renal insufficiency [15, 16]. Compressive alteration of the tubules and vascular impairment are the main structural events. The pathogenesis of primary renal lymphoma is poorly understood, as the renal parenchyma is not a lymphoid organ. It is believed by some investigators that lymphomas in nonlymphoid organs arise in the setting of an inflammatory disease with a lymphoplasmacytic infiltrate [17]. However,

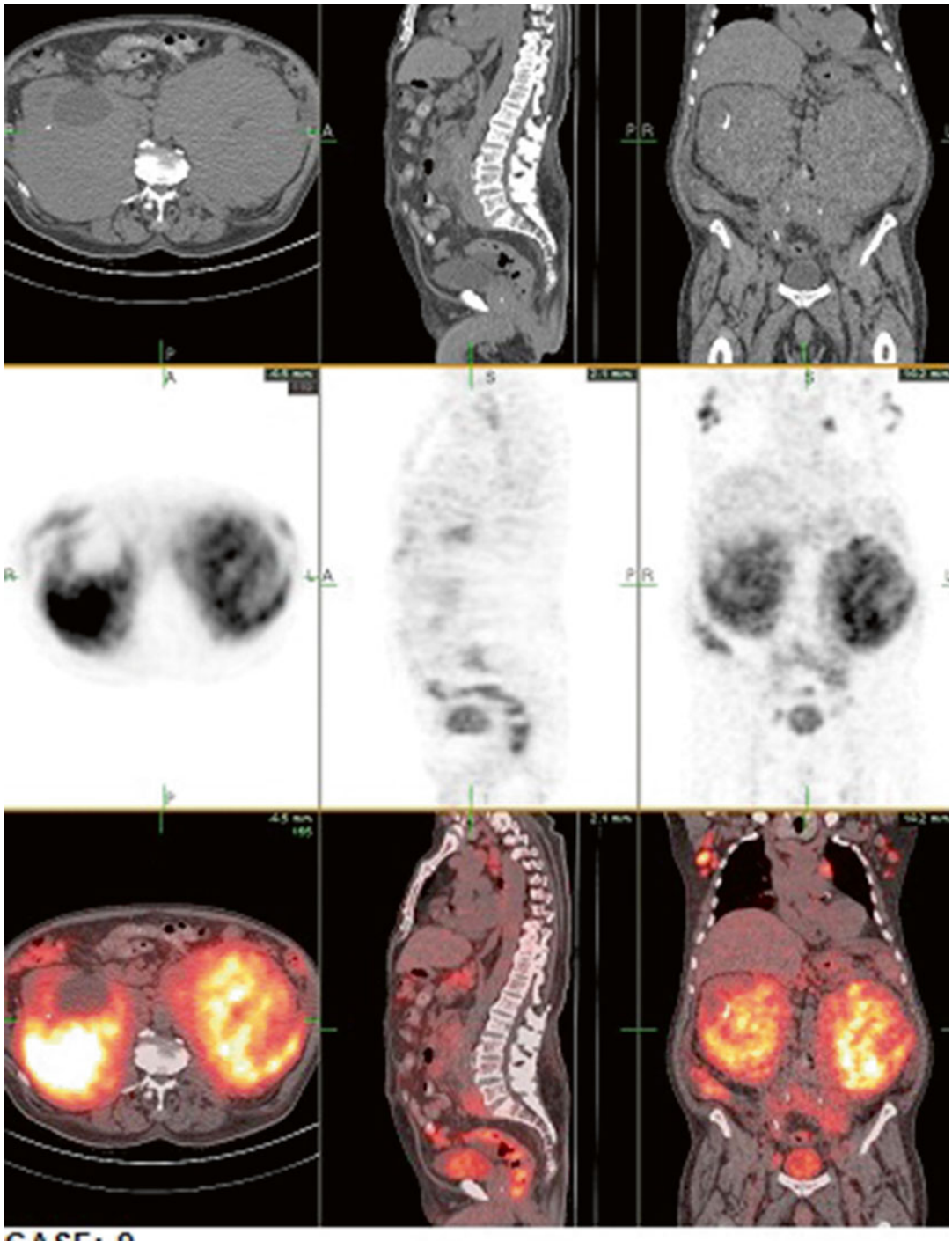

Fig. 9.9

such a pathogenetic mechanism has not been applied to the kidney. Most primary renal lymphomas disseminate rapidly from their renal origin, and mean survival is reportedly less than a year after the diagnosis [18]. Differentiating renal lymphoma from carcinoma, especially in the case of a unilateral lesion, is a diagnostic challenge (Fig. 9.9).

Case 9.10: NK Lymphoma

History

A patient with NK-type nasal lymphoma for initial staging.

Findings

Hypermetabolic right nasopharyngeal mass with destruction of the lower mid bony nasal septum with SUVmax 7.3 (Fig. 9.10). The mass begins in the cavity and extends along the medial wall of the right maxillary sinus to the posterior nasal cavity and superiorly up to the level of the hard palate.

Pearls and Pitfalls

NK-cell lymphoma is the commonest histologic subtype in nasal lymphomas in Asian patients.

Discussion

Natural killer (NK) cells are cytotoxic cells, which are capable of lysing tumor cells, and cells infected by bacteria and virus [19–21]. Nasal NK-cell lymphomas refer generally to tumors arising in the nose and the upper airway [22]. The male to female ratio is approximately 3:1, with disease peaking in the fifth decade of life. NK-cell lymphoma is the commonest histologic subtype in nasal lymphomas in Asian patients [22]. Nasal NK-cell lymphomas present as destructive mass lesions involving the nasal cavity, nasopharynx, paranasal sinuses, tonsils, hypopharynx, and larynx. Destruction of the hard palate leads to a characteristic midline perforation, from which the term “lethal midline granuloma” was originally derived (Fig. 9.10).

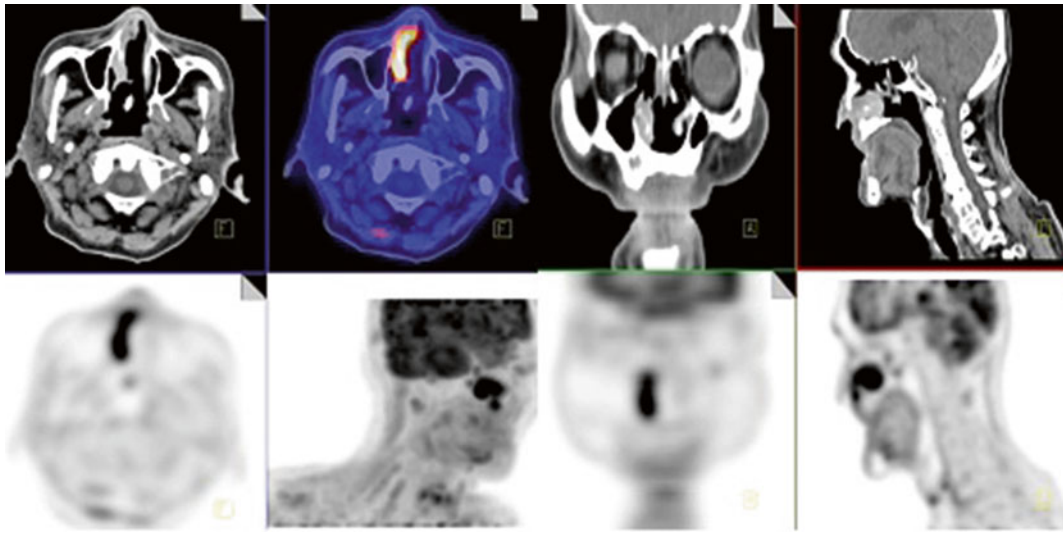

Fig. 9.10

Case 9.11: Orbital Lymphoma

History

A patient with history of orbital lymphoma (MALT), with follow-up showing complete remission.

Findings

There is a right retro-orbital mass, with SUVmax 7.2 consistent with history of lymphoma (top row) (Fig. 9.11). On follow-up there is activity in the bilateral ocular muscles with inactive residua on the right (bottom images).

Pearls and Pitfalls

Orbital lymphoma is almost always non-Hodgkin's lymphoma (NHL) with the most common subtype being low-grade small B-cell lymphoma.

Discussion

Lymphoproliferative lesions of the orbit account for 5–10 % of orbital masses and exist along a spectrum from benign hyperplasia (10–40 %) to lymphoma (60–90 %). Orbital lymphoma is almost always non-Hodgkin's

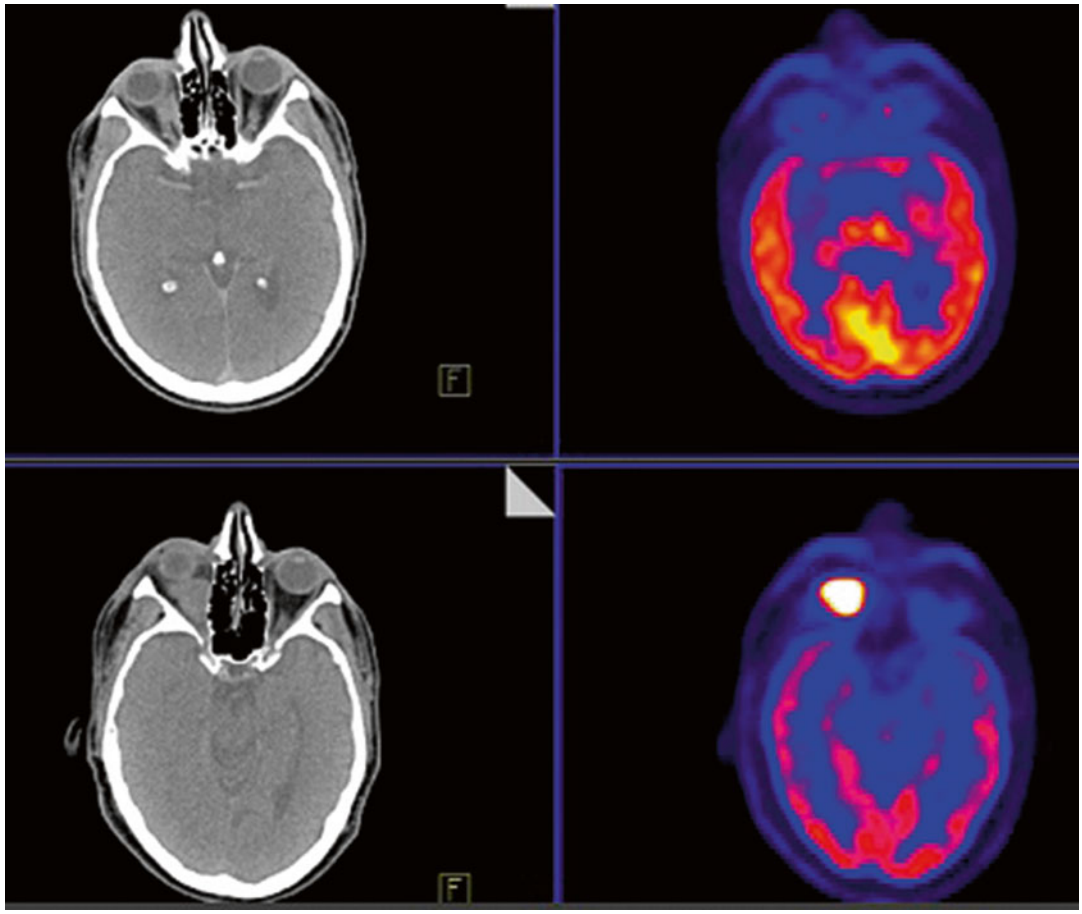

Fig. 9.11

lymphoma (NHL) with the most common subtype being low-grade small B-cell lymphoma. The most common presentation is a painless slow-growing mass. It is commonly extraconal, anterior, superolateral and has a predilection for the lacrimal glands. It is bilateral in 25 % of cases, and 50 % will have globe displacement. Orbital lymphoma is also known to infiltrate the conal or rectus musculature as well as the globe. Fluorine-18 deoxyglucose PET (FDG-PET) can sometimes find systemic extranodal lymphomatous sites that are not detected with conventional imaging studies. This ability yields valuable information in patients with ocular lymphoma, which may result in important changes in staging and also in patient management [23, 24]. PET has been found to have a higher sensitivity than CT scan (86 % vs. 72 %) in detecting distant disease [25] (Fig. 9.11).

References

1. Dave SS, Wright G, Tan B, et al. Prediction of survival in follicular lymphoma based on molecular features of tumor-infiltrating immune cells. N Engl J Med. 2004;351:2159–69.
2. Liu Q, Fayad L, Cabanillas F, et al. Improvement of overall and failure-free survival in stage IV follicular lymphoma: 25 years of treatment experience at The University of Texas M.D. Anderson Cancer Center. J Clin Oncol. 2006;24:1582–9.
3. Mulligan ME, McRae GA, Murphey MD. Imaging features of primary lymphoma of bone. Am J Roentgenol. 1999;173:1691–7.
4. Coley BL, Higinbotham NL, Groesbeck HP. Primary reticulum-cell sarcoma of bone. Radiology. 1950;55:641–58.
5. Boston Jr HC, Dahlin DC, Irvins JC, Cupps RE. Malignant lymphoma (so-called reticulum cell sarcoma) of bone. Cancer. 1974;34:1131–7.
6. Christie DR, Cahill SP, Barton MB. Primary bone lymphoma (osteolymphoma). Australas Radiol. 1996;40:319–23.
7. Díaz-Peromingo JA, Tato-Rodríguez J, Pesqueira-Fontán PM, Molinos-Castro S, Gayol-Fernández MC, Struzik JP. Non-Hodgkin's lymphoma presenting as a primary bladder tumor: a case report. J Med Case Reports. 2010;4:114.
8. Bates AW, Norton AJ, Baithun SI. Malignant lymphoma of the urinary bladder: a clinicopathological study of 11 cases. J Clin Pathol. 2000;53:458–61.
9. Sharkey FE. Systemic evaluation of the World Health Organization classification of salivary gland tumors: a clinicopathologic study of 366 cases. Am J Clin Pathol. 1977;67:272–8.
10. Gleeson MJ, Bennett MH, Cawson RA. Lymphomas of salivary glands. Cancer. 1986;58:699–704.
11. Schusterman MA, Granick MS, Erickson ER, Newton D, Hanna DC, Brighten R. Lymphomas presenting as a salivary gland mass. Head Neck Surg. 1988;10:411–5.
12. Bears OH, Woolner LB, Carveth SW, Devine KD. Surgical management of parotid lesions: a review of 760 cases. Arch Surg. 1960;80:890–904.
13. Freeman C, Berg JW, Cutter SJ. Occurrence and prognosis of extranodal lymphomas. Cancer. 1972;29:252–60.
14. Pervez H, Shaikh M, Potti A, Mehdi SA. Uncommon presentations of non-Hodgkin's lymphoma: case 3-primary renal lymphoma. J Clin Oncol. 2003; 21:567–9.
15. Stallone G, Infante B, Manno C, et al. Primary renal lymphoma does exist. J Nephrol. 2000;13:367–72.
16. Okuno SH, Hoyler JD, Ristow K, et al. Primary renal non-Hodgkin's lymphoma: an unusual extra nodal site. Cancer. 1995;75:2258–61.
17. Brouland JP, Meeus F, Rossert J, et al. Primary bilateral B-cell renal lymphoma. Am J Kidney Dis. 1994;24:586–9.
18. Saito S. Primary renal lymphoma: case report and review of the literature. Urol Int. 1996;56:192–5.
19. Spits H, Lanier LL, Phillips JH. Development of human T and natural killer cells. Blood. 1995;85:2654–70.
20. Kwong YL. Natural killer-cell malignancies: diagnosis and treatment. Leukemia. 2005;19:2186–94.
21. Oshimi K. Progress in understanding and managing natural killer cell malignancies. Br J Haematol. 2007;139:532–44.

22. Cheung MM, Chan JK, Lau WH, Foo W, Chan PT, et al. Primary non-Hodgkin' s lymphoma of the nose and nasopharynx: clinical features, tumor immunophenotype, and treatment outcome in 113 patients. J Clin Oncol. 1998;16:70–7.
23. Valenzuela AA, Allen C, Grimes D, Wong D, Sullivan TJ. Positron emission tomography in the detection and staging of ocular adnexal lymphoproliferative disease. Ophthalmology. 2006;113(12):2331–7.
24. Roe RH, Finger PT, Kurli M, Tena LB, Lacob CE. Whole-body positron emission tomography/computed tomography imaging and staging of orbital lymphoma. Ophthalmology. 2006;113(10):1854–8.
25. Sullivan TJ, Valenzuela AA. Imaging features of ocular adnexal lymphoproliferative disease. Eye. 2006;20(10):1189–95.
26. Tomás JF. The challenge of recurrent follicular lymphoma. Lancet Oncol. 2011;12(8):714–6.
27. Kempton CL, Kurtin PJ, Inwards DJ, Wollan P, Bostwick DG. Malignant lymphoma of the bladder: evidence from 36 cases that low-grade lymphoma of the MALT-type is the most common primary bladder lymphoma. Am J Surg Pathol. 1997;21:1324–33.

10 Musculoskeletal Neoplasms

Aarti Kaushik and Linh T. Ho

Case 10.1: Primary Osseous Lymphoma

History

Patient is a 27-year-old woman with left proximal tibial lesion. Recent MRI showed aggressive mass like marrow replacement throughout the proximal right tibia with cortical thinning and disruption. PET-CT is requested as part of initial staging.

Findings

There is an intensely active left proximal tibial lesion extending approximately 11 cm from the tibial plateau inferiorly with mixed lytic sclerotic changes on CT, predominantly sclerotic, and maximum SUV up to 27.5 (Fig. 10.1). Other smaller hypermetabolic satellite foci are seen within the left proximal tibia. This lesion was subsequently biopsied and consistent with diffuse large B-cell lymphoma. The patient had received chemotherapy followed by radiation treatment.

Impression

- Local disease in the left proximal tibia
- No other active in the remaining body

Pearls and Pitfalls

- FDG PET-CT can detect other disease sites and shows the most active area which is useful for biopsy planning.
- Primary osseous lymphoma can mimic other bone tumors.

P.S. Conti, A. Kaushik (eds.), *PET-CT*, DOI 10.1007/978-1-4419-5811-2_10

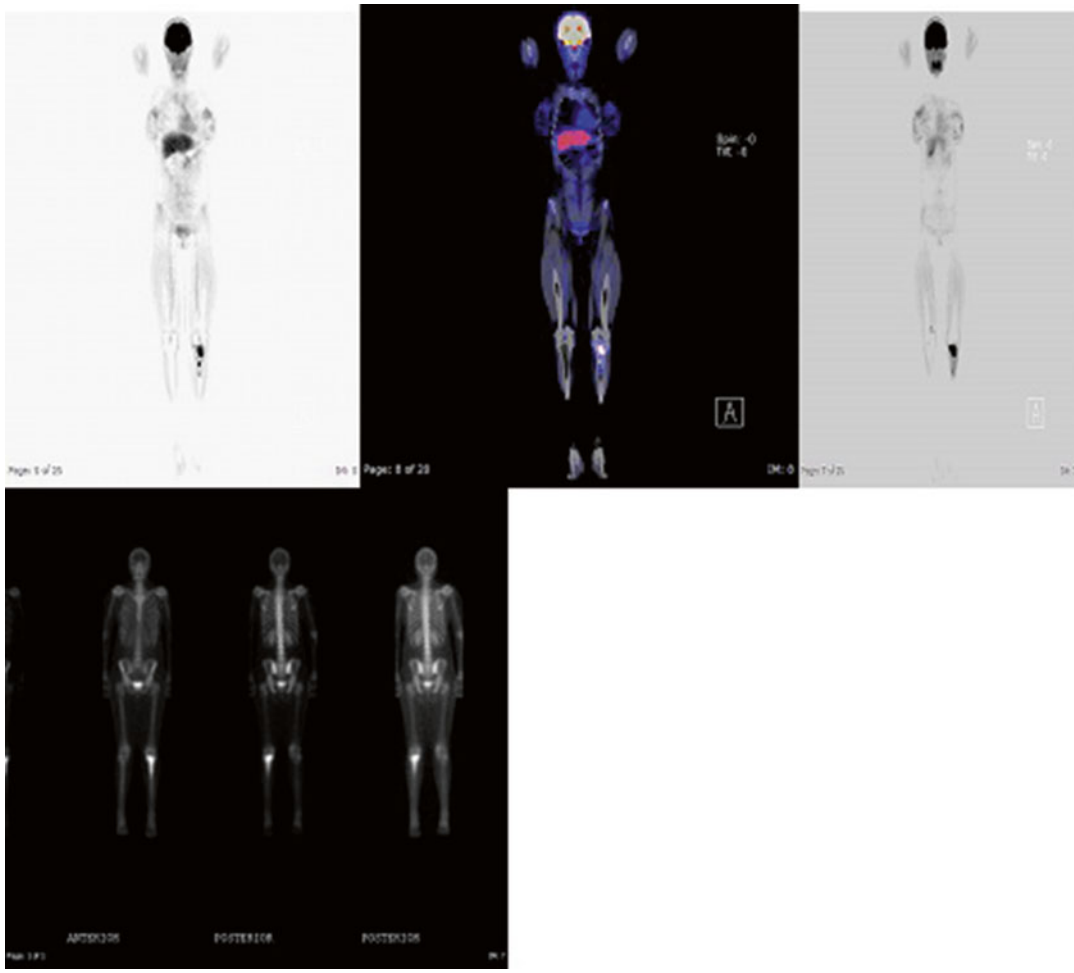

Fig. 10.1

Discussion

Primary lymphoma of the bone is a rare malignant condition that accounts for less than 5 % of all primary bone tumors. The vast majority of cases are of the non-Hodgkin type, with Hodgkin disease accounting for 6 % of cases. It is rare for patients younger than 10 years and occurs slightly more often in males. The femur is the most common site (especially in the metadiaphysis) and is affected in 25 % of cases. Other sites include the pelvis, humerus, head and neck, and tibia. Distinguishing primary bone lymphoma from other bone tumors is important because the former has a better response to therapy and a better prognosis (Fig. 10.1).

Case 10.2: Extra-Adrenal Paraganglioma

History

Patient is a 38-year-old female with newly diagnosed paraganglioma of the lower lumbar spine and upper sacrum.

Findings

There is an intensely active 4.5 × 7.8 × 5.6 cm soft tissue mass (maximum SUV of 8.9) centered in the lower lumbar and upper sacral spinal canal from the level of L4 through S2–3 (Fig. 10.2). This mass demonstrates osseous involvement of the L5, S1, and S2 vertebral bodies and posterior elements, consistent with the documented paraganglioma.

Impressions

- Hypermetabolic soft tissue mass centered in the lower lumbar and upper sacral spinal canal, consistent with the known paraganglioma
- No definite evidence of distant metastasis

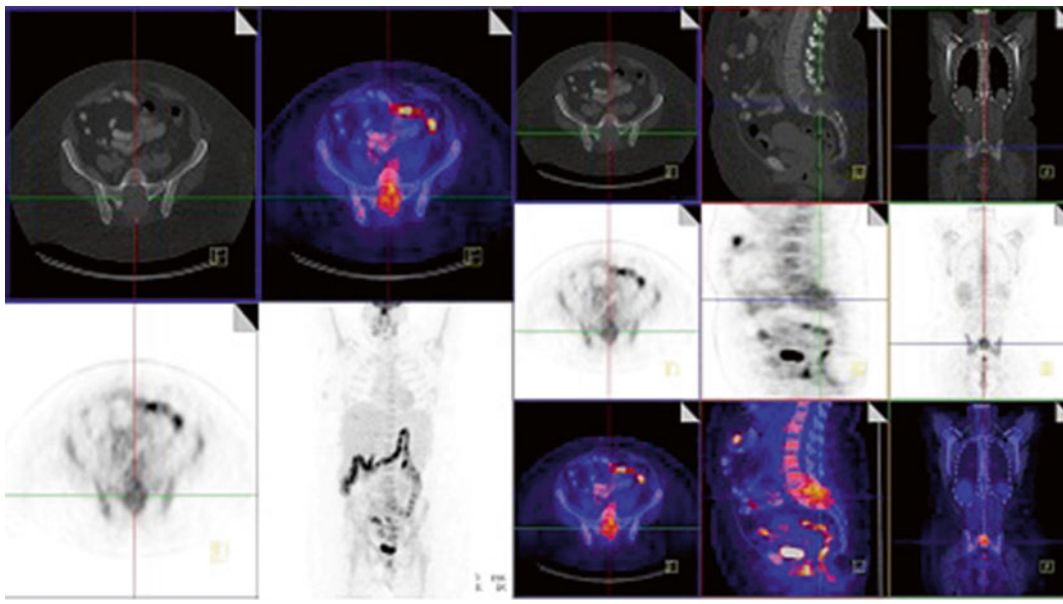

Fig. 10.2

Pearls and Pitfalls

- FDG PET positivity is almost a constant feature of pheochromocytomas and paragangliomas.
- Whole-body PET-CT study is helpful in detecting distant metastases.

Discussion

Pheochromocytomas and extra-adrenal paragangliomas are rare tumors of neuroectodermal origin. They belong to the heterogeneous family of neuroendocrine tumors. Pheochromocytomas and paragangliomas show consistent 18F-FDG avidity, with maximum SUV ranging from 1.9 to 42 in nonmetastatic tumors and 2.3–29.3 in metastatic tumors. FDG PET is superior to 131I-metaiodobenzylguanidine in the majority of metastatic patients (Fig. 10.2).

Case 10.3: Low-Grade Fibromyxoid Sarcoma

History

Patient is a 77-year-old man presented with left thigh mass. He is being seen for staging.

Findings

There is a moderately active $5.7 \times 10.5 \times 15$ cm left distal thigh mass with maximum SUV of 4.6, consistent with neoplasm (Fig. 10.3). The mass has mixed areas of increased and decreased metabolic activity. The patient subsequently had biopsy which was consistent with low-grade fibromyxoid sarcoma.

Impression

- Heterogeneous hypermetabolic soft tissue mass in the left distal thigh, consistent with neoplasm
- No definite evidence of distant metastasis

Pearls and Pitfalls

- Whole-body PET-CT study is helpful in detecting distant metastases.

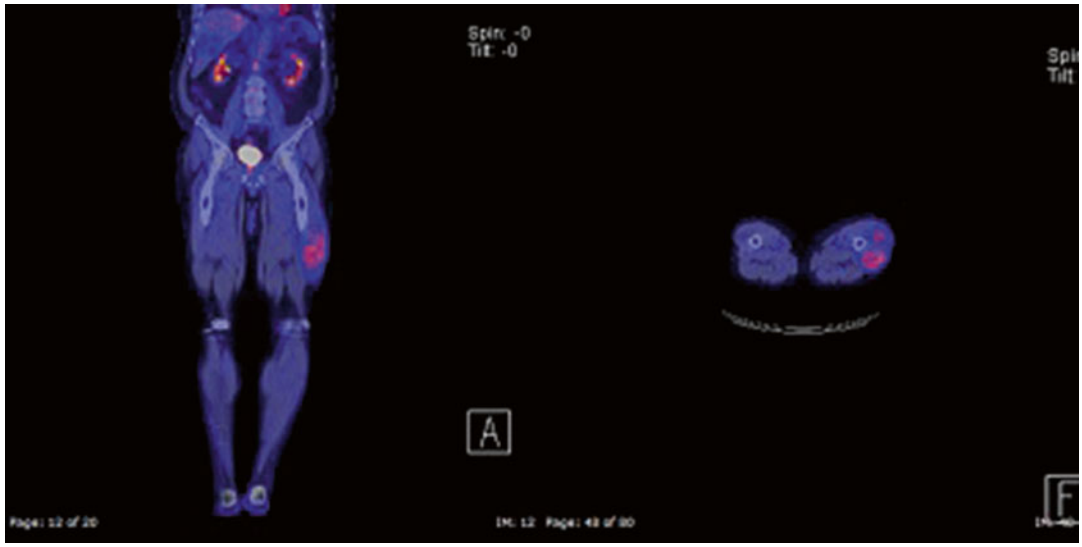

Fig. 10.3

- PET-CT is useful in biopsy planning to show the most metabolically active area of the tumor.
- More accurate staging with FDG PET can help guide and ensure the most appropriate therapy.

Discussion

Low-grade fibromyxoid sarcoma is a rare soft tissue neoplasm with a bland histologic appearance that nevertheless can follow an aggressive course with multiple local recurrences and eventual metastasis to the lung and sometimes bone (Fig. 10.3).

Case 10.4: Elastofibroma Dorsi

History

Patient is a 73-year-old female with history of bilateral breast carcinoma, status post bilateral mastectomies. She is being seen for restaging.

Findings

Moderately active soft tissue densities are seen in bilateral subscapular regions, with maximum SUV of 3.7 on the right and 3.1 on the left (Fig. 10.4).

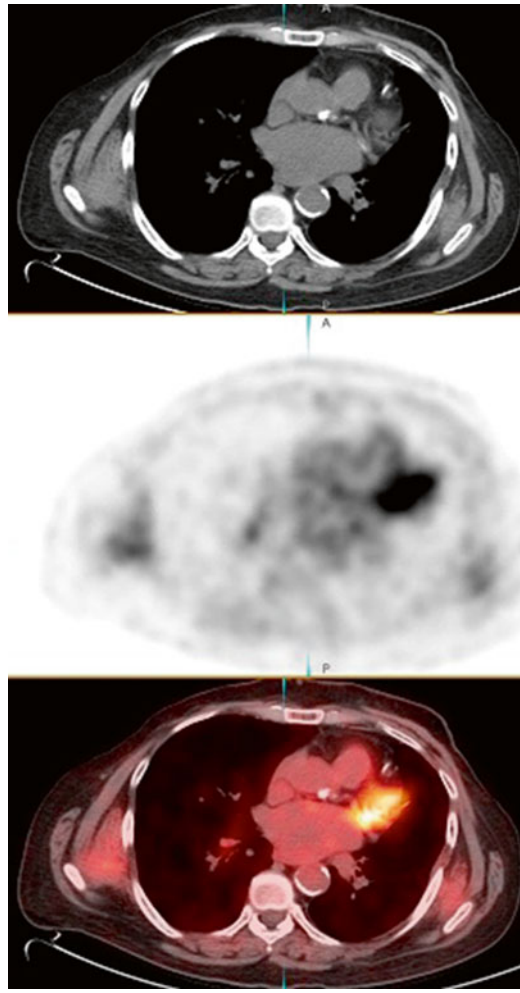

Fig. 10.4

These masses are located just deep relative to the serratus anterior muscles, displacing the muscle laterally. The soft tissue masses are oblong in shape, being longest in the superior-inferior plane. The attenuation of the lesions is similar to that of muscle, consistent with elastofibroma dorsi (EFD).

Impressions

- Bilateral EFD
- No definite evidence of recurrent or metastatic disease

Pearls and Pitfalls

- The diagnosis of EFD is made on the basis of the typical subscapular location of the lesions and the characteristic CT appearance (poorly circumscribed soft tissue with attenuation similar to that of muscle).
- EFD also shows hypermetabolism on FDG PET.

Discussion

Elastofibromas are benign, slowly growing lesions characteristically located in the subscapular region. Elastofibromas are pseudotumorous lesions characterized by fibroblastic proliferation and accumulation of abnormal elastic fibers. They are relatively common lesions; the prevalence revealed on CT was found to be 2 %, and an autopsy series reported an 11–24 % prevalence. A lack of awareness of the CT characteristics of EFD could have resulted in erroneous interpretation of the PET portion of the studies. The FDG hypermetabolism may have been attributed to an inflammatory or neoplastic process (Fig. 10.4).

Case 10.5: Fibrous Dysplasia

History

Patient is a 38-year-old female with history of breast cancer. She is being seen for restaging.

Findings

Expansile cortex with ground-glass appearance of the right posterior seventh rib, with associated moderate activity (maximum SUV of 3.4), consistent with fibrous dysplasia (FD) (Fig. 10.5).

Impression

- Fibrous dysplasia in the right posterior seventh rib
- No definite evidence of recurrent or metastatic disease

Pearls and Pitfalls

- Expansile cortex with ground-glass appearance.
- Fibrous dysplasia shows hypermetabolism on FDG PET.

Discussion

FD is a relatively common, benign skeletal disorder, typically encountered in adolescents and young adults. Rather than a true neoplasm, FD is a developmental anomaly in which the normal medullary space of the affected bone is replaced by fibroosseous tissue. The process may affect

a single bone (monostotic FD) or many bones (polyostotic FD). CT appearance of fibrous dysplasia will vary in direct proportion to the extent of mineralization within the lesion (Fig. 10.5).

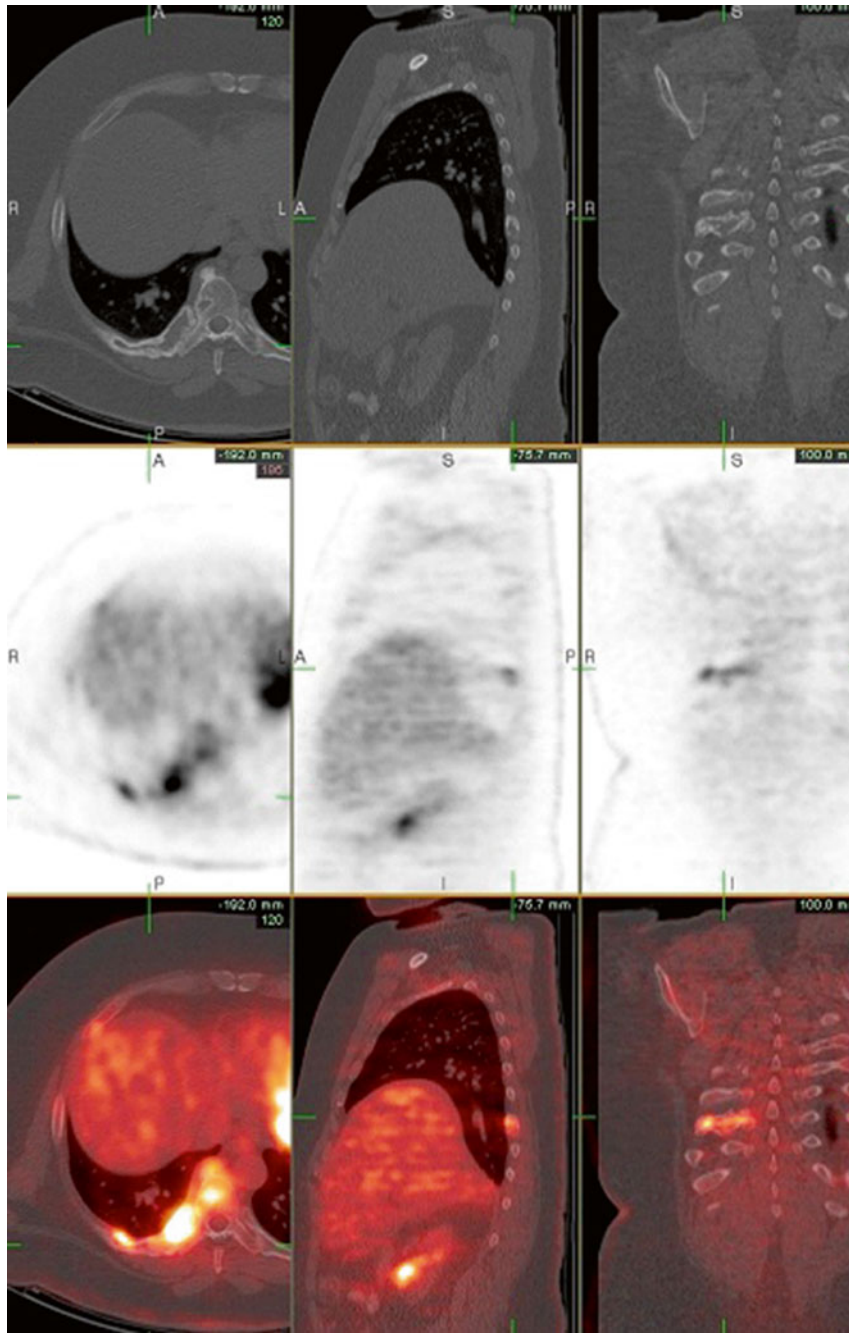

Fig. 10.5

Case 10.6: Squamous Cell Carcinoma of the Lower Extremity

History

Patient is a 40-year-old man with history of recurrent metastatic squamous cell carcinoma involving his left lower extremity. The patient initially had wide excision in June 2010 followed by adjuvant chemoradiation treatment. He subsequently had local recurrence in the pretibial region with metastasis to the left foot. MRI study of the lower extremity showed extensive disease in the left foot including the talus and calcaneus with extension into the adjacent proximal tibia with other smaller lesions noted in the bones of the left foot consistent with metastatic disease. PET-CT is requested for restaging.

Findings

Multiple disease sites are seen below the left knee including the soft tissue masses in the anterior tibial region, destructive lesion in the distal third of the fibula, distal left tibial mass with cortical destruction and extraosseous component, and large destructive heterogeneously hypermetabolic mass involving the hindfoot and posterior midfoot on the left with extension to base of third, fourth, and fifth metatarsal proximally as well as the distal fourth metatarsal, with maximum SUV of 8.2 in the large destructive mass (Fig. 10.6).

In addition, there is metastatic disease involving a left inguinal lymph node and bilateral lungs.

Impressions

- Multiple sites of tumor in the left lower leg below the knee as well as focus of increased activity in the left lateral tibial plateau, probably a site of additional metastasis
- Left inguinal and bilateral pulmonary metastatic disease

Pearls and Pitfalls

- Whole-body FDG PET scan can detect skip metastasis such as left inguinal and bilateral pulmonary metastasis.

Discussion

The association of preexisting scars and sinuses in the extremities with the later development of squamous cell carcinoma is well established. This rare form of carcinoma carries a poor prognosis, with a recurrent rate of 50 %. The most significant prognostic factor predicting recurrence is the histologic grading of the tumor. Amputation is recommended in all grade II or III disease and wide local excision only in very small lesions that can be radically excised or in grade I lesions, with prophylactic nodal irradiation in all grades II and III carcinoma (Fig. 10.6).

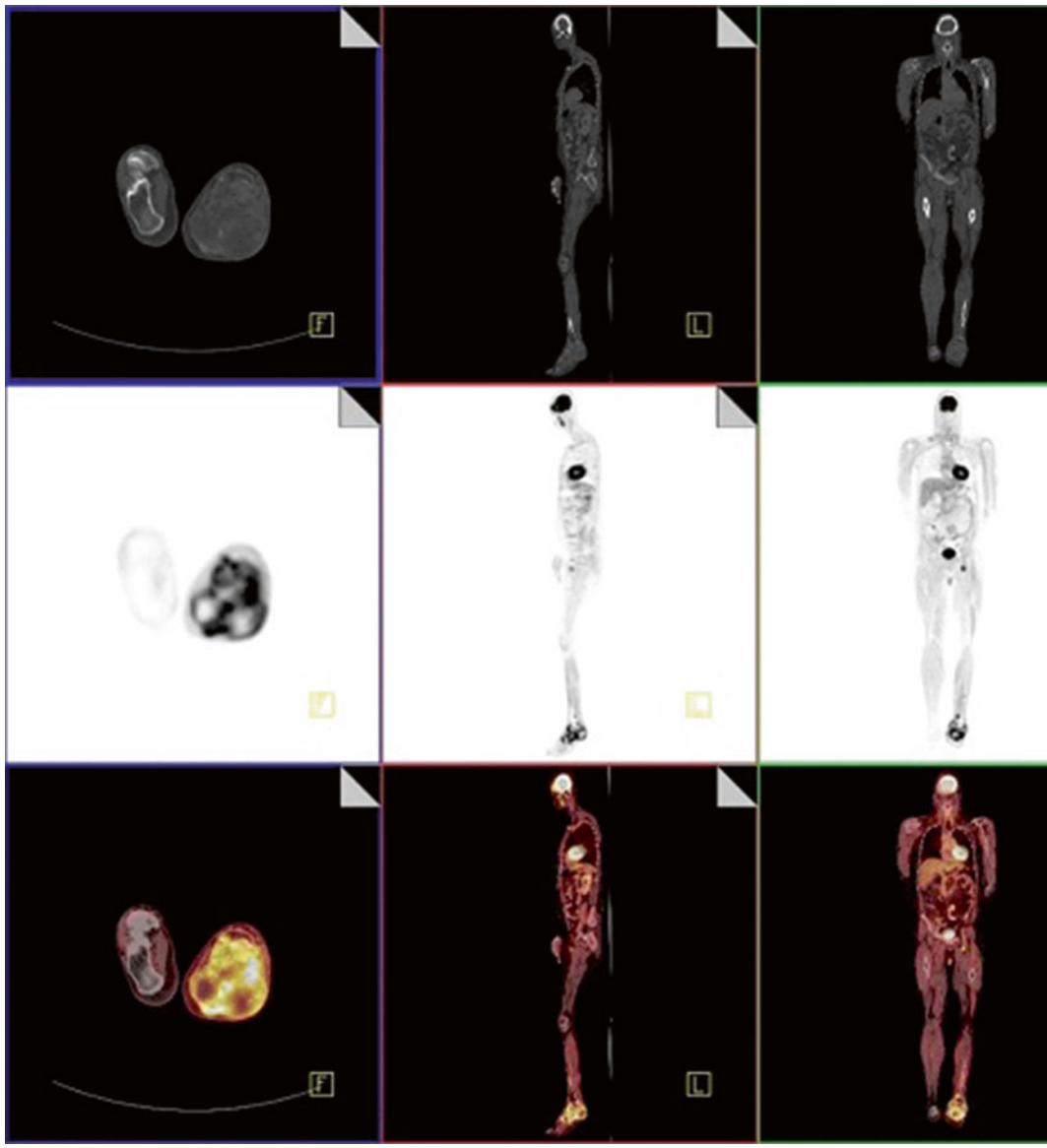

Fig. 10.6

Case 10.7: Low-Grade Chondrosarcoma of the Pelvis

History

Patient is a 73-year-old man with history of low-grade chondrosarcoma of the right pelvis, status post radiation therapy. The current PET-CT is requested for restaging.

Findings

There is a large, heterogeneous pelvic mass with matrix calcifications causing permeative destructive changes within the right iliac bone and acetabulum, demonstrating mild FDG activity at the periphery (Fig. 10.7). This mass measures 20.0 × 16.0 cm and shows heterogeneous activity more significant in the periphery (with maximum SUV up to 4.0).

Impression

Recurrent disease in the right pelvis with permeative destructive changes within the right ilium and acetabulum.

Pearls and Pitfalls

- Whole-body FDG PET is helpful in detecting local recurrences and metastatic disease.
- Low-grade sarcomas are generally less FDG avid than a high-grade sarcoma.

Discussion

Chondrosarcoma, a malignant tumor characterized by the production of a cartilage matrix, accounts for about 11 % of cases of primary malignant bone tumors. The average age at presentation is 46 years (range, 5–82 years). The pelvis is the most common location. Local pain is the most frequently reported initial symptom. The overall 5-year survival rate is 77 %. The recurrent rate is higher for tumors of the shoulder and pelvis than for tumors of long bones. Radiographically, chondrosarcomas have a characteristic appearance, including a combination of bone expansion and cortical thickening. Histologic tumor grade is an important predictor of local recurrence and metastasis (Fig. 10.7).

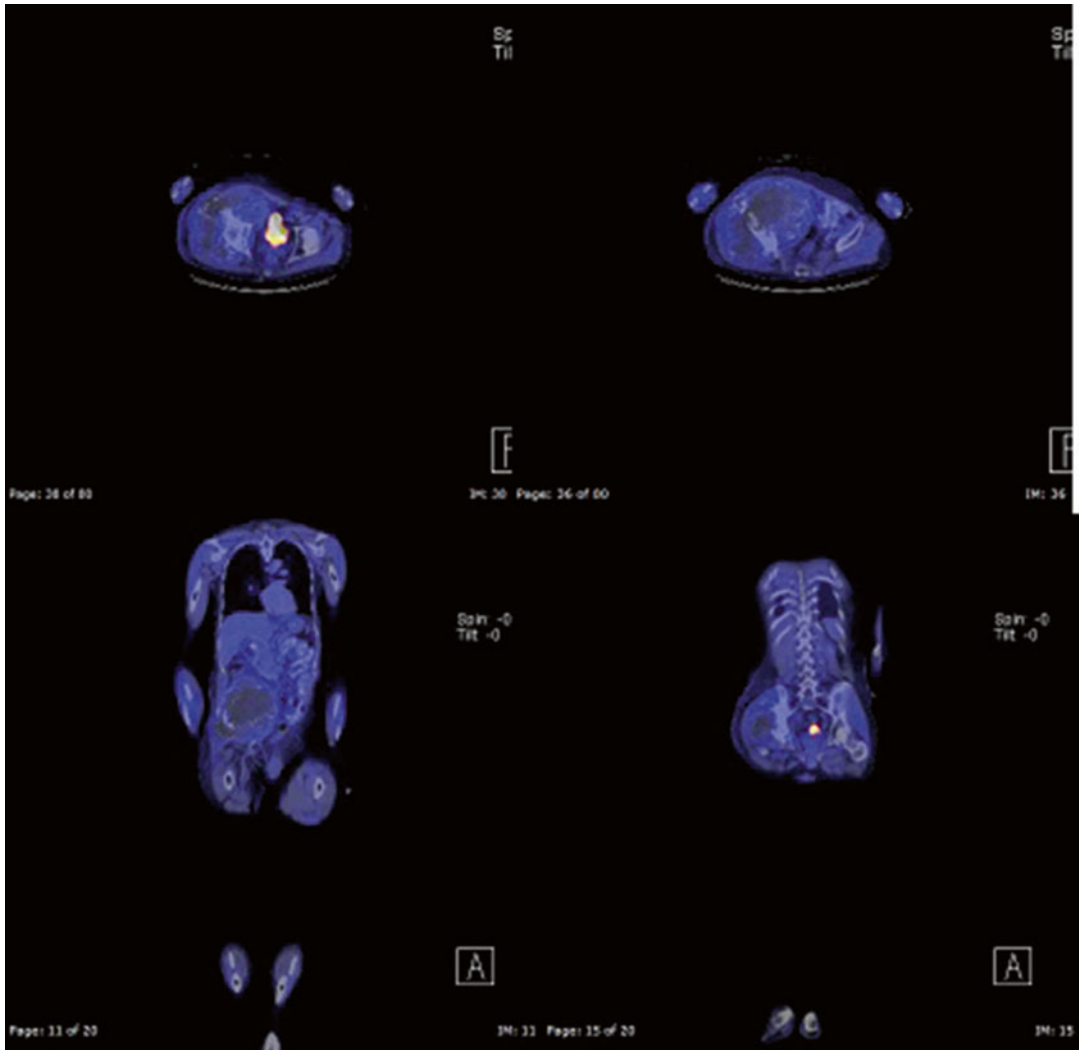

Fig. 10.7

Case 10.8: Multiple Myeloma

History

Patient is a 66-year-old man with history of multiple myeloma, currently on chemotherapy. PET-CT is requested for restaging.

Findings

Multiple hypermetabolic lytic lesions are seen involving the axial and appendicular skeleton, consistent with the documented myeloma (Fig. 10.8). The reference lesions are located in the left posterior parietal bone (maximum SUV of 17.5) and left proximal humerus (maximum SUV of 24.3).

Impression

Multiple hypermetabolic lytic osseous lesions involving the axial and appendicular skeleton, consistent with the known myeloma.

Pearls and Pitfalls

- FDG PET/CT is able to detect bone marrow involvement in patients with multiple myeloma and useful in assessing extent and burden of disease at time of initial diagnosis and for evaluating therapy response.

Discussion

Multiple myeloma (MM) is a malignant hematologic disorder characterized by bone marrow infiltration with neoplastic plasma cells. MM accounts for 10 % of all hematologic cancers. Approximately 5–10 % of patients have a solitary plasmacytoma, and two thirds of these patients progress to multiple myeloma. Patients with stage I MM, with only limited alteration of blood parameters and not more than one skeletal lesion, are followed clinically without therapy. Patients with stage II or III MM require chemotherapy (Fig. 10.8).

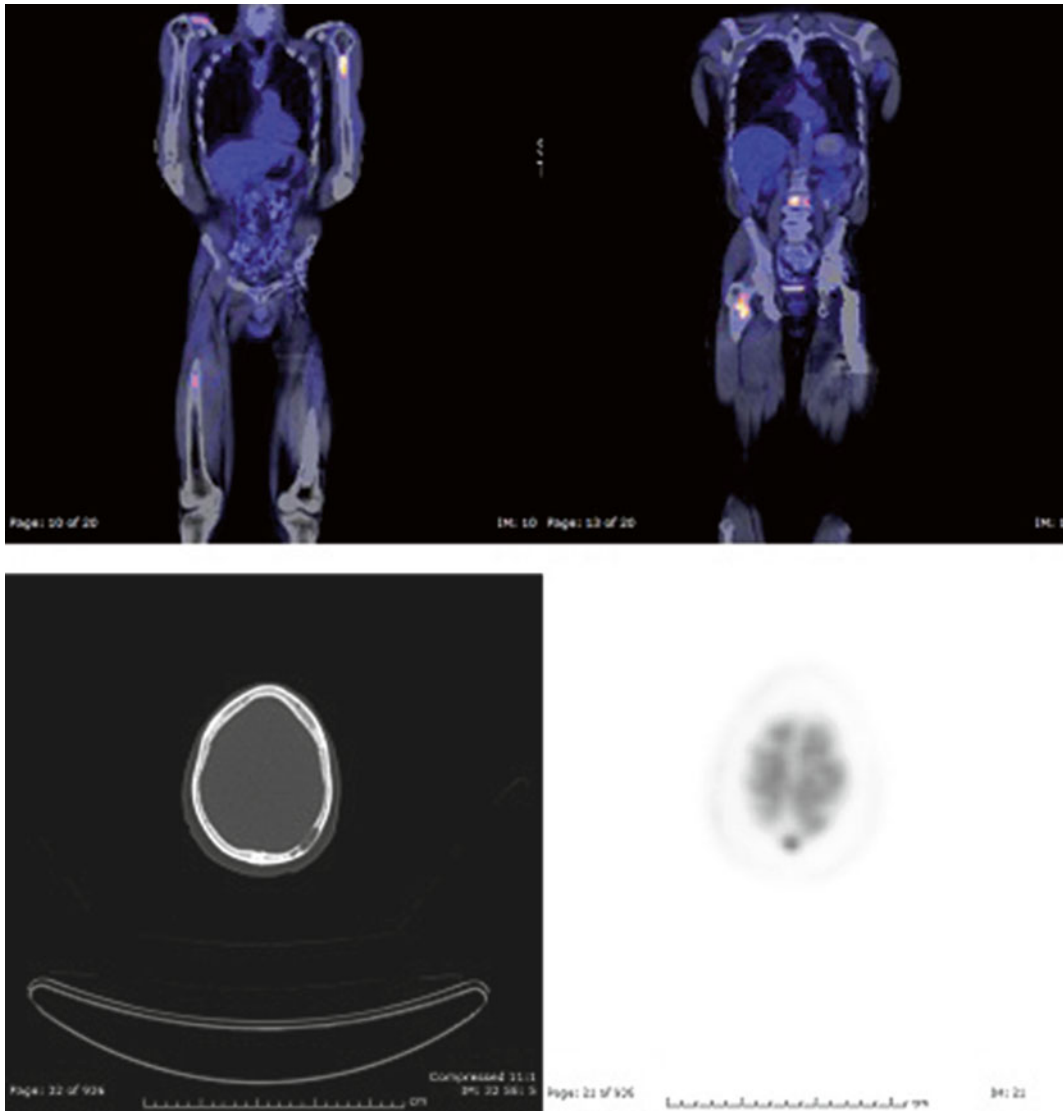

Fig. 10.8

Case 10.9: Low-Grade Soft Tissue Sarcoma

History

Patient is a 77-year-old man presented with left thigh mass with MRI reporting mass consistent with soft tissue sarcoma (biopsy dated February 7, 2011, stating low-grade fibromyxoid sarcoma).

Findings

Moderately hypermetabolic 5.7 × 10.5 × 15 cm left distal thigh soft tissue mass, with maximum SUV of 4.6, consistent with tumor (Fig. 10.9). The mass shows heterogeneous attenuation and metabolic activity. The mass was subsequently biopsied and consistent with low-grade fibromyxoid sarcoma.

Impression

- Hypermetabolic left distal thigh soft tissue mass, consistent with primary tumor
- No definite evidence of distant metastasis

Pearls and Pitfalls

- FDG PET could be useful in rare soft tissue sarcomas to demonstrate possible metastasis and direct biopsy.

Discussion

Low-grade fibromyxoid sarcoma is a rare type of low-grade sarcoma. It is characterized by a long and indolent clinical course and the possibility of local recurrence or distant metastases in a subset of patients. Unlike many other types of cancer, low-grade fibromyxoid sarcoma can metastasize after many years, sometimes decades after the initial presentation of the tumor, to the lung and sometimes bone (Fig. 10.9).

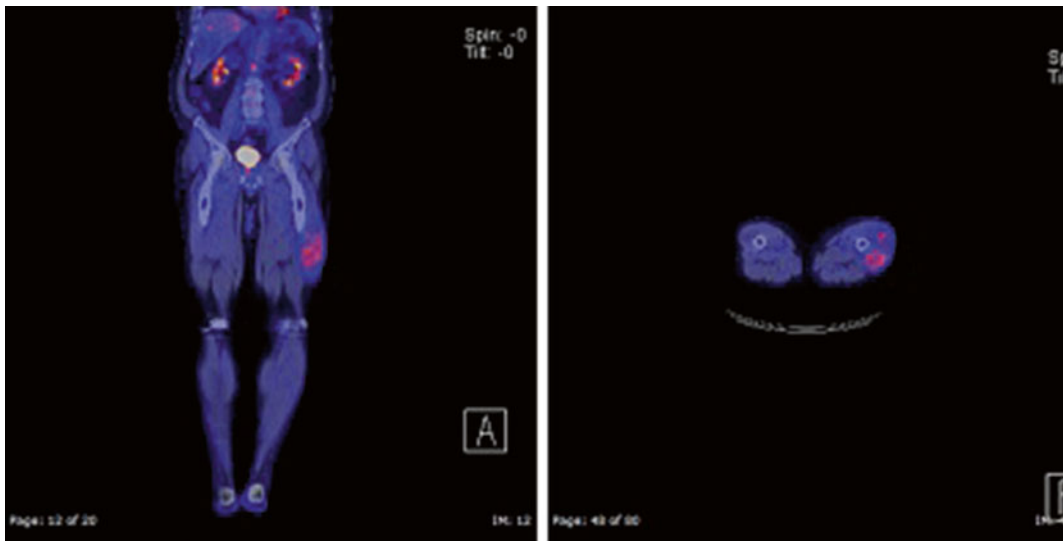

Fig. 10.9

Case 10.10: Myxofibrosarcoma

History

Patient is a 68-year-old female presented with right medial thigh mass. PET/CT is requested for further evaluation.

Findings

A 16.7 × 22.1 × 17.5 cm (in transverse, craniocaudal, and anteroposterior dimensions, respectively) well-defined, compartmentalized, heterogeneous right medial thigh soft tissue mass (Fig. 10.10). This finding demonstrates diffuse heterogeneous activity, with the most active areas located in the superolateral aspect (with SUV max up to 11.4). There are scattered areas of hypoattenuating photopenia within the mass consistent with necrosis. No definite evidence of underlying bony erosion or involvement is noted.

The patient subsequently had right thigh mass biopsy which was consistent with myxofibrosarcoma (MFS), for which she had received chemoradiation treatment.

Impression

1. Large, heterogeneous active right thigh soft tissue mass, consistent with neoplasm
2. No definite evidence of distant metastasis

Pearls and Pitfalls

- FDG PET-CT is useful in detecting distant metastasis and also for biopsy planning.
- MFS shows heterogeneous FDG uptake.

Discussion

Myxofibrosarcoma (MFS), also known as a myxoid subtype of malignant fibrous histiocytomas, is one of the most common sarcomas in the extremities of old patients and is characterized by a high frequency of local recurrence. For high-grade lesions, they tend to form solid parts with a continuous transition to a storiform-pleomorphic-type MFH. No to heterogeneous FDG uptake within MFS was previously reported which probably correlates to the tumor histologic grade (Fig. 10.10).

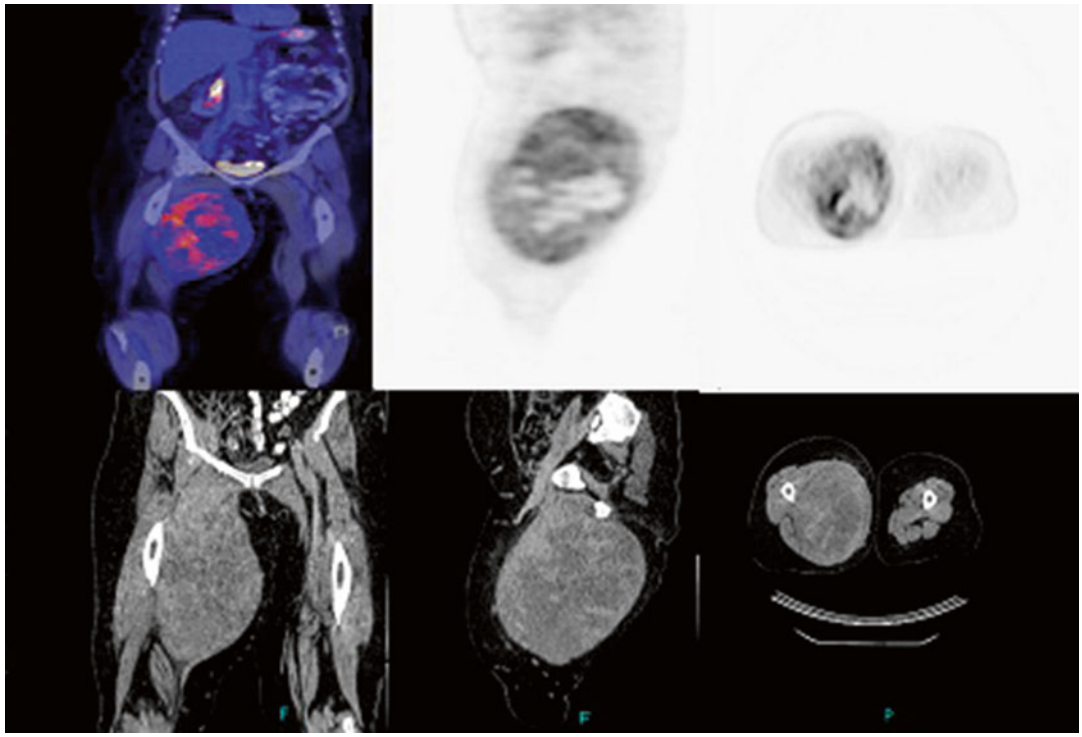

Fig. 10.10

Case 10.11: Osteosarcoma

History

Patient is a 12-year-old female with newly diagnosed left femoral osteosarcoma. PET-CT is performed as part of initial staging.

Findings

There is an intensely active lesion in the left distal femur (maximum SUV of 10.3), corresponding to medullary sclerosis with small area of cortical disruption and associated periosteal reaction medially on CT images (Fig. 10.11). No other abnormal activity is seen in the remaining body.

Impression

1. Intensely active medullary sclerotic lesion with small area of cortical disruption and associated periosteal reaction in the left distal femur, consistent with the documented osteosarcoma.
2. No definite evidence of distant metastasis.

Pearls and Pitfalls

- FDG PET helps to determine the presence and extent of sarcomas and may allow the noninvasive estimation of the histologic grade of these tumors.
- The measured SUV of a sarcoma has been used to predict patient outcome both before and after neoadjuvant therapy. This in turn allows targeted biopsies, which can reduce the likelihood of underestimation of tumor grade and inadequate therapy.
- PET may help to detect intraosseous skip lesions, which may be difficult to differentiate from physiologic hematopoietic marrow at MR imaging.

Discussion

Osteosarcoma, or sometimes referred to as osteogenic sarcoma, is the second most common primary malignant bone tumor, exceeded in frequency only by multiple myeloma. It is the most common primary malignant bone tumor to affect children and adolescents. The intraosseous tumor usually arises in the metaphyses of the long bones, distal femur (44 %), proximal tibia (22 %), and proximal humerus (9 %). It can extend into the diaphysis, epiphysis, or both. The overall prognosis for patients with osteosarcoma depends on the stage of the tumor at presentation. Without metastases, long-term survival is in the order of 60–85 % (Fig. 10.11).

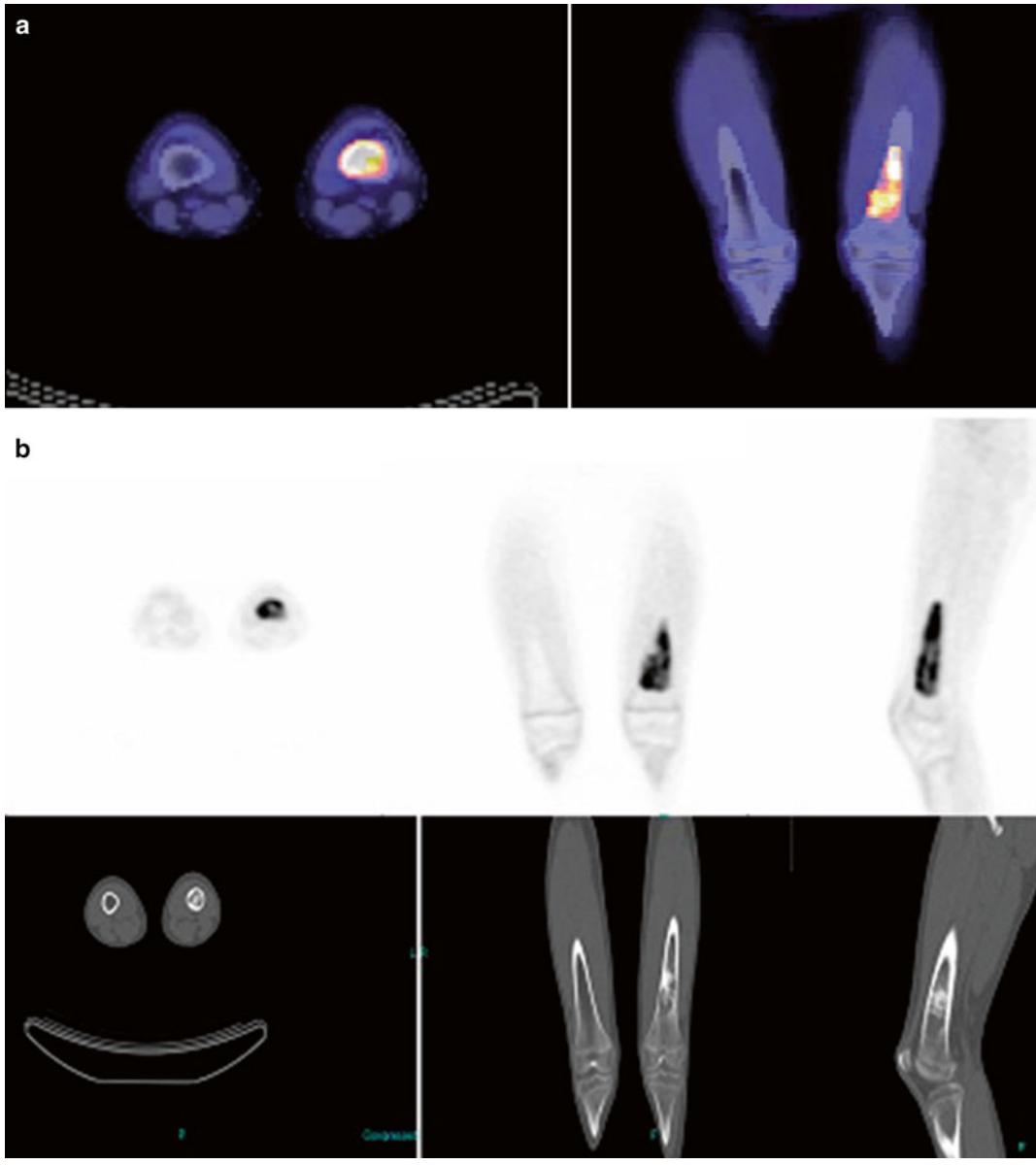

Fig. 10.11

Suggested Reading

Brandser EA, Goree JC, El-Khoury GY. Elastofibroma dorsi: prevalence in an elderly population as revealed by CT. AJR. 1998;171:977–80.

Bredella MA, Steinbach L, Caputo G, Segall G, Hawkins R. Value of FDG PET in the assessment of patients with multiple myeloma. AJR. 2005;184:1190–204.

Eary JF, Conrad EU, Bruckner JD, et al. Quantitative [F-18] fluorodeoxyglucose positron emission tomography in pretreatment and grading sarcoma. Clin Cancer Res. 1998;4(5):1215–20.

Enomoto K, Inohara H, Hamada K, et al. FDG PET imaging of myxofibrosarcoma on the sphenoid sinus. Clin Nucl Med. 2008;33:421–2.
Kimiteru I, Masuda-Miyata Y, Wada S, et al. F-18 FDG PET/CT imaging of bulky myxofibrosarcoma in chest wall. Clin Nucl Med. 2011;36:212–3.
Krishnan A, Shirkhoda A, Tehranzadeh J, et al. Primary bone lymphoma: radiographic-MR imaging correlation. Radiographics. 2003;29:1371–8.
Lifeso RM, Bull CA. Squamous cell carcinoma of the extremities. Cancer. 1985;55:2862–7.
Nishimura G, Sano D, Hanashi M, et al. Myxofibrosarcoma of the hypopharynx. Auris Nasus Larynx. 2006;33:93–6.
Pierce JC, Henderson R. Hypermetabolism of elastofibroma dorsi on PET-CT. AJR. 2004;183:35–7.
Taieb D, Sebag F, Barlier A, et al. 18F-FDG avidity of pheochromocytomas and paragangliomas: a new molecular imaging signature? J Nucl Med. 2009;50:711–7.
Williams HT, Gossage JR, Allred TJ, et al. F-18 FDG positron emission tomography imaging of rare soft tissue sarcomas: low-grade fibromyxoid sarcoma and malignant hemangiopericytoma. Clin Nucl Med. 2004;29:581–4.

11 F-18 Fluoride Bone Scintigraphy

Bhushan Desai and Peter S. Conti

Prostate Cancer

Case 11.1

An 81-year-old male with metastatic adenocarcinoma of prostate, status postradiation therapy, presenting with widespread osseous metastatic disease involving predominantly T4–T7 vertebral bodies along with posterior ribs from T4–T6, likely representing epidural disease with perineural spread (Fig. 11.1). There are also small lesions involving the right lamina T10, proximal right 9th and 10th ribs, L-4 vertebral bodies, and bilateral posterior ilium.

Case 11.2

A 75-year-old male diagnosed with metastatic adenocarcinoma of prostate, presenting with multiple foci of hypermetabolic and sclerotic osseous lesions involving L1, L3, right posterior L4, T12, and left T9 vertebral bodies (Fig. 11.2). Also noted is activity with faint sclerosis in the right anterior iliac bone and posterior left acetabulum.

Case 11.3

A 73-year-old male with history of prostatic adenocarcinoma, presenting with multiple hypermetabolic, predominantly sclerotic osseous lesions i nvolving the left temporal bone, right occipital bone, L1 vertebra, spinous process of L2, left iliac bone, and right iliac bone (Fig. 11.3).

P.S. Conti, A. Kaushik (eds.), *PET-CT*, DOI 10.1007/978-1-4419-5811-2_11

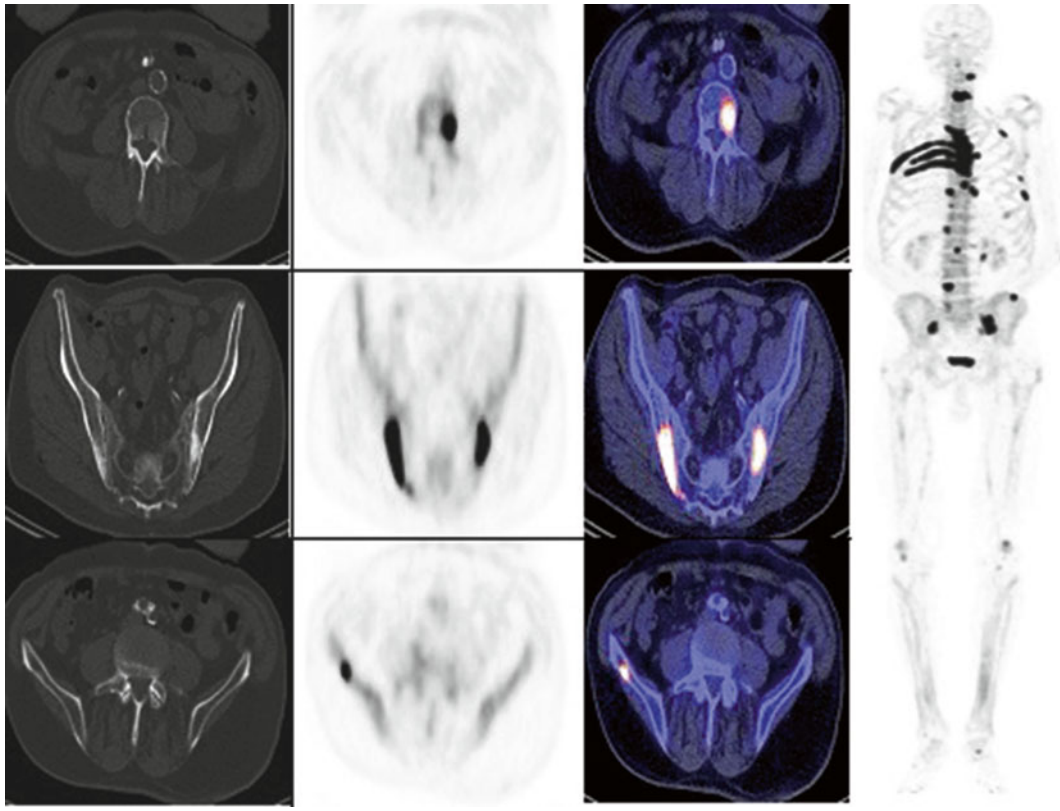

Fig. 11.1

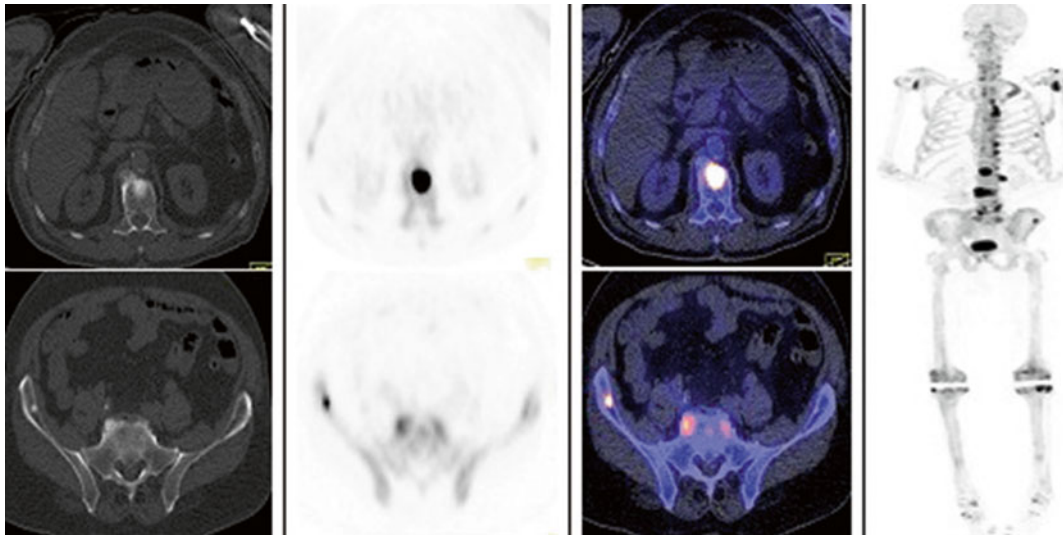

Fig. 11.2

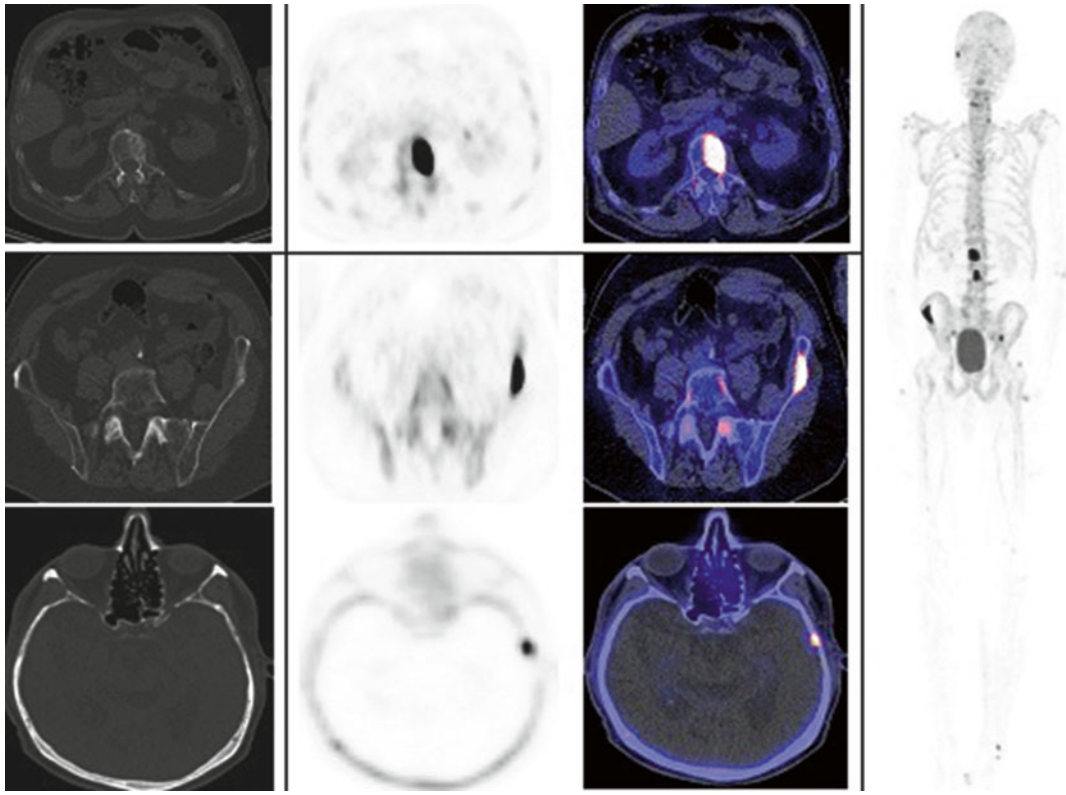

Fig. 11.3

Case 11.4 A 64-year-old male with biochemically recurrent prostate cancer, post radical prostatectomy, and EBRT, presenting with faintly sclerotic but intensely hypermetabolic right L2 metastatic lesion (Fig. 11.4). Tc99m MDP bone scintigraphy was negative. Other nonneoplastic findings include T11 osteophytic activity, Paget's-related increased right hemipelvis activity, and degenerative changes in the knees.

Breast Cancer

Case 11.5 A 54-year-old female with breast cancer presenting with hypermetabolic, predominantly sclerotic osseous lesions noted in T11, right C7 lamina, inferior L4 and sacral promontory, several ribs, left posterior pillar of acetabulum, and right posterior iliac disease (Fig. 11.5).

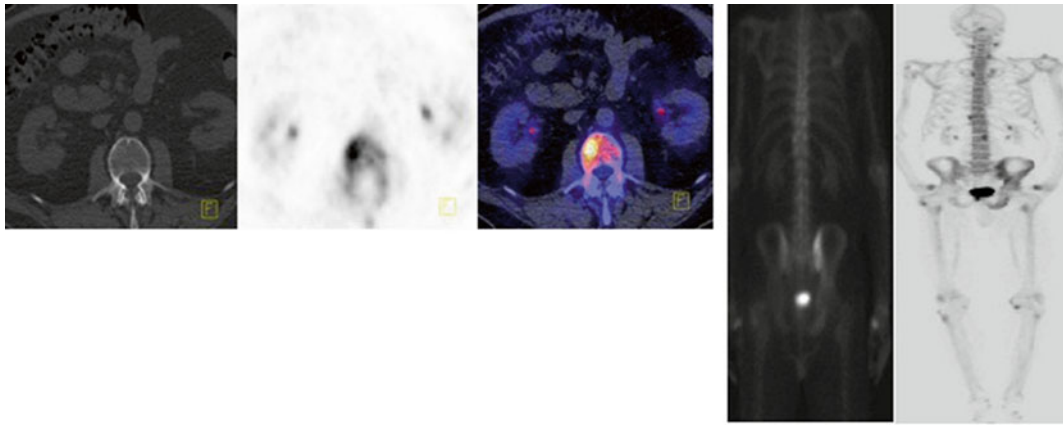

Fig. 11.4

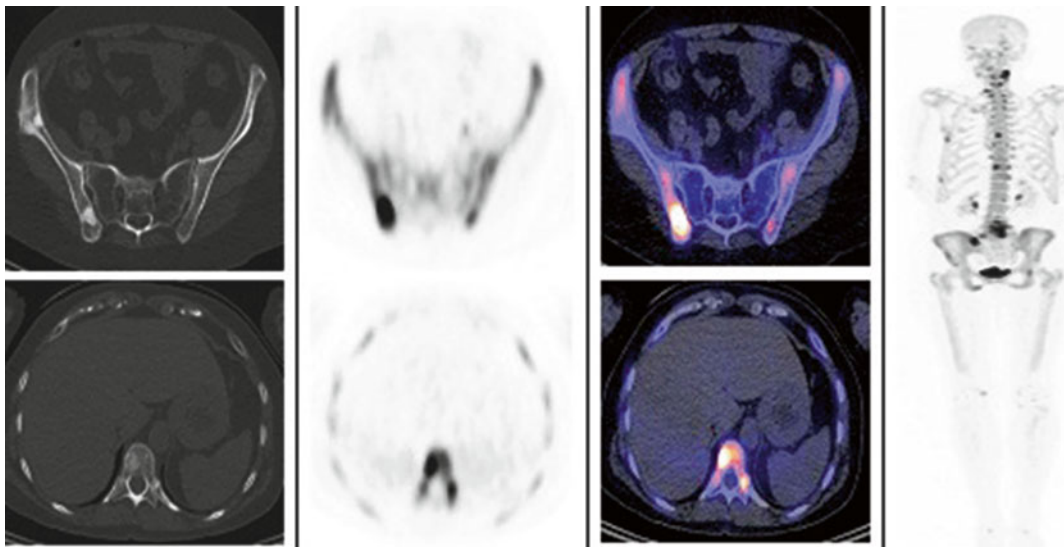

Fig. 11.5

Case 11.6

A 68-year-old female with history of metastatic right breast carcinoma, post right lumpectomy with axillary lymph node dissection, and right lung VATS procedure with talc pleurodesis, presenting with several hypermetabolic osseous lesions seen predominantly in the pelvis and spine (Fig. 11.6). The purely blastic lesions are less avid, and the mixed lytic and sclerotic lesions demonstrate more intense metabolic activity. Mixed lytic and sclerotic lesions are seen at the posterior aspect of the right iliac bone, sacrum, and T8 vertebral body.

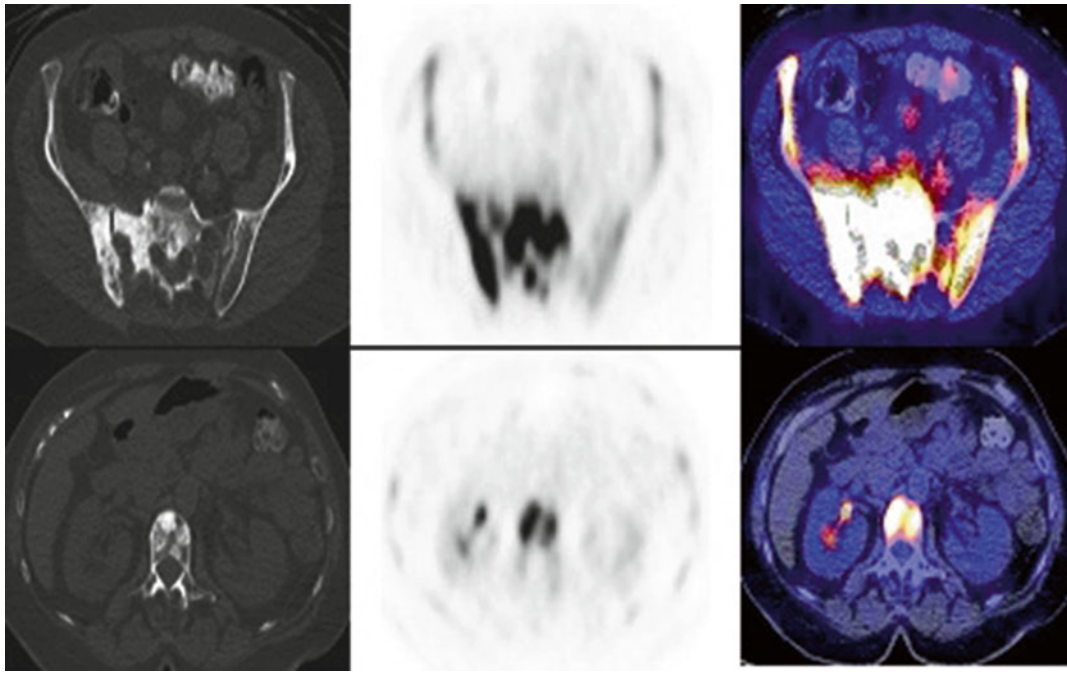

Fig. 11.6

Case 11.7 A 67-year-old female with history of metastatic breast cancer presenting with numerous osseous metastatic lesions involving the sternum, multiple ribs, L1 vertebral body, and left distal humerus (Fig. 11.7).

Lung Cancer

Case 11.8 A 25-year-old male with history of metastatic squamous cell carcinoma of the lung presenting with several hypermetabolic, predominantly lytic lesions involving multiple levels of the cervical, thoracic, and lumbar spine, manubrium and sternum, multiple ribs bilaterally, scapulae, bilateral iliac bones, sacrum, acetabulae, and ischial and pubic bones (Fig. 11.8). There is sparing of the osseous structures of the upper and lower extremities bilaterally.

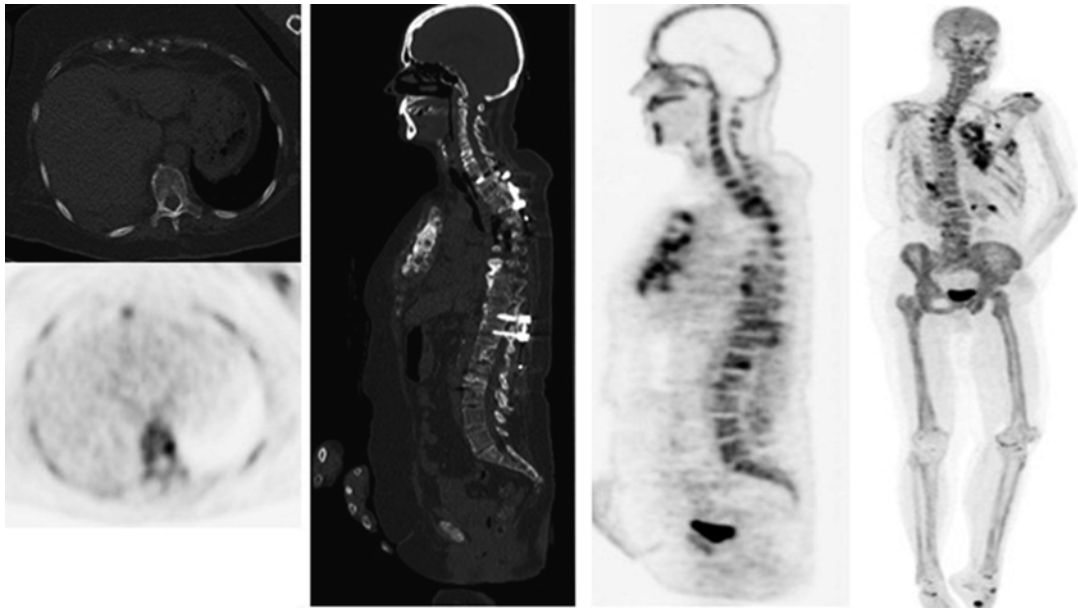

Fig. 11.7

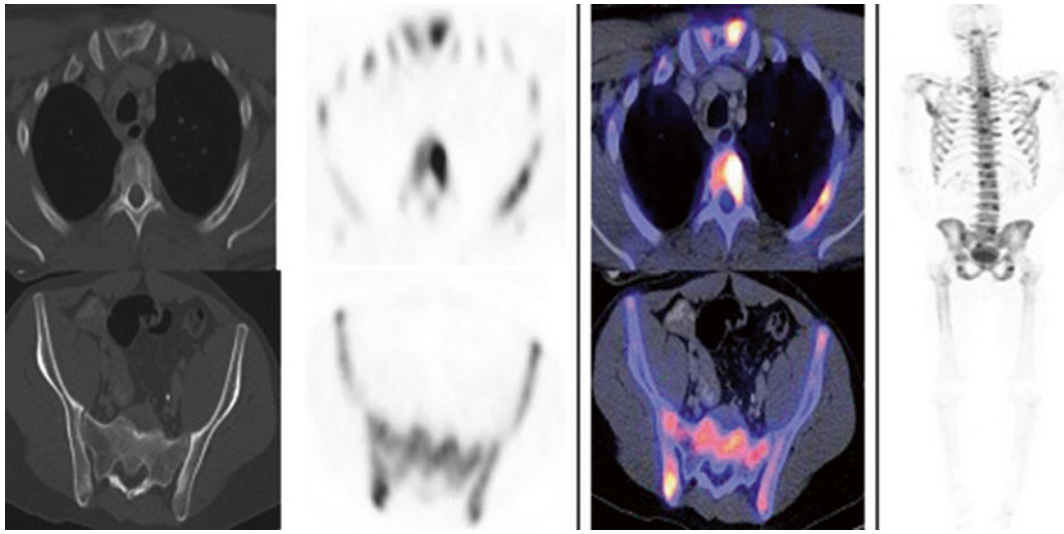

Fig. 11.8

Case 11.9

A 56-year-old male with history of metastatic adenocarcinoma of the lung, presenting with multiple sclerotic and hypermetabolic osseous lesions (Fig. 11.9). These include lesions in medial head of the left clavicle, lower sternum, and T3 vertebral body.

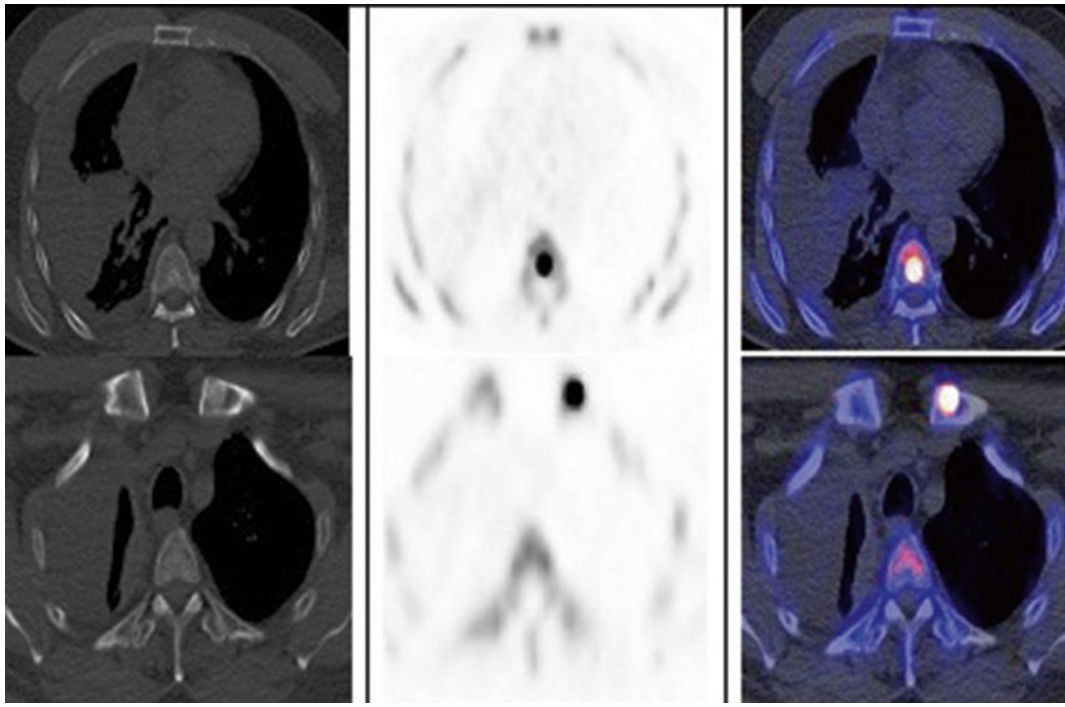

Fig. 11.9

Additional Benign Findings

Case 11.10 (1) Enthesopathic changes, (2) degenerative changes in glenohumeral joint, (3) osteophyte activity in lower thoracic spine, (4) knee arthroplasties, and (5) degenerative disc disease at L3–L4 (Fig. 11.10).

Pearls and Pitfalls

- NaF PET/CT is significantly more accurate than conventional Tc99m MDP bone scintigraphy, SPECT bone scan, and NaF PET only. Sensitivity, specificity, PPV, and NPV: planar BS (70 %, 57 %, 64 %, 55 %), SPECT BS (92 %, 82 %, 86 %, 90 %), NaF PET only (100 %, 62 %, 74 %, 100 %), and NaF PET/CT (100 %, 100 %, 100 %, 100 %) [5].
- 18F-NaF PET/CT superior to standard BS for detection of osteolytic lesions [9].
- NaF PET/CT imaging can be used for evaluation of stress relate injuries and child abuse [8].
- Very early bone reaction in small bone metastases can be seen with 18F-fluoride scintigraphy [2].
- Fluoride studies can reduce the number of invasive bone biopsies and facilitate subsequent follow-up in patients with metabolic bone disease.

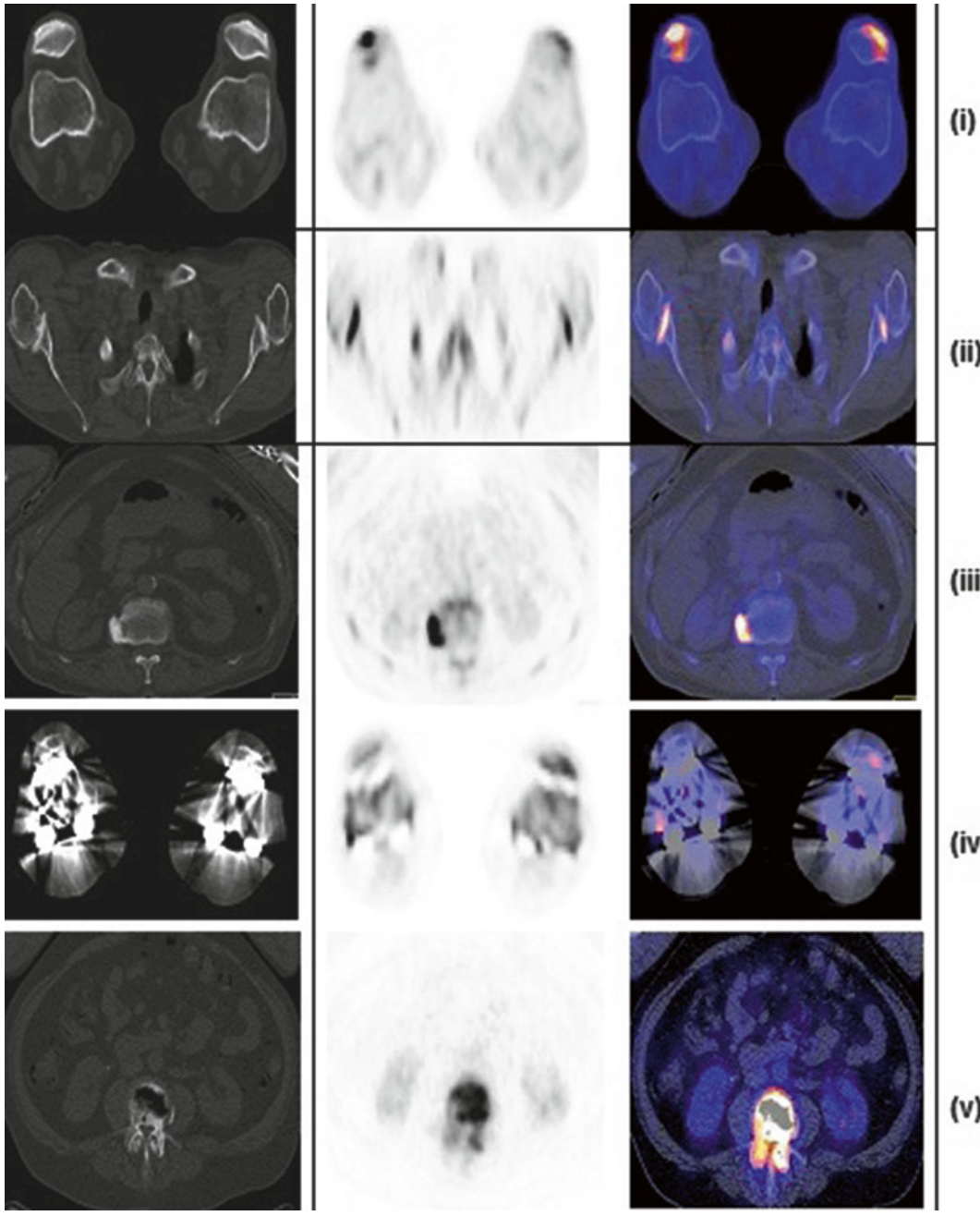

Fig. 11.10

Discussion

At least 99 % of whole-body fluoride is thought to be present in the skeleton, primarily as fluorapatite. 18F-NaF was initially introduced in 1962 as an imaging agent for bone lesions. 18F-fluoride has favorable tracer kinetics as a radiopharmaceutical for bone imaging: it accumulates in bone rapidly to a high concentration and clears quickly from the circulation, allowing a high bone-to-background uptake ratio within a short time [11]. The interest in 18F-fluoride as a bone imaging agent was renewed in the 1990s owing to a wider availability and improved technology of PET scanners, which offer higher spatial resolution and sensitivity than conventional gamma cameras used in planar scintigraphy or single-photon emission computerized tomography (SPECT). In most cases where different imaging modalities were compared, 18F-NaF PET proved to be more sensitive and specific than other techniques. Diagnostic imaging has played a major role in the evaluation of patients with bone metastases, and this application is the focus of the majority of the recent published literature on use of 18F-fluoride PET. For the detection of bone metastases in cancer patients, doses typically ranged from 8 to 12 mCi [12]. In this dose range, excellent image quality with higher spatial resolution than convention BS is obtained. There is evidence that 18F-fluoride PET is more sensitive and selective than conventional BS for diagnosis and detection of bone metastases. The use of low-dose CT in conjunction with 18F-fluoride PET improves sensitivity and specificity and improves the ability to distinguish benign from malignant lesions. Because of these advantages, and advancements in cost-effectiveness, it has been suggested that 18F-fluoride PET will replace conventional bone scan for the detection of bone metastases within several years. In summary, evidence from published studies in cancer patients indicates that 18F-fluoride PET is superior to 99mTc-MDP planar scintigraphy or SPECT in detecting primary bone cancer and skeleton metastases from a wide range of cancers, including cancer of the breast, lung, and prostate [1, 3, 4, 6, 10, 13, 14]. The very high resolution and target-to-background contrast of 18F-fluoride PET can potentially reduce its specificity; however, correlating PET with CT findings substantially helps differentiate malignant from benign lesions. 18F-fluoride PET is also effective in other applications involving altered osteogenic activity, such as detecting skeletal injury, diagnosing causes of back pain, diagnosing osteoporosis, and monitoring effectiveness of bone regeneration therapy, and in cases of child abuse [7].

References

1. Schirrmeister H, et al. Early detection and accurate description of extent of metastatic bone disease in breast cancer with fluoride ion and positron emission tomography. J Clin Oncol. 1999;17:2381–9.
2. Cook GJ, et al. The role of positron emission tomography in the management of bone metastases. Cancer. 2000;88:2927–33.

3. Blake GM, et al. Quantitative studies of bone with the use of 18F-fluoride and 99mTc-methylene diphosphonate. Semin Nucl Med. 2001;31:28–49.
4. Hetzel M, et al. F-18 NaF PET for detection of bone metastases in lung cancer: accuracy, cost-effectiveness, and impact on patient management. J Bone Miner Res. 2003;18:2206–14.
5. Even-Sapir E, et al. Assessment of malignant skeletal disease: initial experience with 18F-fluoride PET/CT and comparison between 18F-fluoride PET and 18F-fluoride PET/CT. J Nucl Med. 2004;45:272–8.
6. Even-Sapir E, et al. The detection of bone metastases in patients with high-risk prostate cancer: 99mTc MDP planar bone scintigraphy, single and multi-filed-of-view SPECT, 18F-fluoride PET and 18F-fluoride PET/CT. J Nucl Med. 2006;47:287–97.
7. Sterner T, et al. The role of [18F] fluoride positron emission tomography in the early detection of aseptic loosening of total knee arthroplasty. Int J Surg. 2007;5:99–104.
8. Beheshti M, et al. Detection of bone metastases in patients with prostate cancer by 18F fluorocholine and 18F fluoride PET-CT: a comparative study. Eur J Nucl Med Mol Imag. 2008;35:1766–74.
9. Grant F, et al. Skeletal PET with 18F-Fluoride: applying new technology to an old tracer. J Nucl Med. 2008;49:68–78.
10. Kruger S, et al. Detection of bone metastases in patients with lung cancer: ^{99m}Tc-MDP planar bone scintigraphy, ^{18}F-fluoride PET or ^{18}F-FDG PET/CT. Eur J Nucl Med Mol Imaging. 2009;36:1807–12.
11. Czernin J. Molecular mechanisms of bone 18F-NaF deposition. J Nucl Med. 2010;51:1826–9.
12. Segall G, et al. SNM practice guideline for sodium 18F-fluoride PET/CT. J Nucl Med. 2010;51:1813–20.
13. Withofs N, et al. 18F-fluoride PET/CT for assessing bone involvement in prostate and breast cancers. Nucl Med Commun. 2010;32:168–76.
14. Iagaru A, et al. Prospective evaluation of Tc99m MDP scintigraphy, 18F NaF PET/CT and 18F FDG PET/CT for detection of skeletal metastases. Mol Imaging Biol. 2011;14:252–9.

12 Neuroradiology: Neoplasms and Epilepsy

Saman Hazany, John Go, Robert W. Henderson, Paul Kim, and Meng Law

Case 12.1: Langerhans Cell Histiocytosis

History

29-year-old female with palpable neck mass.

Findings

Axial post-contrast CT (Fig. 12.1a), FDG-PET (Fig. 12.1b), and PET-CT fusion (Fig. 12.1c) demonstrate hypermetabolic, peripherally enhancing mass inseparable from the posterior parotid gland.

Impression

Biopsy-proven Langerhans cell histiocytosis (LCH).

Pearls and Pitfalls

Differential diagnosis for parotid masses is broad including benign and malignant etiologies. The finding in this case represents involvement of an intra-parotid lymph node. The most common site of involvement by LCH is the bone (90 %) followed by the skin (30 %). FDG-PET is sensitive in detection of multifocal disease and shown to be superior to technetium 99 m methylene diphosphonate bone scans or radiograph in detection of active osseous lesions and response to therapy. There are limited number of studies evaluating utility of FDG-PET in soft tissue involvement by LCH.

P.S. Conti, A. Kaushik (eds.), *PET-CT*, DOI 10.1007/978-1-4419-5811-2_12

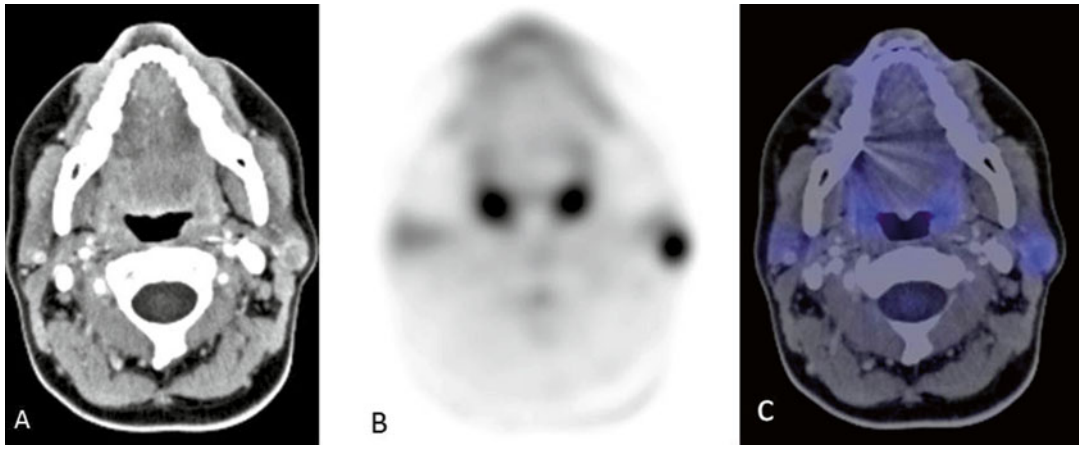

Fig. 12.1

Discussion

LCH is a rare idiopathic "neoplastic" process secondary to monoclonal proliferation of Langerhans-type cells. It is more common in the pediatric population, with a peak incidence between 1 and 3 years of age. There is also a male predilection (M:F 1.2–2.1:1). The course of the disease ranges from spontaneous regression to rapid progression (especially common in young children with multisystem disease). LCH can involve multiple organ systems, single-organ system with multiple sites, or single site. Diagnosis is confirmed histologically by tissue sampling.

The prognosis is variable and depends on disease burden, with single-organ system disease carrying better prognosis than multisystem disease. In 2008 the WHO recommended distinguishing LCH from a more pleomorphic variant know as Langerhans cell sarcoma, which carries a worse prognosis. Treatment ranges from excision or limited radiation for single-focus disease to systemic chemotherapy and steroid administration for multifocal disease and supportive care in cases of endocrine and CNS involvement (Fig. 12.1).

Case 12.2: Crossed Cerebellar Diaschisis

History

43-year-old female with remote history of biopsy-proven oligoastrocytoma within the right cerebral hemisphere status post radiation.

Findings

CT: Areas of calcification with associated volume loss and no appreciable mass effect centered in the right thalamus and internal capsule compatible with known previously treated oligoastrocytoma (Fig. 12.2).

FDG-PET: Relative decreased FDG uptake in the right cerebral hemisphere as compared to left compatible with post radiation change. Relative decreased FDG uptake in the left cerebellar hemisphere as compared to right compatible with crossed cerebellar diaschisis (Fig. 12.2).

MRI: Subtle asymmetric left cerebellar volume loss with no decreased diffusion or signal abnormality (Fig. 12.2).

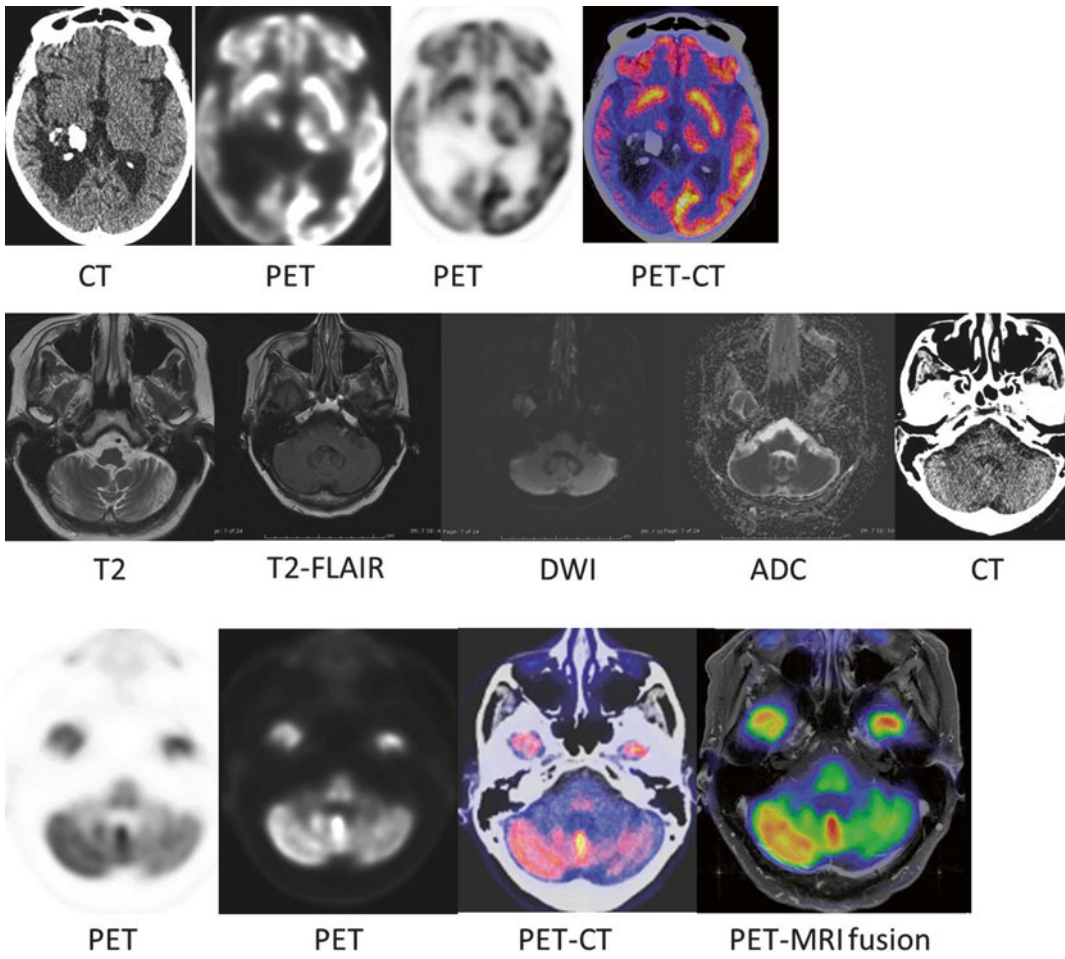

Fig. 12.2

Impression

Crossed cerebellar diaschisis.

Pearls and Pitfalls

Crossed cerebellar diaschisis refers to hypometabolism in a cerebellar hemisphere contralateral to a cerebral hemispheric lesion. Lesions located in the motor cortex, anterior corona radiata, and thalamus (as in this case) produce the most marked suppression of the contralateral cerebellar cortical metabolism. Findings of hypometabolism are seen on FDG-PET. Decreased blood flow to the contralateral cerebellum has also been shown on MR perfusion imaging in setting of MCA territory stroke. In setting of chronic hypometabolism, cerebellar atrophy ensues.

Discussion

Crossed cerebellar diaschisis (CCD) has been reported in patients with ischemic and hemorrhagic hemispheric stroke, during carotid amytal procedure, migraine attack, seizure, space occupying lesion, and focal volume loss of a cerebral hemisphere. CCD is thought to be due to interruption of corticopontocerebellar fibers and subsequent transneuronal metabolic and blood flow alterations that are distant to and on the opposite side of the primary lesion. Border-zone cerebellar infarcts have also been reported in setting of CCD especially in migraines with prolonged aura. In setting of cerebral infarct, CCD is associated with poor clinical outcome (Fig. 12.2).

Case 12.3: Tumor Recurrence/Progression

History

43-year-old female with remote history of treated oligoastrocytoma WHO grade III, within the right cerebral hemisphere status post radiation and chemotherapy about 14 years ago with increased area of enhancement on surveillance MRI (prior MRI is not shown here). Clinical concern for tumor recurrence/progression versus radiation necrosis.

Findings

PET-CT: Focal mass-like area on CT shows abnormal avid FDG uptake which is increased in extent and avidity as compared to prior studies (not shown) (Fig. 12.3).

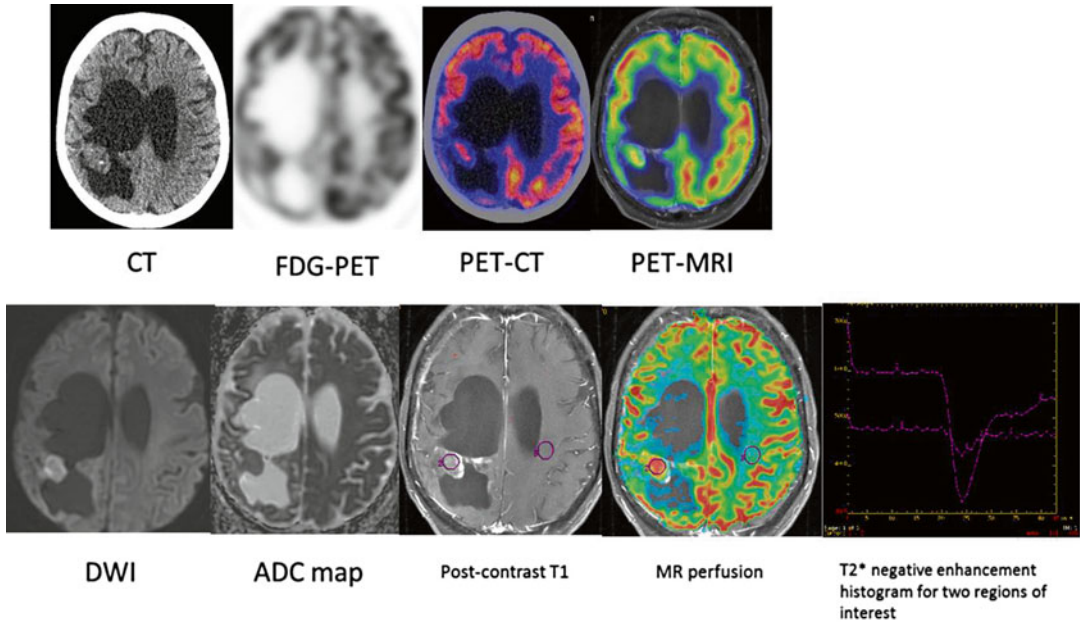

Fig. 12.3

MRI: Approximately 2 cm area of new mild enhancement (prior study not shown) and increased cerebral blood volume (CBV) on dynamic susceptibility contrast-enhanced cerebral blood volume (DSCE-CBV) magnetic resonance imaging (i.e., MR perfusion) with associated decreased diffusion.

PET-MRI: Overlap of abnormality on PET and MRI confirming hypermetabolism and increased CBV (Fig. 12.3).

Impression

Tumor recurrence/progression.

Pearls and Pitfalls

In setting of treated glioma, differentiating radiation necrosis from tumor recurrence/progression on imaging is crucial but often difficult. Findings on conventional imaging are relatively nonspecific and often unable to distinguish the two entities. Utility of fluorodeoxyglucose positron emission tomographic (FDG-PET), which studies tumor metabolism, for differentiation of glioma recurrence/progression from radiation necrosis has been controversial with reported specificities as low as 18 %. However, considering recent advances in MR perfusion imaging, which studies tumor vascularity, combination of the two modalities maybe helpful. These imaging tools have also been for differentiation of high-grade from low-grade tumors and benign lesions.

Discussion

Primary central nervous system neoplasia is one of the most frequent causes of death between 15 and 35 years of age. Gliomas constitute >90 % of primary brain tumors diagnosed after the second decade of life. Despite treatment with chemotherapy and radiation, including proton-beam therapy (PBT) and other radiosurgery, the majority of these tumors progress and/or recur. Moreover, treatment with radiation remains associated with tissue necrosis that may also lead to clinical deterioration. Differentiating recurrent tumor (or progression of tumor) from predominant radiation necrosis has treatment and prognostic implications.

Oligoastrocytomas histologically represent mixed glial cell origin, astrocytoma, and oligodendroglioma with a peak incidence occurring in the third to fifth decade. The incidence among males is higher than females. Prognosis is similar to anaplastic astrocytoma and worsened with increased age of onset, with 5-year survival of greater than 50 % and a 10-year survival of 25–34 %. On histologic evaluation, predominance of oligodendrocytes over astrocytes confers a better prognosis. Treatment is controversial and includes surgical reduction, radiotherapy, and chemotherapy often with corticosteroids and seizure prophylaxis. In our case, surgery was not possible as the tumor was in an eloquent location (Fig. 12.3).

Case 12.4: Stage IVa (T2 N2a M0) Oropharyngeal/ Tonsillar HPV-Positive Squamous Cell Carcinoma

History

42-year-old male with no history of smoking or alcohol consumption presents with neck mass.

Findings

Axial post-contrast CT (A), PET (B), and PET-CT fusion (C) and coronal post-contrast CT demonstrate 2.5 cm FDG-avid mass involving the left palatine tonsil/oropharynx with associated FDG-avid 5.4 cm level 2–4 lymph node (Figs. 12.4 and 12.5). There is also nonspecific FDG uptake in the right palatine tonsil and both sublingual glands, none of which were involved by tumor.

Impression

Stage IVa (T2 N2a M0) oropharyngeal/tonsillar squamous cell carcinoma.

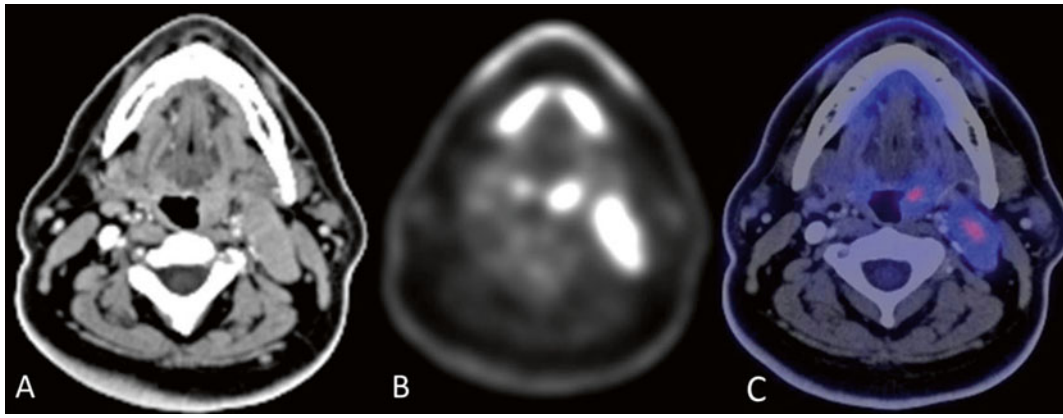

Fig. 12.4

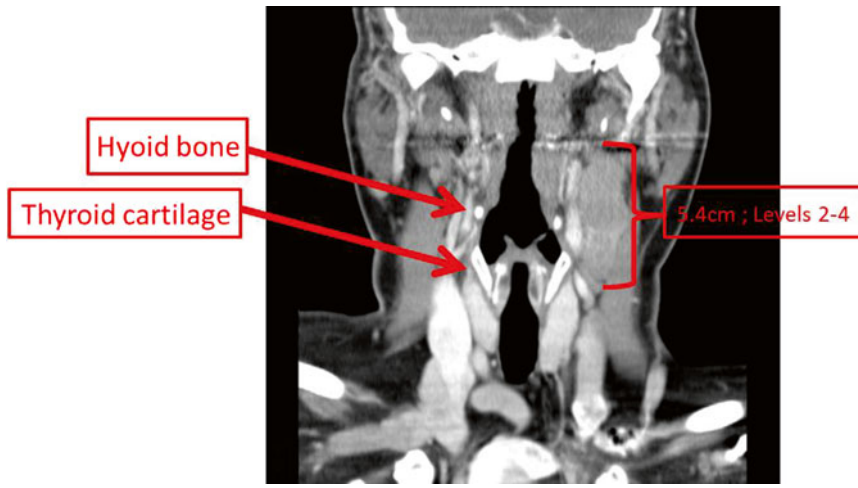

Fig. 12.5

Pearls and Pitfalls

Squamous cell carcinoma (SCC) accounts for the vast majority of malignancies of the oral cavity and oropharynx and is commonly evaluated with radiologic imaging. The symptoms of disease, the routes by which it may spread, and the prognosis vary greatly, depending in large part on the anatomic site at which the primary tumor originates and the stage of the tumor at time of presentation. FDG-PET-CT is used at most centers for detection of otherwise occult primary oropharyngeal SCC (OSCC), as well as determining the local extent and stage of the tumor (including lymph node and distant metastasis). In our case, the tumor was about

2.5 cm with a 5.4 cm ipsilateral lymph node and no distant metastasis, making it T2, N2a, M0, or stage IVA [1]. Tables 12.1 and 12.2 describe TNM staging of oropharyngeal SCC [1].

Discussion

A large body of recent research points out the increasing incidence of human papillomavirus (HPV) as a common cause of oropharyngeal squamous cell carcinoma (OSCC), which includes tonsillar and base of

Table 12.1 TNM staging of oropharyngeal squamous cell carcinoma

Cancer stage	T	N	M
0	Tis	N0	M0
I	T1	N0	M0
II	T2	N0	M0
III	T1, T2, T3	N1	M0
		N0, N1	M0
IVA	T1, T2, T3, T4a	N2	M0
		N0, N1, N2	M0
IVB	Any	N3	M0
	T4b	Any	M0
IVC	Any	Any	M1

Table 12.2 TNM staging of oropharyngeal squamous cell carcinoma

Primary tumor of oropharynx	
Tx	Primary tumor cannot be assessed
T0	No evidence of primary tumor is seen
T1	Primary tumor has a maximal diameter of less than 2 cm
T2	Primary tumor has a maximal diameter of 2–4 cm
T3	Primary tumor has a maximal diameter of more than 4 cm
T4a	Primary tumor involves the larynx, intrinsic or extrinsic muscles of the tongue, medial pterygoid, hard palate, mandible
T4b	Primary tumor involves the lateral pterygoid muscle, pterygoid plates, lateral nasopharynx, skull base, carotid artery
Regional metastasis	
Nx	Regional lymph nodes cannot be assessed
N0	No regional lymph node metastasis is evident
N1	Ipsilateral single enlarged node with a maximal diameter of less than 3 cm
N2a	Ipsilateral single enlarged node with a maximal diameter of 3–6 cm
N2b	Ipsilateral multiple enlarged nodes with a maximal diameter of less than 6 cm
N2c	Bilateral or contralateral enlarged nodes with a maximal diameter of less than 6 cm
N3	Enlarged node with a maximal diameter if more than 6 cm
Distant metastasis	
M0	No distant metastasis is evident
M1	Distant metastasis is evident

tongue cancer. Approximately 25 % of all head and neck cancers and 60 % of all oropharyngeal cancers are HPV positive. This data has made HPV an independent risk factor for OSCC, in addition to smoking and alcohol consumption. Patients with HPV-positive cancer have their first sexual experience at a young age and have multiple partners, suggesting that increased incidence of OSCC in the United States and some countries in northern Europe is because of a new, primarily sexually transmitted HPV epidemic. Oral and vaginal sex and open-mouth kissing have been associated with increased incidence of HPV-associated OSCC. There are >100 HPV types, some found in skin warts and others in mucous tissues. HPV-16 accounts for 90–95 % of HPV-positive OSCC. HPV-associated OSCC has a better prognosis than other types of OSCC, and the knowledge of this association can alter treatment planning. There are no accurate radiologic features to confidently distinguish this entity, but cystic adenopathy (not seen in our case) has been associated with HPV-positive OSCC (Figs. 12.4 and 12.5).

Case 12.5: Adenoid Cystic Carcinoma Recurrence

History

42-year-old female with history of adenoid cystic carcinoma involving the right maxillary sinus status post resection and XRT 13 years ago.

Findings

Axial post-contrast fat-saturated T1 (Fig. 12.6a), T2 (Fig. 12.6b), PET (Fig. 12.6c), PET-MRI fusion (Fig. 12.6d) and coronal non-contrast CT (Fig. 12.6e), and PET-CT fusion (Fig. 12.6f) of the face show enhancing, FDG-avid mass within the right masticator space.

Impression

Adenoid cystic carcinoma recurrence.

Pearls and Pitfalls

The clinical utility of ^{18}F-FDG-PET in evaluating salivary gland malignancies has not been well defined. In a study of 34 patients with newly diagnosed salivary gland cancers, ^{18}F-FDG-PET was more sensitive than CT for the detection of primary salivary gland tumors and cervical metastases [2]. High-grade malignancies had higher mean maximum SUVs than did low- and intermediate-grade malignancies. In a 25 months follow-up,

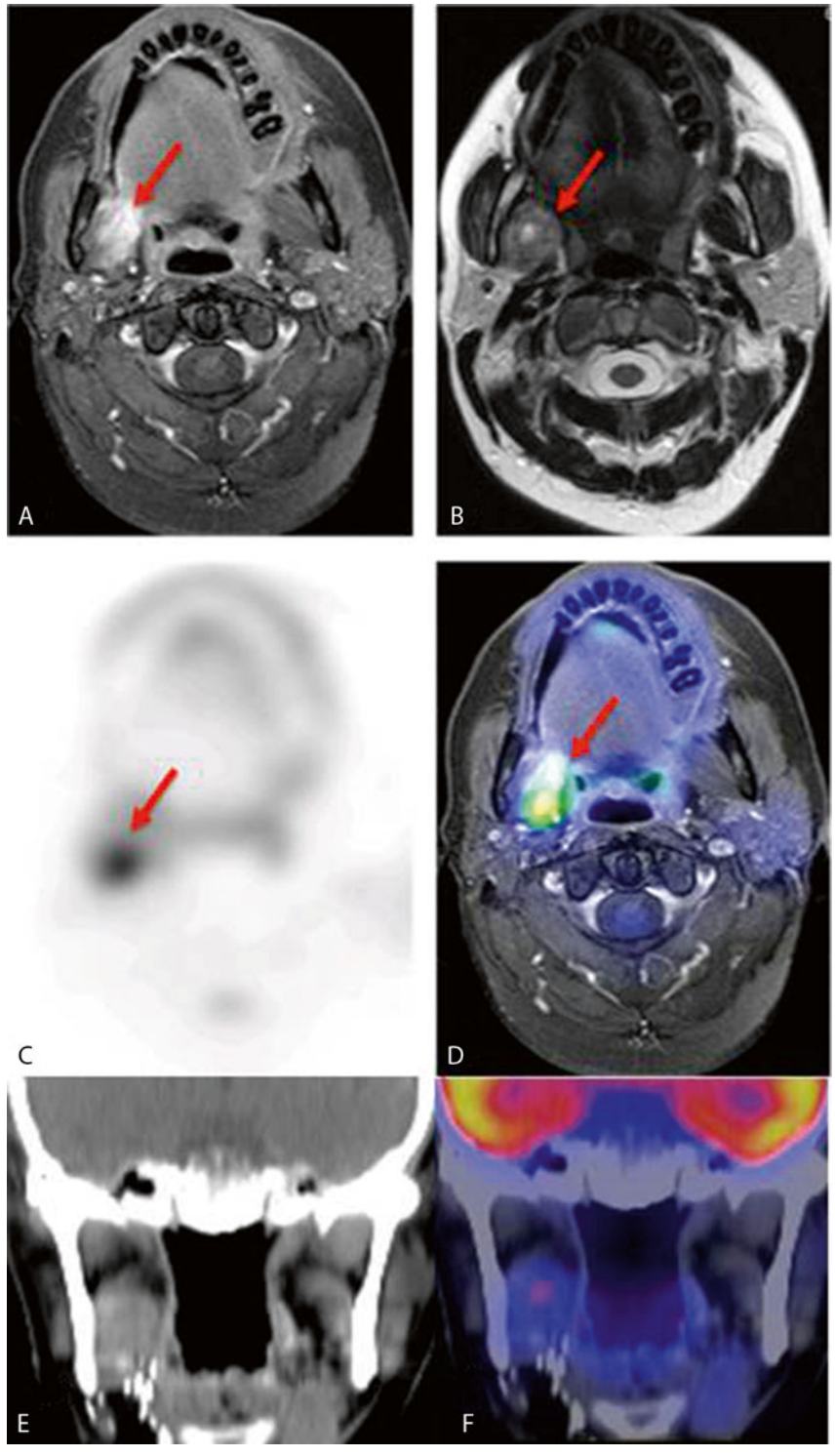

Fig. 12.6

^{18}F-FDG-PEt also correctly diagnosed local-regional recurrences in six patients and new distant metastases in nine patients.

Occasional failure of ^{18}F-FDG-PET in detecting some primary salivary gland tumors has been attributed to normal physiologic uptake of ^{18}F-FDG in the head and neck region, including the salivary glands, and small size of some of the tumors.

Discussion

Adenoid cystic carcinoma most often occurs in the salivary glands, but has also been reported in the breast, lacrimal glands, lung, brain, Bartholin glands, trachea, and paranasal sinuses. It is the third most common malignant salivary gland tumor overall (after mucoepidermoid carcinoma and polymorphous low-grade adenocarcinoma). It represents 28 % of malignant submandibular gland tumors, making it the single most common malignant salivary gland tumor in this region. Salivary gland malignancy is currently managed primarily by resection of the primary tumor, possibly in combination with neck dissection or subsequent radiotherapy. Proper management requires accurate information about the site and extent of tumors (Fig. 12.6).

Case 12.6: Right Vocal Cord Paralysis

History

34-year-old female with recurrent papillary thyroid carcinoma, status post thyroidectomy, and neck dissection with hoarseness.

Findings

Axial FDG-PET (Fig. 12.7a), non-contrast CT (Fig. 12.7b), PET-CT fusion (Fig. 12.7c), axial T1-weighted MRI (Fig. 12.7d), and PET-MRI fusion (Fig. 12.7e) images of the neck demonstrate asymmetric uptake in the left cricoarytenoid muscle.

Axial CT at the level of the vocal cords (Fig. 12.7f) shows subtle medialization of the right vocal fold.

Impression

Right vocal cord paralysis.

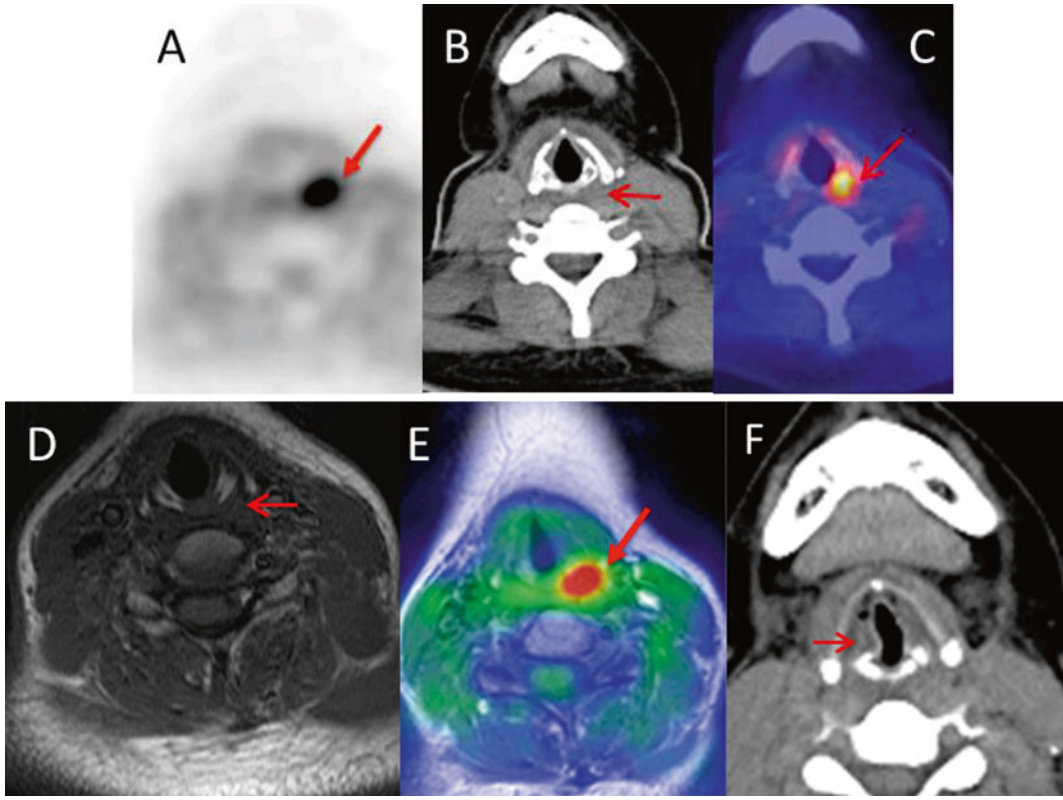

Fig. 12.7

Pearls and Pitfalls

Incidence of permanent recurrent laryngeal nerve (RLN) injury after thyroid surgery is 1–2 % when performed by experienced neck surgeons and higher in hands of less experienced surgeon or in setting of malignant disease. In some cases of thyroid malignancy, the nerve is purposely sacrificed when it runs through the tumor.

Up to 40 % of individuals with vocal cord paralysis may be asymptomatic, making detection of this entity on imaging essential, as vocal cord paralysis can be an initial sign of invasion or compression of the RLN. Detection of vocal cord paralysis can be difficult on conventional imaging (MRI or CT), however usually easily seen on PET. Knowledge of laryngeal anatomy helps the radiologist differentiate this entity from metastatic disease and/or lymphadenopathy.

Discussion

Understanding the anatomy of RLN helps the radiologist in determining the cause of vocal cord paralysis. The vagus nerve descends along the course of the carotid artery into the upper mediastinum bilaterally. The right RLN exits from the vagus nerve anterior to the subclavian artery and

courses posteriorly under the artery at the level of the brachiocephalic bifurcation and courses obliquely toward the right tracheoesophageal groove. The left RLN exits from the vagus nerve at the level of the aortic arch, then courses posteromedially beneath it, and thus passes through the aorticopulmonary window posterior to the ligamentum arteriosum. It then ascends vertically through the superior mediastinum to reach the tracheoesophageal groove. Both RLNs enter the larynx posterior to the cricoarytenoid joints and innervate the intrinsic laryngeal muscles [3] (Fig. 12.7a–f).

Case 12.7: Focal Cortical Dysplasia (ILAE Type IIa)

History

12-year-old male with epilepsy.

Findings

Dysplastic thickened cortex in the superior-medial left parietal lobe with associated subtle signal abnormality on FLAIR and decrease metabolic activity on PET in the interictal state (Figs. 12.8 and 12.9).

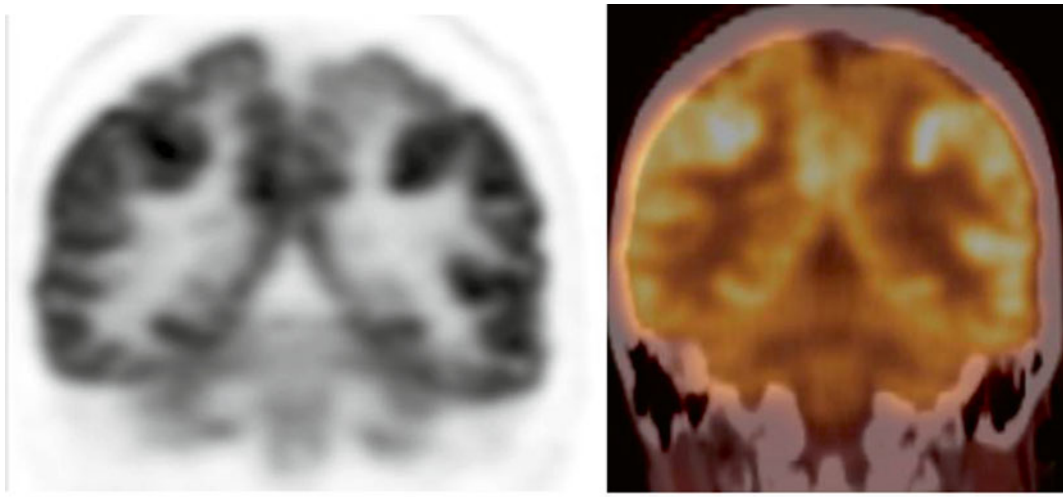

Fig. 12.8

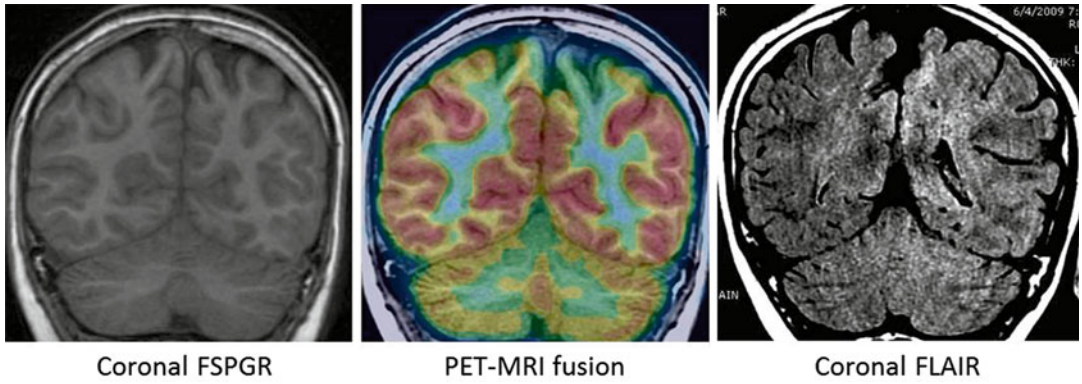

Fig. 12.9

Impression

Focal cortical dysplasia (ILAE type IIa).

Pearls and Pitfalls

FDG-PET/MRI coregistration has been shown to be useful in detecting cortical dysplasia in patients with epilepsy [4]. The addition of FDG-PET/MRI coregistration to the presurgical protocol enhances the ability to detect FCD, especially in patients with type I or type II FCD and non-concordant EEG and MRI findings. Sensitivity of MRI for the detection of FCD has been reported in 53–90 % of patients with surgically proven FCD. An increase in the detection of hypometabolism at the location of the lesion on FDG-PET images when using FDG-PET/MRI coregistration has been shown and considered a useful technique in the presurgical protocol to improve detection of the epileptogenic lesion.

Focal cortical dysplasia is a disorder of cortical formation, which may demonstrate both architectural and proliferative features, and a frequent cause of epilepsy. MR findings of FCD are related to the histologic grade of FCD. Most common finding of FCD on MRI, which is usually seen in severe cortical dysplasia, is indistinct gray-white matter demarcation with T2 prolongation involving the subcortical white matter. FDG-PET is more sensitive in the detection of grades I and II FCD. The histologic abnormalities of bizarre glial cells (balloon cells), ectopic neurons, and abnormalities of myelination may be responsible for the MR abnormality in blurring of the gray-white matter junction with abnormal signal intensity of the subcortical white matter. FCD has been histologically divided into three histologic types by International League Against Epilepsy (ILAE). ILAE type IIa is histologically characterized by cortical dyslamination and dysmorphic neurons without balloon cells (Figs. 12.8 and 12.9).

Case 12.8: Left Medial Temporal Sclerosis

History

22-year-old female with epilepsy scanned in interictal state.

Findings

Coronal PET (Fig. 12.10a), PET-CT fusion (Fig. 12.10b), and PET-MRI fusion (Fig. 12.10c) images show asymmetric decrease in FDG uptake in the left medial temporal lobe (including parahippocampal gyrus) and hippocampus.

Coronal FLAIR image at the level of hippocampal body-tail (Fig. 12.10d) shows small left hippocampus with abnormal configuration and hyperintense signal on FLAIR, characteristic of medial temporal sclerosis.

Impression

Left medial temporal sclerosis.

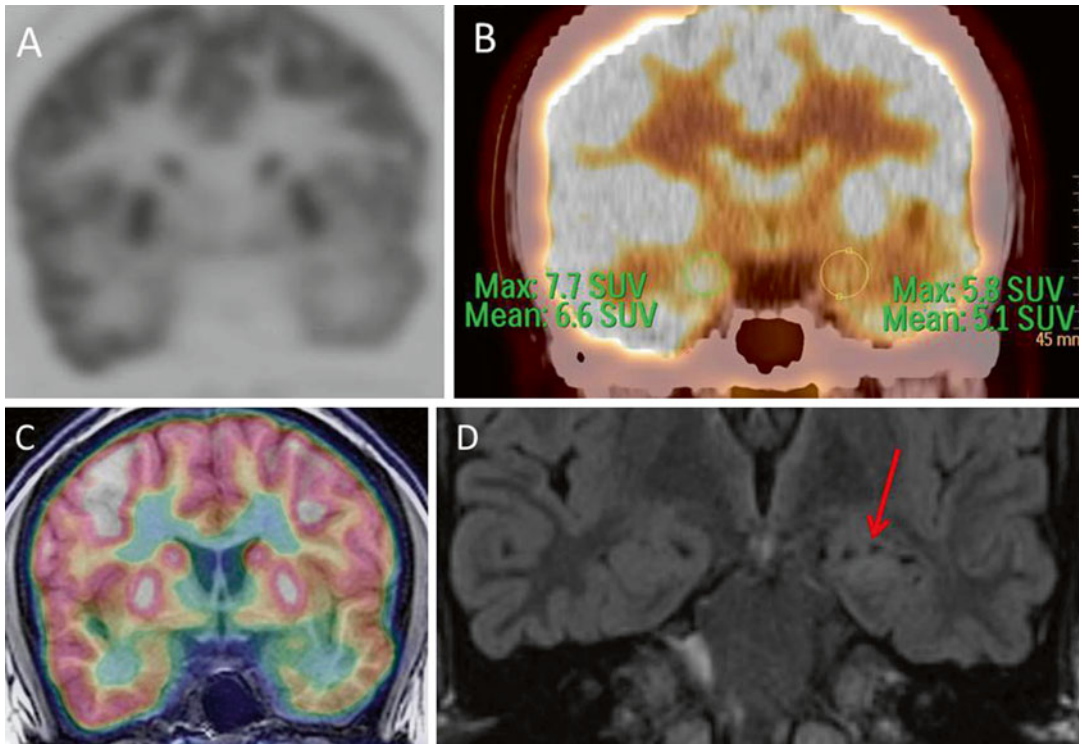

Fig. 12.10

Pearls and Pitfalls

The ultimate goal of PET in epilepsy imaging is to identify and/or confirm the location of a seizure focus which may be completely or partially invisible to other diagnostic techniques (EEG, MRI). PET is generally performed in the interictal state and demonstrates decrease metabolic activity in the epileptogenic focus. Anterior temporal lobe resection has been reported to increase quality-adjusted life expectancy by 7.5 quality-adjusted life years and is the preferred treatment in setting of medial temporal lobe epilepsy. PET imaging and PET-MRI fusion combined with assessment of seizure semiology and extracranial and intracranial EEG findings help the neurosurgeon in determining the extent of epileptogenic focus.

Discussion

Mesial temporal sclerosis (MTS), most common pathological abnormality in temporal lobe epilepsy, is a specific pattern of hippocampal neuron cell loss with associated hippocampal atrophy and gliosis. Cell loss can occur in CA1 and CA4, CA4 alone, or CA1 to CA4 segments. It can be a primary epileptogenic focus or secondary to other epileptogenic focus in the same cerebral hemisphere. PET is useful in determining the location and extent of epileptogenic focus. MRI findings of MTS include small-size, abnormal configuration (including loss of hippocampal head interdigitations) and T2 prolongation or increased FLAIR signal in the hippocampus (Fig. 12.10a–d).

Case 12.9: Sydenham's Chorea

History

11-year-old female with mood change, hearing voices, dysarthria, and choreoathetosis of four extremities. No significant past medical history or family history and no recent infections, pharyngitis, or strep throat. Her brain MRI was unremarkable.

Findings

Axial FDG-PET (Fig. 12.11a), CT (Fig. 12.11b), and PET-CT fusion images (Fig. 12.11c) at the level of the basal ganglia demonstrate symmetric marked increased FDG uptake in caudate and putamen, compatible with Sydenham's chorea. Normal metabolic activity is seen in the remaining brain. Figure 12.11d is an example of normal FDG uptake at the level of basal ganglia.

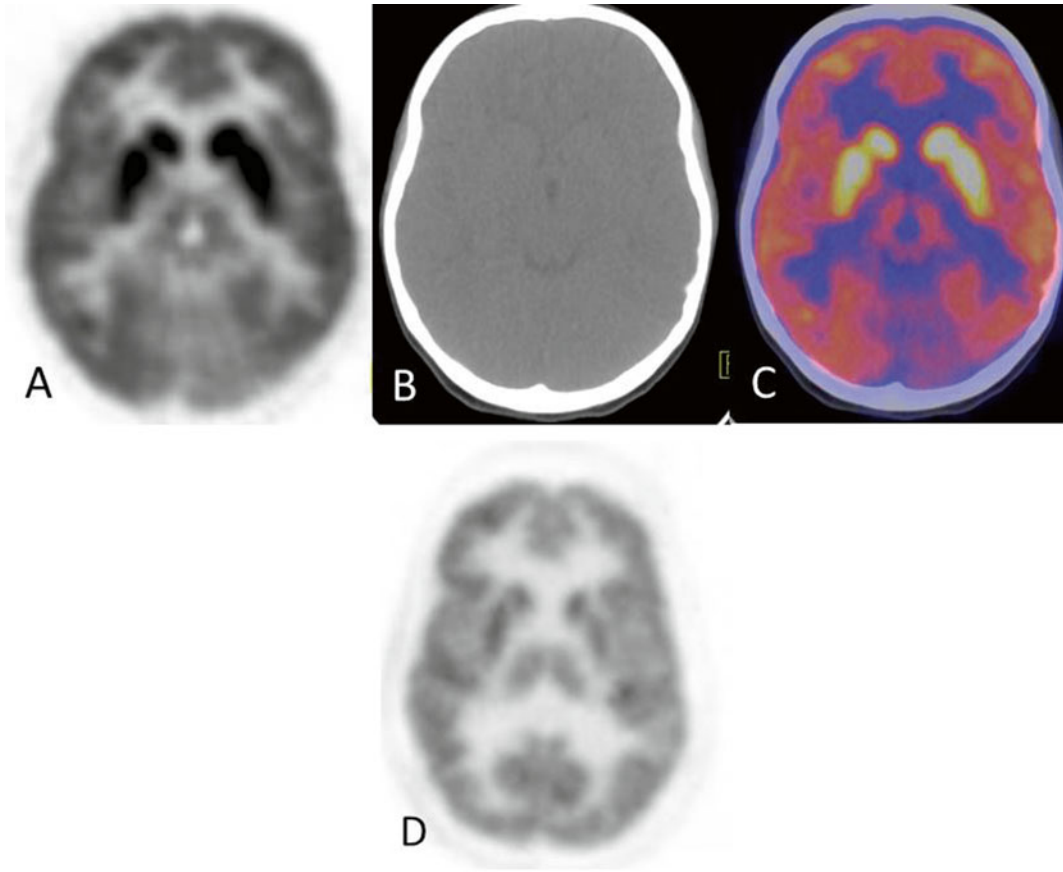

Fig. 12.11

Impression

Sydenham's chorea.

Pearls and Pitfalls

Sydenham's chorea is a late manifestation of rheumatic fever and associated with group A-hemolytic streptococcus. Sydenham's chorea is most common in children and adolescents above the age of 5 (80 %) and twice as common in girls as compared to boys. Preceding or concurrent throat cultures for hemolytic streptococcus can be negative. It is associated with subsequent cardiac valvular heart disease and obsessive-compulsive disorder. A link between multiple tics, pediatric autoimmune neuropsychiatric disorders associated with streptococcal infection (PANDAS syndrome), Tourette syndrome, and Sydenham's chorea has also been suggested.

FDG-PET demonstrates hypermetabolism of the basal ganglia in active Sydenham's chorea. Single-photon emission computed tomography

demonstrates hyperperfusion of the basal ganglia. Magnetic resonance imaging (MRI) studies of patients with active Sydenham's chorea have shown no specific abnormality, but increased size of the caudate, putamen, and globus pallidus has been noted.

Discussion

Recent studies have suggested immunoreactivity as an explanation for Sydenham's chorea. Serum antibodies appear to be an M1 isozyme of pyruvate kinase, which is enriched in the striatum. An initial antibody response to the M streptococcal protein likely cross-reacts with basal ganglia pyruvate kinase. This theory explains the utility of plasmapheresis for treatment in severe Sydenham's chorea. The loss of the hypermetabolic basal ganglia findings in recovery can help explain lack of long-term permanent neurologic sequelae [5] (Fig. 12.11a–d).

References

1. Trotta BM, Pease CS, Rasamny JJ, Raghavan P, Mukerjee S. Oral cavity and oropharyngeal squamous cell cancer: key imaging findings for staging and treatment planning. Radiographics. 2011;31(2):339–54.
2. Roh JL, Ryu CH, Choi SH, Kim JS, Lee JH, Cho KJ, Nam SY, Kim SY. Clinical utility of 18F-FDG for patients with salivary gland malignancies. J Nucl Med. 2007;48(2):240–6.
3. Aquino SL, Duncan GR, Hayman LA. Nerves of the thorax: atlas of normal and pathologic findings. RadioGraphics. 2001;21:1275–81.
4. Goffin K, Van Paesschen W, Dupont P, Baete K, Palmini A, Nuyts J, Van Laere K. Anatomy-based reconstruction of FDG-PET images with implicit partial volume correction improves detection of hypometabolic regions in patients with epilepsy due to focal cortical dysplasia diagnosed on MRI. Eur J Nucl Med Mol Imaging. 2010;37(6):1148–55. Epub 2010 Mar 20.
5. Ho L. Hypermetabolism in bilateral basal ganglia in Sydenham chorea on F-18 FDG PET-CT. Clin Nucl Med. 2009;34(2):114–6.

13 Dementia

Aarti Kaushik and Peter S. Conti

Case 13.1: Alzheimer's Dementia

History

67-year-old female with cognitive impairment.

Findings

There is bilaterally decreased temporal and posterior parietal cortical activity such that it is less than the cerebellar cortical activity (Fig. 13.1). There is sparing of the motor strips, basal ganglia, and visual. Age-appropriate cortical atrophy is noted. There is no evidence of ischemia or mass lesion.

Impression

Abnormal metabolism consistent with dementia of Alzheimer's type.

Pearls and Pitfalls

Alzheimer's disease (AD) is the most common form of dementia. Association cortices are more severely involved, while the primary somatosensory and motor cortices, the basal ganglia, the thalamus, and the cerebellum are relatively spared.

FDG-PET demonstration of the classic metabolic abnormality associated with pathologically verified AD has a sensitivity of 93 %, a specificity of 63 %, and an accuracy of 82 %.

P.S. Conti, A. Kaushik (eds.), *PET-CT*, DOI 10.1007/978-1-4419-5811-2_13

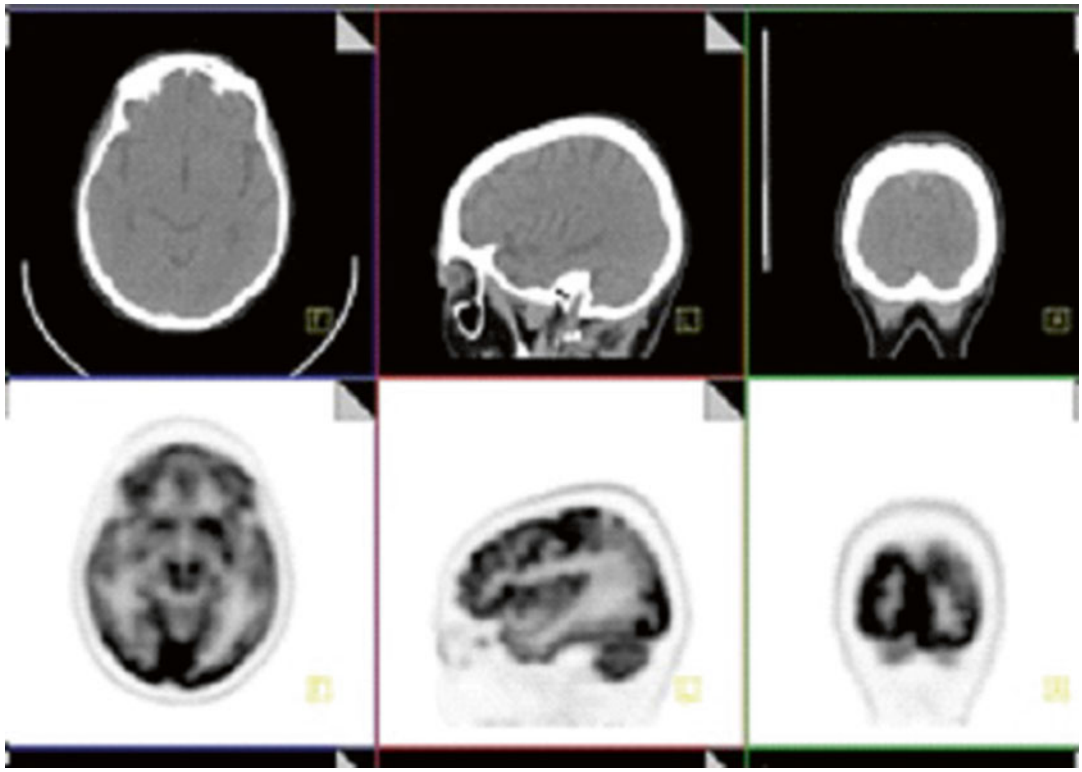

Fig. 13.1

Discussion

It was first described by German psychiatrist and neuropathologist Alois Alzheimer in 1906 and was named after him. Many causes of dementia symptoms exist. Alzheimer's disease is the most common cause of a progressive dementia characterized with gradual decline in cognition and behavior. Accurate early diagnosis of AD is important because early use of medications may improve or delay the cognitive loss that occurs in mild-to-moderate disease. Normal aging of the brain is characterized by a regional decline in the cerebral glucometabolism of the prefrontal cortex (Fig. 13.1).

Case 13.2: Frontotemporal Dementia

History

62-year-old female with 3-year history of progressive decline in cognition accompanied by personality change; with prominent impairment in memory, anomic aphasia, and decreased insight; and with preservation of

visual-spatial. PET/CT is done as part of the investigational workup for neurodegenerative process.

Findings

There is relative symmetric decrease in metabolic activities of the bilateral frontal and temporal regions with sparing of the visual cortex/occipital lobe and deep gray matter activities (Fig. 13.2).

Pearls and Pitfalls

Frontotemporal dementia (FTD) is the most common dementia diagnosed in patients under age 60 and is as common as Alzheimer's disease among patients age 45–64.

Discussion

Cases of elderly patients with progressive language deterioration have been described since Arnold Pick's landmark case report of 1892. FTD

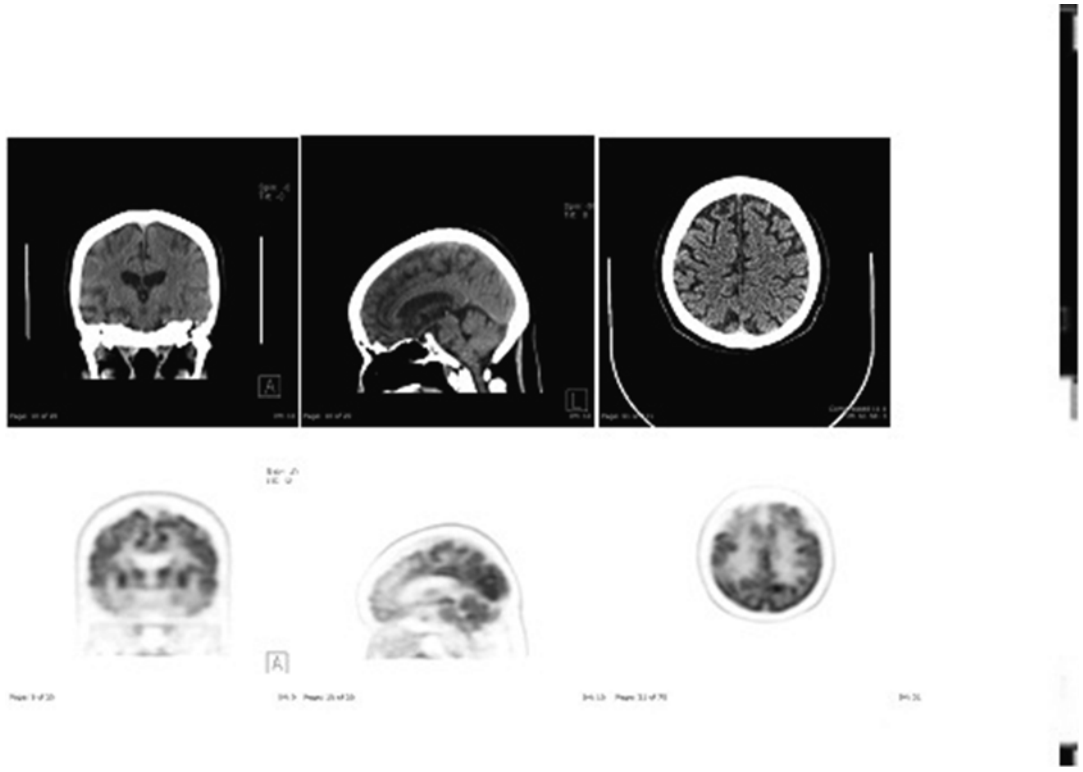

Fig. 13.2

describes a clinical syndrome associated with shrinking of the frontal and temporal anterior lobes of the brain. Originally known as Pick's disease, the name and classification of FTD have been a topic of discussion for over a century. The current designation of the syndrome groups together Pick's disease, primary progressive aphasia, and semantic dementia as FTD (Fig. 13.2).

Case 13.3: Normal Pressure Hydrocephalus

History

75-year-old male with memory loss, incontinence, and history of gait disturbance.

Findings

CT images of the brain demonstrate profound cerebral cortical atrophy and gross ventriculomegaly (Fig. 13.3). There were also calcifications as well as exostoses from posterior sella into the pituitary area.

PET images of the brain demonstrate decrease in metabolic activity appropriate for the cortical atrophy. The deep gray matter structures demonstrated normal and symmetric FDG uptake (not in the images). In the view of relatively normal cortical perfusion, the pattern best fits communicating hydrocephalus.

Pearls and Pitfalls

NPH is treatable cause of dementia.

Discussion

First described by Hakim and Adams in 1965, normal pressure hydrocephalus (NPH) refers to a clinical entity consisting of the triad of gait disturbance, dementia, and incontinence, coupled with the laboratory findings of normal cerebrospinal fluid (CSF) pressures and radiographic findings of ventriculomegaly. Although NPH is a relatively rare cause of dementia, identifying NPH is important because it is one of the few treatable entities. NPH is one of the reasons that all dementia patients should have neuroimaging with either CT scanning or MRI as part of their workup (Fig. 13.3).

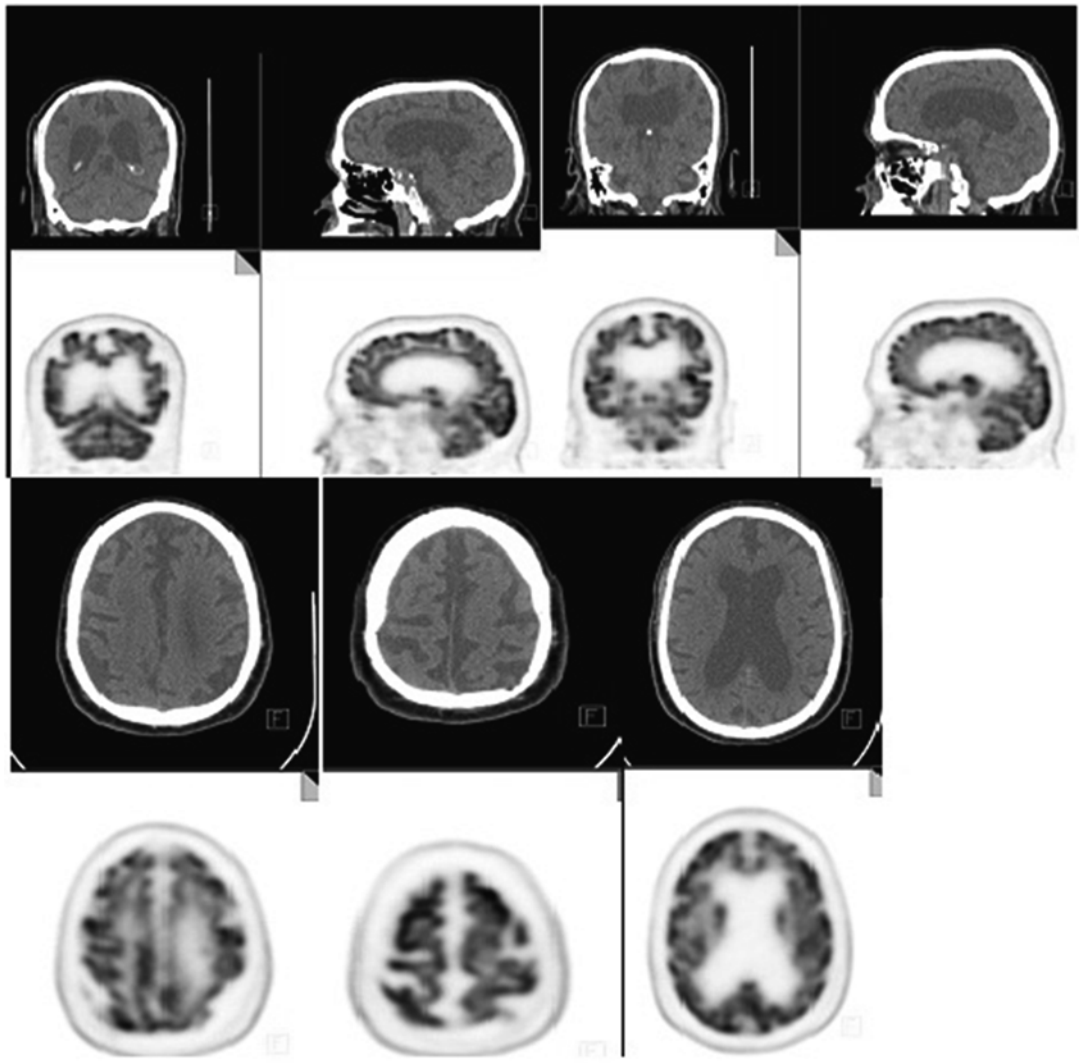

Fig. 13.3

Suggested Reading

Hoffman JM, Welsh-Bohmer KA, Hanson M, et al. FDG PET imaging in patients with pathologically verified dementia. J Nucl Med. 2000;41:1929–32.
Wilson JA, Islam O. Imaging in normal pressure hydrocephalus. Medscape, April 25, 2013.

14 Pediatric Imaging

Shereif H. Gamie, Ella Yevdayev, Aarti Kaushik, and Hollie A. Lai

Case 14.1: Adrenal Cortical Cancer

History

A 15-year-old female with known right adrenal cortical adenocarcinoma, status post chemotherapy treatment. PET/CT scan reported pulmonary metastases in the left lung and increase in size in the right adrenal mass.

Findings

Chest: There are two hypermetabolic left lung pulmonary lesions, one in the lateral lingual segment and second at the base (lower lobe), suggesting persistently active pulmonary metastases (measuring approximately 9–10 mm) (Fig. 14.1). The lingular segment nodule, SUV max 4.07. Left lung base nodule, SUV max of 4.07.

Abdomen: A $8.0 \times 4.5 \times 10.8$ cm right adrenal mass, SUV max 18.7 (Fig. 14.2). There are two separate focal areas of intensely increased FDG uptake superior to the mass, more medial, SUV max 18.7 and 12. 7 in the more lateral nodule. Suggestive for metastatic disease. There is noted subtle ill-defined hypoattenuating lesion in the liver seen on unenhanced CT, which demonstrates no significant corresponding FDG uptake on the PET. Lesions seen in the dome of the liver in segment 8 measure approximately 1.2×2.5 cm.

Impression

PET/CT scan demonstrating hypermetabolic pulmonary nodules and right adrenal mass, suggestive for residual metabolically avid local and metastatic disease.

P.S. Conti, A. Kaushik (eds.), *PET-CT*, DOI 10.1007/978-1-4419-5811-2_14

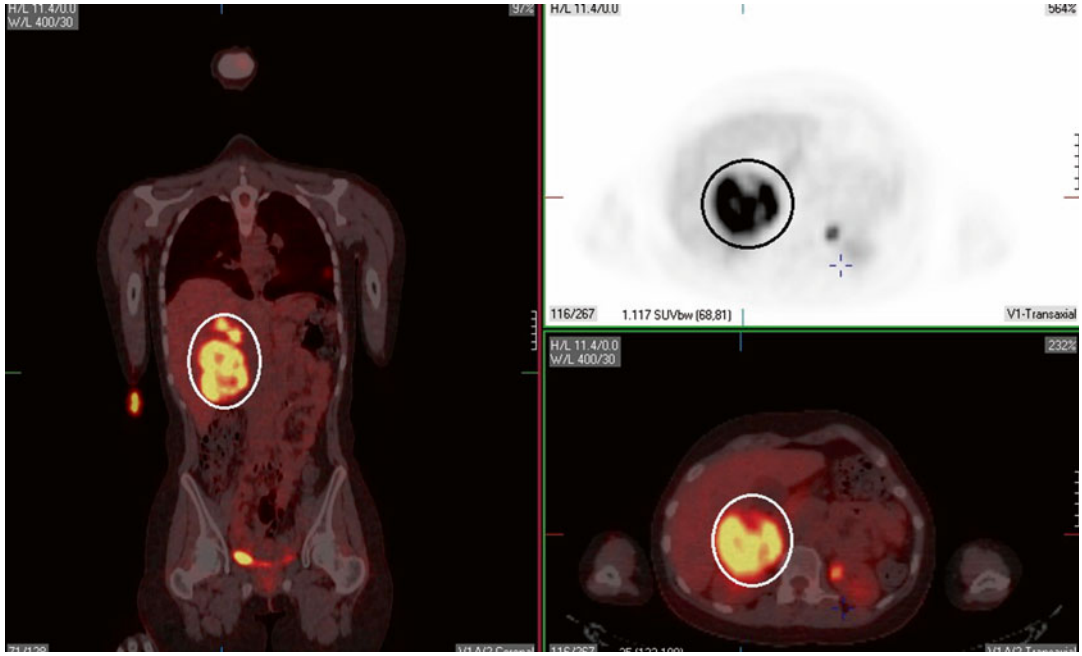

Fig. 14.1

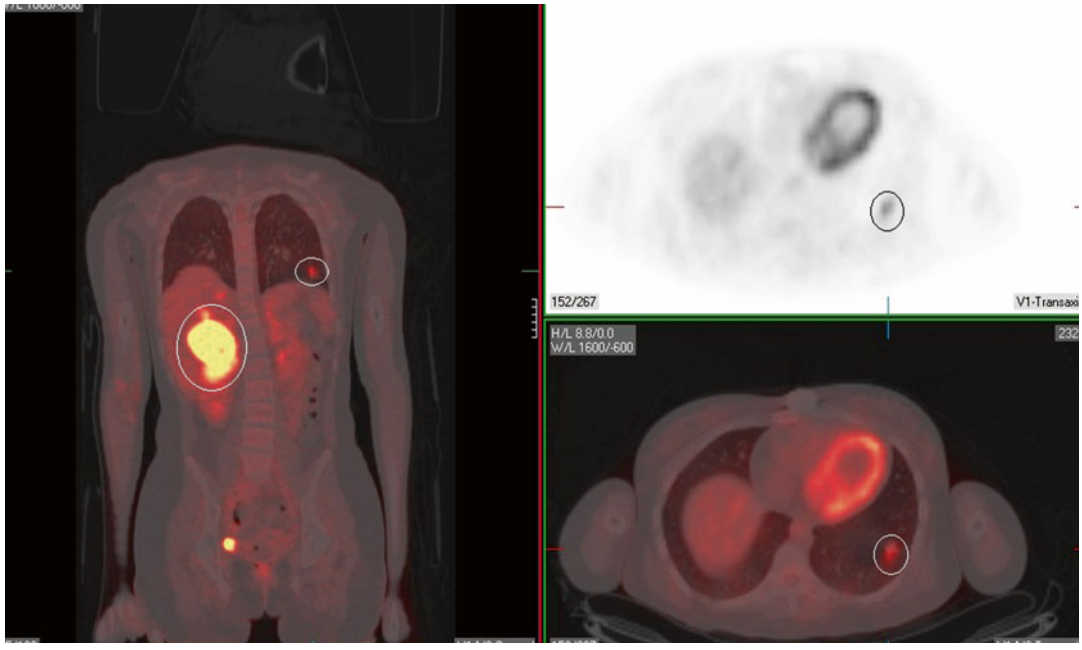

Fig. 14.2

Pearls and Pitfalls

FDG PET for characterization of adrenal lesions showed a sensitivity of 100 %, a specificity of 94 %, and an accuracy of 96 %.

Discussion

Adrenal cortical carcinoma (ACC) is a rare malignant neoplasm with a poor prognosis.

FDG PET showed excellent diagnostic performance in differentiating adrenal lesions detected on CT or MRI. Because FDG PET has the additional advantage of evaluating the primary lesions as well as metastases, it could be cost-effective and the modality of staging. Most adrenocortical carcinomas accumulate and retain FDG and thus can be visualized by PET. However, false-negative findings are possible, especially with very small lesions.

Radical surgery of the primary tumor and of local as well as of distant recurrence is the only effective treatment and requires accurate and early localization of recurrent tumors. All known sites of ACC lesions showed markedly increased FDG uptake (Figs. 14.1 and 14.2).

Case 14.2: Thyroid Cancer: Recurrence

History

A 12-year-old female who was discovered to have a right thyroid lobe nodule on routine physical examination which ultimately turned out to be a T3, N1a, Mx papillary thyroid carcinoma. The patient is status post total thyroidectomy, after which she received 50 mCi of I-131. The patient presented with reportedly elevated thyroglobulin levels. Recent whole-body I-123 scan reported no definitive scintigraphic findings of iodine uptake to suggest a site of locally recurrent and/or metastatic disease.

Findings

Neck: A mildly FDG-avid 4 mm right lower cervical node focus of prominent FDG uptake is seen (SUV max 3.21) (Fig. 14.3). Two or three subtle focal areas of mildly increased FDG uptake are noted in the right lower neck on PET in the midst of the brown fat which appears to correspond to the very subtle subcentimeter-sized nodes on unenhanced CT (Fig. 14.4).

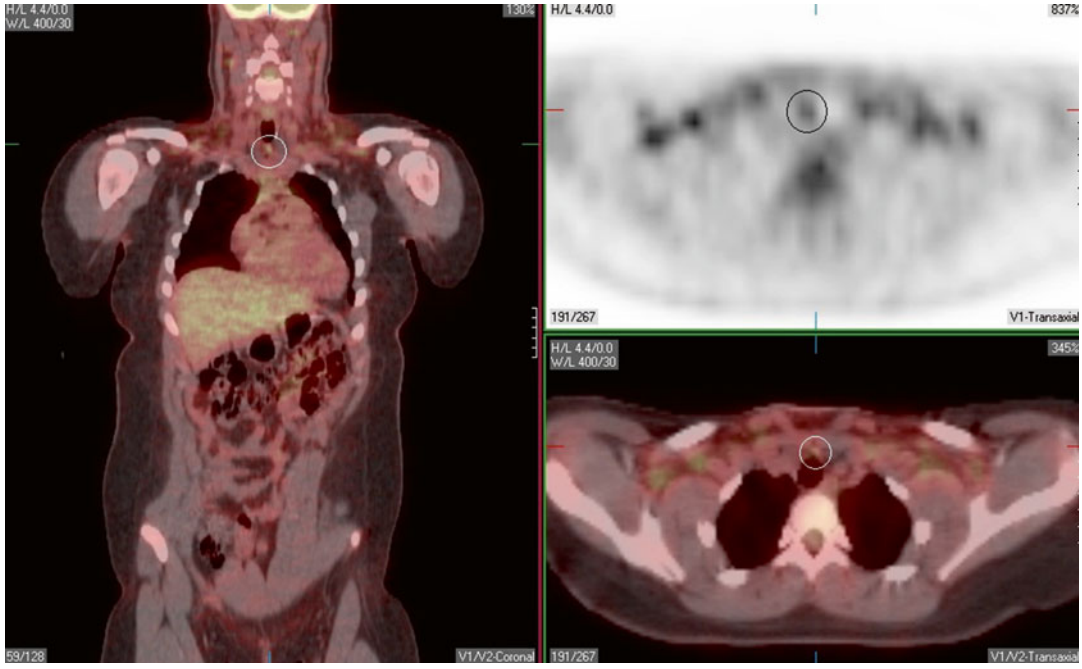

Fig. 14.3

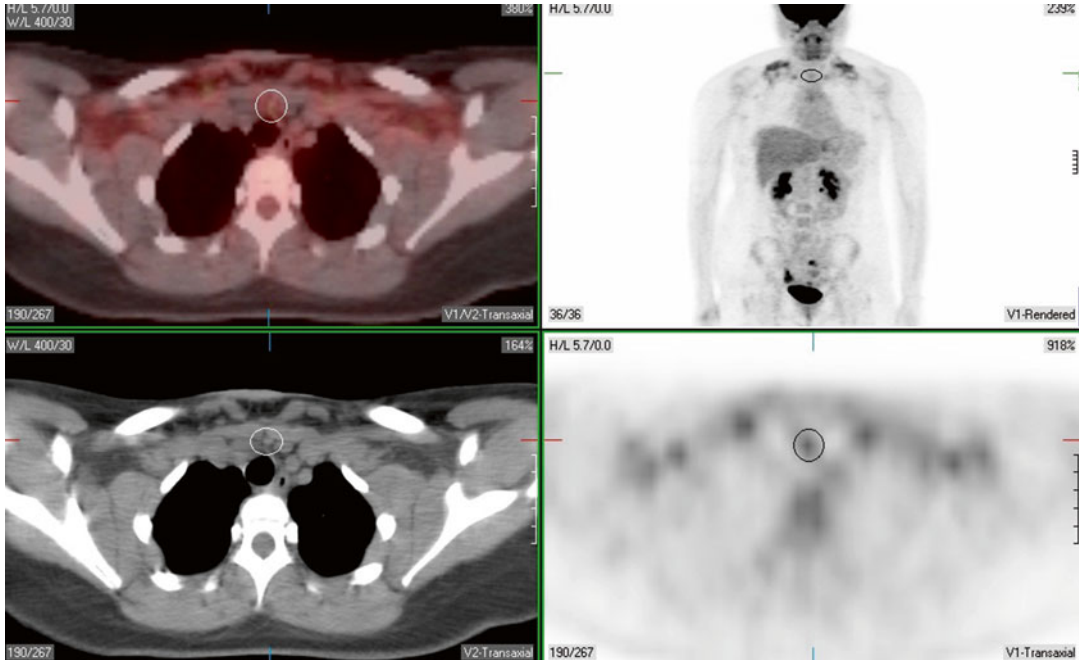

Fig. 14.4

Impression

Restaging PET/CT scan demonstrating subtle subcentimeter-sized mildly FDG-avid nodes in the right lower neck, as detailed above. In the setting of reportedly elevated thyroglobulin levels, these questionable areas of uptake raise concern for possible sites of residual/recurrent disease.

Pearls and Pitfalls

1. Only 50–60 % of papillary thyroid carcinomas and 64–70 % of follicular carcinomas are iodine avid.
2. PET is not indicated for primary thyroid malignancy detection since FDG can accumulate in normal thyroid tissue (about 30 % of patients) and certain benign thyroid disease.
3. A PET study will usually be positive in patients with thyroglobulin level higher than 100 μg/L. PET will detect true positive disease in 11 %, 50 %, and 90 % of patients with hTg levels of <10 μg/L, 10–20 μg/L, and >100 μg/L, respectively.
4. FDG PET/CT is indicated for a known, differentiated, and recurrent papillary/follicular thyroid cancer patients with a negative I-131 scan. Increased expression of GLUT-1 is associated with the loss of radioactive iodine uptake in metastases.

Discussion

Less than 1 % of all cancer death are from thyroid cancer. FNA is best for accurate diagnosis for primary tumor. Coregistered ^{18}F-FDG PET/CT can provide precise anatomic localization of recurrent or metastatic thyroid carcinoma, leading to improved diagnostic accuracy, and can guide therapeutic management. In addition, further assessment of ^{131}I WBS-negative, thyroglobulin-positive patients by ^{18}F-FDG PET/CT may aid in the clinical management of selected cases regardless of the thyroglobulin level (Figs. 14.3 and 14.4).

Case 14.3: Burkitt's Lymphoma

History

A 15-year-old female with reported newly diagnosed Burkitt's lymphoma.

Findings

There are prominent focal symmetric regions of intense FDG uptake bilaterally in the posterior triangle on the upper neck and bilateral supraclavicular regions, which demonstrate no corresponding anatomic correlate on unenhanced CT and likely represent brown fat activity (Fig. 14.5). Tiny, subcentimeter bilateral cervical nodes are seen in the midst of these areas of likely physiologic brown fat activity. There are symmetric regions of intense FDG uptake in the superior mediastinum and bilaterally in the axillae, which demonstrate no corresponding anatomic correlate on CT and also likely represent physiologic brown fat activity (Fig. 14.6). Bilateral symmetric paravertebral intense FDG uptake is seen along the entire thoracic spine, also without corresponding anatomic correlates on CT and also likely physiologic brown fat uptake.

Impression

Prominent most symmetric likely physiologic brown fat activity is seen in bilateral upper neck, supraclavicular regions, superior mediastinum, and axillae. A few scattered subcentimeter nodes are seen in the midst of this brown fat uptake (especially in axillae), in which disease involvement cannot be entirely excluded as detailed above.

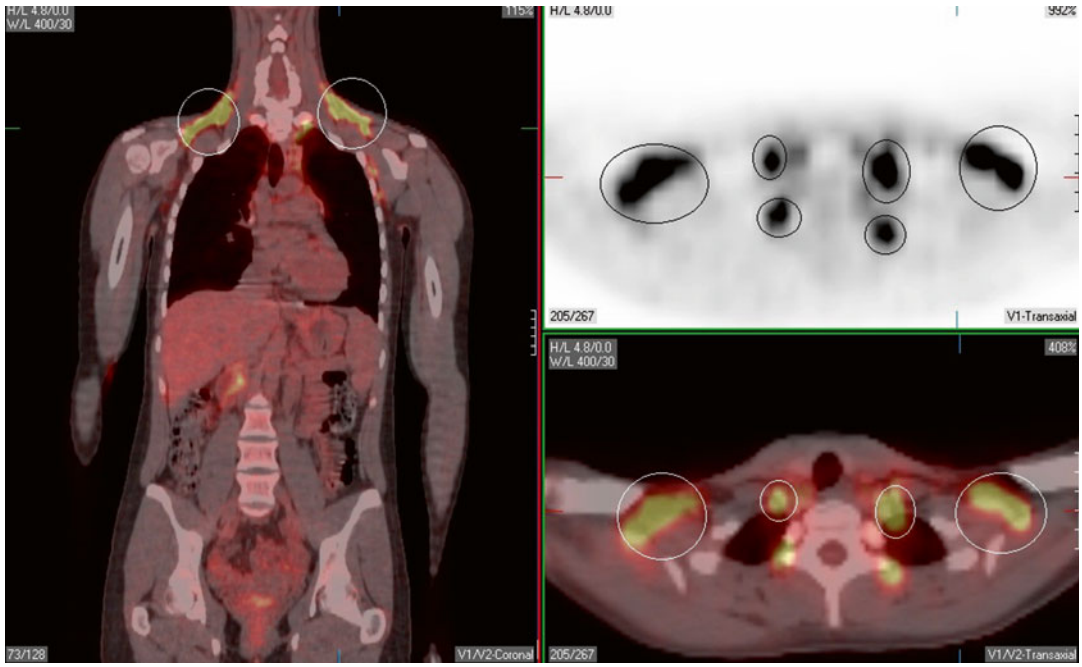

Fig. 14.5

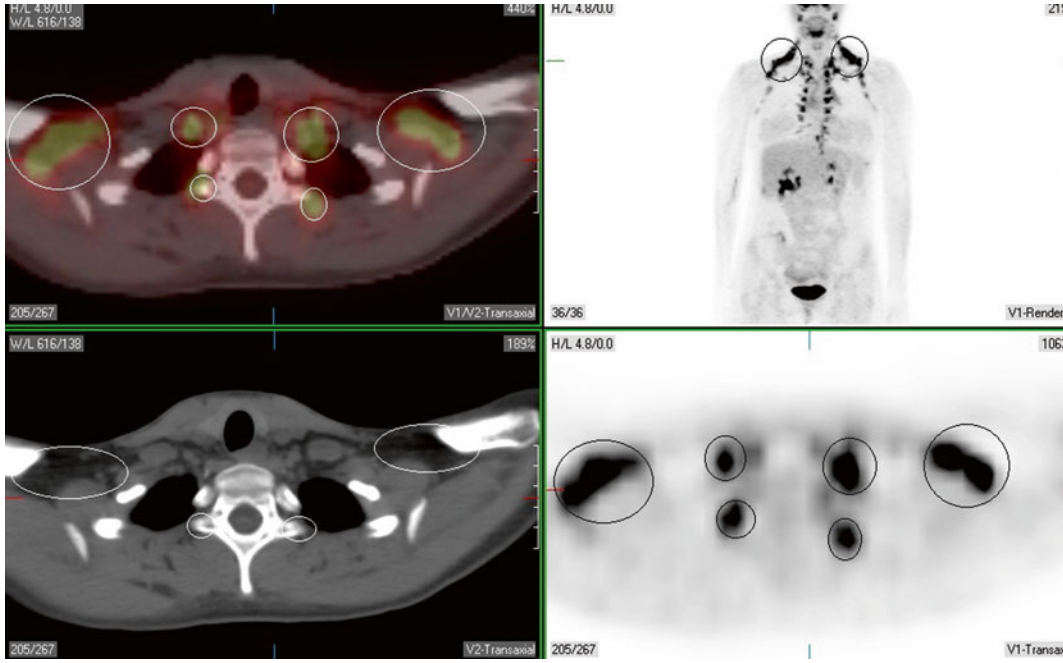

Fig. 14.6

Pearls and Pitfalls

1. Overall sensitivities, specificities, and positive and negative predictive values were 78 %, 98 %, 94 %, and 90 % for F-18 FDG PET and 79 %, 88 %, 90 %, and 46 % for CT, respectively.
2. PET/CT scan with uptake greater than that of the liver is considered positive. Uptake that increased over the background but less than in the liver is equivocal.
3. Coregistered PET/CT images significantly improve the specificity of PET findings. In this case, areas of significant focal FDG uptake in head/neck and chest demonstrate no correlates on CT, enabling differentiation between disease-involved nodes and physiologic brown fat activity.

Discussion

F-18 FDG PET imaging is a useful technique for the staging and follow-up of pediatric patients with lymphoma.

Negative PET/CT scan during routine follow-up for lymphoma in children strongly suggests absence of recurrence, but a positive PET/CT and diagnostic CT scans have low PPV and should be interpreted with caution (Figs. 14.5 and 14.6).

Case 14.4: Hodgkin's Disease

History

A 10-year-old male recently diagnosed with Hodgkin's disease from the left cervical node biopsy and post initiation chemotherapy. Study is performed for scintigraphic staging.

Findings

Head and Neck: Focal region of prominent FDG uptake in seen in the nasopharynx (Waldeyer's ring) more prominent on the left, which corresponds to ill-defined soft tissue fullness on unenhanced CT, which likely represents disease-involved tissue (Fig. 14.7). There is large heterogeneous area of moderate to intense FDG accumulation involving the entire left neck on PET, corresponding to the coalesced-appearing conglomeration of numerous levels II–IV left-sided cervical nodes, which likely represent disease-involved lymphadenopathy. In aggregate, this conglomerate measures approximately 7.5 × 3.6 cm. Several mild to moderate FDG-avid right-sided cervical nodes are seen involving levels II–IV, the largest of these nodes measures approximately 1 × 1.4 cm.

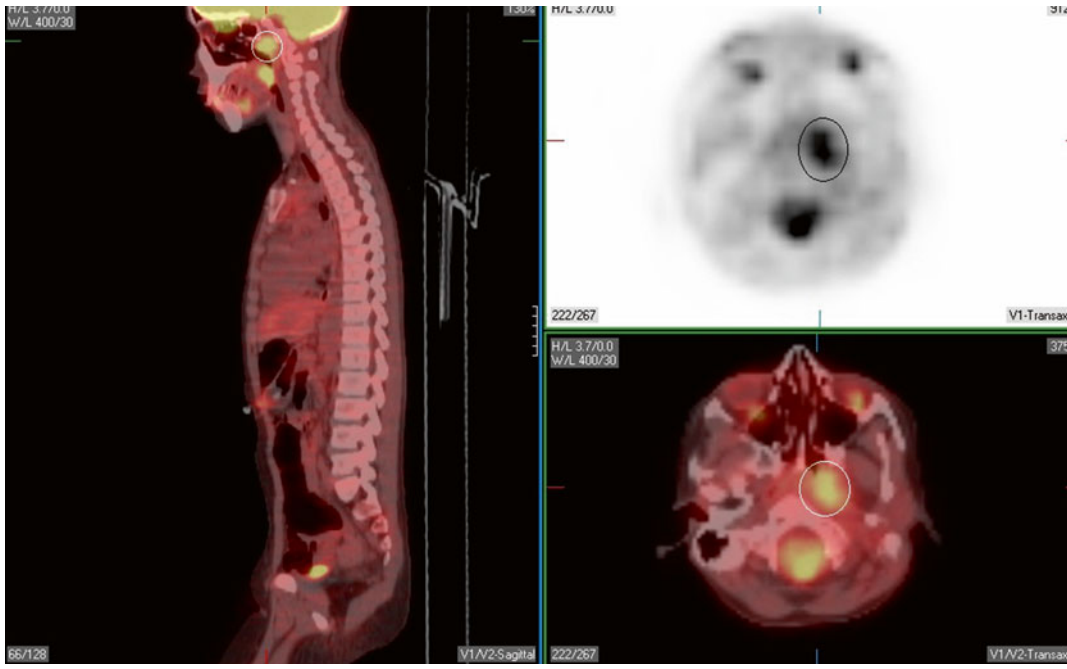

Fig. 14.7

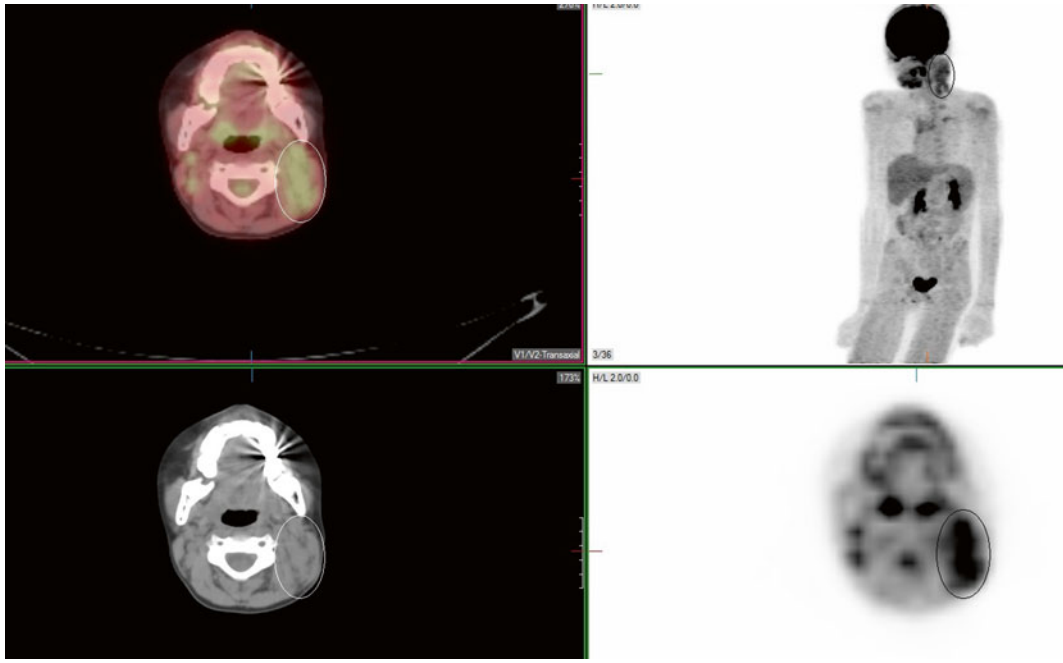

Fig. 14.8

Chest: Diffuse mild curvilinear FDG activity seen in the anterior mediastinum to the left of midline, which may represent reactive/rebound thymic tissue uptake. Left-sided Port-A-Cath seen in the left upper chest.

Abdomen: A focus of intense FDG uptake is seen in the upper anterior abdominal wall, which likely represents reactive uptake in the area of known G-tube (Fig. 14.8).

Impression

PET/CT scan evidence for supradiaphragmatic hypermetabolic lymphadenopathy, predominantly in the Waldeyer's ring and cervical nodes, left more than right, as detailed above.

Pearls and Pitfalls

1. 62–100 % of the FDG-positive patients will relapse after first-line chemotherapy; in contrast, only 4–16 % of the patients with negative PET will relapse.
2. 30–64 % of the residual masses will remain viable following the completion of therapy, demonstrating persistent metabolic uptake.

3. Patient with a negative PET relapse in 16–25 % on a long-term follow-up.
4. 80 % of the patients who relapse do so at another nodal site.

Discussion

The prognosis for children and adolescents with Hodgkin's lymphoma is excellent. However, many patients will show secondary malignancies 15–30 years after the initial diagnosis, which appears to be connected with the intensity of treatment during primary disease. The indication for radiotherapy in patients with early stage Hodgkin's lymphoma should be further refined by using FDG PET for evaluating the response to chemotherapy. Furthermore, in patients at an advanced stage of the disease, it should be determined if sequential FDG PET research during chemotherapy can separate patients into subgroups with an excellent or a poor prognosis.

PET imaging plays an important role in staging, evaluating tumor response, planning radiation treatment fields, and monitoring after completion of therapy for pediatric Hodgkin's lymphoma. This trend will likely increase in the future as a result of PET's superior sensitivity in correlating sites of tumor activity compared to other available functional imaging modalities. Ongoing prospective studies of PET in pediatric patients will increase understanding about the optimal use of this modality in children with cancer and define the characteristics of FDG-avid nonmalignant conditions that may be problematic in the interpretation of tumor activity (Figs. 14.7 and 14.8).

Case 14.5: Rhabdomyosarcoma

History

A 7-month-old infant with reported left thigh rhabdomyosarcoma.

Findings

Chest: Diffuse mild curvilinear FDG activity seen in the anterior mediastinum to the left of midline, which may represent normal physiologic thymic tissue uptake in a 7-month-old infant.

Abdomen: Several moderately to intensely hypermetabolic, likely disease-involved periaortic nodes are seen on PET, the most cranial of which is seen at the level of L3, approximately measuring 0.8 cm (Fig. 14.9).

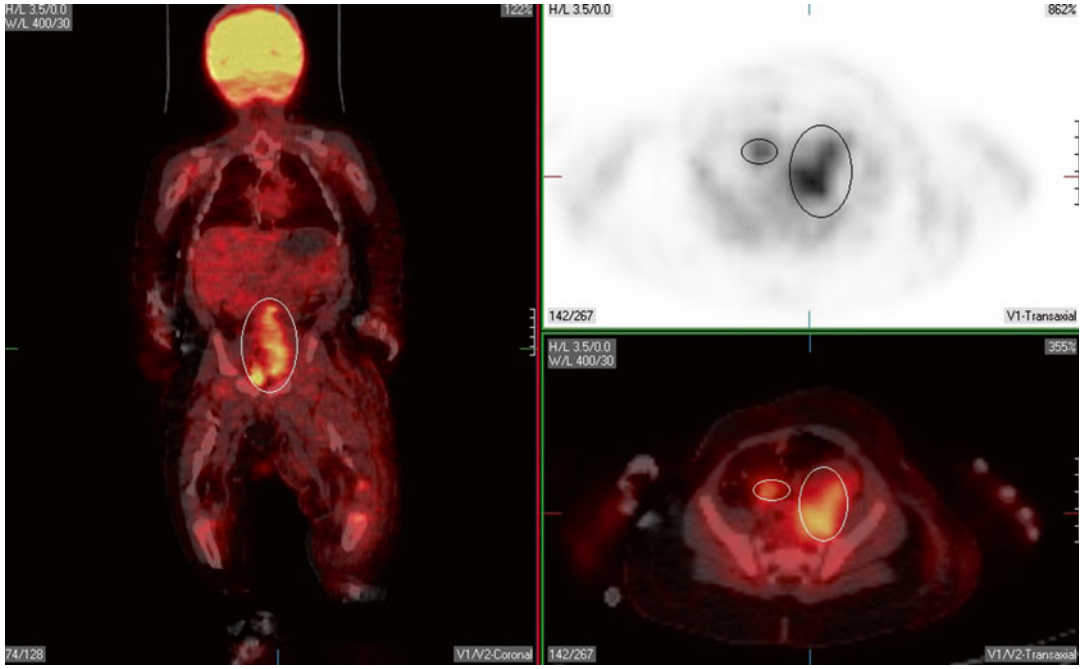

Fig. 14.9

Several adjacent focal regions of moderately intense FDG uptake are seen in the left pelvis/left groin (max SUV 3.69), which corresponds to a cystic appearing confluent mass with a thick periphery in the left pelvis on unenhanced CT, which likely represent bulky left iliac chain necrotic adenopathy, measuring 2.4×1.3 cm.

Several mildly to moderately hypermetabolic left-sided inguinal nodes, the largest of each measures $3 \times 2.1 \times 2.6$ cm on unenhanced CT (Fig. 14.10).

A few scattered mostly subcentimeter right inguinal notes are also seen on unenhanced CT, which demonstrate mild corresponding FDG uptake on PET. Disease involvement cannot be excluded.

Edematous changes are seen in the subcutaneous tissue of the proximal left hip and thigh anteriorly along left thigh edema, likely a mass effect. Undescended right testicle is noted.

Musculoskeletal: Prominent focal region of intensely increased FDG uptake is seen in the posterior and lateral aspect of the left thigh (max SUV 4.87), corresponding to a heterogeneous appearing partially cystic/partially solid bilobed left thigh mass on unenhanced CT, with noted thickened walls and septations (Fig. 14.11). FDG uptake is mostly seen posteriorly in the solid component of this mass, while the more cystic/anterior regions of the mass demonstrate no abnormal FDG uptake.

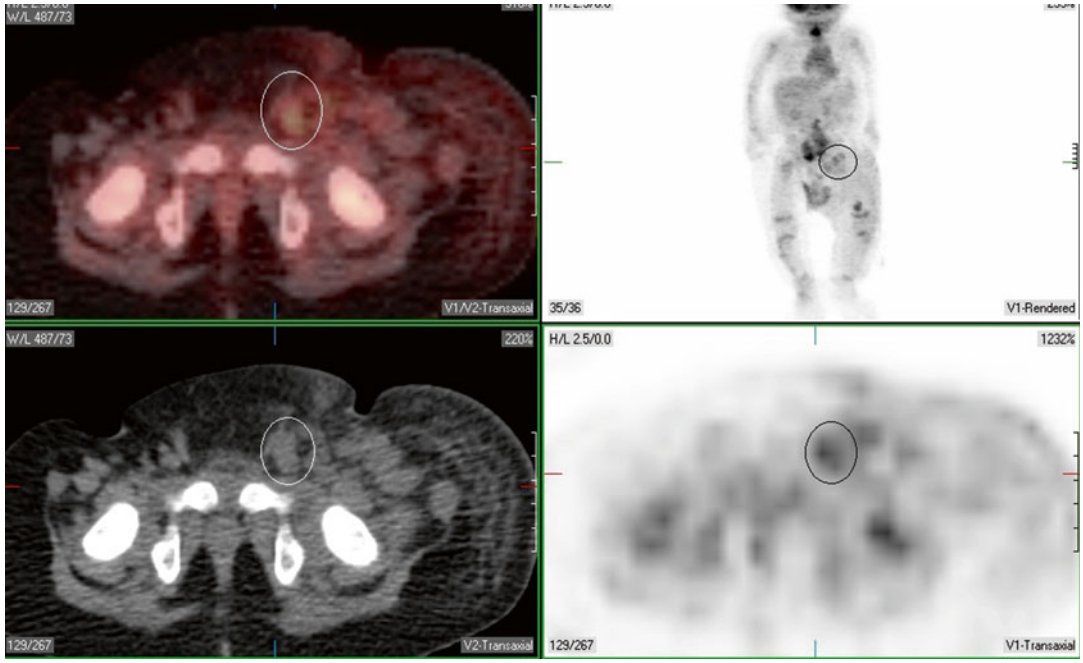

Fig. 14.10

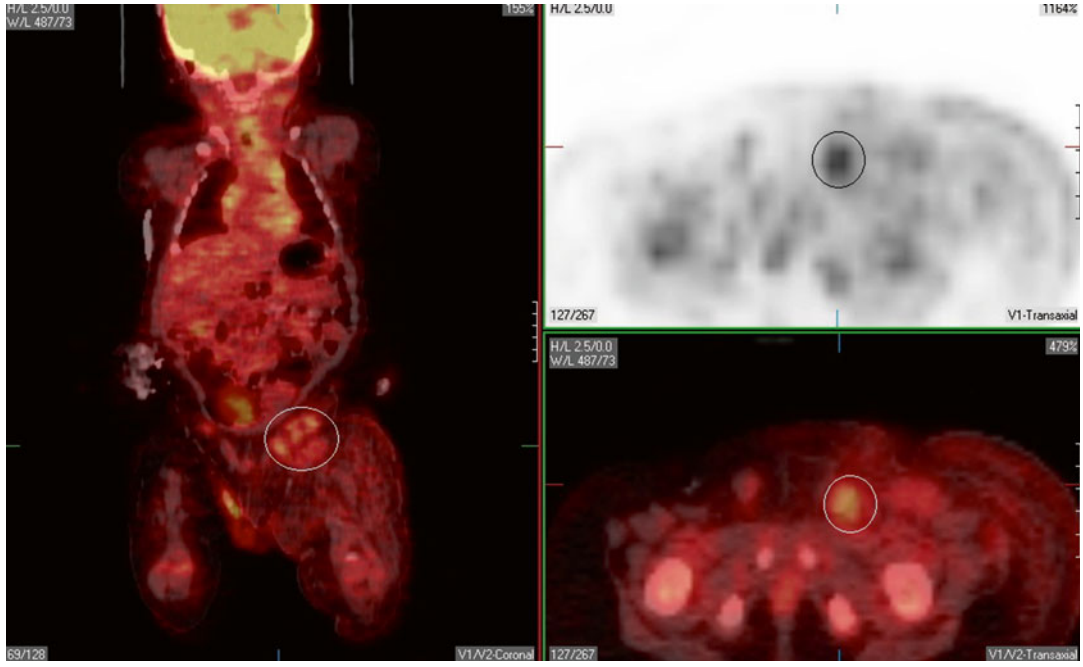

Fig. 14.11

Impression

1. PET/CT scan demonstrates moderately hypermetabolic left thigh mass, which likely represents uptake in the site of the patient's known rhabdomyosarcoma.
2. Moderately to intensely hypermetabolic likely disease-involved periaortic, left iliac, and left inguinal bulky adenopathy, with questionable mildly FDG-avid subcentimeter right-sided inguinal nodes.

Pearls and Pitfalls

1. High-grade sarcomas are generally more FDG-avid than low-grade lesions.
2. Comparing PET with the final clinical determination of disease extent, PET is 77 % sensitive and 95 % specific.

Discussion

PET/CT useful in depicting an unknown primary rhabdomyosarcoma and detecting unsuspected and unusual metastatic sites of childhood sarcomas. It was useful in monitoring response to chemotherapy, radiation therapy, and radiofrequency ablation and aided the postoperative evaluation of tumor resection sites.

^{18}F-fluorodeoxyglucose positron emission tomography (FDG PET) and FDG PET/computed tomography (CT) are becoming increasingly important imaging tools in the noninvasive evaluation and monitoring of children with known or suspected malignant diseases (Figs. 14.9, 14.10, and 14.11).

Case 14.6: Right Kidney Mass and History of Acute Lymphoid Leukemia

History

A 19-year-old female diagnosed with acute lymphoid leukemia as a child who has been in remission since treatment at that time. Recently, the patient reported right abdominal pain, and an abdominal CT reported a 2.8 cm × 2.3 cm × 2.3 cm heterogeneous hyperdense lesion which is partially exophytic in the right lower kidney.

Findings

Abdomen/pelvis: Focal FDG uptake in a 2.8 × 2.3 × 2.3 cm heterogeneous hyperdense lesion in the right lower kidney pole (Fig. 14.12). The SUV max of this lesion is 3.04 on initial whole-body images, and 3.56 on post void delayed spot images of this region (Fig. 14.13). No FDG-avid abdominal and/or pelvic lymph nodes are seen.

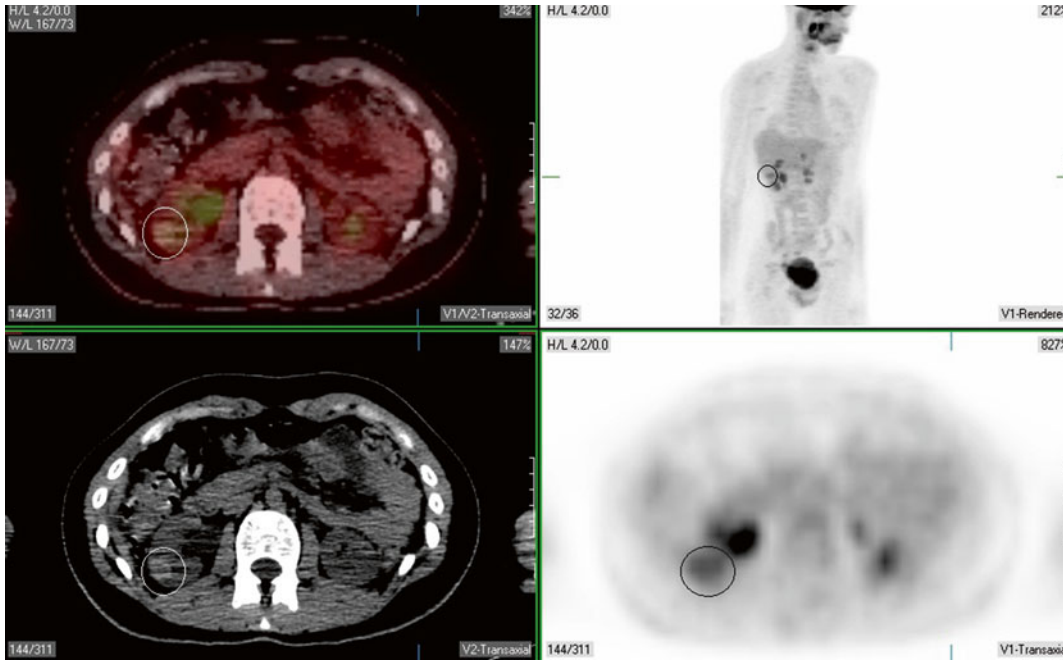

Fig. 14.12

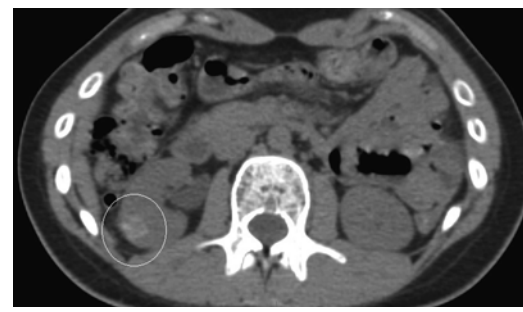

Fig. 14.13

Impression

PET/CT scan demonstrating focal FDG uptake in the right lower kidney pole lesion, which persists on post void/post Lasix augmentation images. Findings raise concern for significant pathology.

Pearls and Pitfalls

FDG PET detected all the sites of distant metastasis revealed by CT, as well as additional metastatic sites, leading to an accuracy of 94 % vs. 89 % for CT. Although PET is more sensitive than CT for the characterization of renal masses, it lacks specificity given a background of physiologic tracer-labeled urine. As such, if we are able to "drive out" all physiologic tracer-labeled urine, we can significantly improve the specificity of PET/CT for these tumors. As such, our now standard acquisition protocol involves injection of 15–20 mg of Lasix IV 25–30 min post FDG administration. Additionally, the acquisition protocol also includes a single post void "bed" of the kidneys, as patient ambulation has proved valuable in allowing gravity to contribute to renal pelvis evacuation.

Additionally, FDG PET has proven to be an efficient tool for the detection of distant metastasis in renal cancer, further suggesting its superiority over CT along. A selection process could be implemented to determine which patients should undergo PET. FDG PET could be performed in the event of a solitary metastasis or doubtful images on CT. Selection could also be based on adverse histological findings from nephrectomy specimens in order to perform staging early after nephrectomy.

Metastatic tumors or secondary lymphoma of the kidney are rare and can often be missed on conventional computed tomography (CT) imaging. On the other hand, many types of metastatic tumor or lymphoma can be detected clearly as hotspots of elevated uptake on FDG PET. However, excreted FDG present in the urinary tract mimics these findings and interferes with image reading. Careful investigation of the renal cortex by FDG PET and review of anatomical images, such as the findings of CT and MRI, have important roles in the detection of renal tumor.

Discussion

F-18 FDG PET may have a role in the diagnostic evaluation of patients with RCC and primary staging of disease. Positive F-18 FDG study may be predictive of the presence of RCC. However, a negative study does not exclude the RCC (Figs. 14.12 and 14.13).

Case 14.7: Chronic Respiratory Disease

History

A 5-year-old male child with reported history of idiopathic interstitial lung disease. The current study is performed to characterize the metabolic nature of areas of most notable inflammatory changes for future comparison to posttreatment scans.

Findings

Chest: The lungs appear hyperexpanded. High-resolution CT of the chest demonstrates diffuse patchy confluent areas of reticular opacities scattered throughout both lungs predominately seen at the lung bases and lower lobes (Fig. 14.14). Corresponding to the confluent reticular opacities is a varying range of mild to moderate intensely hypermetabolic FDG uptake on PET, suggesting metabolic uptake in an area of active inflammatory changes (Fig. 14.15). A region of interest was drawn around the most metabolically active region in the left lung base posteromedially, which demonstrated an SUV max of 1.5 (Fig. 14.16). Another area of curvilinear metabolically increased activity is seen peripherally in the left lower lung lobe with an SUV max of 1.64 (Fig. 14.17). Similarly, the most metabolically active region in the posteromedial right lung base was outlined and showed an SUV max of 1.91 (Fig. 14.18). A focal subcarinal region of

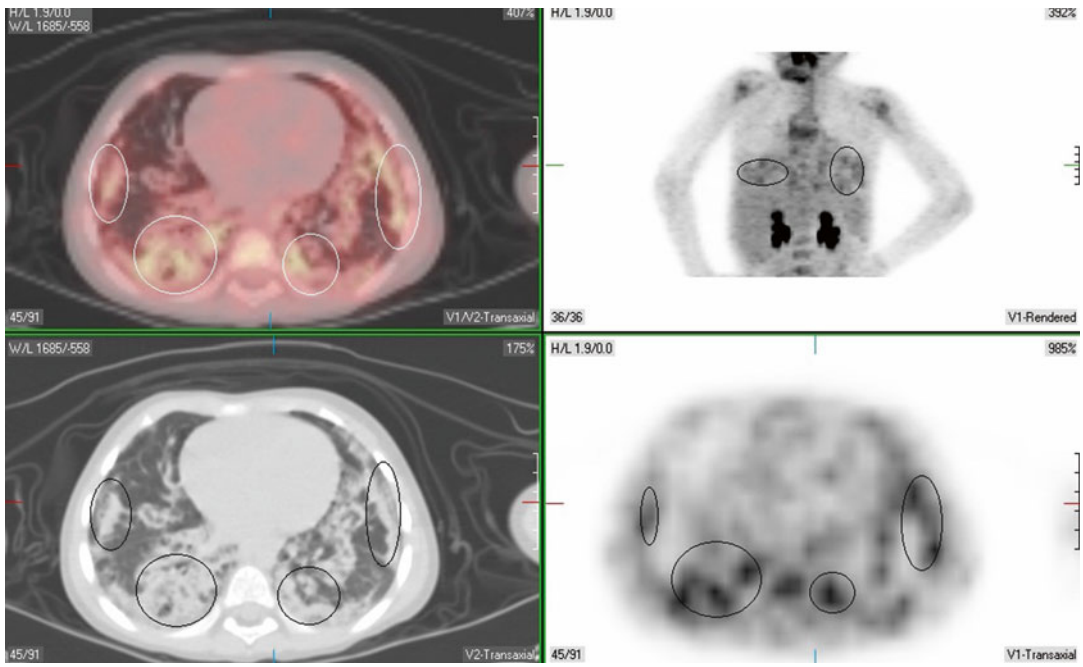

Fig. 14.14

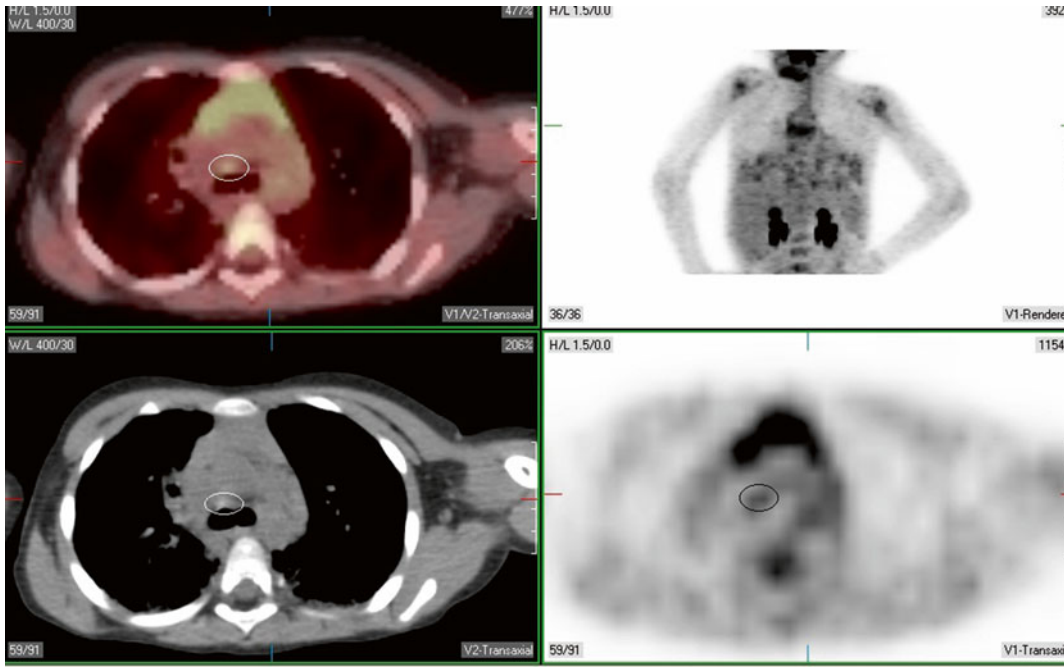

Fig. 14.15

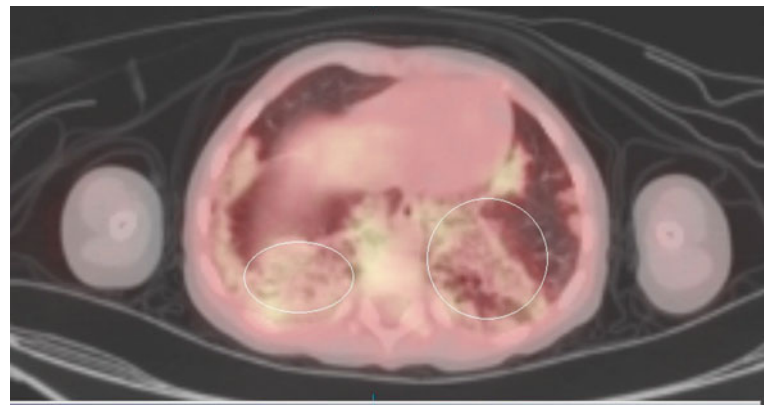

Fig. 14.16

intense FDG uptake is seen with an SUV max of 2.0. Tiny pneumatoceles are seen scattered throughout both lungs along with a few scattered subpleural cysts on unenhanced high-resolution chest CT. A 1.5 cm pneumatoceles is seen at the posterior right lower lung lobe on unenhanced CT, which demonstrates moderately intense FDG uptake on PET. High-resolution images demonstrate mostly parenchymal changes involving bilateral lower lung lobes without peribronchial thickening or bronchiectasis.

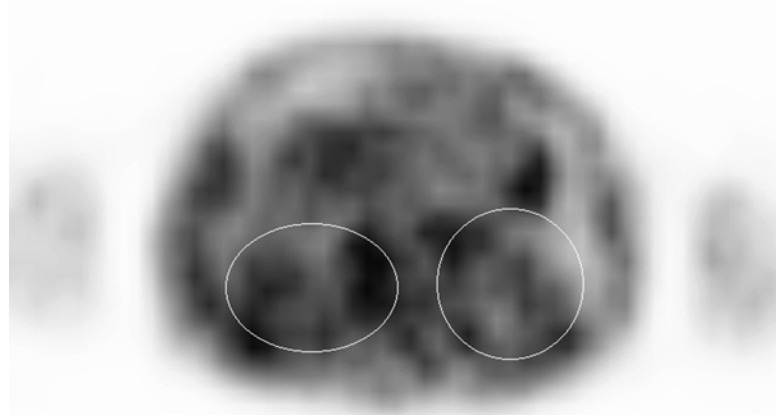

Fig. 14.17

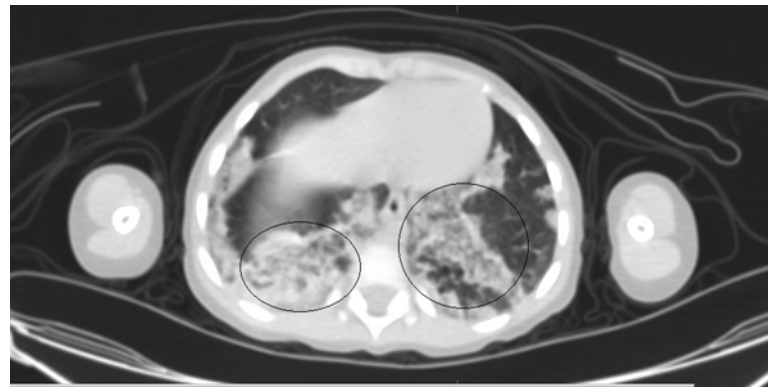

Fig. 14.18

Faint/mild FDG uptake is seen in a 7.0 mm precarinal node. Diffuse nonspecific/similar to background FDG uptake is seen symmetrically in bihilar regions on PET, although evaluation for hilar lymph node enlargement is limited by lack of contrast enhancement. There is no intensely hypermetabolic mediastinal or hilar lymphadenopathy. There are no hypermetabolic axillary lymph nodes. Normal FDG uptake is seen in the heart. Diffuse mild to moderate increased nonspecific likely age-related thymic FDG activity is seen. No pleural or pericardial effusion is seen.

Impression

PET/CT scan demonstrating varying degrees of mild to moderate FDG uptake corresponding to extensive mostly bibasilar lung parenchymal pulmonary opacities with some pneumatoceles and subpleural cysts. SUV max of the most metabolically active regions in both lung bases is as detailed above.

Pearls and Pitfalls

PET does not allow differentiation of IPF from a non-IPF diffuse interstitial pulmonary process.

Discussion

Lung (18)FDG uptake was considered to reflect a gravity-dependent tissue density in the normal lung. Though the lung (18)FDG uptake as well as the CT density tended to be higher in chronic ILD patients, it may be difficult to distinguish them in normal dependent regions from those related to chronic ILD in some cases.

Pulmonary 18F-FDG uptake predicts measurements of health and lung physiology in all patients with IPF and other forms of DPLD. 18F-FDG metabolism is higher when the site of maximal uptake corresponded to areas of reticulation/honeycomb on HRCT than to those with ground-glass patterns (Figs. 14.14, 14.15, 14.16, 14.17, and 14.18).

Case 14.8: Lymphoma

History

A 9-year-old male with recently diagnosed lymphoma. The current study is performed to scintigraphically stage the patient's disease.

Findings

Face/neck: Large bulky conglomerates of hypermetabolic adenopathy are seen involving both sides of the neck which likely represent disease-involved lymphadenopathy (Fig. 14.19).

The largest left neck mass in the posterior triangle measuring approximately $2.3 \times 2.6 \times 2.7$ cm on unenhanced CT, demonstrating an SUV max of 12.1 on PET. Additionally, a separate intensely hypermetabolic nodal mass is seen in the posterior lower left neck/left supraclavicular region measuring 2.3×1.1 cm on unenhanced, with an SUV max of 7.95.

On the right side, the largest nodal mass is seen along the jugular vein measuring $1.5 \times 1.7 \times 2.7$ cm on unenhanced CT demonstrating an SUV max of 10.01 (Fig. 14.20).

Diffuse mild enlargement of the soft tissue of the left posterior pharynx is seen on unenhanced CT with diffuse intensely increased FDG uptake on PET.

Asymmetric tonsillar FDG activity is seen significantly more prominent on the left, corresponding to a more prominent appearing left tonsil in comparison to the right on unenhanced CT. The SUV max on the left tonsil was seen to be 7.98 on PET, measuring 1.4 cm on unenhanced CT.

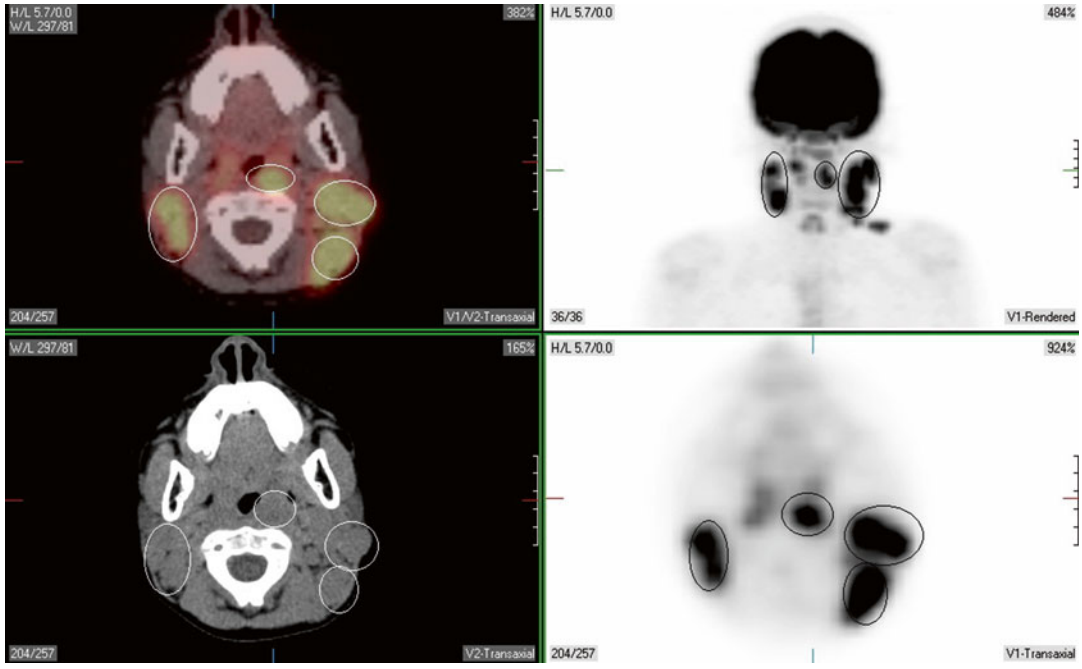

Fig. 14.19

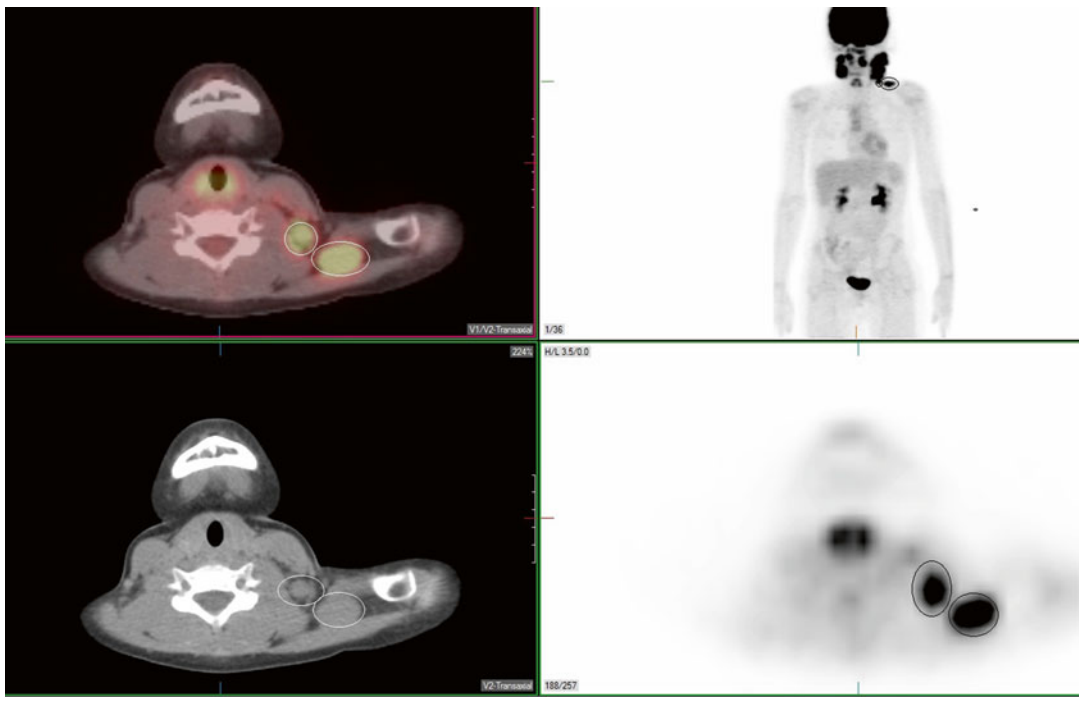

Fig. 14.20

Impression

1. PET/CT scan demonstrating bulky hypermetabolic bilateral cervical and left supraclavicular adenopathy, all of which are likely disease involved.
2. Findings concerning for disease involvement of the posterior pharynx and tonsils (left > right), as detailed above.

Pearls and Pitfalls

1. Overall sensitivities, specificities, and positive and negative predictive values were 78 %, 98 %, 94 %, and 90 % for F-18 FDG PET and 79 %, 88 %, 90 %, and 46 % for CT, respectively.
2. PET/CT scan with uptake greater than that of the liver is considered positive. Uptake that increased over the background but less than in the liver is equivocal.

Discussion

F-18 FDG PET imaging is a useful technique for the staging and follow-up of pediatric patients with lymphoma.

Negative PET/CT scan during routine follow-up for lymphoma in children strongly suggests absence of recurrence, but a positive PET/CT and diagnostic CT scans have low PPV and should be interpreted with caution (Figs. 14.19 and 14.20).

Case 14.9: Leiomyosarcoma

Clinical History

The patient is an 18 -year-old male with a history of metastatic leiomyosarcoma diagnosed in 2007. He has received several rounds of chemotherapy, with the most recent dose in May 2012. The PET scan is requested to evaluate response to therapy.

Findings

Head and Neck: There is a hypermetabolic 1.4 × 0.9 cm left level II lymph node, with a max SUV of 5.2 (Fig. 14.21).

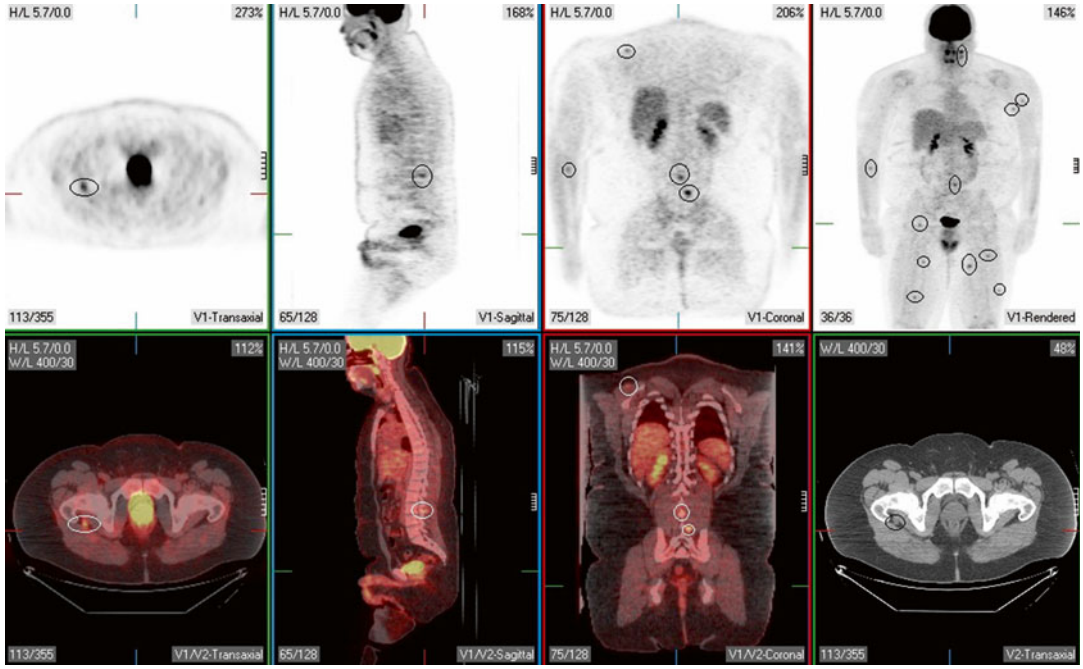

Fig. 14.21

Musculoskeletal System

A small focus in the right upper back posterior to the scapula in or adjacent to the right infraspinatus muscle has a max SUV of 3.5. Two foci are seen in the left upper arm in or adjacent to muscle; this area is suboptimally imaged on CT. Activity in the right upper medial forearm may represent tracer activity at the injection site.

There is a focus of intense activity associated with the paraspinous muscle at the L4 level on the left, max SUV 8.2. A 1×0.7 cm soft tissue density is seen in fat posterior to the right femoral neck, max SUV 5.3. A minimally active 5 mm subcutaneous soft tissue density in the right back at the L1/2 level is of uncertain significance.

Several foci are seen in the lower extremities bilaterally, including in the right upper posterior medial thigh in or adjacent to muscle, max SUV 4.4; a 1×0.6 cm soft tissue density in fat posterior to the right distal femur, max SUV 6.2; a small focus in the right tibialis posterior muscle, max SUV 5.5; a soft tissue density in the left upper anteromedial thigh in fat deep to the sartorius muscle, max SUV 5.1; in the left mid thigh in or closely adjacent to the femur anterolaterally, max SUV 4.7; in the left lateral thigh in muscle; posterior to the left lower femur in or adjacent to muscle; and in muscle in the left medial foot, max SUV 4.0.

Several foci of abnormal activity are seen in bone. The most active (max SUV 8.2) is associated with an approximately 1.2×0.7 cm destructive bone lesion medially in the head of the left mandible. In the right mandible, there is a tiny focus (max SUV 5.3) medially adjacent to the

most posterior molar. Other foci include in the left posterolateral elements of C5 (max SUV 4.9) and in the right side of the spinous process of L3 (max SUV 4.8).

Impression

1. PET/CT imaging demonstrates numerous foci of abnormal tracer uptake in soft tissue of the torso, arms, legs, and left foot and in bone, including in the left and right mandibular heads, the posterolateral elements of c5, the l3 spinous process, and possibly a small focus in the left mid femur.
2. Prominent hypermetabolic left level II lymph node worrisome for malignant involvement.

Pearls and Pitfalls

FDG PET is considered as a useful tool in differentiating a benign lesion from a malignant lesion from benign. However, FDG PET scan was not able to correctly distinguish leiomyosarcoma from benign characteristic of nodular fasciitis. The SUV max in the nodular fasciitis was as high as 7. High glucose uptake in benign lesions was unusual because they normally grow more slowly and are metabolically less active. Why does nodular fasciitis, a benign tumor, has such high FDG uptake? The rapid growth, rich cellularity, and high mitotic activity.

Discussion

FDG PET correctly detected disease in patients with anaplastic thyroid cancer, pleural mesothelioma, myxoid liposarcoma, malignant fibrous histiocytoma, synovial cell sarcoma, and uterine leiomyosarcoma. These findings suggest that PET is useful in the evaluation of a variety of rare tumors both for initial preoperative staging and post-therapy assessment. FDG PET can identify both local and distant recurrences of tumor as a one-step procedure and will detect other metastases (Fig. 14.21).

Case 14.10: Epithelial Malignant Neoplasm

History

The patient is an 18-year-old female with liver cancer (epithelial malignant neoplasm, NOS).

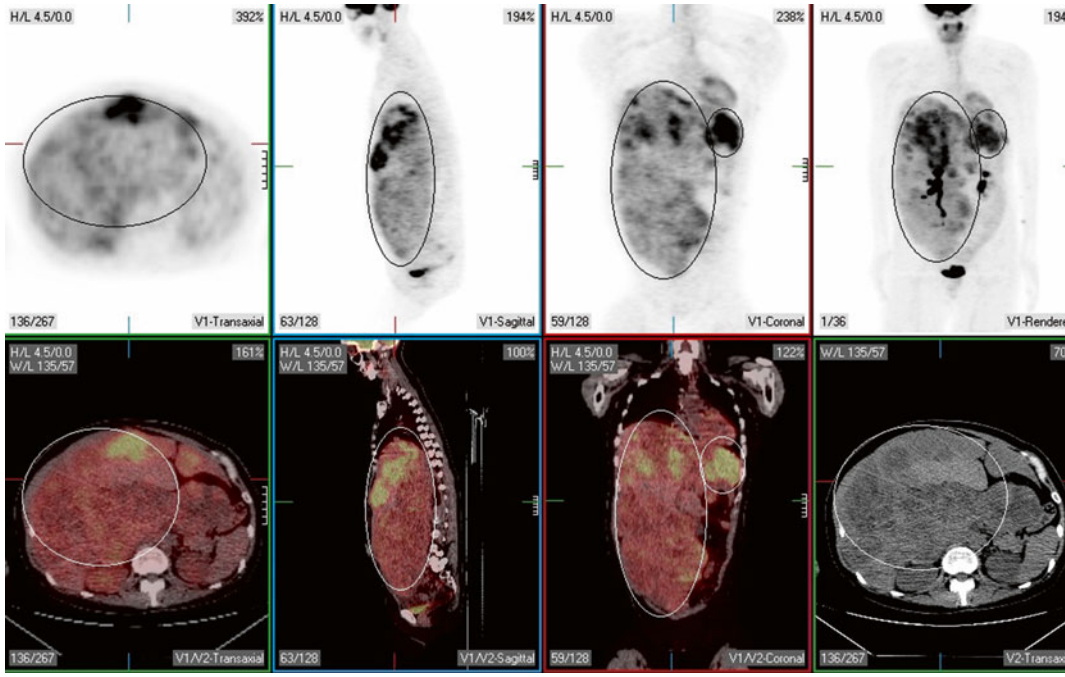

Fig. 14.22

Findings

Abdomen/Pelvis: The liver is studded with numerous hypermetabolic lesions in both lobes corresponding to large confluent hypoattenuating lesions (Fig. 14.22). For reference purposes, the lesion in the anterior right hepatic lobe (segment IV with SUV max of 6.03) and the lesion in the left lateral segment at the same level have an SUV max of 5.0. The spleen measures approximately 9.2 cm.

Impression

PET/CT scan demonstrating numerous large hypermetabolic bilobed hepatic lesions.

Pearls and Pitfalls

1. Data suggests that FDG PET imaging may be able to effectively monitor the efficacy of regional therapy to hepatic metastases. FDG PET is more accurate than lipiodol retention on CT in predicting the presence of residual viable tumor. The presence of residual uptake in some lesions can help in guiding further regional therapy.

2. The sensitivity of FDG PET for detection of HCC is 64 %. A correlation was found between the degree of FDG uptake and the grade of malignancy. Therefore, FDG imaging may have a prognostic significance in the evaluation of patients with HCC. HCCs that accumulate FDG are associated with markedly elevated alpha-fetoprotein levels. However, FDG PET has limited value for the differential diagnosis of focal liver lesions in patients with chronic hepatitis C virus infection because of the low sensitivity for detection of HCC and the high prevalence of this tumor in that population of patients.

Discussion

Ninety percent of malignant primary liver tumors are tumors from epithelial origin: hepatocellular carcinoma (HCC) and cholangiocarcinoma. FDG PET detects only 50–70 % of HCC, but has a sensitivity greater than 90 % for all other primary (cholangiocarcinoma and sarcoma) and metastatic tumors to the liver. FDG PET imaging appears helpful to differentiate malignant from benign hepatic lesions, with the exception of false-negative HCC, false-negative infiltrating cholangiocarcinoma, and false-positive inflammatory lesions. It is not helpful to identify HCC in patients with cirrhosis and regenerating nodules. In patients with hepatic primary malignant tumors trapping FDG, FDG PET imaging does identify unexpected distant metastases (although miliary carcinomatosis is often false negative) and can help in monitoring therapy. Scintigraphic tumor detectability depends on both the size of the lesion and the degree of uptake, as well as surrounding background uptake and intrinsic resolution of the imaging system. Small lesions may yield false-negative results which can be due to partial volume averaging, leading to underestimation of the uptake in small lesions (Fig. 14.22).

Case 14.11: Brown Fat

Findings

Extensive uptake in the neck corresponding to brown fat uptake (Fig. 14.23).

Pearls and Pitfalls

1. Combined ^{18}F FDG PET/CT provides precise anatomic correlation, which allows differentiation between ^{18}F FDG uptake corresponding to fat-attenuation tissue at CT and uptake from pathologic causes.
2. Brown fat ^{18}F FDG uptake can also be avoided by administering diazepam, fentanyl, or propanolol prior to injection.

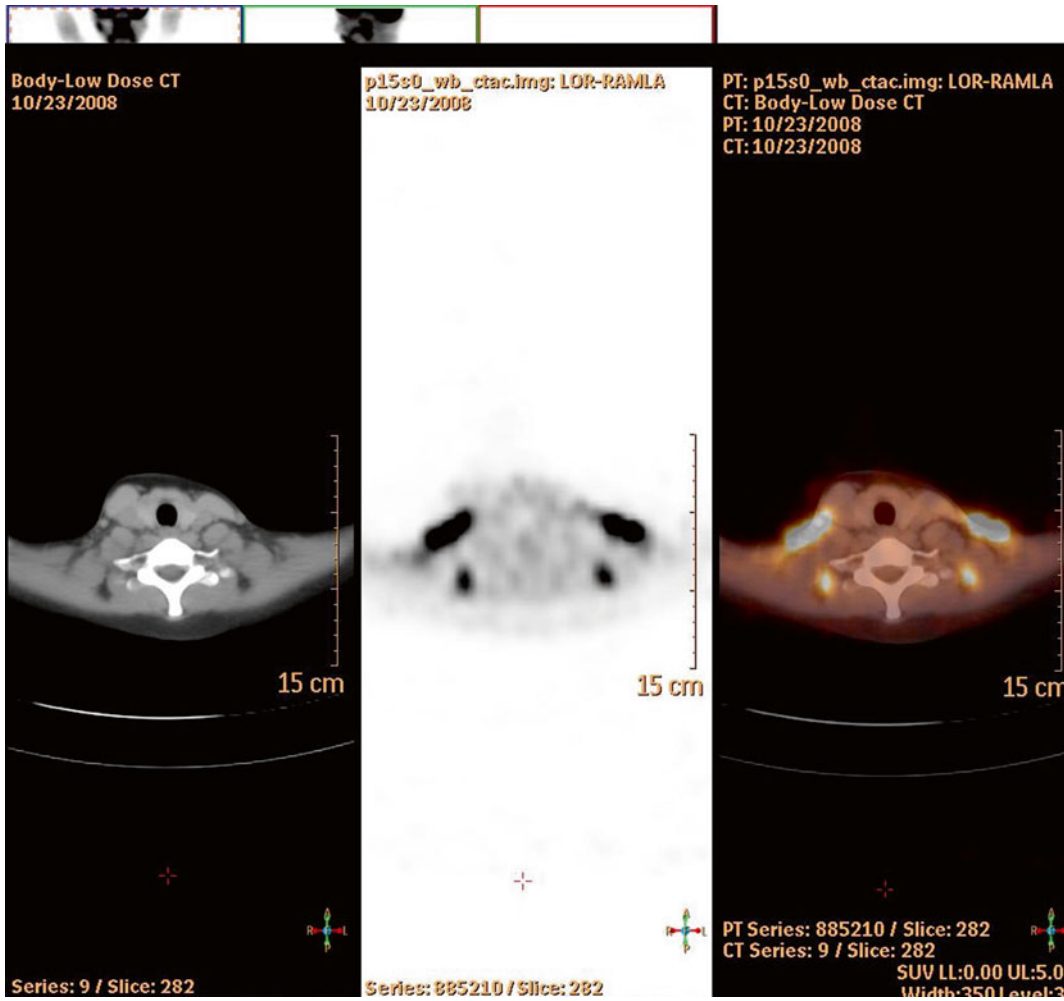

Fig. 14.23

Discussion

The development of PET/CT has led to the recognition that metabolically active fat, referred to as brown fat, can accumulate FDG and represents a possible source of false-positive scans in oncology patients. Physiologic high uptake can be observed along the distribution of activated brown adipose tissue in the neck, supraclavicular regions, axillae, mediastinum, and paravertebral and perinephric regions. Uptake of ^{18}F FDG, a glucose analog, occurs when glucose transporters in brown adipose tissue have been activated. Since the introduction of PET, physiologic ^{18}F FDG uptake in activated brown adipose tissue has been known to be a source of false-positive results. ^{18}F FDG uptake in brown fat is typically bilateral and symmetric. However, focal and asymmetric uptake can occur in the neck or mediastinum, leading to false-positive results. Combined ^{18}F FDG

PET/CT provides precise anatomic correlation, which allows differentiation between ^{18}F FDG uptake corresponding to fat-attenuation tissue at CT and uptake from pathologic causes. Uptake in brown fat is more common in children than in adults and is most common during the winter. Warming the patient prior to injection and during the uptake phase is a simple approach that is used routinely at our institution to reduce brown fat uptake. Brown fat ^{18}F FDG uptake can also be avoided by administering diazepam, fentanyl, or propanolol prior to injection (Fig. 14.23).

Case 14.12: Normal Thymus

Findings

Normal thymic uptake (Fig. 14.24).

Pearls and Pitfalls

Both the higher metabolic activity of the thymus in the first years of life to puberty and the known phenomenon of the occurrence of thymus hyperplasia after chemotherapy were considered.

Discussion

The thymus is a lymphoid organ and endocrine gland responsible for directing and stimulating the adaptive immune system. The thymus gland is located in the superior and anterior mediastinum, behind the sternum. Thymus shape and size demonstrate marked age-related and interindividual variability on ultrasonographic (US), computed tomographic (CT), and magnetic resonance (MR) imaging studies, particularly in early childhood. The thymus is disproportionately large in infants and gradually undergoes involution with fatty replacement by adolescence or early adulthood. The normal thymus is typically triangular or bilobed in shape with homogeneous parenchyma and absence of mass effects on adjacent structures. The thymus responds to systemic stress related to infection, neoplasm, chemotherapy, and surgery by rapid atrophy. Once the stressful event has ended, the thymus may regrow to its original size and beyond. In patients with malignant mediastinal tumors, the thymus typically regresses during chemotherapy, with possible rebound enlargement after completion of therapy (Fig. 14.24).

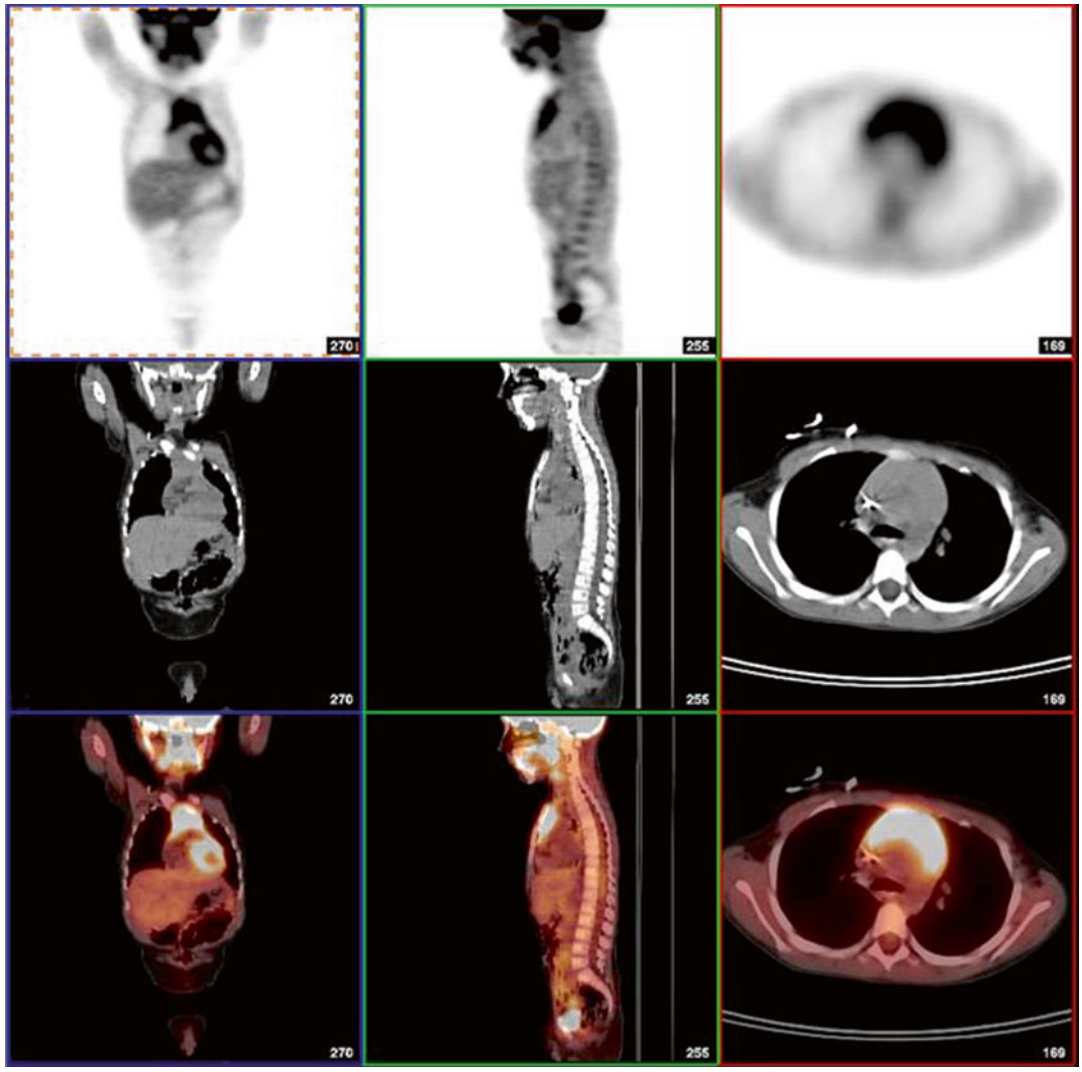

Fig. 14.24

Case 14.13: Pediatric Lymphoma

Findings

Uptake in multiple left lymph nodes (Fig. 14.25). Biopsy was consistent with Hodgkin's lymphoma.

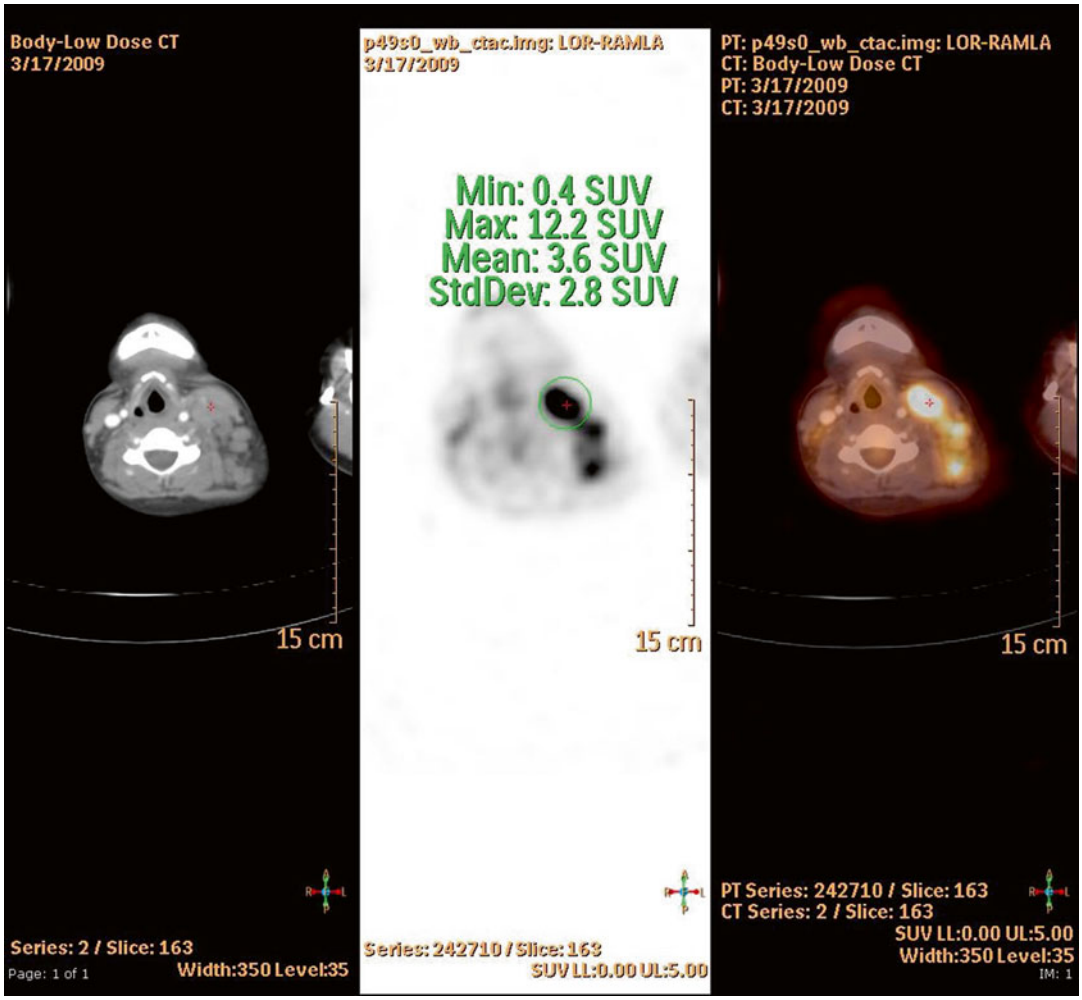

Fig. 14.25

Pearls and Pitfalls

Bone marrow biopsy is the reference standard for BMI; it can miss localized disease outside the site of bone marrow biopsy. FDG PET/CT may be used at initial staging of pediatric lymphoma as it may uncover unsuspected bone marrow involvement.

Discussion

PET/CT in pediatric lymphoma is more accurate than other imaging modalities for initial staging, evaluating treatment response and follow-up (Fig. 14.25).

Case 14.14: NUT Midline Carcinoma

Findings

Uptake in chest corresponds to the patient's primary NUT midline carcinoma (Fig. 14.26). There are also osseous metastases to the humeri, spine, femurs, and tibias (Fig. 14.27).

Discussion

NUT midline carcinoma is a very rare, poorly differentiated, highly aggressive cancer originating from midline body locations, most often in

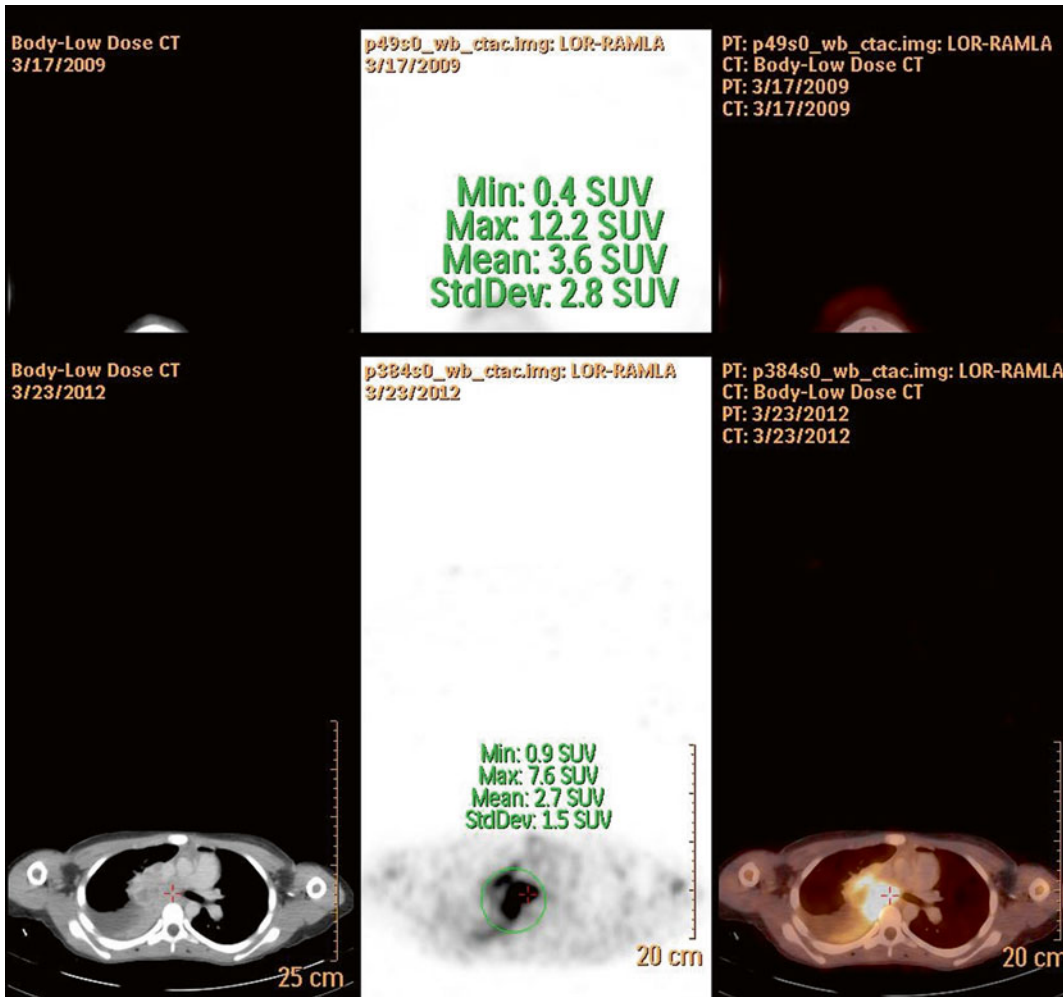

Fig. 14.26

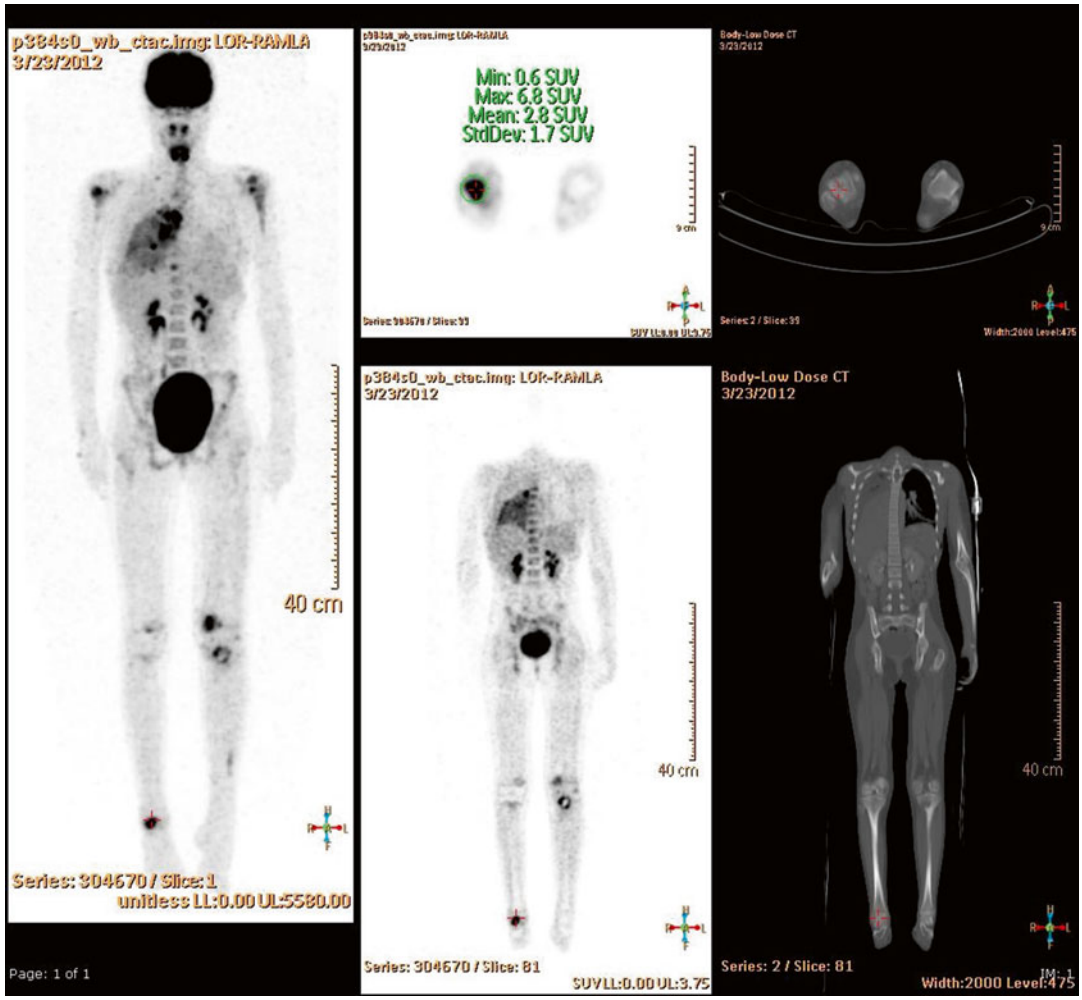

Fig. 14.27

adolescents or young adults. Advanced local disease and distant hematogenous metastases are typical. NMC is genetically defined by chromosomal rearrangements of the NUT gene on chromosome 15q14 forming a BRD4-NUT fusion oncogene which blocks epithelial differentiation, resulting in uncontrolled cell growth (Figs. 14.26 and 14.27).

Case 14.15: Recurrent Left Frontal Anaplastic Astrocytoma

Findings

Arrows point to a recurrent left frontal anaplastic astrocytoma (Fig. 14.28).

Discussion

High-grade gliomas (HGG)—glioblastoma multiforme (GBM), anaplastic astrocytoma, oligodendroglioma, and oligoastrocytoma—nearly always recur, with median overall survival (OS) ranging from 4 to 8 months from the time of progression (Fig. 14.28).

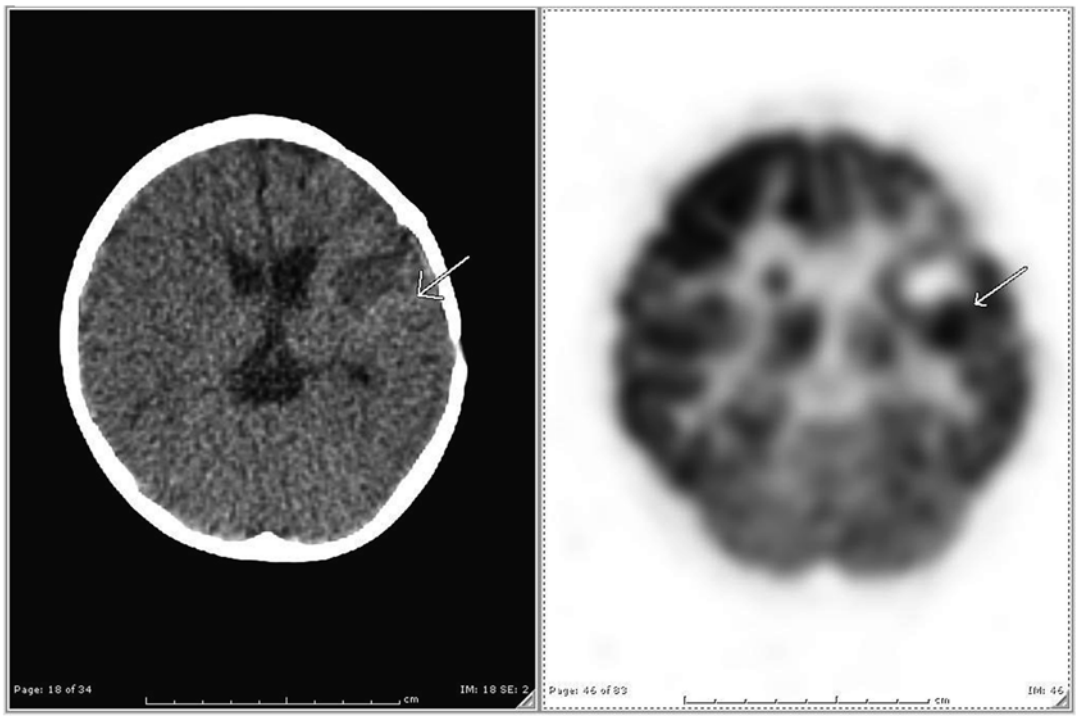

Fig. 14.28

Case 14.16: Ewing Sarcoma

Findings

There is increased uptake corresponding to the sclerotic lesion in the distal right tibia (Fig. 14.29).

Discussion

Ewing sarcoma family tumors account for approximately 3 % of all pediatric cancers, making them the second most common bone malignancies in children and adolescents. Radiologic evaluation of Ewing sarcoma can help detect and accurately assess the extent of disease prior to treatment, determine whether metastatic or recurrent disease is present, and monitor therapy response (Fig. 14.29).

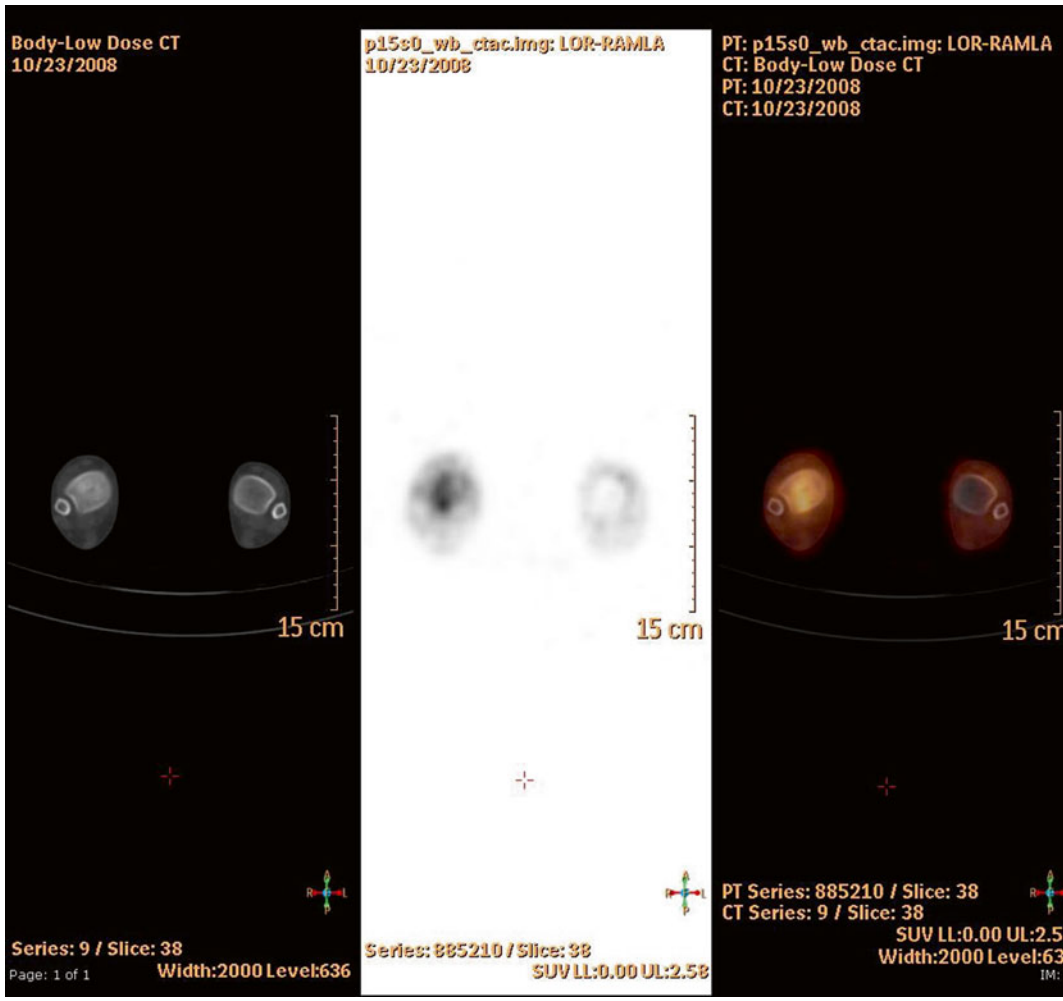

Fig. 14.29

Case 14.17: Posttransplant Lymphoproliferative Disorder

Findings

There is a soft tissue mass with FDG uptake in the right pelvis adjacent to the patient's transplanted kidney (Fig. 14.30).

Discussion

Posttransplant lymphoproliferative disease (PTLD) is a severe complication after solid organ or bone marrow transplantation. In pediatric transplant recipients, PTLD is the most common malignancy (Fig. 14.30).

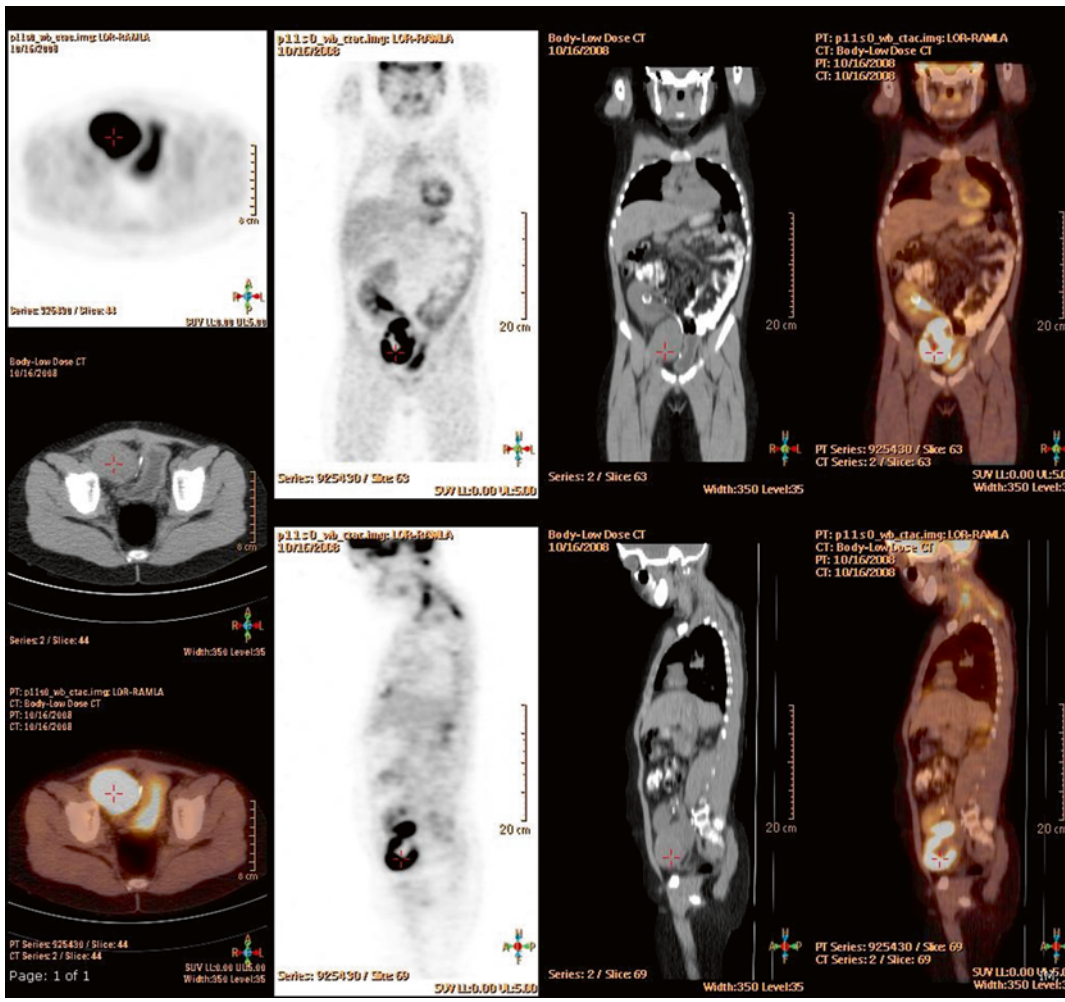

Fig. 14.30

Suggested Reading

1. Agrawal K, Mittal B, Harisankar C, Kuruva M, Bhattacharya A, Bansal D, Trehan A, Marwaha RK. Can F-18 FDG PET/CT avoid bone marrow biopsy in pediatric Hodgkin's lymphoma? India J Nucl Med. 2011;52 Suppl 1:399.
2. Aide N, Cappele O, Bottet P, Bensadoun H, Regeasse A, Comoz F, Sobrio F, Bouvard G, Agostini D. Efficiency of [(18)F] FDG PET in characterising renal cancer and detecting distant metastases: a comparison with CT. Eur J Nucl Med Mol Imaging. 2003;30(9):1236–45.
3. Ak I, Can C. F-18 FDG PET in detecting renal cell carcinoma. Acta Radiol. 2005;46(8):895–9.
4. Becherer A, Vierhapper H, Pötzi C, Karanikas G, Kurtaran A, Schmaljohann J, Staudenherz A, Dudczak R, Kletter K. FDG-PET in adrenocortical carcinoma. Cancer Biother Radiopharm. 2001;16(4):289–95.
5. Bestic JM, Peterson JJ, Bancroft LW. Use of FDG PET in staging, restaging, and assessment of therapy response in Ewing sarcoma. RadioGraphics. 2009;29:1487–500.
6. Brink I, Reinhardt MJ, Hoegerle S, Altehoefer C, Moser E, Nitzsche EU. Increased metabolic activity in the thymus gland studied with 18F-FDG PET: age dependency and frequency after chemotherapy. J Nucl Med. 2001;42(4):591–5.
7. Choi JY, Lee KS, Kim H-J, Shim YM, Kwon OJ, Park K, Baek C-H, Chung JH, Lee K-H, Kim B-T. Focal thyroid lesions incidentally identified by integrated ^{18}F-FDG PET/CT: clinical significance and improved characterization. J Nucl Med. 2006;4:609–15.
8. Clarke JR, Brglevska S, Lau EW, Ramdave S, Hicks RJ. Atypical brown fat distribution in young males demonstrated on PET/CT. Clin Nucl Med. 2007;32(9):679–82.
9. Coccia P, Ruggiero A, Rufini V, Maurizi P, Attiná G, Riccardo M, Natale L, Leccisotti L, Calcagni ML, Riccardi R. Cardiac metastases of Ewing sarcoma detected by 18F-FDG PET/CT. J Pediatr Hematol/Oncol. 2012;34(3):236–8.
10. Delbeke D, Martin W. Update of PET and PET/CT for hepatobiliary and pancreatic malignancies. HBP. 2005;7(3):166–79.
11. Freudenberg LS, Antoch G, Jentzen W, Pink R, Knust J, Görges R, Müller SP, Bockisch A, Debatin JF, Brandau W. Value of ^{124}I-PET/CT in staging of patients with differentiated thyroid cancer. Eur Radiol. 2004;14:2092–8.
12. Gawande RS, Khurana A, Messing S, Zhang D, Castañeda RT, Goldsby RE, Hawkins RA, Daldrup-Link HE. Differentiation of normal thymus from anterior mediastinal lymphoma and lymphoma recurrence at pediatric PET/CT. Radiology. 2012;262(2):613–22.
13. Groves AM, Win T, Screaton NJ, Berovic M, Endozo R, Booth H, Kayani I, Menezes LJ, Dickson JC, Ell PJ. Idiopathic pulmonary fibrosis and diffuse parenchymal lung disease: implications from initial experience with 18F-FDG PET/CT. J Nucl Med. 2009;50(4):538–45.
14. Hernandez-Pampaloni M, Takalkar A, Yu JQ, Zhuang H, Alavi A. F-18 FDG-PET imaging and correlation with CT in staging and follow-up of pediatric lymphomas. Pediatr Radiol. 2006;36(6):524–31.
15. Hudson MM, Krasin MJ, Kaste SC. PET imaging in pediatric Hodgkin's lymphoma. Pediatr Radiol. 2004;34(3):190–8.
16. Inoue K, Okada K, Taki Y, Goto R, Kinomura S, Fukuda H. (18)FDG uptake associated with CT density on PET/CT in lungs with and without chronic interstitial lung diseases. Ann Nucl Med. 2009;23(3):277–81.

17. Jadvar H, Fischman AJ. Evaluation of rare tumors with [F-18] Fluorodeoxyglucose positron emission tomography. Clin Positron Imaging. 1999;2(3):153–8.
18. Kabickova E, Sumerauer D, Cumlivska E, Drahokoupilova E, Nekolna M, Chanova M, Hladikova M, Kodet R, Belohlavek O. Comparison of ^{18}F-FDG-PET and standard procedures for the pretreatment staging of children and adolescents with Hodgkin's disease. Eur J Nucl Med Mol Imaging. 2006;33(9):1025–31.
19. Kaneta T, Hakamatsuka T, Yamada T, Takase K, Sato A, Higano S, Kinomura S, Fukuda H, Takahashi S, Yamada S. Case Report: FDG PET in solitary metastastic/secondary tumor of the kidney: a report of three cases and a review of the relevant literature. Ann Nucl Med. 2006;20(1):79–82.
20. London K, Cross S, Onikul E, Dalla-Poza L, Howman-Giles R. 18F-FDG PET/CT in paediatric lymphoma: comparison with conventional imaging. Eur J Nucl Med Mol Imaging. 2011;38(2):274–84.
21. Louis DN, Ohgaki H, Wiestler OD, et al. The 2007 WHO classification of tumours of the central nervous system. Acta Neuropathol. 2007;114:97–109.
22. Lucas JD, O'Doherty MJ, Wong JC, Bingham JB, McKee PH, Fletcher CD, Smith MA. Evaluation of fluorodeoxyglucose positron emission tomography in the management of soft-tissue sarcomas. J Bone Joint Surg Br. 1998; 80(3):441–7.
23. Ludwig JA. Ewing sarcoma: historical perspectives, current state-of-the-art, and opportunities for targeted therapy in the future. Curr Opin Oncol. 2008;20(4):412–8.
24. Mackie GC, Shulkin BL, Ribeiro RC, Worden FP, Gauger PG, Mody RJ, Connolly LP, Kunter G, Rodriguez-Galindo C, Wallis JW, Hurwitz CA, Schteingart DE. Use of [^{18}F]Fluorodeoxyglucose positron emission tomography in evaluating locally recurrent and metastatic adrenocortical carcinoma. J Clin Endocrine Metab. 2006;91:2665–71.
25. Makis W, Lisbona R, Derbekyan V. Hodgkin lymphoma post-transplant lymphoproliferative disorder following pediatric renal transplant: serial imaging with F-18 FDG PET/CT. Clin Nucl Med. 2010;35(9):704–5.
26. McCarville MB, Christie R, Daw NC, Spunt SL, Kaste SC. PET/CT in the evaluation of childhood sarcomas. Am J Roentgenol. 2005;184(4):1293–304.
27. Mirzaei S, Knoll P, Kohn H. Diagnosis of recurrent astrocytoma with fludeoxyglucose F18 PET scanning. NEJM. 2001;344:2030–1.
28. Niederkohr RD, Cameron MJ, French CA. FDG PET/CT imaging of NUT midline carcinoma. Clin Nucl Med. 2011;36(9):e124–6.
29. Nusair S, Rubinstein R, Freedman NM, Amir G, Bogot NR, Izhar U, Breuer R. Positron emission tomography in interstitial lung disease. Respirology. 2007;12(6):843–947.
30. Rhodes MM, Delbeke D, Whitlock JA, Martin W, Kuttesch JF, Frangoul HA, Shankar S. Utility of FDG-PET/CT in follow-Up of children treated for Hodgkin and Non-Hodgkin lymphoma. J Pediatr Hematol Oncol. 2006; 28(5):300–6.
31. Riad R, Omar W, Kotb M, Hafez M, Sidhom I, Zamzam M, Zaky I, Abdel-Dayem H. Role of PET/CT in malignant pediatric lymphoma. Eur J Nucl Med Mol Imaging. 2010;37(2):319–29.
32. Sahani DV, Kalva SP. Imaging the liver. The Oncologist. 2004;9(4):385–97.
33. Shammas A, Lim R, Charron M. Pediatric FDG PET/CT: physiologic uptake, normal variants, and benign conditions. RadioGraphics. 2009;29:1467–86.
34. Shammas A, Degirmenci B, Mountz JM, McCook BM, Branstetter B, Bencherif BB, Joyce JM, Carty SE, Kuffner HA, Avril N. ^{18}F-FDG PET/CT in patients with suspected recurrent or metastatic well-differentiated thyroid cancer. J Nucl Med. 2007;48(2):221–6.

35. Tateishi U, Hosono A, Makimoto A, Nakamoto Y, Kaneta T, Fukuda H, Murakama K, Terauchi T, Suga T, Inoue T. Comparative study of FDG PET/CT and conventional imaging in the staging of rhabdomyosarcoma. Ann Nucl Med. 2009;23(2):155–61.
36. von Falck C, Maecker B, Schirg E, Boerner AR, Knapp WH, Klein C, Galanski M. Post transplant lymphoproliferative disease in pediatric solid organ transplant patients: a possible role for [^{18}F]-FDG-PET(/CT) in initial staging and therapy monitoring. Eur J Radiol. 2007;63:427–35.
37. Wang K-B, Tsai S-C, Chen Y-C. A possible musculoskeletal pitfall in 18F-FDG PET: nodular fascitis. Ann Nucl Med Sci. 2010;23:165–8.
38. Yun M, Kim W, Alnafisi N, Lacorte L, Jang S, Alavi A. ^{18}F-FDG PET in characterizing adrenal lesions detected on CT or MRI. J Nucl Med. 2001; 42(12):1795–9.

15 Myocardial Viability

Shahram Bonyadlou and Sindu Sheth

FDG Viability Scintigraphy

Introduction

Among all methodologies in the diagnosis of hibernating myocardium, ^{18}F-FDG PET has remained a significant diagnostic tool. In combination with myocardial perfusion scintigraphy, FDG PEt allows differentiation between scar and viable myocardium and extent of disease with remarkable certainty. This leads to appropriate patient selection for invasive revascularization procedure. FDG PET has also been helpful in patients with diagnosis of cardiac sarcoidosis and evaluation of patients with cardiomyopathy for resynchronization therapy or who are being considered for revascularization or heart transplant.

Overview

Normal myocardium utilizes free fatty acids or glucose to generate energy. Under aerobic conditions, free fatty acids are the main sources of energy unless there is circulating insulin to facilitate glucose consumption. During severe ischemia (viable), myocardium switches to anaerobic metabolism, utilizing glucose as the sole source of energy. Therefore, ^{18}F-FDG PET will detect an ischemic myocardium (hibernating).

Technique

Perhaps the most important factor in obtaining a quality image is patient preparation. The following protocol has been successfully implemented in our institution.

P.S. Conti, A. Kaushik (eds.), *PET-CT*, DOI 10.1007/978-1-4419-5811-2_15

[^{18}F]-FDG Cardiac Viability Imaging Protocol

Scheduling Considerations

A resting myocardial perfusion study must be obtained within the month prior to the PET scan, and there must be no change in the patient's clinical status between the perfusion scan and the viability scan.

Patient Preparation

Obtain patient history including allergies, risk factor, diabetes, medication, known cardiovascular therapy, and prior cardiovascular tests (echocardiography, SPECT, MRI, or invasive coronary angiography).

The patient must have a resting myocardial perfusion scintigraphy (thallium, Myoview/MIBI, or rubidium) prior to viability scintigraphy.

Glucose management for diabetic cardiac patients is individually reviewed by the nuclear medicine physician, radiologist, or nurse. However, generally diabetic patients are instructed to eat a high-protein/low-carbohydrate dinner the evening before the scan. Diabetics using oral hypoglycemic agents are asked to take the normal dose of medication and no breakfast the day of the study (early morning schedule).

If the study must be scheduled for the afternoon, the patient is instructed to eat a high-protein/low-carbohydrate light breakfast, take a full dose of morning hypoglycemic agent or insulin, and abstain from eating lunch.

Tube feeding and intravenous dextrose solution must be placed on hold 3–6 h prior to study. Nicotine and caffeine consumption must be held 24 h prior to viability scintigraphy.

Radiopharmaceutical Dosage

Adult dose: ^{18}F-FDG 10–20 mCi IV or 0.22 mCi/kg.

Pediatric dose: adjusted pediatric dose schedule = (0.14–0.21 mCi) [^{18}F] IV not to exceed 10 mCi.

Clinical Imaging Procedure

1. Height, weight, and blood glucose are measured. An intravenous catheter is placed and left throughout the study.
2. Cardiac monitoring.
3. Obtain serum fasting blood glucose (BG).
4. Glucose is administered PO.
5. **Nondiabetic**

Oral glucose loading:

(a)	If BG < or = 150 mg/dl	50 g oral glucose + regular insulin 3 units IV
(b)	If BG 151–300 mg/dl	regular insulin 5 units IV
(c)	If BG 301–400 mg/dl	regular insulin 7 units IV
(d)	If BG > 400 mg/dl	consult physician

IV glucose loading (if unable to load PO): see below

FDG administration: After glucose load and sliding scale insulin injections, administer F-18 FDG at least **45 min** after glucose loading and when BG < or = 150 mg/dl.

6. **Diabetic**
   Oral glucose loading:

(a)	If BG < or = 150 mg/dl	25 g oral glucose
(b)	If BG 151–180 mg/dl	regular insulin 5 units IV
(c)	If BG 181–200 mg/dl	regular insulin 7 units IV
(d)	If BG 201–300 mg/dl	regular insulin 12 units IV
(e)	If BG > 400 mg/dl	consult physician

IV glucose loading (if unable to load PO): see below

FDG administration: After glucose load and sliding scale insulin injections, administer F-18 FDG at least **60 min** after glucose loading and when BG ≤ 150 mg/dl.

7. 15 min following administration of oral glucose load, obtain blood glucose level and repeat every 15 min and administer IV regular insulin as per above protocol.
8. Residual activity in the syringe and tubing is assayed and used to determine the actual administered activity.
9. Following uptake period, the patient is transferred to the imaging table.
10. The patient is positioned with their arms up (preferred) or at their side. Scout images are acquired to determine position and whether there is adequate FDG uptake in the myocardium.
11. Routine cardiac imaging should not begin sooner than 40 min post injection. If myocardial uptake is still negligible after 40 min, the nuclear medicine physician must be notified.
12. The blood glucose level must be >80 mg/dl prior to discharge. The patient will be observed for signs of hypoglycemia during the entire procedure while in the PET center. If blood sugar is ever less than 80 mg/dl after insulin administration, start D5W @ 100 cm^3/h IV. Recheck blood glucose in 15 min.

IV Glucose Loading Instruction

(a) If the fasting glucose level is <150 mg/dl, 25 g dextrose-50 is given intravenously. (20–25 mg of hydrocortisone should be added to the dextrose-50 prior to injection to reduce the irritation of the veins.)
(b) For fasting glucose levels between 150 and 200, administer 12.5 g dextrose-50 dose.
(c) For fasting glucose levels >200, implement sliding scale insulin to lower the blood sugar using the following formula:

$$\text{Units of regular insulin IV} = \frac{\text{BS} - 50}{25}.$$

Note: Up to 10 units IV per dose (i.e., no single dose greater than 10 units of regular insulin should be given).

(d) After each insulin dose, blood sugar should be checked 15 min after the dose is given.
(e) If blood sugar is ever less than 80 mg/dl after insulin administration, start D5W @ 100 cm^3/h IV. Recheck blood glucose in 15 min.
(f) If hypoglycemia occurs (patient becomes diaphoretic, tachycardic, disoriented, etc.), give dextrose-50, 1 ampule IV, and start D5W @ 100 cm^3/h IV.
(g) Insulin is administered by physician or PET nurse only.
(h) If the blood sugar is = or < 150 mg/dl following sliding scale protocol, FDG can be injected.
(i) If the blood sugar remains >150 mg/dl, continue sliding scale insulin formula prior to injection of the FDG.

Case 15.1 History

A 57-year-old male with known history of coronary artery disease, status post CABG, was referred for myocardial viability.

Rows 1 and 3 (short-axis images) demonstrated a large area of perfusion abnormality at rest (SPECT myocardial perfusion scintigraphy—^{99m}Tc-tetrofosmin) involving the inferior left ventricular wall (Fig. 15.1). Rows 2 and 4 ^{18}F-FDG viability scintigraphy demonstrated a nonviable myocardium.

Top row (vertical axis) image resting SPECT myocardial perfusion scintigraphy (^{99m}Tc-tetrofosmin) (Fig. 15.2). Bottom row ^{18}F-FDG viability scintigraphy demonstrated no viable myocardium in the inferior wall.

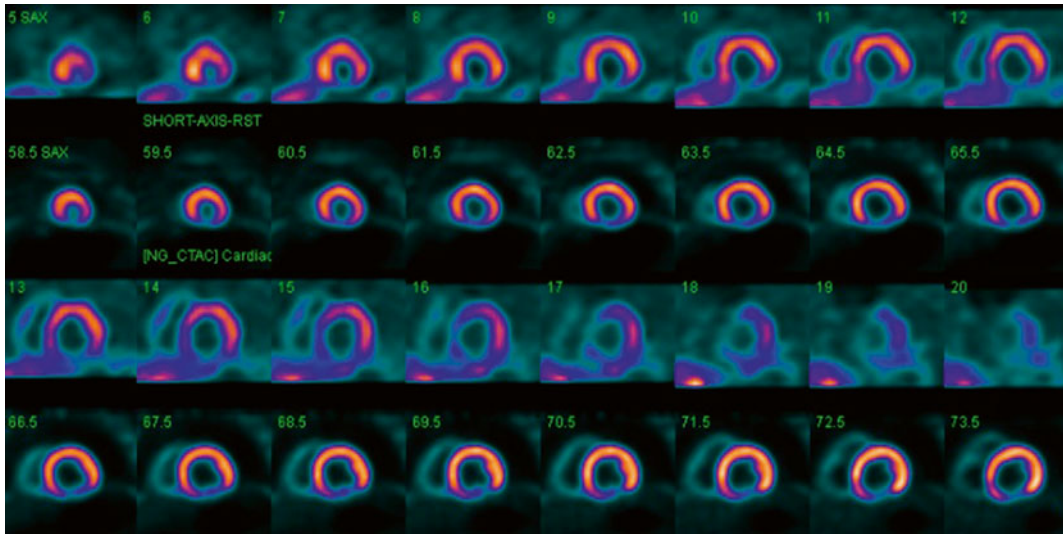

Fig. 15.1

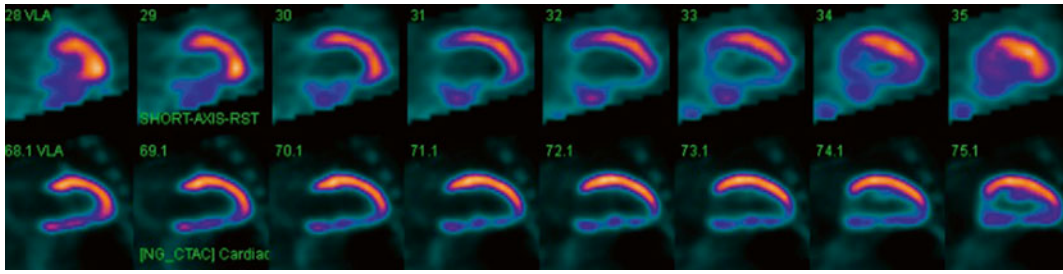

Fig. 15.2

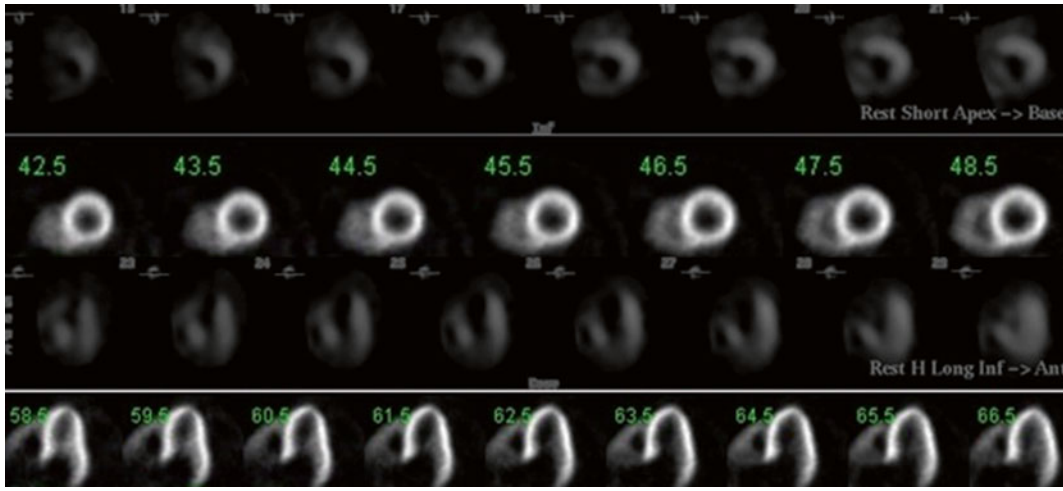

Fig. 15.3

Case 15.2 History

A 72-year-old male with known history of coronary artery disease, status post PTCA stent of RCA, was referred for evaluation of myocardial viability. Image 2 showed a moderate size perfusion abnormality involving inferoseptal left ventricular myocardium. This region demonstrated physiologic activity on FDG scintigraphy, indicating a viable myocardium.

Rows 1 and 3 demonstrated a large area of perfusion abnormality at rest SPECT myocardial perfusion scintigraphy (^{201}thallous chloride) (Fig. 15.3). Rows 2 and 4 demonstrated a viable myocardium on ^{18}F-FDG PET scintigraphy.

Artifacts Associated with PET-CT Myocardial Perfusion Scintigraphy

Misregistration of PET and CT Transmission Data

Misregistration of PET and transmission data is common in cardiac PET imaging, resulting in false interpretation. As a quality control measure, assessment of registration images of PET and CT must be performed routinely. This is important for processing PET data based on underlying soft tissue attenuation level. As a result, over- or undercorrection of PET data may occur.

Case 15.3

A 54-year-old male with hypertension and diabetes and abnormal ECG, complaining of chest pain of suspected ischemic origin (Fig. 15.4). Patient underwent routine rubidium-82 myocardial perfusion scintigraphy. Stress fusion images (PET rubidium-82 cardiac perfusion and CT transmission scan) demonstrate misregistration of the lateral wall of the left ventricle within low attenuating tissue of the lung parenchyma. The resting fusion images demonstrated appropriate registration.

Attenuation-corrected rubidium-82 cardiac perfusion PET demonstrates hypoactivity of the lateral wall at stress and normal activity at rest, most suspected for ischemia (Fig. 15.5).

Images demonstrate appropriate registration of rubidium-82 cardiac perfusion and transmission scans (manual correction was made) (Fig. 15.6). Note: Alignment must be made in 3-D format.

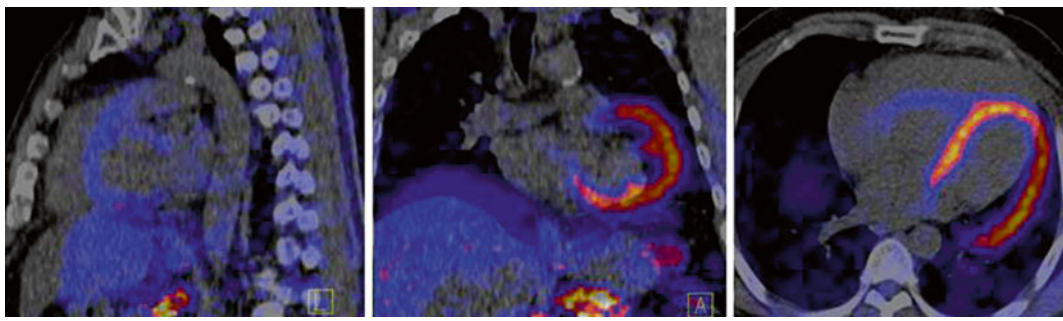

Fig. 15.4

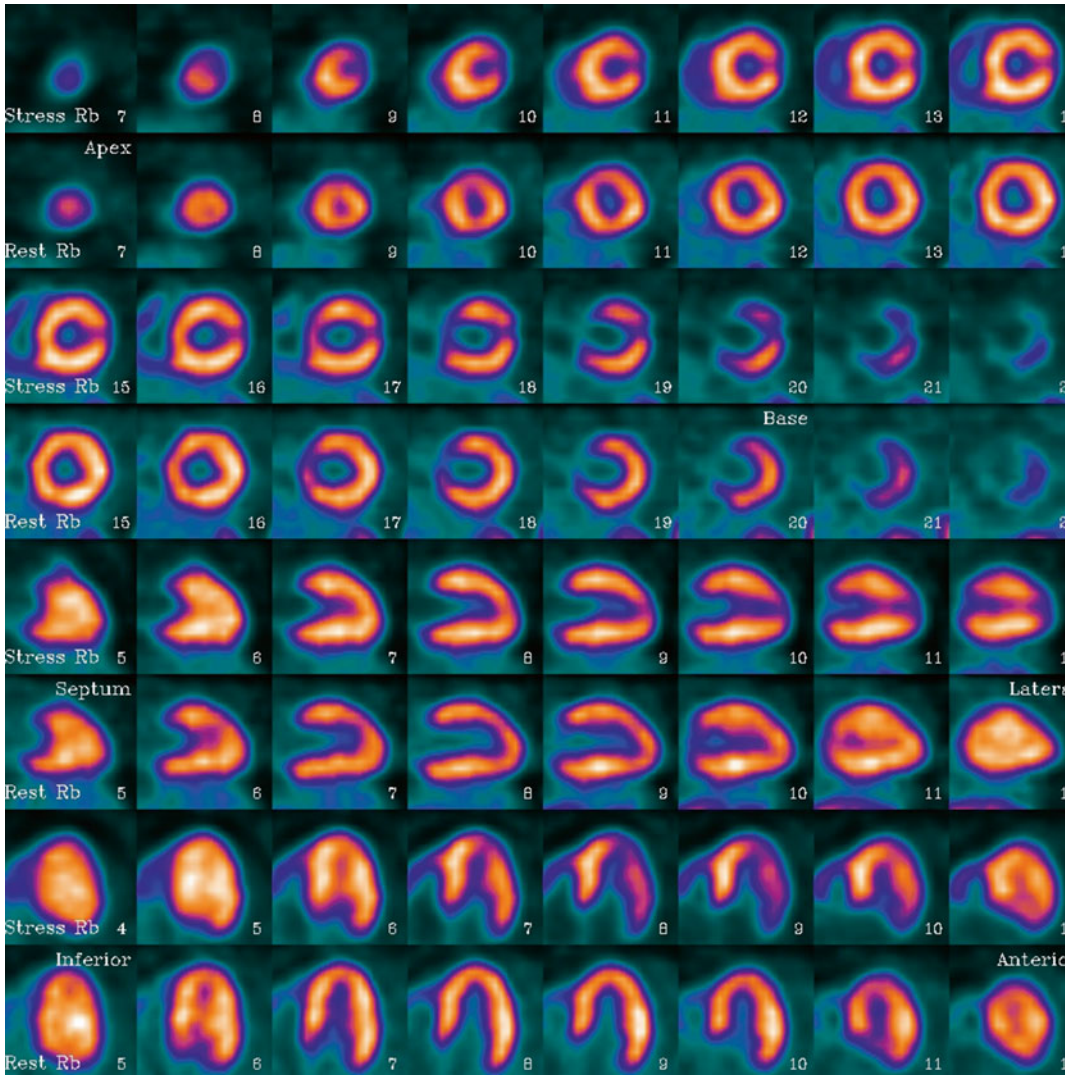

Fig. 15.5

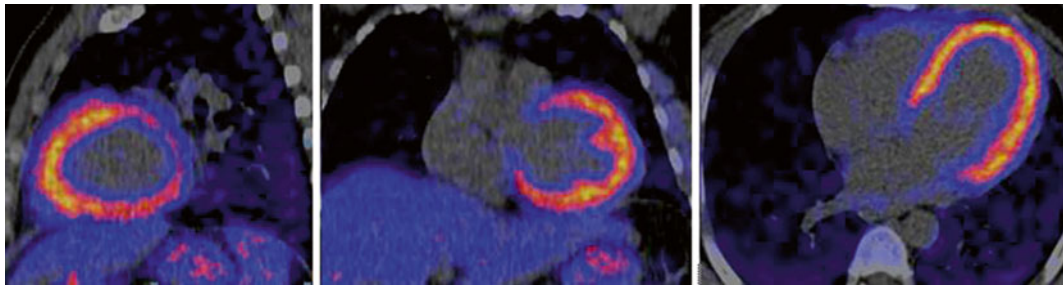

Fig. 15.6

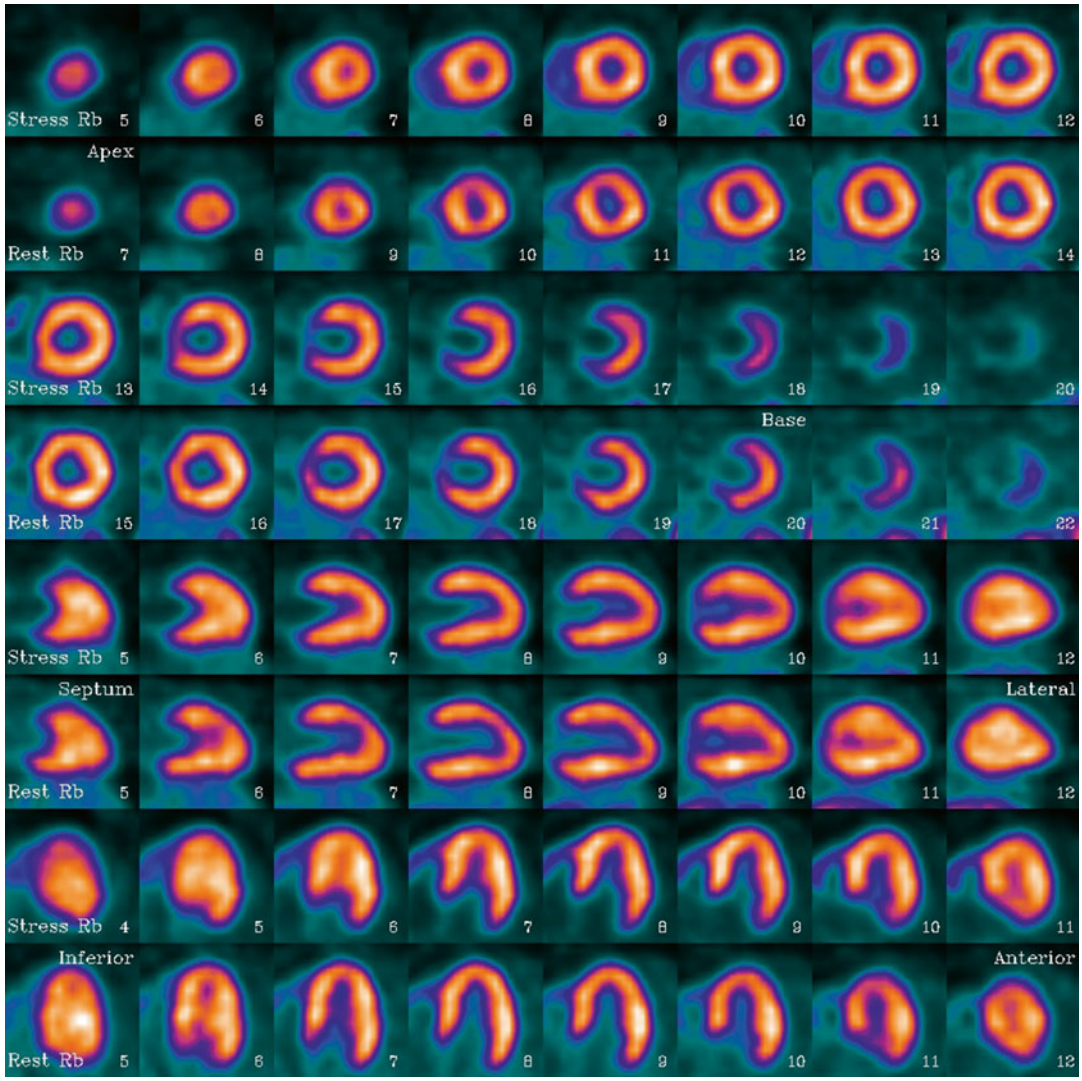

Fig. 15.7

Following correction of registration data, rubidium-82 cardiac perfusion images demonstrate resolution of hypoactivity of the lateral wall (Fig. 15.7).

Breast Attenuation Artifact

Although markedly reduced, attenuation associated with soft tissue of the breast must be excluded.

Case 15.4

Following images demonstrate hypoactivity of the anterior wall in a 64-year-old female with long-standing hypertension and hyperlipidemia, complaining of chest pain and shortness of breath. The anterior wall hypoactivity appears more pronounced at rest than stress (Figs. 15.8 and 15.9). Acquisition of gated data was at the time of peak stress, representing a true stress wall motion and wall thickening. Figures 15.10 and 15.11 demonstrate end-diastolic and end-systolic gated images, respectively. There is appropriate thickening of the anterior wall at end-systolic images, confirming attenuation artifact attributed to breast parenchyma.

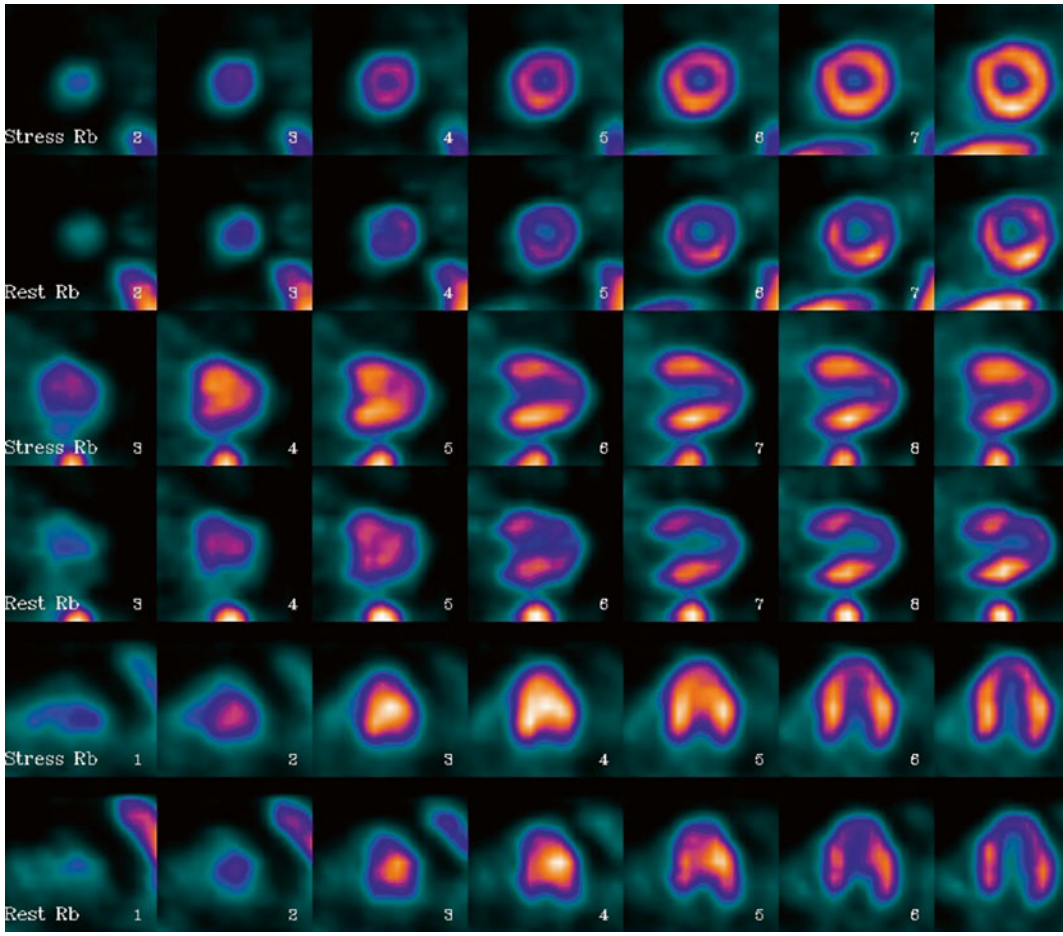

Fig. 15.8

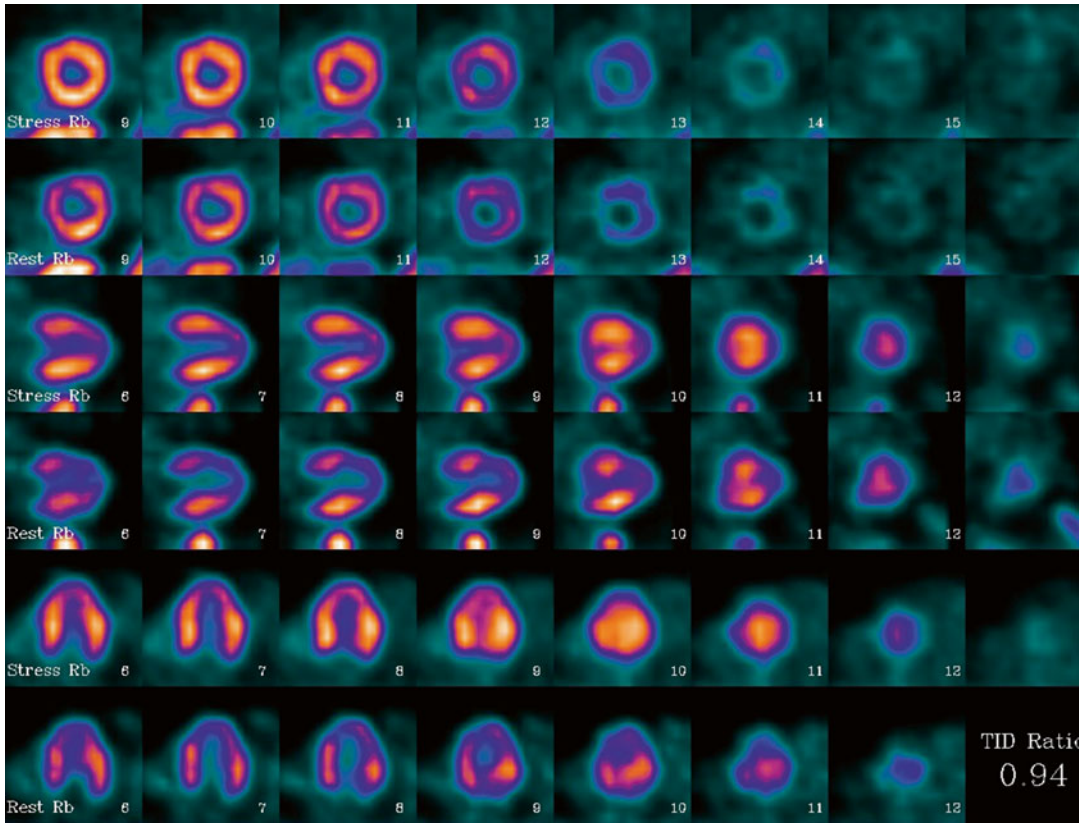

Fig. 15.9

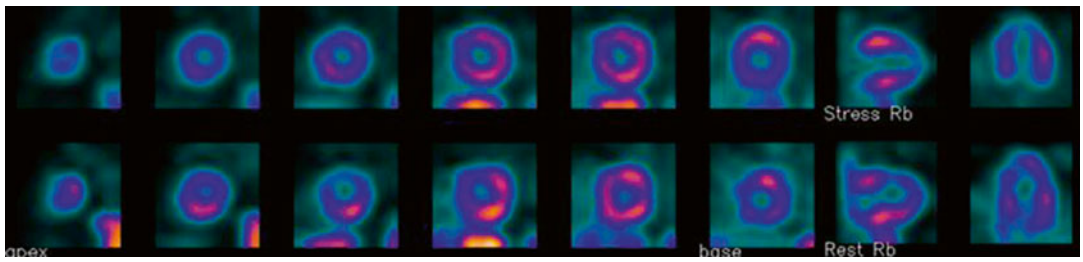

Fig. 15.10

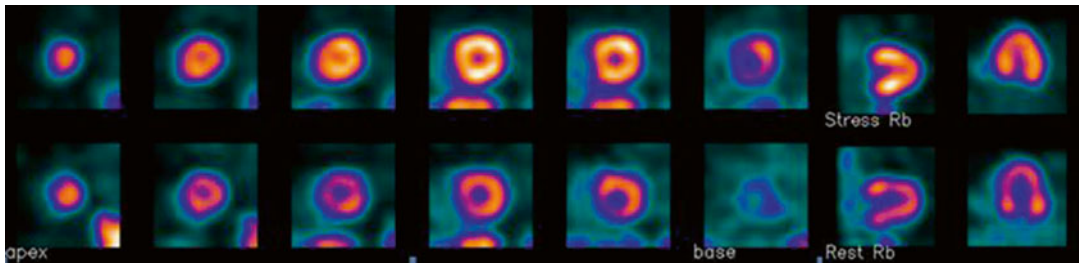

Fig. 15.11

Attenuation Attributed to Large Region of Interest

Whether automatic or manual, there would be an Region of Interest (ROI) drawn within processing matrix to normalize the left ventricular count profile. The field of view may or may not include noncardiac activities. This adversely affects the normalization process, therefore affecting myocardial activity.

Figures 15.12 and 15.13 demonstrate initial (automatic) placement of ROI that included the left ventricle as well as intense subdiaphragmatic activity. Normalization was based on the most active region within ROI. The stress images were normalized to left ventricular myocardial activity, whereas resting images were normalized to subdiaphragmatic activity (Fig. 15.13).

Figure 15.14 demonstrates manual correction of ROI only to the left ventricle. Note following correct placement of ROI, the resting left ventricular activity is appropriately normalized at rest (Fig. 15.15).

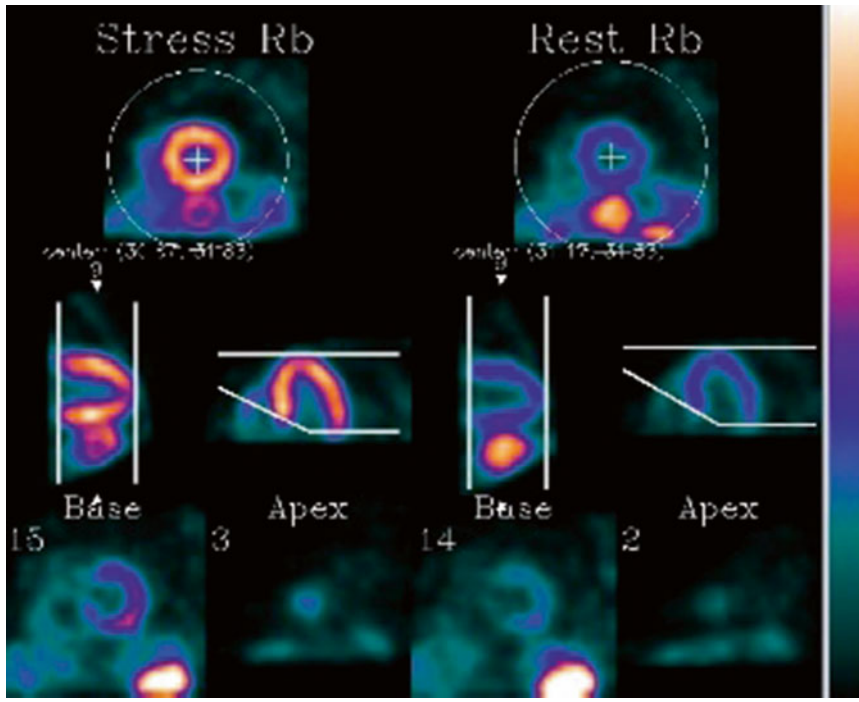

Fig. 15.12

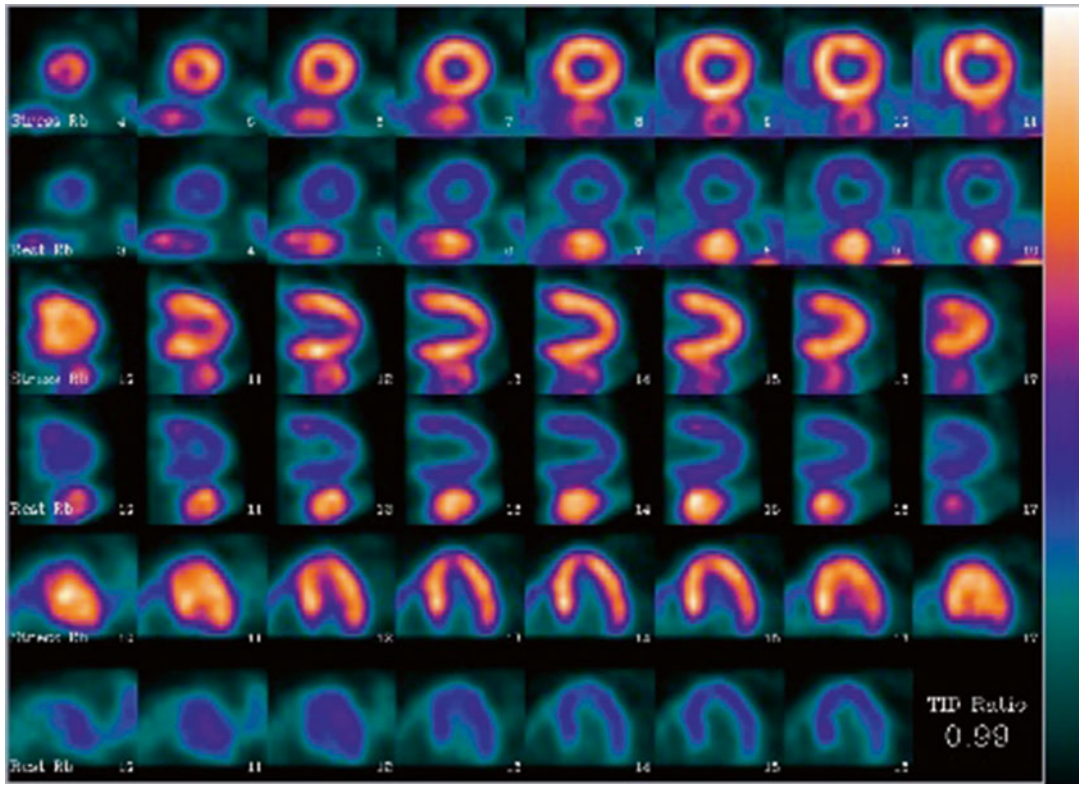

Fig. 15.13

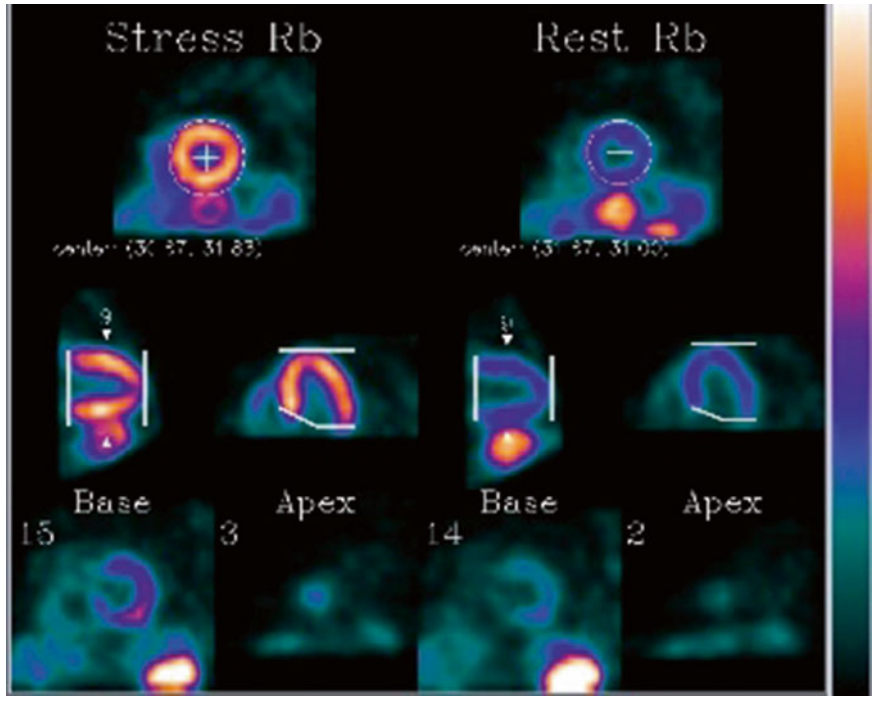

Fig. 15.14

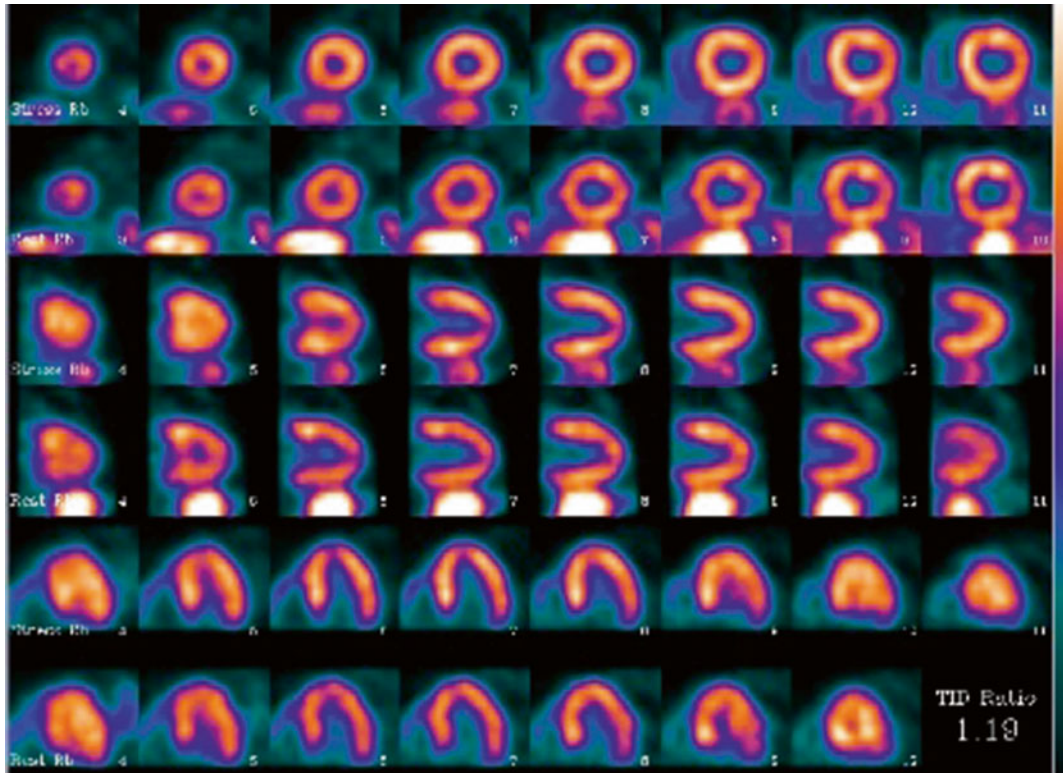

Fig. 15.15

Noncardiac Findings

1. PET
   (a) Chest: mediastinal, esophageal, pulmonary, skeletal, breast, thyroid, cervical, and subdiaphragmatic.

   Attention must be made to noncardiac activities during the evaluation process, similar to conventional SPECT scintigraphy as radiotracer activity may localize to pathological processes such as a tumor. Careful evaluation of raw data during quality control (registration assessment) process is a must.
2. CT
   (a) Nonmalignant: mediastinal, pulmonary, skeletal, esophageal, cervical, and nodal.
   (b) Malignant: primary and metastatic.

   Most PET myocardial scintigraphies are performed, using hybrid equipments (PET-CT). Quality of transmission CT scan images is poor secondary to low level of radiation (50–70 mAs) and acquisition during mild respiration. However, one must carefully examine the transmission CT dataset as it may reveal benign or malignant lesions.

Case 15.5

Transmission scan of rubidium myocardial perfusion scintigraphy (Fig. 15.16) demonstrates heterogeneous attenuation through liver parenchyma, highly suspicious of malignancy. Patient was referred for a FDG PET-CT scan for further clarification.

PET-CT scintigraphy (Fig. 15.17) demonstrated hypermetabolic activity associated with hypoattenuating liver lesions. Tissue sampling revealed metastatic disease from colon carcinoma.

Case 15.6

A 70-year-old male with hypertension, hyperlipidemia, and family history of coronary artery disease was being evaluated for chest discomfort of suspected ischemic origin. Axial CT transmission scan images demonstrated large hiatal hernia and vertebral body hemangioma (Fig. 15.18). Rubidium myocardial perfusion scintigraphy was unremarkable. No prior anatomical imaging was performed prior to rubidium scintigraphy. Patient's symptom was attributed to hiatal hernia and GERD. Subsequent management of GERD resulted in complete cessation of symptoms.

Case 15.7

A 55-year-old female with hypertension and family history of coronary artery disease was referred for assessment of coronary artery disease. Axial CT transmission images demonstrated large retrotracheal/mediastinal

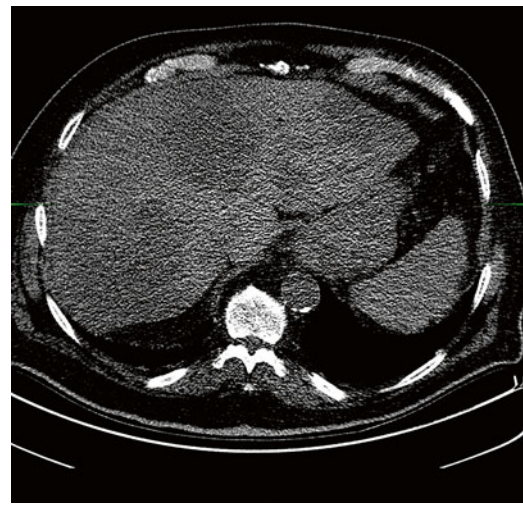

Fig. 15.16

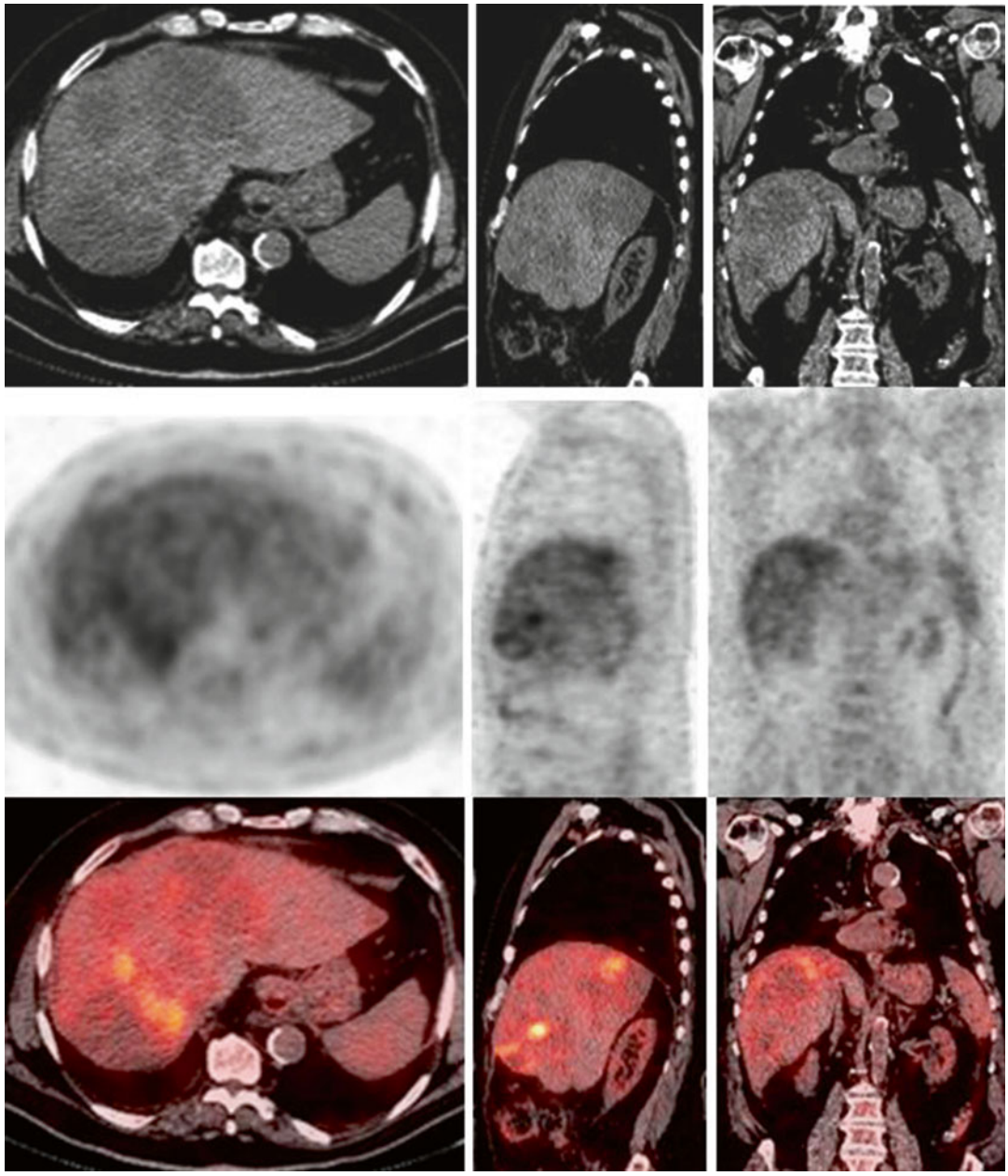

Fig. 15.17

mass that was worrisome for malignant etiology (Fig. 15.19). Further correlation with ^{18}F-FDG PET-CT scan identified the mass as mediastinal extension of a large goiter. Subsequent management of goiter resulted in resolution of chest pain.

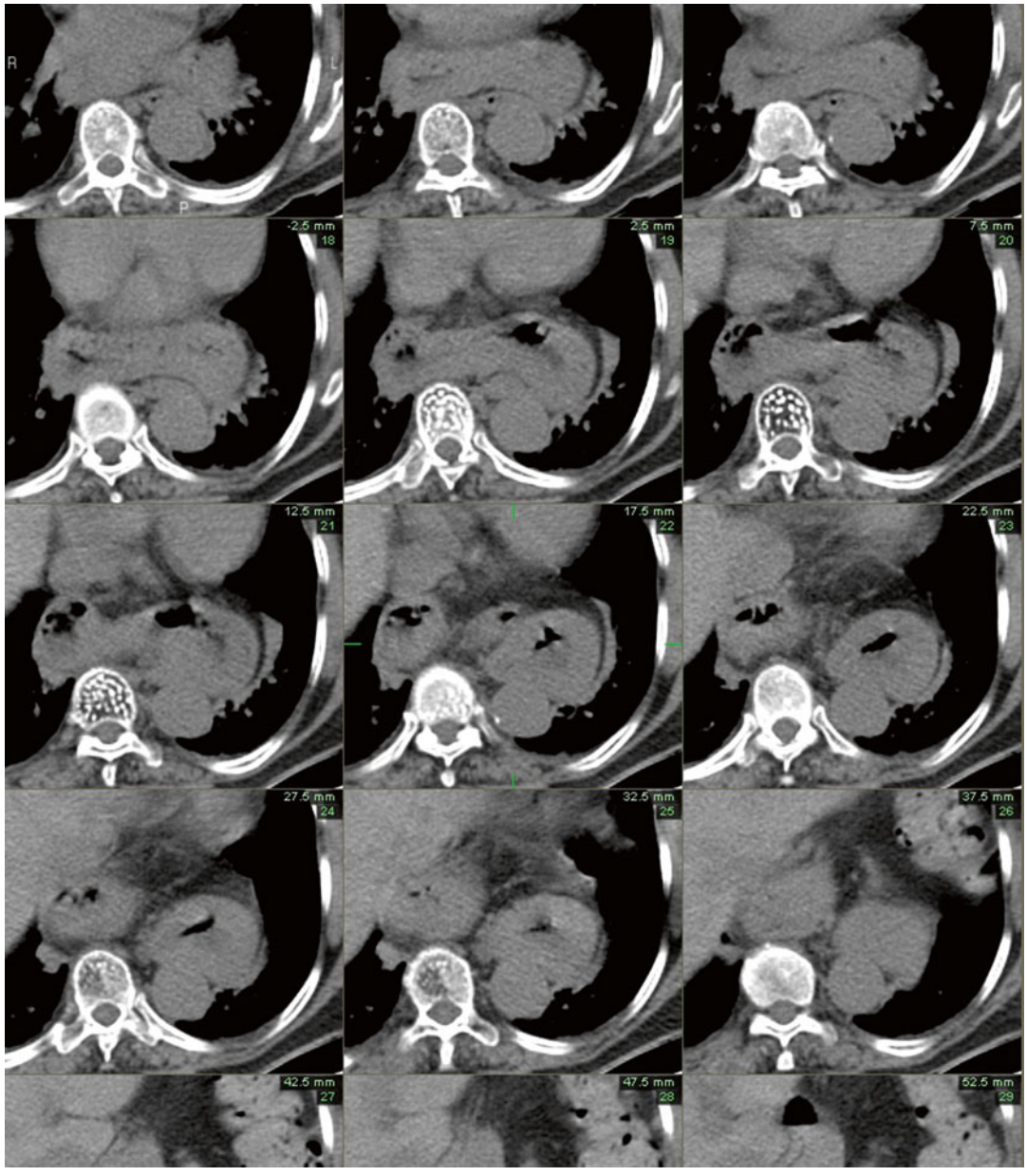
R
L
P
-2.5 mm
18
2.5 mm
19
7.5 mm
20
12.5 mm
21
17.5 mm
22
22.5 mm
23
27.5 mm
24
32.5 mm
25
37.5 mm
26
42.5 mm
27
47.5 mm
28
52.5 mm
29

Fig. 15.18

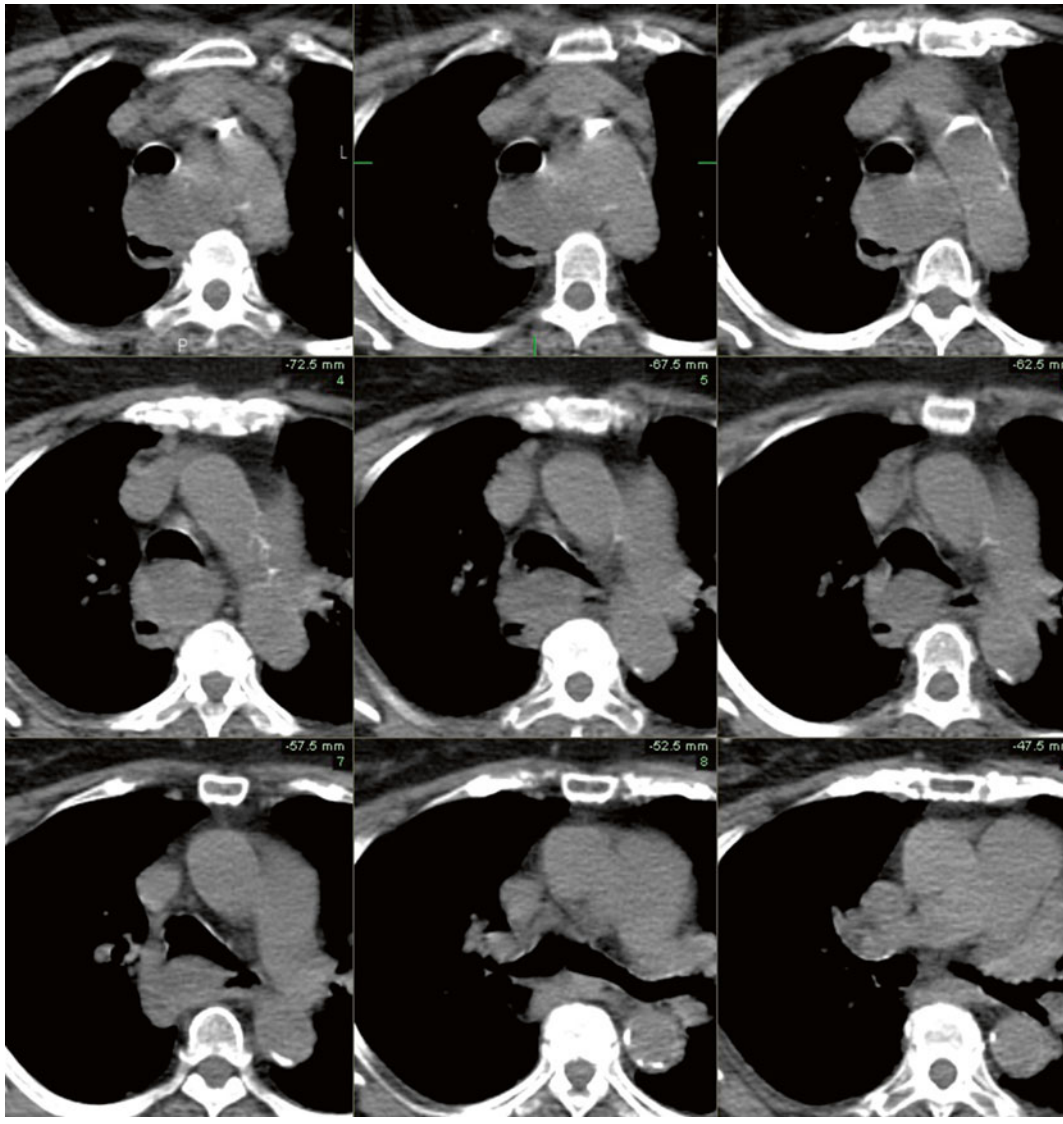

Fig. 15.19

Case 15.8

A 63-year-old male with hyperlipidemia, hypertension, and chest pain was referred for assessment of coronary artery disease. Spiculated left upper lobe mass on transmission scan (Fig. 15.20) was identified. The mass was pathologically confirmed following wedge resection as primary pulmonary neoplasm.

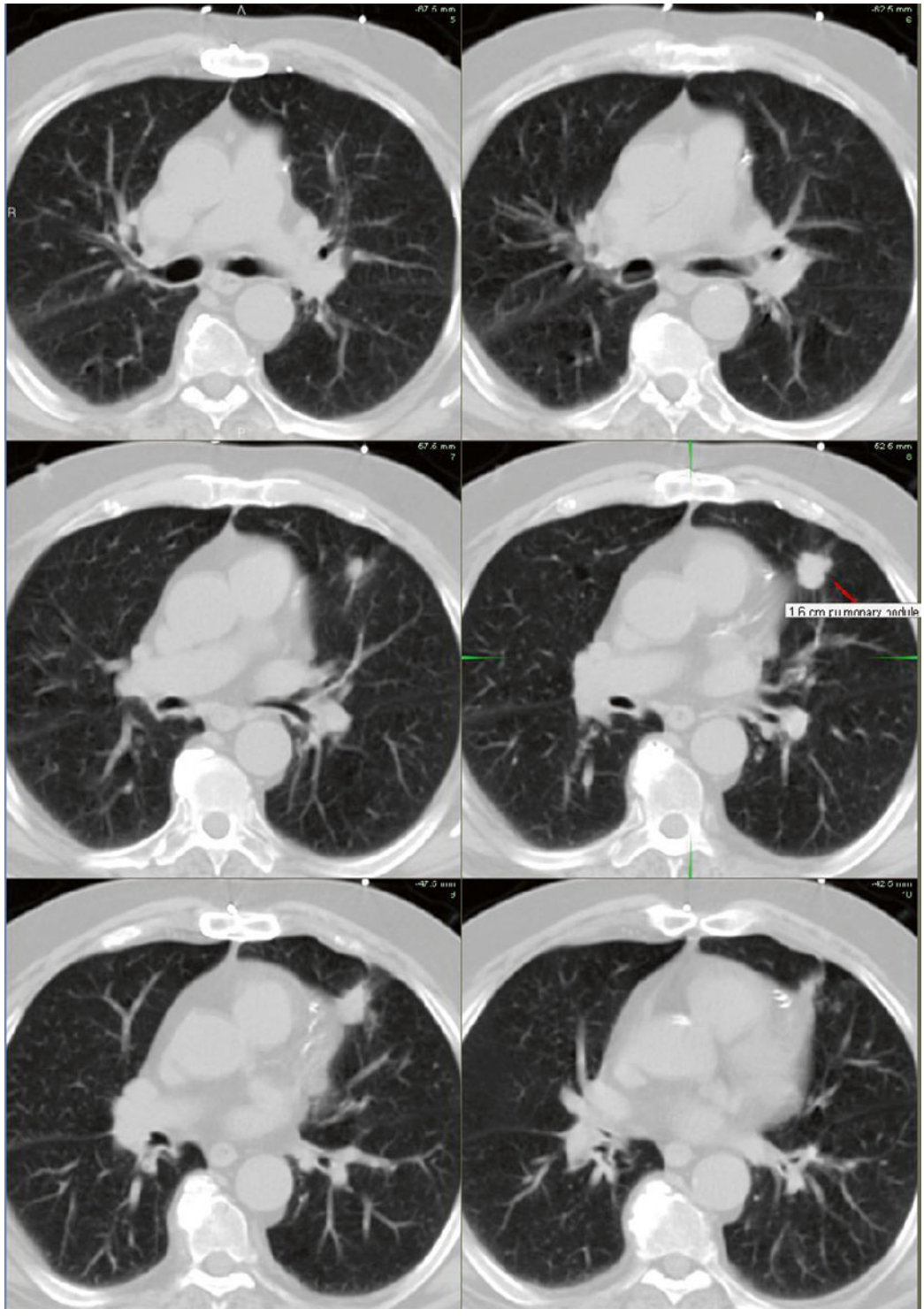

Fig. 15.20

Suggested Reading

Abraham A, Nihhol G, Williams KA, et al. F-18-FDG PET imaging of myocardial viability in an experienced center with access to F-18-FDG and integration with clinical management teams: the Ottawa-FIVE sub study of the PARR 2 Trial. J Nucl Med. 2010;51:567–74.

Bax JJ, Veening MA, Visser FC, et al. Optimal metabolic conditions during fluorine-18 fluorodeoxyglucose imaging: A comparative study using different protocols. Eur J Nucl Med. 1997;24:35–41.

Bax JJ, Visser FC, Poldermans D, et al. Feasibility, safety and image quality of cardiac FDG studies during hyperinsulinemic-euglycemic clamping. Eur J Nucl Med. 2002;29:452–7.

Brix G, Lechel U, Glatting G, et al. Radiation exposure of patients undergoing whole-body dual-modality F-18 PET/Ct examinations. J Nucl Med. 2005;46:608–13.

Brogsitter C, Gruning T, Weise R, et al. F-18-FDG PET for detecting myocardial viability: validation of 3D data acquisition. J Nucl Med. 2005;46:19–24.

Di Carli MF, Murthy VL. Cardiac PET/CT for the evaluation of known or suspected coronary artery disease. Radiographics. 2011;31(5):1239–54.

Eckerman KF, Endo A, editors. MIRD: radionuclide data and decay schemes. Reston: Society of Nuclear Medicine; 2008. p. 52.

Fukuchi K, Ohta H, Matsumura K, et al. Benign variations and incidental abnormalities of myocardial FDG uptake in the fasting state as encountered during routine oncology positron emission tomography studies. Br J Radiol. 2007;80(949):3–11. Epub 2006 Sep 27.

Go RT, Marwick TH, MacIntyre WJ, et al. A prospective comparison of rubidium-82 PET and thallium-201 SPECT myocardial perfusion imaging utilizing a single dipyridamole stress in the diagnosis of coronary artery disease. J Nucl Med. 1990;31:1899–905.

Hays MT, Watson EE, Thomas SR, et al. MIRD dose estimate report no. 19: radiation absorbed dose estimates from F-18-FDG. J Nucl Med. 2002;43:210–4.

Hernandez-Pampaloni M, Bax JJ, Morita K, et al. Incidence of stunned, hibernation and scarred myocardium in ischaemic cardiomyopathy. Eur J Nucl Med Mol Imaging. 2005;32:314–21.

Huitink JM, Visser FC, van Leeuwen GR, et al. Influence of high and low plasma insulin levels on the uptake of fluorine-18 fluorodeoxyglucose in myocardium and femoral muscle, assessed by planar imaging. Eur J Nucl Med. 1995;22:1141–8.

Langah R, Spicer K, Gebregzlabher M, et al. Effectiveness of prolonged fasting F-18-FDG PET-CT in the detection of cardiac sarcoidosis. J Nucl Cardiol. 2009;16:801–10.

Lehman SJ, Abbara S, Cury RC, et al. Significance of cardiac computed tomography incidental findings in acute chest pain. Am J Med. 2009;122(6):543–9.

Lewis P, Nunan T, Dynes A, et al. The use of low-dose intravenous insulin in myocardial F-18 FDG PET scanning. Clin Nucl Med. 1996;21:15–8.

Loghin C, Sdringola S, Gould KL. Common artifacts in PET myocardial perfusion images due to attenuation-emission misregistration: clinical significance, causes, and solutions. J Nucl Med. 2004;45(6):1029–39.

Martin WH, Jones RC, Delbeke D, et al. A simplified intravenous glucose loading protocol for fluorine-18-florodeoxyglucose cardiac single-photon emission tomography. Eur J Nucl Med. 1997;24:1291–7.

Martinez-Möller A, Souvatzoglou M, Navab N, et al. Artifacts from misaligned CT in cardiac perfusion PET/CT studies: frequency, effects, and potential solutions. J Nucl Med. 2007;48(2):188–93.

Matsunari I, Kanayama S, Yoneyama T, et al. Myocardial distribution of F-18-FDG and Tc-99m-sestamibi on dual-isotope simultaneous acquisition SPET compared with PET. Eur J Nucl Med. 2002;29:1357–64.

Mesotten L, Maes A, Van de Werf F, et al. PET radiopharmaceuticals used in viability studies in acute myocardial infarction: a literature survey. Eur J Nucl Med. 2002;29:3–6.

Metrard G, Girault S, Capitain O, et al. Uncommon breast tumor attenuation artifact on radionuclide ventriculography. Clin Nucl Med. 2008;33(4):288–9.
Mettler FA, Bhargavan M, Thomadsen BR, et al. Nuclear medicine exposure in the United states, 2005–2007: preliminary results. Semin Nucl Med. 2008;38:384–91.
Mirpour S, Khandani AH. Extracardiac abnormalities on rubidium-82 cardiac positron emission tomography/computed tomography. Nucl Med Commun. 2011;32(4):260–4.
Mueller J, Jeudy J, Poston R, et al. Cardiac CT angiography after coronary bypass surgery: prevalence of incidental findings. Am J Roentgenol. 2007;189(2):414–9.
Nye JA, Esteves F, Votaw JR. Minimizing artifacts resulting from respiratory and cardiac motion by optimization of the transmission scan in cardiac PET/CT. Med Phys. 2007;34(6):1901–6.
Sandler MP, Bax JJ, Patton JA, et al. Fluorine-18-fluorodeoxyglucose cardiac imaging using a modified scintillation camera. J Nucl Med. 1998;39:2035–43.
Schelbert HR. F-18-deoxyglucose and the assessment of myocardial viability. Sem Nucl Med. 2002;32:60–9.
Schinkel AFL, Bax JJ, Valkema R, et al. Effect of diabetes mellitus on myocardial F-18-FDG SPECT using acipimox for the assessment of myocardial viability. J Nucl Med. 2003;44:877–83.
Stankewicz MA, Mansouir CS, Eisner RL, et al. Myocardial viability assessment by PET: Rb-82 defect washout does not predict the results of metabolic-perfusion mismatch. J Nucl Med. 2005;46:1602–9.
Stewart RE, Schwaiger M, Molina E, et al. Comparison of rubidium-82 positron emission tomography and thallium-201 SPECT imaging for detection of coronary artery disease. Am J Cardiol. 1991;67:1303–10.
Stone CK, Holden JE, Stanley W, et al. Effect of nicotinic acid on exogenous myocardial glucose utilization. J Nucl Med. 1995;36:996–1002.
Van Campen CMC, Viser FC, van der Weerdt AP, et al. FDG PET as a predictor of response to resynchronization therapy in patients with ischaemic cardiomyopathy. Eur J Nucl Med Mol Imaging. 2007;34:309–15.
Waxman AD, Barondess P. Preparing patients for PET imaging: the importance of prescan communication. Discussion in PET Imaging. New York: CMP Healthcare Media; 2004.

16 Granulomatous Diseases

Nova M. Isaac and Robert W. Henderson

Case 16.1: Sarcoidosis

History

50-year-old male, with history of esophageal cancer, status post esophagectomy with gastric pull-through.

Findings

Symmetrically intense FDG activity seen within bihilar and mediastinal lymph nodes, demonstrating hypermetabolism of similar intensity (Figs. 16.1 and 16.2).

Impression

Findings compatible with sarcoidosis by scan pattern (which was proven on surgery, during esophagectomy and gastric pull-up).

Pearls and Pitfalls

The hypermetabolic lymph nodes could have been mistaken for metastatic disease.

Discussion

Etiology for granulomatous disease (noncaseating) is unknown.

P.S. Conti, A. Kaushik (eds.), *PET-CT*, DOI 10.1007/978-1-4419-5811-2_16

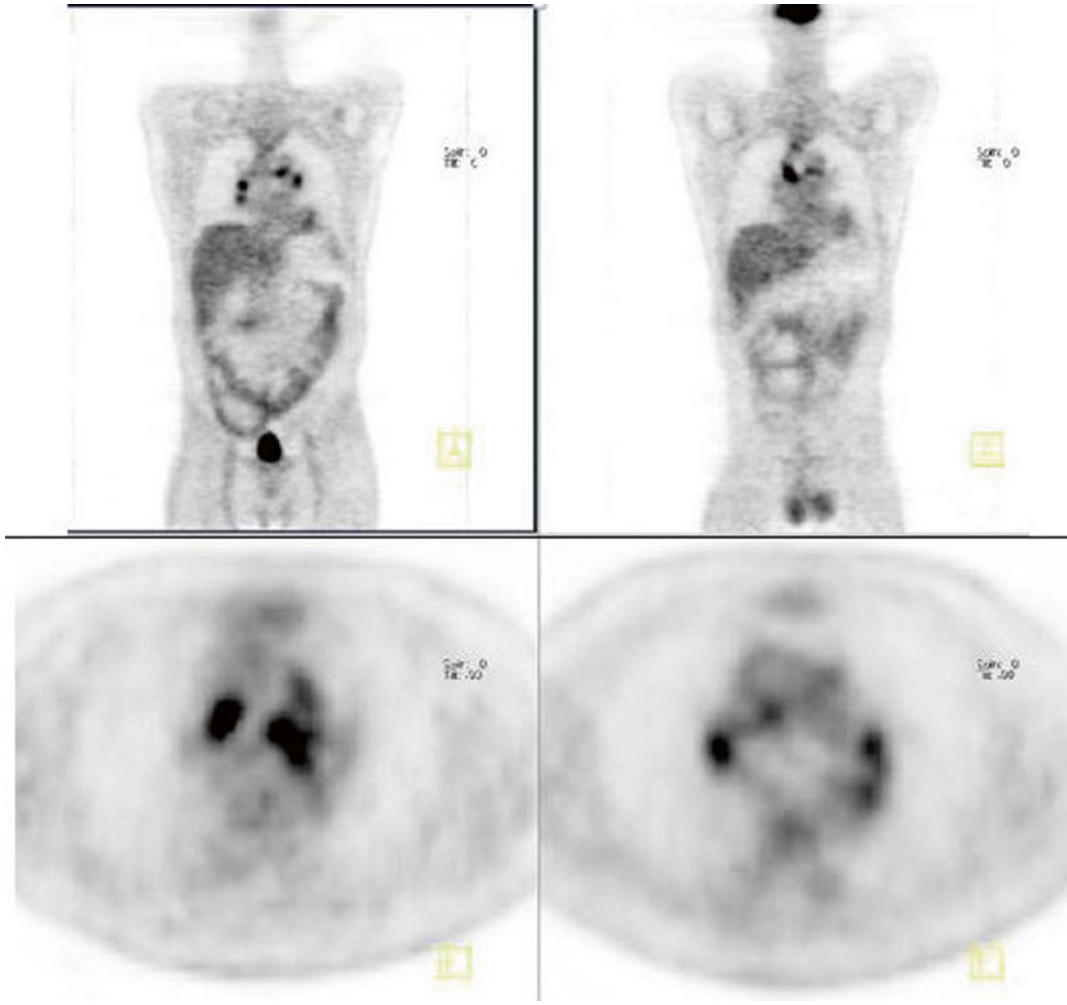

Fig. 16.1

Characteristic scan pattern: nodal disease involving mediastinal (lower paratracheal, aortopulmonary window, subcarinal), bilateral hilar, and interlobar lymph nodes.

Parenchymal disease is a late feature; by then nodal disease may have regressed.

^{18}FDG-PET scan pattern is similar to ^{67}Ga scan (lambda pattern) in the region of the chest.

Symmetric FDG avid bihilar lymphadenopathy would be a rare pattern for metastatic disease (Figs. 16.1 and 16.2).

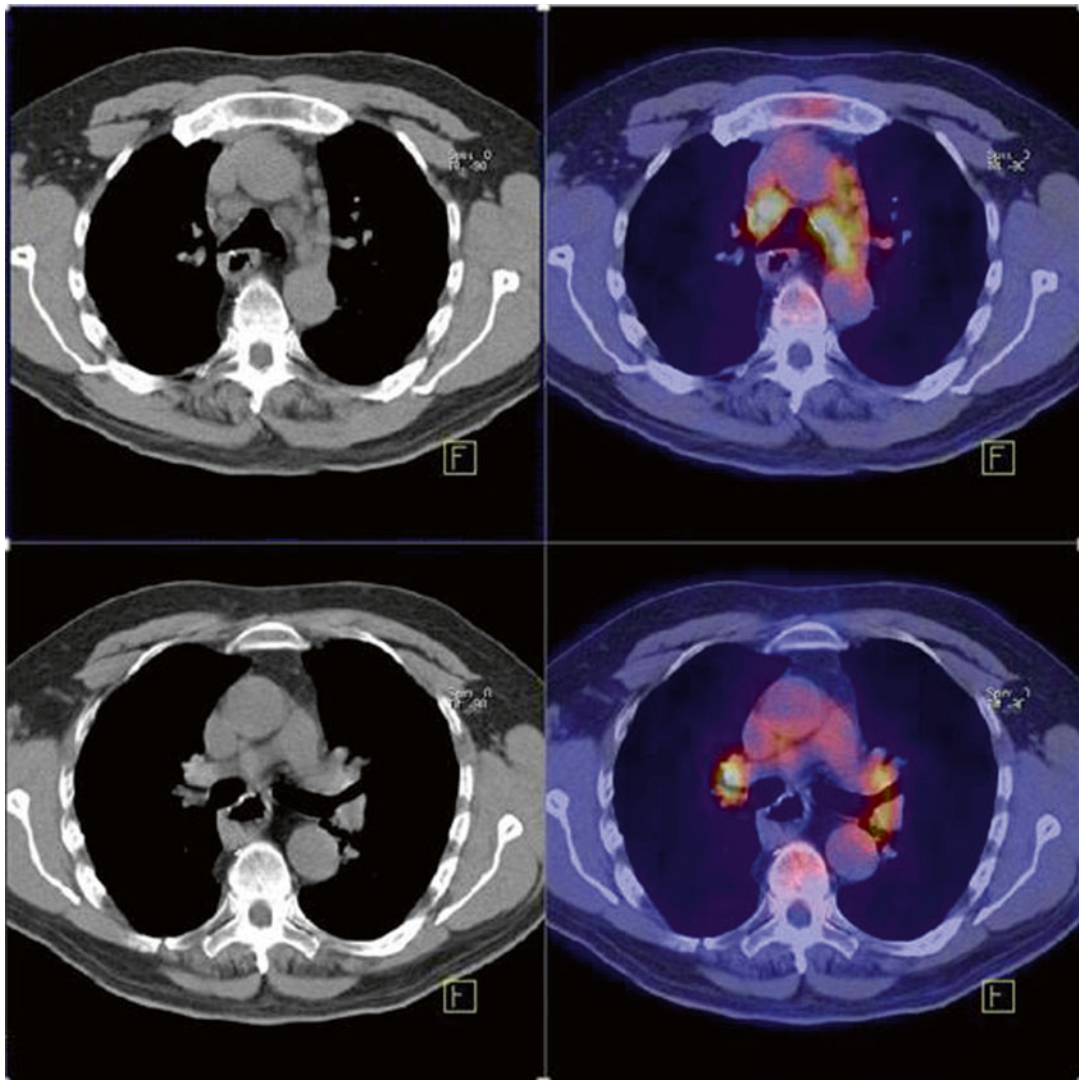

Fig. 16.2

Case 16.2: Pneumoconiosis

History

55-year-old male, sand blaster by occupation, presents with chronic cough.

Findings

Lambda pattern of lymphadenopathy involving mediastinal and bihilar nodal regions (Fig. 16.3, *yellow arrow*). Particles predominantly seen in the upper lobes of the lung, as shown here in the right upper lobe image (Fig. 16.4, *red arrow*).

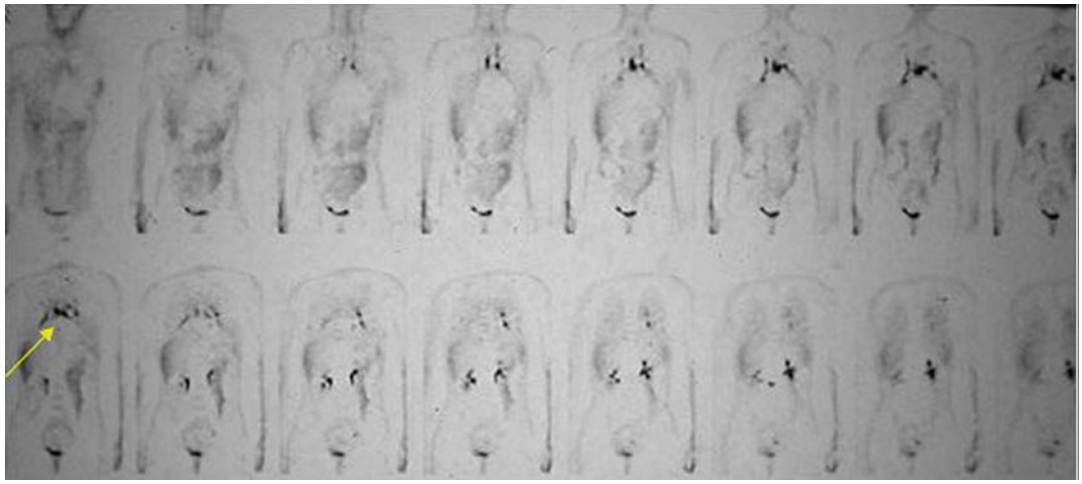

Fig. 16.3

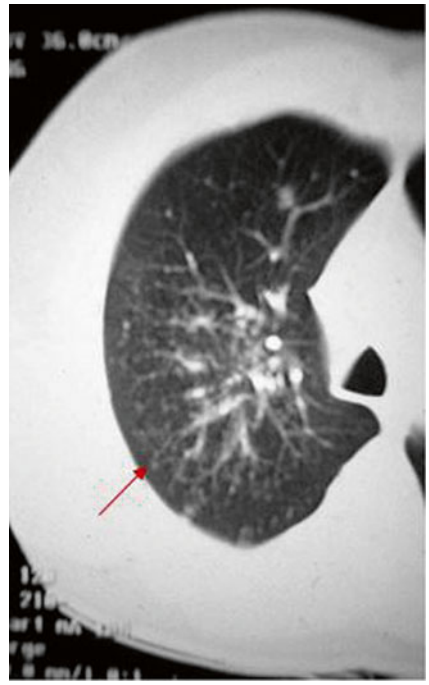

Fig. 16.4

Impression

Silicosis based on correlation with patient's occupational exposure history, presence of hypermetabolic mediastinal and bihilar lymph nodes (lambda pattern), and visualization of multiple small pulmonary nodules, predominantly in the upper lobes.

Discussion

- Involvement of upper lobes predominantly. This is related to lymphatic drainage, which is better in the lower chest, as it is assisted by more excursion.
- Particles that pass the respiratory bronchioles into the alveoli are drained by lymphatics, due to lack of cilia.
- Exception, being asbestosis (whose needles are not cleared by lymphatics) (Figs. 16.3 and 16.4).

Case 16.3: Asbestosis

History

55-year-old male with asbestosis.

Findings

Fibrotic changes in the lower lung fields demonstrating low-grade FDG activity on PET and PET/CT fused images (Fig. 16.5). Pleural plaque in the left lower lobe (*red arrow*).

Impression

Sequela to prior asbestosis exposure.

Discussion

- Differentiating idiopathic pulmonary fibrosis from asbestosis is important because of legal and compensatory issues (Fig. 16.5).

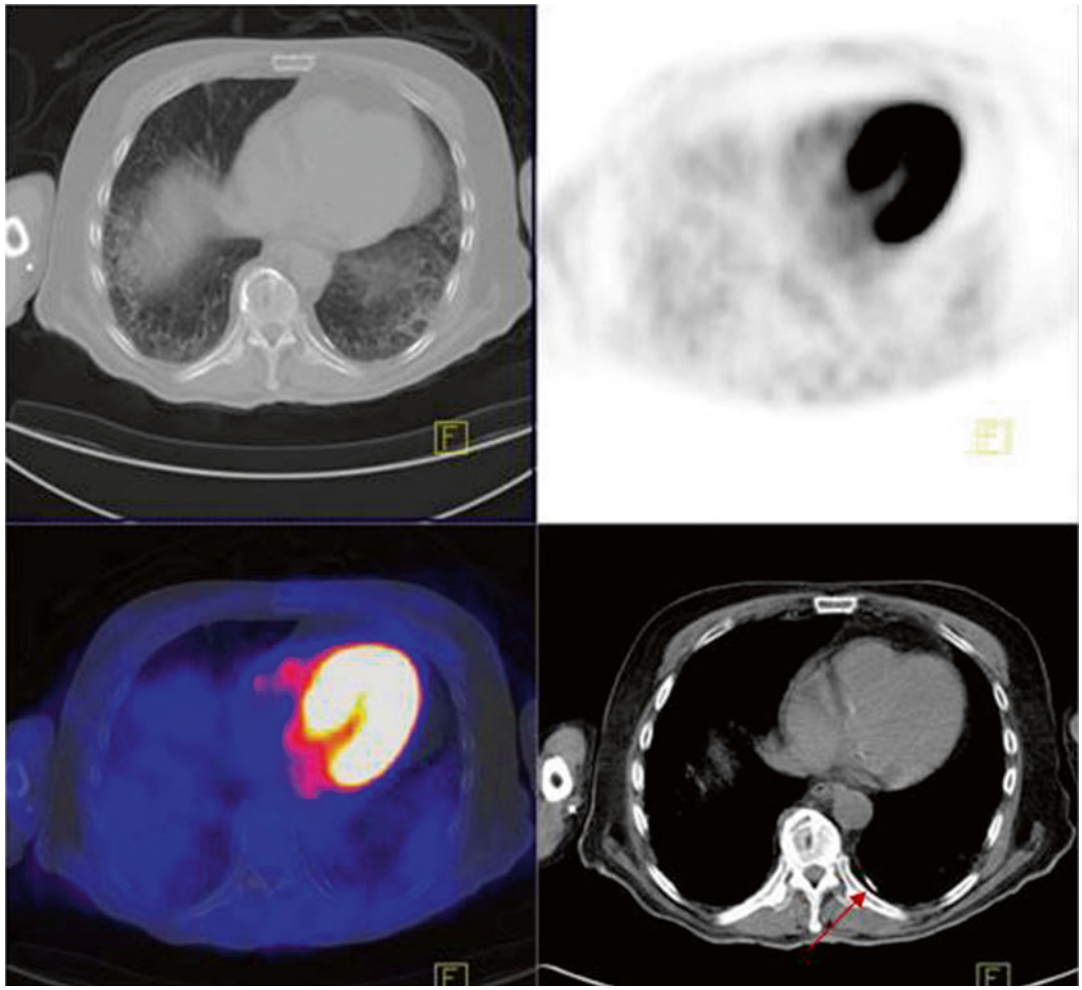

Fig. 16.5

Case 16.4: Prior Tuberculosis/Old Granulomatous Disease

History

Patient with known history of prior tuberculosis (TB).

Findings

Symmetric bihilar nodal activity within normal-sized lymph nodes (Fig. 16.6).

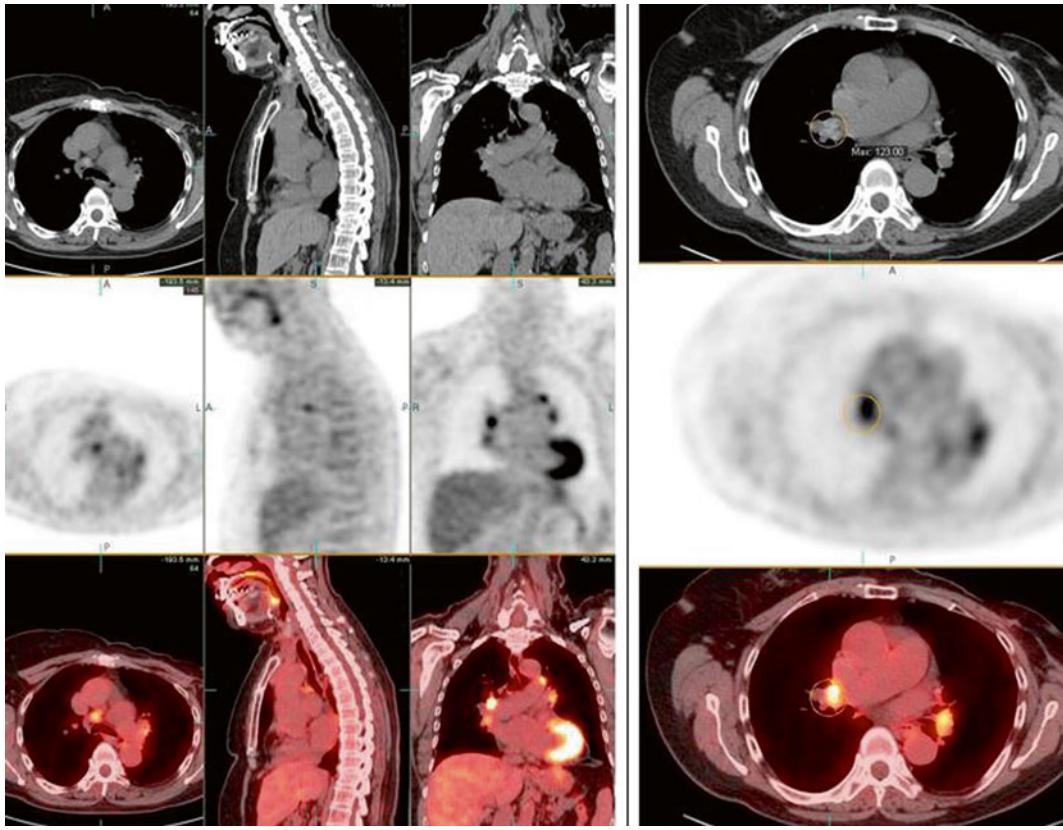

Fig. 16.6

Impression

Granulomatous disease by scan pattern.

Pearls and Pitfalls

Granulomatous disease (GD) is by far the commonest false-positive finding for nodal disease in the chest. In majority of the time, the hilar and med iastinal lymph nodes cannot be readily biopsied. Therefore, the classic scan pattern for GD must be identified on PET/CT.

Discussion

- Active nodes common.
- Does not imply active infection or need for treatment.
- May or may not be associated with calcifications.
- Nodes usually are normal size.
- Usually bilateral (Fig. 16.6).

Case 16.5: Granulomatous Disease in the Midst of Hodgkin's Lymphoma

History

56-year-old male, with history of Hodgkin's disease (HD) below the diaphragm and prior history of tuberculosis. PET/CT images during chemotherapy (Fig. 16.7, *top images*); post chemotherapy PET/CT (Fig. 16.7, *bottom images*).

Findings

Axial CT and fused PET/CT images (top) demonstrate new enlarged, hypermetabolic right hilar lymph nodes with the rest of the body demonstrating good response to chemotherapy (Fig. 16.7). Follow-up PET/CT images (bottom) at the same level demonstrate resolution of right hilar lymph nodes without anti-TB treatment.

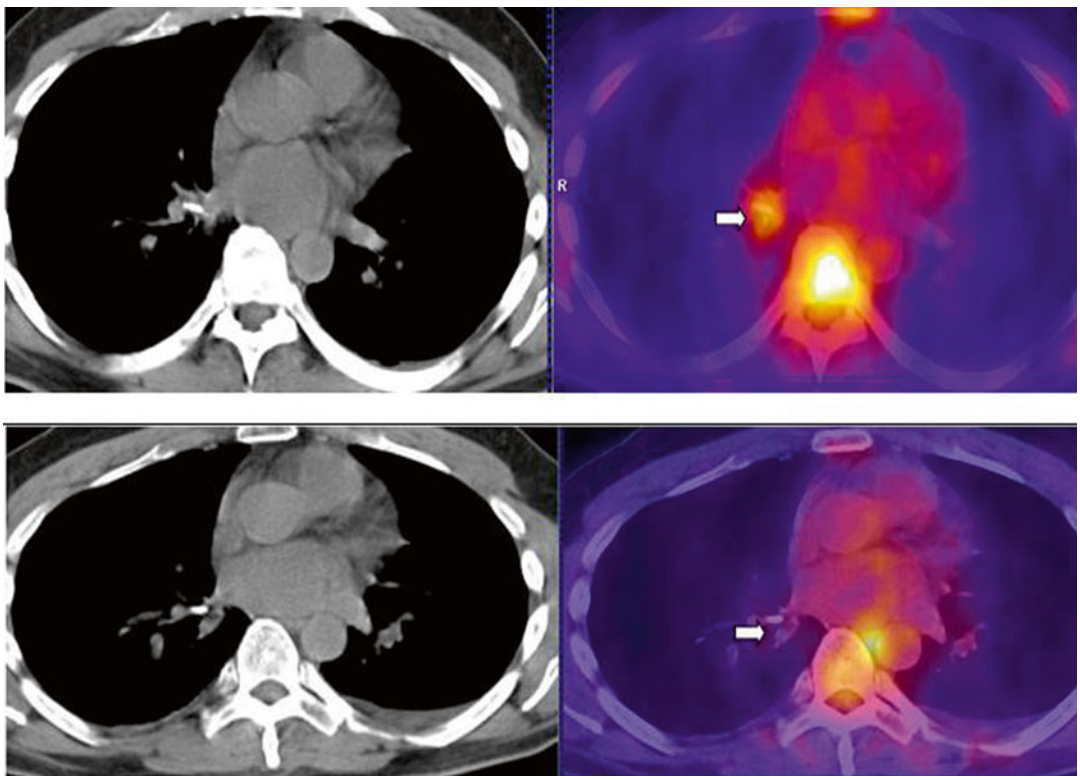

Fig. 16.7

Impression

Reactivation of granulomatous disease during chemotherapy.

Pearls and Pitfalls

The PET/CT reader might call the post-therapy scan as persistent Hodgkin's disease or progression of HD. (False-positive) PET/CT scans in patients with HD are not always due to residual or progressive disease.

Discussion

- Association seen between increased incidence of granulomatous disease and HD patients undergoing chemotherapy.
- Familiarity with scan pattern of 18F-FDG uptake in GD is essential as it significantly impacts prognosis and management.
- Clinicians may need to maintain a low threshold of confidence for basing their diagnosis on histopathological evaluations when PET/CT results appear to be incongruent with the patient's clinical response [1] (Fig. 16.7).

Case 16.6: Granulomatous Disease Coexisting with Lymphomatous Disease

History

Patient presents with lymphoma recurrence in the left external iliac lymph node.

Findings

Normal-sized, calcified bihilar lymph nodes; granulomatous disease by scan pattern (Fig. 16.8, *yellow arrow*). Enlarged hypermetabolic left external iliac lymph node (Fig. 16.8, *red arrow*) is compatible with recurrence of lymphoma.

Impression

Coexistence of granulomatous disease and lymphomatous disease.

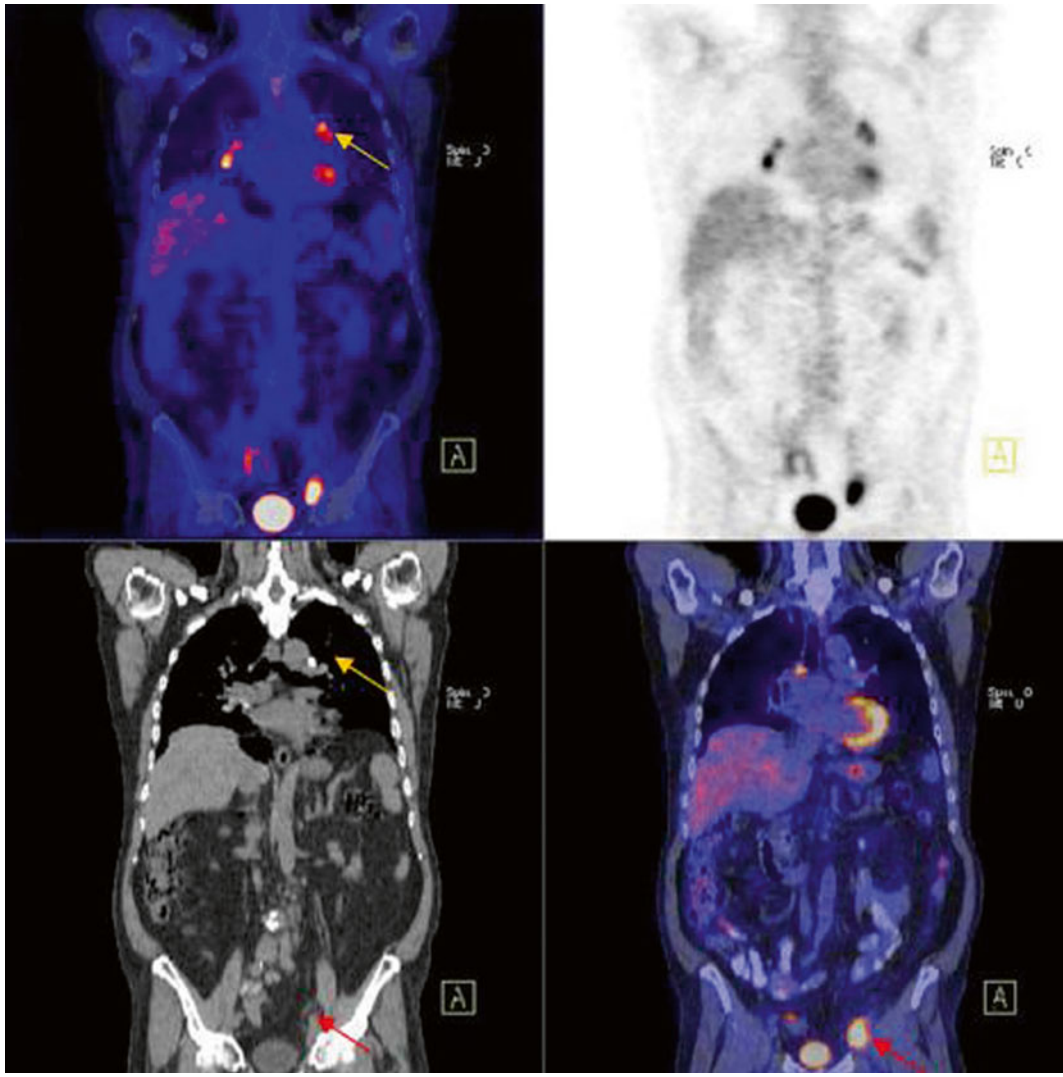

Fig. 16.8

Discussion

- Presentation of unilateral hilar disease, mediastinal lymphadenopathy without hilar disease, or posterior mediastinal adenopathy are rarely seen with sarcoidosis and are more suggestive of lymphoma, metastatic cancer, or other granulomatous infections [2] (Fig. 16.8).

Case 16.7: Granulomatous Disease and Metastatic Disease in the Chest

History

62-year-old male with known metastatic lung cancer with prior history of mycobacterium tuberculosis.

Findings

Enlarged, intensely avid, left hilar lymph nodes representing metastatic disease (Fig. 16.9, *circled*) from lung primary. Calcified, normal-sized bihilar (*yellow arrow*) and subcarinal lymph nodes demonstrating mild FDG activity, representing old granulomatous disease.

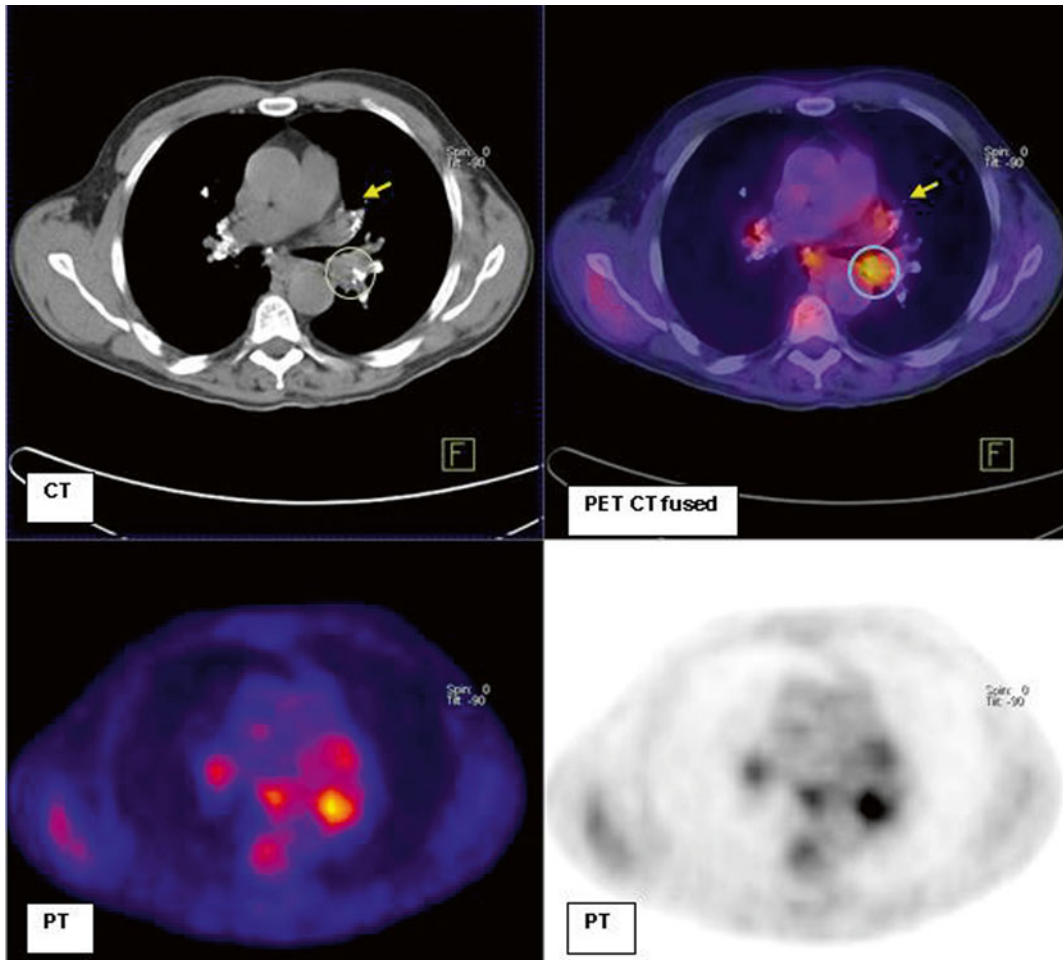

Fig. 16.9

Impression

Metastatic left hilar lymph nodes with coexisting sequela of prior granulomatous disease.

Discussion

Granulomatous disease and metastatic disease in the chest [2].

- Lymph node calcification (occasionally eggshell pattern) can be seen in up to 25 % of cases with prior granulomatous disease, usually in long-standing disease.
- In addition to lung cancer, malignancies that may metastasize to thoracic lymph nodes include breast, melanoma, head and neck, genitourinary, and gastrointestinal carcinomas including esophageal carcinoma and melanoma.
- Metastatic lymph node involvement is usually asymmetric (as opposed to granulomatous disease) (Fig. 16.9).

Case 16.8: Mycobacterium Avium Complex

History

65-year-old female with history of bronchiectasis.

Findings

Increased linear and focal hypermetabolic activity in the right upper lobe on PET (Fig. 16.10, *black arrow*). Increased hypermetabolism in the lingula (*red arrow*). Both PET findings correspond to clusters of pulmonary nodules seen in a background of bronchiectatic changes in the lung parenchyma on CT.

Impression

Non-immunocompromised mycobacterium avium complex (MAC).

Pearls and Pitfalls

FDG-PET/CT is considered as a useful diagnostic tool to assess the exact extent and activity of disseminated MAC infection [3]. Moreover, PET/CT is advantageous over CT and magnetic resonance imaging to assess the treatment response and time course of the disease.

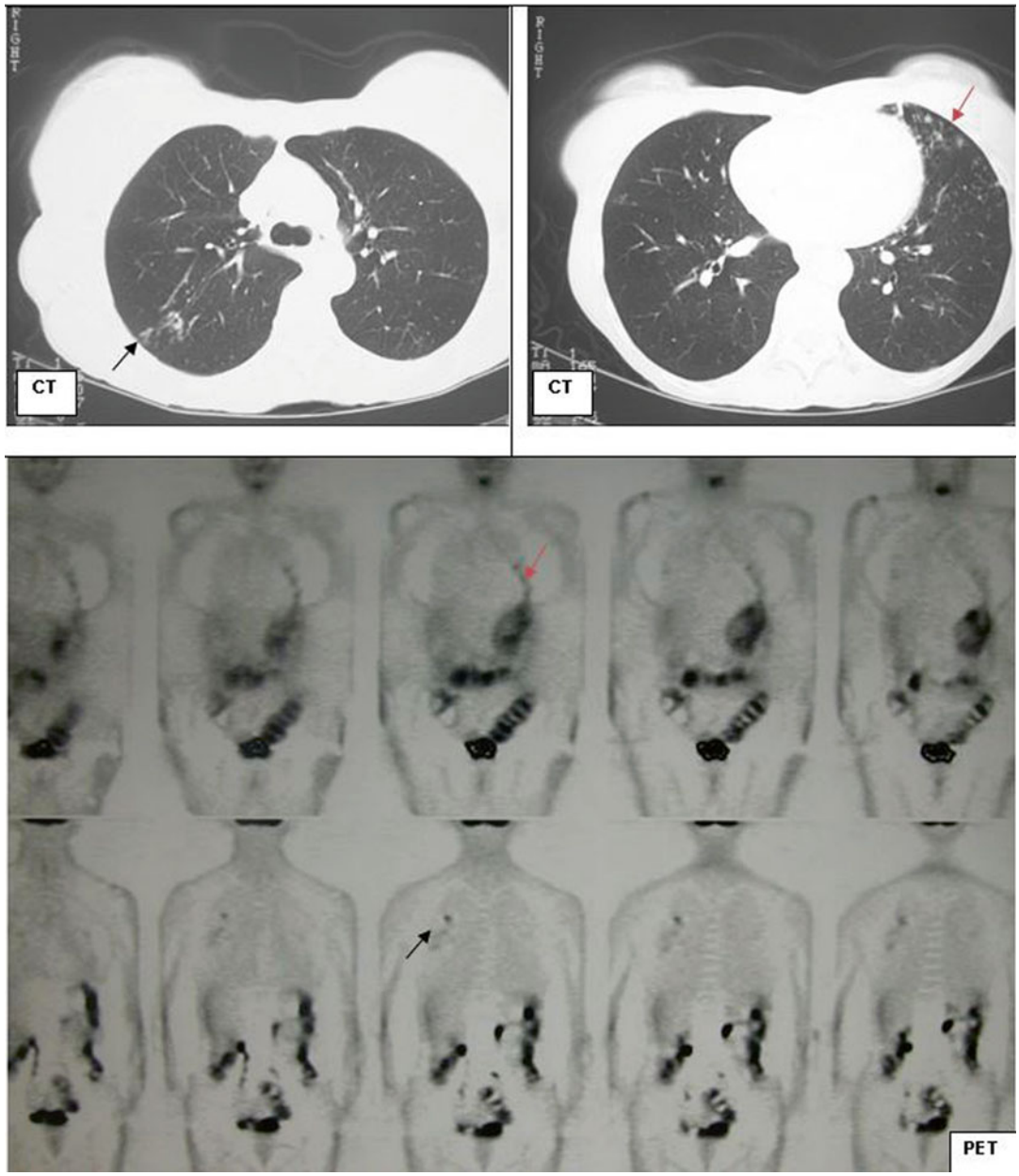

Fig. 16.10

Discussion

- Older women, 60s–70s.
- 80 % have bronchiectasis.
- Clustered nodules occur in areas of regional bronchiectasis.
- May be asymptomatic.
- Symptomatic cases (cough, constitutional symptoms) more likely demonstrate lymph nodes which are 18F-FDG avid (Fig. 16.10).

Case 16.9

History

45-year-old male with history of Hodgkin's disease, in remission since many years, presents with new right upper lobe (RUL) lung nodule. Biopsy of pulmonary nodule revealed fungal infection.

Findings

New pulmonary nodule in RUL, hypermetabolic on PET, SUV max 3.0 (Fig. 16.11, *images on left*). Resolution of pulmonary nodule, 3 months following antifungal therapy (Fig. 16.11, *images on right*).

Impression

Pretherapy images: hypermetabolic RUL pulmonary nodule, worrisome for neoplastic process. Post-antifungal therapy scan: interval response to antifungal therapy with resolution of RUL pulmonary nodule.

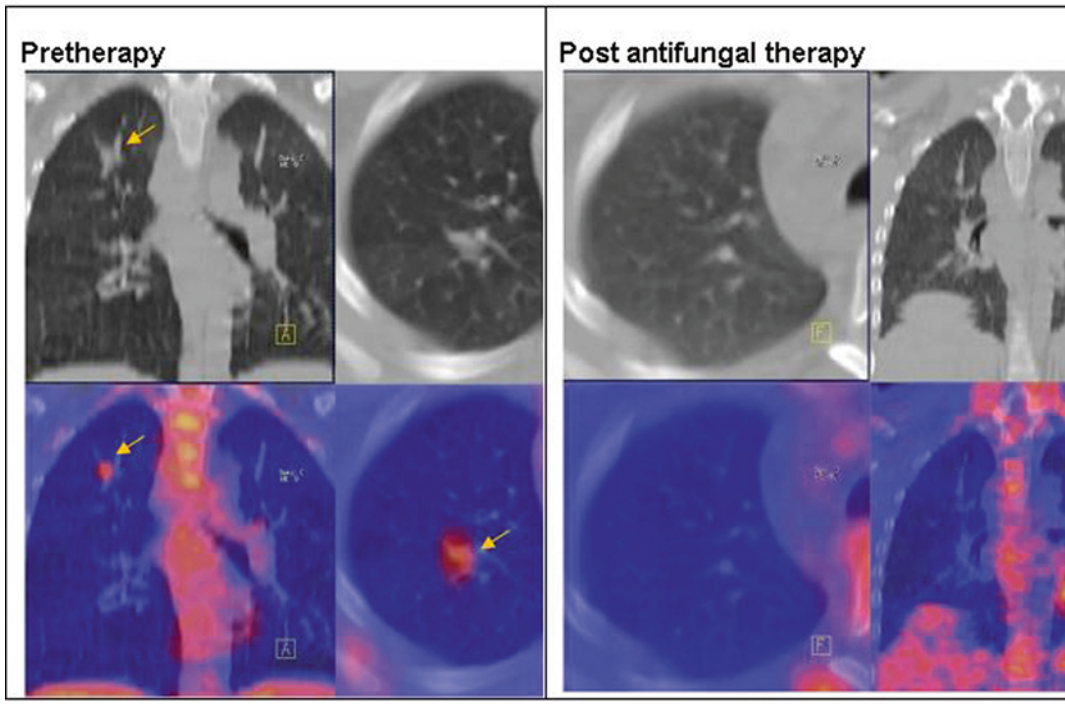

Fig. 16.11

Pearls and Pitfalls

Fungal infection can be a cause for false positive on PET.

Discussion

- Infectious and inflammatory processes aggregate metabolically active macrophages, which also have increased demand for glucose, causing false-positive results on FDG-PET [4] (Fig. 16.11).

Case 16.10

History

65-year-old female, status post left ventricular aneurysm repair with patch in 2009. PET/CT images provided below were obtained in 2012.

Findings

Status post left ventricular aneurysm patch repair demonstrating intense FDG accumulation on PET images (Fig. 16.12, *yellow arrow*), secondary to foreign body reaction.

Impression

Foreign body reaction in a left ventricular aneurysm repair patch.

Pearls and Pitfalls

FDG uptake secondary to inflammation/infection is the most common false-positive finding on PET/CT. Differentiation between low-grade infection within a prosthetic graft and foreign body reaction remains difficult.

Discussion

It is likely that a large portion of patients with synthetic vascular grafts will display high 18F-FDG accumulation in the graft material on PET/CT, even after a long time following surgery and without a graft infection [5]. The basis for this 18F-FDG accumulation may be due to chronic inflammation known to occur on the surface of synthetic graft material. Although not statistically significant, the 18F-FDG accumulation appears

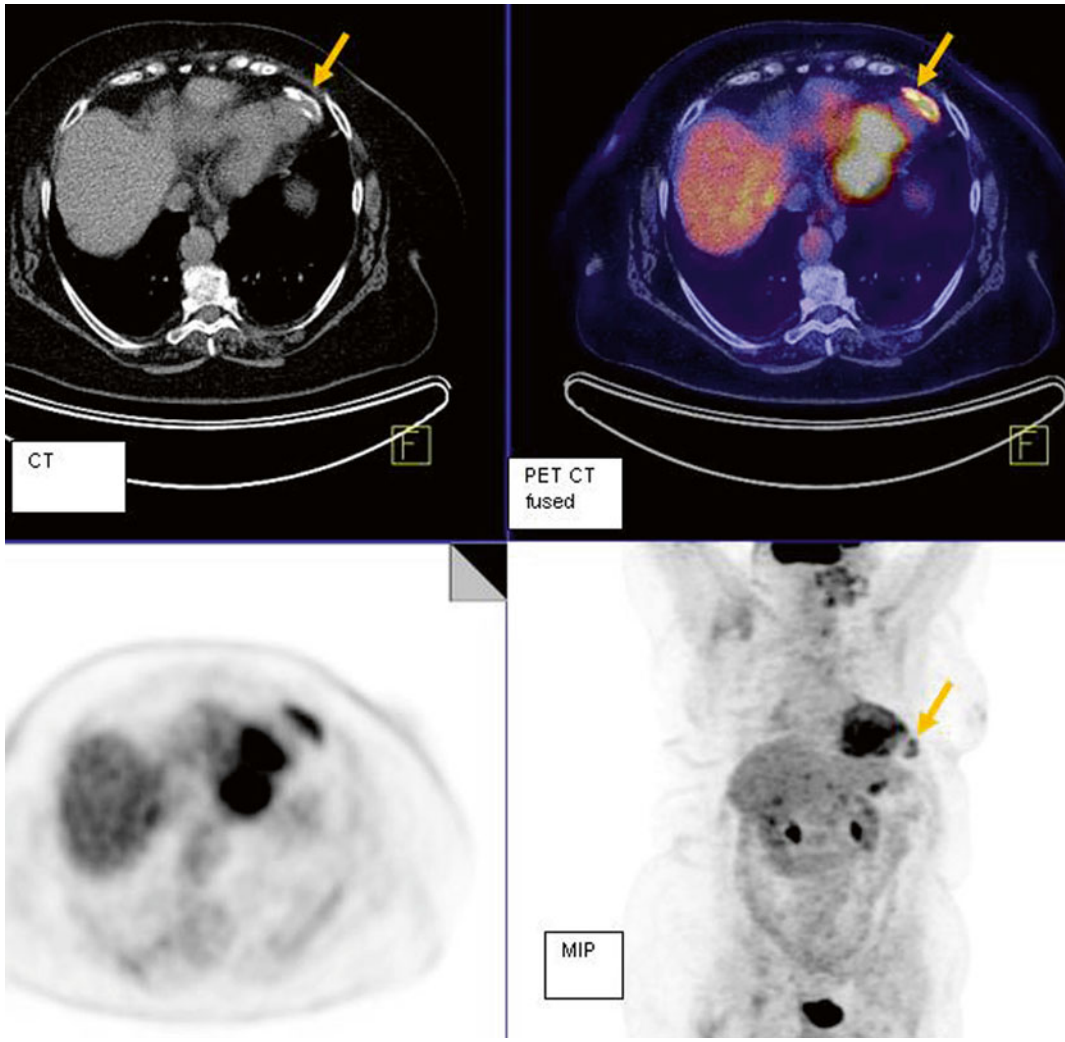

Fig. 16.12

to be less prominent in endovascular grafts than in conventional grafts (Fig. 16.12).

Case 16.11 History

42-year-old female, status post soft tissue augmentation with Juvederm injections, 2 weeks post procedure.

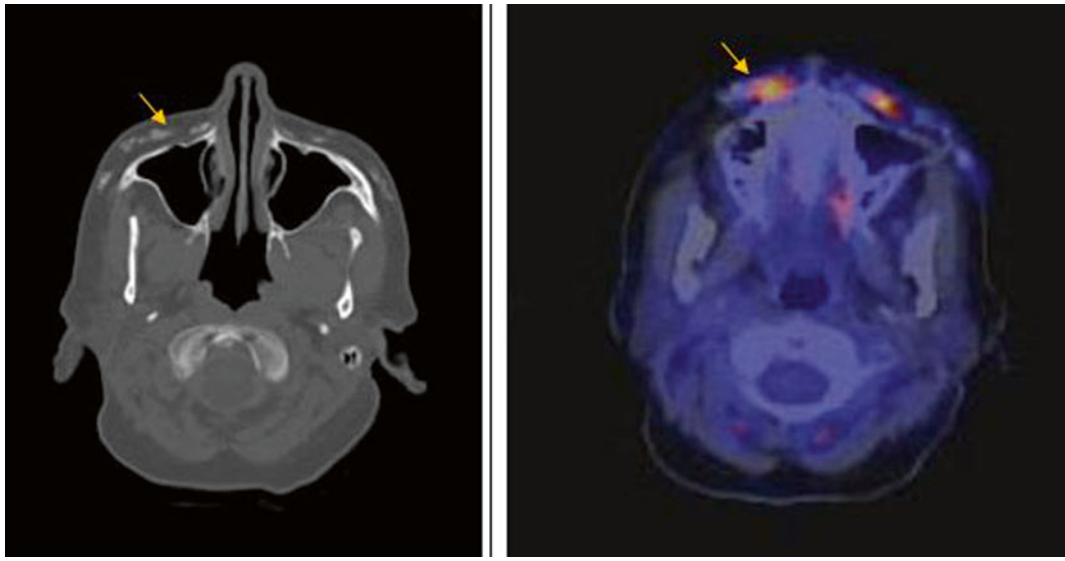

Fig. 16.13

Findings

Subcutaneous hyperdense material in bilateral malar regions on CT with corresponding linear hypermetabolism, consistent with known history of cosmetic injections in the cheeks, 2 weeks post procedure (Fig. 16.13).

Impression

Foreign body reaction in bilateral malar regions secondary to hyaluronic acid gel (soft tissue filler) injection.

Pearls and Pitfalls

Foreign body reaction is a potential source for false-positive results. Clinical history and correlation of PET with CT findings is crucial in making the diagnosis of foreign body reaction scan pattern, which can vary in intensity and persist for many years following surgery/procedure.

Discussion

- Hyaluronic acid gel is also called Hydrafill. Approved by FDA in June 2006 for correction of moderate to severe facial wrinkles and folds.
- Derived from *Streptococcus equi* and manufactured by a bacterial fermentation process [6] (Fig. 16.13).

References

1. Cherk MH, et al. ^{18}F-fluorodeoxyglucose positron emission tomography-positive sarcoidosis after chemo radiotherapy for Hodgkin's disease: a case report. J Med Case Rep. 2011;5:247. doi:10.1186/1752-1947-5-247.
2. Suwatanapongched T, et al. CT of thoracic lymph nodes. Part II: diseases and pitfalls. Br J Radiol. 2006;79:999–1006. doi:10.1259/bjr/82484604.
3. Sato M, et al. Usefulness of F-18 FDG PET/CT in the assessment of disseminated Mycobacterium avium complex infection. Ann Nucl Med. 2009;23(8):757–62. Epub 2009 Sep 29.
4. Workman RB, Coleman RE. PET in lung cancer. In: Workman RB, Coleman RE, editors. PET/CT: essentials for clinical practice. New York: Springer; 2006. p. 50.
5. Wasselius J, et al. High ^{18}F-FDG uptake in synthetic aortic vascular grafts on PET/CT in symptomatic and asymptomatic patients. J Nucl Med. 2008;49:1601–5. doi:10.2967/jnumed.108.053462.
6. Allemann IB, et al. Hyaluronic acid gel (Juvéderm™) preparations in the treatment of facial wrinkles and folds. Clin Interv Aging. 2008;3(4):629–34.

17 Newer Tracers

Aarti Kaushik and Peter S. Conti

18F-AV-45 and 18F-FDG

Case 17.1 Findings

The 18F-FDG PET brain images (Fig. 17.1, top) demonstrate normal tracer distribution in the gray matter and in the bottom 18F-AV-45 PET images demonstrate normal white matter uptake (Fig. 17.1).

Case 17.2 Findings

The 18F-FDG brain PET images of the brain (Fig. 17.2, top) demonstrate bilateral temporal hypometabolism consistent with dementia of Alzheimer's type by pattern and the 18F-AV-45 PET images of brain (Fig. 17.2, bottom) demonstrate diffuse uptake in the brain with loss of gray and white matter demarcation unlike in case 1 (Fig. 17.2).

64Cu-ATSM (64Cu-ATSM: Copper (II)-Diacetyl-Bis(N4-Methylthiosemicarbazone) and 18F-FDG)

Case 17.3 Findings

18F-FDG PET/CT images (Fig. 17.3, left) demonstrate mild to intense uptake in cervical mass with uptake in bladder above it. 64Cu-ATSM PET/CT images (Fig. 17.3, right) show peripheral rim of uptake in one

P.S. Conti, A. Kaushik (eds.), *PET-CT*, DOI 10.1007/978-1-4419-5811-2_17

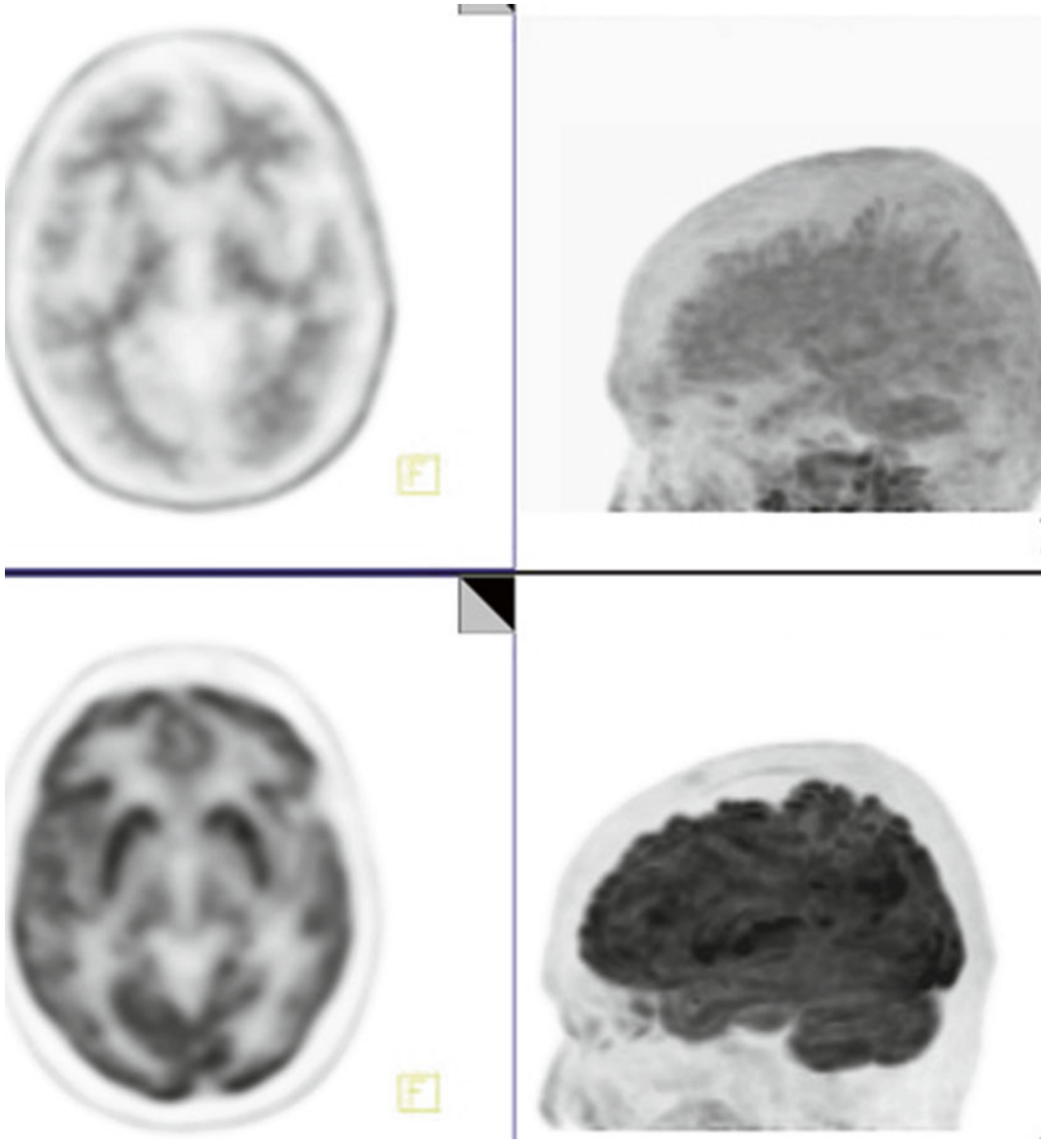

Fig. 17.1

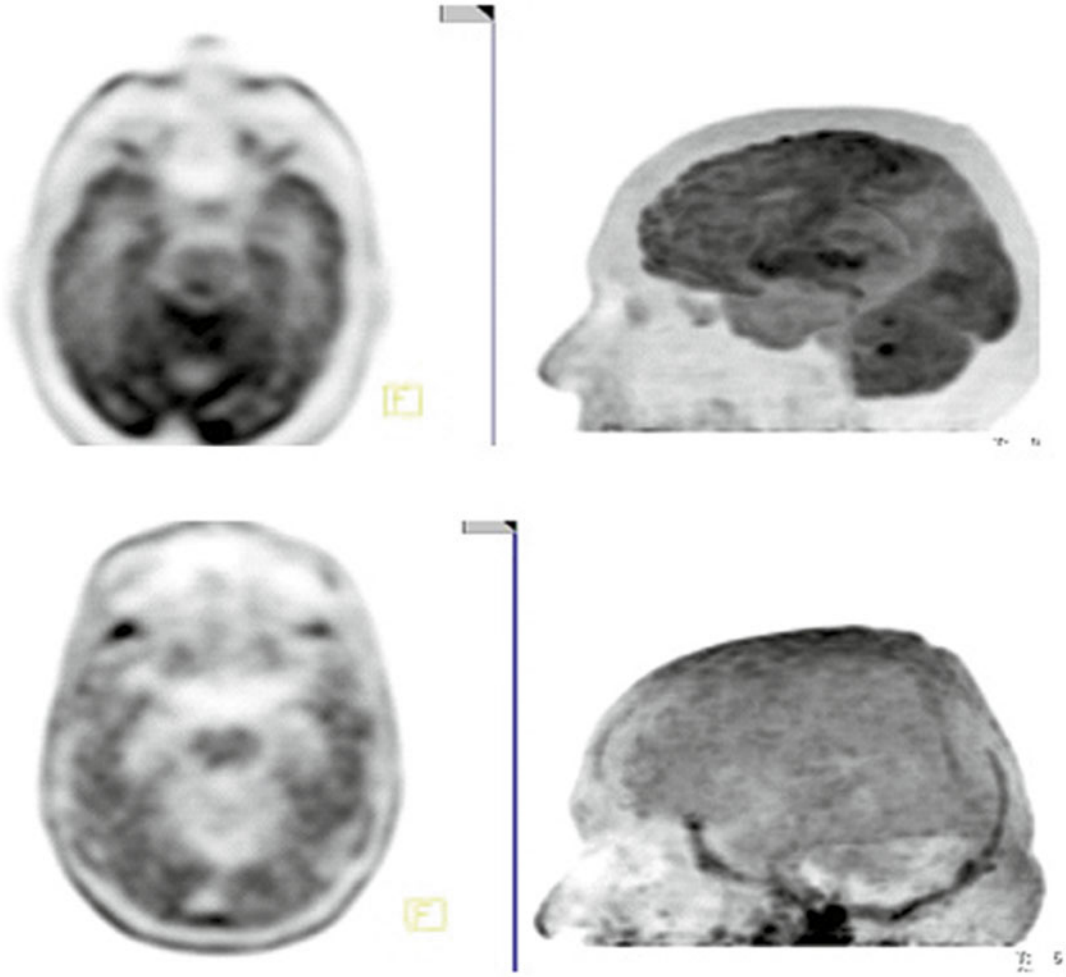

Fig. 17.2

region of tumor and intense uptake in the other (Fig. 17.3, bottom). The 64Cu-ATSM is retained in hypoxic tissues, but rapidly washes out of normoxic tissues (Fig. 17.3).

18F-MISO (18F-Fluoromisonidazole)

Case 17.4 Findings

Images of 18F-MISO PET/CT scan of the brain show focal uptake in the right parietal region (Fig. 17.4). [^{18}F]MISO is the prototype hypoxia imaging agent. Uptake is homogeneous in most normal tissues, reflecting

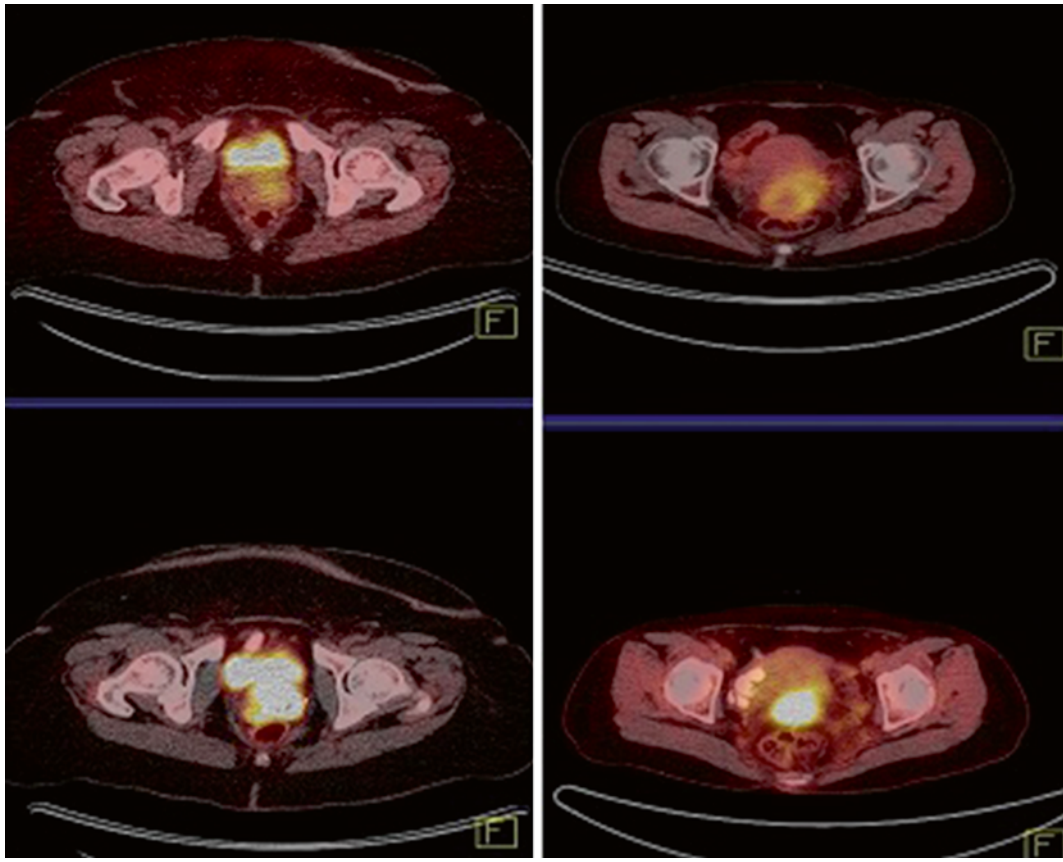

Fig. 17.3

its high partition coefficient (near unity), and delivery to tumor's is not limited by perfusion. [18F]MISO binds to large molecules in tumor cells that have a low level of oxygen and therefore hypoxic and resistant to treatment (Fig. 17.4).

F-18 FLT

Case 17.5

Findings

18F-FLT PET/CT images show physiologic uptake in bone marrow, but there is pathologic uptake in right breast mass (Fig. 17.5).

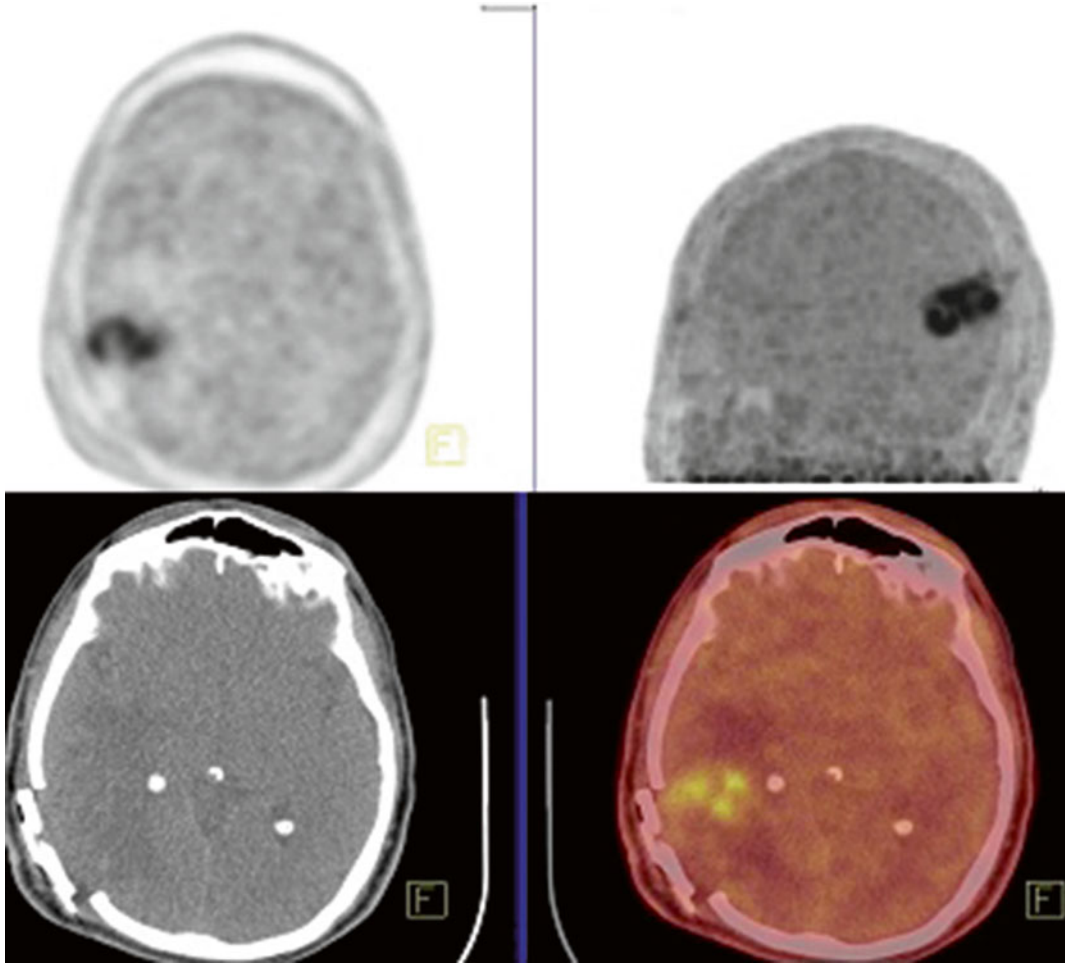

Fig. 17.4

Case 17.6

Findings

The 18F-FLT PET/CT images show thymic uptake before (Fig. 17.6, left) and is decreased after chemotherapy (Fig. 17.6, right). There is physiologic uptake in the marrow and pathologic uptake in the right breast mass (Fig. 17.6).

Case 17.7

Findings

18F-FLT PET/CT images of patient with melanoma with uptake in the left lung metastasis as well in the primary lesion in the right mid arm, medially (Fig. 17.7). There is physiologic uptake in the bone marrow (Fig. 17.7).

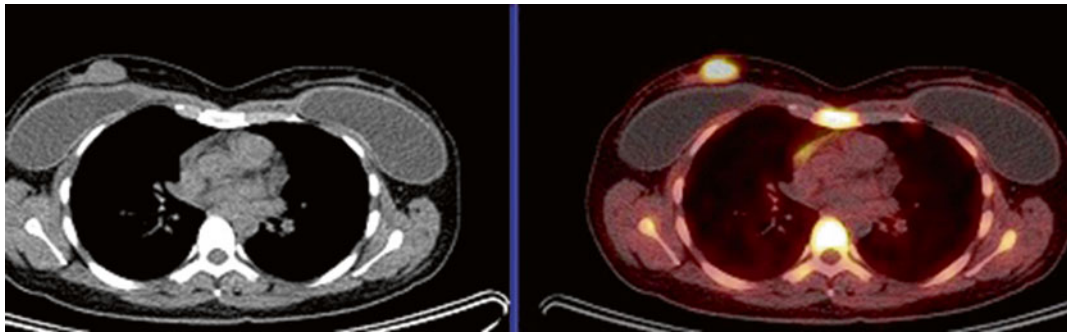

Fig. 17.5

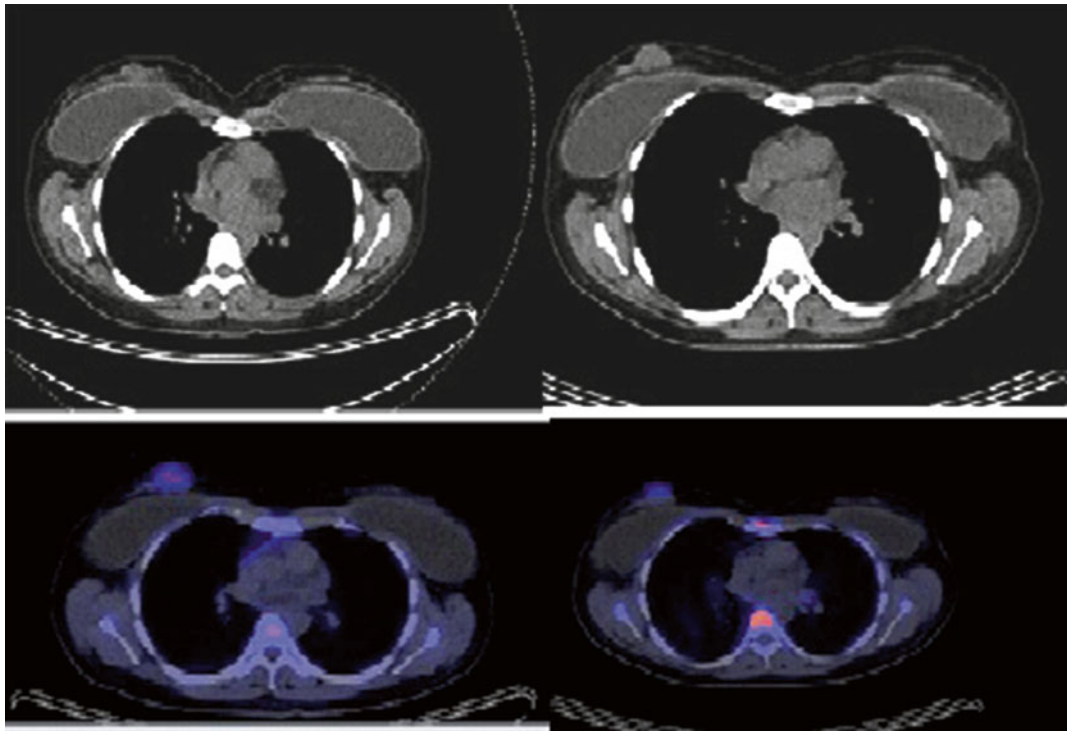

Fig. 17.6

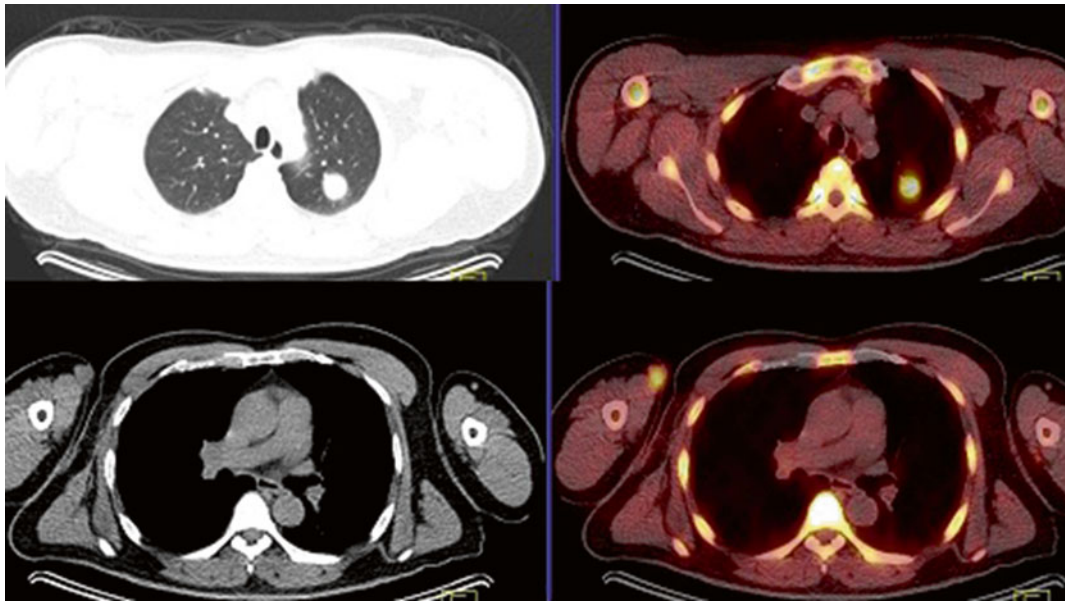

Fig. 17.7

Case 17.8

Findings

18F-FLT PET/CT images of a patient with transitional cell carcinoma of the bladder with metastases to the lungs (Fig. 17.8).

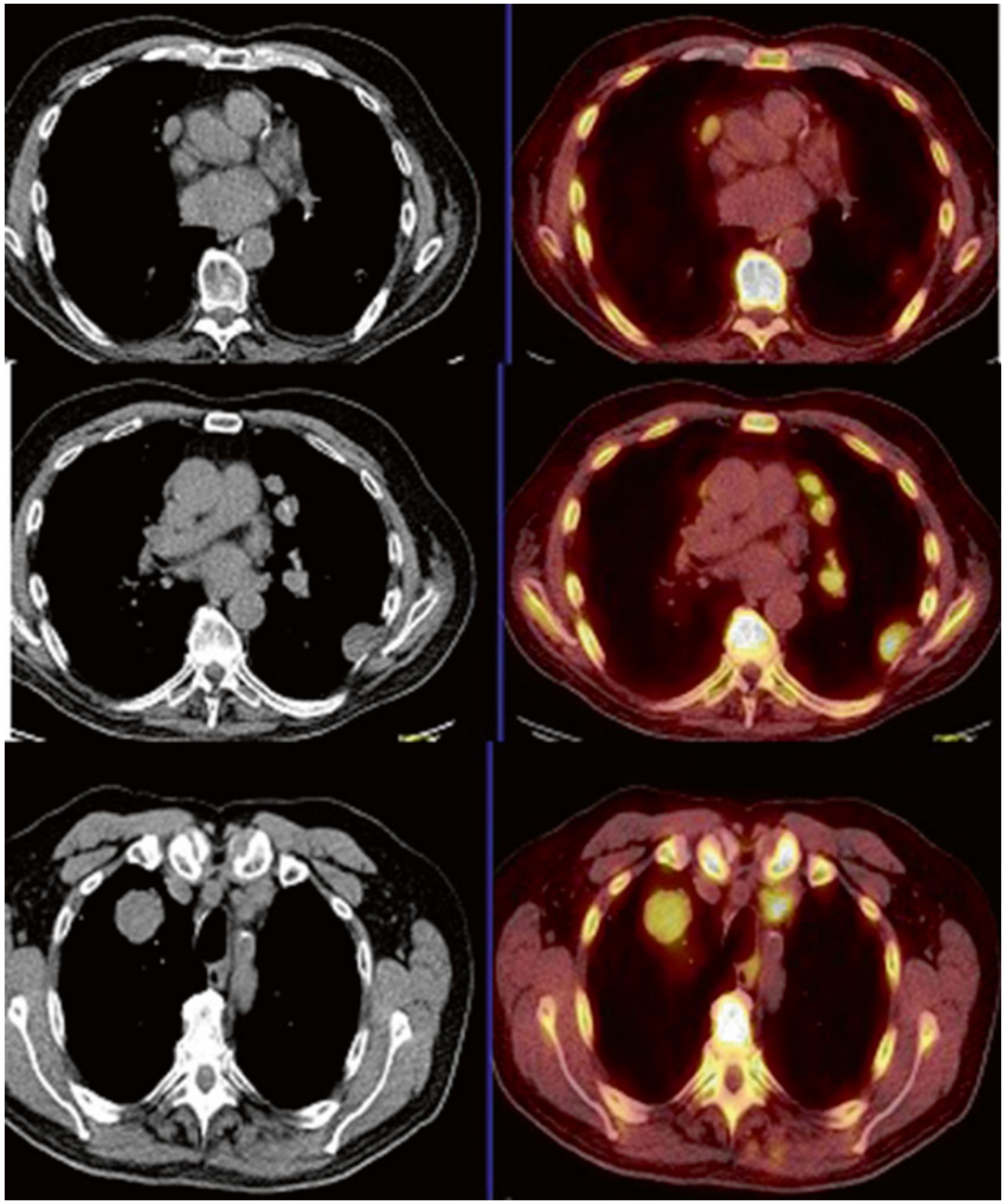

Fig. 17.8

Index

P.S. Conti, A. Kaushik (eds.), *PET-CT*, DOI 10.1007/978-1-4419-5811-2